PNC TN4600 88-005(2)

# 海外加速器調査報告書

## —資料編—

昭和63年11月

動力炉・核燃料開発事業団

動力炉・核燃料開発事業団（Power Reactor and Nuclear Fuel Development Corporation）

# 資　料　編　目　次

# 資料４－１

# 長寿命放射性廃棄物の消滅処理法

# 長寿命放射性廃棄物の消滅処理法

松　本　高　明*
植　松　邦　彦**

## 1. はじめに

消滅処理（nuclear incineration）法とは原子力のゴミ焼きの1種であるが，普通の化学的な焼却法とは違って，核転換または核種変換（nuclear tansmutation）法ともいわれるように，放射線による核反応を利用して，廃棄物中の長寿命放射性核種を短寿命または安定な核種に変換する方法である．消滅処理によって廃棄物の放射能は短期的には増大するが，長寿命の放射性核種が減少するために処分時の問題を軽減することができる．いわゆる“放射線を制するに放射線を以ってする”類である．

消滅処理に使用する放射線としては，原子炉，核融合炉及び加速器により発生する中性子線がよく研究されている．また加速器による陽子線およびガンマ線の使用も最近研究されている．1973年に原子力産業会議によって消滅処理法の研究のレビューが出されている[1]．その後世界各国で精力的な研究が行なわれてきた．本文では主に最近の研究に焦点を当てて，原子炉，核融合炉および加速器のそれぞれについて消滅処理の研究を紹介する．

## 2. 消滅処理対象の長寿命放射性核種

使用済燃料の再処理工場において発生する高レベル放射性廃棄物（HLW）の中には，（i）未回収の燃料アクチニド（Uおよび Pu），（ii）原子炉内で核転換により生成した廃棄アクチニド（Np，Am，Cm など）および（iii）核分裂生成物 F.P.（$^{137}$Cs，$^{90}$Sr など）の放射性核種が含まれている．図1に軽水炉燃料の HLW について，これら放射性核種による毒性(注) の時間変化を示す．30 年程度の冷却期間後に残る長期的な毒性はアクチニド，$^{90}$Sr，$^{137}$Cs，$^{129}$I および $^{99}$Tc によるものである．表1にこれらの核種の半減期などを示す．これらの長寿命放射性核種が消滅処理の対象となる．ことに廃棄アクチニドはα線の放出体で毒性が強く，超長寿命であるため，消滅処理を試みる動機が強い．

将来，わが国も含めた世界において相当量の廃棄アクチニドが累積することが予想されている．米国では 1988 年から 2010 年の間に約 770トン[2]の廃棄アクチニドが原子力発電により生成す

(注) 毒性の定義は次式で与えられる；

$$\phi=\sum_i \phi_i=\sum_i Q_i/MPC_i$$

$Q_i$：$i$ 核種の量
$MPC_i$：$i$ 核種の最大許容濃度

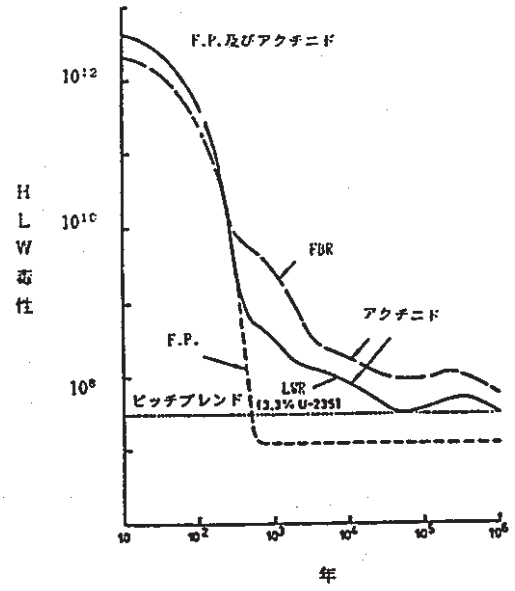


図1　HLW 毒性の時間変化

* *Takaaki MATSUMOTO*：北海道大学工学部 原子力工学科 助教授
** *Kunihiko UEMATSU*：動力炉・核燃料開発事業団 理事

表 1　代表的な長寿命放射性核種

| | | 半減期 (年) | 生成量 (kg/100万kWe.年) | 熱中性子断面積 ($b$) |
|---|---|---|---|---|
| 廃棄アクチニド | $^{237}$Np | $2.1\times10^{6}$ | 16.6 | 370 |
| | $^{241}$Am | 433 | 1.2 | 33 |
| | $^{243}$Am | 7,370 | 2.8 | 70 |
| | $^{244}$Cm | 17.9 | 0.63 | 20 |
| F.P. | $^{90}$Sr | 28.1 | 18.1 | 0.9 |
| | $^{137}$Cs | 30.1 | 41.4 | 0.11 |
| | $^{129}$I | $1.6\times10^{7}$ | — | 17.0 |
| | $^{99}$Tc | $2.1\times10^{5}$ | 28.3 | 19.0 |

ることが見込まれている．また OECD 加盟国全体で 2000 年には約 80 トン[3]，わが国では約 24 トン累積する[4]．これら多量の廃棄アクチニドは処分するばかりでなく，積極的な有効利用を考える必要がある．

## 3.　消滅処理法の原理

一般に物質を放射線で照射した場合，物質はガンマ粒子放出，荷電粒子放出，核分裂などの種々の核反応を起こして異なった核に転換する．新たに生成した核は一般に不安定で，放射性崩壊を起こしてさらに別の核に転換する．これら一連の核転換過程において，核種の生成・消滅の量は次の方程式で求めることができる．

$$\frac{dx_i}{dt}=\sum_{j=1}^{N} l_{ij}\lambda_j x_j + \phi\sum_{j=1}^{N} f_{ij}\sigma_j x_j-(\lambda_i+\phi\sigma_i)x_i+s_i \quad (1)$$

$$i=1,2,\cdots,N$$

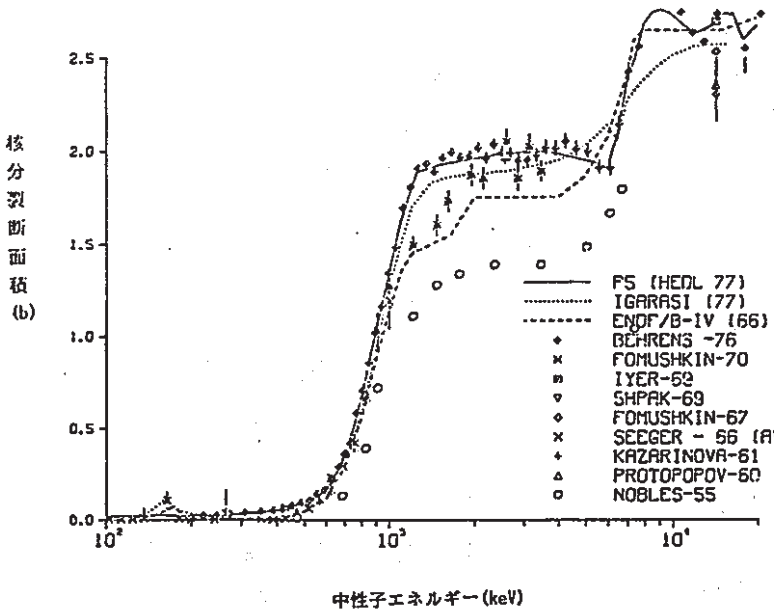


図 2　$^{241}$Am の核分裂断面積

ここに

$x_i$：核種 $i$ の原子数密度

$\lambda_i$：核種 $i$ の崩壊定数

$l_{ij}$：核種 $j$ の放射性崩壊により核種 $i$ が生成する割合

$f_{ij}$：核種 $j$ の核反応により核種 $i$ が生成する割合

$\phi$：空間とエネルギーで平均した放射線束

$s_i$：核種 $i$ の系への入出率

$N$：考慮している核種の数

式（1）の右辺第1項および第2項はそれぞれ放射性崩壊および核反応によって核種 $i$ が生成する総和である．また第3項は核種 $i$ が放射性崩壊と核反応によって消滅する割合である．

消滅効果の定量的な計算は式(1)を解くことであるが，その前に放射線の輸送計算を行なって放射線束 $\phi(r,E)$ を求め，$\sigma_i(E)$ の平均化を行ない一群の $\sigma,\phi$ を計算する必要がある．中性子線を利用する場合，輸送計算は $S_N$ 法など炉物理計算でお馴染みのコードが用いられる．また消滅計算ではアクチニドの場合，燃焼計算コード ORIGEN[5] がそのまま使用できるのでよく用いられる．

廃棄アクチニドの場合，中性子の核分裂及び吸収断面積が大きいので，消滅処理には中性子線の利用がよく研究されている．ただし中性子吸収では廃棄アクチニドより生成した核種は同じくアクチニドであるので照射の効果が軽減する．むしろ中性子による核分裂反応の方が，$\alpha$ 放出体のアクチニドから $\beta\cdot\gamma$ 放出体の核分裂生成物に転換できるので毒性の減少が大きく有効である．

式（1）において核分裂反応の項を分けて書き，アクチニドの全核種について総和をとると，アクチニドの核種間に保存則が成立するので，

$$\frac{dx}{dt}=-\langle\phi\sigma_f\rangle x+s \quad (2)$$

ここに

$x$：全アクチニドの原子数密度

$s$：全アクチニドの系への入出率

$\langle\phi\sigma_f\rangle$：空間およびエネルギー平均した核分裂反応率

原子力工業

表 2　単一核種照射時の特性

| | 核分裂反応しきい値 (MeV) | $\alpha=\sigma_c/\sigma_f$ | | 核分裂の半減期 (年) | | 核転換の半減期 (年) | | 毒性の減少比 $f_\infty$* | | $\eta$ | |
|---|---|---|---|---|---|---|---|---|---|---|---|
| | | LWR | FBR | LWR | FBR | LWR | FBR | LWR | FBR | LWR | FBR |
| $^{237}$Np | 0.6 | 64 | 5.5 | 8.3 | 2.4 | 4.0 | 1.0 | 0.06 | 1.5 | 0.82 | 1.72 |
| $^{241}$Am | 0.8 | 92 | 4.7 | 6.9 | 2.6 | 0.48 | 1.3 | 30 | 655 | 0.93 | 1.71 |
| $^{243}$Am | 0.9 | 141 | 8.8 | 11.6 | 4.1 | 1.4 | 2.3 | 3.0 | 24 | 1.15 | 1.58 |
| $^{244}$Cm | 0.7 | 9.4 | 1.3 | 10.3 | 3.2 | 6.0 | 1.9 | 3.7 | 62 | 1.13 | 1.10 |

* $f_\infty=\phi$ 初期/$\phi$20 年照射　照射後 $10^3$ 年

定常状態 ($dx/dt=0$) では，アクチニドの平均寿命 $\langle l\rangle$ は次のようになる．

$$\langle l\rangle=x/s=1/\langle\phi\sigma_f\rangle \qquad (3)$$

式 (3) より $\langle l\rangle$ の小さい有効な中性子消滅処理を行なうには，$\langle\phi\sigma_f\rangle$ が大きくなければならない．図 2 に 1 例として $^{241}$Am の中性子核分裂断面積 $\sigma_f$ のエネルギー依存性を示す．一般に廃棄アクチニドは数百 keV 近辺に核分裂のしきい値を持つ場合が多いので，スペクトルの硬い中性子場が廃棄アクチニドの消滅処理に有利になる．また $\phi$ の大きい高中性子束場が有利なことはいうまでもない．

一方，$^{90}$Sr，$^{137}$Cs などの長寿命の F.P. については中性子吸収による核転換の方法が検討されている．この場合，熱中性子スペクトル場の方が有効である．しかし中性子吸収の断面積が余り大きくないために，陽子線による破砕反応やガンマ線による巨大共鳴反応を利用することも研究されている．

## 4.　原子炉による消滅処理

1972 年米国 Oak Ridge 国立研究所の Claiborne が軽水炉 (PWR) を用いた廃棄アクチニドの消滅処理を最初に検討した[6]．それ以来，原子炉による消滅処理法は数多く研究され，現在では原子炉による廃棄アクチニドの消滅法の可能性は理論的に確立されている．原子炉を用いる方法は次節以降で述べる他の方法に比べて，原子炉本体に特別な研究開発が必要でなく，現在の技術で充分に可能であるため最も有望視されている．

廃棄アクチニドを原子炉中で照射する場合，核種が転換する形式は原子炉燃料が燃焼する場合と同様である．図 3 に U-Pu サイクルの核転換形式を示す．Np，Am，Cm などの廃棄アクチニドは核分裂反応によってより短寿命の核分裂生成物に転換される．同時に中性子吸収及び放射性崩壊によって廃棄アクチニドの一部は U または Pu の燃料アクチニドに転換される．両者の過程の重要性は $\alpha$ 値 ($\alpha=\sigma_c/\sigma_f$) を見れば分る．表 2 に代表的な廃棄アクチニドの $\alpha$ 値を軽水炉と高速炉で比較してある．軽水炉の場合，一般に中性子吸収の割合が大きいので，廃棄アクチニドの燃料アクチニドへの核転換による減少効果が重要であることが分る．

実際の照射時には廃棄アクチニドは複数の核種の混合体の形で照射されるが，その前に単一の核種の照射特性を見てみよう．消滅の見通しを得る上で有効である．表 2 の第 4，5 欄には単一核種を照射した場合，核分裂反応による半減期を示してある．値はそれぞれ 20 年間照射した場合の平均値である．高速炉では 2 ～ 4 年の半減期であるが，軽水炉では約 3 倍長い．また表 2 の第 6，7 欄には核分裂反応の他に，(n, $\gamma$)，(n, 2 n)

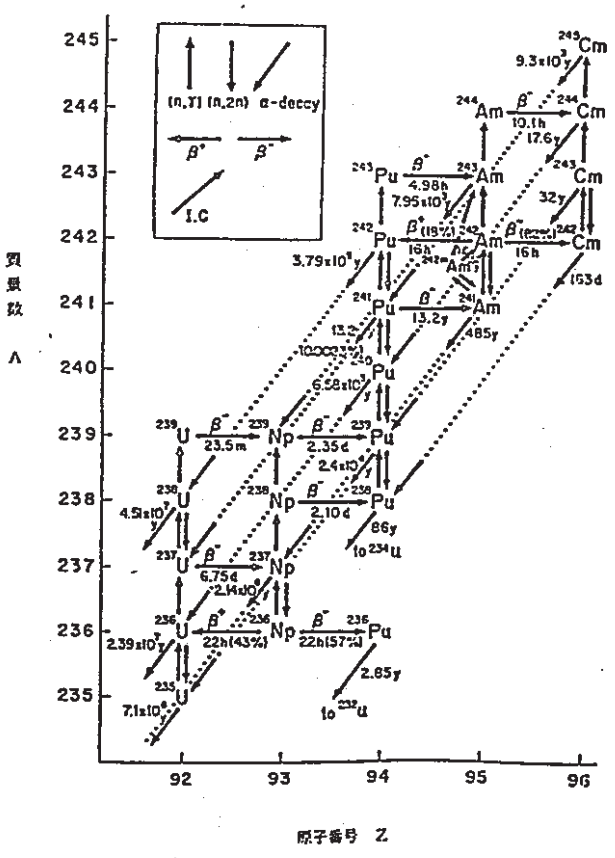


図 3　アクチニドの生成・消滅

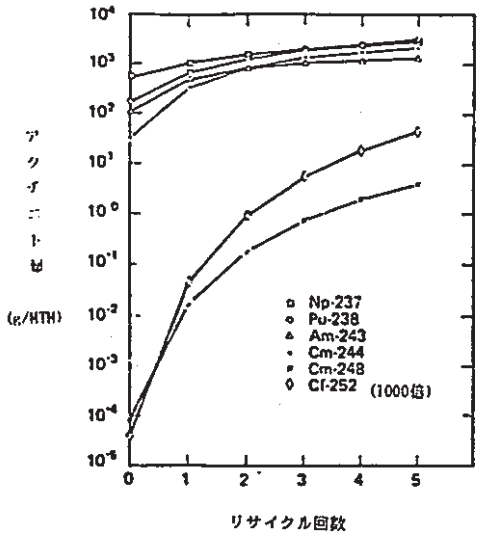


図 4　廃棄アクチニドの炉内蓄積

反応および放射性崩壊をも含めた場合の核転換の半減期を示す．高速炉では１～２年で，核分裂反応だけの場合に比べて約半分である．一方軽水炉の場合は核種によってバラツキが大きく，$^{241}$Am，$^{243}$Am，では高速炉よりも早く消滅することが分る．

表２の第８．９欄には 20 年間照射した場合，照射後 1,000 年後の毒性（水に対して）の減少比を示す．$^{237}$Np の場合，軽水炉照射では Pu の生成によってむしろ毒性が増大している．全般的には，高速炉の方が核分裂反応の割合が大きいために毒性の減少度が大きいといえる．

次に廃棄アクチニドの反応度への影響も原子炉運転上重要である．表２の第 10，11 欄には $\eta$ 値（中性子吸収に対する放出中性子数の比）を示す．軽水炉では $^{237}$Np および $^{241}$Am は負の，

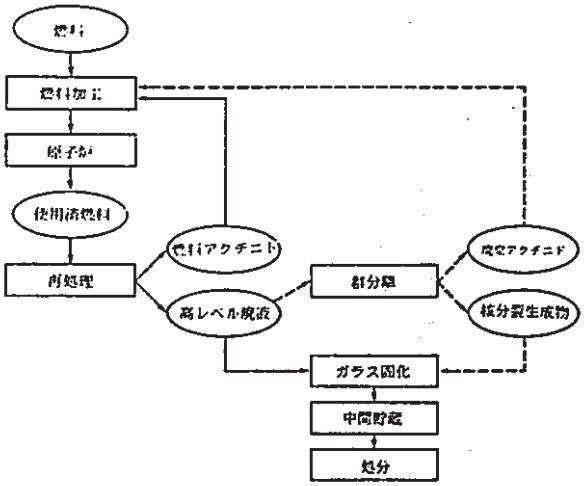


図 5　消滅処理時の燃料サイクル

表 3　1000日照射時の廃棄アクチニドの消滅（%）

| | | $^{237}$Np | $^{241}$Am | $^{243}$Am | $^{244}$Cm | $^{245}$Cm |
|---|---|---|---|---|---|---|
| LWR ($3\times10^{13}$ n/cm$^2$·s) | 核転換 | 60 | 82 | 18 | 38 | 84 |
| | 核分裂 | 14 | 22 | 14 | 32 | 84 |
| FBR ($1\times10^{16}$ n/cm$^2$·s) | 核転換 | 62 | 63 | 24 | 46 | 81 |
| | 核分裂 | 40 | 41 | 22 | 40 | 81 |

$^{243}$Am および $^{244}$Cm は正の反応度効果を持たらす．量的には前者の方が大きいので，リサイクリング毎に燃料を追加する必要がある．一方高速炉の場合は，全て正の反応度効果を持つので燃料の節約になる．

廃棄アクチニドの混合体の照射に話をもどそう．原子炉による廃棄アクチニドの消滅の理論的研究は多く行なわれている．熱中性子炉は大部分軽水炉を対象にしている．また高速炉による消滅の研究もかなり多い．消滅の特性は，使用済燃料の種類・燃焼度，再処理方法，照射方法（均質照射かターゲット照射），照射期間，中性子束，燃料交換方式などによって異なる．したがって各研究結果の相互比較は困難である．

表３に軽水炉と高速炉の代表的な場合についての消滅特性を示す．廃棄アクチニドを 1,000 日間照射した場合の核転換と核分裂の割合を示す．表より核転換および核分裂の割合はかなり小さいことが分る．また高速炉の優位性は考えられていた程大きくない．廃棄アクチニド全体で見ると約２～３年の半減期であり，炉の負荷率，炉外時間および燃料中の中性子束減少などの種々の負の効果を考慮すると約２倍になるであろう．すなわち全廃棄アクチニドを 0.1% に減少させるには約 50年かかることになる．このことは廃棄アクチニドを何回もリサイクリングして照射する必要があることを意味する．

原子炉内照射の計算の例として図４に軽水炉にリサイクリングした場合の廃棄アクチニド量の変化を示す[7]．１回の照射は 33,000 MWD/MTM まで行ない，１年冷却後再照射する．反応度は BOC 時に $^{235}$U の量を調整して増倍係数 $k_\infty$=1.10 になるようにしている．Cm および Cf 以外の元素は早く平衡状態に到達するが，Cm および Cf は５サイクル時ではまだ平衡になっていない．５サイクルで約 50% の廃棄アクチニドが核分裂生成物に転換される．リサイクリングを繰

り返すことによって，炉内の廃棄アクチニドのインベントリーが増大して短期的な危険性が増す．これは従来 HLW に流れて行っていた廃棄アクチニドの長期的な危険性を減少するために支払わなければならない代償であるといえる．

消滅処理では廃棄アクチニドを繰り返しリサイクリングしなければならないため，従来の核燃料サイクルの変更が必要になる．図5に消滅処理を導入した場合の核燃料サイクルを示す．図中点線で示されている部分が消滅処理のために追加される流れである．すなわち，HLW から群分離によって廃棄アクチニドを回収し，燃料に加える工程である．

消滅処理のために必要な核燃料サイクルの変更は図5では小さいように見えるが，実際には大きな変更になる．これは廃棄アクチニドによる中性子と崩壊熱の放出が大きいため，燃料の加工・輸送・貯蔵・再処理などにおいて遠隔操作などの新たな設備投資が必要になるからである．しかし Pu リサイクリングの燃料サイクルでは遠隔操作が前提であるために，消滅処理の採用は余り大きなインパクトを与えない．

リサイクリングが多数回必要であるので，廃棄アクチニドの損失も重要な因子である．1回のリサイクリングによる廃棄アクチニドの損失をL，炉内での燃焼率をBとすると，$n$回リサイクリング時の損失は $L\{(1-B)(1-L)\}$ になる．したがってリサイクリングを多数回行なった際の廃棄アクチニドの全損失Tは次のようになる．

$$T=\frac{L}{1-(1-B)(1-L)} \qquad (4)$$

図6に全損失Tを示す．廃棄アクチニドの損失が多量になり，それらが回収されないで廃棄物の流れに混入すれば消滅処理の意味がなくなる．図より全損失を少なく抑えるには，炉内での高燃焼度照射およびサイクル内での低損失が必要である．

廃棄アクチニドの消滅処理が実際に導入されるためには，核的な可能性だけでなく種々の面からの検討が必要である．OECD[8]，ORNL[9] および IAEA[10] において消滅処理技術全般のアセスメントが実施されている．これらのアセスメントによると，（イ）原子炉による消滅法の核的な可能性は確立されている，（ロ）群分離技術の工業的規模の実現には多くの研究開発が必要である，（ハ）消滅処理によって逆に短期的な危険性が増大する，（ニ）長期的な危険性の減少は地層処分技術の進展と競合する，（ホ）消滅処理による核燃料サイクルコストの上昇は約 5% であるなどの点が指摘されている．（原子炉利用の消滅処理法の文献リストは文献9を参照）．

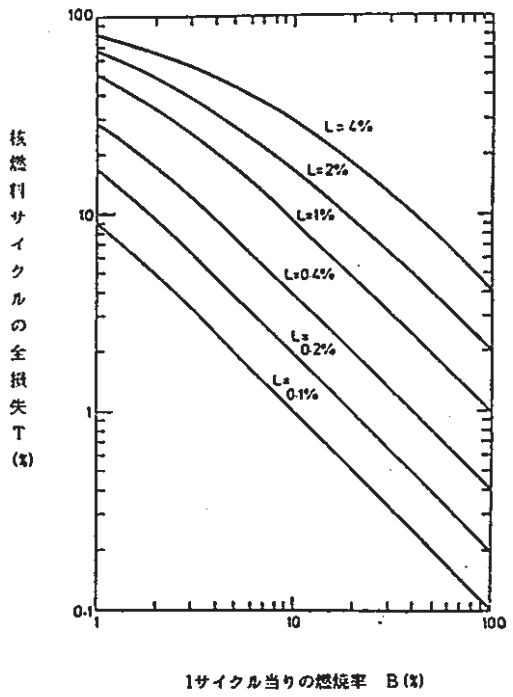


図6 廃棄アクチニドの全損失

## 5. 核融合炉による消滅法

D-T 反応による核融合炉は原子炉に比べて，高中性子束で高いエネルギースペクトル場が得られるため消滅炉として研究されている．トカマク炉[11)~13)]およびレーザー炉[14)~15)]の両方が検討されている．廃棄アクチニドは大部分の場合，ブランケット領域に装荷される．したがって核融合炉の場合でも原子炉の場合と同様に，廃棄アクチニドは HLW より群分離して燃料加工する必要がある．

トカマク炉を用いた廃棄アクチニドの消滅法は1973年米国 AEC によって研究が始められた[11]．その後，EPRI が引継いで詳細な検討を行なった[12]．EPRI によるトカマク炉を利用した消滅炉の配置を図7に示す．中性子の輸送計算は ANISN および DOT コードにより1次元及び2次元モデルで行なった．PWR，FBR および

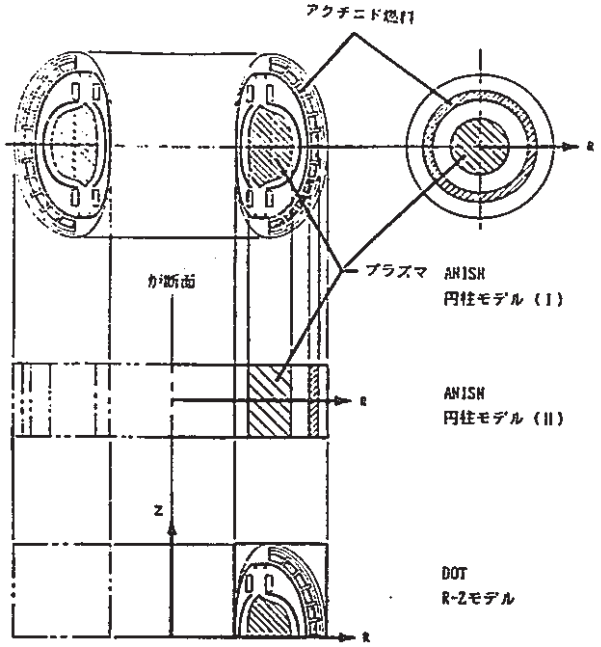


図 7　トカマク消滅炉

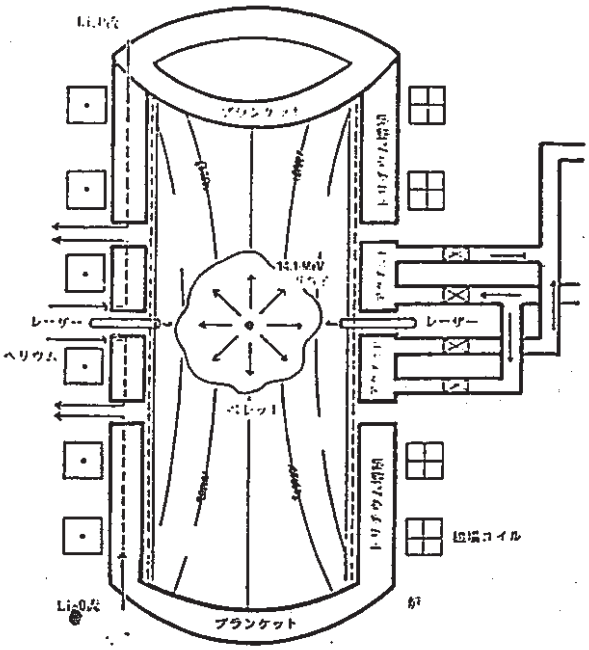


図 9　レーザー消滅炉概念図

PWR-Pu の使用済燃料から取出した廃棄アクチニドの消滅を比較している．ORIGEN コードによる計算結果の１例として，図８に PWR 燃料の場合の毒性の減衰を示す．ここではウラン鉱石の毒性を１としてある．パラメータとして第１炉壁の中性子負荷を変えている．約 $10^5$ 年における危険指数の一時的な増大は $^{226}Ra$ および $^{210}Pb$ による寄与である．結論として毒性を 100 分の１に減少させるためには，4～5 MW/m² の中性子負荷で 30 年，または 1 MW/m² で 50 年の照射が必要である．

一方，Duderstadt らは レーザー炉での廃棄アクチニドの消滅を検討している[14]．図９にレーザー消滅炉の概要を示す．燃料はアクチニド・錫の溶融合金で，核分裂生成物は連続処理されるものとしている．核融合炉のように外部中性子源を使用する場合には，ブランケット領域内で中性子束が急速に減衰する欠点がある．彼らはブランケットの実効増倍係数 keff を１に近く設計して減衰を小さくしている．XSDRNPM コードを用いて $S_N$ の中性子輸送計算を行ない，ORIGEN コードによって消滅計算を行なっている．図 10 に消

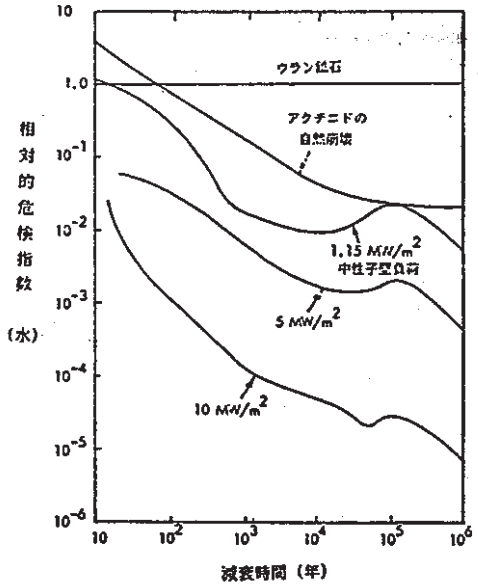


図 8　トカマク消滅炉の性能

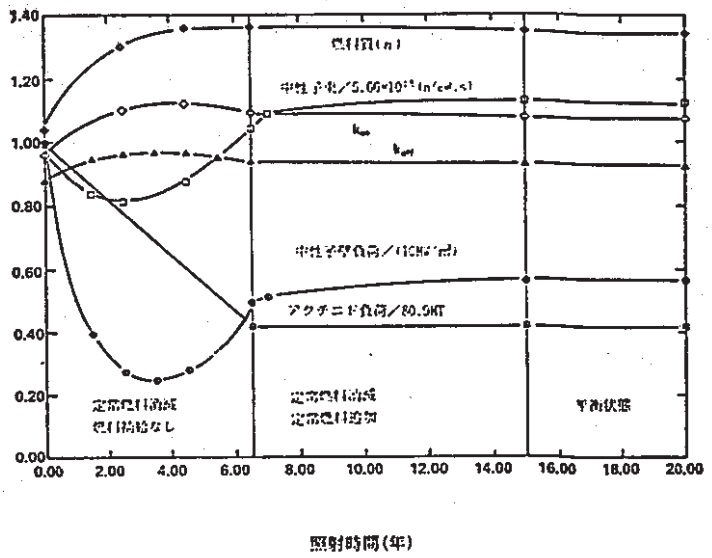


図 10　レーザー消滅炉の性能

原子力工業

滅炉の特性を示す．計算の結果，第1壁負荷 5.7 MW/m$^2$，中性子束 $6.4\times10^{15}$ n/cm$^2$·sec において7.6 MT/年の廃棄アクチニドの処理が可能になっている．この量は 100 万 kWe の軽水炉 135 基分の廃棄アクチニドに相当する．

核融合炉による消滅は原子炉に比べて，核的に有効な設計が可能であるが，炉本体に多くの研究開発が必要であることはいうまでもない．

## 6. 加速器による消滅法

最近加速器技術の進展が目覚しく，大電流の陽子または電子ビームの入手が可能になり工業的利用の途が開拓されつつある．その1つとして 1 GeV 程度の陽子ビームによる消滅処理法[16)~18)]が核燃料増殖法と併行して研究されている．またごく最近になって電子ビームによる高エネルギーガンマ線を利用した消滅処理法が提案されている[19)~20)]．加速器を用いる場合，加速に必要なエネルギーは何らかの方法で稼なわなければならない．

米国の Brookhaven 国立研究所では，高エネルギー陽子ビームにより廃棄アクチニドおよび F. P. を消滅させる計画が立案されている[16)]．図 11 に消滅炉内の熱中性子束分布を示す．中心に鉛ターゲットを置き，周囲を $^{137}$Cs および $^{90}$Sr 酸化物の水溶液及び黒鉛減速材で包っている．陽子エネルギー 1.5 GeV，ビーム電流 300 mA の場合，$^{137}$Cs および $^{90}$Sr の核転換率はそれぞれ自然崩壊率の 11.0 および 14.8 倍になり，陽子1個当り核転換される核の数は 20.8 および 10.1（核／陽子）である．また1年間の核転換量はそれぞれ 273 および 89 kg/年となる．一方，カナダの Harms らは陽子ビームと長寿命 F.P. との直接衝突による破砕反応を利用した消滅を検討している[17)]．この場合，廃棄アクチニドの場合と違ってエネルギー収支が困難になる．

筆者らは陽子ビームの破砕反応により発生する中性子による核分裂反応を利用した廃棄アクチニドの消滅炉を研究した[18)]．中心のターゲットには鉛を使用し，燃料領域は $^{237}$Np の酸化物と MgO 希釈材の混合である．冷却材として He と Na を比較している．$^{237}$Np による核分裂を充分に利用すれば，充分な消滅性能ばかりでなく，加速器に必要な電力以上の発電が可能になる．この場合，未臨界で運転のできる消滅兼発電炉である．

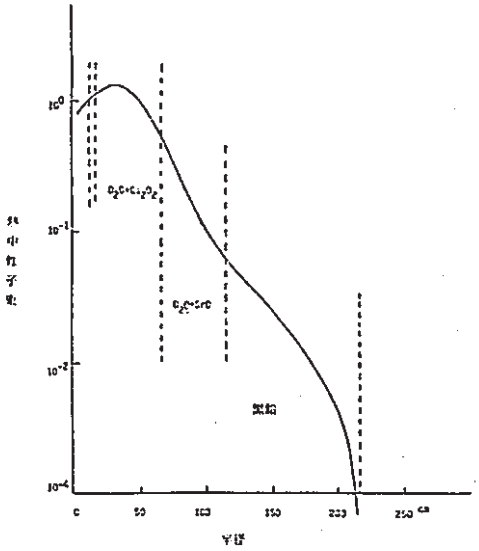

図 11 加速器消滅炉の熱中性子分布

ごく最近になって電子ビームによって発生する高エネルギーガンマ線を利用した消滅法が提案されている．この場合，$(\gamma, n)$ 反応または $(\gamma$，核分裂$)$ 反応の巨大共鳴を利用する．これらの反応断面積は比較的小さいが，大電流の電子ビームにより高ガンマ線束が得られる利点がある．廃棄アクチニドおよび F.P. の消滅処理ができる可能性がある．ことに廃棄アクチニド元素の $(\gamma, n)$ 反応および $(\gamma$，核分裂$)$ 反応の巨大共鳴のしきい値が約 10 MeV と低いため，ガンマ線スペクトルを調整すればガラス固化体中の廃棄アクチニドだけを選択的に消滅できる可能性がある．またこの方法は超ウラン元素 (TRU) 廃棄物中のアクチニド消滅にも利用できる[20)]．

## 7. ま と め

原子炉，核融合炉および加速器を用いた消滅処理法について概説した．消滅処理の効果が最も期待される廃棄アクチニドについては，中性子利用の方法が適している．理論的には消滅処理の可能性は確立している．ことに原子炉を用いた消滅処理法については，核的な側面の研究ばかりでなく，群分離，燃料加工，輸送，照射方法など具体的な検討がなされている段階である．消滅処理を導入するか否かの判断は，コスト／利益の考えに基づいて行なわれるが，HLW の長期的な危険性は地層処分技術の改良によっても減少されるので，こ

れら関連技術の総合的な評価の上になされることになる．消滅処理が実際に導入されるのは 21 世紀に入ってからになろうという意見が大勢である．この間，消滅処理を施されないガラス固化体が多量に発生するので，加速器による消滅処理法の研究開発も供せて行なうことが重要である．

現在，一般廃棄物または他の産業廃棄物が焼却処理されるのは当然のことのように考えられているが，これらの技術についても高々 50 年から 100 年の歴史を有するに過ぎない．ガラス固化体の地層処分が実施されれば，きわめて長期間にわたり放射性廃棄物を埋設することになる．この長い歴史の間にいずれ人類は科学技術の進歩によって何らかの処理方法を見い出すであろう．そういう意味で消滅処理は研究の緒についたばかりと言える．レーザーによる分離技術，種々の放射線源など未来技術を積極的に活用して，消滅処理法の活発な研究開発を行なうべきである．

幸い昭和 62 年度より消滅処理法の研究開発を行なうフェニックス計画がスタートする．計画は原子力先端技術の一つとして位置付けられており，産学官界の有機的な協力体制のもとに進められる予定である．多くの研究者が斬新なアイディアを積極的に提案して頂きたいと考える．

## 参考文献


1) 日本原子力産業会議：「核分裂生成物等総合対策懇談会報告書」(1973 年)
2) Blomeke, J. O. et al.: CONF-76701 (1976)
3) Schmidt, E.: EUR-5690 e (1977)
4) Uematsu, K.: 京都大学原子エネルギー研究所紀要 (1984)
5) Bell, M. J.: ORNL-4628 (1973)
6) Claiborne, H. C ORNL-TM-3964 (1972)
7) Gorrell, T. C.. DP-1496 (1978)
8) McKay, et al.: EUR-5801 (1977)
9) Wachter, J. W.: ORNL/TM-6983 (1980)
10) IAEA: 'Evaluation of Actinide Partitioning and Transmutation', Tech. Rep. 214 (1982)
11) Wolkenhauer, W. C. et al.: BNWL-1772 (1973)
12) Rose, R. R.: EPRI-ER-451 (1976)
13) Matsumoto, T. et al.: 北海道大学工学部研究報告 111号(1982)
14) Duderstadt J. J. et al・Nucl. Technol. 42, 34 (1979)
15) Parish, T. A. et al.: Nucl. Technol. 47, 324 (1980)
16) Takahashi, H. et al.: BNL-28779 (1980)
17) Harms, A. A. et al.: Nucl. Instr. Meth. 185 (1981)
18) Matsumoto, T. et al.: 動燃事業団研究成果報告書 PNC-SJ-168-85-02 (1985)
19) Konashi, K.: 公開特許公報，昭 59-48698 (1984)
20) Matsumoto, T. et al.: 動燃事業団研究成果報告書 PNC-SJ-5600-86-02 (1986)


## 図書紹介

経セミ増刊

### チェルノブイリ原発事故

定価 1600 円　日本評論社・刊

チェルノブイル原発事故は核の暴走という大事故で，世界の人々の原子力に対する信頼を揺がせた．本書は昨年行なわれたエントロピー学会のシンポジウムを中心に，座談会やインタビュー，さらにソ連が IAEA に提出した報告書を載せた“反原発読本”とでいうべきもの．

主な項目を列挙すると，チェルノブイリ事故と日本，私とチェルノブイリ，チェルノブイリ事故の全貌，チェルノブイリ事故の衝撃，最後に資料編として，ソ連原発事故報告書，という構成となっている．この中で久米氏は「反対派も含めて想定不適当であるとしてきました事故が，しかも実用の商業炉で，はじめて起ったということ．チェルノブイリ事故の意味はそれに尽きる……」．また小出氏は「日本だけは，自前の技術で原子炉を開発してこなかった非常に特異な国なのです（中略）．自分で独自の技術をも開発してこなかった国というのは，よけい恐しい気がします」などという指摘は注目すべきことと思われる．

### 原子炉危険性国際研究

—世界の原子力発電所の設計と運転上の特徴と原子炉事故の危険性—

頒価 300 円　原子力資料情報室刊

本書はグリーンピースの委託によって西ドイツ・ハノーバーの Gruppe Ökologie を中心に，7 カ国の研究者からなる国際パネルが組織され，世界各国で商業利用されている炉型およびその事故についての危険性を比較検討したものの一部分を小冊子化したものである．

ここでは PWR，BWR，RBMK，CANDU，マグノックス炉および AGR などの炉型をとりあげ，それぞれの炉の危険性を示そうしたものである．たとえば，PWR については蒸気発生器の弱点はもちろんに圧力容器もとりあげ，非常に多くの中性子にさらされ，“この圧力容器が高い応力下でどんな作用をするかは，充分知られていないし，予測できない”．とし，それなのに，圧力容器は絶対に破壊することはないとしている，と指摘．また BWR は PWR から派生したもので，設計の簡素化と熱効率の高度化をはかろうとしたものだが，“この改良の試みは少なくとも安全性の視点からすれば失敗であった”としている．

原子力工業

# 資料５－１

# Combined transmutation system of Nuclear wastes

# Combined transmutation system of nuclear wastes

K. Konashi

Power Reactor and Nuclear Fuel Development Corporation

## 1. INTRODUCTION

A large amount of high radioactive wastes has been produced and accumulated by operations of nuclear reactors. For the time being, one of the methods available for the permanent disposal of radioactive wastes is to solidify them into glass or cement in order to store in monitored places until the radioactivity of wastes decay and to despose them underground. The safety of high radioactive wastes containing long-lived radionuclides such as $^{137}Cs$ and $^{90}Sr$, however, must be assured for a long period, and it entails difficult problems of selection and maintenance of storage places as the volume of wastes incleases.

Thus, the disposal method of radioactive wastes by a transmutation of long-lived radionuclides into stable nuclides or short-lived radionuclides to reduce the level of radioactivity is very beneficial for the disposal of radioactive wastes. One potential method is to transmute radionuclides by nuclear reactions, and to reduce radioactivity in a short period.

## 2. CONCEPT OF COMBINED TRANSMUTATION SYSTEM

A number of devices have been proposed for the transmutation of nuclear wastes; fission reactor, fusion reactor and accelerators etc. The important question is whether the transmutation concepts would meet the following criteria to establish the alternative disposal method by transmutation.

(1) Risk reduction criterion : The overall risk of disposal method by transmutation must be reduced the over allrisk by comparison with the reference management scheme.

(2) Transmutation rate criterion : The transmutation rate of the nuclear wastes must be several times faster than the natural decay rate. To be a highly successful process, the effective half-life by the transmutation should be about several years.

(3) Energy balance criterion : The transmutation method must not consume more energy than was originally obtained when the waste was created.

The criterion (1) and (2) are fundamental requirements for the waste management strategy based on nuclear transmutation. The criterion (3) is valid only so long as fission power reactors contributing significantly to the energy economy. If fission power were no longer necessary, this criterion is no longer one of feasibility but of practicality.

There are two available devices in the present technology, i.e. fission reactors and accelerators. The transmutaions by these two devices are characterized as follows; Large quantities of radioactive nuclides can be transmuted in one fission reractor. The transmutation process also can generate energies and can easily meet the criterion (3). However its transmutation rate is slow because of low neutron flux.

In the case of the transmutation by accelerator, its advantage is in the fact that high transmutation rate can be obtained by focusing of accelerator beam. On the other hand, the transmutation method by accelerator also has disadvatage concerned with criteria (3), since the method consumes the large energy in transmutations. This is the reason why transmutation method by accelerators was ruled out as alternatives of nuclear wastes disposal.

As a practical way, combined system of accelerator and reactor was proposed in this paper. As seen in Fig.1, the combined system has two steps of transmutation process in order to meet both criteria (2) and (3). In the first step, a large quantity of nuclear waste is transmuted with slow transmutation rate in fission reactors. When the transmutation by fission reactors is finished, small quantity of nuclear waste is remained. In the second step, the remained nuclear wastes are transmuted by accelerators with a fast transmutation rate. In this combined system, the overall transmutation rate is between these of two steps.

Figure 2 shows an example of the transmutation of $^{137}Cs$ by the combined system. In the first stage, nuclear wastes are accumulated by the operation of nuclear power reactors. No transmutation device is operated in this stage. In the second stage, the operation of the transmutation reactors start. In this stage, quantities of nuclear waste reachs the constant value, which is determined by the equilibrium between the transmutation and the generation of radionuclides. In the third stage, the power reactors are stopped and total quantities of nuclear wastes decrease by the transmutation. As decrease of nuclear wastes, the transmutation reactors are stopped one by one. At the end of the third stage, all transmutation reactors are stopped and the quantities of nuclear wastes reach the minimum value which can be transmuted by the fission reactor. The last stage, the remained nuclear wastes are transmuted by accelerators with fast transmutation rate. In this example, the overall transmutation rate correspods to that of single step transmutation with the half-life of 5 years. The energy balance of total step is positive.

## 3. FISSION REACTOR AND ACCELERATOR FOR TRANSMUTATION

High flux reactor is neccesary for the transmutation. Taube proposed the fast reactor with inner thermal region. His concept is employed in the combined system.

Electron and proton accelerators have been proposed as the transmutation device. In this paper, the electron accelerator was selected, since the electron accelerators have large experiences

of industrial use compared with proton accelerators. The electron accelerator is used as a generator of photons by bremsstrahlung.

In this paper, photonuclear reaction was considered for the transmutation of nuclear wastes. It is well known that so called giant resonance are observed in nuclear absorption process of the photon with the energy of 10 - 20 MeV. That is ($\gamma$ ,n) reaction. The probability of ($\gamma$ ,n) reaction was calculated by EGS4 code to be 0.03 under the condition when an electron with the energy of 100MeV incidents in Cs target. In order to transmute Cs of 1 Kg in a year by photonuclear reaction, a electron beam with a current of 0.74A is necessary. This estimation shows that total current to transmute nuclear waste should be high and high current electron machine is required for practicality.

## 5.CONCLUSIONS

The combined system of accelerator and reactor was proposed for the transmutation of nuclear wastes. This system can meet both criteria of energy balance and transmutation rate.

Fig-1 COMBINED TRANSMUTATION SYSTEM

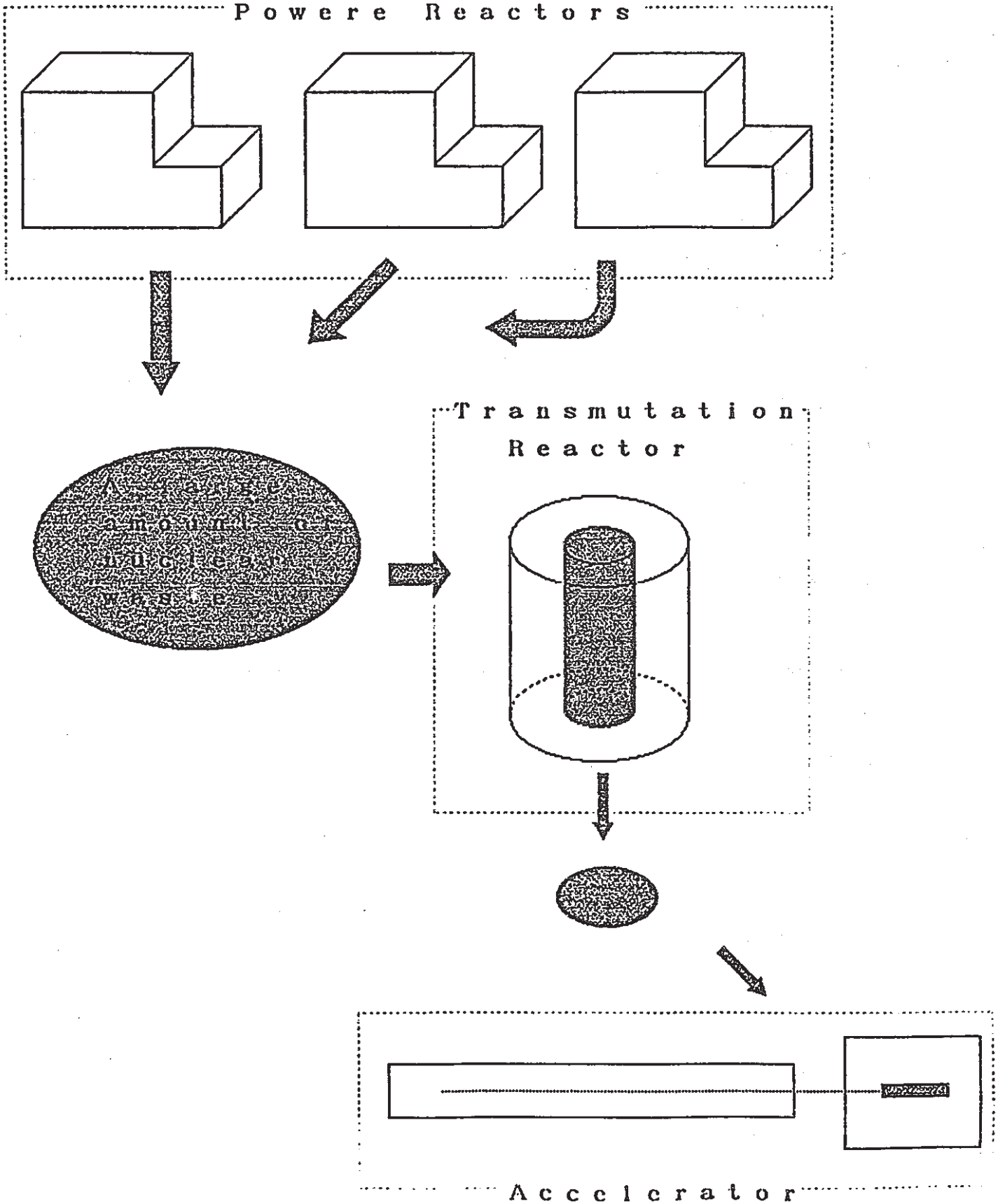

# Fig. 2 TRANSMUTATION PROCESS

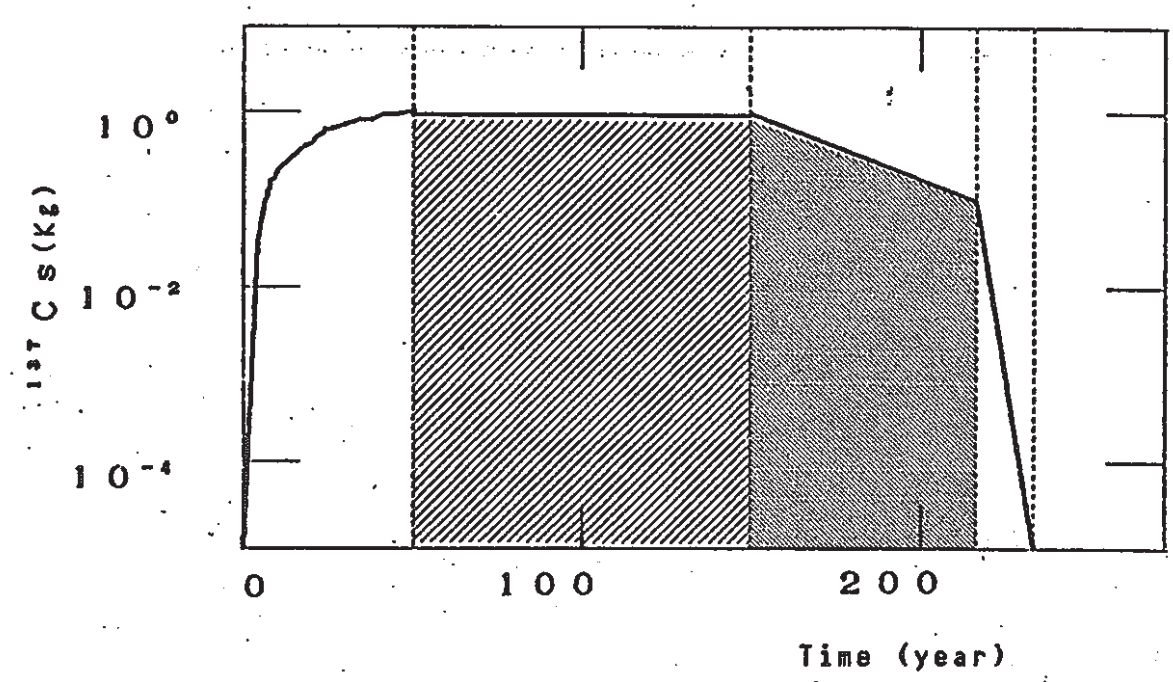


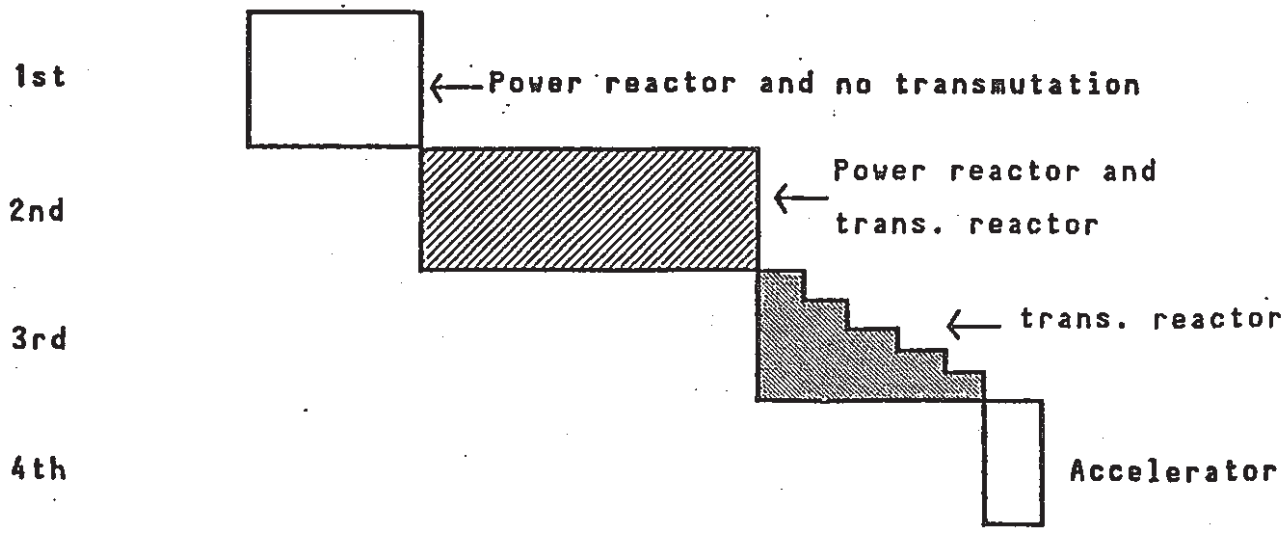

# 資料６－１

# 消滅処理用電子加速器の概念

## ３．加速器の概念設計

工学実証段階で求められる電子線の特性を満すための加速器の概念設計を行った。この加速器の設計パラメータを表３－１に示した。

電子ビームの特性は、エネルギー100MeV，電流値100mAとした。

ライナックの構成は、ビーム不安定性を考慮し実績をもとに１ビームライン20mAとし全体で５ビームラインで100mAとした。

周波数は、加速可能な電流値を仮定してビーム効率の良い1000MHzを選んだ。

加速管は、加速効率の良い定在波形加速管を選び運転モードは電源効率の良いＣＷを選んだ。ライナックの全体構成を図３－１にライナックのビームラインの１つを図３－２に示した。

１つのビームラインは、インジェクター部と１４のライナックセグメントから成り、１ライナックセグメントには、加速管３本より構成され１つの400KWのクライストロンよりマイクロ波が分割されて供給される。図３－３にインジェクター部を示した。

インジェクター部は、電子銃，プレバンチャ，３つのバンチャ加速管より成り、電子銃は100KVでドライブする予定である。プレバンチャ及び３つのバンチャ加速管は400KWのクライストロンでドライブされ、20mA，5MeVの加速をする。加速管と加速管との間にはＱ電磁石を配置し、ＢＢＵの抑制をはかっている。

加速部には、３つのレギュラー加速管から構成される加速ユニット１４個から成り加速管と加速管との間には、バンチャ加速管と同様Ｑ電磁石を配置した。加速部の加速ユニットを図３－４に示した。

ＲＦ系は、クライストロンにValvoのＣＷクライストロンＹＫ１２５０を用い各々インジェクターに１本、加速部ライナックセグメントに１４本合計１５本／１ライン用いている。各種大出力クライストロンを図３－５に示した。

表3-1

## Design Parameters of Test Linac

| | |
|---|---|
| **1. Beam characteristics** | |
| Electron energy | 100 MeV |
| Average current(total) | 100 mA |
| Duty factor | 100 % |
| **2. Linac Parameters** | |
| Concept | c w |
| Number of linac beam lines | 5 |
| Number of linac segments/line | 14 |
| Number of accelerating structures /segment | 3 |
| Segment length | 6.7 m |
| Accelerating structure length | 1.7 m |
| Type | side coupled standing wave |
| Frequency | 1 GHz |
| Shunt impedance | 42MΩ/m |
| **3. R F** | |
| Type Klystron | YK1250 |
| Output power | 400 KW |
| Duty factor | 100 % |
| Number of Klystrons/line (including for buncher) | 15 |
| **4. Injector parameters** | |
| Gun energy | 100 KV |
| Injection energy | 5 MeV |
| Avarage current/lime | 20mA |
| Bunch length | <3degree |
| Number of bunching structures | 3 |
| Type of prebuncher | re-entrant |

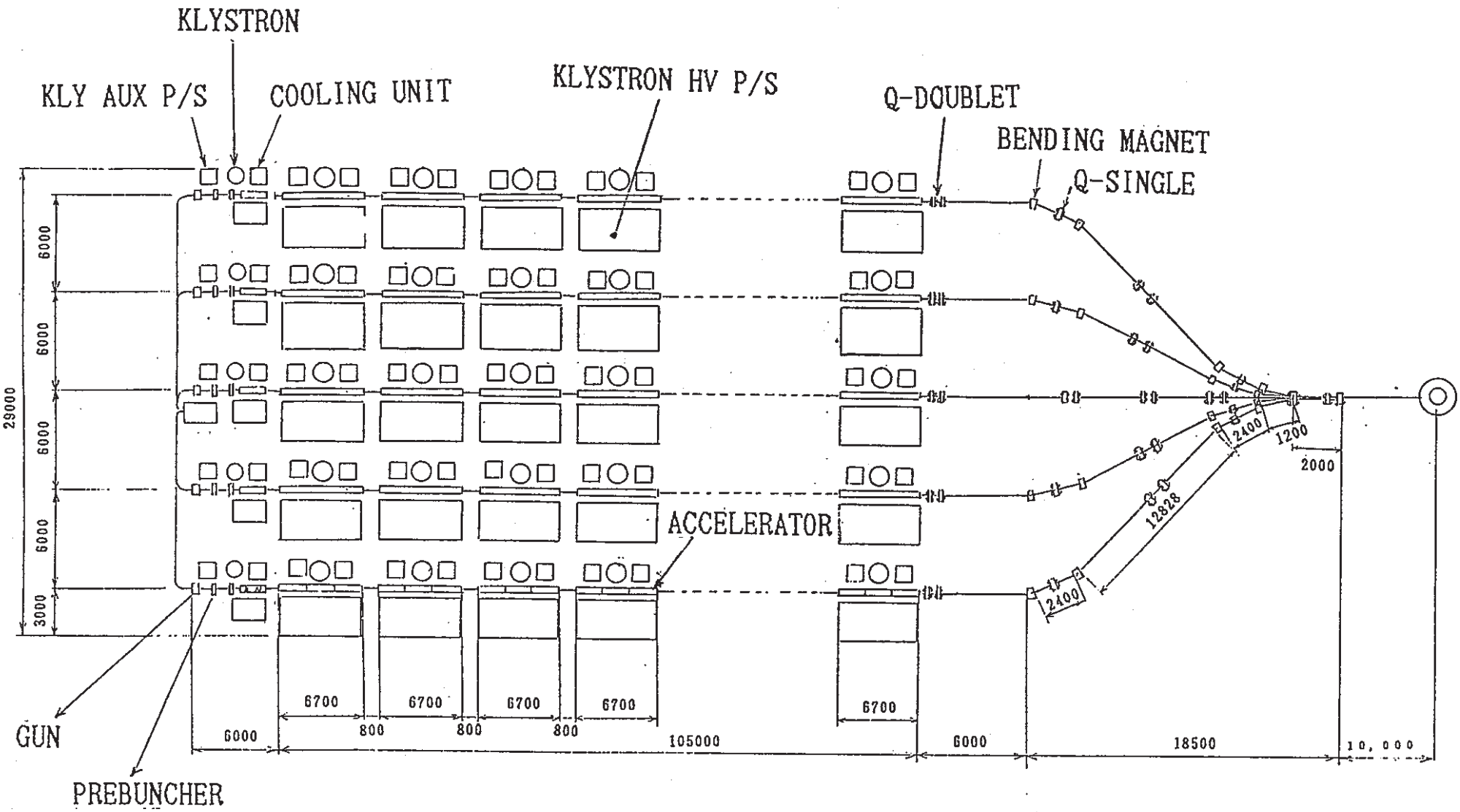


図３－１　消滅処理用電子線加速器概念図（工学実証用）

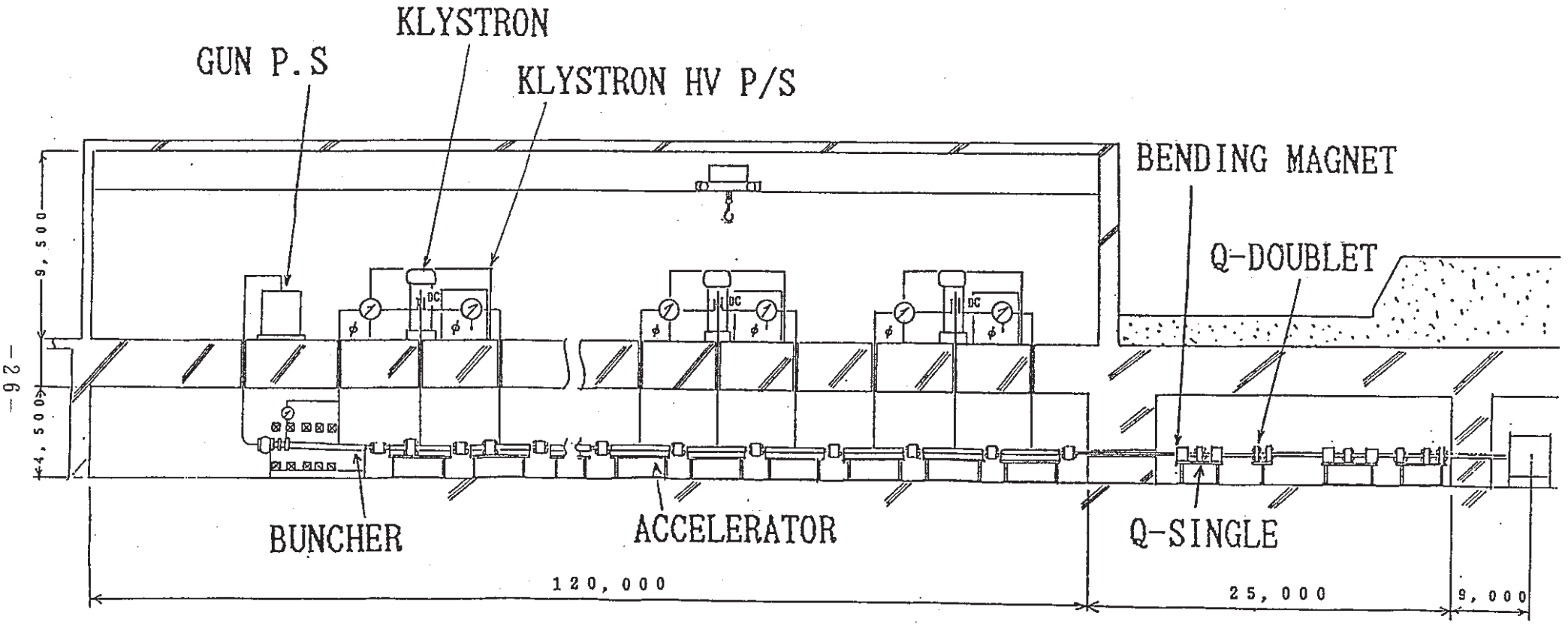


図３－２　消滅処理用電子線加速器ビームライン及びクライストロンギャリー

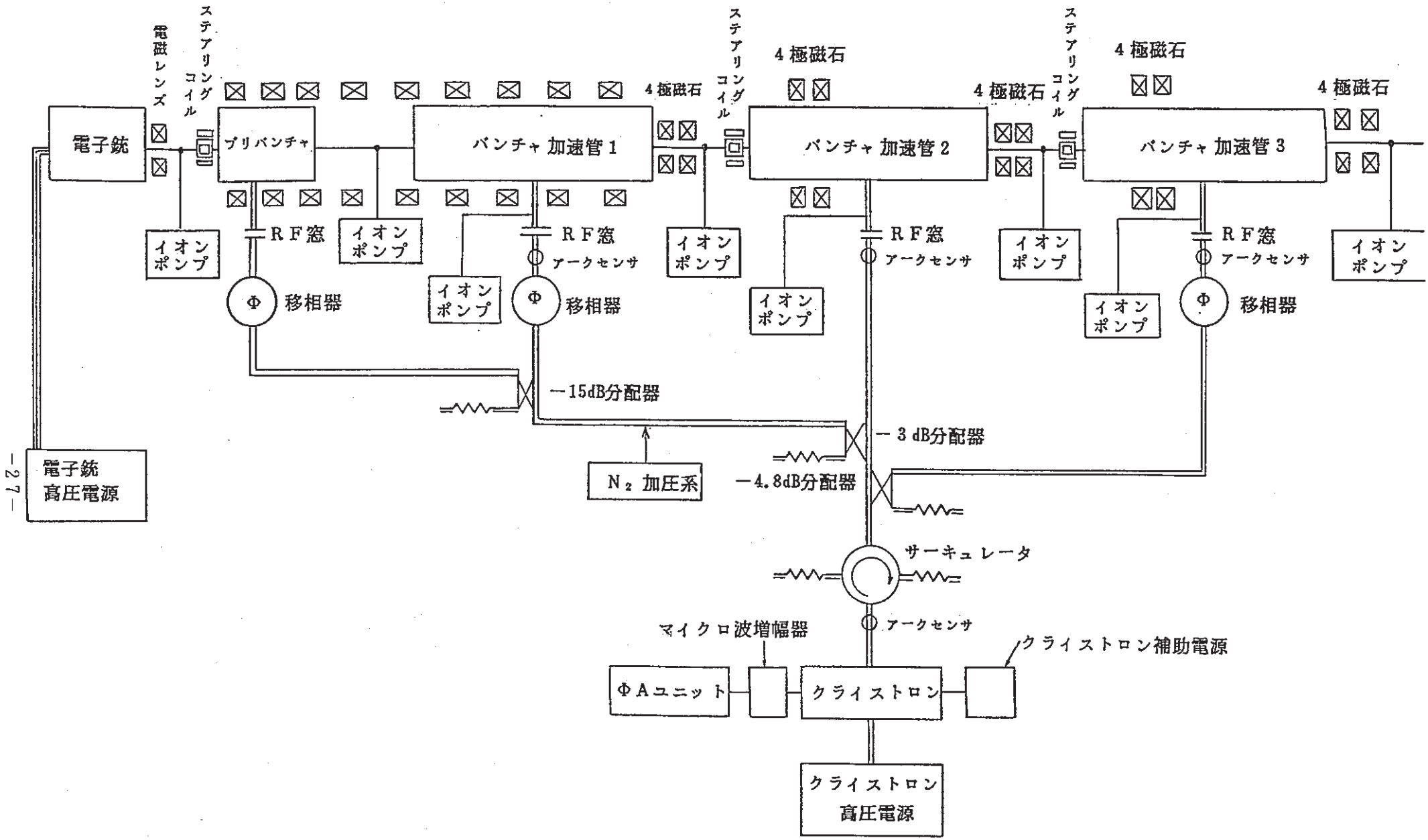
電磁レンズ
ステアリングコイル
電子銃
プリバンチャ
バンチャ加速管1
バンチャ加速管2
バンチャ加速管3
4極磁石
RF窓
アークセンサ
イオンポンプ
Φ 移相器
−15dB分配器
−3dB分配器
−4.8dB分配器
N₂ 加圧系
サーキュレータ
マイクロ波増幅器
ΦAユニット
クライストロン
クライストロン補助電源
電子銃高圧電源
クライストロン高圧電源

図3－3　入射部構成機器

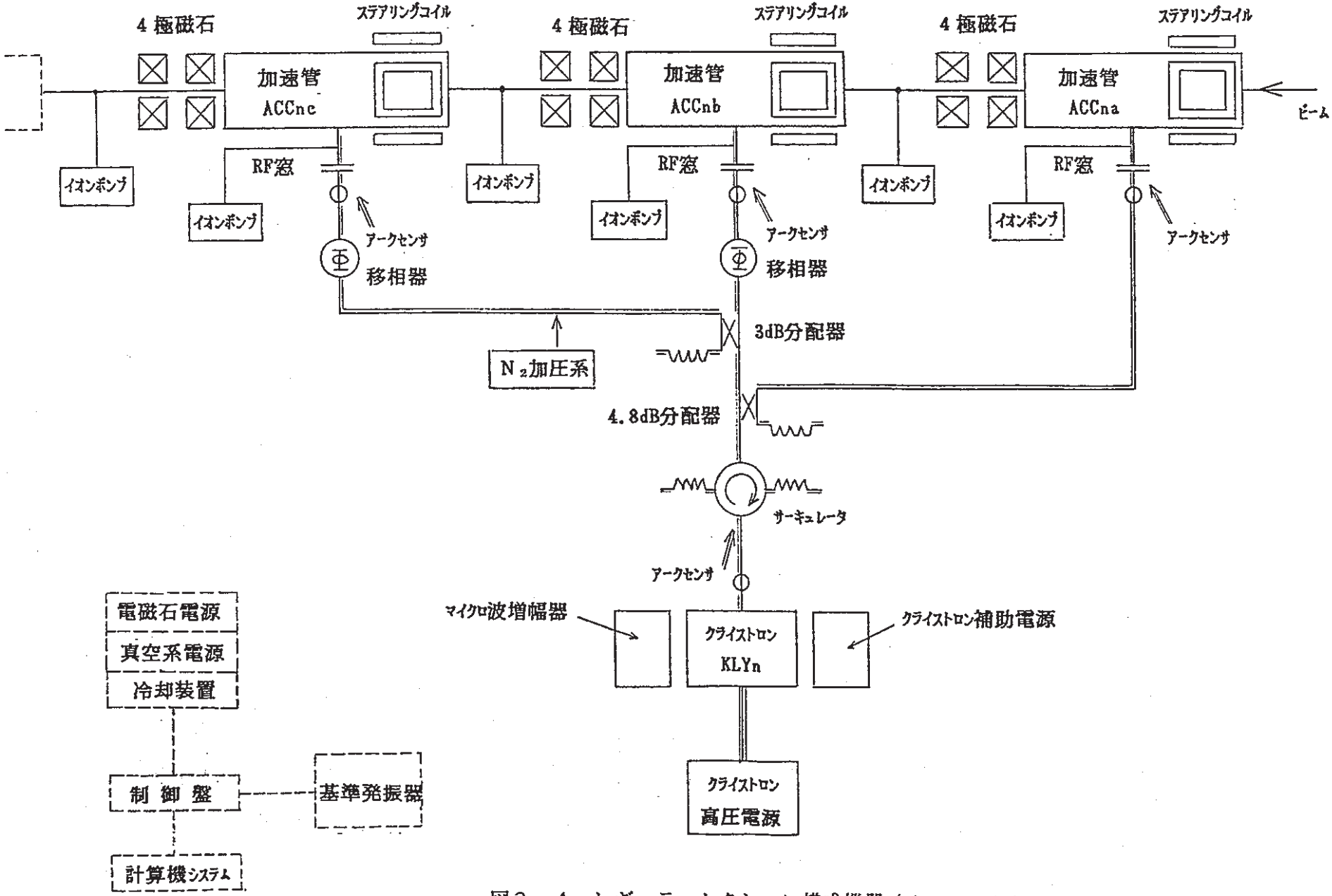


図3－4　レギュラーセクション構成機器（1ユニット）

MITSUBISHI ELECTRIC CORPORATION

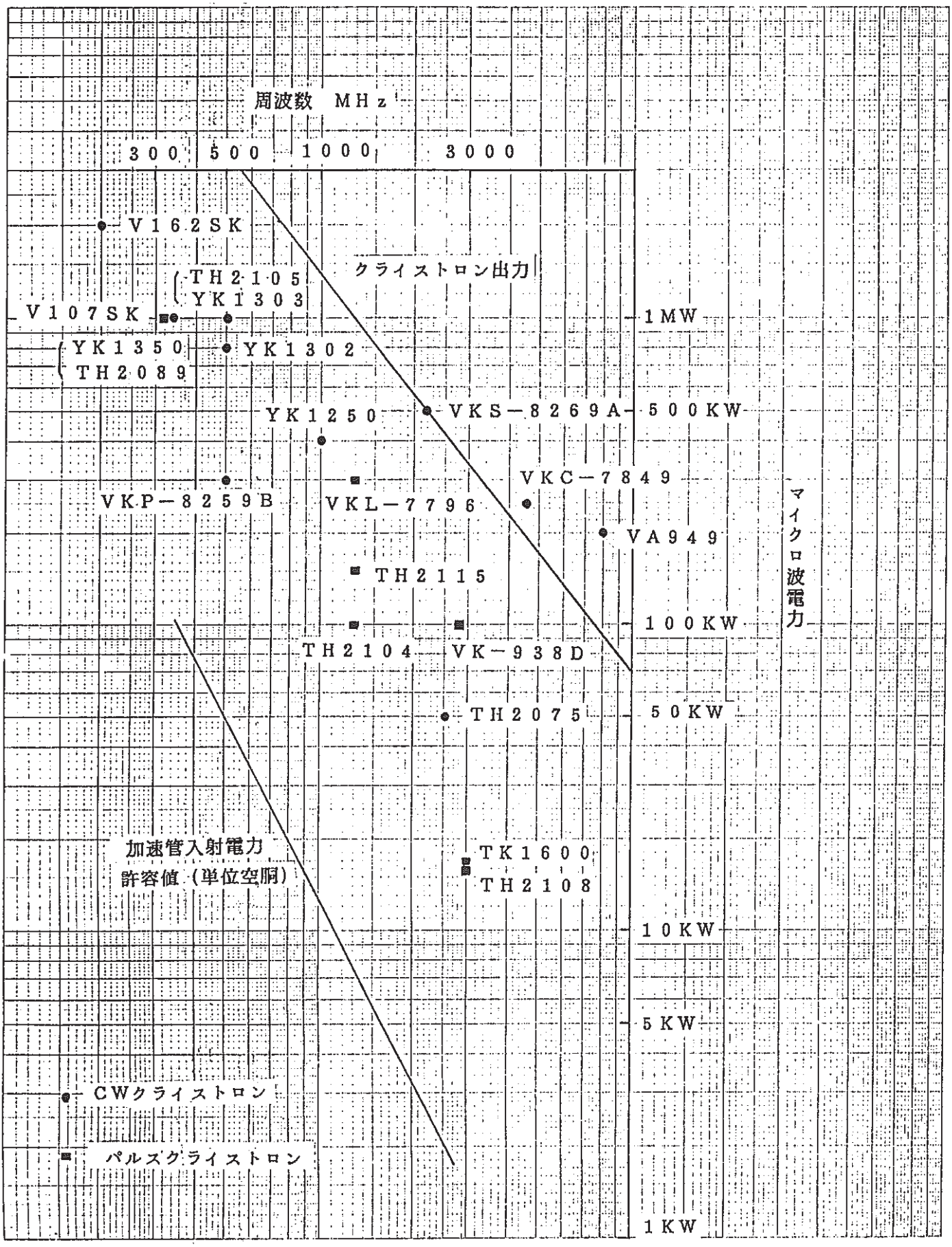


図3－5　大出力クライストロン特性図

- 資料７－２

Chalk River Nuclear Laboratoriesの事前調査

- 資料７－２　文献－１
  ＥＴＡの運転経験報告
- 資料７－２　文献－２
  500kWリニアック計画

- 資料７－３

大出力リニアック加速管の熱歪解析

- 資料７－４

1988年ヨーロッパ加速器会議のIMPELA報告

- 資料７－５

SPALLATION & RADIATION PHYSICS AT CRLN

- 資料７－６

PRESENTATION TO PNC

- 資料７－７

Chalk River研究所のカタログ

資料７－２　　Chalk River Nuclear Laboratories　の事前調査

１。組織

AECLの研究開発部門は CANDU型原子炉をはじめ多くの成果を挙げてきたが、最近は商業ベースでの活動が可能な部門は民間企業として分離し、他の部門にも効率化の努力を勧め、また社会へのサービスを要求する方針を取っているとのことである。名称もResearch Companyを名乗っており、1986頃から研究報告にも使っているようである。

組織の主要部を下に示す。

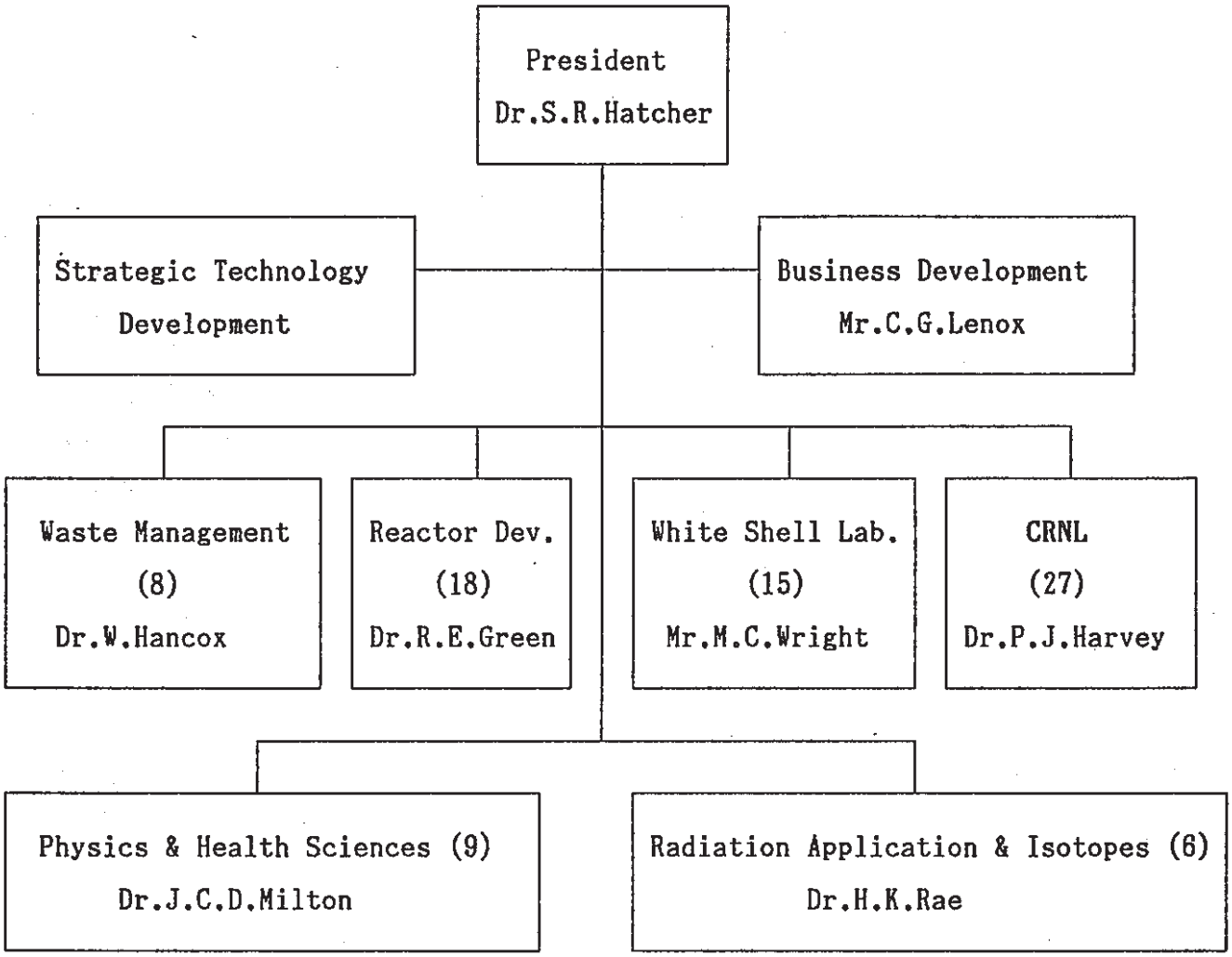


それぞれを統括するVice-presidentの名前を括弧内に記した。但しWhite Shell lab.は最近CRNLに統合されたとのことである。各部には括弧内に記した数の R&D部門がある。

２。ＣＲＮＬ

所員は2000名で、そのうち研究者と技師が 500名、テクニシャンが 500名である。

Ottawaから 190kmの距離にある研究所の敷地は4000ヘクタールの広さがあり、人里から隔絶した森と水の環境に恵まれている。

目立つ施設は二基の原子炉NRX,NRV とTASCC で、その他に今回の訪問の目的の一つで、大強度プロトンリニアック開発の中途段階で作られたCW電子リニアックETA 、RFQ およびアルバレ型リニアック、200MeV以上のエネルギーのプロトン加速用に開発された on-axis結合型定在波加速管、その技術を使用して製作中の大強度産業用電子リニアックIMPELAなどがある。大強度イオン源も加速器による核燃料増殖プロジェクトのなかで開発され、現在は半導体技術に利用されているとのことである。

註　TASCC=Tandem Super Conducting Cyclotron

## 3。ＡＥＣＬの電子リニアック技術

医療用のS-バンド電子リニアックをカナダ、米国その他に販売してきたが、1987年にやめた。Varianとの競争に敗れたようである。

他方では1963年から追求してきた加速器による核燃料増殖技術開発プログラムのなかで、ロスアラモスのLAMPF をCW運転としたときの問題点を調べるために同じ805MHzのSide-couple 型加速管を作り、電子ビームによる陽子ビーム ローディングのシミュレーションヨン実験を行なってきた。これが ETAである。核燃料プロジェクトが1984年に打ち切られる以前からETA は工業用その他の電子線応用技術開発にも使用されてきたが、以後は実用性のあるプロセシング用大電力加速器の設計のデータを得るための測定が主任務となった。

その任務もほぼ終了し、現在は工業応用専用機として商品化することを目標とするIMPELAの建設が開始されている。以下はAECL製の医療用以外のリニアック一覧表である。

| 機種名 | 周波数 | ｴﾈﾙｷﾞｰ | ﾋﾞｰﾑ電力 | タイプ | duty f. | 完成年 | 用　途 |
|---|---|---|---|---|---|---|---|
| ETA | 805MHz | 4MeV | 20kW | side-coupled | CW | 1976 | ﾋﾞｰﾑﾛｰﾃﾞｨﾝｸﾞ効果、産業応用 |
| I-10/1 | 3GHz | 10MeV | 1kW | on-axis coupled | pulse | 1987 | 実用機ﾌﾟﾛﾄﾀｲﾌﾟ |
| IMPELA | 1.3 GHz | 10MeV | 50kW | on-axis coupled | pulse | 1989 | ﾌﾟﾛｾｽ 実用機 |

この他、通常の進行波型の40 MeVのリニアックもあるように聞いているが、詳細は不明で、CRNL以外の場所にあるのかも知れない。I-10/1はWhite Shell Lab.にOttawaから移動している。Ottawaでは制御システムの組込みとともに1987年に同市で開かれた放射線応用国

際会議での展示にも使われたようである。

4。添付した報告の内容

McKeowonのグループからは多くの報告がでているが、ここには今回の訪問による調査の趣旨に最も添っていると思われる二つを選んだ。

4-1 "Operational Experience with Coupled Cavity Structures in a High Duty Factor Accelerators",IEEE NS-26 (1979) 4108

ETA は、ロスアラモスの805MHz LAMPFをCW運転としたときの問題を調べるためのシミュレーターとして製作されたが、これはその運転経験報告である。

ETA はModel-4 と命名された11セルの速度変化領域用加速部と、18セルの定速度部用のModel-3 からなっており、両者はビームパイプで繋がっている。それぞれは更に二つに分割されていて、Bridge Couplerで結合されている。このカプラーに取り付けられているSlug tunerにより、それぞれのセル群の共振周波数を限られた範囲ではあるが、変えることができる。

問題はCW運転による加速管の温度変化で生じる共振周波数変化が大きく、また二つの加速管グループの周波数変化特性が異なっていて、励振初期の電力注入に工夫を要することで、これがこの報告の主題である。

ETA ではその対策として、約15分の立ち上がり時期には各加速管グループに個別の可変周波オシレーターを結合して、共振周波数の変化に追随して電力供給をし、冷却水は循環のみとして温度上昇を早める方法を取っている。設計温度に達したら共通のマスターオシレーターに切り替え、水温調節を始める。また共振周波数アナライザーによる共振維持機構も働かせてから、初めてビームの入射をする。(Fig.8およびその下のコメント) この過程は短時間の停止後であれば 5分程度で済むとのことである。これらの動作は計算機により制御されているが、将来多数の加速管を使用する場合は低コストのマイクロプロセッサー群に置き換えることができるとしている。

但しこの方式ではビームの入射を加速管の熱平衡状態の達成まで待たなければならないから、リニアックを他の連続運転用、例えば蓄積リングや産業用プロセシングに使用する場合は温水を利用するか、周波数調節能力の大きいSlug tunerの開発が必要となると述べている。

4-2 "Design of a High Power Electron Linac",Linac'84,Seeheim,(1984) 186

1979年の時点でもある程度予感されていたことであるが、加速器による核燃料生産あるいは放射性廃棄物の処理技術開発に対する支持が早急には得られないので、ETA で得られた技術を産業用プロセシング（高分子改質、滅菌、食品保存など）に適した大電力リニアックの開発に振り向ける努力が、1980年代に入って強化された。照射利用技術に関しても活動を行なっているが、この報告では10MeV,で最大 500kWの出力の可能なリニアックの設計が述べられており、今回の見学対象にも含まれているはずのIMPELA型の目指すところを窺うことができる。周波数を2.45GHz とした理由も述べられている。但し、1986年の加速器応用の会議に提出された大電力励振下での加速管の熱変形と共振周波数変化を解析した報告では、1.35GHz の構造の使用を前提としており、1987年 9月から製作が開始されたIMPELAに先ずどちらが使用されているかは明確ではない。

CRNLで開発されたOn-axis coupled cavityの大電力使用には、Web とその真ん中にあるNose cone の冷却が重要で、水管をAccel.cavity とCoupling cavity の間の薄い Web 内に通さなければならない。加工技術的にはCavityが大きく、Web を厚くできる1.35GHz のほうが有利であるのは自明であるが、実効シャントインピーダンスは2.45GHZ が大きい。しかし、1984年の報告が1.35GHz を採用しなかったのはそれよりも、500kW のビーム加速の目標に適したクライストロンがなかったためであると思われる。現在建設中のIMPELAの目標ビーム電力は50kWであるから、使用可能なクライストロンの選択余地は遥かに広い。したがって、加工技術あるいは冷却の安全係数の点から、1.35GHz の使用にCRNLのグループが目を向けることは当然あり得ることであろう。

IEEE Transactions on Nuclear Science, Vol. NS-26, No. 3, June 1979

# OPERATIONAL EXPERIENCE WITH COUPLED-CAVITY STRUCTURES IN A HIGH DUTY FACTOR ACCELERATOR

Gerald E. McMichael* and Joseph McKeown*


## Abstract

The Chalk River Electron Test Accelerator is a facility to study beam behaviour in a multi-tank accelerator and to develop control systems for high power operation. Two standing-wave structures have been operated at energy gradients of 0.75 MeV/m and their accelerating fields held constant under 50% beam loading. During start-up, the control systems must accommodate resonant frequency shifts exceeding ten bandwidths in both of the dissimilar structures and their resonant frequencies must differ by less than a tenth of a bandwidth before locking to the accelerator frequency. The central mini-computer controls the run-up and among other things controls the structure temperature.


## Introduction

The Chalk River Electron Test Accelerator[1] (ETA) comprises an electron gun and buncher cavity as the injector, a graded-β and a β=1 structure, all operating at 100% duty factor. Operation of the graded-β structure at up to 50% beam loading has been described previously[2]. In the last two years the problems of multi-structure operation have been solved and 16 mA has been accelerated to 4 MeV without fundamental difficulty.

This paper describes the operation of the two dissimilar structures at 100% duty factor and the modular control systems which should permit straightforward expansion to a much larger accelerator.

## Accelerating Structures

Model 4 (graded-β structure) and Model 3 (β=1 structure) have 11 and 18 accelerating cells respectively and each consists of two almost equal, (identical in the case of Model 3), sections joined by a bridge coupler. Both are adaptations of the LAMPF side-coupled structure with improved cooling for the increased power dissipation associated with 100% duty factor operation. A movable slug tuner in the bridge coupler of each structure provides a convenient means of varying the resonant frequency as shown in Fig. 1.

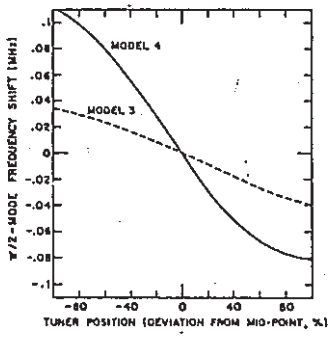


Fig. 1　π/2-mode Frequency Shifts Caused by Tuner Movement

The resonant frequency also depends on the temperature of the structure and the rf power dissipation. Because of different cavity profiles, small differences are found between the two structures, but on average the resonant frequency changes 0.014 MHz/°C for changes in structure temperature, and 0.070 MHz/kW/cell for changes in rf field. During accelerator operation, all structures must be excited from a single oscillator and the resonant frequencies of the individual structures must not deviate by more than a few kHz from the accelerator frequency. The control systems to meet this requirement have been described previously[3]. More recently, improvements to our instrumentation have allowed us to further investigate the behaviour of the structures under cw conditions.

Ignoring beam loading effects, there are two main perturbations to the structures - the temperature gradients between the cooling water and various parts of the structure due to the power dissipation of several kW/cell, and the detuning of the bridge by the tuner. Except for machining tolerances, all cells in Model 3 are of identical profile, thus it is a simpler structure than Model 4. After final tuning, bead pull measurements showed the fields in all Model 3 accelerating cells were equal at low power. Amplitude and phase tilts induced when the power is varied from 0 to 3.5 kW/cell are shown in Figs. 2 and 3. Within the uncertainty of the measurements, no phase tilts were found and the amplitude tilts are less than + or -1%.

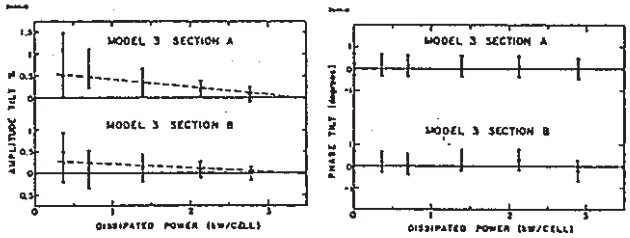


Figs. 2 and 3　Model 3 Amplitude and Phase Tilts

Measurements made while the tuner was moved over its full range show that the tuner also does not cause a detectable phase tilt, however it has an appreciable effect on amplitude as shown in Fig. 4. Calculations with a coupled circuit model predicted that a 1% amplitude tilt would be induced in each section when the bridge was detuned so as to shift the π/2-mode frequency by 75 kHz. (These calculations assumed that the structure was perfectly tuned to begin with.) The observed tilts (2.5% in Section B and 1.5% in Section A) are roughly in agreement with this prediction, however the fact that they differ, plus the 2% shift from A to B indicates some asymmetry in the tuning. The observed bridge coupler-to-section tilt however, (18%), is an order of magnitude larger and of the opposite sign to that predicted. While not a problem for ETA, the large effect of the tuner on the cell being detuned could be important for accelerator structures with tuners in one or more of the accelerating cells. It is probable that in addition to the frequency shift, the tuner causes a change in the coupling. This is not taken into account in the model. Further investigations are planned to account for the magnitude of this effect and find ways to reduce it.

Unlike the Model 3 structure, which is critically coupled without beam, Model 4 is overcoupled (VSWR = 1.36) and becomes critically coupled with a beam power of 11.7 kW. The Model 4 tuner has a similar effect to that observed in Model 3, but the tilt from bridge to section is only about 8%. Whether this is due to the different coupling or the different number of cells in the structures has not been determined. The reflected/forward power ratio for Model 4 was measured


* Atomic Energy of Canada Limited
Physics Division, Chalk River Nuclear Laboratories
Chalk River, Ontario, Canada K0J 1J0


0018-9499/79/0600-4108$00.75 © 1979 IEEE

as a function of tuner position and is shown in Fig. 5. This change in reflected/forward power ratio represents a change in the match to the transmission line from a VSWR of 1.33 to 1.37.

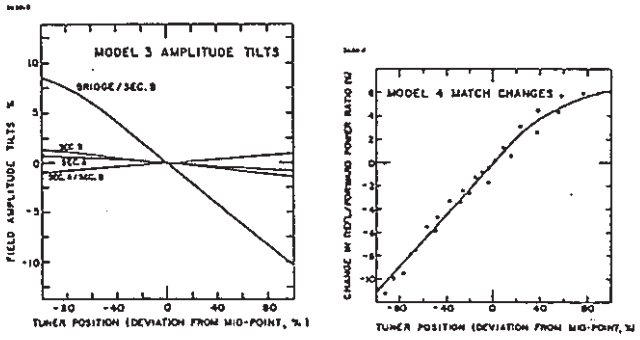


Figs. 4 and 5 Effects of Tuner Movement

## Structure Start-up and Control

Three control loops[3] provide the required accelerating field amplitude and phase stability and maintain the structure resonant frequency sufficiently close to the accelerator frequency. As shown in Fig. 6, the amplitude and phase controllers adjust the drive to the klystron, while the structure resonance (Fig. 7) is controlled by adjustments to the tuner and the cooling system. The cooling system is a closed loop with a heat exchanger through which a fraction of the structure cooling water may be passed.

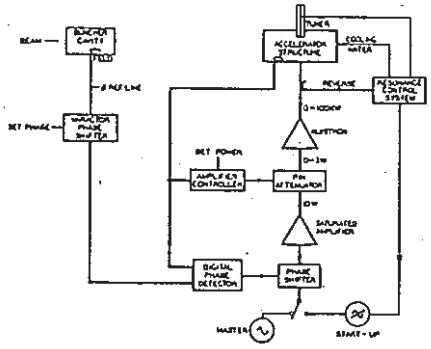

Fig. 6 Accelerator Structure Control System Block Diagram

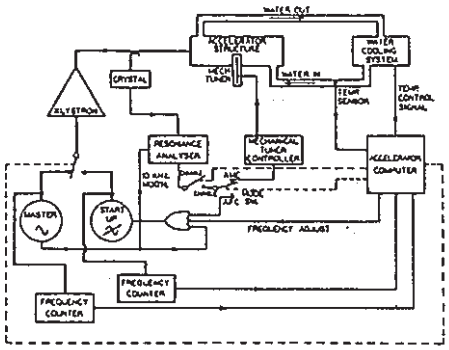

Fig. 7 ETA Resonance Control System

As can be seen in Fig. 7, start-up oscillators which can track the structure resonant frequency are provided for each structure. This simplifies the start-up procedure and also permits rf heating to be used to bring the structures up to operating temperature. The alternatives of a hot water system for heating, or tuners with sufficient range to accommodate the frequency shift of start-up are therefore not required, provided, as will be explained later, the beam can be shut down while the start-up oscillator is in use.

Although ETA is a two-structure accelerator, one of the purposes of the project is to develop equipment and techniques applicable to accelerators with many structures. For this reason, a control computer[4] was obtained early in the project, to develop hardware and software which could be useful for a multi-tank accelerator. At present, both structure temperature and start-up are completely controlled by the system computer but with hardware and software to permit future transference of the tasks to dedicated microprocessors.

The use of separate oscillators and mechanical tuners makes the start-up of the ETA structures simple and straightforward. To illustrate this, the time history of several parameters during computer start-up of Model 4 from an initial temperature of 5°C is shown in Fig. 8.

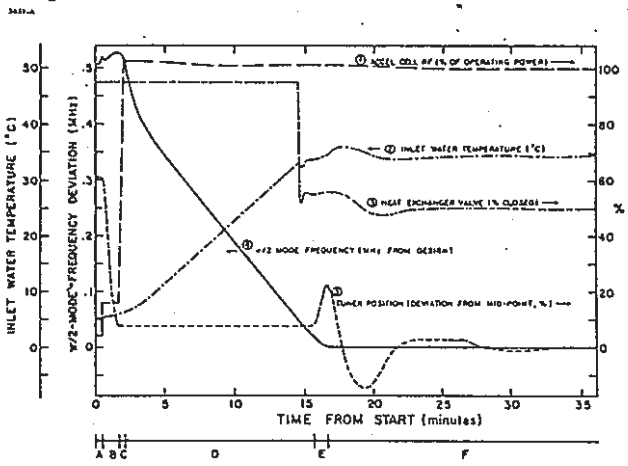


Fig. 8 Computer Controlled Start-up of Model 4

| Time Interval | Comments |
|---|---|
| A. | Resonance control loop is disabled (Fig. 7), minimum drive applied to the klystron, and the frequency (4) (Fig. 8) swept until resonance (minimum reflected/forward power ratio) found. |
| B. | Rf field (1) is increased to a level at which the resonance controller can operate, tuner control engaged and the frequency (4) adjusted to move the tuner (5) to within 10% of the mid-point of its travel. |
| C. | AFC mode (frequency slaved to structure resonance) is selected and the rf field (1) increased to operating level. |
| D. | Heat exchanger valve (3) is kept closed so that the structure (and water in the cooling system (2) ) is brought to operating temperature is quickly as possible. With the increasing structure temperature, and the temperature gradient due to the power dissipation, the frequency (4) approaches the accelerator frequency. By about the 15 minute mark, the temperature (2) has approached the calculated optimum temperature for that power and frequency and the heat exchanger valve (3) is rapidly adjusted to slow the temperature rise. |

E. Both frequency and temperature have approached operating levels and the tuner control is engaged, leaving the start-up oscillator controlled only by the computer. The frequency is then adjusted to within 1 kHz of the accelerator frequency, and the klystron drive switched from "start-up" to "master" oscillator. At this point the structure is ready to accelerate the beam and the start-up program terminates.

F. The temperature control program (which is always running) continues to make valve adjustments (3) until the tuner is returned to the mid-point of its range.

Under normal circumstances, the cooling system pump provides sufficient power to the system (3 to 4 kW) to keep it close to operating temperature even when the rf is off. As shown in Fig. 9, for a restart under these conditions, both the frequency shift and time until the structure is ready to accelerate a beam are reduced by about a factor of 3, with the structure ready for beam in about 5 minutes.

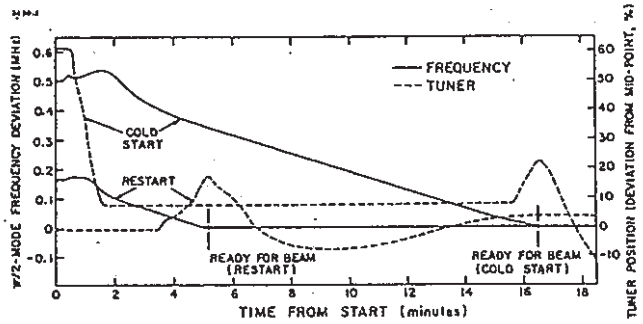


Fig. 9 Model 4 Start-ups from 5 and 33°C

Although the system described here would be relatively inexpensive to implement with microprocessors for a large multi-structure accelerator, it is suitable only for those cases (such as ETA) where the beam is off until all structures are ready. For electron rings, or a recently proposed 12 MeV accelerator for radiation processing[5], the beam must be drifted through an unpowered module. The accelerating module is brought into service with the beam on, and therefore would have to be at the accelerator frequency. This requires tuners with sufficient range to handle the frequency shift on start-up and/or a source of hot water, which could possibly be economically provided by tapping into the outlet of the klystron collector cooling system. These alternatives are being investigated.

## Conclusions

The ETA program has demonstrated that accelerator structures and control systems are available which can accelerate high intensity electron beams in cw mode. The phase and amplitude tilts of the accelerating field due to power dissipation up to 3.5 kW/cell are less than ± 0.5 degrees and ± 1% respectively. Start-up and operation are greatly simplified by using a movable slug tuner in one cell to adjust the resonance of the coupled-cavity system, however this can introduce appreciable field amplitude tilts. A hardware and software system for automated start-up of accelerator structures, has been developed. Such a system could be easily and inexpensively expanded for a many-structure accelerator.

## References


1. J.S. Fraser, S.H. Kidner, J. McKeown and G.E. McMichael, "The Chalk River Electron Test Accelerator", Proc. 1972 Proton Linear Accelerator Conf., LA-5115, 226 (1972).
2. J.S. Fraser, J. McKeown, G.E. McMichael and W.T. Diamond, "Operation of the Graded-β Electron Test Accelerator", Proc. 1976 Proton Linear Accel. Conf., Atomic Energy of Canada Limited, Report AECL-5677, 166 (1976).
3. J. McKeown, J.S. Fraser and G.E. McMichael, "Field Control in a Standing Wave Structure at High Average Beam Power", ibid. 291.
4. G.E. McMichael, J.S. Fraser and J. McKeown, "The Control Computer for the Chalk River Electron Test Accelerator", Atomic Energy of Canada Limited, Report AECL-5720 (February 1978).
5. J.S. Fraser, "High Power, Low Energy Linac for Radiation Processing", Proc. of 5th Conf. on Applications of Small Accelerators to be published in February 1977 IEEE Trans. on Nucl. Sci.

# DESIGN OF A HIGH POWER ELECTRON LINAC

J. McKeown, R.K. Elliott, L.W. Funk, S. Gowans, J.-P. Labrie, C.E. Langlais and D.G. Logan
Atomic Energy of Canada Limited, Research Company
Chalk River Nuclear Laboratories
Chalk River, Ontario, Canada K0J 1J0

## Summary

The conceptual design of a cw electron linac to produce 500 kW of beam power at 10 MeV is described. Examination of klystron availability, structure efficiency and system physical size has led to the selection of 2.45 GHz as the operating frequency. The development of accelerating structures operating at 2 MeV/m and beam loaded at 63% allows the system to operate with two 500 kW klystrons. A new scheme for start-up is modeled on cw microtron procedures, providing pulsed diagnostic information during a gradual run up to full power.

## Introduction

CRNL has a long-standing interest in the development of high power particle accelerators. The past decade has seen the development of a cw linac[1] which has accelerated 20 mA of electrons to 4 MeV in the study of highly beam-loaded cw accelerators. This is a topic of interest to designers of electron storage rings, cw microtrons and linacs for electronuclear breeding. Experimental work has proceeded in parallel with theoretical studies in beam dynamics, coupled-cavity structure design, beam-cavity interaction and thermal stress analysis. This paper describes the results of a study undertaken to determine the feasibility of designing and building a cw electron linac to provide beam currents up to 50 mA at energies up to 10 MeV for industrial applications. Most components are commercially available and only modest development is required on others.

## Basic Design Choices

The three main factors determining the basic characteristics of the accelerator are energy gradient, operating frequency and structure type. For many potential applications of a cw linac, a premium is placed on reducing the overall length so operation with a high accelerating gradient is desirable. Accelerating gradients have increased sharply in recent years, for example, in cw tests of CRNL[2] and LANL/NBS[3] structures gradients of 1.9 MeV/m and 2 MeV/m respectively have been reported. Calculations[4], reported elsewhere at this conference, indicate that values as high as 3.7 MeV/m should be attainable in room-temperature structures with reasonable coolant flows.

The choice of gradient is closely related to the choice of operating frequency, because the power required to produce a given accelerating field varies inversely as the square root of the frequency, and because klystrons of suitable size are available at only a few of the frequencies that may be of interest. Figure 1 is a plot of the structure power required to produce a total energy gain of 10 MeV for three different gradients. With the well-tested Mainz structure[5] as a reference point it illustrates the advantage of choosing a high frequency which has the additional advantage of smaller structures and hence lower material costs. However, it also implies a lower current limit, more brazed joints, more demanding machining tolerances, reduced vacuum conductances and higher surface power densities.

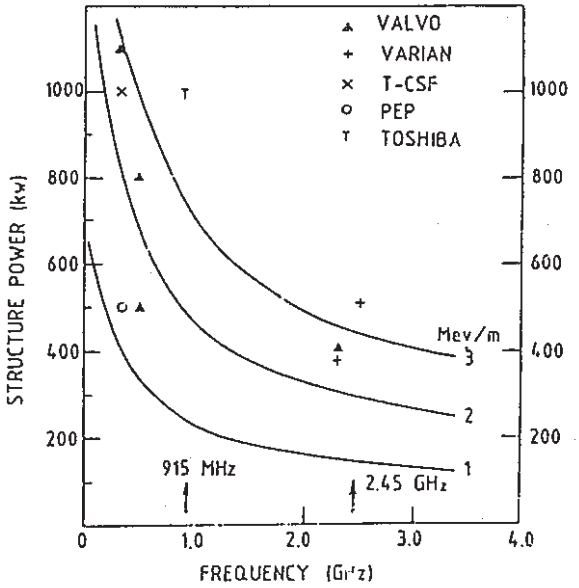


Fig. 1 Structure power and frequency for three different energy gradients. Commercially available klystrons are identified by manufacturer. The number of klystrons at low frequency is the consequence of recent developments for high energy storage rings. The industrial frequencies of 915 MHz and 2450 MHz are highlighted.

These considerations have led to the choice of a system based on two VKS-8269A 500 kW klystrons operating at 2450 MHz. The klystrons have recently been developed by Varian Associates for the Princeton fusion program[6]. At an accelerating gradient of 2 MeV/m, from Fig. 1 we find that 300 kW will be dissipated in the structures, and 500 kW will go into the beam, leaving a 200 kW margin for waveguide and other losses.

Either side-coupled and on-axis coupled resonator structures would be suitable for the linac. We have chosen the on-axis coupled system, with its somewhat easier tuning and greater vacuum conductance. The 5 m of accelerating cavities would be subdivided into four structures, as shown in Fig. 2, one graded in β and the others designed for β=1. Each section consists of 21 accelerating cells and requires about 75 kW to establish the accelerating fields.

The power-handling capability of the structures has been analyzed with the thermal stress analysis code MARC. Sufficient cooling channels have been added to the web to reduce the temperature difference between the nose and the outer wall, that the limit on power dissipation within the structure is determined by the onset of film boiling not the mechanical distortion arising from the temperature difference. For the present design, the limiting power dissipation is well above the reference value of 60 kW/m. Wall and web cooling channels are internally connected in series and parallel respectively. Simplified cross sections of the channels are shown in Fig. 3a and 3b. Further details of the design will be found in a companion paper at this conference[4].

Two tuners are required in each structure to compensate for the cold/hot frequency shift of 900 kHz. Calculations with the LOOPX code[7] indicate that a first neighbour coupling constant of 8% is required to keep the field tilts associated with tuner operation to the acceptable level of 7.3%.

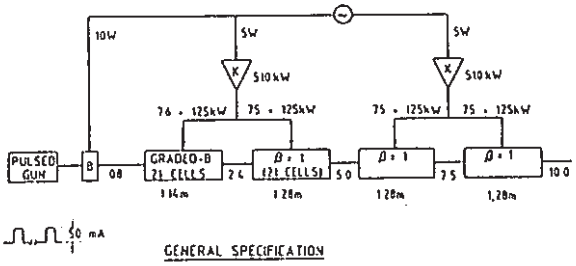


Fig. 2 Distribution of the rf power to provide the accelerating field and the power for a 50 mA beam.

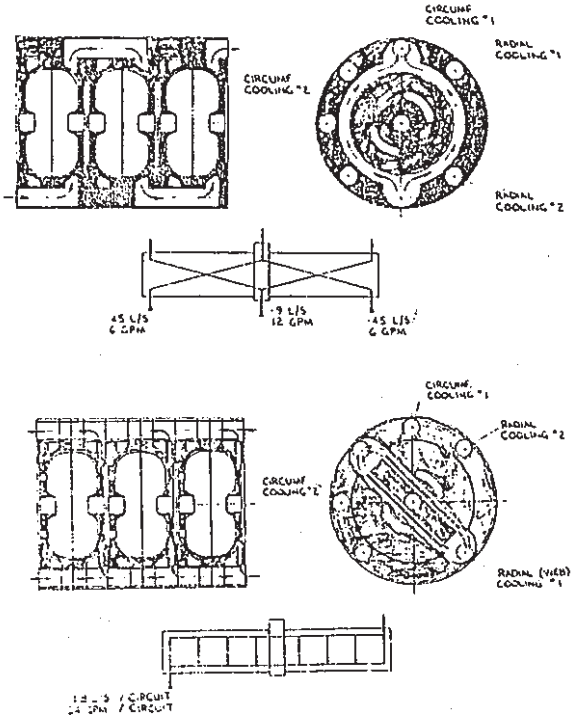


Fig. 3 The cooling system used for high energy gradients of 2 MeV/m.
(a) circumferential (b) web cooling.

## Beam Transport and Dynamics

The electron gun is a new, grid controlled design specifically developed for use on a cw linac. It is similar to the Hermosa[8] Model 7-1 built for the National Synchrotron Light Source at Brookhaven, but with a redesigned copper anode structure provided with external water cooling. The pulser uses VMOS transistor technology and fibre optic links to bring the trigger signal up to the 80 kV high voltage deck. The gun provides 200 ns duration pulses at pulse repetition frequencies variable from 500 Hz up to 5 MHz. At the upper end of this range a special "lock-up" circuit provides a true dc output.

The advantage of this unique pulsed/cw capability is that it provides a means to tune up the beam transport system at the full peak current, but with an average current sufficiently low that beam-line components are not at risk if the beam is mis-steered. For this pulsed beam operation the rf structures operate in stored-energy mode, with a field depression of 18% by the end of the pulse.

The design of the injector has been developed using the computer code, PARMELA[9]. Figure 4 shows the zero-current transverse acceptance figure of the single-harmonic buncher/graded-β linac combination. The acceptance ellipse area is $4.1 \times 10^{-3}$ π cm·rad while the emittance of the gun is $10^{-3}$ π cm·rad - comfortably smaller than the acceptance. Beam loss, mainly that not captured longitudinally, occurs primarily at low energy in the graded-β structure. PARMELA computations predict acceleration of 65% of the input current to design energy. To meet the 50 mA beam specification the gun is designed for 80 mA emission.

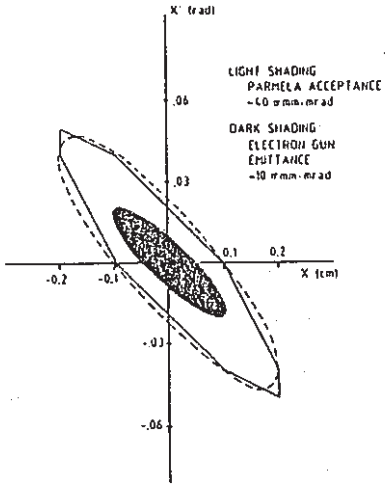


Fig. 4 Zero current acceptance of the injector and estimated emittance of an 80 mA beam from the proposed pulsed electron source.

Beam loading is 63% for all structures at the design current. The rf system, critically coupled to the linac at full current, is designed to accommodate the VSWR of 2.6 at zero current. Appropriate inter-tank spacing and waveguide run lengths are used to deflect the reverse power from a hybrid tee into a matched load, while the klystron is protected from load imbalances by a circulator designed for the full 500 kW forward power.

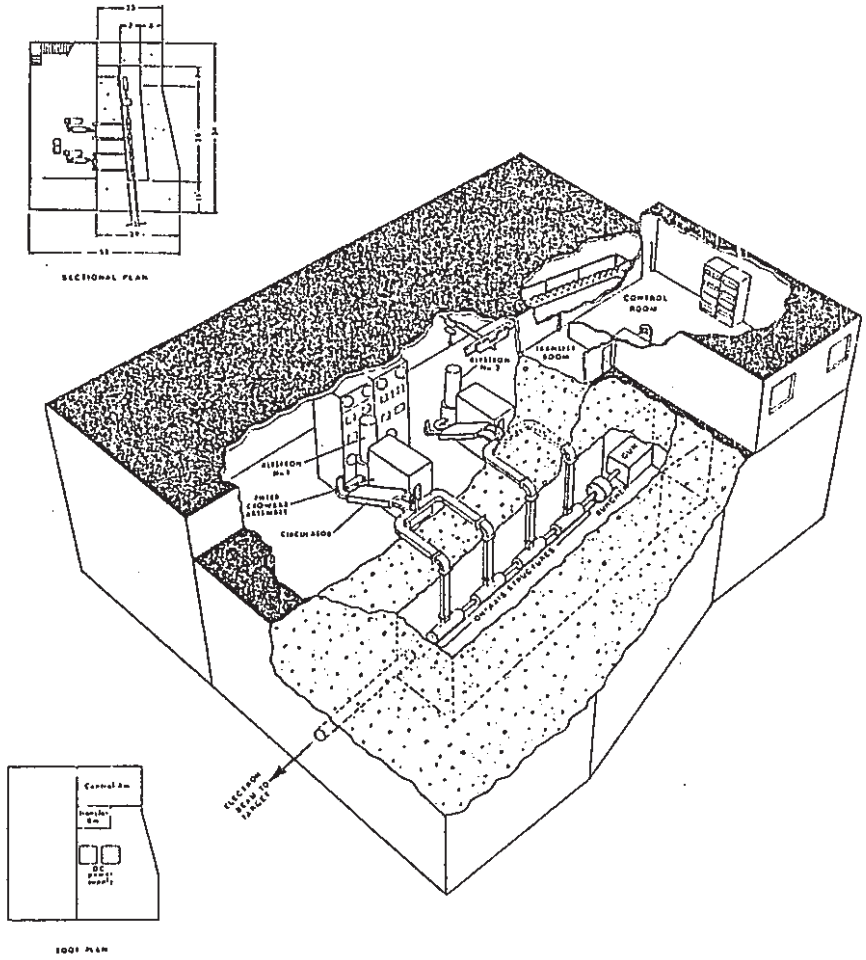

Fig. 5　Artist's view of proposed accelerator inside its concrete shield.

## Shielding and Services

Figure 5 shows a drawing of the accelerator inside its concrete enclosure. The tapered wall has 2.44 m of normal concrete at the source end and 3.35 m at the 10 MeV end. The forward peaked angular distribution of the bremsstrahlung requires a thickness of 4.37 m on the end wall. This assures that radiation outside the tunnel is less than 2.5 mSv/h. The doses calculated[10] with exponential attenuation were corrected by dose build-up factors. The shielding will attenuate neutron doses from $(\gamma,xn)$ reactions in copper and steel by a factor of $10^{11}$ hence no appreciable radiation dose from neutrons will exist outside the shield.

Power and water requirements are 2.5 MVA and 7300 L/min to cool a primary circuit of distilled deionized water (2650 L/min) for klystron and accelerator cavity cooling.

## References


1. J.S. Fraser, G.E. McMichael, J. McKeown and S.H. Kidner, "The Chalk River Electron Test Accelerator", Proc. of 1972 Proton Linear Accelerator Conference, LA-5115, p.226.
2. J. McKeown, R.T.F. Bird, K.C.D. Chan, S.H. Kidner and J.-P. Labrie, "High Power, On-Axis Coupled Linac Structure", Proc. of the 1981 Linear Accelerator Conference, Santa Fe, NM, LA-9234-C, 332 (1982).
3. L.M. Young and J.M. Potter, "CW Side-Coupled Linac for the Los Alamos/NBS Racetrack Microtron", IEEE Trans. Nucl. Sci., NS-30 (4), 3508 (1983).
4. J.-P. Labrie, H. Euteneuer and J. McKeown, "Energy Gradient Limits in Room Temperature CW Linacs", this conference.
5. H. Euteneuer, "Design, Performance and Blow-up Properties of the MAMI Structure", Proceedings on the Conference on Future Possibilities for Electron Accelerators, University of Virginia, January 1979, P-1.
6. N. Bowen, A. Bohr, H. Burrin, J.O. Lawson, W. Newman and F. Schnabl, "2.45 GHz System for Lower Hybrid Current Drive" on the Princeton Large Torus, Princeton University internal report.
7. LOOPX, A Coupled-Loop Circuit Model Computer Code, written by S.O. Schriber, CRNL.
8. Hermosa Electronics, California 94025.
9. K.R. Crandall, private communication.
10. K.C.D. Chan, internal communication, CRNL.

880　Nuclear Instruments and Methods in Physics Research B24/25 (1987) 880–883
North-Holland, Amsterdam

# THREE-DIMENSIONAL FINITE ELEMENT HEAT TRANSFER AND THERMAL STRESS ANALYSIS OF RF STRUCTURES

Truc TRAN NGOC, Jean-Pierre LABRIE and Saleh BASET

*Atomic Energy of Canada Limited, Research Company, Chalk River Nuclear Laboratories, Chalk River, Ontario, Canada K0J 1J0*

Thermal expansion and thermal stress induced strain cause the detuning and limit the power level of radiofrequency (rf) structures. Two-dimensional finite element modeling has been used to determine the operating power limits of coupled cavity systems [1], but for complex high power accelerator structures without axial symmetry, a three-dimensional analysis is necessary. This paper describes results of a three-dimensional finite element temperature and thermal stress analysis. The analysis was performed for a high power coupled cavity linac structure operating at 1350 MHz. The results of the analysis are used to determine changes in the structure rf parameters as a function of power level and cooling water velocity.

## 1. Introduction

Two dimensional finite element thermal stress analysis has been used to determine the power handling capability of coupled cavity linac structures [1]. Some rf structure geometries do not have axial symmetry and hence a three-dimensional analysis is required. In this paper, a 1350 MHz on-axis coupled cavity with complex cooling circuits and coupling slots is analyzed using three-dimensional modeling techniques. This allows a more accurate study of the deformation and stress patterns which cause the detuning, limit the operating power level and determine the behaviour of the rf structure. The results from the heat transfer and thermal stress analyses have been used for a parametric study of the changes in rf parameters as function of coolant flow velocity and power level.

## 2. Description of the linac structure and the finite element model

The 1350 MHz accelerator structure is made from OFHC copper. Fig. 1 shows the structure and its cooling circuits. Each segment of the structure consists of one-half accelerating cavity and one-half coupling cavity, it has an outside diameter of 200 mm and a thickness of 56 mm. The cooling circuits are composed of a series of 20 through flow circumferential cooling channels (10 mm diameter), 4 web headers (10 mm diameter)

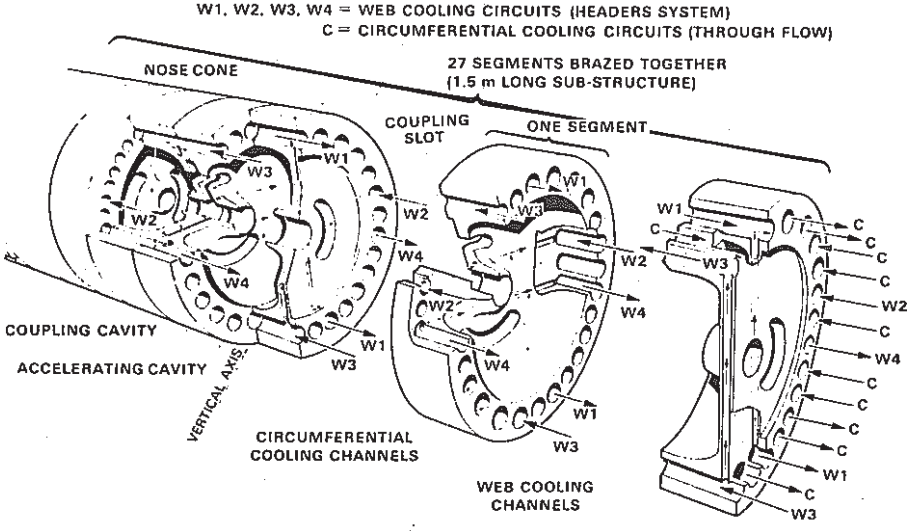


Fig. 1. Cooling circuits of the 1350 MHz on-axis coupled structure.

0168-583X/87/$03.50 

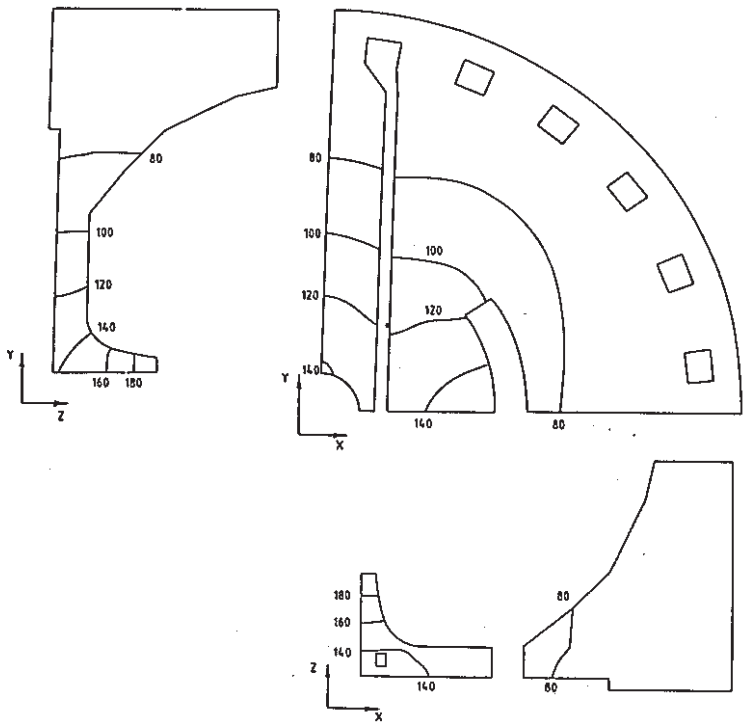


Fig. 3. Isotherms on selected faces of the cavity at a power level of 150 kW/m. A uniform initial temperature of 40 ° C was assumed (temperature in ° C).

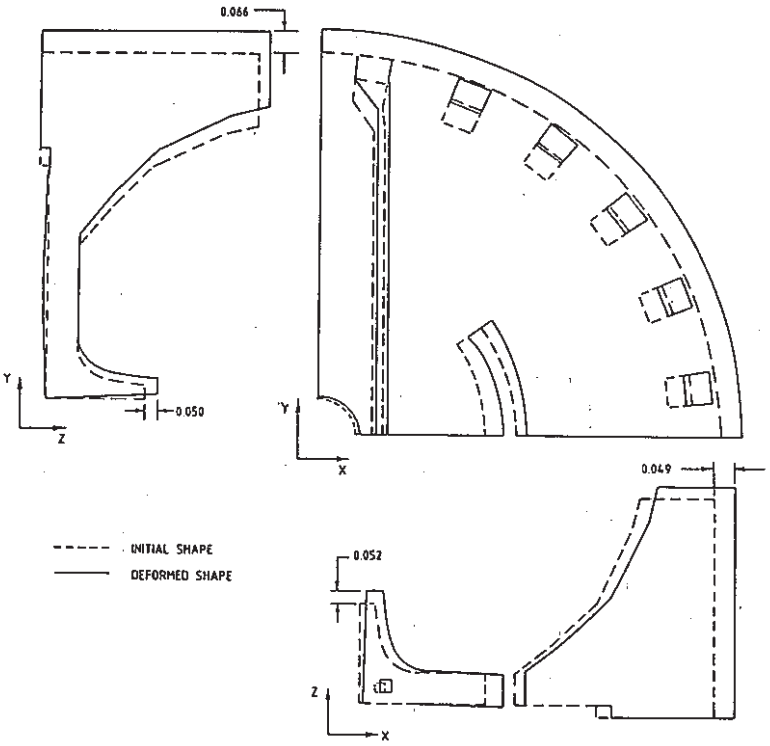


Fig. 4. Cavity deformation at a power level of 150 kW/m (displacements in mm).

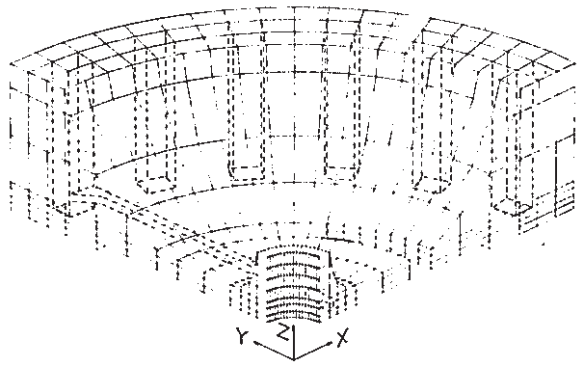


Fig. 2. The three-dimensional finite element model of a rf cavity segment.

and 2 web channels (3 mm diameter). The circuits are arranged in counterflow to minimize temperature differences in the structure.

Due to symmetry, only one quarter of a full segment needs to be modeled. The three-dimensional finite element model is shown in fig. 2. A total of 1117 elements and 1638 nodes are required. First order isoparametric, 8-node elements are used with 1 and 3 degrees of freedom per node for the heat transfer and thermal stress analyses respectively. The circular cooling channels were approximated by a quadrilateral hole with the same total heat transfer surface area.

The computer code SUPERFISH [2] was used to calculate the rf generated heat fluxes on the surface of the accelerating cavity. The power distribution is axisymmetrical and varies from a maximum of 16.5 W/cm$^2$ at the nose cone to 5.9 W/cm$^2$ at the maximum radius of the accelerating cavity for a power level of 50 kW/m. Average film heat transfer coefficients and cooling water temperatures of each channel, estimated from a thermohydraulic analysis of the whole structure, vary nonlinearly with the power level. The thermal expansion coefficient is given as a linear function of temperature between 0 and 300°C, all other material properties are specified at a reference initial temperature of 40°C. Convective cooling around the outer perimeter of the structure is neglected.

### 3. Discussion of the results

Detailed results of the analysis are presented for the case of 150 kW/m power level with a cooling water velocity of 3 m/s. They are given in figs. 3, 4 and 5 on three different views, i.e., *XZ*, *YZ* faces and a cross-section in the *XY* plane through the web wall of the cavity (see fig. 2).

Fig. 3 gives the temperature distribution in the cavity wall. As expected, the temperature is highest at the nose tip and lowest at the maximum radius. Although the temperature profile remains fairly axisymmetrical in the circumferential and nose cone areas, some perturbations could be noticed in the web wall of the cavity. In the region between the beam aperture and the coupling slots, the presence of web cooling channels contributes to reduction of the temperature which otherwise would be higher due to the discontinuity in the conduction heat path at the gap.

Fig. 4 shows the deformed shape of the cavity wall under thermal loading and reveals the following:

(1) At the central area of the coupling slot the deformed gap dimension is reduced. This causes a reduction in the first neighbour coupling coefficient of the cavities.

(2) The beam aperture has deformed nonuniformly in the *Z* direction; it has tapered off from the accelerating cavity toward the coupling cavity. A cross-sectional view of the beam aperture in the *XY* plane shows some ellipticity in the radial deformation. This introduces some changes in the accelerating field azimuthal distribution.

(3) The web wall is subjected to some degree of warping that buckles it up toward the coupling cavity side and hence reduces the volume of the latter. At the center of the coupling slot, it causes some offset shearing movement of the web walls. This introduces changes in the structure stopband frequency gap.

(4) The outer diameter of the cavity expands slightly more in the *Y* than in the *X* direction.

The general behaviour of the cavity noted above is due to the relatively free movement of the web wall at the coupling slots. This discontinuity enables the internal stresses to be relieved by more radial motion of the web wall. The buckling of the web wall described in (3) is due to a combination of the bending moment transmitted from the expanding nose cone and a relatively low thermal expansion of the massive, cooler circumferential area. The tapered deformation of the beam aperture is due to the strong variation of the temperature profile in the nose cone.

Von Mises stress contours obtained from an elastic analysis of the cavity are shown in fig. 5. These should be compared to the yield point of the cavity material, $\sigma_y = 69$ MPa. Stresses vary significantly on the surface of the beam aperture and are highest in the *XZ* plane on the coupling cavity side. For example, the maximum stress at a power level of 150 kW/m is 146 MPa which exceeds the fictitious elastic limit of $2\sigma_y$ for a self-limiting load [3]. Therefore this part of the cavity wall will undergo plastic deformation every time the thermal cycle is applied. In the zones where stresses stay between $\sigma_y$ and $2\sigma_y$, plastic deformation only occurs in the first thermal cycle; the structure is allowed to shake down to an elastic response during the subsequent cycles.

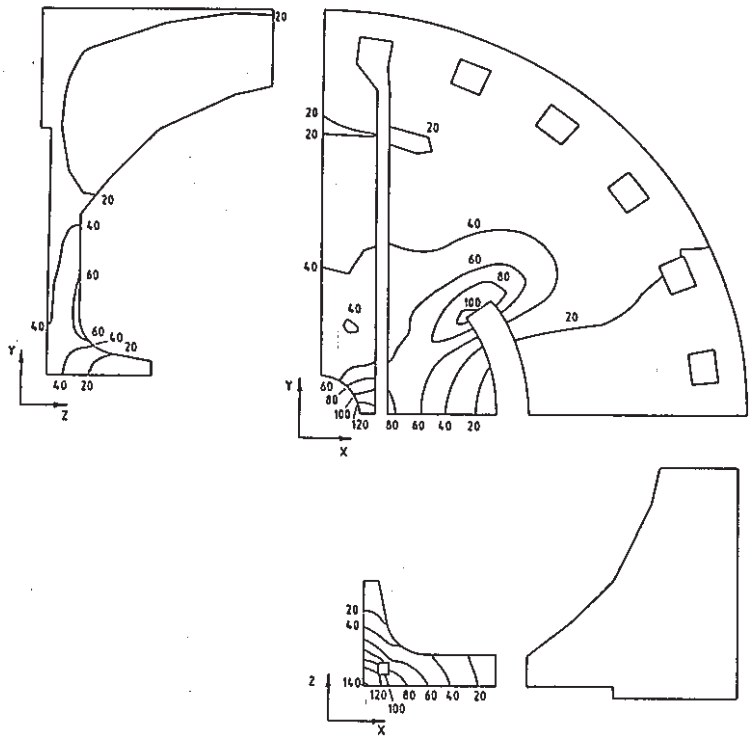

Fig. 5. Von Mises stress contours in the cavity wall at a power level of 150 kW/m (stresses in MPa).

Due to stress concentration, stresses are also high at the ends of the coupling slots. This is enhanced by the squared corner coupling slot on the finite element model. The real stress pattern would differ somewhat with the one shown in fig. 5 if an elastic-plastic analysis had been carried out for the cavity.

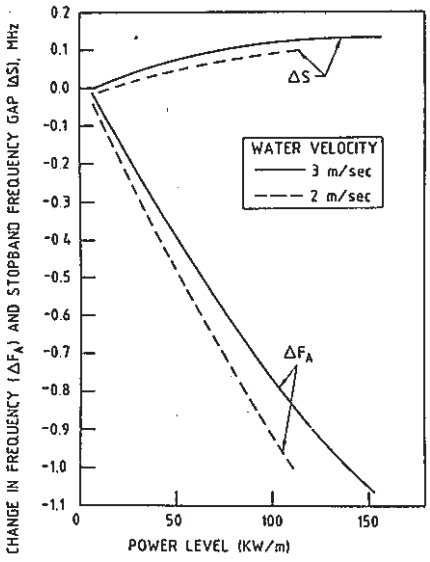


Fig. 6. Variation of rf frequency and stopband frequency gap as a function of power level and cooling water velocity.

The frequency shift and the change of the stopband frequency gap have been calculated and results are shown in fig. 6 as function of power level for two cooling water velocities. Results are in general agreement with measurements on a similar structure operating at 2450 MHz [1].

## 4. Conclusion

This paper demonstrates the capability and usefulness of three-dimensional modeling in heat transfer and thermal stress analysis of complex accelerator structures. The technique allows a more accurate study of the behaviour of a 1350 MHz on-axis coupled structure. It exposes interesting features that could not have been obtained from an analysis using only axial symmetry and has the capability for the analysis of more complicated rf structures.

## References

[1] J.-P. Labrie and H. Euteneuer, Nucl. Instr. and Meth. A247 (1986) 281.
[2] K.H. Halbach and R.F. Holsinger, Part. Accel. 7 (1976) 213.
[3] H. Henry and P.E. Bednar, Pressure Vessel Design Handbook (Van Nostrand Reinhold Company, 1981).

# 資料７－４　1988年ヨーロッパ加速器会議のＩＭＰＥＬＡ報告

## IMPELA: AN INDUSTRIAL ACCELERATOR FAMILY

J. Ungrin, N.H. Drewell, N.A. Ebrahim, J-P. Labrie,
C.B. Lawrence, V.A. Mason, and B.F. White

Atomic Energy of Canada Limited, Research Company
Chalk River Nuclear Laboratories
Chalk River, Ontario, Canada KOJ IJO

### Summary

The IMPELA family of industrial accelerators is being developed by AECL to complement its isotope-based irradiators. These accelerators use an on-axis coupled standing wave structure and operate in the long pulse mode. The first member of the family, IMPELA-10/50 (10 Mev, 50 kW), is now being assembled.

### Introduction

The use of electron accelerators in industry has grown rapidly over the past two decades and it is estimated that in excess of 40 MW of electron beam power is now installed in the world for industrial applications. This growth in demand has been accompanied by an increase in the power of individual units. Accelerators already exist with beam powers in the 100-200 kW range; however, the technologies commonly in use for these high power machines limit their energy to less than 5 MeV and therefore limit the penetration of beams to thicknesses equivalent to 2-3 g/cm$^2$. The rf linear accelerator, which has had many years of development for research and medical therapy applications, is the only technology tested in diverse applications that is capable of producing higher energy beams at the power and reliability levels required.

A small number of rf linacs have been operated in industry over the past 20 years but the power levels available from these have generally been less than 10 kW. Atomic Energy of Canada Limited, the world's largest supplier of industrial irradiators, has recognized this need for higher power accelerators in the energy range above 5 MeV [1,2] and is developing a family of rf linacs engineered specifically for the industrial market.

Accelerators used in industry place special demands on their designers. The need for a small energy spread and good emittance normally placed on research machines is replaced by requirements of high reliability, ruggedness, simplicity of operation, high dose uniformity and economy. The IMPELA (Industrial Materials Processing Electron Linear Accelerator) family of linacs is designed specifically to address these requirements.

This family of accelerators, controlled by industrial computers, is based on standing wave, L-band, on-axis coupled linacs operated in the long pulse mode. A modular design approach is used to achieve beam powers in the range of 20-500 kW at various energies, with the same basic components coupled to the required power supply and klystron. The long pulse approach with modest accelerating gradients has been chosen as the most appropriate for industrial applications. This approach is intermediate to the high-gradient short-pulse systems used in the medical field and the lower gradient systems used in research accelerators. The desired range of power can be achieved using the same components by increasing the duty factor from 1-2% to cw operation while maintaining the same beam loading and peak stress levels from one accelerator to the next.

The first member of this accelerator family, IMPELA-10/50 (10 MeV, 50 kW) is now being constructed at the Chalk River Nuclear Laboratories in the shielded enclosure that formerly housed the 4 MeV, 80 kW Electron Test Accelerator (Fig. 1). The 50 kW average beam power is achieved by operating the accelerator at a nominal duty factor of 5% (200 μs pulses at a pulse repetition frequency of 250 Hz). This paper describes the major sub-systems and reports the construction status. A companion paper at this conference describes the control system for the prototype accelerator in greater detail [3].

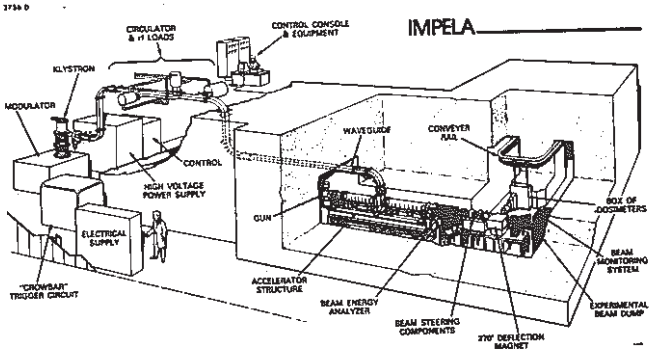


Fig. 1: Cut-away artist's conception of IMPELA-10/50

### Accelerator Design

#### Injector

The IMPELA family is designed for direct injection at a relatively low voltage, 40 kV, from an electron gun with triode geometry, mounted directly on the accelerating structure. To achieve the rf system simplicity essential for industrial applications no prebunching of the beam is used. Commercially available 0.5 cm$^2$ dispenser cathodes are used in the electron gun. Both gridded and ungridded cathodes are being tested.

The cathode is held at the dc injection voltage and beam pulses are formed by pulsing the control element voltage relative to the cathode. Fine control of the beam current is achieved by adjusting the bias of the control element pulse-to-pulse. The pulse length and repetition frequency can be readily adjusted to meet the duty factor required of the accelerator. The pulser and dc power supply are located in a high voltage cabinet outside the accelerator vault away from high radiation fields.

The gun housing design facilitates rapid replacement of the cathode and maximizes vacuum pumping speed in the cathode region. A short gap lens and a set of steering coils are incorporated in the gun assembly. The total drift distance from the cathode surface to the centre of the first accelerating cell is only 20 cm.

The beam requirements for the IMPELA family have been kept relatively conservative. IMPELA-10/50 will produce the rated power at a 5% duty factor with a beam current of only 100 mA. Using a typical beam transmission of 25% through an accelerator without a buncher translates to a modest injection current of

400 mA. A transmission of >40% has been achieved on a similar short pulse 13 MeV, 4 kW S-band linac at CRNL through the addition of a short focussing solenoid over the structure. A similar solenoid will decrease the gun current requirements on the IMPELA-10/50 below this estimate.

Accelerating Structure

The accelerating structure chosen for the IMPELA family is the on-axis coupled cavity, standing wave structure which has been developed and extensively investigated at the Chalk River Nuclear Laboratories [4]. A low duty factor, 3 GHz version of this structure is used on a 10 MeV, 1 kW industrial irradiator, the I-10/1, which is now in operation at the Whiteshell Nuclear Research Establishment [5].

A modular approach has been adopted for the accelerating structure. With this approach an optimum accelerating gradient and high beam loading can be chosen for any particular combination of energy and beam power. Three types of structure modules, graded beta, constant beta and rf coupling, are used. The modules terminate at the centre of an accelerating cell and are bolted together to form a single rf and vacuum cavity. The vacuum seal is made with conventional (ConFlat) flanges that are furnace-brazed to the structure modules during assembly. The flanges also provide the mechanical pressure for the copper-to-copper rf seal formed at the cell wall and are used as headers for the water cooling system. The MAMI accelerating structure at the University of Mainz [6] (2.45 GHz) which used this assembly technique has been operated successfully at 100% duty factor.

The prototype IMPELA-10/50 accelerator consists of 58 cavity segments, joined in four modules to form 29 accelerating and 28 coupling cavities. The injection module consists of four graded-beta accelerating cavities. It is followed by two constant-beta modules which are separated by the coupler module. The total length of the structure is 3.25 m corresponding to a conservative accelerating gradient of 3 MeV/m.

The accelerating cavity geometry has been optimized at 1.3 GHz for the large 19 mm diameter axial hole using SUPERFISH. The shunt impedance and Q for the structure, calculated neglecting the effect of coupling slots and pumping ports, are 67 MΩ/m and 24 500, respectively. Low-power rf measurements on the assembled structure indicate that ~85% of these theoretical values have been achieved. A relatively large cell-to-cell coupling constant of 7.6% has been used to ensure field flatness along the full length of the structure.

Based on the measured shunt impedance, the peak rf structure power for IMPELA-10/50 is 540 kW. With the nominal duty factor of 5% and a 100 mA beam current, the beam loading is ~65%. The coupling of the waveguide to the structure has been adjusted to an initial VSWR of 2.8 to achieve near-critical coupling at this loading level.

Extensive finite-element thermal analyses of the IMPELA structure with the computer code MARC have been used in the design of the cavity cooling to ensure stable, distortion-free operation up to a 100% duty factor. The integrated SUPERFISH and MARC calculations, lead to a design where the structure is cooled with a series of counterflowing circuits which are an integral part of the cavity segments. Two long web cooling channels are used in each segment to minimize the shift in the cavity frequency with power. The predicted shift in frequency over the range from zero to full rf power is less than 70 kHz for IMPELA-10/50.

The assembled structure is mounted on a strongback and vacuum manifold (Fig. 2). A vacuum manifold that provides a very high pumping capacity is used with this prototype structure to accommodate the wide range of experiments planned to investigate its operating limits. The vacuum manifold is connected to the structure at five points and is pumped by a 60 L/s ion pump supplemented by a titanium sublimation pump. An 8 L/s ion pump is mounted on the coupling module just below the rf window to ensure good pumping in this critical area.

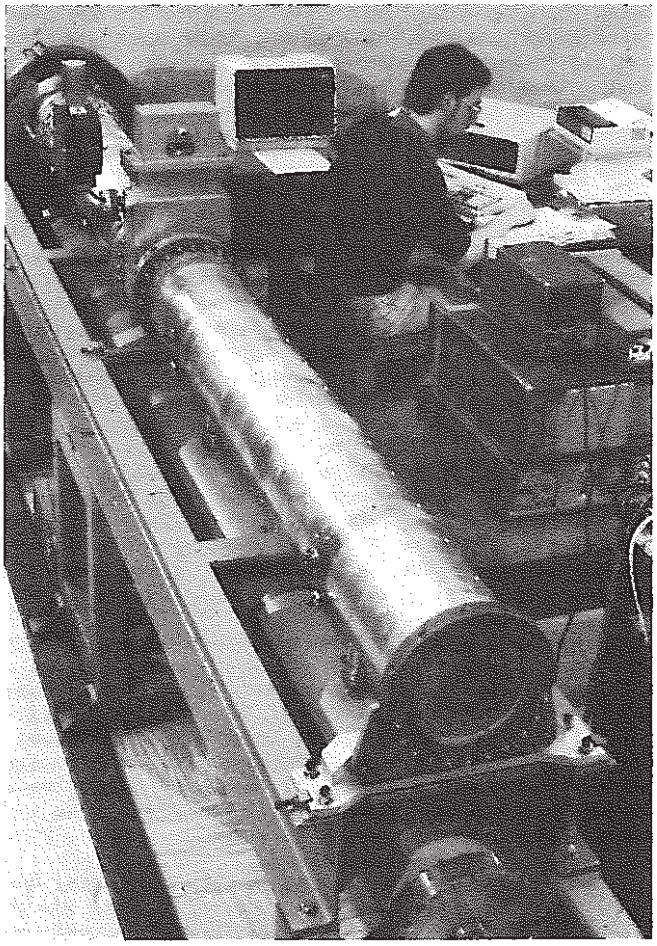

Fig. 2: Assembled four-module IMPELA-10/50 structure.

Radio Frequency System

The IMPELA family is based on a long pulse rf system using modulated anode klystrons. With this approach the same low-stress design and efficient beam loading can be maintained across a wide range of average power by varying either the pulse length, the pulse repetition frequency, or both.

A simplified schematic diagram of the IMPELA-10/50 rf system is shown in Fig. 3. The main klystron is a 2 MW peak, 150 kW average TH2115 klystron developed for the IMPELA program by THOMSON-CSF. The drive for this klystron is provided by a 1 kW TH2437 klystron which acts as an amplifier for the voltage controlled oscillator and input control circuitry. The accelerating cavity rf field strength is chosen to set the beam energy and is controlled by independent loops to keep the field amplitude and frequency at a constant level.

The TH2115 klystron typically requires an 82 kV 55 A pulse to produce the peak output of 2 MW. This pulse is provided by a 100 kV, 4 A dc power supply

which is coupled to four 1 μF capacitors. The capacitors are located in a 2.7x1.5x1.3 m high oil tank that also contains the modulator, the klystron filament supply and supports the klystron. The stored energy in the capacitors at 90 kV is a relatively modest 16 kJ. The size of the capacitor bank was chosen as a compromise of size, stored charge and voltage droop during the long pulse.

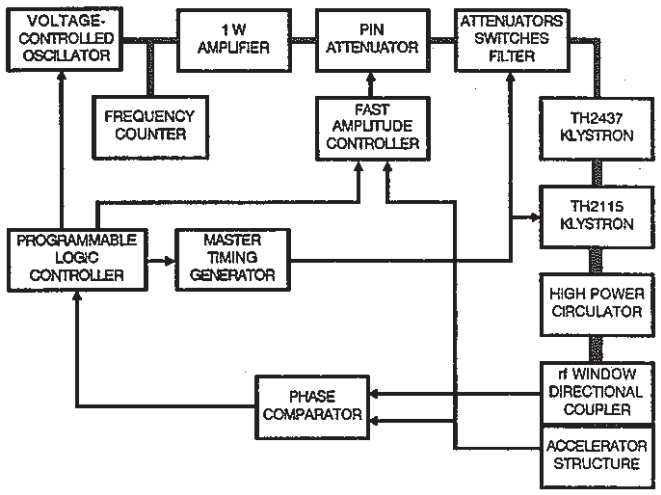


Fig. 3: Simplified diagram of 1.3 GHz, 2 MW rf system.

The design of the modulator follows closely that used on the Millstone Hill Radar Site [7]. One major difference is in the use of a single switch tube and a pull-down resistor instead of two switch tubes. The switch tube used is a TH5188 tetrode.

Power from the TH2115 klystron is fed to the accelerator through 15 m of WR650 waveguide pressurized with $SF_6$. The klystron is isolated by a high power THOMSON-CSF circulator which is designed to sustain a continuous VSWR of 3.0.

Two protective systems are used on the IMPELA-10/50 to ensure that the energy deposited in the klystron by a potential internal arc is kept below a damage threshold of 20 J. The first system uses a high-speed triggered crowbar to divert the energy from the klystron. The second uses surge resistors rated for high energy in series with the klystron to limit the fault current to 2 kA and thereby limit the arc voltage to <30 V [8].

Beam Delivery System

IMPELA-10/50 is designed to deliver the beam over an 80 cm wide zone 15 cm from the end of a scan horn with a dose variation, at a depth of 2 cm in water, not to exceed ±5%. The beam is scanned in a plane orthogonal to the accelerator axis and will be available either at 0° or at 90° after a bend through 270°. A 270° bending system ensures that high energy photons from the scraping of electrons with energy exceeding 10.0 MeV are directed away from the product as is required if the accelerator is used for food irradiation [9].

The initial beam delivery system will produce a spot scan at 0° at the end of a 1.3 m scan horn with a scan frequency of ~5 Hz. The optical design of this system has been developed using the TRANSOPTR code with phase-space parameters determined from modeling the beam dynamics through the linac with PARMELA. A 10 cm diameter beam spot is obtained at the air/vacuum window with careful matching of the dispersal and scanning magnets. The beam exits through a 0.13 mm thick titanium window. Heating effects and thermal stresses in the window have been modeled using the MARC code. The effects of scattering by the window and air are calculated with the COPSI code [10].

The modular approach for the IMPELA family has been incorporated in the physics and engineering design of the major components of the beam delivery system. The scan horn assembly can be used in both the 0° and 270° configurations.

The prototype accelerator differs from future production accelerators in that it incorporates a 45° analyzing magnet in the 0° line for measurements of the energy spectrum under various operating conditions. No provision is made in the present shielded cell for a product conveyor and maze but extensive diagnostics for on-line monitoring of exposure dose distributions has been incorporated.

Control System

The control system for IMPELA-10/50 is based on an industrial programmable logic controller with a distributed input/output system. Custom electronic modules have been developed for interfacing the sensors that are unique to pulsed accelerators, the machine protection systems and the fast rf feedback control loop. The hard-wired personnel safety system is fully separate from the control system.

A separate paper at this conference describes the control system in detail [3].

## Status

As of 1988 June 01, the accelerator structure is fully assembled and ready for final installation in the shielded tunnel. The rf system is 90% assembled and delivery of the klystron is expected within several weeks. The PLC is installed and the programming required for rf testing of the klystron is essentially complete. Acceptance tests of the klystron are expected to be complete in August and first beam from the accelerator is scheduled in 1988 December.

## References

[1] J. McKeown, J-P. Labrie and L.W. Funk , "An Intense Radiation Source", Nucl. Inst. & Meth. B10/11, (1985), 846.

[2] J. McKeown, "Radiation Processing Using Electron Linacs", IEEE Trans. Nucl. Sci., NS-32, (1985), 3292.

[3] C.B. Lawrence et al., " The IMPELA Control System", paper presented at the 1988 EPAC conference, to be published in a special edition of Nuovo Cimento.

[4] J-P. Labrie and H. Euteneuer, "Power Handling Capability of Water Cooled CW Linac Structures", Nucl. Inst. & Meth. A247, (1986), 281.

[5] G.E. Hare, "The I-10/1 Electron Linear Accelerator For Irradiation Research and Pilot Scale Operations", Radiat. Phys. Chem., V31, (1988), 309.

[6] H. Euteneuer, private communication.

[7] B. Norander, private communication.

[8] G.R. Mitchell, "High-Current Vacuum Arcs", Proc. IEEE, V117, (1970), 2315.

[9] United Nations Food and Agriculture Organization/W.H.O. Codex Alimentarius Commission; Codex Alimentarius, Vol XV, (1984), CODEX-STAN 106-1983.

[10] G.E. Lee-Whiting and G.A. Petrovich, "The Program COPSI", Atomic Energy of Canada Limited Report AECL-9502, (1987).

資料７－５

# SPALLATION & RADIATION PHYSICS AT CRNL

(M.A. Lone)

- INTRODUCTION
- SPALLATION - N SOURCE
- SPALLATION - BREEDER
- HLW - TRANSMUTATION

# INTRODUCTION

# SPALLATION & RADIATION PHYSICS AT CRNL

SCOPE

## SPALLATION PHYSICS

- a specific nuclear reaction process
- light charged particle projectile
- prolific neutron source
- prolific nuclear transmutation of target — Fissile Breed / Incineration

## RADIATION PHYSICS

- physical characteristics of radiation
- production - source characteristics
- detection - dosimetry
- interactions with matter
    - induced activity
    - fissile material breeding
    - transmutation
- applications in industrial processing
    - process configuration optimization

# OBJECTIVES

## LONG TERM

ENHANCE NUCLEAR POWER OPTION
- advanced CANDU fuel cycle
  - thorium cycle
  - electro-nuclear breeding

(-) high level waste management
  - nuclear transmutation & neutralization

## SHORT TERM

ESTABLISH ADVANCED INDUSTRIAL TECHNOLOGIES
- high power accelerators
- industrial processing
- isotopes

ADVANCED NEUTRON SOURCES
- research
  - physics
  - material sciences
  - nuclear engineering

# STRATEGY I

## 1952 - 1968

### DEFINE REFERENCE DESIGN FOR DEMONSTRATION SPALLATION SOURCE

- develop & validate spallation physics theory/codes/data base
- establish spallation source characterisitics
- high current accelerator technology scope
- reference design of intense neutron generator (ING)
  - 1 GeV proton
  - 65 mA
  - Pb-Bi eutectic target
  - $10^{19}$ n/s yield
  - $10^{16}$ n/cm$^2$·s thermal neutron flux

# STRATEGY II

## 1969 - 1984

## MULTI-STAGE PLAN

## REFERENCE DESIGNS FOR MID-STREAM DEVICES

- **RFQ**

- **CANUTRON 2.5 MeV - 10 mA - Protons**
  - **clean neutron source for radiography**

- **ZEBRA 10 MeV - 300 mA**
  - **zero energy breeder accelerator**
  - **neutron source for materials testing**

- **EMTF 200 MeV - 70 mA**
  - **electro-nuclear materials test facility**
  - **source for research and target development**

- **AB 1000 MeV - 70 mA**
  - **pilot accelerator breeder (ING with new name)**

# SPALLATION - N SOURCE

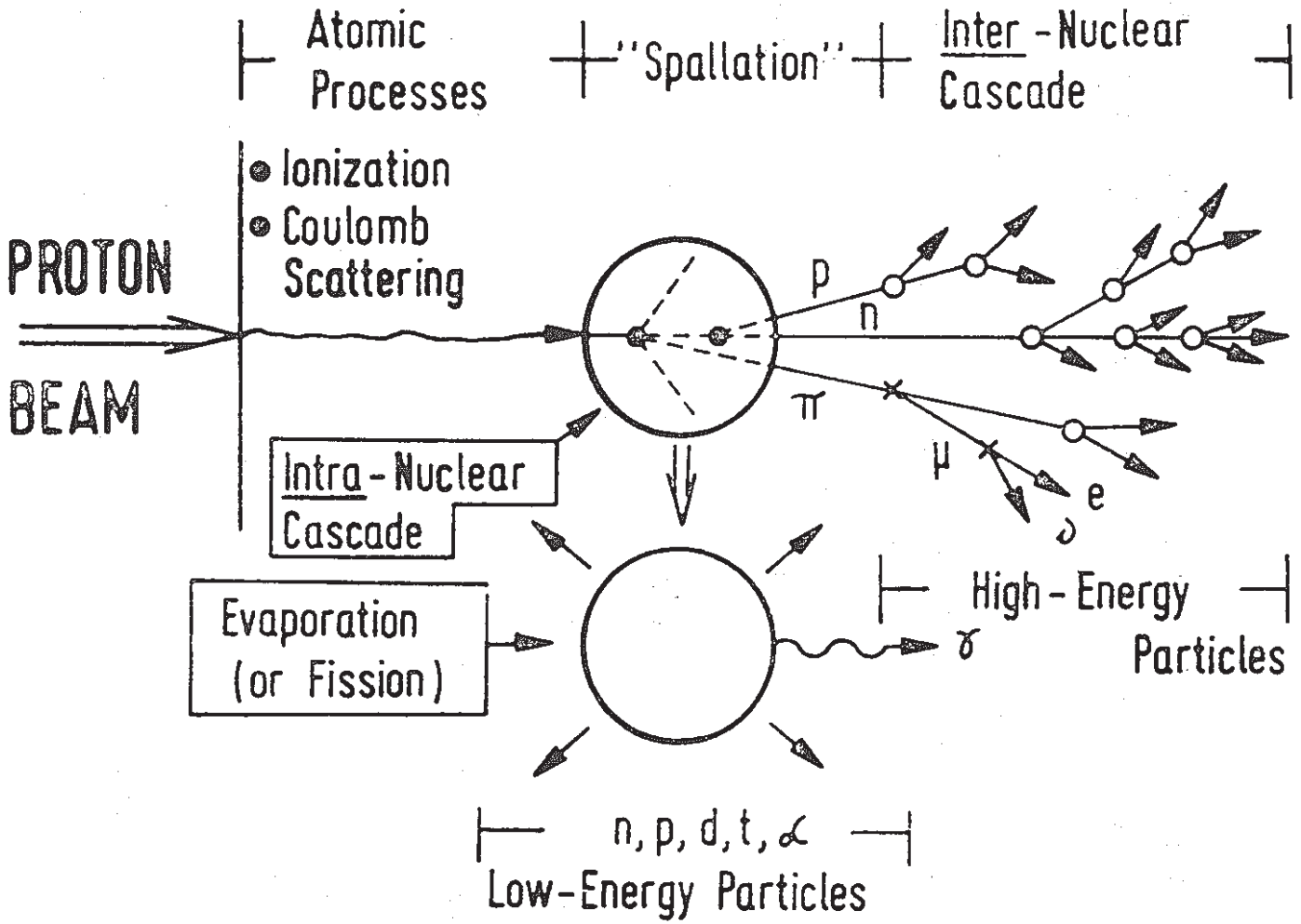
Atomic Processes
"Spallation"
Inter-Nuclear Cascade
Ionization
Coulomb Scattering
PROTON BEAM
p
n
π
μ
e
Intra-Nuclear Cascade
Evaporation (or Fission)
High-Energy Particles
γ
n, p, d, t, α
Low-Energy Particles

# SPALLATION REACTION -PROTON BEAM

## PROBABILITY Pn OF NUCLEAR REACTION IN Pb TARGET

| E (MeV) | RANGE R(g/cm$^2$) | R/$\lambda$ | Pn |
|---|---|---|---|
| 100 | 17 | 0.09 | 0.08 |
| 300 | 105 | 0.54 | 0.42 |
| 500 | 230 | 1.2 | 0.70 |
| 800 | 458 | 2.3 | 0.90 |
| 1100 | 705 | 3.6 | 0.97 |

$Pn = 1\text{-}exp(-R/\lambda)$

Interaction length $\lambda = 33\ A^{0.33}\ g/cm^2;\ E > 100\ MeV;\ A > 1$

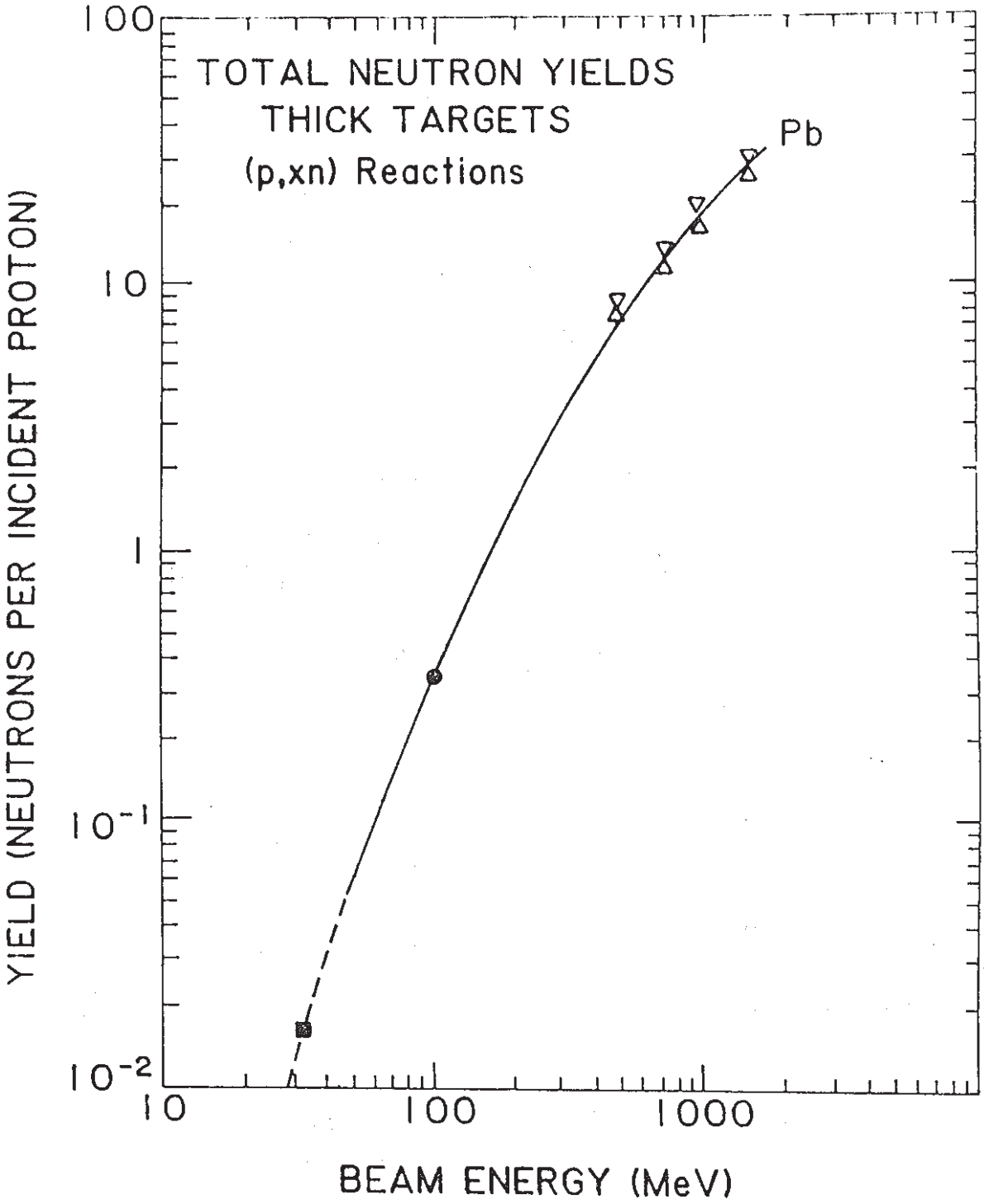
TOTAL NEUTRON YIELDS
THICK TARGETS
(p,xn) Reactions
Pb
100
10
1
10⁻¹
10⁻²
YIELD (NEUTRONS PER INCIDENT PROTON)
10
100
1000
BEAM ENERGY (MeV)

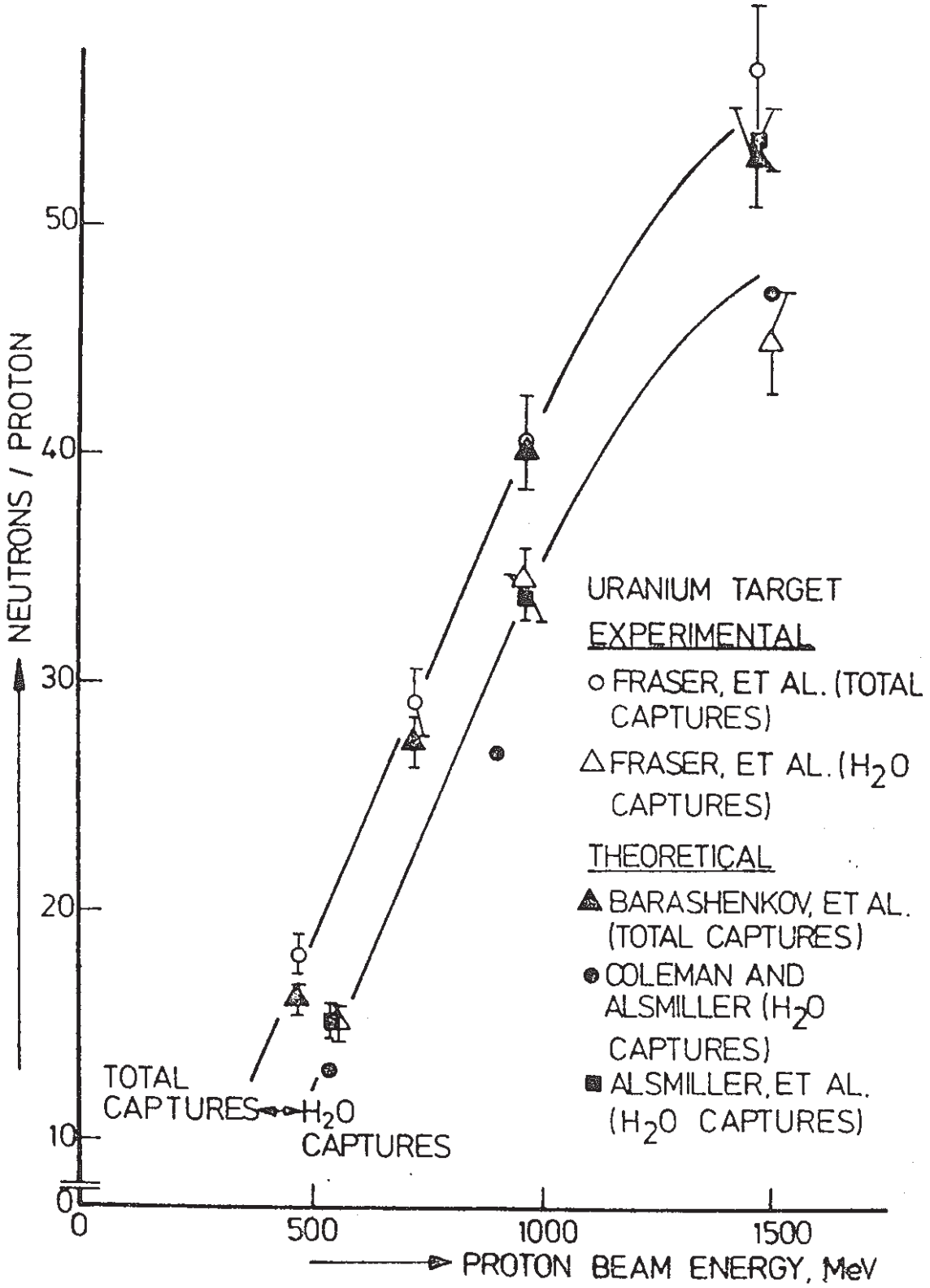
NEUTRONS / PROTON
50
40
30
20
10
0
0
500
1000
1500
PROTON BEAM ENERGY, MeV
TOTAL CAPTURES
$H_2O$ CAPTURES
URANIUM TARGET
EXPERIMENTAL
FRASER, ET AL. (TOTAL CAPTURES)
FRASER, ET AL. ($H_2O$ CAPTURES)
THEORETICAL
BARASHENKOV, ET AL. (TOTAL CAPTURES)
COLEMAN AND ALSMILLER ($H_2O$ CAPTURES)
ALSMILLER, ET AL. ($H_2O$ CAPTURES)

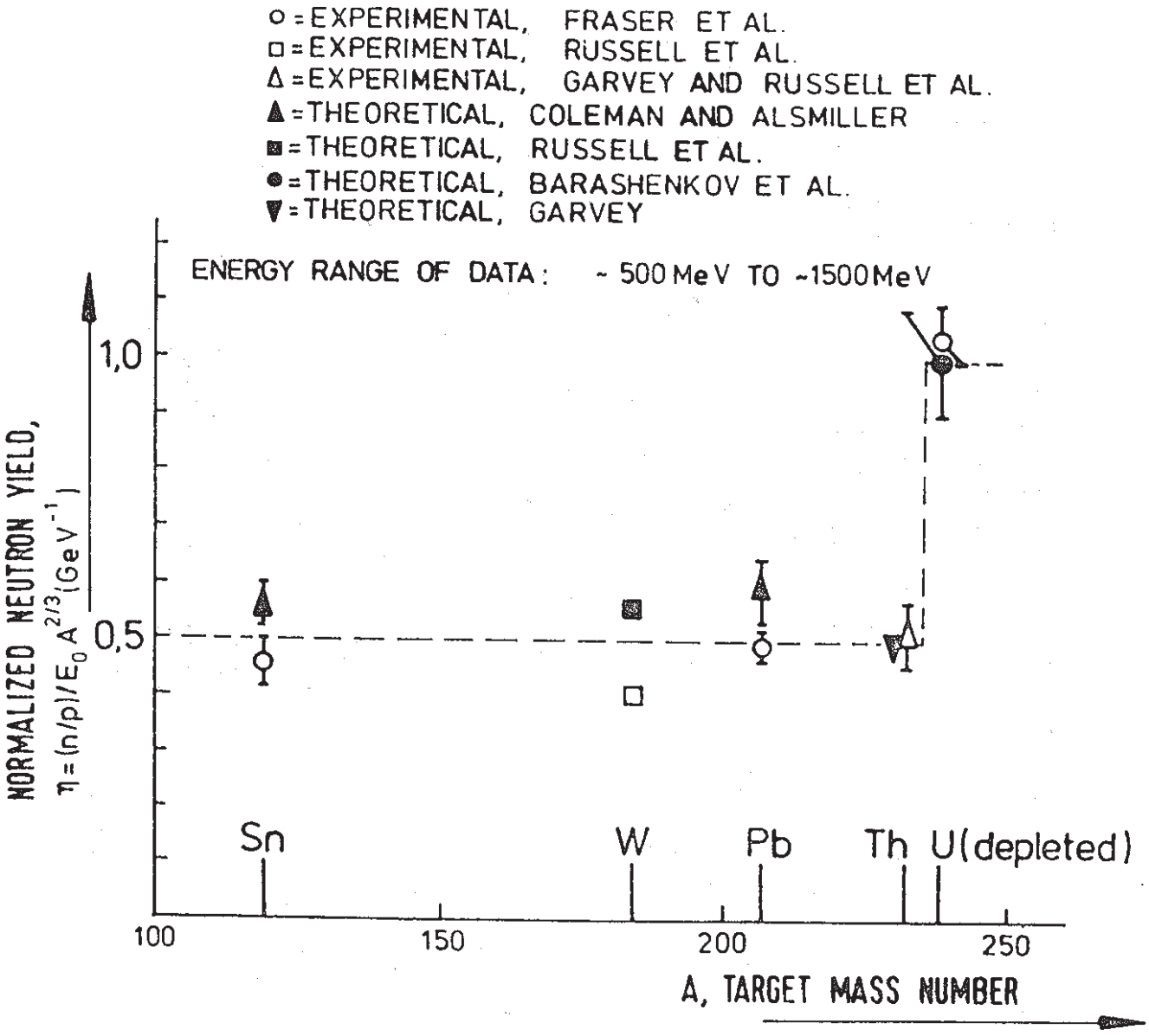
○ = EXPERIMENTAL, FRASER ET AL.
□ = EXPERIMENTAL, RUSSELL ET AL.
Δ = EXPERIMENTAL, GARVEY AND RUSSELL ET AL.
▲ = THEORETICAL, COLEMAN AND ALSMILLER
■ = THEORETICAL, RUSSELL ET AL.
● = THEORETICAL, BARASHENKOV ET AL.
▼ = THEORETICAL, GARVEY
ENERGY RANGE OF DATA: ~ 500 MeV TO ~1500 MeV
NORMALIZED NEUTRON YIELD,
$\eta = (n/p)/E_0 A^{2/3} (GeV^{-1})$
1,0
0,5
Sn
W
Pb
Th
U(depleted)
100
150
200
250
A, TARGET MASS NUMBER

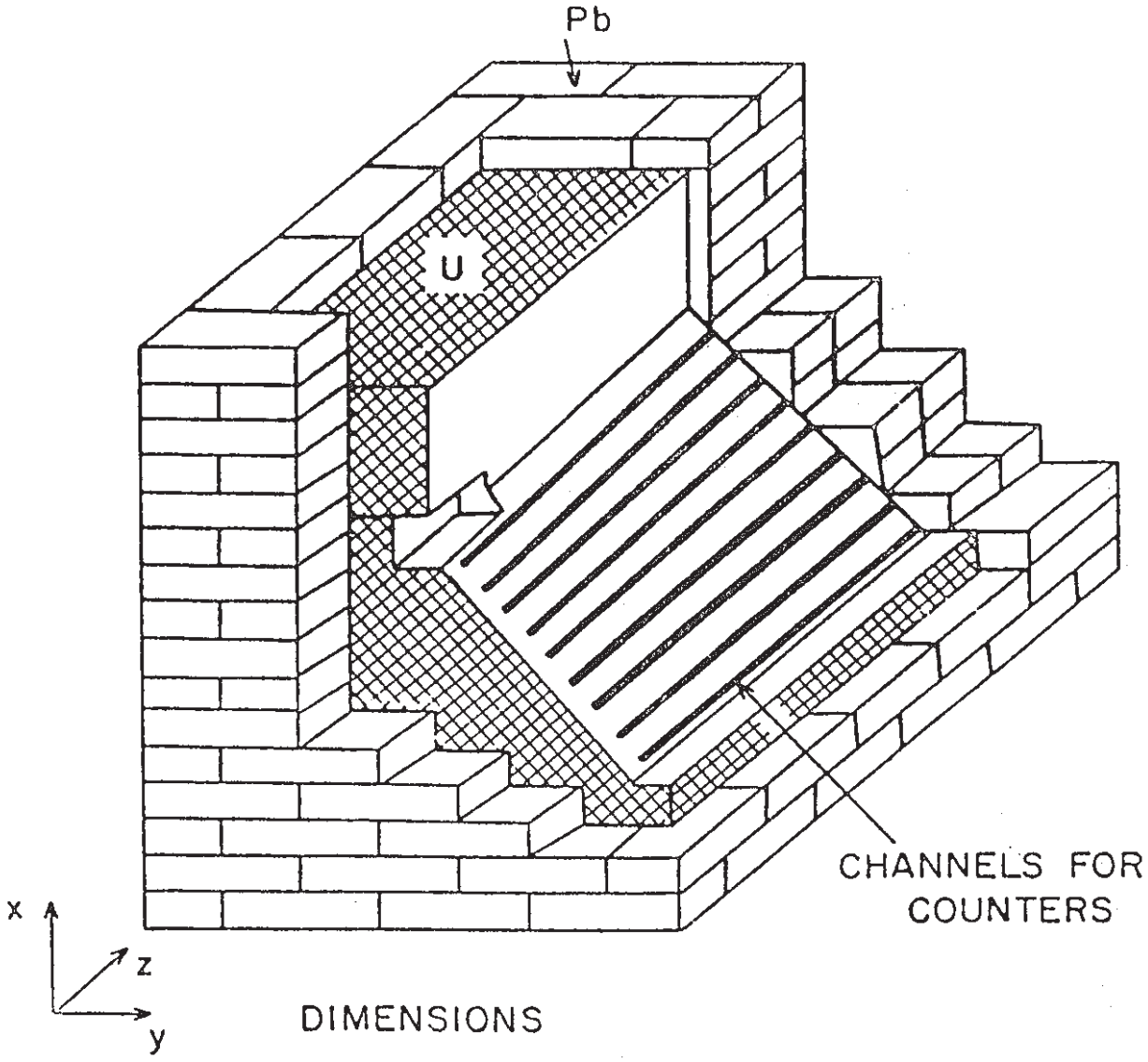


DIMENSIONS

CORE: $56 \times 56 \times 64\ cm^3$

BEAM HOLE: $8 \times 8 \times 16\ cm^3$

WIDTH OF Pb WALL: 10 cm OR 20 cm

PROTON BEAM DIAMETER: 4~5 cm

# SPALLATION REACTION

## DEPLETED $^{238}U$ EXTENDED TARGET

| PROCESS | E(MeV) | (PER PROTON) EXPERIMENT | THEORY |
|---|---|---|---|
| capture $^{238}U$ | 1000 | | 100 ± 10 |
| capture $^{238}U$ | 660 | 46 ± 4 | 42.6 ± 4.8 |
| fission $^{238}U$ | 660 | 14.3 ± 1.3 | 11.3 ± 1.2 |
| fission $^{235}U$ | 660 | 3.9 ± 0.4 | 2.4 ± 0.2 |
| total fission | 660 | 18.2 ± 1.7 | 13.7 ± 1.4 |

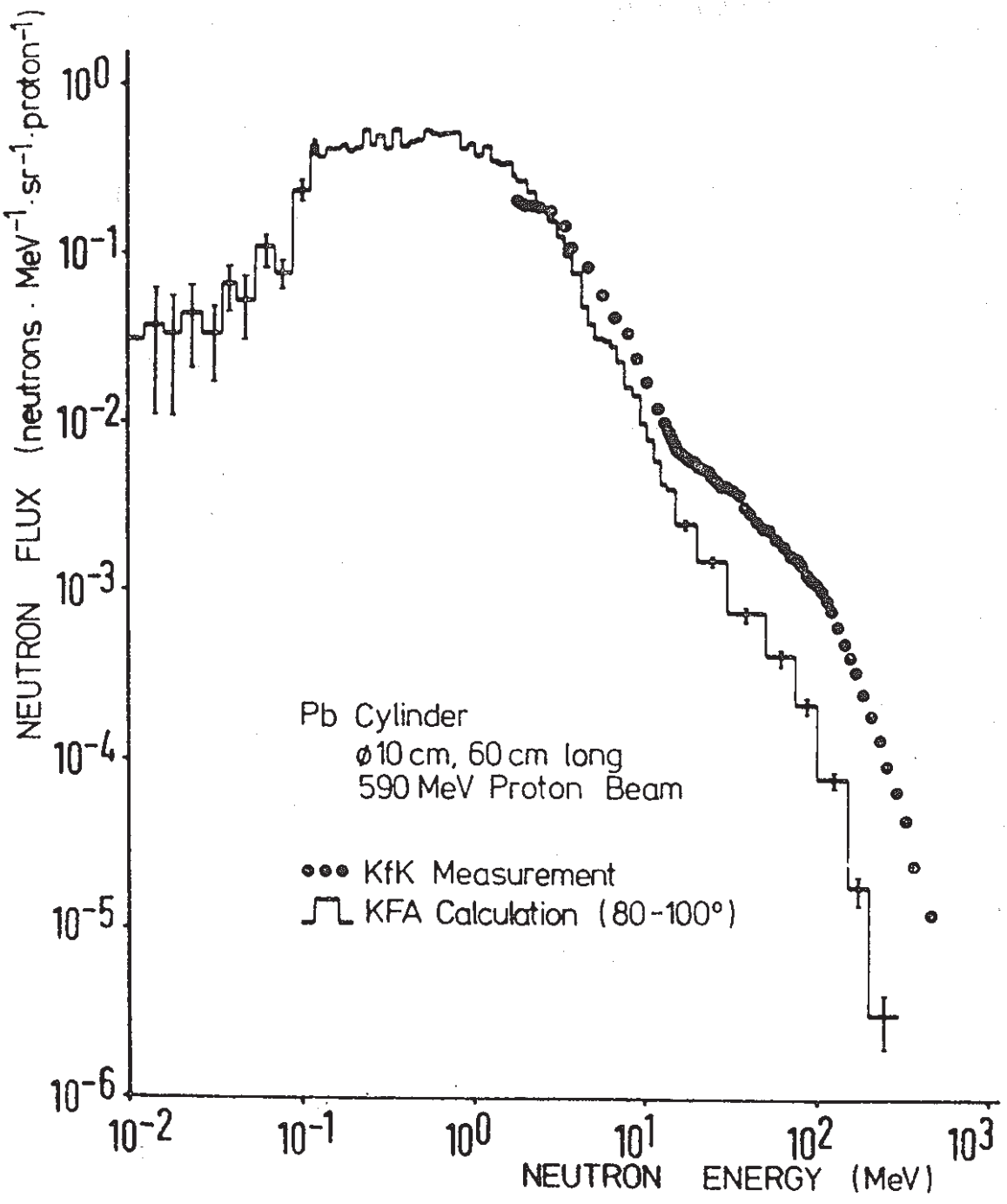
NEUTRON FLUX (neutrons · MeV$^{-1}$ · sr$^{-1}$ · proton$^{-1}$)
$10^{0}$
$10^{-1}$
$10^{-2}$
$10^{-3}$
$10^{-4}$
$10^{-5}$
$10^{-6}$
Pb Cylinder
ø10 cm, 60 cm long
590 MeV Proton Beam
KfK Measurement
KFA Calculation (80-100°)
$10^{-2}$
$10^{-1}$
$10^{0}$
$10^{1}$
$10^{2}$
$10^{3}$
NEUTRON ENERGY (MeV)

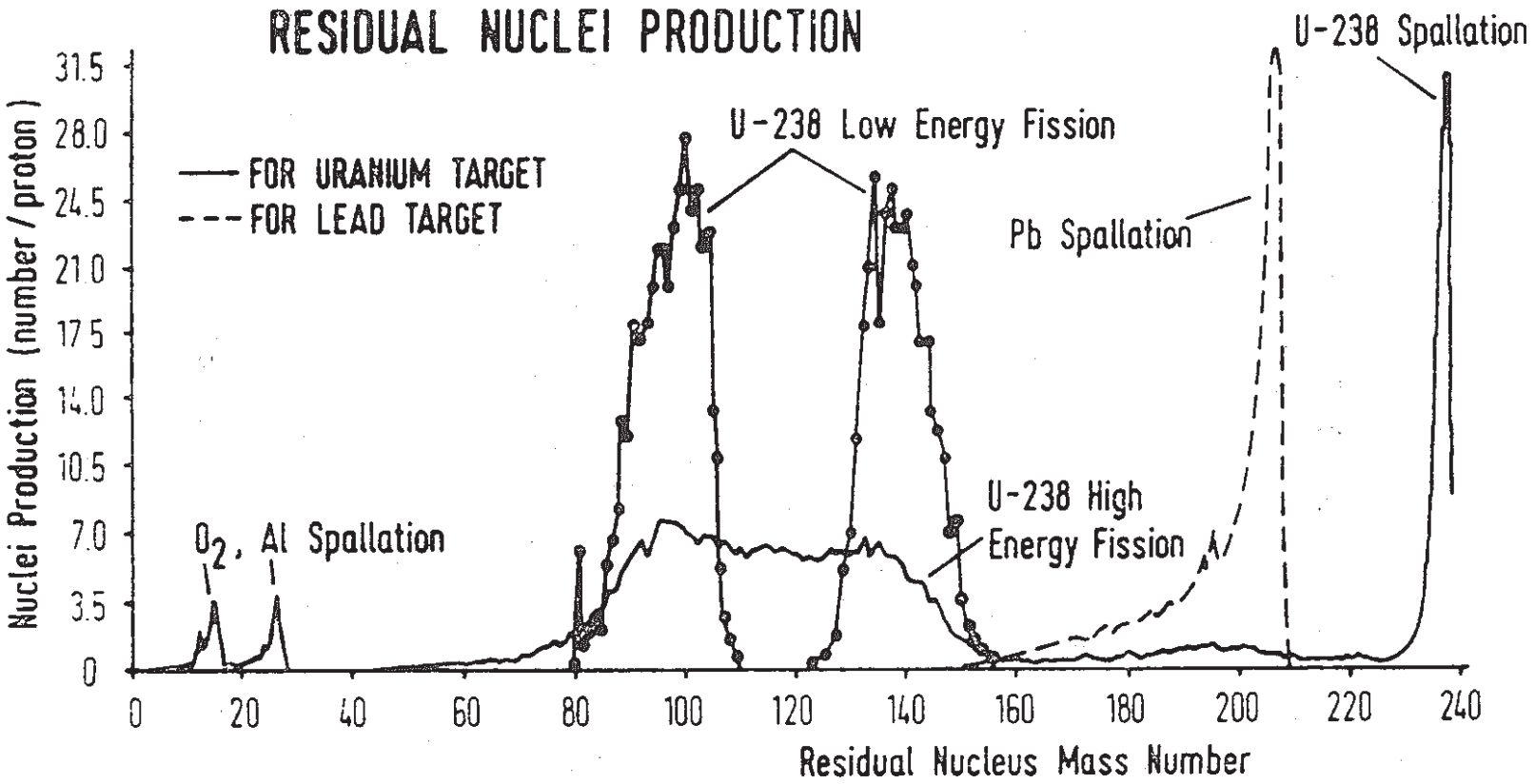
RESIDUAL NUCLEI PRODUCTION
Nuclei Production (number / proton)
31.5
28.0
24.5
21.0
17.5
14.0
10.5
7.0
3.5
0
FOR URANIUM TARGET
FOR LEAD TARGET
U-238 Low Energy Fission
U-238 Spallation
Pb Spallation
U-238 High
Energy Fission
O2, Al Spallation
0
20
40
60
80
100
120
140
160
180
200
220
240
Residual Nucleus Mass Number

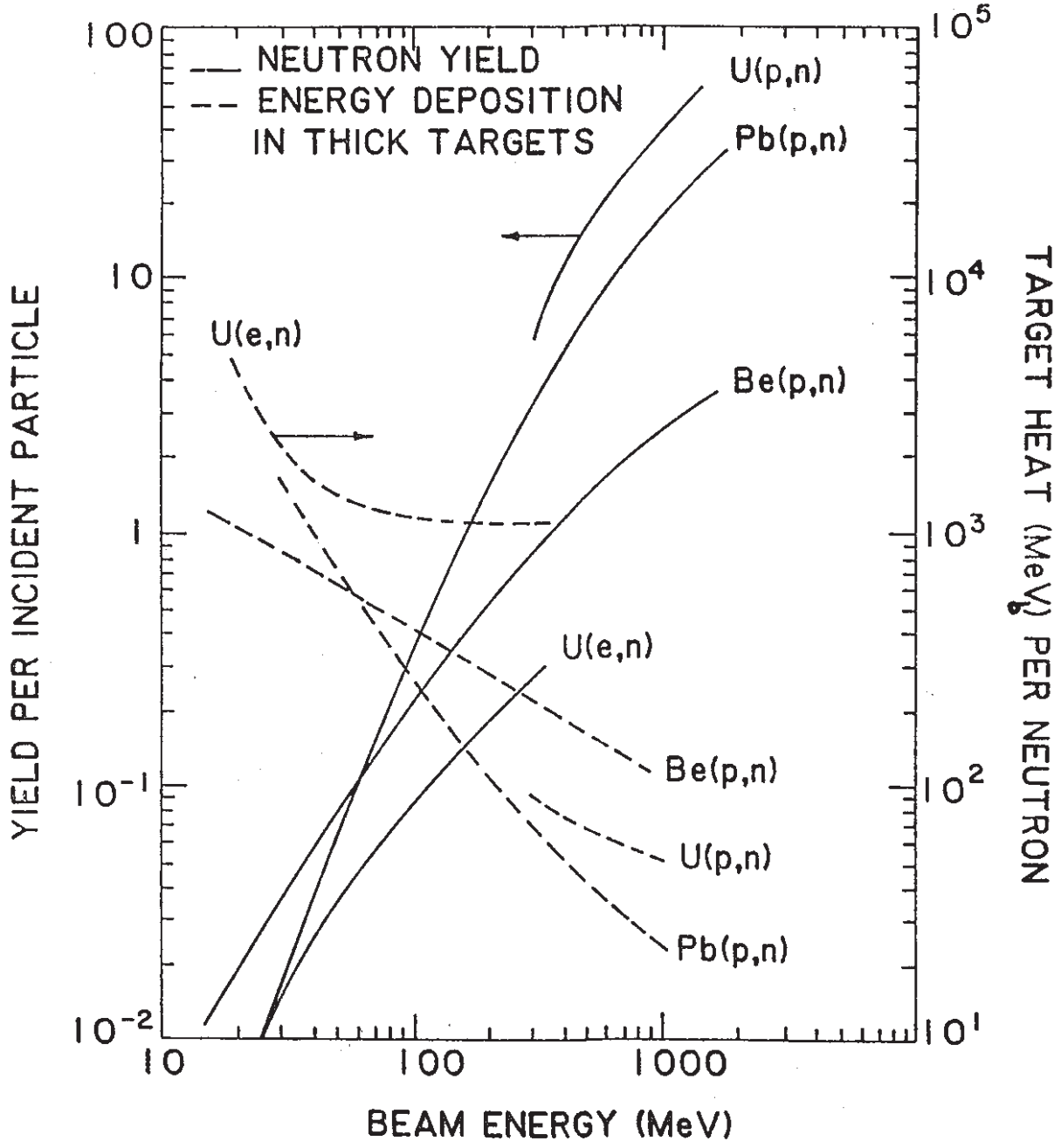


– if each neutron from a separate nucleus.

# SPALLATION - BREEDER

SYSTEM 1

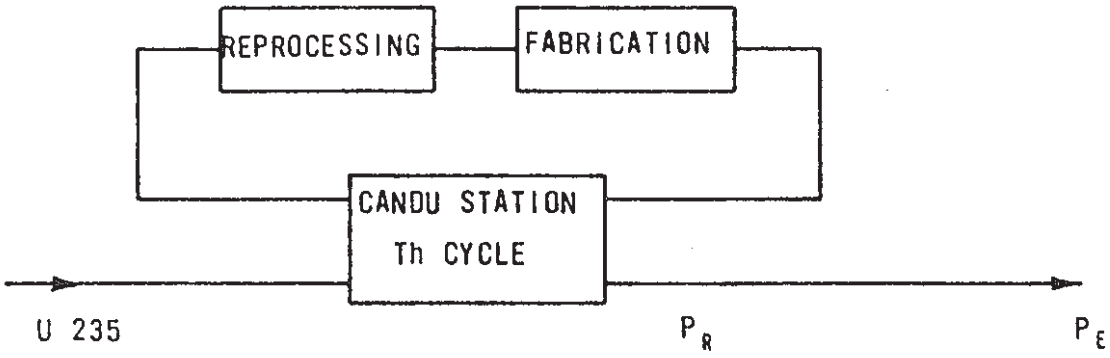


SYSTEM 2

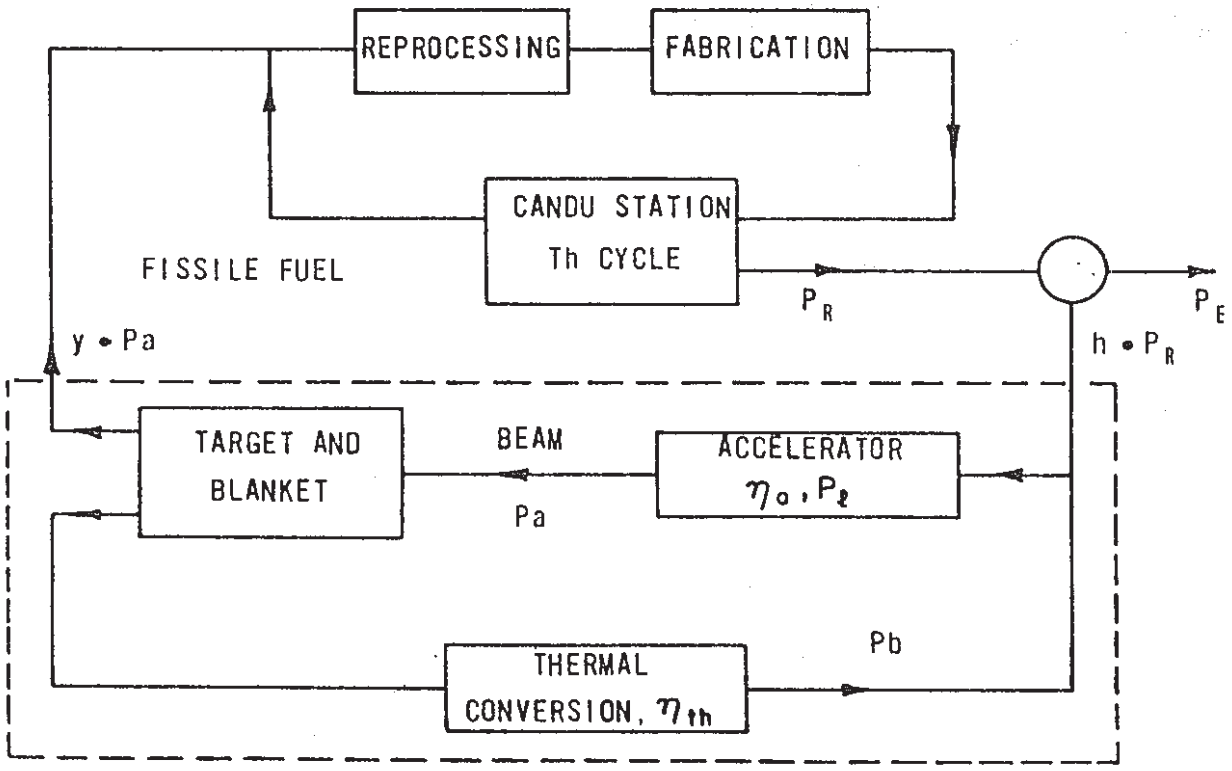

# SPALLATION OF HEAVY NUCLEI

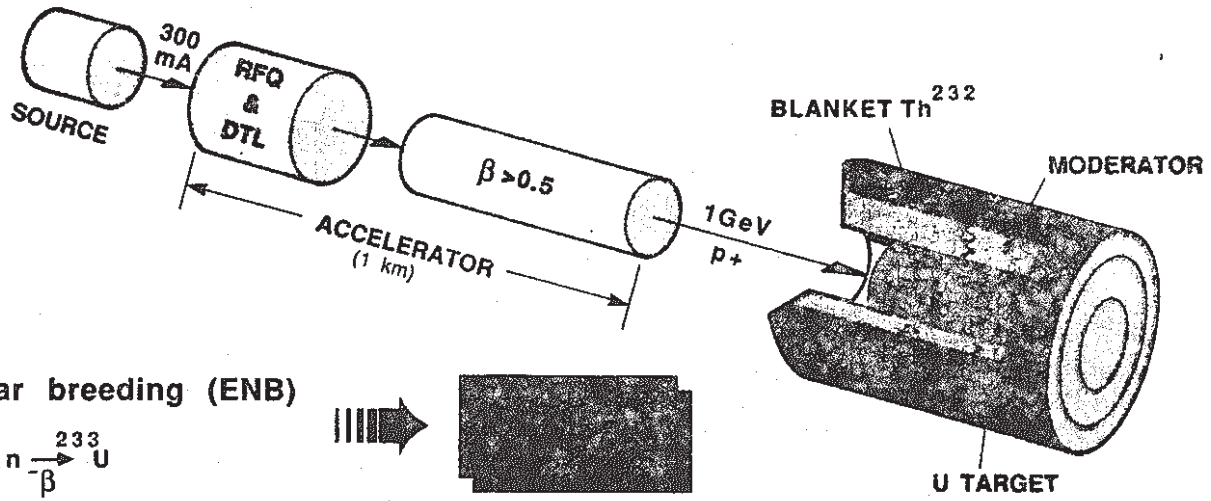


**1.) Electro-nuclear breeding (ENB)**

$$^{232}Th + {}^{1}_{0}n \xrightarrow[-\beta]{} {}^{233}U$$



**2.) Direct Fission**

- ENERGY GAIN (=4)
- TRU burn-up

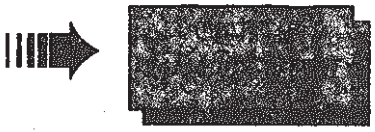

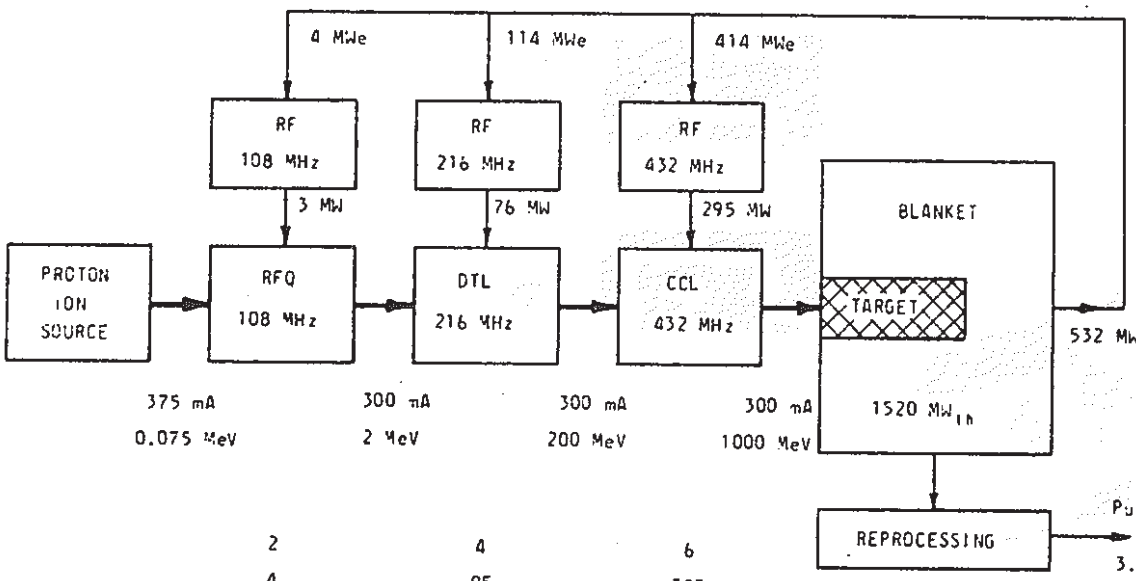


| | | | | |
|---|---|---|---|---|
| BORE DIA. (cm) | | 2 | 4 | 6 |
| LENGTH (m) | | 4 | 95 | 383 |
| SHUNT IMPEDANCE (MΩ/m) | | | 31.3 | 37.8 |
| GRADIENT (MeV/m) | | | 2.09 | 2.09 |
| COST | $0.8 M | $0.5M | $21M | $73.5M |
| RF COST | | $2.0M | $53M | $206 M |

$357M

$797 M(TARGET/BLANKET)

30

1981 CB
AECL 7260.

# ACCELERATOR-BREEDER CHARACTERISTICS

## BEAM POWER 300 MW

## TARGET/BLANKET POWER 1520 MW

| BLANKET MATERIAL | FISSILE MATERIAL PRODUCED | NET PRODUCTION RATE kg/efpd | ANNUAL (70%) Mg/Yr |
|---|---|---|---|
| URANIUM | Pu 239 | 3.4 | 0.87 |
| THORIUM | U 233 | 2.3 | 0.59 |

*efpd = effective full power days*

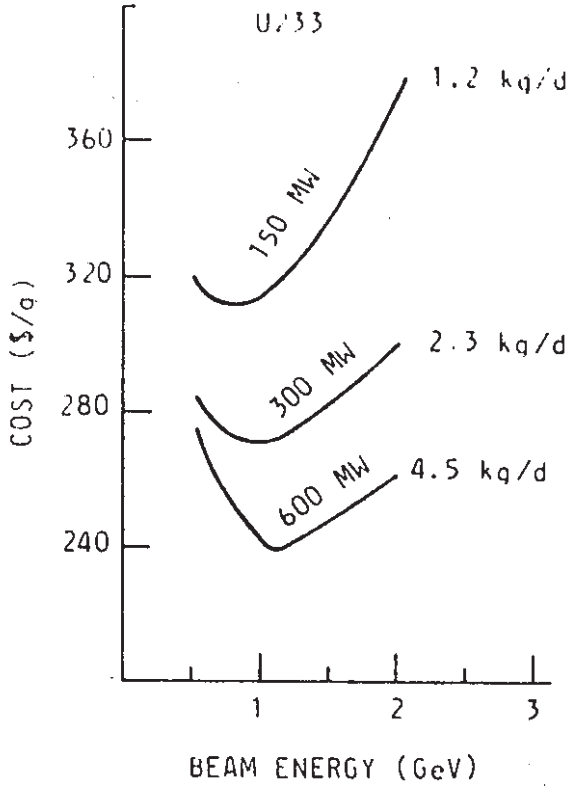


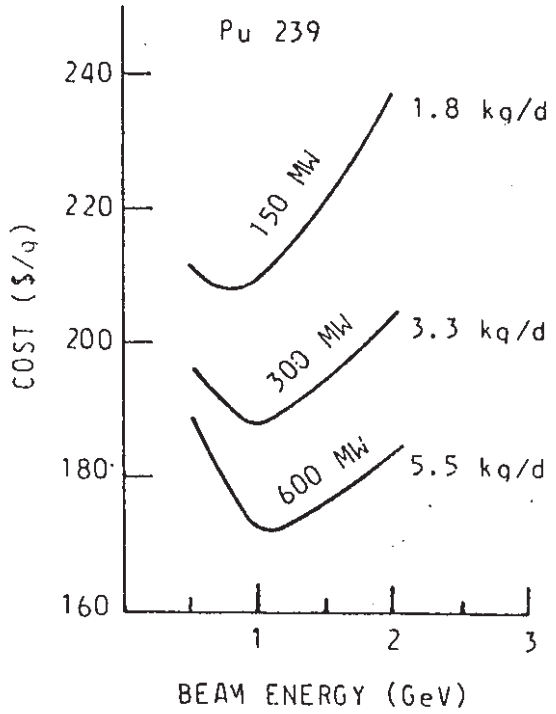


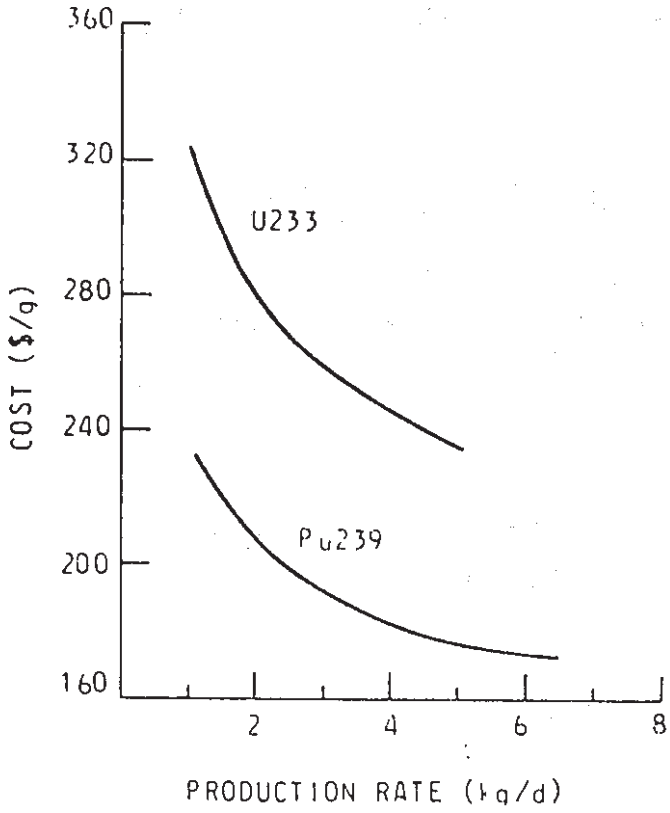


AECL-7260
1981 CB

# HLW - TRANSMUTATION

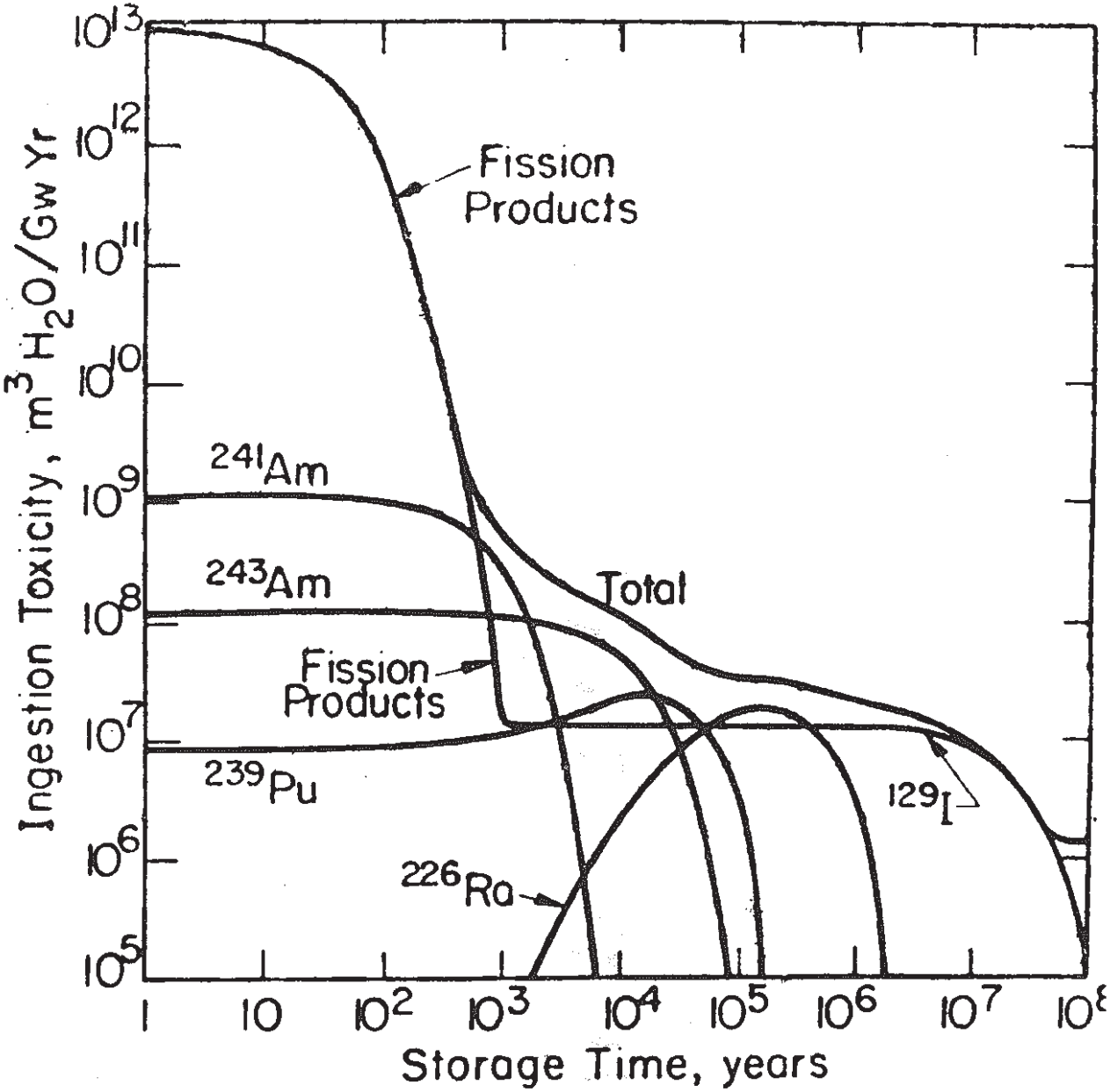
Ingestion Toxicity, $m^3 H_2O$/Gw Yr
$10^{13}$
$10^{12}$
$10^{11}$
$10^{10}$
$10^{9}$
$10^{8}$
$10^{7}$
$10^{6}$
$10^{5}$
Fission Products
$^{241}Am$
$^{243}Am$
Total
Fission Products
$^{239}Pu$
$^{129}I$
$^{226}Ra$
1
10
$10^2$
$10^3$
$10^4$
$10^5$
$10^6$
$10^7$
Storage Time, years

# HIGH LEVEL WASTE MANAGEMENT

## WASTE CATEGORY - SURVIVAL TIME

A - less than 1000 years
B - greater than 1000 years

## OPTIONS

- immobilise and store in isolation from biosphere
- transmute and neutralize category B.
- time scales of category B waste disposal transcends man's experience and the viability of his social and governmental institutions.
- Transmutation option relaxes the need to guarantee integrity of disposal process over time spans comparable to major geological changes in earth's crust.

# NUCLEAR TRANSMUTATION

## FEASIBILITY CRITERIA

- Waste balance - less created than burnt
- Energy balance - less than originally produced
- Inventory - adequate transmutation rate
- Economics - competitiveness
- Urgency/Funding Priorities
- Socially acceptable

## HAZARD INDEX

- Survival time
- Dose/Energy/Penetration
- Mobility/Solubility
- Toxicity

# TRANSMUTATION OPTIONS

## PROLIFIC TRANSMUTATION NUCLEAR REACTIONS

- neutron capture or emission
- fission in actinides

## TRANSMUTATION SOURCE FOR WASTE BALANCE

- waste survived n/$\gamma$ field in a thermal reactor
- must provide n/$\gamma$ fluences or energy much different from total encountered in a thermal reactor

FAST BREEDER/FUSION REACTOR
- high energy neutrons

HIGH ENERGY PROTON ACCELERATOR
- spallation neutron source

HIGH ENERGY ELECTRON ACCELERATOR
- high energy gamma rays
- bremsstrahlung radiation
- synchrotron radiation

TRANSMUTATION OF HLW SCIENTIFICALLY FEASIBLE

# HLW ANNUAL INVENTORY

## 1000 MWe THERMAL REACTOR 80% OPERATION

| | |
|---|---|
| TOTAL FISSILE LOAD | 878 kg |
| FISSION PRODUCTS | 863 kg |
| NO. OF FISSIONS | $2.3 \times 10^{27}$ |
| TOTAL ENERGY | $4.8 \times 10^{29}$ $MeV_t$ (1 kg) |

## CATEGORY B ACTINIDES

| PRODUCT | CANDU | PWR |
|---|---|---|
| Am + Np mass | 3.2 kg | 15.6 kg |
| atoms | $0.8 \times 10^{25}$ | $3.5 \times 10^{25}$ |
| total energy $MeV_e$ | $1.6 \times 10^{29}$ | $1.6 \times 10^{29}$ |
| energy/atom $MeV_e$ | 20000 | 4000 |
| Pu mass | 474 kg | 234 kg |
| energy/atom $MeV_e$ | 130 | 270 |

# HLW ANNUAL INVENTORY

## 1000 MWe THERMAL REACTOR 80% OPERATION

**TOTAL FISSION PRODUCT MASS 863 kg**
**NO. OF FISSIONS 2.3 X $10^{27}$**
**TOTAL ENERGY 4.8 X $10^{29}$ $MeV_t$ (1.2kg)**

## CATEGORY B FISSION PRODUCTS

| MATERIAL | CANDU | PWR |
|---|---|---|
| isotopic mass | 55 kg (30*) (6%) | 57 kg (33*) (6%) |
| | | Se, Kr, Sr, Zr*, Nb, Mo*, Tc, Pd*, Ag, Sn, I, Cs, Eu, Gd |
| element mass | 350 kg (135*) (40%) | 344 kg (138*) (40%) |
| element atoms | 2.1 x $10^{27}$ | |
| energy | 1.6 x $10^{29}$ $MeV_e$ | |
| energy/atom | 74.8 $MeV_e$ | |
| transmutation allowance | $\leq$ 7.5 $MeV_e$ | |
| beam energy/atom (10%) | | |

# TRANSMUTATION SCOPE

- CHEMICAL SEPARATION
- CATEGORY A - NOT FEASIBLE
  B - ACTINIDES - FEASIBLE
  FISSION PRODUCTS - TOO MANY

## FAST BREEDER

- FISSION PRODUCTS - MAYBE
- ACTINIDES FEASIBLE
- ACTINIDE INVENTORY BUILD UP IN REACTOR
- REAL GAIN AFTER 100 YEARS RECYCLE

## SPALLATION

- FISSION PRODUCTS - TOO MANY
- ACTINIDES - FEASIBLE
- ONE ACCELERATOR - 3 TO 10 PWR
  (300 MW$_b$) (10-30% ENERGY)

## ELECTRON

- FISSION PRODUCTS - NO
- ACTINIDES - ?
- BREMSSTRAHLUNG SOURCE ENERGY BALANCE AND REACTION RATES MARGINAL
- SYNCHROTRON SOURCE - HARDER SPECTRUM GIVES HIGH EFFICIENCY DUE TO GDR

資料７－６

# PRESENTATION TO PNC

BY

J. UNGRIN

CHALK RIVER NUCLEAR LABORATORY

SEPTEMBER 27, 1988

## ELECTRON ACCELERATORS

EXPERIENCE DATES TO ~ 1970.

ETA - CW (CONTINUOUS WAVE)
- 20 MA AT 4 MEV
- 805 MHz
- HIGH BEAM LOADING
- CONTROLS DEVELOPMENT

THERAC - SHORT PULSE
- 3 GHz
- COMPLEX BEAM DYNAMICS

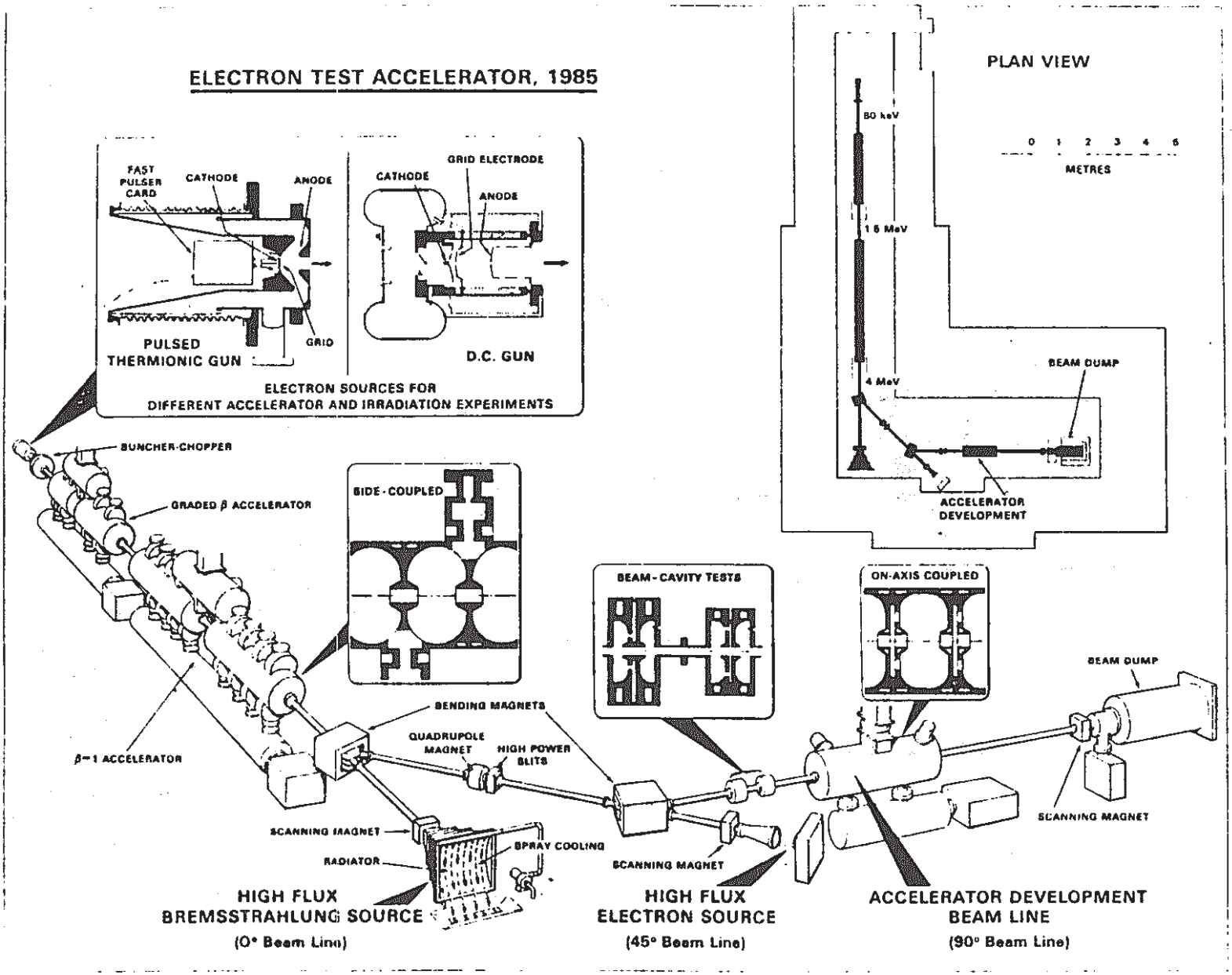
ELECTRON TEST ACCELERATOR, 1985
PLAN VIEW
0 1 2 3 4 5
METRES
80 keV
16 MeV
4 MeV
BEAM DUMP
ACCELERATOR DEVELOPMENT
FAST PULSER CARD
CATHODE
ANODE
GRID
PULSED THERMIONIC GUN
GRID ELECTRODE
D.C. GUN
ELECTRON SOURCES FOR DIFFERENT ACCELERATOR AND IRRADIATION EXPERIMENTS
BUNCHER-CHOPPER
GRADED β ACCELERATOR
β=1 ACCELERATOR
SIDE-COUPLED
BEAM-CAVITY TESTS
ON-AXIS COUPLED
BENDING MAGNETS
QUADRUPOLE MAGNET
HIGH POWER SLITS
SCANNING MAGNET
RADIATOR
SPRAY COOLING
HIGH FLUX BREMSSTRAHLUNG SOURCE
(0° Beam Line)
HIGH FLUX ELECTRON SOURCE
(45° Beam Line)
ACCELERATOR DEVELOPMENT BEAM LINE
(90° Beam Line)

3666-J

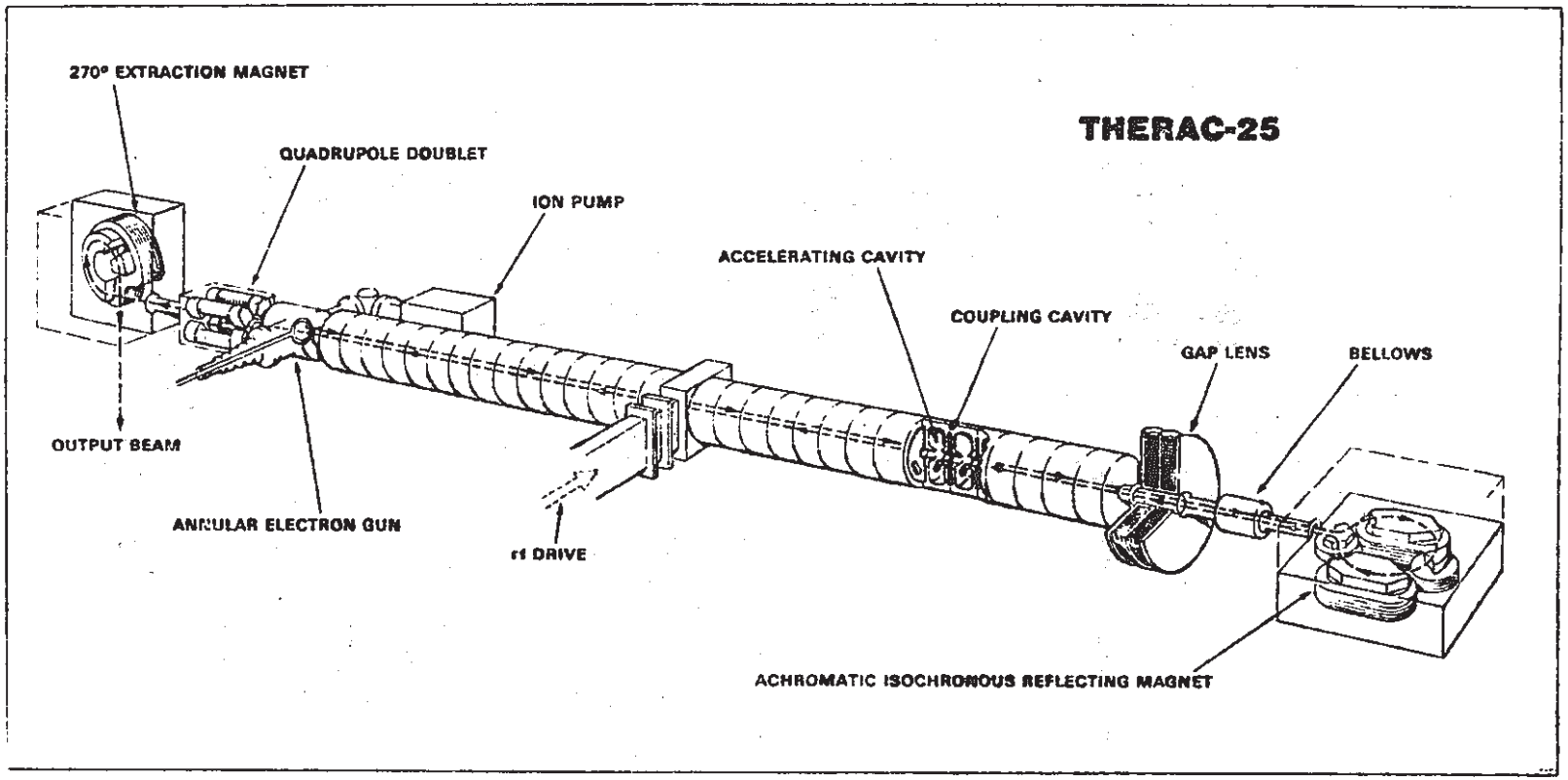
THERAC-25
270° EXTRACTION MAGNET
QUADRUPOLE DOUBLET
ION PUMP
ACCELERATING CAVITY
COUPLING CAVITY
GAP LENS
BELLOWS
OUTPUT BEAM
ANNULAR ELECTRON GUN
rf DRIVE
ACHROMATIC ISOCHRONOUS REFLECTING MAGNET

## STRUCTURE STUDIES

- STANDING WAVE, $\pi/2$ MODE

- SIDE COUPLED
- ON-AXIS COUPLED
- CO-AXIAL COUPLED

- OPTIMIZE EFFICIENCY
- THERMAL STABILITY

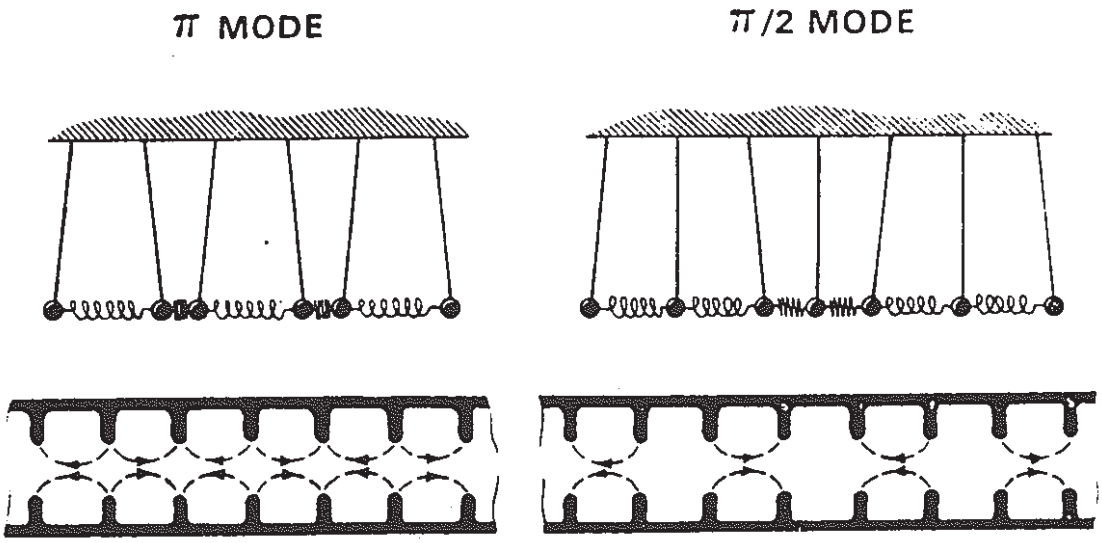


2.45 GHz, 13 ACCELERATING CELL STRUCTURE

$K_1 = 0.04$, $K_2 = 0.004$

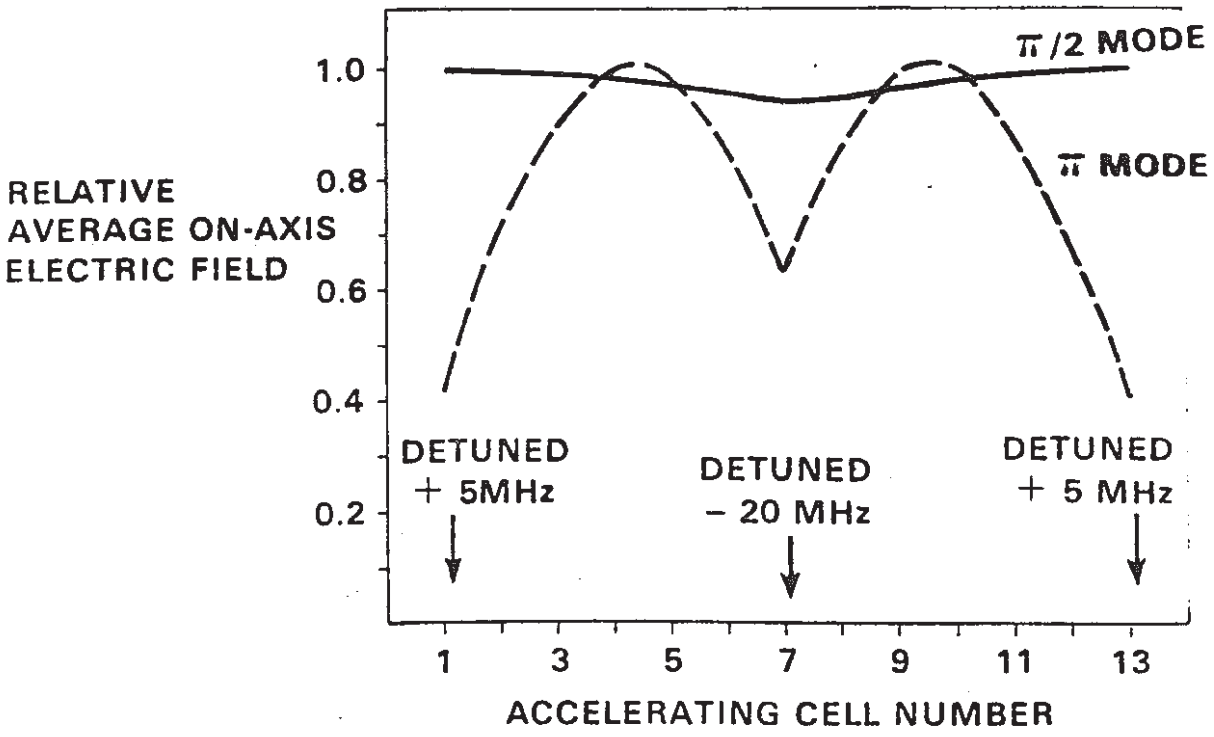

## EXAMPLES OF $\pi/2$ – MODE STRUCTURES

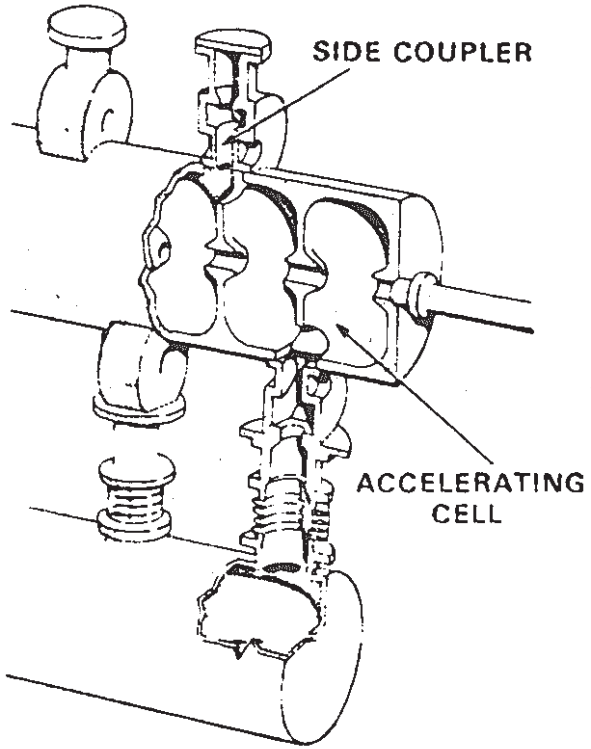


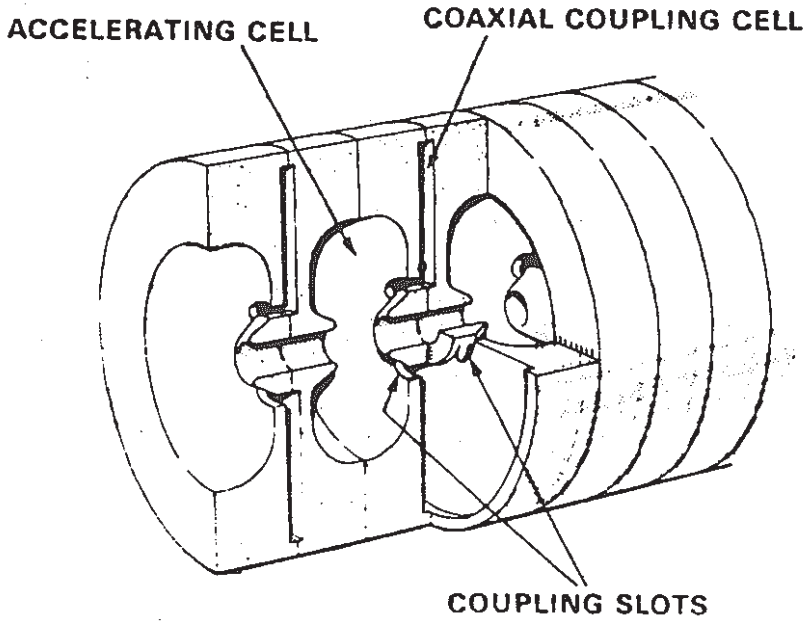

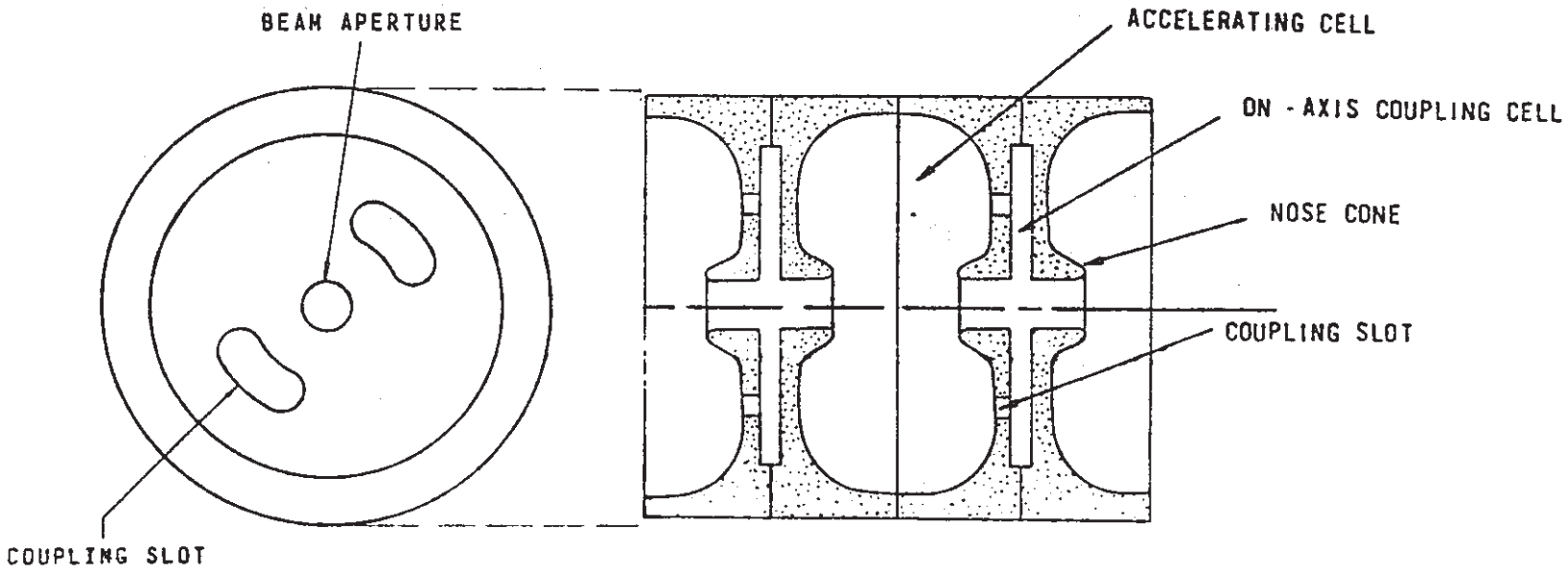


MACHINED SEGMENT

## STRUCTURE EFFICIENCY

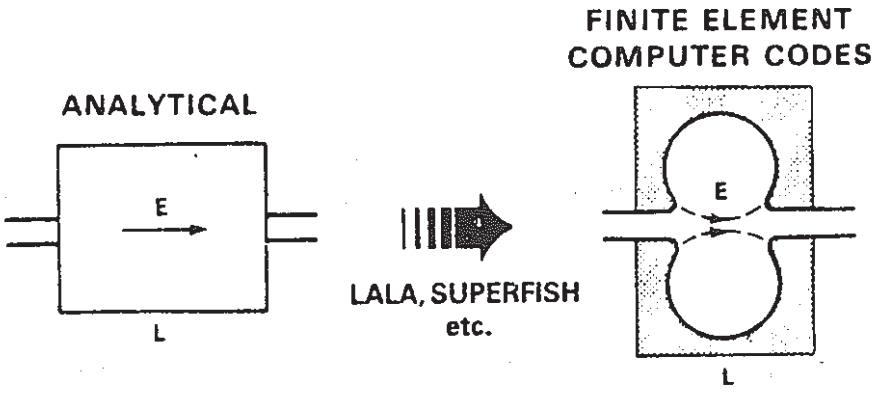


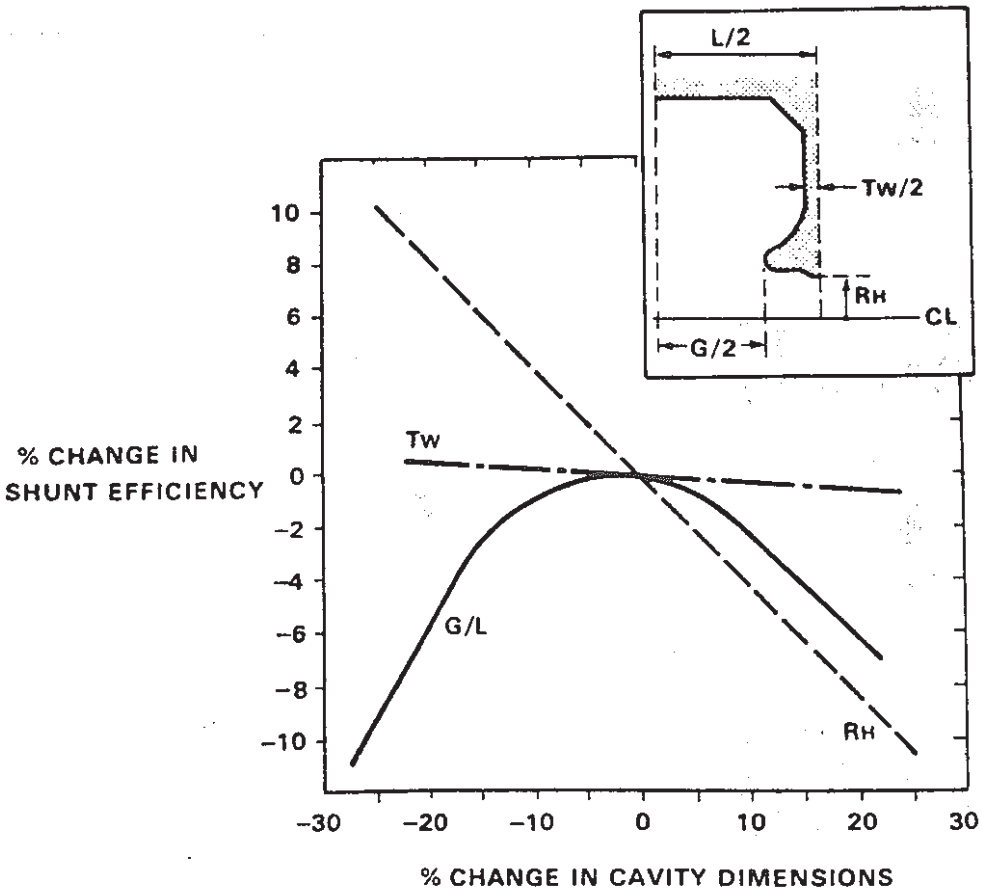

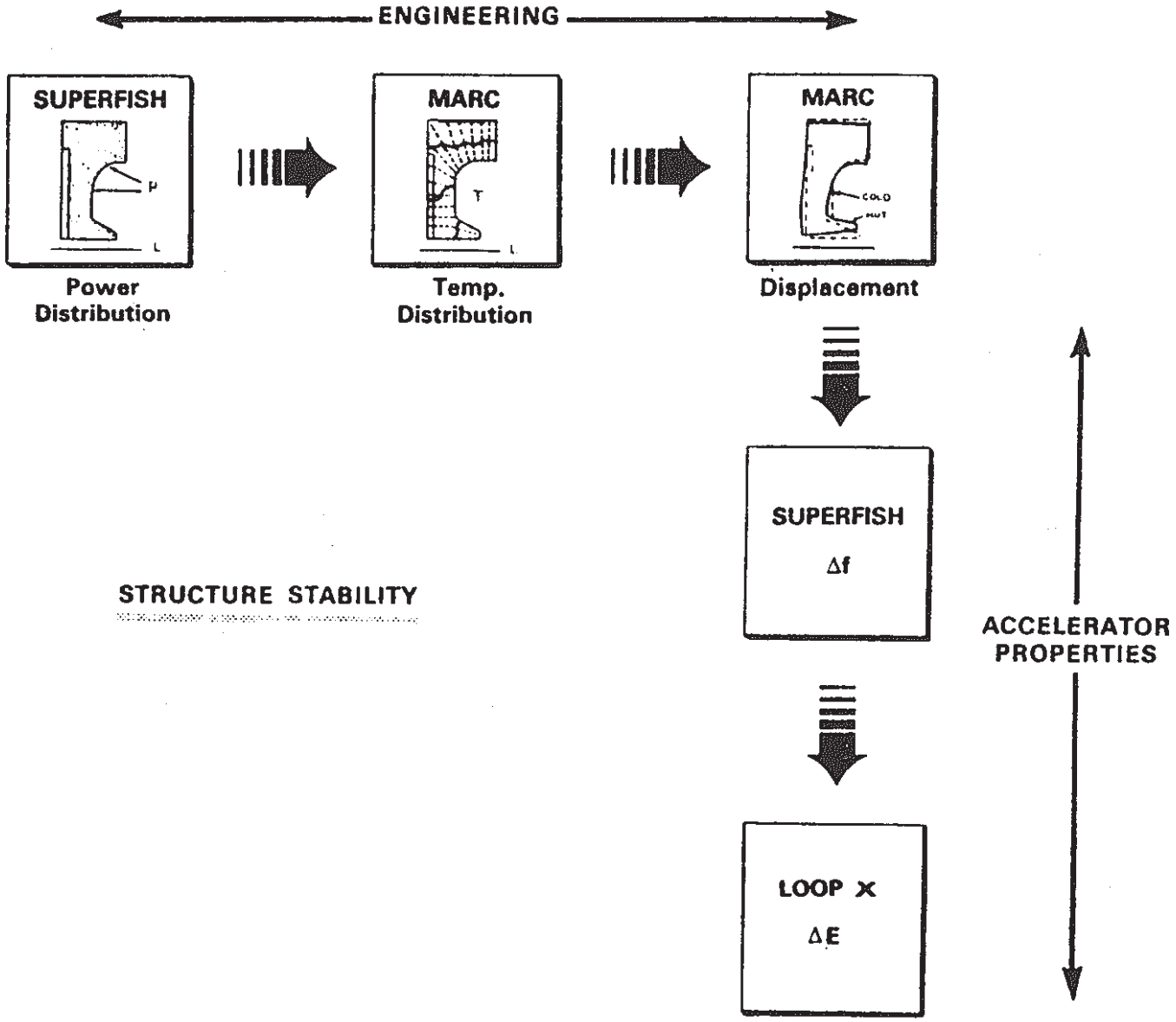
ENGINEERING
SUPERFISH
Power Distribution
MARC
Temp. Distribution
MARC
Displacement
SUPERFISH
Δf
LOOP X
ΔE
ACCELERATOR PROPERTIES
STRUCTURE STABILITY

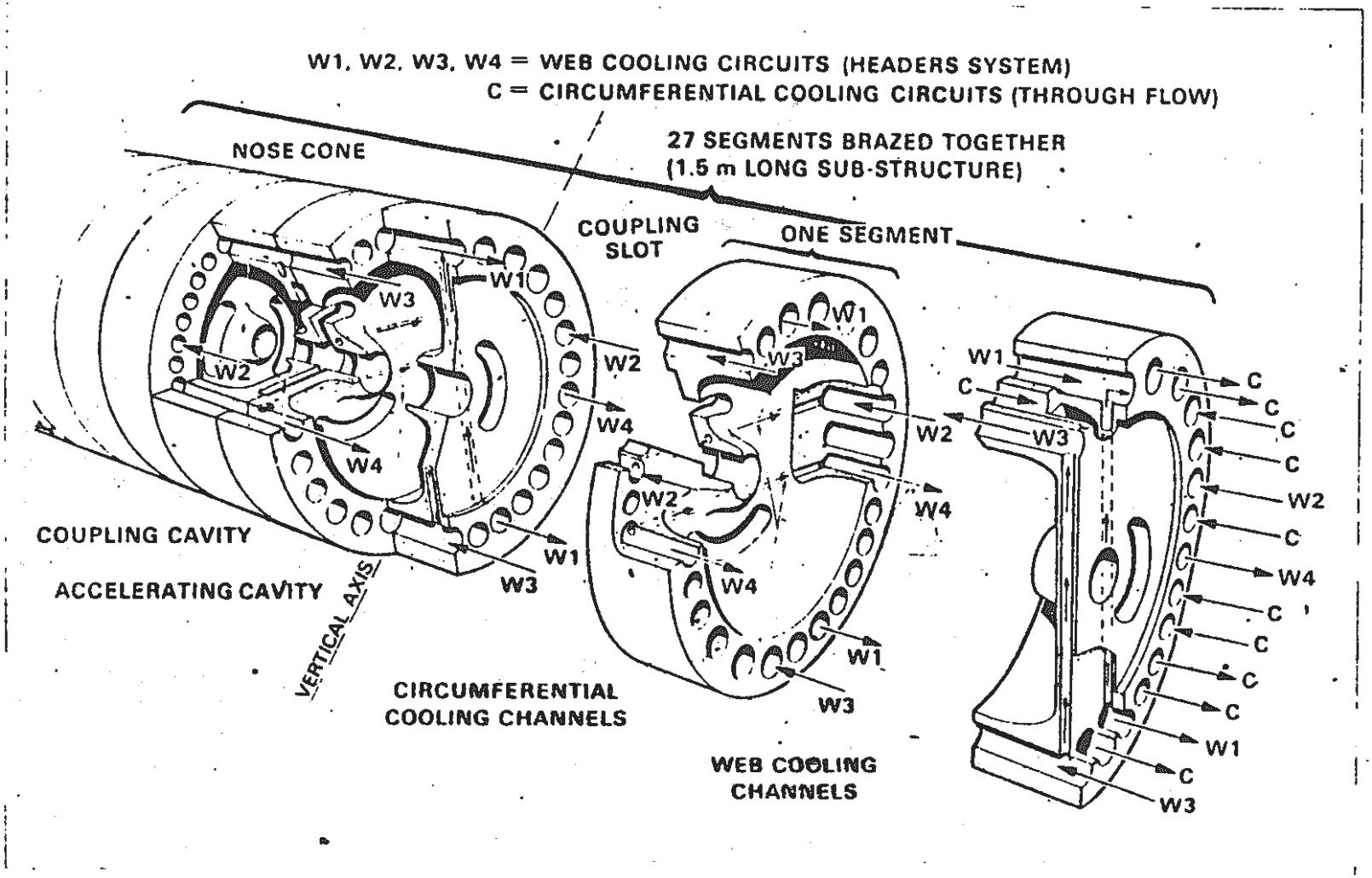
W1, W2, W3, W4 = WEB COOLING CIRCUITS (HEADERS SYSTEM)
C = CIRCUMFERENTIAL COOLING CIRCUITS (THROUGH FLOW)
NOSE CONE
27 SEGMENTS BRAZED TOGETHER
(1.5 m LONG SUB-STRUCTURE)
COUPLING SLOT
ONE SEGMENT
COUPLING CAVITY
ACCELERATING CAVITY
VERTICAL AXIS
CIRCUMFERENTIAL COOLING CHANNELS
WEB COOLING CHANNELS
W1
W2
W3
W4
C

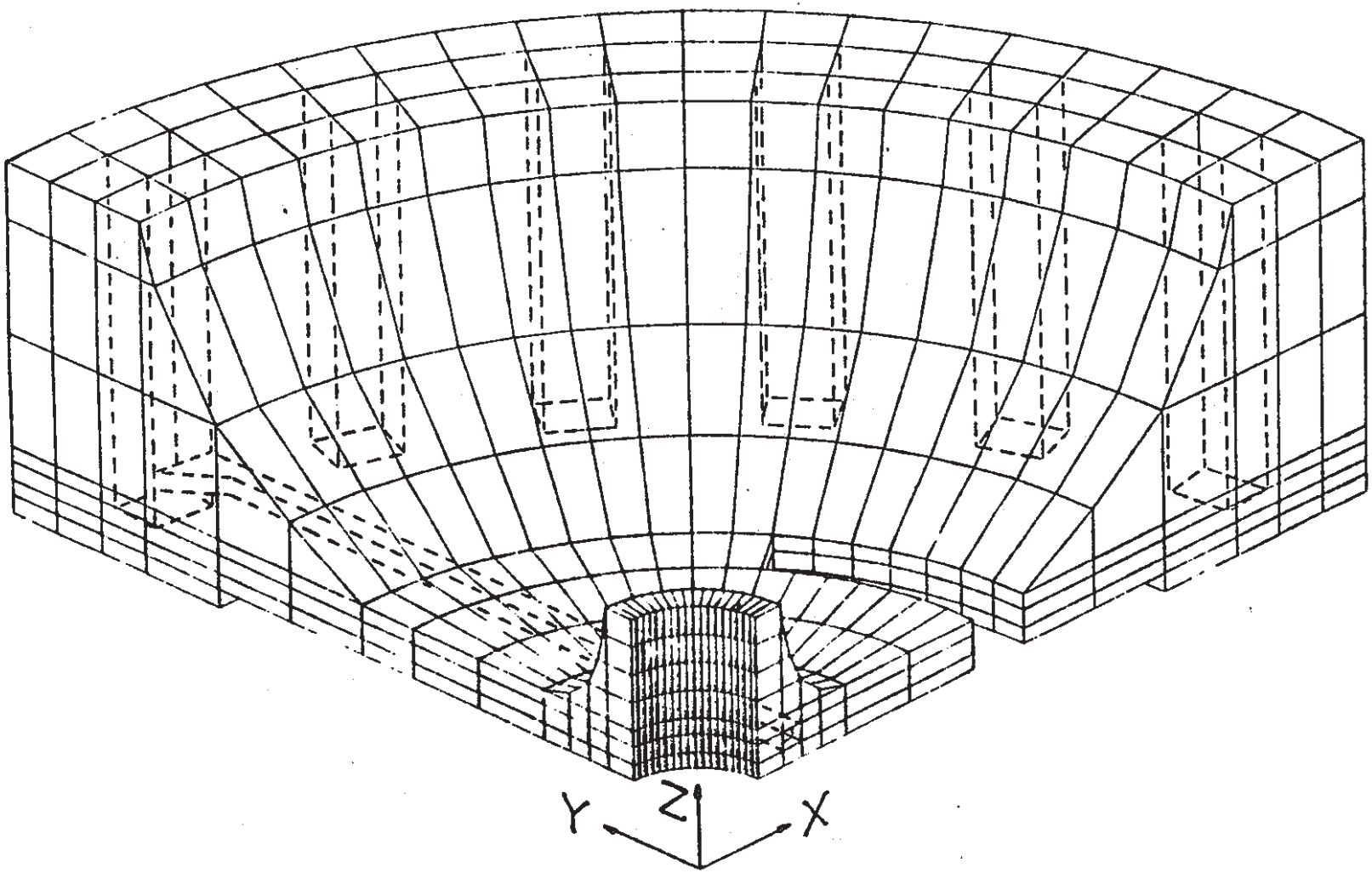


Fig. 5 The three-dimensional finite element model of a rf cavity segment.

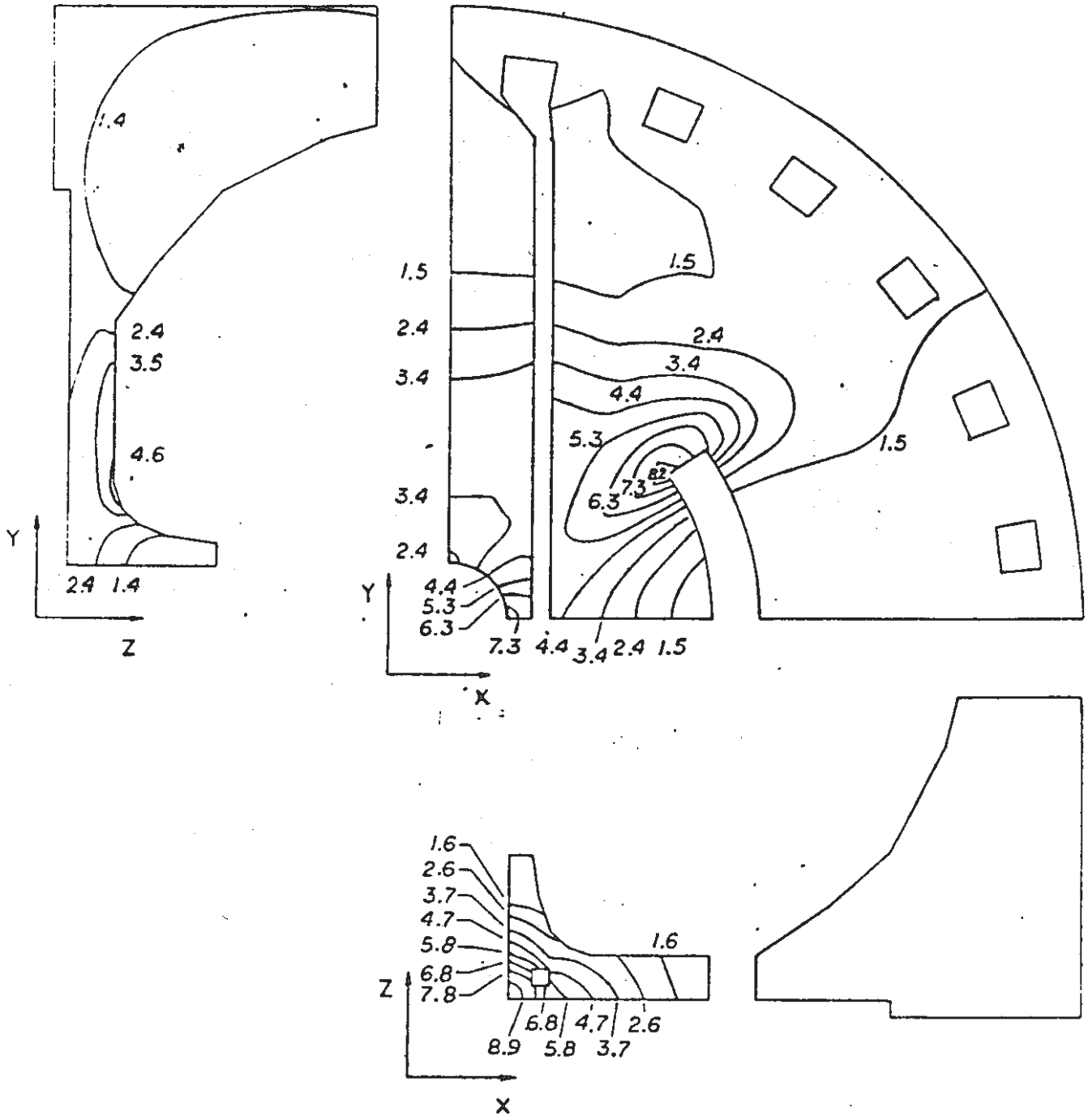
1.4
2.4
3.5
4.6
Y
2.4 1.4
Z
1.5
2.4
3.4
3.4
2.4
1.5
2.4
3.4
4.4
5.3
6.3
7.3
8.2
1.5
Y
4.4
5.3
6.3
7.3 4.4 3.4 2.4 1.5
X
1.6
2.6
3.7
4.7
5.8
6.8
7.8
Z
1.6
6.8 4.7 2.6
8.9 5.8 3.7
X

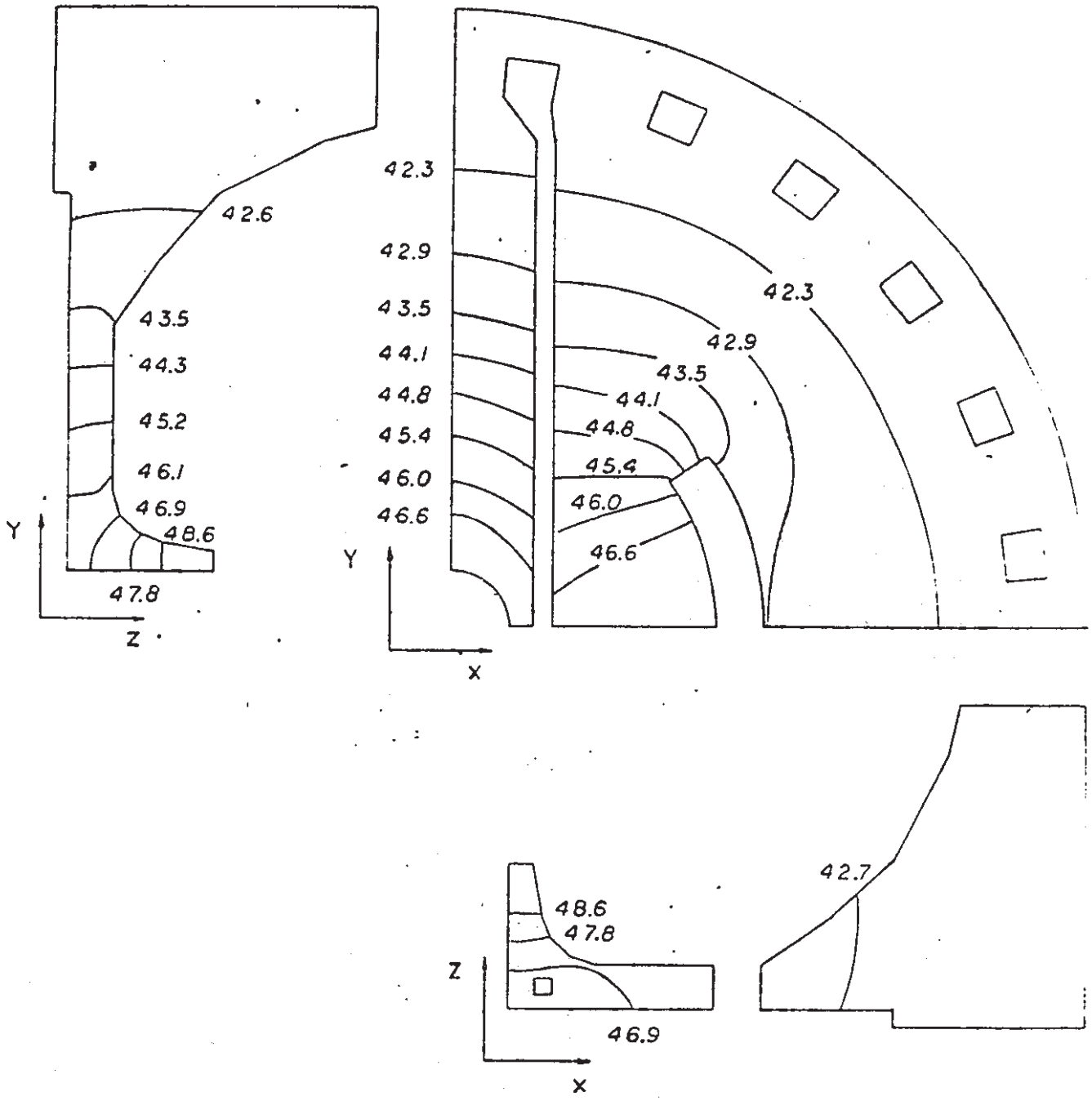
42.6
43.5
44.3
45.2
46.1
46.9
48.6
47.8
Y
Z
42.3
42.9
43.5
44.1
44.8
45.4
46.0
46.6
Y
X
42.3
42.9
43.5
44.1
44.8
45.4
46.0
46.6
48.6
47.8
Z
46.9
X
42.7

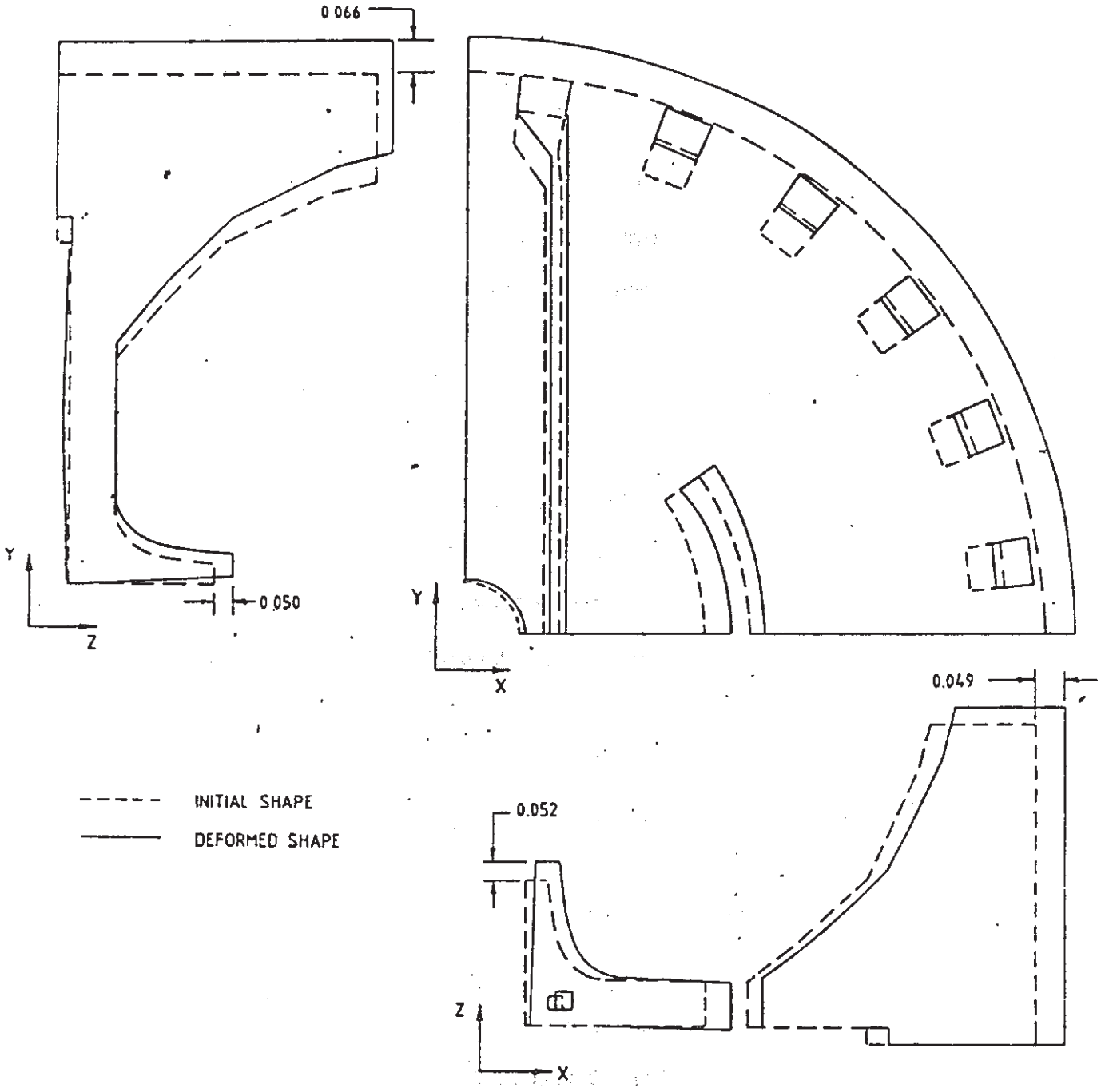
0 066
0 050
Y
Z
Y
X
0.049
0.052
Z
X
INITIAL SHAPE
DEFORMED SHAPE

# IRRADIATOR PROGRAMS

## LOW POWER - SHORT PULSE, BASED ON 3 GHz T-25

### I-10/1. PROCESS DEMONSTRATION ACCELERATOR

- NOMINAL 10 MeV, 1 kW
- MAGNETRON DRIVEN
- COMMERCIAL UNIT

### PHELA

- QUASI EXPERIMENTAL
- NOMINAL 13 MeV, 4 kW
- KLYSTRON DRIVEN
- COMMERCIAL IRRADIATIONS (75% OF TIME)

## HIGH POWER - LONG PULSE, MODULATED ANODE KLYSTRON

### IMPELA FAMILY

- 20-500 kW
- L-BAND FREQUENCY
- LONG PULSE MODE
- CONTROLLED BY INDUSTRIAL PROGRAMMABLE CONTROLLERS

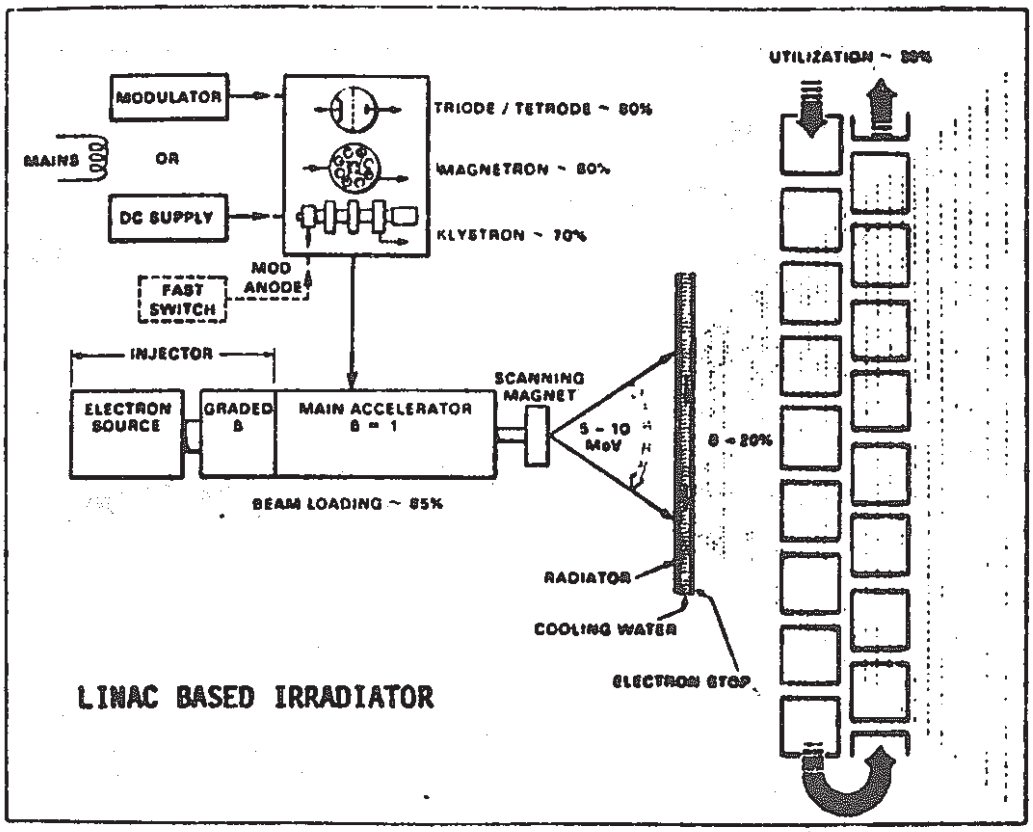
UTILIZATION ~ 90%
MODULATOR
MAINS
OR
DC SUPPLY
TRIODE / TETRODE ~ 80%
MAGNETRON ~ 60%
KLYSTRON ~ 70%
MOD ANODE
FAST SWITCH
INJECTOR
ELECTRON SOURCE
GRADED B
MAIN ACCELERATOR B = 1
SCANNING MAGNET
5 - 10 MeV
B = 20%
BEAM LOADING ~ 85%
RADIATOR
COOLING WATER
ELECTRON STOP
LINAC BASED IRRADIATOR

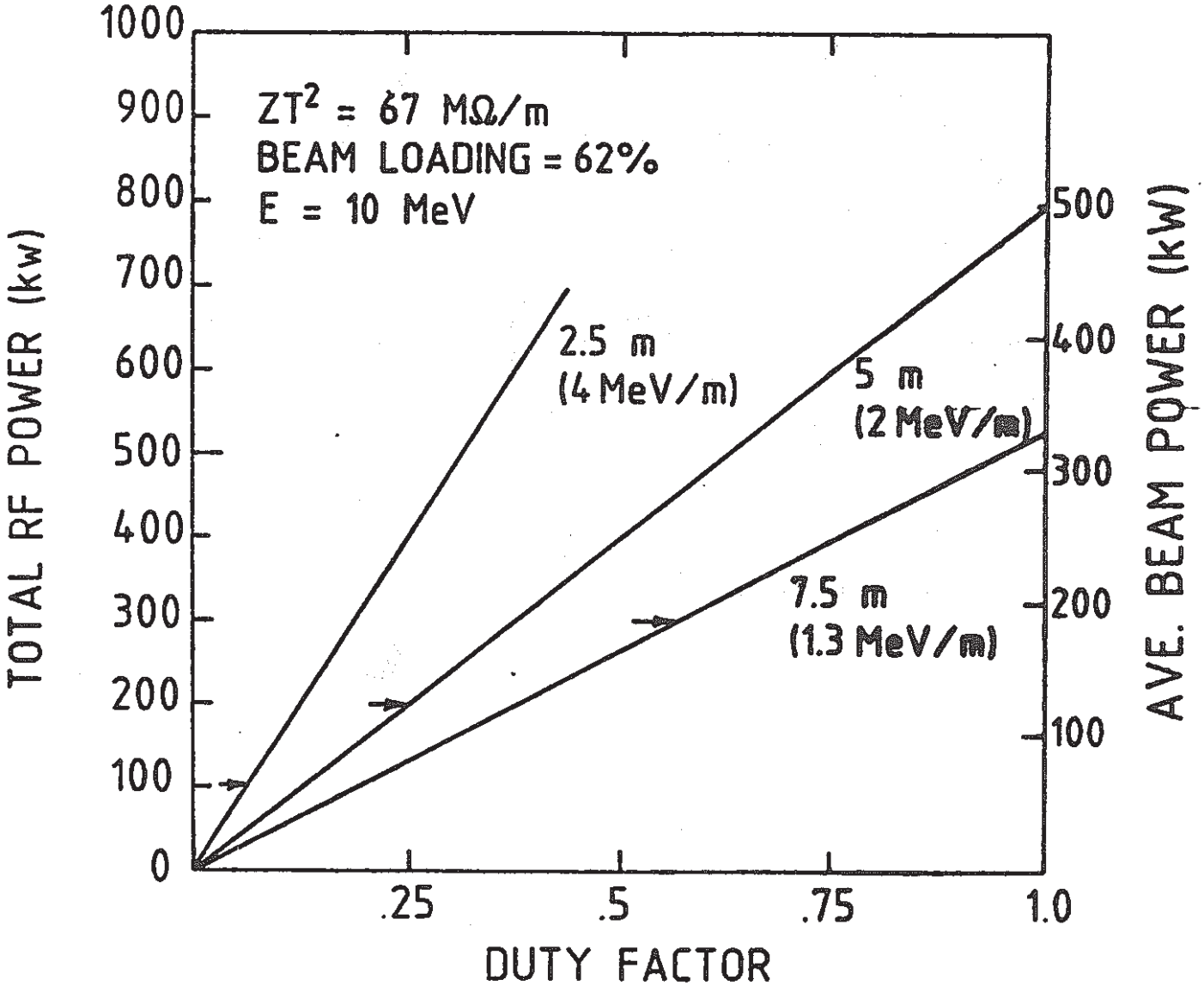
1000
900
800
700
600
500
400
300
200
100
0
$ZT^2$ = 67 MΩ/m
BEAM LOADING = 62%
E = 10 MeV
2.5 m
(4 MeV/m)
5 m
(2 MeV/m)
7.5 m
(1.3 MeV/m)
TOTAL RF POWER (kw)
AVE. BEAM POWER (kW)
500
400
300
200
100
.25
.5
.75
1.0
DUTY FACTOR

M50

# IMPELA

## Industrial Materials Processing Electron

## Linear Accelerator

**IMPELA 10/50 is a 50 kW (average power), nominal 10 MeV, electron irradiator based on a 5% duty factor, L-band, bi-periodic, $\pi/2$ mode, on-axis coupled, standing-wave linac.**

AECL-*Accelerators*

# IMPELA 10/50

- IMPELA 10/50 is a prototype accelerator and test facility.

- Provide design, performance and cost data on which to base proposals for widely differing applications.

- Demonstrate reliability of approach

AECL-*Accelerators*

# DESIGN TARGETS

- **RELIABLE**
  **97 % or greater availability based on 5 day week**

- **FLEXIBLE**
  **Modulated anode rf system**

- **SIMPLE OPERATION**
  **Computer Controlled**

- **EFFICIENT**
  **High beam loading**

AECL-*Accelerators*

# MODULAR CONCEPT

BUILDING SECTIONS

INJECTOR

ACCELERATOR

Low Gradient

High Gradient

COUPLER

UNIT

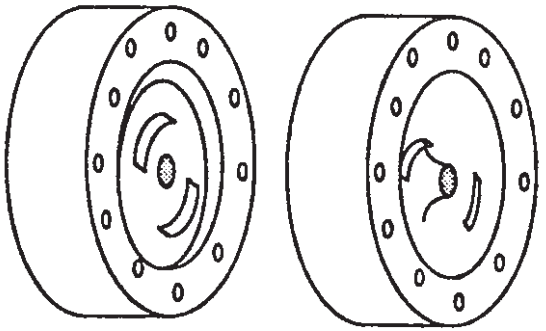

ACCELERATOR OPTIONS

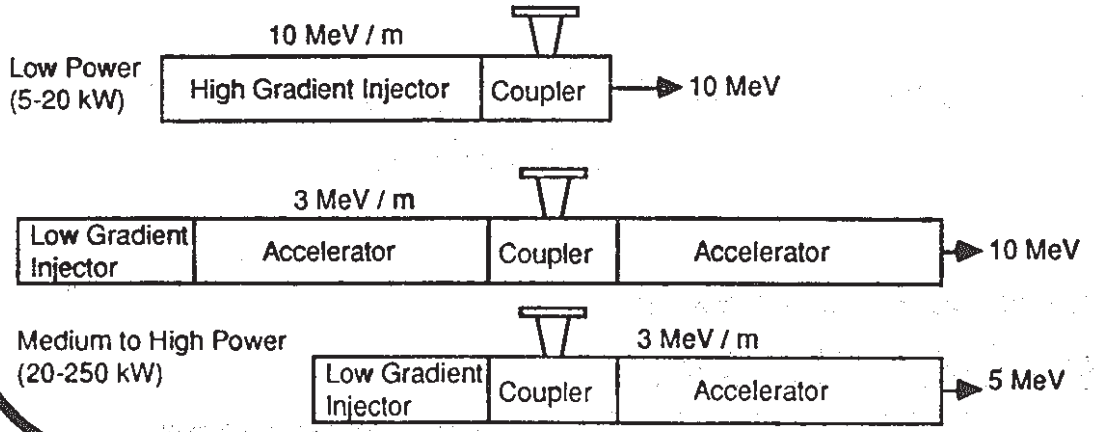


AECL-*Accelerators*

# MODULATED ANODE KLYSTRON (THOMSON-CSF)

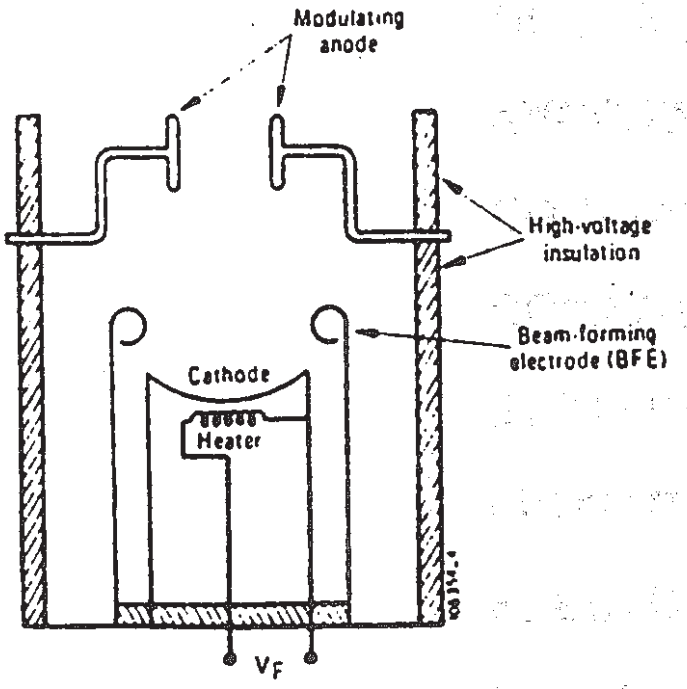


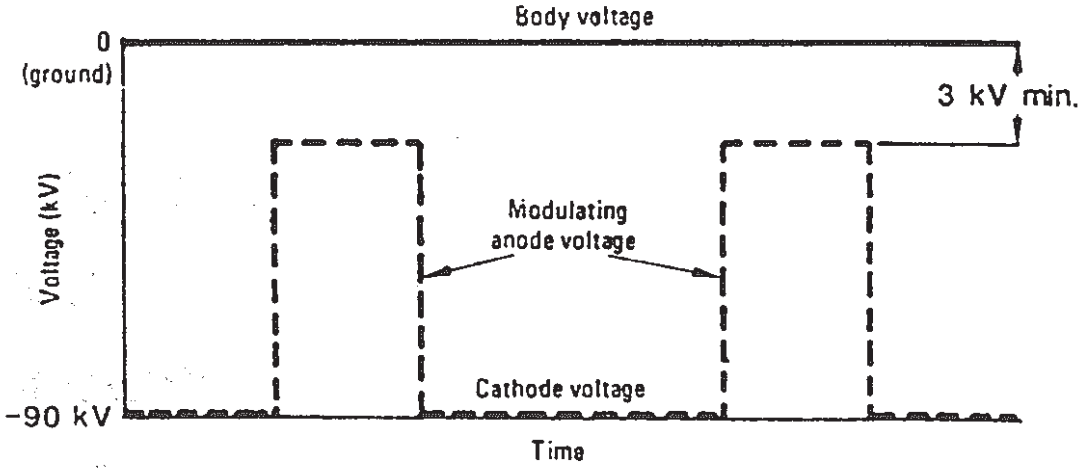


AECL-*Accelerators*

# MAJOR IMPELA SUBSYSTEMS

RF POWER

ELECTRON GUN

LINAC STRUCTURE

BEAM DELIVERY

COMPUTER CONTROL

COOLING

VACUUM

DOSIMETRY , DIAGNOSTICS

SHIELDING

AECL-*Accelerators*

3736-D

# IMPELA

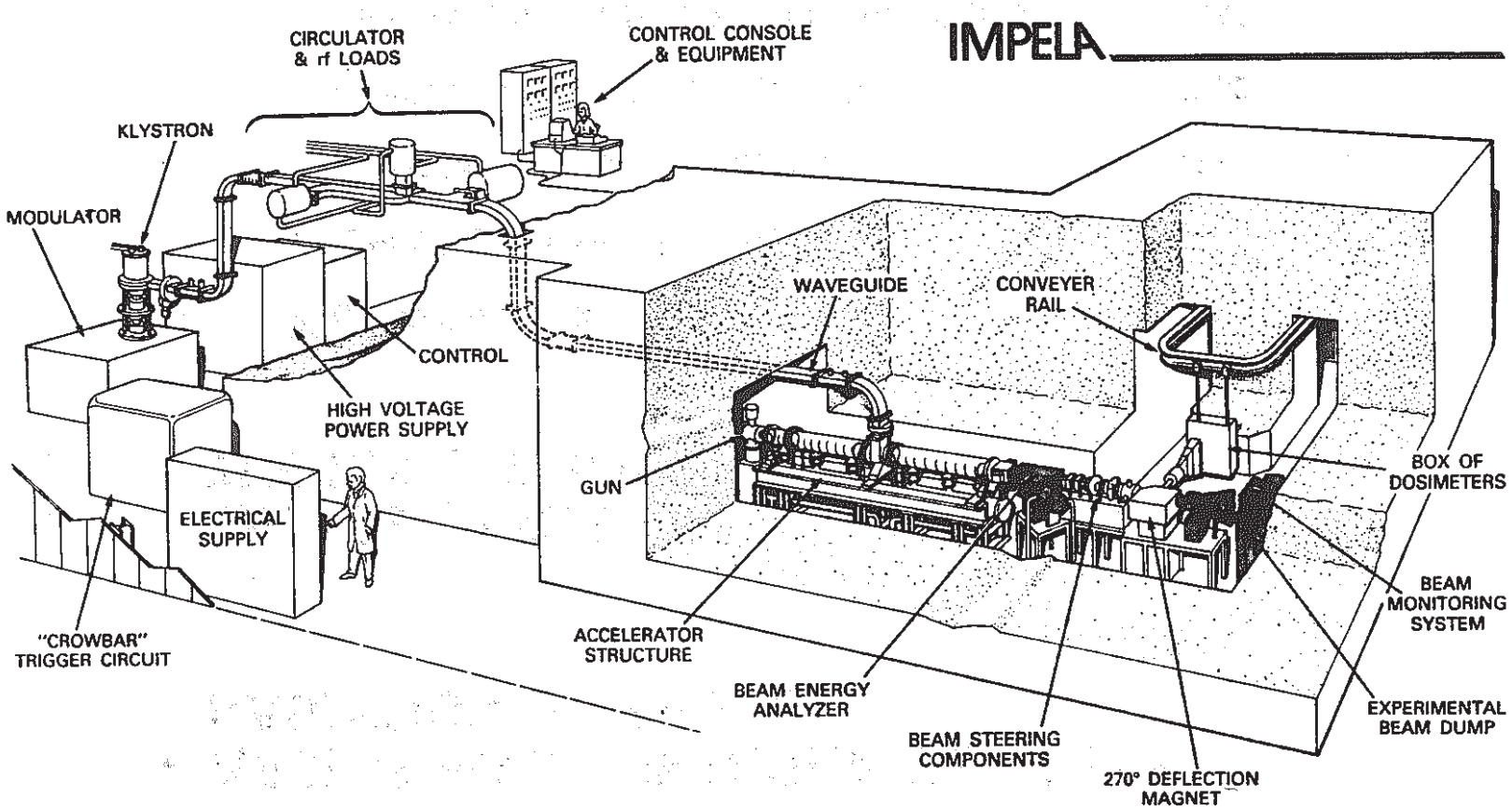


**AECL-*Accelerators***

# COMMITMENT

- **AECL IS FULLY INTEGRATED IN THE RADIATION BUSINESS**

- **WE ARE IN THE RADIATION BUSINESS FOR THE LONG TERM**

| | |
|---|---|
| $^{60}$Co TECHNOLOGY DEVELOPMENT | 1962 |
| ACCELERATOR DEVELOPMENT | 1965 |
| - MEDICAL ACCELERATORS | 1971 |
| - INDUSTRIAL ACCELERATORS | 1985 |
| - RADIATION APPLICATIONS RESEARCH | 1985 |

AECL-*Accelerators*

# TEAM EXPERIENCE

- ACCELERATOR STRUCTURE DEVELOPMENT
- BEAM HANDLING EXPERIENCE
- RF EXPERIENCE
- CONTROL SYSTEM

AECL-*Accelerators*

資料７－７　Chalk River研究所のカタログ

## *Chalk River Nuclear Laboratories*

# *The World of the Atom*

Approaching the laboratories by water, you might think of the voyageurs, led by Samuel de Champlain in 1613, who made their way up the Ottawa River. Travelling by road, along the Trans-Canada Highway, more recent pioneers come to mind. At the Village of Chalk River brightly coloured signs welcome you: "Visit Inner Space," they say, "The World of the Atom – Chalk River Nuclear Laboratories."

Chalk River's scientific era began in 1944 when the federal government decided to build a Canadian nuclear reactor and chose a 4000 hectare site of woods, lakes and sandy beaches adjoining the Petawawa Army base. The laboratories were operated as part of the National Research Council until 1952, when the Canadian government created the Crown corporation Atomic Energy of Canada Limited (AECL). Today, nuclear power provides a stable and economic source of electricity throughout much of the world and Canada's CANDU® reactor is a top performer. AECL has grown into three companies with sites across Canada: CANDU Operations, an engineering company responsible for selling and servicing CANDUs; the Radiochemical Company, which markets radioisotopes and irradiation equipment, and the Research Company which provides the underlying research and development support for Canada's nuclear program, through Chalk River Nuclear Laboratories in Ontario and Whiteshell Nuclear Research Establishment in Manitoba.

This brochure gives you a glimpse of the challenges and excitement at a large scientific laboratory, one that gave birth to a new Canadian industry and is still working to apply nuclear and related technologies to the maximum benefit of Canadians.

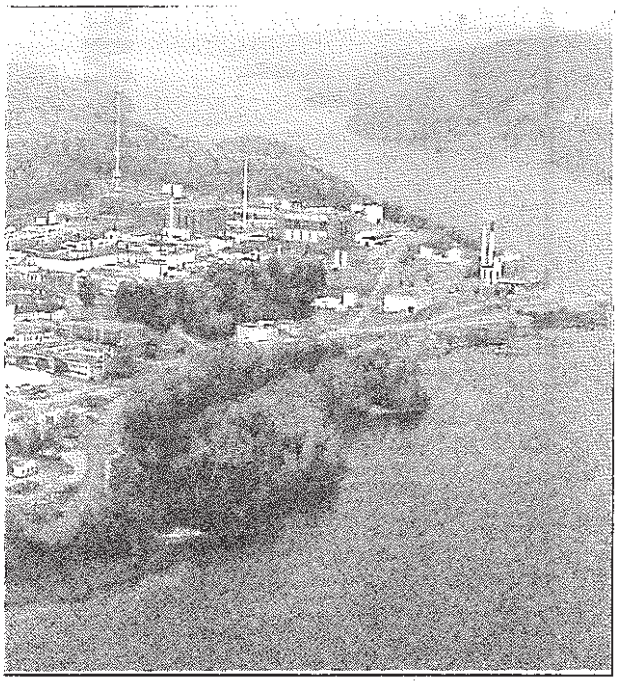

*Chalk River Nuclear Laboratories provides underlying research and development support for Canada's nuclear program. It has major responsibilities for reactor development, new radiation applications and isotopes, and physics and the health sciences.*

### Physics – Key to Inner Space

Since the discovery of radioactivity in 1896 and that of fission in 1938, physicists have gained a good understanding of uranium-235 and how its atoms can be "split". Once scientists appreciated that energy is released during fission, they began to build atomic "piles" or reactors. The first was in Chicago in 1942. The new discoveries led not only to the development of nuclear power but to improved radiation therapy and to medical diagnosis using radioisotopes.

AECL gives high priority to its national physics program. Today, nuclear physicists probe even further into the nucleus of the atom through use of high-powered accelerators or "atom-smashers" such as the Tandem Accelerator Superconducting Cyclotron (TASCC), designed and built at the laboratories. TASCC is used by researchers across Canada.

Our condensed matter physicists use beams of neutrons from the NRU research reactor to study how atoms and molecules are arranged in solids and liquids, how they move and what holds them together. Our theoretical physicists are studying newly discovered particles, such as quarks and leptons, now thought to be nature's basic building blocks. Discoveries made by physicists today may lead to new technologies in the future.

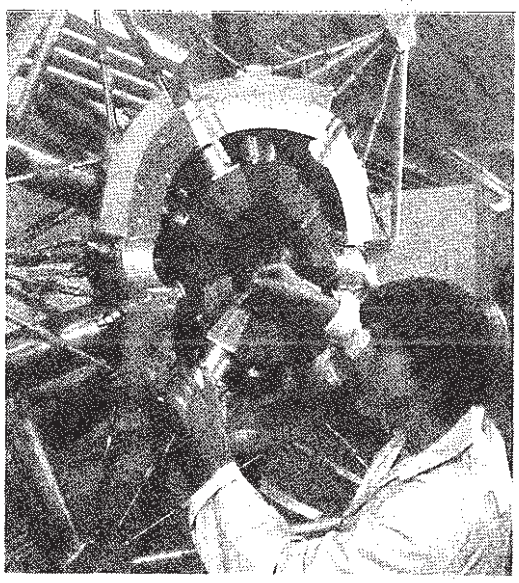

*Canadian university students come to Chalk River to use the Tandem Accelerator Superconducting Cyclotron, a powerful "atom-smasher" which allows researchers to study the nucleus of the atom.*

### Our First Reactors

Physicists led the way towards nuclear power but engineers and materials scientists have been essential in its development. At our laboratories, it all began with ZEEP (Zero Energy Experimental Pile), the first reactor to start

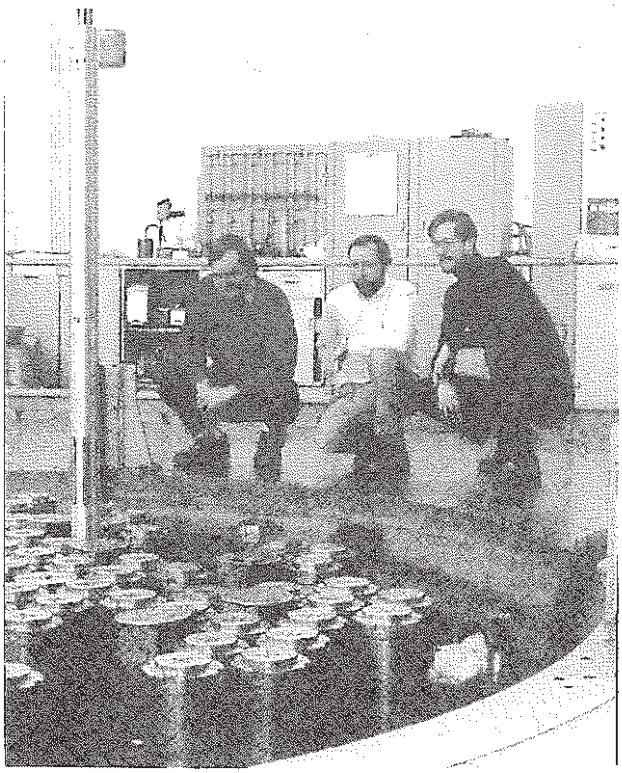

*NRU is a versatile research reactor which produces most of the free world's medical isotopes. Here, fusion test equipment is inserted into its core.*

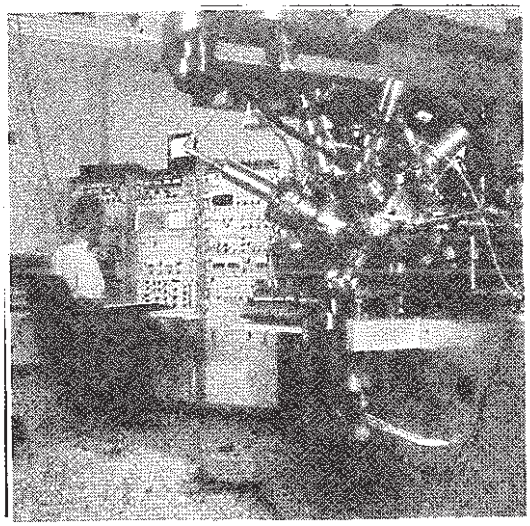

*Scientific staff at Chalk River use state-of-the-art equipment such as this spectrometer which provides information about the surface layers of different materials.*

up outside the United States, in 1945. A much more complex reactor, NRX (National Research EXperimental), followed ZEEP in 1947. At the time, NRX had the highest neutron "flux" (flow of neutrons) of any reactor in the world. It has been used to develop fuels and materials for CANDU, to produce radioisotopes for medicine and industry, and as a neutron source for physics experiments. An accident in 1952 showed that nuclear accidents need not be public disasters and taught engineers valuable lessons in reactor safety and design. Today, it is the oldest operating research reactor in the world, starting up when needed as a backup for the NRU (National Research Universal) reactor.

NRU, a more powerful research reactor, started up in 1957. Innovations made in this reactor – such as the use of heavy water as a moderator and the ability to refuel without shutting down – were later adopted in the CANDU reactor design. NRU contributes to fuels and materials testing and physics research and is the world's major supplier of medical isotopes. Two smaller research reactors also operate on-site.

## Commercial Reactors – Great and Small

With experience gained from the research reactors, AECL set to work on its first Canadian power reactor, the NPD (Nuclear Power Demonstration) reactor which started up in 1962. A special group, including engineers from industry, engineering consultants and Canadian electrical utilities, joined Chalk River scientists and engineers in this project. In 1958, a new division of AECL, now known as CANDU Operations, was launched to undertake design of future power stations.

Today, the AECL Research Company's Reactor Development group supports existing CANDUs and develops improvements, a process designed to keep CANDU a top-performing reactor. As well, new families of Canadian reactors are being designed and developed: advanced CANDUs incorporating leading-edge technology; new small reactors – SLOWPOKE and the Nuclear Battery – designed to generate heat and/or electricity in special environments such as remote locations and underwater vehicles, and the MAPLE series of research and isotope-producing reactors.

## Specialized Skills

Our specialized staff provides a wide range of skills to meet the exceptional demands of the nuclear industry. Materials scientists determine the best alloys and metals; experts in corrosion and wear, and nondestructive inspection, analyze any flaws and recommend new designs, manufacturing techniques or operating procedures; safety experts study the behaviour of the various parts of the reactor in hypothetical accident conditions; instrument and electronics engineers make state-of-the art improvements to hardware and software. Increasingly, we are finding that other industries are interested in benefitting from our research and development. For example, the technology behind the high-performance and highly reliable CANDU pump seals is now being applied to the O-ring seals in NASA's space shuttle booster rocket. The Research Company generates a significant portion of its own funding by selling its expertise and offers new products and processes for license to the private sector.

## Accelerators: Electrons in Our Lives

Nuclear technology plays a significant role in our lives. Many products we come across every day have been treated with radiation – gamma rays or

electrons – to give them special properties. Car tires are often "vulcanized" and paints and plastics cured with radiation; it is also an effective way of sterilizing surgical products. In the future, irradiation of food, to eliminate salmonella bacteria and increase shelf-life, will be more common.

AECL pioneered the gamma processing industry and today the Radiochemical Company supplies cobalt-60 irradiators throughout the world. A special group of Research Company and Radiochemical Company staff is presently working to develop a line of electron accelerators, applying Chalk River's long experience with high-power accelerators to industrial processing. Our sister site in Manitoba is identifying new uses for this technology.

## Radioisotopes for Medicine and Industry

Used to diagnose disease and injury and to treat cancer, radioisotopes play a major role in medicine today. NRU reactor now produces 60 to 70 per cent of the free world's medical isotopes: the versatile technetium-99m, used to "scan" most body organs and the cardiovascular system; xenon-133, for lung studies; iodine-125, for liver and kidney scans and in-vitro testing, and many others. Cobalt-60 is used in cancer treatment. Its gamma rays reach deep-seated tumors and kill cancer cells. The most important industrial isotope, iridium-192, is used in the pipeline industry to check for flaws in welds and metal castings. Isotopes from Chalk River are purified, packaged and marketed by the AECL Radiochemical Company in Ottawa.

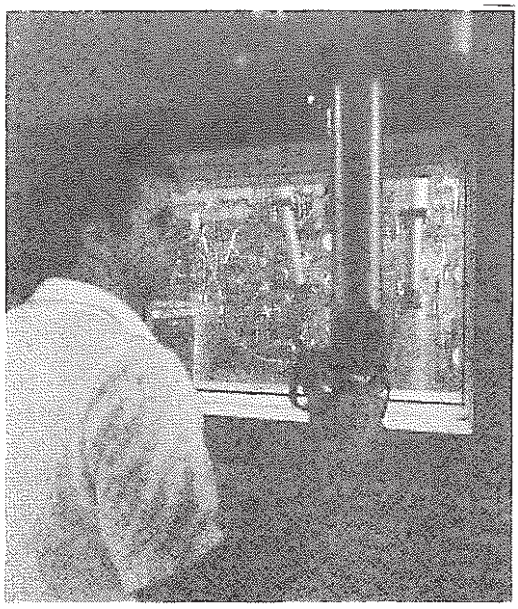

*Molybdenum-99 is the most important radioisotope produced at Chalk River. Its radioactive decay product technetium-99m provides more than 25 million patient diagnoses every year. Here an operator processes the "moly" remotely in a shielded cell.*

## Radiation and the Cell

In a living cell, the target most sensitive to radiation and many toxic substances is the genetic material, DNA. Chalk River's biologists are studying damage to DNA from radiation and other environmental agents, and the cell's ability to repair itself. Some people's cells are less able to repair damage to their DNA, and our researchers are developing a test to identify these more cancer-prone individuals. The major aim of our biological studies is to gain more knowledge about damage and repair mechanisms in living organisms, and to assess the radiation standards used for health protection. The long-term effects on man of relatively small amounts of radiation are constantly reviewed.

*Chalk River biologists perform experiments to study damage to cells from radiation and other environmental agents. Here a technologist separates fragments of DNA, the genetic material in the human cell, to assess repair capability in different human cell lines.*

## Guarding our Environment

Chalk River's environmental scientists are studying how radioactive materials and other toxic agents move through the ground, water and air. The laboratories' setting provides an ideal natural environment for this research. Glass blocks incorporating radioactive waste and buried in the Perch Lake basin show that it isn't easy for radioactive contaminants to move through soil – after 30 years, the amount that has escaped from the blocks is insignificant.

AECL has more detailed plans, however, for managing the radioactive wastes that result from producing nuclear electricity and using radioisotopes in hospitals and industry. Our Whiteshell laboratory is responsible for assessing ideas for long-term disposal of CANDU fuel. Chalk River's main responsibility is to design a disposal method for the other radioactive wastes.

*About 1200 skilled tradesmen, administrative staff and many others supply all the services you would find in a small city. Here, a certified ASME welder provides the finishing touches to an air-absorber tank intended for use at low temperatures.*

## Fusion: Planning for the Future

While fission is a process of releasing energy from "inner space", fusion also releases energy from matter and is a process that occurs naturally in outer space – in the sun and stars.

AECL manages the National Fusion Program which includes the Tokamak de Varennes, a fusion test facility near Montreal, and the Canadian Fusion Fuels Technology Project (CFFTP) in Toronto. AECL and CFFTP support a strong research and development program at Chalk River, concentrating on the lithium "blanket", which breeds the fusion fuel, tritium. The Canadian program emphasizes international cooperation, ensuring our access to fusion technology as it develops worldwide.

## CRNL: A Scientific "City"

Two thousand people work at Chalk River but not all are scientists, engineers and technical staff. About 1 200 skilled tradesmen, administrative staff and many others supply all the services you would find in a small city – fire protection, security, transport, electrical, design and construction, as well as computer and information services, for example. Plumbers, welders and metal workers provide quality work in well-equipped "shops".

At Chalk River, we are all proud of our past and look forward to the future, working with our colleagues at other AECL sites to improve the lives of Canadians.

## Can we help you?

Our Public Affairs staff can supply free brochures for school or university projects, a film list for teachers and prearranged tours for schools and other groups. In summer, we welcome visitors seven days a week. We can also arrange for a member of our Speakers' Group to address your school or organization. For more information, contact:

The Public Affairs Office
Chalk River Nuclear Laboratories
Atomic Energy of Canada Limited Research Company
Chalk River, Ontario
Canada K0J 1J0
Phone: (613) 584-3311

Atomic Energy of Canada Limited Research Company L'Énergie Atomique du Canada Limitée, Société de Recherche

August 1987 Printed in Canada

# WHAT NUCLEAR ENERGY MEANS TO CANADA

## • Jobs

30,000 direct jobs, many of them high-tech.
Equivalent of nearly 100,000 jobs overall.

## • The Economy

$4 billion per year contribution in 1986, a level of contribution similar to the chemical and automobile industries.

Ontario has already saved $7 billion in foreign exchange by using uranium rather than coal. Accumulated benefits of Ontario's nuclear program will amount to $20 billion by the year 2000.

## • World Leader in Uranium Exports

Canada's 1986 production of 11,720 tonnes contained more than twice the energy available from Canada's total annual oil production and more than the combined total of Canada's annual oil and gas production.

Canada is the world's leading exporter of uranium bringing in one billion dollars per year in sales.

## • Excellent Return on Nuclear Research Investment by Government

The most effective in the western world in terms of electricity produced per research dollar spent to the end of 1985.

| | Electricity per US $ spent (kWh) | Total Expenditure (US $ billion) |
|---|---|---|
| Canada | 189 | 2.5 |
| U.K. | 127 | 6.0 |
| U.S.A. | 103 | 31.6 |
| Japan | 94 | 9.6 |
| France | 84 | 12.2 |
| W. Germany | 56 | 11.2 |
| Italy | 25 | 3.4 |

## • Low Cost Electricity

One half of Ontario's electricity now comes from CANDUs which helps keep Ontario rates among the cheapest in the world.

| | Cents per kWh | Minutes Worked to buy 1 kWh |
|---|---|---|
| Ontario | 5.4 | 0.28 |
| Sweden | 6.2 | 0.47 |
| San Franscisco | 11.5 | 0.54 |
| France | 11.9 | 1.15 |
| Detroit | 12.8 | 0.45 |
| Tokyo | 19.4 | 1.43 |
| New York City | 20.7 | 0.97 |

Average Residential Rates – August 1986

## • Reliable Performance

CANDU stations are world leaders in reliability of operation. CANDUs have been consistently rated in the top ten of more than 300 reactors world-wide.

## • Prevention of Environmental Damage

If Ontario Hydro had used coal-fired generating plants to produce the same amount of electricity as has been made by its nuclear plants to date, it would have released six million tonnes of acid gas into the atmosphere and produced almost 20 million tonnes of ashes.

All of the used fuel from Canada's nuclear plants would fill an ice hockey rink to about waist high. The coal ashes would require about 25,000 times as much space if coal had been used. What's more the used nuclear fuel still has the potential for recycling to produce much more energy.

## • The World Scene

Most industrial countries have a strong commitment to nuclear energy. By 1990 there will be over 500 power reactors in service. At 400,000 MWe this represents more capacity than all the world's hydro-electric plants.

## • Reactor Exports

CANDUs currently hold 5% of the world reactor power market which is expected to grow rapidly through the turn of the century. This is a larger share than for most other industries.

## • Spin-Off Benefits

Nuclear energy offers many additional beneficial uses and Canada is at the forefront of these developments.

Health and Medicine – Diagnosis, Cancer Therapy, Instruments and Dressings Sterilisation.

Food and Agriculture – Crop Improvement, Pest Control, Food Preservation, Animal Husbandry.

Industry – Gauging, Analysis, Tracers, Navigation Aids.

## • Still to Come

Many important potential developments are waiting in the wings – Major district heating concepts, tar-sands extraction, fusion energy, etc.

For further information about Nuclear Energy in Canada contact:
CANADIAN NUCLEAR ASSOCIATION
111 ELIZABETH STREET, TORONTO, ONTARIO
M5G 1P7 (416) 977-6152

Revised March 1987

French Overleaf

# CE QUE SIGNIFIE L'ENERGIE NUCLÉAIRE POUR LE CANADA

## Emplois

30,000 emplois directs, dont bon nombre dans le domaine de le haute technologie. L'équivalent de plus de 100 000 emplois au total.

## Economie

Contribution annuelle de 4 milliards de $ en 1986, une contribution qui est comparable à celle des industries de produits chimiques et d'automobiles.

L'utilisation de l'uranium plutôt que de charbon a permis à l'Ontario d'économiser jusqu'à maintenant 7 milliards de $ en devises étrangères. La valeur totale des avantages que l'Ontario retire de son programme nucléaire totalisera 20 milliards de $ en l'an 2000.

## Chef de file mondial en matière d'exportation d'uranium

Les 11 720 tonnes d'uranium produites au Canada en 1986 représentaient plus du double de l'énergie provenant de notre production annuelle totale de pétrole et plus que la production annuelle totale de pétrole et de gaz.

La valeur des commandes annuelles d'exportation d'uranium du Canada s'élève à environ un milliard de $.

## Rendement de l'investissement dans la recherche nucléaire par le gouvernement

L'investissement le plus rentable dans l'hémisphère occidental en termes d'électricité produite par dollar investi dans la recherche jusqu'à la fin de 1985.

| | Electricité produite par $ investi (kWh) | Dépenses totales (milliards de $US) |
|---|---|---|
| Canada | 189 | 2.5 |
| Royaume-Uni | 127 | 6.0 |
| Etats-Unis | 103 | 31.6 |
| Japon | 94 | 9.6 |
| France | 84 | 12.2 |
| Allemagne de l'Ouest | 56 | 11.2 |
| Italie | 25 | 3.4 |

## Electricité bon marché

La moitié de l'électricité produite en Ontario provient des réacteurs CANDU qui aident la province à maintenir ses tariffs parmi les moins élevés au monde.

| | Cents par kWh | Minutes travaillées pour acheter 1 kWh |
|---|---|---|
| Ontario | 5.4 | 0.28 |
| Suède | 6.2 | 0.47 |
| San Franscisco | 11.5 | 0.54 |
| France | 11.9 | 1.15 |
| Detroit | 12.8 | 0.45 |
| Tokyo | 19.4 | 1.43 |
| New York (ville) | 20.7 | 0.97 |

Tariff residentiels moyens - août 1986

- ## Rendement fiable

  Les centrales CANDU possèdent la meilleure fiche de fiabilité du fonctionnement. Les réacteurs CANDU se classent constamment parmi les dix premiers au monde sur plus de 300 réacteurs.

- ## Prévention de la pollution

  Si Ontario Hydro avait utilisé des centrales au charbon pour produire la même quantité d'électricité que celle produite par ses centrales nucléaires jusqu'à ce jour, elle aurait libéré dans l'atmosphère six millions de tonnes de gaz acide et produit près de vingt millions de tonnes de cendres.

  Le total du combustible irradié provenant des centrales nucléaires pourrait être contenu dans une patinoire de hockey jusqu'à une hauteur de trois pieds. Si on avait, par contre, utilisé des centrales au charbon, les cendres seule auraient occupées environ 25 000 fois ce volume. En outre, le combustible nucléaire irradié peut être recyclé pour produire beaucoup plus d'énergie.

- ## Sur la scène mondiale

  La plupart des pays industrialisés sont fortement engagés envers l'énergie nucléaire. D'ici 1990, plus de 500 réacteurs nucléaires seront en service dans le monde. Cette capacité totale de 400 000 MWe sera supérieure à celle de toutes les centrales hydro-électriques existantes.

- ## Exportations de réacteurs

  La part des CANDUs du marché mondiale des réacteurs nucléaires est actuellement de 5% et devrait s'accroître sensiblement vers le tournant du siècle. Cette part d'un marché mondial est proportionnellement plus grande que pour la plupart des industrie.

- ## Retombées économiques

  L'énergie nucléaire se prête à bon nombre d'autres applications utilitaires, pour lesquelles le Canada se situe au premier plan.

  Santé et médecine – diagnostic, traitement contre le cancer, instruments et pansements, stérilisation.

  Aliments et agriculture – amélioration des récoltes, lutte contre les insectes, conservation des aliments, élevage.

  Industrie – jaugeauge, analyse, traceurs, aides à la navigation.

- ## Perspectives d'avenir

  Bon nombre de développements importants figurent parmi les projets étudiés, notamment le concept du chauffage de districts urbains, l'extraction des sables bitumineux, l'énergie thermonucléaire, etc.

Pour de plus amples renseignements sur l'énergie nucléaire au Canada, communiquez avec:
L'ASSOCIATION NUCLEAIRE CANADIENNE
111 RUE ELIZABETH, TORONTO (ONTARIO)
M5G 1P7 (416) 977-6152

Révision, mars 1987



Anglais au verso

# Waste Treatment Centre

The Waste Treatment Centre at Chalk River was constructed to develop and demonstrate processes to reduce the volume of solid and liquid low-level radioactive wastes and to convert them to a form most suitable for storage and disposal. The solid low-level radioactive wastes are separated, at source, into incinerable and non-incinerable containers. The burnable wastes are handled in a two-stage, starved-air incinerator. Exhaust gases are carefully filtered to ensure that most of the radioactivity remains in the ash. The volume reduction factor for this process is greater than 150 to one. The ash is currently being stored in drums, but will eventually be immobilized.

The non-incinerable low-level radioactive waste is compacted to a reduction of nearly eight to one. Baled waste is currently being stored but will eventually be transferred to a permanent disposal area. Liquid wastes with low-level radiation originate from active drains in the reactor buildings, laboratories, and the decontamination centre. These wastes are filtered, then forced through semi-permeable membranes. Almost all of the radioisotopes present in the waste are retained and concentrated. This liquid must be further processed by blending it with emulsified bitumen in the solidification plant. At this point, the dilute aqueous low-level radioactive waste has been concentrated by a factor of about 1500 to one.

The Waste Treatment Plant provides a full-scale integrated waste management system and is being used to generate performance and cost data, and to serve as a marketing tool for this technology.

# Accelerator Development Laboratory

The Accelerator Physics Branch at Chalk River comprises 47 physicists, engineers and technologists who are working on projects that include both basic accelerator science and commercial exploitation of accelerator technology.

The basic science component investigates limits of accelerator knowledge and technology, especially in areas likely to prove important to future applications in industry, medicine and research. The programs include experiments and development of accelerator structures, high current ion sources, advanced accelerator concepts, control systems, diagnostic devices and computer codes for accelerator design. Current commercial work includes design and fabrication of accelerating cavities for a large accelerator complex in Germany, development of an industrial irradiator based on a 10 MeV electron accelerator, development of a neutral beam injector for plasma diagnostics, and specialized irradiations using our high-power electron accelerator.

Work on accelerator structures will be described. This work ranges from experiments in the forefront of accelerator development, such as the laser-plasma beat-wave accelerator in collaboration with INRS Energie, Varennes, to applications for business development opportunities, such as the 10 MeV, 50 kW IMPELA industrial irradiator program.

# The ChalkRiver Accelerator Physics Branch

Chalk River Nuclear Laboratories, Atomic Energy of Canada Limited Research Company March, 1987

**Introduction:** The Accelerator Physics Branch had its beginnings in the mid 1960s during the Intense Neutron Generator (ING) study. The study proposed construction of a 1 GeV, 65 mA cw proton linear accelerator (linac) with a liquid PbBi eutectic target. High energy protons, in collision with high atomic number nuclei, generate large numbers of neutrons through the spallation process; ING would have given neutron fluxes in excess of $10^{16}$ / $cm^2/s$ – considerably greater than that available from reactors – and was to have been the centre-piece of an excellent research facility. ING was cancelled in 1968 but the branch continued working on the development of high current cw accelerators, mainly towards the development of electro-nuclear breeding, and at the same time pursued other accelerator development programs. Some of our past achievements and current programs are described below. We expect these programs to change as new aspects of accelerator technology emerge and offer promise. Despite this evolution of our programs, they will remain anchored in applied electromagnetics.

The 47 physicists, engineers and technologists in the branch are working on projects that include both basic accelerator development and commercial exploitation of our technology. The basic component investigates limits of accelerator knowledge and technology, especially in areas likely to prove important to future applications in research, medicine and industry. The programs include experiments and development on accelerator structures, high current ion sources, advanced accelerator concepts, control systems, diagnostic devices and computer codes for accelerator design. Current commercial work includes design and fabrication of accelerating cavities for a large accelerator complex in Germany, development of an industrial irradiator based on a 10 MeV electron accelerator, development of a neutral beam injector for plasma diagnostics and specialized irradiations using our high-power electron accelerator.

All radiofrequency (rf) accelerators have evolved from the original concept of R. Wideröe, illustrated in Figure 1. Clusters of charged particles, or bunches, enter from the left. A row of conducting "drift" tubes is connected alternately to the terminals of an rf voltage source and the particles are accelerated by a succession of impulses received in the gaps between adjacent drift tubes. Each bunch arrives at the first gap when the electric field will accelerate the particles. Bunches are screened from the reversing electric field by a drift tube until they reach the second gap; the frequency and drift-tube length are chosen to give an accelerating impulse at this and succeeding gaps. Drift-tube length increases with particle velocity to maintain this essential synchronism. Development of this concept over six decades has resulted in an impressive number of ingenious variations, some of which are described in following sections.

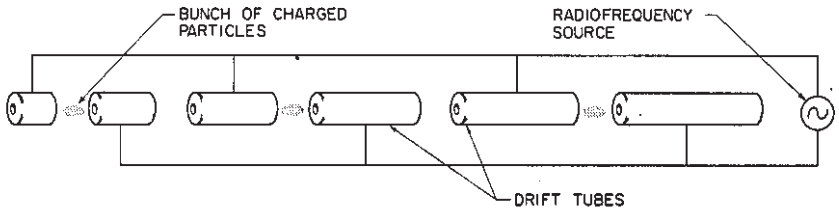


*Figure 1 Schematic of Wideröe accelerator.*

**High-Power Structure Development:** Understanding and predicting the properties and high-power behaviour of rf structures is a fundamental part of accelerator development. The design of a high-power particle accelerator, whether of a new concept or of an established type, involves three interactive steps – (1) beam dynamics calculations to decide what rf fields are required to accelerate the beam, (2) structure design and modeling to determine if the required fields can be achieved and (3) thermal stress analysis to optimize the cooling system and determine the dynamic behaviour of the structure from cold startup to high-power operation. Thus the design of an rf structure is a complex process requiring a broad base of experience, both from physical understanding and engineering points of view.

Accelerating structures may be roughly divided into two categories, low β or high β ($\beta = v/c$) depending on the velocity of the beam. For example, a particle with an initial velocity much less than the velocity of light ($\beta << 0.1$) needs a very different accelerating structure than a relativistic particle ($\beta \approx 1$). We have contributed to the fundamental development of structures of both types covering a broad range of frequencies. RF structures studied at CRNL over the last 20 years include magnetron and crossed field amplifiers, drift tube (Alvarez) structures, coupled cavity linacs, loaded quarter wave resonators (for the Superconducting Cyclotron), re-entrant folded coaxial cavities (for the HERA project in West Germany) and radiofrequency quadrupoles (RFQs).

All these structures may, in principle, be analyzed by solving Maxwell's equations with the appropriate boundary conditions. In practice, however, full 3-dimensional codes to model actual structures are not yet within the practical capability of present computer systems. Two dimensional codes are available but they can model only a simplified, idealized geometry. Thus, theoretical analysis is usually accompanied by physical modeling and extensive measurements of the various resonant frequencies and spatial distributions of rf fields in the structure.

To ensure the reliability of an accelerator structure, 3-dimensional thermal stress analysis can be used to op-

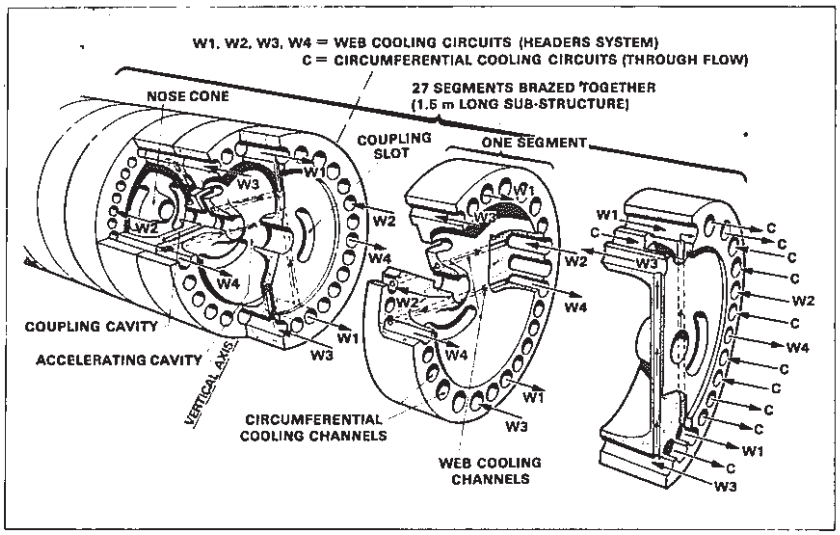


*Figure 2 Cooling channels in a high-power on-axis coupled accelerating structure.*

timize cooling. Figure 2 shows the various cooling circuits used for a high-power on-axis coupled structure. Limitations of linac structure design and changes in a structure's rf characteristics at high power are determined from finite element analysis. The possibility of reducing coolant flows by using a two phase coolant is being investigated.

Computer simulations are used to develop the fast control systems required to maintain the resonant frequency and accelerating field amplitude in a structure during high power operation. Side coupled, on-axis coupled and coaxial coupled high power L-band and S-band accelerator structures have been studied at CRNL to optimize their control under heavy beam loading and determine the conditions leading to beam breakup which limits the beam current and reduces the linac's efficiency.

**RFQ1:** A new accelerator variant is the Radio Frequency Quadrupole (RFQ), which was first described by Russian scientists in 1970, but remained undeveloped until work began in the USA almost ten years later. In its simplest form, an RFQ consists of four parallel modulated rods connected in opposing pairs to the terminals of an rf generator as shown in Figure 3. The oscillating quadrupolar electric field set up in the region between the rods confines the beam of charged particles radially. Each pair of rods has identical modulations, but the hills of the vertical pair are located opposite the valleys of the horizontal pair, giving a longitudinal electric field component on the axis. By systematically increasing modulation amplitude and wavelength the longitudinal field can bunch and accelerate a beam of charged particles. RFQ's are particularly useful at the beginning of an accelerator where they are increasingly being used to replace cumbersome high voltage dc injectors.

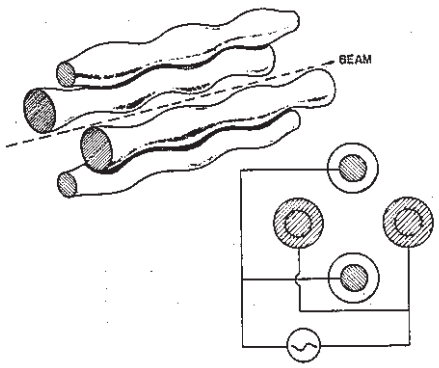


*Figure 3 Conceptual illustration of a short length of a Radio-Frequency Quadrupole (RFQ) accelerator.*

We are developing high current, high duty factor proton accelerators in the 500 keV – 2 MeV range as injectors for higher energy accelerators and for the production of neutrons. Presently, emphasis is on RFQ1, a 75 mA cw proton linac which includes a 50 keV, 100 mA dc injector, and a 270 MHz, 600 keV RFQ accelerator. A four-vane RFQ design was chosen here, rather than a 4-rod, for mechanical reasons. The vanes, with a wedge-like cross-section, are mounted radially in a long pipe, with their copper tipped modulated edges defining the central beam channel. The whole structure, with vacuum pumps and appendages, is about 1.5 m in diameter. The vanes (Figure 4) have had their tips machined to a precise profile designed for maximum capture fraction and optimum acceleration. First operation of this facility is scheduled for late 1987; at 75 mA, it will be the highest current cw RFQ ever operated.

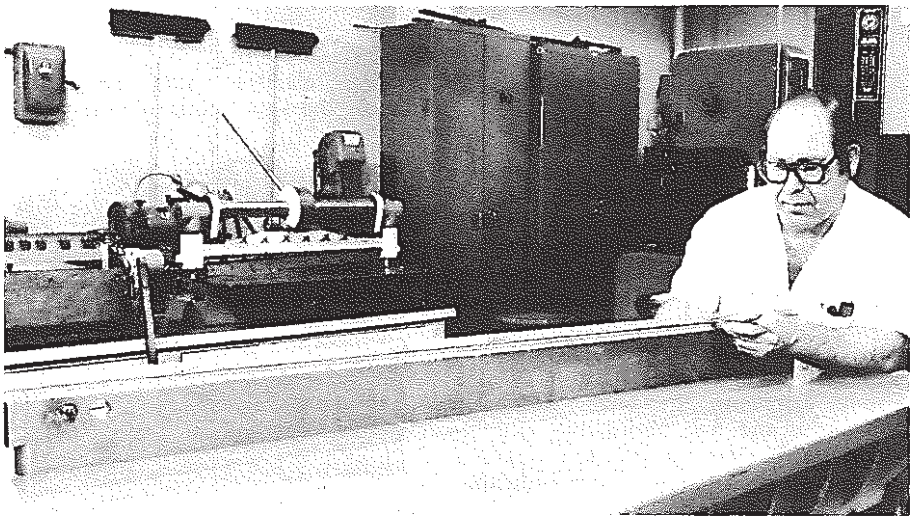

*Figure 4 One of the four vanes for RFQ1, a 1.5 m long, 600 keV proton accelerator.*

**Superconducting Cyclotron:** Figure 5 shows a quite different type of accelerator, the Chalk River superconducting cyclotron. The idea was originally proposed by Bruce Bigham and Harvey Schneider of the Accelerator Physics Branch and is now being pursued by several laboratories around the world. It was chosen as the most economical booster for the existing MP tandem Van de Graaff electrostatic accelerator – these two coupled accelerators form the TASCC (Tandem Accelerator Superconducting Cyclotron) facility. The cyclotron was designed and built by the Accelerator Physics Branch to satisfy a Nuclear Physics Branch request for an accelerator with a high quality beam capable of accelerating all ions – light ions like carbon to 600 MeV with energy increas-

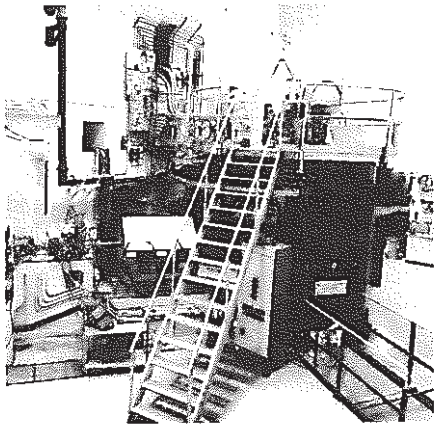

*Figure 5 View of the superconducting cyclotron. Ions from the tandem Van de Graaff accelerator are injected through the beam line at the left.*

ing with ion mass to 2400 MeV for uranium.

The advantage of a superconducting magnet for a cyclotron is that the high magnetic fields attainable make the machine only one-third the diameter of a conventional machine of similar capability. The extra costs associated with building and operating a magnet with coils at liquid helium temperature are more than compensated by the savings achieved by the smaller size. The choice of a superconducting magnet makes novel techniques readily available to other subsystems of the cyclotron, for example, cryopumping of the accelerating cavity vacuum and a superconducting extraction channel.

Two of the many challenges encountered in the cyclotron design were extracting the beam from the cyclotron and fine tuning the magnetic field. The former problem was solved by using small superconducting coils and magnetically saturated iron bars to counter the main coil field and the latter by using moving saturated iron rods in the poles (the "trim rods"). It is the only superconducting cyclotron in the world which does not use trim coils wrapped round the poles for field trimming.

Detailed design of the cyclotron began in 1974. By the end of 1981 the two major systems, the magnet and the accelerating structure had been independently tested and proven and in 1982 the full rf accelerating cavity was operated at power in the calibrated field of the cyclotron magnet. The magnet was then moved to its shielded vault in the TASCC facility. Commissioning with beam from the tandem began in Summer 1985, acceleration of I-127 to the extraction radius at an energy of 1.27 GeV was achieved on September 12 and first beam extracted outside the cyclotron on November 19. The first nuclear physics experiment using the cyclotron beam started on 1986 March 03. Accelerator Physics Branch continues to provide design effort for upgrades and improvements to the cyclotron.

**Electron Linear Accelerators:** Work on electron accelerators at CRNL has concentrated on standing wave linacs. This work began in the late 1960's with the Electron Test Accelerator (ETA). This 4 MeV accelerator, which used the $\pi/2$-mode side-coupled structure developed at Los Alamos for LAMPF, was designed to model, with electrons, the behaviour of protons in high energy accelerating cavities. The ETA linac, powered by klystrons at a frequency of 805 MHz, was the first $\pi/2$ mode accelerator to be operated cw. Beam powers up to 80 kW and beam loading up to 85% were achieved before this accelerator was shut down in 1985.

A second electron linac program began at almost the same time with the objective of developing low duty factor ($\approx$ 0.1%) compact accelerators that could be used for producing high energy electrons and photons for cancer therapy. Work on this program led to the CRNL development of the on-axis coupled accelerating structure (see Figure 6) which is simpler to fabricate than the side-coupled structure and is now used on a number of accelerators – for example on the University of Mainz 1 GeV Microtron. The physical size constraints on the medical therapy accelerators produced a number of accelerator physics challenges. The "double-pass" linac concept in which a beam from an annular electron gun traverses the same accelerating structure twice in opposite directions was developed at CRNL to produce a compact accelerator with a wide range of electron energies. Powered by a 3 GHz pulsed magnetron, it produced electron beams from 6-25 MeV for electron and photon therapy with an accelerator only 1.2 m long. It was marketed by AECL Medical Products Division as the THERAC 25.

Electron accelerators now play a large role in industrial processes, ranging from cross-linking of polymers and radiation curing with 100-500 keV units, to sterilization of medical disposables with 10-15 MeV accelerators. The IMPELA (Industrial Material Production Electron Linear Accelerator) program is developing 10-15 MeV linacs with 10-50 kW beam powers for industrial applications. These developments are based largely on the experience gained in the ETA and medical accelerator programs. One particular linac, the Pulsed High Energy Linear Accelerator (PHELA), an on-axis coupled 3 GHz structure powered by a 0.1% duty factor pulsed klystron, produces average beam powers in the 2-5 kW range for commercial irradiations and serves as a test bed for various accelerator concepts.

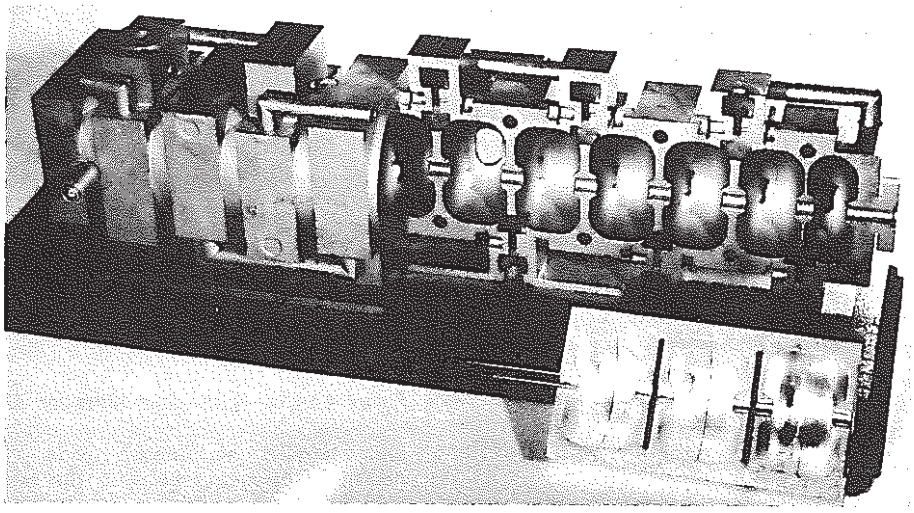

*Figure 6 Cutaway view of a 3 GHz side-coupled accelerating structure and a short section of on-axis coupled structure. The 55 cm long side-coupled accelerator produced 4-8 MeV electron beams.*

**PETRA II Accelerating Cavities:** Perhaps the best-known use of particle accelerators is in high energy physics. The Branch presence in the field is based on consultation and construction of equipment for programs at other laboratories. The largest interaction has been with the HERA project at the DESY laboratory, in Hamburg.

The HERA facility will study collisions between 30 GeV electrons and 820 GeV protons. It will consist of two parallel chains, each consisting of

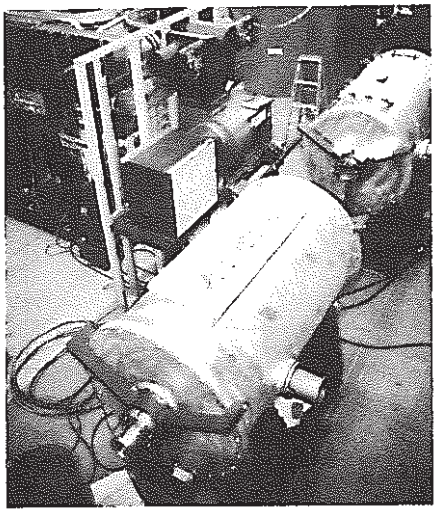

*Figure 7 52 MHz PETRA II rf system during assembly at CRNL prior to shipment to Germany. The 0.9 m diameter cavities are seen in the right foreground*

an injector linac and three synchrotrons, for electrons and protons. German federal and Hamburg state government approval of the approximately 500 M$ project required significant international contributions to the construction phase. The Canadian contribution, the first committed, involves CRNL and TRIUMF in the supply of proton system elements. The Institute of Particle Physics (IPP) is co-ordinating the contribution, with support from the Natural Sciences and Engineering Research Council (NSERC).

CRNL has contracted with IPP to supply two accelerating cavities and associated rf equipment, control systems and power supplies (see Figure 7) for the second proton synchrotron, PETRA II, which feeds the superconducting main ring. The cavities, modeled on the Fermilab Antiproton Accumulator cavities, are tuned (51.6 – 52.0 MHz) to match proton velocity variation, using a loop- coupled coaxial line, loaded with perpendicularly biased ferrite. They provide 100 kV to accelerate proton bunches during the 2-minute acceleration cycle, and 200 kV to compress them prior to transfer to the main ring. The grounded-grid triode amplifiers, loop-coupled directly into the cavities, are capable of dissipating 25 kW each, most of which goes into compensating for beam loading. The fast analog control system counters beam instability with feedback (loop gain of 50) and feedforward. The control computers operate the system under direction from the DESY computer.

This 18-month, 2.1 M$, project will end 1987 May 01. A companion project to provide two similar cavities for the main HERA proton synchrotron by 1988 October 31, is presently being considered by NSERC for funding.

**Ion Sources:** Ion sources are an important component of any ion accelerator and are also used directly in industry and research. We have concentrated on the development of high-current dc ion sources and our experience is being applied to isotope separation, ion implantation and plasma diagnostics as well as accelerator injectors.

All high-current ion sources extract beam from the surface of a plasma but differ in how the plasma is generated. Two plasma generator concepts used at CRNL are the duoplasmatron and the duoPIGatron. In a duoplasmatron, an arc discharge between a hot cathode and an anode is pinched at an intermediate electrode by an inhomogeneous magnetic field to generate a very high plasma density. The duoPIGatron adds a fourth electrode, the so-called anticathode. Electrons oscillating between the intermediate electrode and the anticathode increase the plasma density still further. Both of these plasma generators have been mated to multi-aperture triode extraction columns optimized to reduce aberrations while giving high brightness and freedom from sparking.

A wide range of ion beams, ranging from $H^+$ to $Xe^+$, has been generated at extraction voltages of 10 to 50 kV. Extraction current densities up to 600 mA • $cm^{-2}$ for hydrogen have been achieved and as much as 850 mA has been extracted from a thirteen aperture duoPIGatron. Ion source development at CRNL is now concentrated on a version of the duoPIGatron that will accept non-volatile (solid) feeds, with emphasis on improvements in beam purity and reliability. These properties are especially important for industrial applications of low-energy ion beams.

**Diagnostics:** A general requirement of all particle accelerators is diagnostic equipment to monitor beam characteristics, such as position, energy and intensity. Although techniques for measuring these properties are well known, very high power beams present a special problem since any equipment which intercepts the beam is liable to be melted very quickly. Thus our development program has focused upon non-intercepting diagnostic techniques for intense ion beams.

Recent work has demonstrated beam profile and beam divergence monitors that use the light emitted by the beam as it passes through the residual gas in the vacuum chamber. At low gas pressures light intensity is proportional to beam intensity, thus profile measurements of light emission across the beam yield the beam profile. Similarly, ions or atoms in the beam can emit light. A measurement of the Doppler broadening of this emission can be used to determine the divergence of the beam.

Electric fields are created by the high charge density of intense ion beams, and knowledge of the distribution of these fields within the beam is very important for designing beam transport systems. A new technique to measure these electric fields is being developed. Stark quenching of Balmer emission lines from residual hydrogen gas in the vacuum is measured by an rf-optical method. This permits the average field within the ion beam to be determined. Further enhancements to the techniques are planned to determine the spatial distribution of the electric fields.

**Laser Plasma Beatwave Experiment:** Ever since Cockroft and Walton first produced nuclear reactions by means of a particle accelerator, physicists have channeled their collective talents towards the development of ever more powerful machines. This development has required the invention of a new accelerator technology roughly every decade to maintain the rate of increase in available particle energy. The present challenge is to achieve 100-1000 TeV energies in a reasonable physical size and no existing technology can meet it.

In a collaborative research program between CRNL and the Université du Quebec at Varennes in Quebec, we are studying novel methods of accelerating electrons with high power lasers in a plasma medium. The trick is to turn the transverse field of the laser (which is not in the right direction for accelerating electrons) into a longitudinal field. This is achieved by illuminating the plasma with two laser beams of angular frequency $\omega_1$ and $\omega_2$. If the beat frequency $(\omega_1 - \omega_2)$ is equal to the plasma frequency, it will resonate with the plasma and bunch the plasma. The bunching results in a longitudinal electrostatic field which can accelerate particles. Using a high power pulsed carbon dioxide laser operating at 9.6 and 10.6 $\mu$m wavelengths and a plasma at an electron density of $10^{17}$ electrons-$cm^{-3}$ produced by the same laser beams, we have, for the first time ever, accelerated externally injected electrons using laser generated electric fields. The acceleration gradient, produced over a 1.5 mm length, was greater than 1 GeV/m. These observations open up new possibilities for accelerating particles to ultra-high energies.

SPECIAL REPORT

F O O D • I R R A D I A T I O N:

# A NEW ERA IN FOOD PRESERVATION IS COMING

If current predictions are correct, the coming decade will usher in a new era in food preservation around the world. Pressure is growing for wider use of a nuclear technique known as irradiation to assume some of the duties now performed by a myriad of chemicals and processes in the food industry. The pressure is coming from governments, consumer organizations, food-processing interests and the existing irradiation industry, which has been waiting in the wings like a nervous understudy for nearly 30 years.

Food irradiation is a process by which food is exposed to ionizing energy emitted by radioactive isotopes, usually cobalt-60, or from fast-moving electrons produced by accelerators, or from X-rays. Cobalt-60 is produced in CANDU power reactors for commercial use in the existing industrial irradiation industry and as a source of radiation for cancer therapy machines.

What interests the food and agricultural industries is the fact that ionizing radiation can perform four distinct functions in the processing of food. Depending on the amount of radiation applied and the type of food exposed, radiation can:

- preserve food by destroying the micro-organisms that cause normal spoilage,
- kill food-borne parasites and pathogenic micro-organisms such as trichinella and salmonella,
- slow the ripening of some fruits and inhibit the sprouting of potatoes and onions,
- sterilize or kill the adults, larvae and eggs of insects.

From the standpoint of food industry and consumer benefits, these characteristics translate into longer shelf lives for many items

such as poultry, fish, meats and some fresh fruits and vegetables. The possibility of food poisoning is reduced. It has been demonstrated, for example, that fresh, irradiated poultry can be kept for as long as two weeks (as opposed to three days) under refrigeration and strawberries for an additional 10 days. It must be noted that irradiation is not suitable for all foods and it cannot be used to make an inferior product better.

At the cellular level, ionizing radiation breaks down some of the chemical bonds in micro-organisms including those of DNA (deoxyribonucleic acid) molecules, killing the affected cells. This is the property that destroys organisms that contaminate food. In a limited way, the same action slows the ripening process of some fruits. The amount of exposure needed to kill organisms varies, depending on the organism, but generally the simpler the organism the higher the dose needed.

**Radiation passes through food, killing insects, pathogenic organisms and spoilage bacteria.**

The equipment and procedures used to irradiate food are relatively simple. Food products are conveyed through a thick-walled room containing a source of ionizing radiation. Radiation passes through the food and the packaging surrounding it, killing insects, pathogenic organisms and spoilage bacteria on its way. The amount of radiation food receives (called the dose) is critical because too little will not produce the desired effect and too much may create unwanted changes in flavor and texture. The dose of radiation a product receives depends on the amount of time it is exposed and the intensity of the radiation source. After foods have been irradiated, they can be eaten immediately.

Food irradiation is of particular interest to Canada, since this country, through Atomic Energy of Canada Limited (AECL), is the world's largest supplier of industrial irradiators and cobalt-60. Of the world's 140 industrial irradiators, 85 were supplied by AECL.

Advocates of the process claim it has several advantages over chemical fumigants and preservatives. It leaves no residue; it can be applied after food has been packaged to prevent re-infection; and it penetrates food, killing pests such as the mango seed weevil that have bored into the interior — something chemical pesticides cannot do.

Because research has shown that irradiation destroys pathogenic bacteria such as salmonella, it could also help prevent many outbreaks of food-related illnesses. It's estimated that four million people

# FOOD • IRRADIATION:

in North America become ill from salmonella poisoning every year. Poultry is the major carrier.

Not everyone agrees that food irradiation is as good as it's cracked up to be. Critics question the economics of the process and call for further study on the wholesomeness of irradiated food, although there have been countless studies and papers on the subject over the past three decades. The World Health Organization, the United Nations Food and Agricultural Organization and the International Atomic Energy Agency declared it safe in 1983.

Another factor that has raised the hackles of many critics and consumers has been the overselling of the process, especially during earlier days when it was touted as a cure-all for food-related problems. Unrealistic claims on the economics, on its ability to extend the shelf-life of foods and on its potential for easing world hunger were recognized and condemned as overt boasting. There is little doubt radiation can play a role in these areas, but it too, say the specialists, has its limitations. Like freezing or canning, it is useful for some items and useless for others.

**Several recent events have pushed food irradiation into the spotlight.**

Despite the benefits claimed for food irradiation by its advocates, it has been little used because early classification as a food "additive" rather than a process such as freezing or canning, meant irradiated foods had to undergo lengthy and expensive testing programs for toxicity. But several recent events have pushed food irradiation into the spotlight.

One was the 1984 continent-wide banning of a chemical called ethylene dibromide (EDB), which for years served as a fumigant in the food industry. It was used by everyone from Canadian grain millers to Hawaiian papaya growers to control insects. When EDB was found to be carcinogenic, it exited the North American stage quickly.

Although the banning was extensively covered by the media, its significance was largely lost. What it did was call into question other chemical fumigants and additives, sending officials and scientists in government and industry scurrying for alternative methods of disinfesting and preserving food. One of those alternatives was irradiation, a technology that has already made a name for itself sterilizing disposable medical products such as rubber gloves and syringes, and certain consumer products like tampons and baby soothers — products that were once sterilized almost exclusively by either chemicals or heat in the form of steam or boiling water.

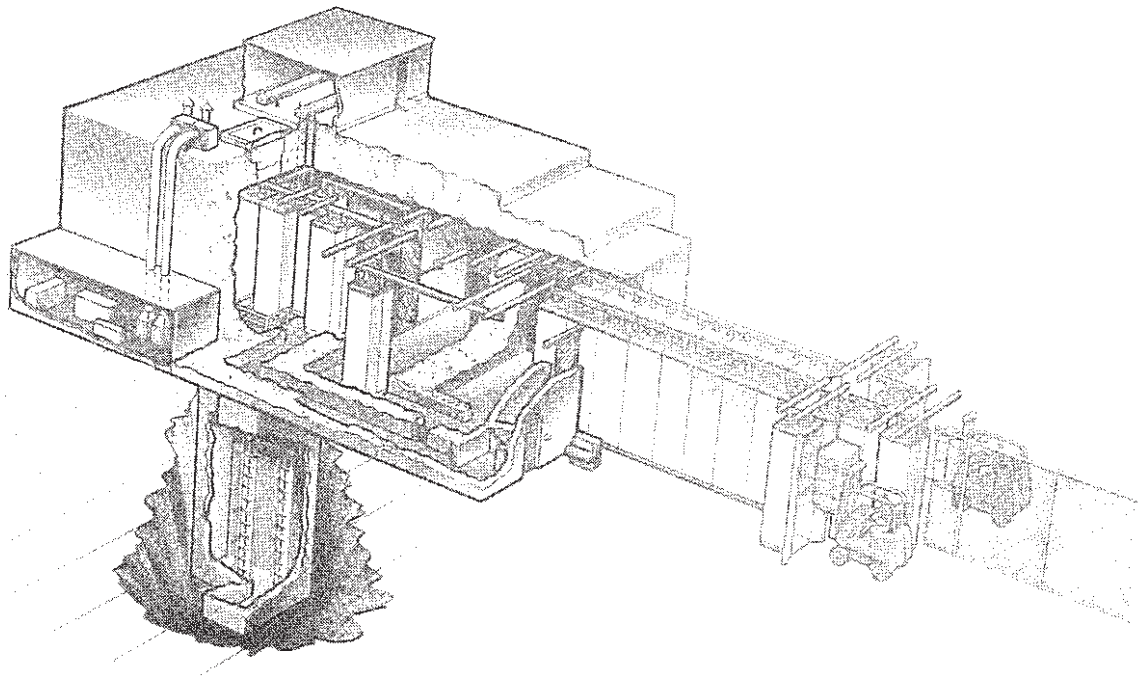

*Food irradiation is of particular interest to Canada because this country, through AECL, is the world's largest supplier of industrial irradiators such as this one designed to process palletized goods.*

# F O O D • I R R A D I A T I O N:

As a relatively new industy, it has established a good record for safety, economy and convenience and is currently competing toe to toe with chemicals and heat processes. An estimated 50% of all medical disposables are now sterilized in gamma irradiators around the world.

Dr. George Giddings, food scientist and food irradiation consultant, is actively promoting the use of ionizing radiation for food processing. "There's a pressing need for a long-term alternative to chemical fumigants," he maintains. "One by one, the chemicals are expected to be eliminated. Insects must be controlled and it's unlikely biological controls alone will be able to handle the job. Bandage solutions have been tried, but the full, complete solution is radiation."

The move away from chemicals is not the only factor giving impetus to food irradiation. In 1983, after years of deliberation and study, the Codex Alementarius Committee of the United Nations, representing some 125 countries, set specific standards for the irradiation of foods and ruled that foods processed to these standards retained their wholesomeness. Although the standards are not binding on any of the nations represented, they do provide a foundation on which national regulations can be built, and they add credibility and impetus to the process itself. The Codex standards, coupled with the fact that food irradiation is gradually being introduced abroad, particularly in Europe, means Canada and the United States must move on decisions affecting its future in North America to ensure that the international trade in food does not become additionally complicated.

Knowledge of the process stretches back to 1905 when two U.S. patents were issued for inventions to preserve food using radiation to eliminate micro-organisms, but it wasn't until the 1950s that the U.S. Atomic Energy Commission and the U.S. Army began extensive research on food irradiation. At the same time, Atomic Energy of Canada Limited stepped into the field with a lab-sized irradiator called the Gammacell-220, donating about a dozen of the units to Canadian universities to stimulate research into the process. During the next two decades, Canada and the United States became world leaders in food irradition studies.

*After foods have been irradiated, they can be immediately eaten.*

Although Canada and the United States took first place in developing the technologies and the techniques associated with food irradiation, they fell behind other countries such as the Netherlands and South Africa in actually using the process, which has been kept on the back burner here by government regulations and by the availability of inexpensive alternatives, including chemicals, to deal with pests or serve as preservatives. Food processors, nervous about consumer acceptance of anything associated with nuclear technology, have been content to adopt a wait-and-see attitude.

Nevertheless, some scientists, engineers, government officials and irradiation specialists believed in the process enough to continue research and development efforts. Over the years they have evolved better techniques to ensure that irradiated foods will one day be fully accepted. Irradiated steak, ham, bread and other staples are eaten by astronauts aboard the U.S. space shuttle and by patients with immune-deficient diseases.

Some scientists and researchers believe that food irradiation will some day revolutionize the food industry. Others are more conservative, claiming only that the process is one of many and will find a special niche for itself. ■

*Goods are loaded for sterilization in an industrial irradiator.*

# WHY THE CRITICS DON'T LIKE IT

For whatever reason, there is some organized opposition to food irradiation in North America, perhaps because the technology is poorly understood. Since irradiated foods are not readily available, consumers have not been able to judge them as they assess other foods.

In the United States, Ralph Nader's Public Citizens Health Research Group is critical of food irradiation because it feels more research is needed. It prefers other methods of preservation instead. And in San Francisco, a group which calls itself the Coalition to Stop Food Irradiation objects to the process for both nutritional and social reasons. The coalition takes the position that the process offers social justification for the U.S. Department of Energy's By-products Utilization Program under which cesium-137, a by-product of the U.S. nuclear energy and weapons programs, is being marketed to the irradiation industry. Canadian-processed cobalt-60 is a deliberately produced isotope not related to the nuclear weapons industry.

Speaking for irradiation in the United States is the irradiation industry, the Department of Energy, the United States Council for Energy Awareness and the Coalition for Food Irradiation, a spinoff of the National Food Processors Association, which represents some of the country's largest food processors, including General Foods, Ralston Purina, Campbell Soup and Hershey Foods. These groups are working to expand the role of food irradiation

In Canada, Energy Probe and the Canadian Coalition for Nuclear Responsibility are the two major anti-nuclear groups who vocally oppose the technique. In general, the anti-nuclear groups are not well

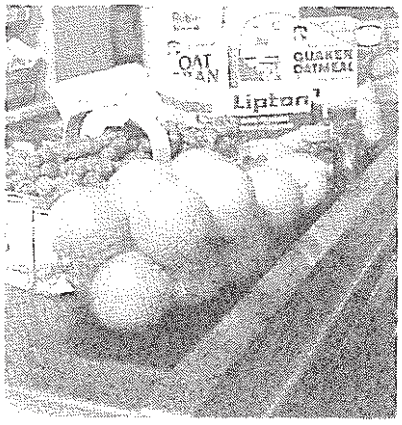


informed and use emotional sensationalism to obtain media attention.

Like its American counterpart, the Canadian food industry has formed an organization with an interest in informing the public about food irradiation. The Canadian Council for the Advancement of Food Technology was formed in 1987 to provide unbiased information on food technologies, including irradiation.

**Most criticism falls on the question of wholesomeness.**

The Canadian irradiation industry, composed of several private-sector firms plus Atomic Energy of Canada Limited, are strong advocates of food irradiation in this country and have worked for many years to demonstrate its commercial and practical attractiveness. AECL designs, manufactures and sells gamma-processing equipment around the world.

Aside from the cesium-137 issue, which is restricted to the United States, the focus of most criticism falls on the question of wholesomeness. There is concern that irradiated food suffers some nutritional losses and may contain radiolytic products not yet fully identified and studied. The irradiation industry responds by pointing out that the process has been studied more intensively than any other and has been given a clean bill of health by authorative international bodies such as World Health Organization, the United Nations Food and Agricultural Organization and the Codex Alimentarius Commission of the United Nations. The U.S. Food and Drug Administration and Health and Welfare Canada have also found no health problems associated with the process.

While acknowledging that radiation produces some nutritional losses, most noticeably of vitamins, the industry points out that these losses are no greater (and often less) than with other processes. Specialists say that the amount of energy used is too small to affect the major components of food — the proteins, lipids and carbohydrates. Similarly, it answers questions about the radiolytic products (substances formed by the rearrangement of molecules in the food) by noting that they are also formed by heat processing, freezing, and most other processes. The irradiation industry argues that extensive international research has shown that the chemical changes in irradiated foods do not pose any health problems.

Some activist groups suggest that while radiation may solve some microbiological problems, it could create others by leaving certain organisms a clear field in which to multiply. Irradiation industry experts argue that this concern, as well as others regarding the microbiological safety of irradiated food has been studied by the International Union of Microbiological Societies, who in 1983, affirmed

that irradiation up to 10 kilograys is safe.

**Consumers must be informed when foods have been irradiated.**

Consumer groups are concerned with the question of labelling, insisting that consumers must be informed when foods on their supermarket shelves have been irradiated. The food and irradiation industries generally agree, but are nervous about how such labelling will initially be perceived, fearing that consumers may think the food is radioactive. This issue has raised disputes over the wording of labelled products. On a related matter, critics worry that there are no simple tests to determine whether or not a food has been irradiated, a point that could create problems in international food trade. How does an importer know for certain whether or not the food he is bringing into the country has been irradiated or whether it has been irradiated properly? The industry sees these questions answered by regulation, multilateral agreements and inspection.

Advocates of food irradiation claim that a quarter of the world's food production is destroyed after harvesting. In Third World tropical regions such losses may reach 50%. They offer radiation processing as a partial solution. Much of these post-harvest crop losses are due to vermin such as rats and mice, against which radiation is useless, but insects and spoilage micro-organisms could be controlled by the process. Such treatment would be most effective if the food could then be stored under conditions that would prevent reinfestation. Even better, if the food could be irradiated in packaging that is impenetrable to insects and micro-organisms, it could be stored for a considerable time without becoming recontaminated. These techniques would help, not solve, food shortage problems in the Third World, industry officials say.

Yet food irradiation is seen by critics as inappropriate for the Third World because, they say, it is an expensive, centralized, high-tech solution that would make them dependent on developed countries for technology and expertise. A Pollution Probe report summarizes this argument. "The use of irradiation to solve the Third World's food shortage constitutes what may be called a technological fix and should be acknowledged as an unrealistic solution. Technology transfer from industrialized to less developed countries will not cure starvation there."

Frank Fraser, vice-president of the market development division of Atomic Energy of Canada's Radiochemical Company, responds: "We have put irradiators into many developing countries and they are up and running. Because we sell the cobalt-60 they use as a source of radiation, it's in our interest to make sure the equipment keeps op-

*Irradiation can destroy spoilage bacteria and pathogenic organisms to increase the shelf-life of many foods such as fresh fish, poultry, meats and some produce.*

erating. It's in our interest to make them successful on a long-term basis as opposed to a one-shot equipment sale. Also, you have to consider that many of these countries can earn the foreign exchange they need by exporting disinfested produce that they can't export now."

**Worry about the safety of the public and workers at irradiation plants.**

Critics also dislike the idea of transporting radioactive source materials such as cobalt-60 to and from irradiators and are concerned with what happens to sources which are no longer radioactive enough to do their job (but are still dangerous). And they worry about the safety of the public and workers at and around irradiation plants. Industry officials point to the 140 commercial irradiators now operating in more than 40 countries around the world, processing various products. To date, only two deaths associated with irradiators (not Canadian equipment) have been recorded — one in Italy and another in Norway. Further, not all food would be irradiated with radioactive isotopes. Foods such as cereals may be processed with high-speed electrons produced by an electrical device. No transportation or waste materials will be involved. In the case of AECL's cobalt-60, the company guarantees to remove all cobalt at the request of the user.

In summary, advocates claim irradiation will help solve some of the problems of Third World hunger; will replace expensive heat and refrigeration processes in some instances; and will reduce the incidence of food-borne disease. Further, they state that irradiated food is wholesome and that the process may improve public health by reducing the amount of chemical fumigants and preservatives in our foods.

Critics are leery of many claims by the advocates and fear the process is being over-sold. A report by one group states that consumers fear irradiation because they have not been given enough information about it and almost nothing in language they can understand. It says there needs to be more information and public discussion. The food and irradiation industries agree that a public information and education program will be needed if irradiated foods are to be accepted by consumers when they arrive on supermarket shelves. ■

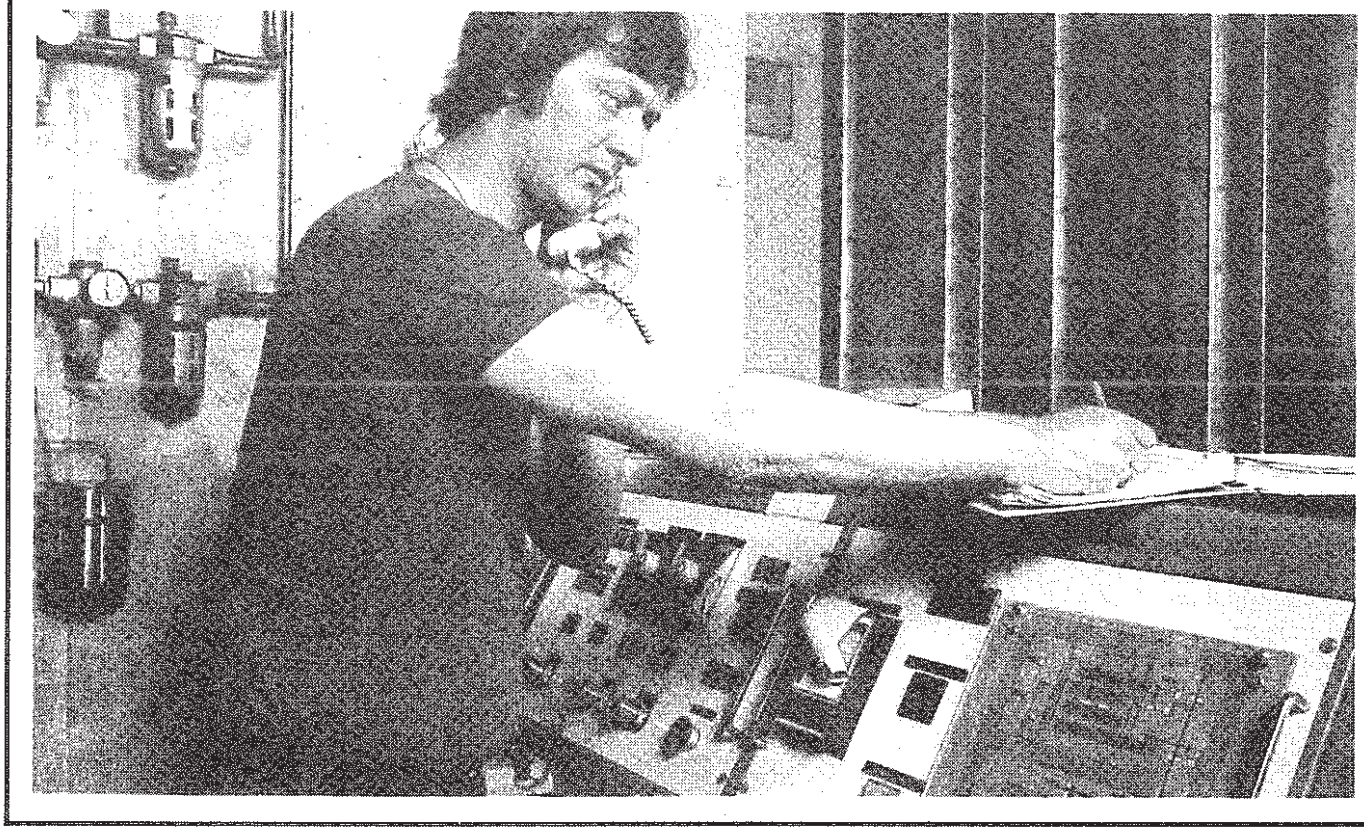

*In response to critics who worry about the safety of irradiation plants, the industry points out that 140 commercial irradiators now operate in more than 40 countries.*

# CHANGING THE REGULATIONS

One reason food irradiation is little used in Canada and the United States stems from its early classification in both countries as an additive rather than a process such as canning or freezing. The additive classification means treated foods must undergo lengthy, expensive testing programs for toxicity in which irradiated food is fed to test animals over long periods of time. Given the host of chemical alternatives coupled with consumer jitters about radiation, food processors took a pass.

At present, both countries permit the irradiation of a few foods such as potatoes and onions to inhibit sprouting, wheat and wheat flour for disinfestation and spices for microbial decontamination. But even in these permitted areas, the process is uncommon. In the United States, the Federal Food and Drug Administration (FDA), is satisfied that the process is safe. It cleared the process for the irradiation of pork to prevent trichinosis in humans in 1985. It also made a general clearance for fresh foods to a maximum of 1 kilogray (1 kGy) or 100 kilorads (100 Krads) to kill insects and inhibit growth, ripening, and spoilage of fruits and vegetables. (A kilogray or kilorad is a unit of absorbed energy.)

Representatives of the irradiation industry and to a large extent the food industry feel the new clearances will offer only limited use of the technology, but could open the door for more widespread use in the future.

The Coalition for Food Irradiation, representing some of the largest U.S. food processors, has taken the position that 100 kilorads does not provide significant commercial application but if approved it could allow parties to petition for higher levels. The coalition feels 300-500 kilorads will be necessary for most commercial food-processing applications.

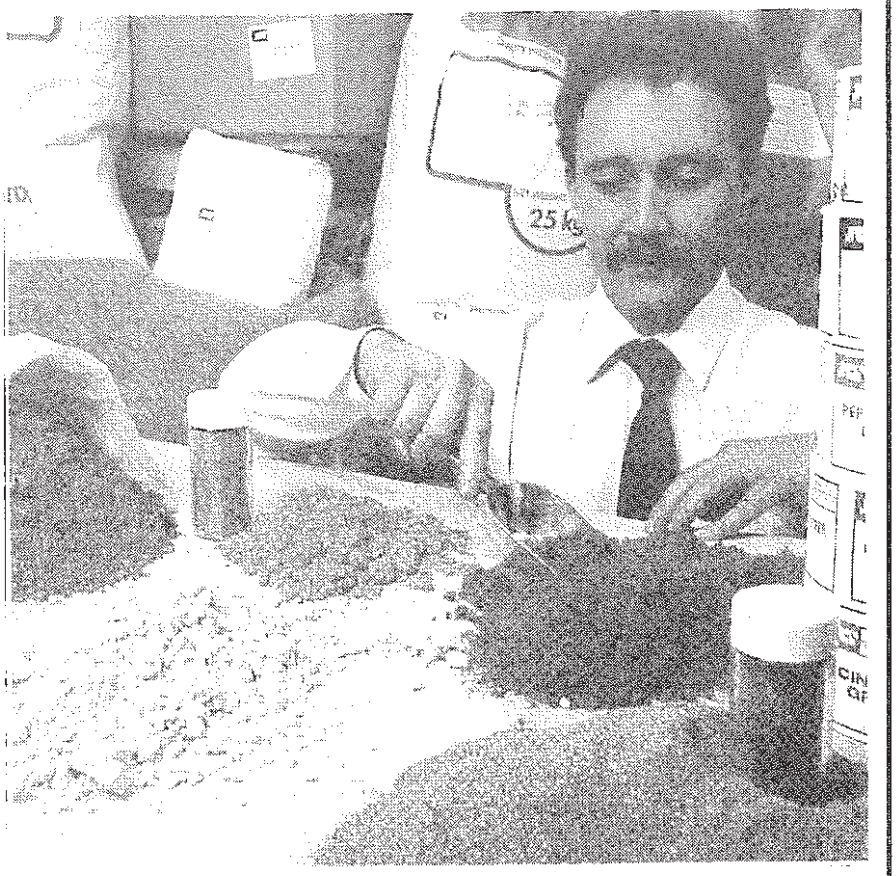

*Spices have been cleared for radiation processing in Canada and the United States to eliminate insect infestation. They are among a handful of foods that have received clearance.*

Dr. George Giddings, well-known American food scientist and food irradiation consultant agrees. "The first regulation is limited, but it is the icebreaker. It draws the fire and flack and when the dust settles, there's a chance for ammendment."

**"The pre-clearance requirements for additives are not appropriate for irradiation."**

In Canada, it appears regulations will be changed as well. Dr. B.H. Lauer, scientific evaluator with the Health Protection Branch of Health and Welfare Canada, explained: "Right now, irradiation is considered an addititive, but we have concluded that the pre-clearance requirements for additives are not appropriate for irradiation. We have recommended removing irradiation from the additive regulations and setting up their own pre-clearance regulations."

The branch published proposals

# FOOD • IRRADIATION:

in 1983 to revise the regulations for control of food irradiation. The proposals were sent out to concerned parties for comment. Revised regulations are expected by early 1988.

Frank Fraser, vice-president of the market development division of Atomic Energy of Canada Limited's Radiochemical Company, the subsidiary responsible for manufacturing and marketing irradiation equipment, feels the Canadian government is heading in the right direction. "I think the Canadian government is moving along very positively. The way it is proceeding is the right way."

The regulatory changes in both countries are the initial steps in the gradual integration of irradiation into the food-processing industry in North America. The changes are being prompted by the growing mistrust of chemicals in the food industry, and by international trends toward the irradiation process. Because of the close relationship of the food industries in Canada and the United States, the question of regulations is an important one. And since vast quantities of food move between North America and the rest of the world, regulations established here should harmonize with international regulations covering the types of food which may be irradiated, permissible dosages, methods of handling and labelling.

AECL's Frank Fraser adds: "If we can't get irradiated food into the United States, what's the use of the process? Japan is another lucrative market. Ethylene dibromide is likely to be banned there shortly, but they can't risk fruit coming in with pests. So irradiation is likely the answer. It's this international aspect that's taking a bit of time."

North American regulatory agencies were given some direction by the approval in October 1983, of a general standard for irradiated food established by the Codex Alimentarius Commission, a United Nations body with representation from more than 125 countries. The standard permits the irradiation of certain food products to an average dose of 10 kilograys. This is not a level above which irradiated foods become unsafe; rather it is a level at or below which safety has been established. Although it's not binding on UN members, many are using it as a guide for national standards.

What government officials, the irradiation industry, consumer groups and opponents of food irradiation are stumbling over at the moment is the problem of how to inform consumers that the food they are purchasing, whether in supermarkets or restaurants, has been irradiated. In Canada, consumer groups, health officials and industry representatives have been discussing labelling since about mid-1983.

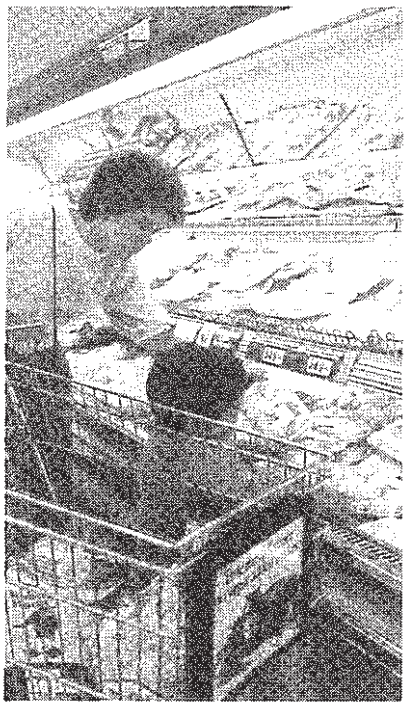

*The irradiation and food industries generally agree that gamma-processed products must be labelled as such. One suggestion is that this international symbol be used on irradiated products.*

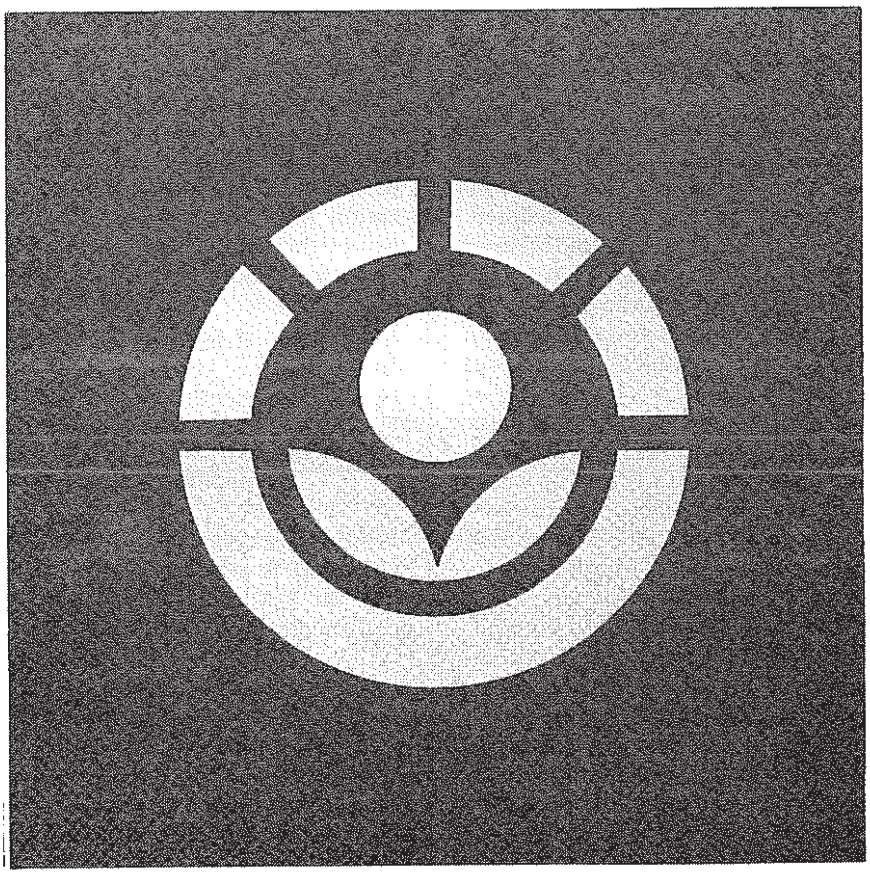

*Frank Fraser is vice-president of the market development division of Atomic Energy of Canada Limited. Fraser's group is actively promoting the use of gamma processing for food.*

**Processors fear consumers may avoid products bearing a special label.**

Some food processors argue that if irradiation is re-classified as a process, it should be treated like canning or freezing or any other process — no special label. They fear consumers may avoid products bearing a special label. Consumer groups and others point out that supermarket customers can easily spot food that has been frozen, canned or dried, but have no way of identifying irradiated food unless it's labelled. Most people dealing with the question feel some form of labelling will be required for items such as fresh strawberries, poultry, fish, and other such foods. The question gets thornier when it touches on something like a dried soup mix in which some of the ingredients, say the spices, have been irradiated.

Then there's the question of food purchased in restaurants and fast-food outlets. Some or all of the ingredients may have been irradiated. Should consumers be told? How? Someone dining at a restaurant has no way of telling if the grilled trout has been frozen or whether or not the accompanying asparagus was tinned unless he asks the waiter or unless his taste buds tell him. In the case of irradiation, taste buds will be of no use and neither the waiter nor, indeed, the chef, may know.

Speaking at a conference on food irradiation in 1983, Marilyn Young, chairman of the Consumers' Association of Canada's food committee, said irradiated food must be labelled but favors wording along the lines of "gamma-processed products" or "treated with ionizing energy" because consumers associate the word radiation with negative images. The CAC has also favored the idea of tagging irradiated food with an international symbol that shows it has been irradiated.

Mike O'Connor, vice-president and technical director of Robin Hood Foods in Toronto, said he feels the food industry in general is interested in the process but is concerned with labelling and consumer education. "There must be an education program and people must accept the process as safe — they must see irradiated foods as premium products," he said. "This is something the government should spearhead."

**Some day the symbol will represent to consumers a quality product.**

Frank Fraser agrees with Young's view and is convinced that some day the symbol will represent to consumers a "quality" product. "They will know that chicken bearing the symbol is free of salmonella and that a bag of potatoes marked with it won't sprout," he said.

Fraser has stated that the interesting thing for North Americans is that our Caribbean and South American trading partners are ready to go and are waiting for us to pass legislation. "Canadian and American legislation will have almost as much impact on the international scene as the Codex recommendations. Canada and the United States still seem to be the key to widespread use of this technology."

Summarizing a recent week-long International Symposium on Food-Irradiation Processing sponsored by the Food and Agricultural Organization of the United Nations and the International Atomic Energy Agency, a panel of scientists and food experts representing 10 countries delivered a report outlining recommendations to expand the commercial use of food irradiation.

"We know more about the safety of food irradiation through years of research and development than most other food-preservation techniques," panel chairman Dr. J.S. Sivinski told symposium participants. "It is up to governments to recognize the safety and technical efficacy of food irradiation and take the necessary steps to see that it is made available for the benefit of mankind." ■

F O O D • I R R A D I A T I O N:

# THE WORLD IS WAITING

Because enormous quantities of food products move between North America and the rest of the world, specialists in the food and irradiation industries see Canadian and American acceptance of food irradiation as the key to widespread international use of the process. Although North American acceptance is at hand, it may be several years before irradiated chicken and strawberries turn up on supermarket shelves here. Meanwhile, other countries using the technique today are limited to their own national boundaries or, at best, to their own global neighborhoods. Still, many are making advances to clear foods for treatment and to establish national food-irradiation programs.

Most of these countries are adopting the standards and procedures for food irradiation set by the United Nations' Codex Alimentarius Committee in 1983 as models for their national programs. Canada and the United States are expected to follow suit, an important point since large-scale global use of the technology will require reasonably standard, multilateral agreements and regulations to facilitate trade in irradiated food products.

As it stands, Canadian and American requirements for petitions to approve the irradiation of specific foods restricts its use. The Canadian government is shortly expected to re-classify the technique as a process with its own set of test procedures and regulations, a move that will make it easier for food processors to use. Even then, most experts feel food irradiation will not take off like a rocket in North America, but will be introduced gradually at a rate dictated by consumer acceptance and economic viability. But at least North America will be integrated into the global network that is beginning to form around the process.

*While irradiation is not a substitute for the family freezer, it is expected to help preserve some foods beyond their natural shelf-life, an important feature in many parts of the world where refrigeration is scarce.*

## Canada: The world's first irradiators

Canadians did much of the early work in developing food irradiators. In 1961, Atomic Energy of Canada Limited built the world's first mobile cobalt-60 food irradiator for use as a demonstration unit. Four years later, the firm manufactured and installed the world's first commercial food irradiation plant, a potato irradiator near Montreal. AECL, from its Radiochemical Company subsidiary in Kanata, Ontario, now builds and sells irradiation equipment for the sterilization of medical equipment and food around the globe. It also supplies most of the world's cobalt-60.

Although irradiated food is not currently sold in Canada, the government has approved the technique to prevent sprouting in potatoes and onions; to eliminate insect infestation of wheat, and to eliminate insects and reduce bacterial contamination in spices amd seasoning preparations.

There are currently three industrial irradiators operating in this country sterilizing medical products, but all are capable to some degree of processing food. A fourth, non-profit, commercial-size facility, the Canadian Irradiation Centre, opened in 1987 in Laval, near Montreal. This demonstration, training and product-testing facility is operated as a co-operative project by AECL and Institut Armand-Frappier of the University of Quebec.

Canada has conducted a number of studies and projects on the irradiation of different foods, the most recent of which was an efficacy test

on poultry to eliminate salmonella with gamma energy. The project was sponsored by Agriculture Canada.

Test irradiations were carried out at the Isomedix plant in Whitby, Ontario, just east of Toronto. As a result of the project, AECL officials are hoping Canada will adopt radiation processing as a method of salmonella control.

## United States: An irradiated banquet

In April 1985, the Idaho Section of the American Nuclear Society threw a banquet for 175 guests, including members of the general public, at a church hall in Idaho Falls. They dined on irradiated fish, pork, shrimps, oranges, apples, tangerines, pears and vegetables. Unirradiated baked potatoes, rolls and dessert rounded out the meal. Most of the diners approved of the food and most of the negative comments related more to preparation and presentation than irradiation. Left overs were taken to the Boise legislative open house three days later for a "tasting."

Irradiated food may still be hard to find at most banquets in the United States, but there's little doubt they'll begin to show up on more and more plates over the next few years if current trends continue.

Until 1985, U.S. regulations generally parallelled Canada's, with clearances for wheat, wheat flour, potatoes and spices. But in 1985, the U.S. Food and Drug Administration extended approval for the irradiation of pork for prevention of trichinosis, additional spices and food enzymes. It also approved the irradiation of fresh foods in 1986. The FDA is also expected to remove the irradiation process from the "additive" status and place it in its own category.

*The irradiation industry feels that with solid consumer education programs on food irradiation, shoppers will one day view a gamma-processed food item as a premium product.*

FOOD PRODUCT CLEARANCES

*This chart was published by the International Atomic Energy Agency to highlight the unconditional and provisional clearances of major food products in different countries around the world (as of March 1985).*

| | Argentina | Bangladesh | Belgium | Canada | Chile | Denmark | France | Hungary | Israel | Italy | Japan | Netherlands | Norway | Philippines | Poland | South Africa | Spain | Thailand | Uruguay | USA | USSR |
|---|---|---|---|---|---|---|---|---|---|---|---|---|---|---|---|---|---|---|---|---|---|
| Potatoes | ● | ● | ● | ● | ● | ● | ● | | ● | ● | ● | ● | | ● | ● | ● | ● | ● | ● | ● | ● |
| Onions | | ● | ● | ● | ● | | ● | ● | ● | ● | | ● | | ● | ● | ● | ● | ● | | | ● |
| Garlic | | | ● | | | | ● | | ● | ● | | | | ● | | ● | | ● | | | |
| Shallots | | | ● | | | | ● | | ● | | | | | | | | | | | | |
| Wheat, flour, whole wheat flour | | ● | | ● | ● | | | | | | | | | | | | | | | ● | |
| Spices | | ● | ● | ● | ● | ● | ● | ● | ● | | | ● | ● | | | | ● | | ● | ● | |
| Chicken | | ● | | | ● | | ● | | ● | | | ● | | | | | ● | | ● | | |
| Fish and fish products (chilled, frozen) | | ● | | | ● | | | | | | | ● | | | | | | | ● | | |
| Frozen shrimps | | ● | | | | | | | | | | ● | | | | | | | ● | | |
| Frog legs | | ● | | | | | | | | | | ● | | | | | | | | | |
| Rice and ground rice products | | ● | | | ● | | | | | | | ● | | | | | | | ● | | |
| Rye bread | | | | | | | | | | | | ● | | | | | | | | | |
| Egg powder | | | | | | | | | | | | ● | | | | | | | | | |
| Fresh fruit and vegetables | | | | | | | | | | ● | | ● | | | | | | | | ● | |
| Cocoa beans | | | | | ● | | | | | | | ● | | | | | | | ● | | |
| Dates | | | | | ● | | | | | | | | | | | | | | ● | | ● |
| Pulses | | ● | | | ● | | | | | ● | | | | | | | | | ● | | |
| Papaya | | ● | | | ● | | | | | ● | | | | | | | ● | | ● | | |
| Mango | | ● | | | ● | | | | | ● | | | | | | | ● | | ● | | |
| Strawberries | | | ● | | ● | | | | | ● | | | ● | | | | ● | | ● | | |
| Paprika | | | ● | | | | | | | | | | | | | | | | | | |
| Pork | | | | | | | | | | | | | | | | | ● | | | ● | |
| Bananas (fresh, dried) | | | | | | | | | | ● | | | | | | | ● | | | | ● |
| Litchis | | | | | | | | | | | | | | | | | ● | | | | |
| Dehydrated vegetables | | | ● | | | | ● | | ● | | | | ● | | | | ● | | | ● | ● |
| Grain | | | | | | | | | ● | | | | | | | | | | ● | | ● |
| Dried fruits | | | | | | | | | | | | | | | | | | | | | ● |
| Mushrooms | | | | | | | | | ● | | | | ● | | | | | | | | |
| Endive | | | | | | | | | ● | | | | | | | | | | | | |
| Asparagus | | | | | | | | | ● | | | | ● | | | | | | | | |

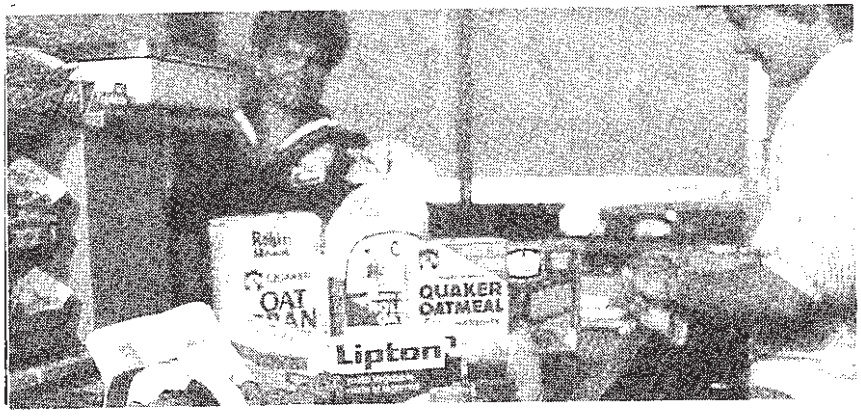

For further information contact: Atomic Energy of Canada Limited, Corporate Public Affairs
275 Slater St., Ottawa, Ontario K1A 0S4 (613) 237-3270



# F O O D • I R R A D I A T I O N

The United States has nearly 40 commercial irradiators in operation, most of which use cobalt-60 as a source of gamma radiation, but the Department of Energy (DOE) has announced its intention to sponsor construction of five demonstration food irradiators for agricultural commodities, and at least one of these will use cesium-137, a waste product of the nuclear-weapons program. DOE is attempting to market cesium-137 as an alternative to cobalt-60. Since it takes about seven times more cesium-137 (in its present form) than cobalt to accomplish the same amount of processing, reports that all available cesium-137 has been spoken for by American companies interested in radiation food processing may well be accurate.

## South Africa: The tea party

In November 1984, officials in South Africa discovered that 30,000 tonnes of locally grown herbal tea was contaminated by salmonella. After investigation, it was decided that the only realistic way to save the tea was to irradiate it. Regulatory approvals followed swiftly and a contract went to a local radiation processing firm. Within a few months from the time of discovering the problem, the tea was being processed and safe to consume.

The incident typifies the attitude toward food irradiation in South Africa, which, with three gamma-irradiation facilities processing certain fruits and other foods commercially, is considered one of the most advanced countries in the use of this technology. Discussions are reportedly underway between South Africa and neighboring countries to establish bilateral and multilateral trade agreements covering irradiated foods.

## Southeast Asia: Not waiting for the rest of the world

Several Asian and Pacific Rim countries — Australia, Bangladesh, Indonesia, Republic of Korea, Malasia, Philippines, Thailand and Japan — met in 1985 to take steps to clear the way for trading irradiated foods in the region. They agreed to evaluate shipping trials of irradiated foods from these and other countries affiliated with the Asian Regional Co-operative Project (ARCP) on Food Irradiation, and to promote the acceptance of the Codex standard and code of practice on food irradiation. ARCP's second phase is aimed at finding ways to transfer the technology of food irradiation to local industries in the region. It has also co-ordinated research and pilot-scale studies on products of particular interest in the region, namely fish products, tropical fruits, onions and spices.

A demonstration irradiation facility for food processing is currently under construction in Bangkok as part of a co-operative program between Canada and Thailand.

Japan has already installed a food-irradiation facility to inhibit the sprouting of potatoes. It is currently processing 20,000 tonnes a year.

## Europe: From strawberries to fish

Some 14 European countries have authorized the irradiation of food products over the past 15 years. The Netherlands, for example, is processing about 100 tonnes of food per week — everything from strawberries to poultry, fish and spices. In fact, the greatest range of food products for which irradiation is accepted can be found in that country.

The United Kingdom is moving more slowly, but an advisory committee to the U.K. Department of Health has recently found no problems for foods irradiated to internationally recommended standards. The department is expected to approve the technique shortly.

In West Germany the story is different. There the process has received a major setback from the local Green Party, which opposes food irradiation. Since the Greens wield considerable political clout, they have been able to block legislation that would permit the irradiation of food. Further, they are pressuring the government to ensure that irradiated food is not imported into the country. The result is that West Germany is travelling in the opposite direction to its European partners.

Nevertheless, the rest of the world is not expected to follow Germany's example. For most countries, radiation processing offers enough advantages to make it an attractive alternative to other preservation techniques. ■

*AECL builds irradiators at its Radiochemical Company in Kanata, Ontario, for shipment to customers around the globe.*

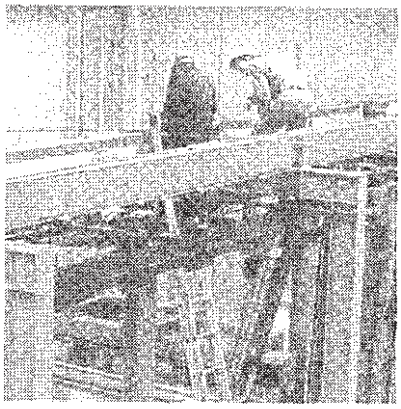

*The government has approved the technique to prevent sprouting potatoes and onions; to eliminate insects in wheat, flour and whole wheat flour and spices; and to reduce bacteria in onion powder.*

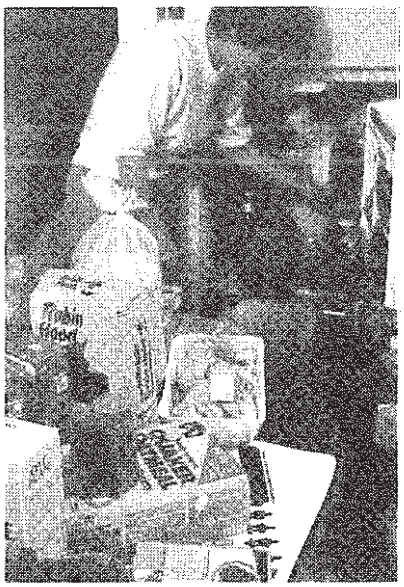

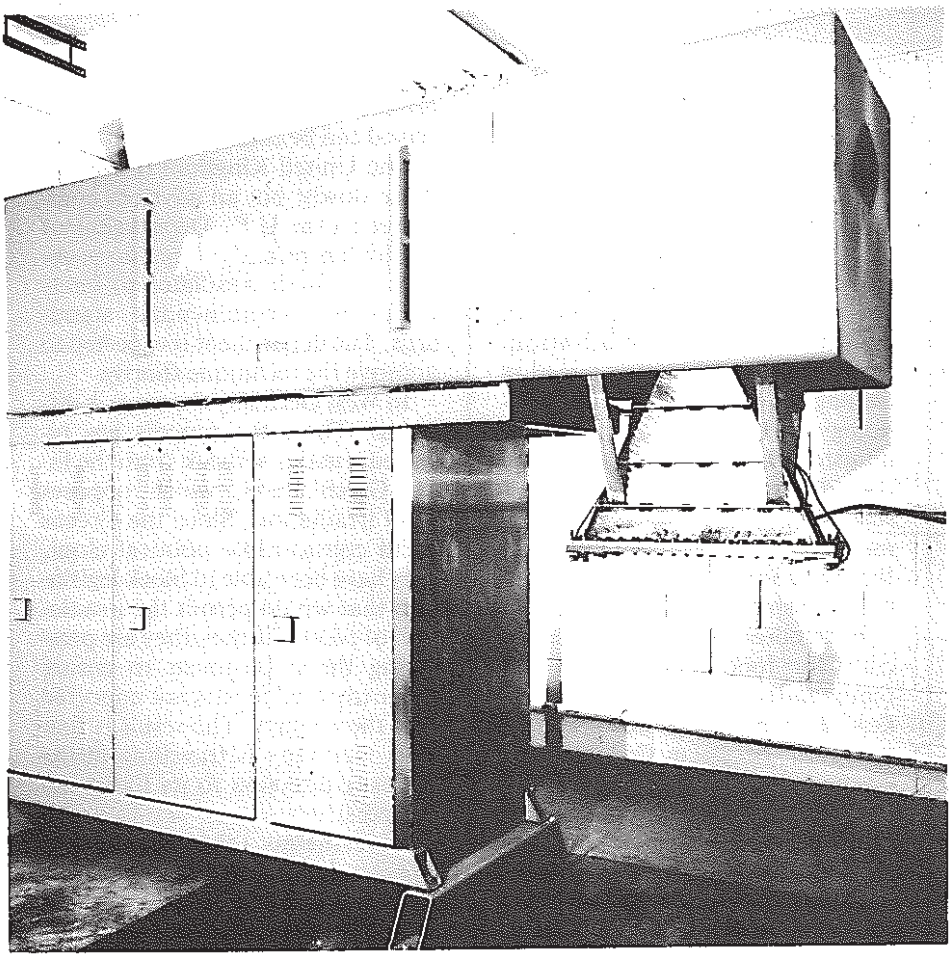

# AECL Accelerator Systems

## Industrial Electron Accelerator AECL I-10/1

**A tool for developing industrial electron irradiation and material processing, and for use in low throughput production processing.**

## Features

- 10 MeV electron beam accelerator
- treatment rates to 135 kg/h at 1 kGray (1 Mrad)
- accurate energy and dose control
- scanned electron beam allowing treatment of product up to 60 cm wide
- compact high-voltage and radiofrequency power system
- automatic operation, control, and monitoring through a programmable industrial process controller
- conveyor speed control linked to beam power
- simple to use

## Uses

The I-10/1 can form the centrepiece of a corporate, government, or university facility for evaluating the process benefits of electron beam treatment. It is useful in studies of

- biological effects (control and elimination of pathogens in cosmetic, hygiene, medical, and food products, animal feed, and waste materials; reduced spoilage rates)
- materials enhancement (curing of dense, large-cross-section rubber and plastic materials without heat or solvents; improved strength, handling, and temperature properties)
- cellulose processing (lignin modification; wood polymer processing; bacteria, fungus, and nematode control)
- chemical production (pretreatment of materials by modification of long-chain molecules)
- production optimization (product handling on continuous conveyor systems)
- mineral analysis (on-line and batch analysis of ore composition)

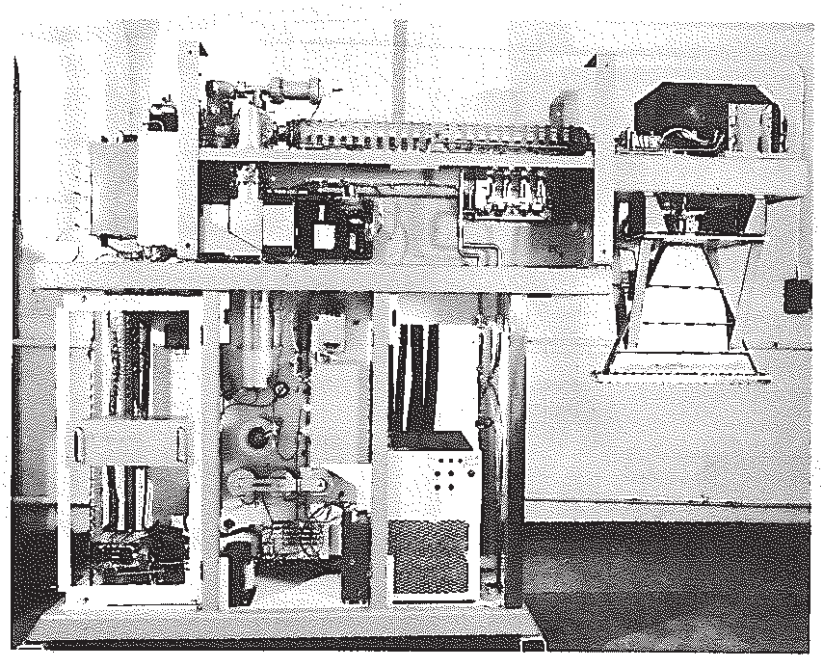

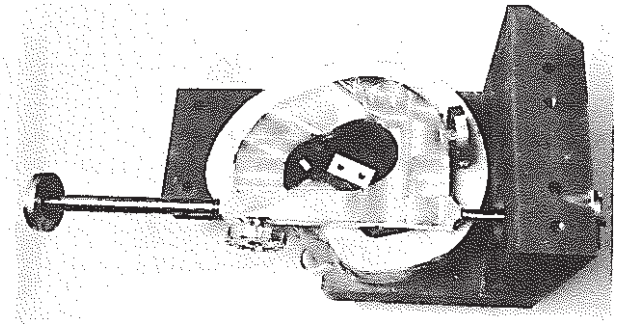

▲ The I-10/1 energy analyzer magnet removes all electrons with energies greater than 10 MeV, in accordance with Codex Alimentarius requirements.

◀ Bending magnet and scan horn assembly.

The I-10/1 research and pilot scale accelerator was designed by Atomic Energy of Canada Limited (AECL) to satisfy the need for an irradiator able to provide a source of electrons with control of energy, exposure, and beam distribution suitable for process development as well as research. Its magnetron-driven, short-pulsed technology is the most economical for low-power applications and can be used for commercial processing.

The scanned 10 MeV beam complies with all international recommendations on food irradiation, and provides good uniform dose distribution. The same uniformity can be achieved for more than twice the thickness if the product is irradiated from two sides, as shown in Figure 1.

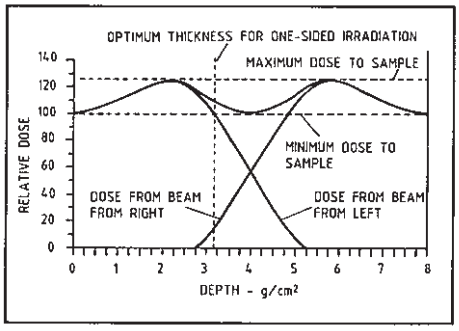


Figure 1: Depth dose distribution for one- and two-sided irradiation with a 10 MeV electron beam

A conveyor speed interface is provided for simulating full-scale industrial processing.

## Accelerator System

The beam accelerating system of the I-10/1 uses a space-charge limited triode electron gun as its source of electrons. The accelerator structure employs a "pancake-coupled" S-band design driven by a magnetron rf power tube.

The Codex Alimentarius† requirements are met by passing the accelerated beam through an energy-analyzing magnet and removing all electrons with energies greater than 10 MeV. The beam then enters an evacuated horn and is scanned through an angle of 38° to provide uniform dose distribution across wide samples.

## Electron Beam Parameters

**Energy**
The mean electron beam energy at the point where the beam leaves the accelerator is 9.5 MeV ±0.2.

**Output**
Electron beam power is 0.75 (+0.25,-0.0) kW delivered in pulses about 4 μsec long at a repetition rate of 300 Hz. The minimum dose that can be delivered with uniform distribution over the full width of the scan depends on the diameter of the beam reaching the target, the scanning speed, and the pulse repetition rate. In the I-10/1, the beam is scanned in a complete sweep, across the sample conveyor and back, four times every second. The beam diameter at the sample is 3 ±0.5 cm. The minimum dose achievable with good uniformity is approximately 1 kGy.

**Scan Width**
To minimize energy degradation, beam diffusion, and the generation of ozone due to scattering of the electron beam in air, an evacuated scan horn is attached to the output window. This allows the beam to be scanned in vacuum. It extends out to 100 cm from the accelerator beam axis.

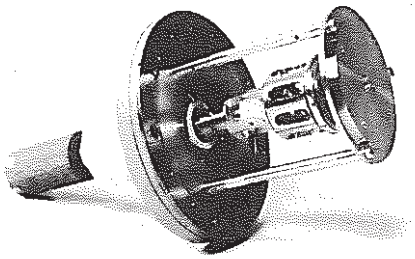

▲ The I-10/1 uses a space-charge limited triode electron gun as its source of electrons.

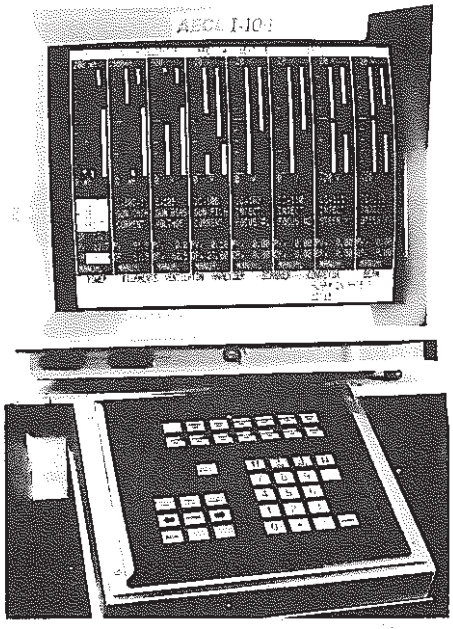

A GEC GEM 80/252 programmable industrial process controller performs digital control functions in the I-10/1. ▶

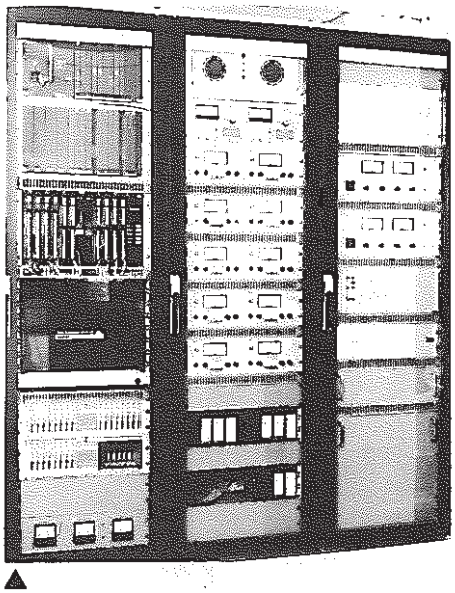

▲ Electronic control cabinet.

## Controls

The I-10/1 uses a combination of electrical, electronic, and digital controls. The digital control functions are performed by a GEC GEM 80/252 programmable industrial process controller.

During normal operation, the machine is run from a control keyboard with dedicated function keys. This membrane keyboard ensures reliable operation in industrial environments. "Face plate" VDT color displays are provided for all important operating parameters.

**Precalibrated**
The following parameters are controlled by adjustment during periodic calibration procedures

- pulse repetition rate time base
- beam alignment fields
- magnetron magnetic fields

**Servo-controlled**
Parameters under automatic control include

- energy
- power
- frequency
- beam current
- high voltage supply

**System Displays**
The operating values of the following parameters can be viewed at "face plate" displays on the color monitor

- pulse repetition rate*
- gun filament current
- beam current injected into the accelerator
- beam current after acceleration*
- magnetron cathode current*
- magnetron voltage*
- forward and reflected power at the rf input*
- pulse forming network voltage*
- water temperature
- accelerator temperature
- water flow rate
- vacuum pressure

## Installation Requirements

**Radiation Shielding**
To ensure radiation levels are kept at those allowable to the general public, a shield thickness of up to 3.5 m (11'6") of standard density concrete or its equivalent is required.

**Electricity Supply**
The supply required is 12 kVA, 208 V ±7%, 3 phase, 4 wire, 50 or 60 Hz.

**Water**
A cooling water supply of 12 litres/min (3.5 U.S. gal/min) at not more than 20°C (68°F) is required.

**Ventilation**
The I-10/1 will operate in an ambient temperature of 10°C to 25°C and a relative humidity below 75%. The additional thermal load it generates is 5 kW (11.5 kBTU/h). To ensure satisfactory removal of any ozone generated, a ventilation rate of one room change of air per minute is recommended.

†United Nations Food and Agriculture Organization/ World Health Organization Codex Alimentarius Commission; Codex Alimentarius, Volume XV, Ed 1, 1984 CODEX STAN 106-1983.

*direct signal outputs also provided

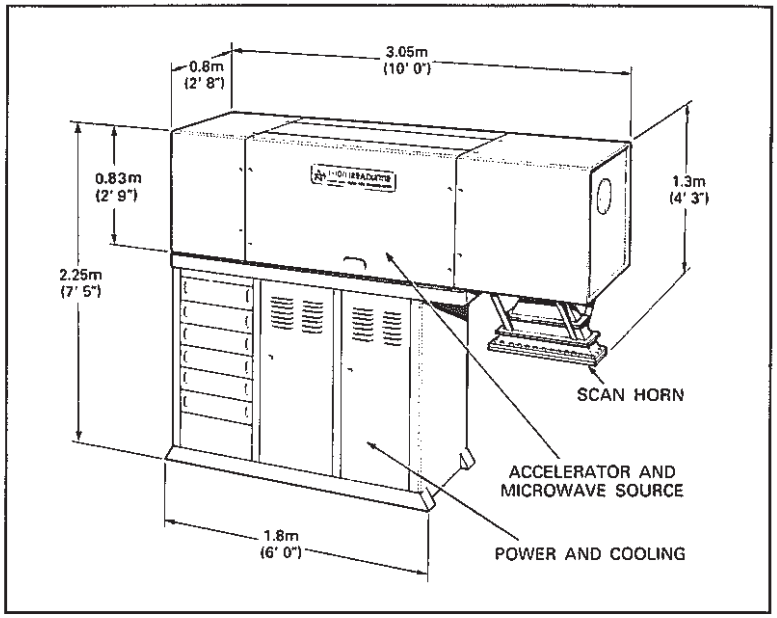


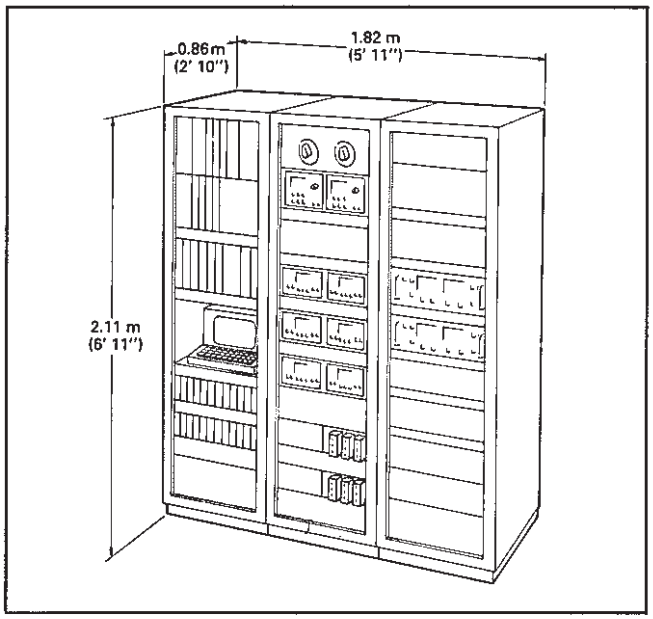


Outside dimensions of I-10/1

## Specification Summary

**Beam energy (mean)** 9.5 ±0.2 MeV

**Beam power (maximum)** 0.75 kW at output window

**Useful beam dimensions at product surface** 60 cm in the direction of scanning and 3 cm in the non-scanned direction at 15 cm from the output window

**Scan rate** 4 Hz

**Rf frequency** S band (3 GHz)

**Nominal pulse length** 4 µsec

**Pulse repetition rate** 300 pulses per second

**Magnetron** English Electric M5193

**Electricity supply** 12 kVA, 208 V ±7%, 3 phase, 4 wire, 50 or 60 Hz

**Cooling water requirements** 12 litres per minute at not more than 20°C

This summary describes a reference operating point. The irradiator can be set to operate at other energy and power levels. Further details can be provided on request.

**For Information**
Accelerator Business Unit
AECL Research Company
413 March Road, P.O. Box 13500
Kanata, Ontario, Canada K2K 1X8
Tel: (613) 592-2790 Telex: 053-4162 Fax: (613) 592-6937

# AECL's Industrial Accelerator Program – an Overview

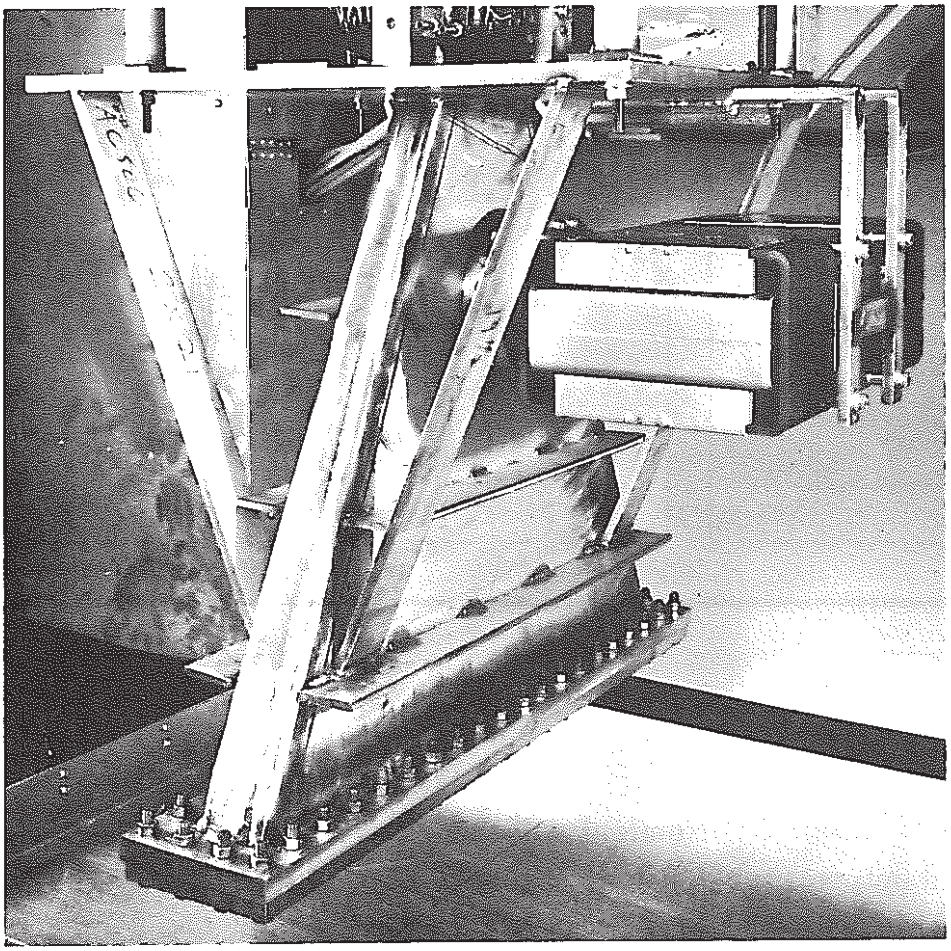

Scan horn assembly of the I-10/1 Research and Pilot Scale Accelerator.

## Radiation Processing and Industrial Linacs

Atomic Energy of Canada Limited (AECL) pioneered the gamma processing industry through development of the cobalt-60 technology and handling mechanisms which make gamma processing a practical and efficient industrial process today. The company's research and development program includes radiation processing technology, continuing fundamental studies on photochemical interactions and their potential applications, and the development of new technology to exploit these discoveries.

Cobalt-60 is a source of ionizing radiation characterized by its ability to penetrate thick and/or dense materials. Many new applications would be economic if large quantities of moderately penetrating radiation could be produced at a low unit cost. These applications include sterilization of sewage and biological wastes, treatment of large volume bulk commodities, curing of thick plastic parts, and irradiation of some processed foods requiring "on-line" treatment to take advantage of a synergism between thermal processing and irradiation. Some of these new requirements can be met by industrial electron linacs with energies above 5 MeV.

AECL has more than 20 years' experience in the development of high-power particle accelerators and over 30 years' experience in the design, manufacture, sales and service of cobalt-60 sourced gamma irradiators. As well, there are more than 80 AECL medical accelerators in use for cancer therapy. This experience is now being directed towards development of high-energy, high-power electron beam equipment and techniques for industrial radiation processing.

AECL is confident that a strong future exists for both gamma and electron beam radiation processing. The continuing growth of the industry will be encouraged by the development of AECL's industrial linacs, which will complement AECL's line of cobalt-60 irradiation units.

## Technology

AECL's high-power accelerator technology is based on extensive research into an alternative to fast breeder reactors for producing a greater range of nuclear fuels.

When early forecasts indicated that the demand for nuclear power would lead to a shortage of uranium fuel, AECL's quest to develop new fuels led to a program in electronuclear breeding. In this process, neutrons produced in a target irradiated with high-energy protons, are absorbed by natural thorium to produce new fissile isotopes.

Design studies indicated that an accelerator for this application would be over 1 km long and would cost more than one billion dollars. An experimental program was carried

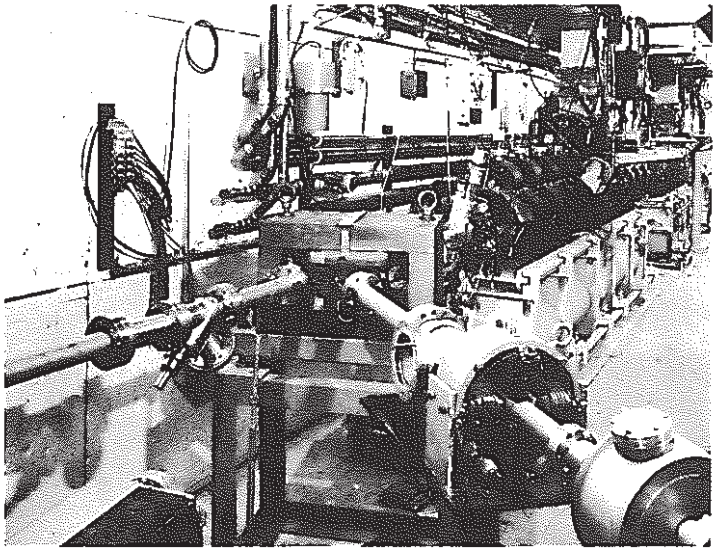

Some features of Chalk River's Electron Test Accelerator (ETA) will be used in a family of high-power industrial machines being designed by AECL.

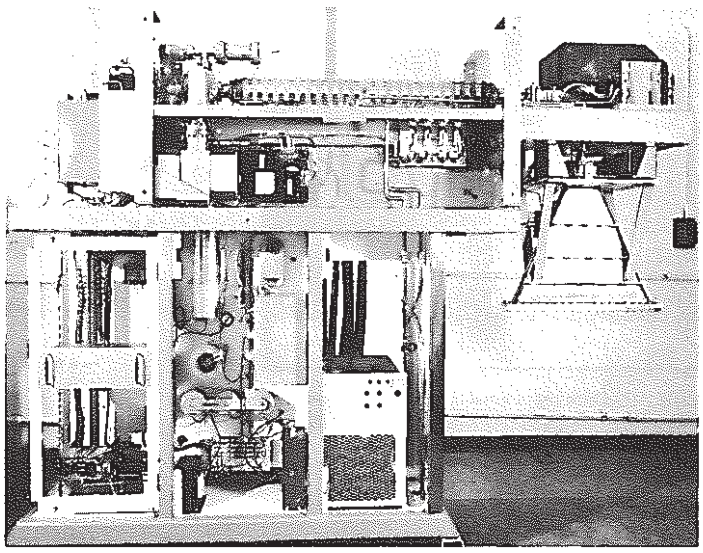

The I-10/1 is a high quality research and development tool for electron processing studies.

out, on a reduced scale, to evaluate primary beam-cavity interactions. Since electrons can be accelerated more easily to relativistic energies, an electron accelerator was built to model this behavior.

This machine was called the Electron Test Accelerator (ETA), and it provided a 4 MeV electron beam at 80 kW continuous output power, using a standing wave electron linac. AECL pioneered Continuous Wave (CW) accelerator operation (100% duty factor) with ETA, and this machine was used to develop extensive expertise in designing high-power accelerator structures. One of these, the on-axis coupled configuration, has been chosen for a family of high power industrial machines. AECL's accelerator expertise is now being directed to potential industrial uses of the ETA technology.

Details of the ETA design can be found in the technical paper, "The Chalk River Electron Test Accelerator: A Prototype for Industrial Irradiator Designs", by J.P. Labric, K.C.D. Chan and J. McKeown, I.E.E.E Transactions on Nuclear Science Vol. 30 No. 2, 1983, pp. 1634-1637.

AECL's other experience in accelerator technology results from its dominant position in the field of cancer radiotherapy using cobalt-60. To expand the range of treatments available, AECL introduced a family of electron and x-ray treatment machines using linear electron accelerators. The company has manufactured, installed and continues to provide service support for more than 80 of these units.

## The Impela Industrial Accelerator

A CW machine like ETA is large and has a number of accelerating structures operating in series. This requires a complex system of phase-locked control loops to distribute the rf power. Conventional short-pulsed machines, on the other hand, require high peak power and current to achieve the desired average power and this leads to high thermal and electrical stresses. AECL combined the best features of both concepts, adopting a long pulse, pseudo-CW technology to ensure a single-structure, high-energy, high-power industrial machine which would be compact and reliable.

AECL's IMPELA (Industrial Materials Processing Electron Accelerator) family of industrial accelerators is based on this new concept. IMPELA machines will be configured from standard components to meet customer applications with energies from 5-15 MeV and up to 500 kW of power. Its design is discussed in detail in "Radiation Processing Using Electron Linacs", by J. McKeown, I.E.E.E Transactions on Nuclear Science Vol. 32, No. 5, 1985, pp. 3292-6.

A 10 MeV, 50 kW prototype IMPELA is under construction at AECL's Chalk River Nuclear Laboratories and AECL is seeking partners for the first demonstration of this machine in industrial installations.

## The I-10-1 Research and Pilot Scale Accelerator (10 MeV, 1 kW)

Industrial radiation processing using gamma sources was greatly assisted by the availability of a range of small self-contained, research irradiators, using cobalt-60. Growing interest in the use of electron beams is generating a need for a research accelerator which can provide a source of electrons with energy, exposure and beam distribution suitably controlled for irradiation research and process development.

The I-10/1 Research and Pilot Scale Accelerator has been designed by AECL to satisfy this need. Many proven medical accelerator components were selected for the I-10/1. Its magnetron-driven, short pulsed technology was chosen as most

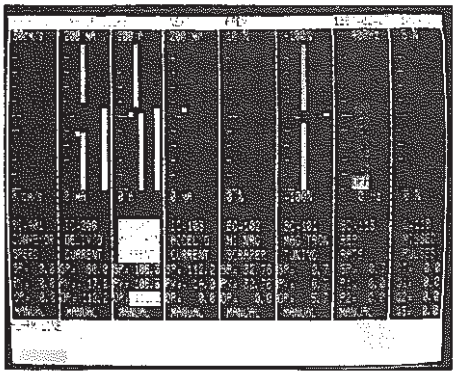

A GEC GEM 80 programmable industrial process controller performs digital control functions in the I-10/1.

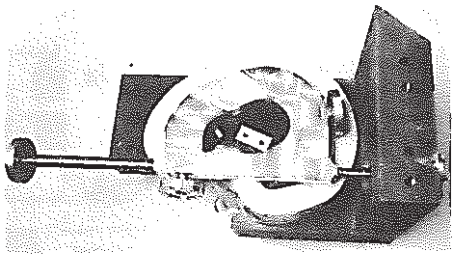

The I-10/1 uses a space-charge limited triode electron gun as its source of electrons.

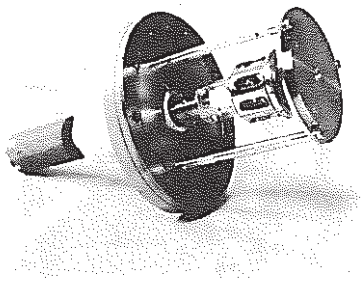

The I-10/1's energy analyzing magnet removes all electrons with energies greater than 10 MeV, in accordance with Codex Alimentarius requirements.

economical for this low power application.

The first unit will be installed at the AECL Radiation Applications Research Branch at Whiteshell Nuclear Research Establishment in Pinawa, Manitoba, for use in radiation processing studies. Full beam characterization and evaluation of operation will be completed in 1987 and commercial versions will then be made available.

The I-10/1 is a high-quality research and development tool for electron processing, allowing the user to explore product handling at throughput rates high enough for pilot-scale tests. The scanned 10 MeV beam complies with the Codex Alimentarius recommendations on food irradiation. Materials, such as plastics, feed, grain, wastes, packaged goods and liquids, can be irradiated with good control of dose distribution. A conveyor speed interface is provided for simulating full-scale industrial processing.

The beam accelerating system of the I-10/1 uses a space-charge limited triode electron gun as its source of electrons. The accelerator structure employs a "pancake" coupled "S" band design driven by a magnetron rf power tube. The Codex Alimentarius requirements are met by passing the accelerated beam through an energy analyzing magnet and removing all electrons with energies greater than 10 MeV. The beam then enters an evacuated horn and is scanned through an angle of 38° to provide uniform dose distribution across wide samples.

The I-10/1's control system has been designed to minimize operator intervention while ensuring safe, uniform, repeatable and recorded radiation exposures. The main component of the control system is a GEC GEM 80 programmable controller which monitors over 70 machine operating parameters and system interlocks. This industrially proven controller can be interfaced to provide conveyor speed control. It has extensive diagnostic and record keeping abilities and can be operated for routine irradiations with a minimum of expert knowledge.

The I-10/1 requires 12 kVA of electric power and can operate from 50 or 60 Hz supplies. A cooling water supply of twelve litres per minute at not more than 20°C is also necessary. The accelerator is installed in a shielded room, which can be arranged according to application.

Additional information on the I-10/1 is available in a technical paper entitled "The I-10/1 Electron Accelerator for Irradiation Research and Pilot Scale Operations", by G. Hare, presented at the 6th International Meeting on Radiation Processing, May 1987, (to be published in the Journal of Radiation Physics and Chemistry).

## AECL's I-10/1 Demonstration Facility

The facility housing the prototype I-10/1 at AECL's Whiteshell Nuclear Research Establishment is a special pilot-scale design allowing experimental irradiation of solids, liquids and gases in simulated industrial configurations. It can also handle packaged products in quantity on a conveyor system which operates at a controlled rate and carries packages through the complete system – from the receiving area, through the radiation shielding maze, past the irradiation chamber and out to the shipping area. Static and loop experiments are assembled and tested in a special room before installation.

The facility's irradiation chamber is large enough to accommodate a higher power machine in the future, and the wide maze will permit a more bulky system to be installed with relative ease. A large crawl space below the facility will allow new services to be installed without major reconstruction. Main bio-

Scientists at Whiteshell Nuclear Research Establishment are studying new industrial radiation processing applications using ionizing radiation from radioisotopes and electron accelerators.

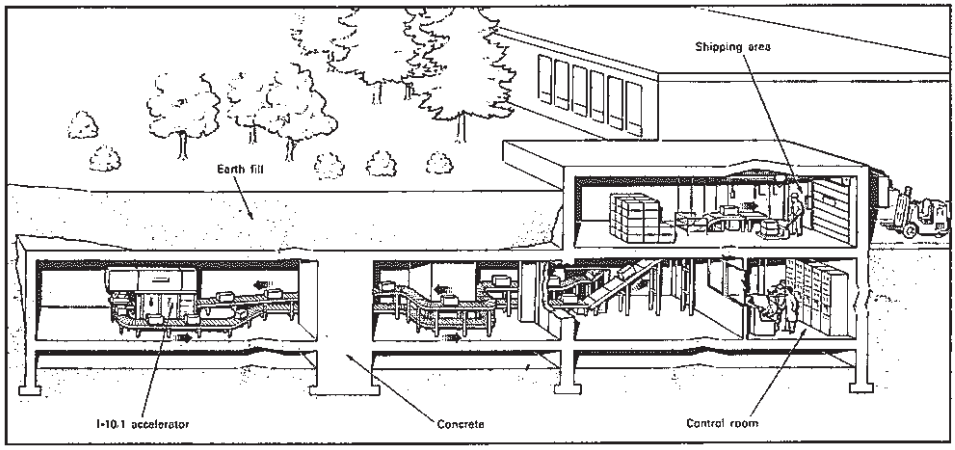


A prototype version of the I-10/1 is being installed at Whiteshell Nuclear Research Establishment.

logical shielding is provided by an earth berm.

## Applications R&D at AECL

AECL formed the Radiation Applications Research Branch at the Whiteshell Nuclear Research Establishment in March 1985. The group's mission is to research and develop new industrial radiation processing applications using ionizing radiation from radioisotopes and electron accelerators. A staff of 11 scientists and engineers and 10 technical support personnel is responsible for research and development and operation of the I-10/1 demonstration facility. In addition to AECL-funded projects, the branch carries out research in collaboration with industries and will perform proprietary research and testing under direct contract.

Areas under study include

- application of radiation pasteurization, at various stages in food production, to reduce or eliminate the incidence of Salmonella
- use of combined heat and radiation processing to extend shelf life of foods and create new shelf-stable products
- effects of radiation in the curing, ross-linking, grafting and polymerizing of thick-section structural plastics
- electron dosimetry in industrial electron beam applications
- time-dependant effects of electron beam irradiation

More details on the work of the branch can be found in the following technical papers: "Radiation Applications Research and Facilities at AECL", by S.L. Iverson, and "Electron Dosimetry for 10 MeV linac" by K.K. Mehta, R. Chu and G. VanDyk, presented at the 6th International Meeting on Radiation Processing, May 1987, (to be published in the Journal of Radiation Physics and Chemistry).

## Summary

Gamma radiation processing using cobalt-60 and electron beam irradiation have complementary areas of application. AECL's commitment to radiation processing using cobalt-60 will continue as its industrial accelerator program develops. The I-10/1 accelerator will satisfy the immediate need for an economic research and pilot-scale tool for applications development, and the IMPELA family of accelerators will provide the power necessary for commercial installations.

AECL is committed to becoming the first company in the world that designs and manufactures both gamma and electron beam processing systems to satisfy the needs of present and future markets.

For more information please contact

Dr. Andrew Stirling
General Manager
Accelerator Business Unit
AECL Research Company
413 March Road
P.O. Box 13500, Kanata, Ontario
Canada K2K 1X8

Dr. Joe McKeown
Director, Science and Technology
Accelerator Business Unit
AECL Research Company
Chalk River Nuclear Laboratories
Chalk River, Ontario, Canada K0J 1J0

Dr. Stuart Iverson
Manager
Radiation Applications Research Branch
AECL Research Company
Whiteshell Nuclear Research Establishment
Pinawa, Manitoba, Canada R0E 1L0

Mr. Frank Fraser
Vice-President
Industrial Irradiators
AECL Radiochemical Company
Industrial Irradiation Division
413 March Road
P.O. Box 13500, Kanata, Ontario
Canada K2K 1X8

# 資料８－１

# A HIGH DUTY FACTOR 400MeV HIGH RESOLUTION ELECTRON LINEAR ACCELEARTOR

# A HIGH DUTY FACTOR 400 MeV HIGH RESOLUTION ELECTRON LINEAR ACCELERATOR*

J. HAIMSON

*Massachusetts Institute of Technology*
*Cambridge, Massachusetts*

## Introduction

An increasing need for electron beams of higher intensity, resolution, and duty factor, in high energy nuclear physics research, provided stimulus for the re-appraisal and extension of existing microwave accelerator concepts, and the investigation of alternate new techniques. Most of the high duty factor microwave electron accelerator projects presently being pursued in a number of laboratories throughout the world comprise either, (a) "conventional" linacs and microtrons, which utilize high power RF generators and high dissipation waveguides or (b) superconducting linacs and microtrons, which hold promise of eventually achieving the ultimate in high duty factor-high energy performance, namely, continuous operation. In the former category, system design concepts were previously limited due to the nonavailability of suitable high duty factor RF generators. In recent years, however, the reliable demonstration of very high levels of RF power over a range of different frequency bands enabled several high duty factor accelerator projects to be initiated. 1,2,3

The MIT electron linac described in this paper utilizes 2856 MHz klystrons which operate over a wide dynamic range of peak RF power from 4 MW to 1 MW with a corresponding average RF power range of 80 kW to 65 kW, i.e., a range of RF duty factors from 2 percent to 6.5 percent. High duty operation with this technique, however, imposes unusual technical and economic restrictions on the design of the linac because of the weak accelerating field strengths associated with the low values of peak RF power, and the uncommonly high levels of average

* Work supported by the U. S Atomic Energy Commission and the Massachusetts Institute of Technology.

power, that must be dissipated in the thermally phase sensitive and dispersive elements of the system, such as the accelerator sections and the rectangular waveguide feeds.

For example, in order to compensate for loss in energy gain due to the reduced field gradients there is a strong design tendency to maximize the length and total attenuation ($\tau$) of the waveguide sections consistent with the requirements of phase and temperature stability ($\Delta\theta/\Delta f = 2\tau Q/f$, $\Delta f/\Delta T = 48$ kHz/°C). Also, the waveguides generally require water cooling systems which are designed to operate with large flows and high velocities, and which incorporate means for the accurate automatic temperature control of the phase shft through the section. In this regard, control of the inlet water temperature with a sensitive metal temperature detector located at a unique temperature—phase "fulcrum" point on the waveguide is found to be effective in maintaining a given phase relationship, regardless of variation of input RF power or beam loading.

Since, with a linac system of the above type, high duty performance is obtained by operating at a maximum repetition rate of several thousand pulses per second and pulse lengths in excess of 10 $\mu$ sec, it is clear that adjustment of these parameters can cause large variations of dissipated power throughout the system. A requirement that the RF and injection systems be designed for reliable and stable performance over very wide limits of pulse operation is characteristic of this high duty factor approach.

Quite apart from the principal advantage of increasing the beam intensity, high duty operation manifests another particularly valuable feature; namely, that despite inherently low field gradients, high duty factor linacs are subject to considerably less beam loading than conventional low duty high gradient machines of the same beam energy and average current. (For a given klystron and waveguide configuration and a constant average current the beam loading parameter is inversely proportional to the square root of the duty factor). This characteristic is instrumental in reducing several of the larger contributions to beam energy spread and is primarily responsible for the inherent capability of high duty factor linacs to produce electron beams of higher resolution than conventional duty machines.

A comprehensive description of system optimization and design procedures for high duty factor linacs has been given recently elsewhere,[3] and the following discussion refers specifically to the 400 MeV linac currently under construction at the Laboratory for Nuclear Science, MIT, and performance data obtained during preliminary tests on several of the prototype sub-systems.

## Design Objectives

In determining a suitable concept for the MIT linac, the study of various RF and beam optics problems established two important design objectives. The first was to elevate the threshold current level of the cumulative type of beam break-up (BBU) well above the normal operating levels of the machine, bearing in mind that high duty operation necessitated low field gradients and long pulse lengths — conditions which were known to be conducive to the BBU instability phenomenon. The second objective was to exploit as fully as possible (to the extent permitted by limited funds) the high duty factor capability of producing sharp spectra beams of high intensity. In this regard, design emphasis was placed on achieving input RF power and beam injection of high quality and on maintaining an accurate phase relationship and a central beam trajectory within each waveguide.

The design objectives for the three prime RF operating parameters, phase, field strength, and frequency were, respectively, $<2$ degrees of intrapulse phase variation (droop and ripple), with respect to the phase of the drive power, for pulses up to 15 $\mu$ sec in length; $<\pm 0.125$ percent of intrapulse variation of the field gradient at the waveguide input couplers; and $<1.5$ kHz long term frequency variation of the master exciter. These RF objectives led to the choice of an ultrastable phase-locked solid state exciter, cw booster drive klystrons using 0.02 percent voltage regulated dc power supplies and pin-diode modulated RF input signals, direct HV series switching of the main klystrons (hard tube modulators) without the use of pulse transformers, and temperature-phase control of the critical RF systems.

Consistent with the inherent high resolution capability of a lightly loaded accelerator operating with pulses an order of magnitude longer than the fill-time of the waveguides, the injector design studies placed emphasis on the attainment of very narrow bunch widths. A 2 degree design objective was established for the longitudinal phase space of bunches emergent from the injector linac at energies greater than 6 MeV and for peak currents of up to 25 mA. Owing to space charge and waveguide space harmonic considerations[3], the above requirements led to the choice of a high potential electron gun (maximum of 500 kV), an RF chopper prebuncher system, and a slightly tapered phase velocity buncher waveguide designed to operate at a high level of dissipation.

Choice of a high gun potential, a small cathode diameter, a long focal length, and the use of narrow collimating apertures, in combination with a low value of longitudinal phase space ($<10^{-2}$) at injection to the buncher waveguide, held promise of demonstrating a considerably lower beam emittance than that previously obtained with higher perveance, lower potential, injection systems. These features were consistent also with the desire to inject and accelerate small cross-section beams and to maintain the trajectories as close as practicable to the central axis. To assist in this objective, two pairs of beam steering

Helmholtz coils are located at each waveguide section in close proximity to the RF input couplers, and solenoidal focusing has been provided for the first five waveguide sections with several quadrupole doublet assemblies thereafter.

## General Description of Machine

A schematic layout of the microwave distribution system, the injector linac, and the accelerator waveguide arrangement is illustrated in Figure 1. Ten high power klystrons are paired into five groups, each pair being video driven from a common hard tube modulator and RF driven from a common driver klystron. A highly stabilized master driver klystron is used to excite the five driver klystrons via a phase stabilized coaxial line.

Ten rectangular waveguide networks are utilized to interconnect the high power klystrons to 24 accelerator waveguide sections. The first klystron is reserved for the two series-connected sections of the injector linac; each of the following seven klystrons drive two waveguide sections; and each of the last two klystrons energize four accelerator sections. The use of quadruplexed waveguide sections at the end of the linac provided a satisfactory compromise between the technical desire to maximize beam energy and the economic requirement to minimize initial expenditure. The approach has an added attraction in that the machine can be up rated at a later date, without affecting the beam centerline components, by adding another transmitter and retrofitting a portion of the RWG network in the gallery.

The 24 accelerator waveguide sections comprise a buncher in series with a 3.7 meter section, four 3.7 meter sections, and eighteen 7.35 meter sections. The accelerator waveguides are divided into six groups of different microwave design, shown in Figure 1 as AA, BB, A, B, C, and D, in order to (a) provide a higher gradient at the beginning of the linac and (b) counteract the cumulative type of BBU.

## Description of Linac Characteristics

### Principle Performance Specifications

| | |
|---|---|
| Beam energy at zero loading | 430 MeV at 1.8% duty |
| Beam energy at an average current of 150 mA | 400 MeV at 18% duty |
| Energy spread at 150 mA average | $>$ 50% current in $\pm$0.2% |
| Beam emittance at 400 MeV | $2 \times 10^{-6}$ rad $\times$ cm |

### Main Features

| | |
|---|---|
| Number of klystrons | 10 |
| Linac design operating frequency | 2856 $\pm$ .05 MHz |
| Number of modulators | 5 |

| | |
|---|---|
| Number of waveguide sections | 24 ($2\pi/3$ design) |
| Overall electrical length | 152 meter |
| Overall physical length | 180 meter |

**Master Driver**

**Crystal controlled solid state oscillator**

| | |
|---|---|
| Frequency range (manual control) | 2856 ± 6 MHz |
| Vernier adjustment (electronic control) | ± 150 kHz |
| Long term stability | 1 part in $10^7$ |
| Power output (cw) | 400 mW |
| Trigger logic controlled diode modulation | |

| | |
|---|---|
| **Master driver klystron** | Type 4K3SN-1 |
| Power output (cm rating) | 1 kW |
| Bandwidth (Output) | <0.1 db variation for 2856 ± 0.5MHz |
| Beam voltage | 6.2 kV dc |
| Beam current | 470 mA dc |
| Drive power (nominal) | 75-150 mW |
| Electrical length | 2240 degrees at 7 kV |
| Filament power | 6.0 V dc x 4.8 A dc |
| Focus | Permanent magnet |
| Collector cooling | 3 GPM at 23 psi |
| Body cooling | 1 GPM at 6 psi |

**High Voltage power supply**

| | |
|---|---|
| Voltage range | 0 - 8 kV dc |
| Current range | 0 - 600 mA dc |
| Voltage ripple and regulation | $<\pm 0.01\%$ |
| HV vernier control | 0.03% |

**Main Drive Line**

| | |
|---|---|
| 1 - 5/8 inch coaxial line | 190 meter long |
| Group velocity | $0.98c < vg < 1.02c$ |
| Phase velocity | $> 0.997c$ |

218

| | |
|---|---|
| Coaxial directional couplers | 5 at 2W peak output<br>1 at 5W peak output |
| Coaxial expansion joints | 4 |
| Temperature control | $\pm\frac{1}{2}$° C |
| Pressure control (dry $N_2$) | 1/10 psi |
| Overall phase stability | 1 degree |
| **Driver Klystrons** | 5 (Type 4K3SN-1, as above) |
| HV dc power supplies | 5 (as above) |
| **Main Klystrons** | 10 (Type VA938) |
| Operating frequency | 2856±0.2 MHz |
| Peak output RF power | 4 MW to 1 MW |
| Peak beam voltage (max) | 130 kV to 80 kV |
| Peak beam current | 91 A to 44 A |
| Microperveance | 2.0 ± 0.1 |
| Average output RF power | 80 kW to 65 kW |
| Minimum efficiency | 35% to 30% |
| Minimum gain for saturation | 41 db |
| Maximum body current | 3% |
| Filament power (max) | 700 W |
| Focus | Electromagnetic (4 coils) |
| Collector cooling | 75 GPM at 70 psi |
| Body and window cooling | 10 GPM at 10 psi |
| Single RF output through ceramic window | |
| Window pressurization (dry $N_2$) | 50 psi (max) |
| **Modulators (Hard Tube)** | 5 (Type ESI) |
| Peak Power | 23 MW at 1.25 kHz, 7MW at 4 kHz |
| Average Power | 520 kW |
| Peak voltage | 140 kV |
| Peak current | 200 A |
| Load dynamic impedance | 1400 to 1700 ohm |
| Switch tubes | Four Litton - L5097 rated 165 kV |
| Capacitance bank | 1.8 μF |
| Crowbar protection | Maximum energy release < 50 joule |
| Pulse duration (99% flat-top) | Continuously variable up to 15 μsec in accordance with duty factor and peak power (see Figure 4) |

249

| | |
|---|---|
| Voltage pulse flat-top specification | 0.2% (objective 0.1%) |
| Pulse repetition rate | Continously variable up to 5 kHz in accordance with duty factor and peak power (see Figure 4) |
| RF duty factor | 2% to 6.5% |
| Video duty factor | 2.5% to 8% |

**Main Waveguide Sections** (4 short and 18 long)

$2\pi/3$ mode, approx. constant gradient.

Length
3.675 and 7.35 meter

Number of cavities
105 and 210

Disc thichness
5.84 and 5.84 mm

Number of uniform segments per section
11 and 11

Range of shunt impedance
53.8-57.7 and 48.0-56.5 MΩ/m

Range of group velocity ($v_g/c$)
0.0156-0.007 and 0.0389-0.0093

Average attenuation parameter
0.75 and 0.825 neper

Average Q
13400 and 13750

Filling time
1.12 and 1.27 μsec

Zero current energy gain at $P_o = 1.8$ MW
16.6MeV and 23.2MeV

Zero current energy gain at $P_o = 0.8$ MW
15.5MeV

Cooling
12 × 11 mm I.D.and 8 × 16 mm I.D. tubes

Water flow per section
6.3 and 6.3 litre per sec.

Construction
Hyndrogen braze (copper-silver eutectic) and vacuum jacket

Beam pulse length
Variable up to 14 μsec in accordance with duty factor and peak RF power.

Beam duty factor
1.8% at $P_o$=4 MW and 5.8% at $P_o$=1 MW.

250

Steering coils at each input coupler, no solenoids for long sections.

**Injector Linac Design**

| | |
|---|---|
| Electron gun maximum potential | 500 kV |
| Nominal operating potential | 400 kV |
| Nominal cathode current | 100 mA |
| Mod electrode potential | 2 to 5 kV (-500 V bias) |
| Chopper cavity | $TE_{102}$ mode |
| Prebuncher cavity | $TM_{010}$ mode |
| Drift length | 1.3 meter |
| Injected bunch width | $<$ 10 degrees |
| Buncher waveguide | Tapered phase velocity, $2\pi/3$ design, 1.2 meter long. |
| Series-connected waveguides | $v_p=c$, $2\pi/3$, 3.7 meter long |
| Buncher zero load energy | 6.9 MeV at $P_0=2.5$ MW |
| Beam design emittance at 6 MeV | $10^{-4}$rad $\times$ cm |
| Focus | Thin lenses and solenoids |

## RF System

At high duty factor, the provision of a reliable, phase stable RF drive system extending over the full length of the accelerator presents a severe design problem owing to the high levels of power dissipation. This problem can be avoided by the use of intermediate drive klystrons which are excited via a common coaxial line and a master RF driver as shown in Fignre 1. Tne use of a rigid coaxial cable for a main drive line is highly decirable in a multi-klystron driven accelerator since the group velocity can be closely approximated to the velocity of light; and because of low dispersion characteristics, a coaxial cable is more tolerant to small changes of frequency and ambient temperature than a rectangular waveguide. On the other hand, unlike a rectangular waveguide, a coaxial line which is subject to wide variations and moderate levels of dissipation is difficult to phase stabilize owing to the inaccessibility of the center conductor. With the above technique, however, the drive line dissipation level remains low even at the maximum duty factor, and attention nead only be directed at controlling the ambient enviroment. Another advantage of the coaxial line is that its geometry

readily allows the use ot bellows type expansion joints, and by judicious location of these joints, it is possible to anchor the drive line at each of the directional coupler feed points. This allows the phase relationship between each of the driver klystron feed points to be spatially locked, and the telescoping action within each segment prevents the drive line from being seriously stressed.

While the use of driver klystrons offers several distinct advantages, especially the very low power rating permitted for many of the components, extreme care must be taken to avoid radiative feedback into what is essentially a long distributed high gain amplifier system. A potential source of interference is the RF leakage associated with isolated collector high power klystrons; and low—level drive line components such as couplers, flanges, etc. should be well shielded and/or remotely located in a shielded duct.

The RF master exciter consists of a tunable phase-locked crystal-controlled solid state oscillator which drives a water-cooled klystron. All phase-locked and oscillator components are oven-controlled for high stabillity, and pin-diode modulation capabillity of the 400 milliwatt oscillator output enables optional cw or pulsed operation of the klystron. The klystron is rated at 1 kW cw, requires a drive of 150 mW (nominal) and is energized by a remotely adjustable HV regulated dc power supply having a voltage ripple of less than 0.02 percent peak to peak. Power from the main 1-5/8 inch coaxial drive line is coupled out to excite the five 1 kW driver klystrons, each of which provides drive for two high power klystrons. With this approach, even at 10 percent duty, the total dissipation in the main drive line is limited to less than 70 watts, and the drop-out lines (2W peak) and components connecting to the driver klystrons operate at an average power of a few hundred milliwatts. The five driver klystrons are identical in design to the master driver klystron and are energized from similar highly stabilized dc power supplies. Thus, all driver klystrons operate with dc beams and derive pulsed input RF signals from a triggerlogic-controlled modulation of the master oscillator output. This drive system concept was chosen as the most likely to reliably provide a 1 degree phase stability for the main klystron drive signals as well as for the main drive line in its role as a master reference for phasing the accelerator.

Figure 2 shows the completed master driver cubicle (background) and a high precision phase bridge capable of resolving phase differences of less than 0.1 degree between signals connected to the two input arms of a carefully matched and balanced magic Tee. Typical phase performance data obtained during final tests on the master driver system are shown in Figures 3(a) and (b). These phase measurements were taken at 5000 pulses per second, with one arm of the bridge sampling the output of the solid state exciter and the other arm sampling the pulsed output of the driver klystron when operating at a peak power of 800 watts. Figure 3 (a) shows the flat phase characteristic obtained for

a pulse length of 33 μsec. For calibration purposes, as shown in Figure 3(b), a 1 degree phase shift off-set is superimposed on the 33 μ sec pulse trace of the phase bridge output, i.e. the RF phase stability over the full length of the pulse flat top is <0.3 degrees. This RF flat-top phase stability has also been demonstrated over a wide range of repetition rates and with pulse lengths extending into the millisecond region, which is consistent with the cw beam operation of the driver klystron, a 1 volt peak to peak ripple of the HV power sypply, and a klystron transit length of 2420 degrees at 6 kV. The long term (24 hours) freguency drift of the master driver unit is between 200 and 300 Hz, which is well within the operational requirements of the linac. It should be noted that the pin-diode presently beinq used to modulate the cw output of the exciter introduces a relatively large transient phase shift (~2 degrees) during initial switching, and a delay of approximately 6 μsec is required before the steadystate condition is reached. Further development work is being planned to investigate this phenomenon.

The high power klystrons are of five cavity construction, each requiring a peak RF drive of approximately 50 watts and using a single waveguide output feed which is terminated in a half wavelength (solid block) water-cooled ceramic window. A short section of thick-wall, pressurized waveguide, terminated with a similar RF window, connects the klystron to the evacuated rectangular waveguide system. This section serves the dual role of providing additional cooling for the klystron window (average power 80 kw) and enabling klystron replacement without disturbing the vacuum system. It also provides a convenient location for the four directional couplers used for RF protection and monitoring purposes. The evacuated rectangular waveguide networks are similar to those used at SLAC, with the exception that an extra water cooling channel has been added to the high power sections between the klystrons and the power splitters. RF monitoring couplers are located on either side of the driver and main klystrons and in the rectangular waveguide feeds immediately prior to each accelerator waveguide input coupler. In order to minimize transverse momenta contributions to the beam, due to coupler asymmetries, the rectangular waveguides are arranged as vertical input feeds from above (A) and below (B) the accelerator structure in an ABBA BAAB ABBA BAAB BA BAAB configuration, as shown in Figure 1. To further cancel the effects of coupler asymmetry, the input and output RF feeds are located on the same side of each accelerator waveguide; and, to provide local correction, two pairs of beam steering Helmholtz coils are located at each input coupler. In keeping with a philosophy to avoid unnecessary evolution of gas within the vacuum system, especially during long pulse operation, the accelerator waveguide output feeds are connected to water loads which are isolated from the vacuum by two quarter wavelength ceramic windows separated by a short section of air-filled rectangular waveguide.

Again, this section serves the dual purpose of providing a convenient location for the output RF power monitor and avoiding a catastrophic situation in the event of a window failure. Since there are no high power phase shifters in the system, reliance is placed on the accurate determination and manufacture of the rectangular waveguide lengths, and on final tuning of the waveguides after installation, to provide correct phase relationships within individual networks.[4]

## Prototype Transmitter Performance

Hard tube modulators and direct series switching were chosen for the MIT linac because of the need for high quality video pulses and a maximum repetition rate of 5000 pulses per second, and the desire to continuously vary the peak RF power and pulse length over the full dynamic range of the system. The operational limits of RF pulse width and repetition rate for the transmitter are related to the klystron peak RF power and permissible duty factor as indicated in Figure 4.

The absence of pulse transformers, made possible by the direct high voltage switching approach, enables pulse ripple and droop contributions due to leakage reactance and stray capacitance to be reduced to very low values. The prototype transmitter described below utilized two paralleled switch tubes in series connection with each klystron. These switch tubes use magnetron injection gun geometry, with the cathode well protected from arcs, and are of gridless construction. The high plate resistance of the two switch tubes in parallel (more than twenty times the dynamic impedance of the klystron) is an essential characteristic which provides the regulation necessary for meeting the jitter and drift specifications and allows economy in the capacitor banks.

Video and RF preliminary tests were conducted recently on the prototype transmitter using one klystron and two switch tubes. The results of these tests were particularly impressive, especially in regard to pulse quality and stability, and a summary of the performance data is given below.

The klystron was operated as a diode load for the video power tests, and the body current was carefully monitored and maintained at a low level throughout the test period. Continuous adjustment capability of the video peak power was demonstrated by operating at a variety of klystron beam conditions between 126 kV, 88.3 amps (11.1 MW) and 67 kV, 35 amps (2.3 MW) with a 16 μsec flat-top pulse at 660 pps. High average video power tests were also conducted at both high and low peak power conditions, e.g., 10.9 MW peak at 1.9 percent flat-top duty (152 μsec flat-top at 1250 pps), and 3.27 MW peak at 6.0 percent flat-top duty (15.6 μ sec flat top at 3850 pps). In addition, video pulse modulation, droop and jitter measurements were taken at peak power levels of 122 kV, 84 amps (10.3 MW), and 79 kV, 45 amps (3.5 MW).

The maximum observed intrapulse voltage amplitude modulation was <0 05 percent for both peak power conditions (Specification is 0.2 percent except during the first and last microsecond).

The droop in pulse current after 15 μ sec was measured as <0.05 percent in the high peak power condition and 0.11 percent rise in the low peak power condition (specification is ≤0.5 percent).

Short term jitter pulse instabilities were measured over the range of permissible repetition rates at both the low and high peak power conditions. The voltage jitter was approximately 0.03 percent (specification is 0.17 percent) with occasional current pulse jitter values of about 0.05 percent (specification is 0.25 percent).

Figure 5 shows some of the prototype transmitter components including the dual capacitance bank, the crowbar protection assembly, the modulator tank with its HV bushing, and the tank containing the HV dc power supply. Figure 6 is a view of the interior of the modulator tank showing two of the switch tubes and a high power klystron.

The master driver described earlier, and shown in Figure 2, was used to excite the main klystron during the RF preliminary tests. The klystron output rectangular waveguide was pressurized with dry $N_2$ and instrumented for excess reverse power protection, arc protection, and forward power measurements, and was terminated in a matched water load calorimeter. Data obtained during these preliminary tests verified peak RF power outputs over the range of 4.4 MW to 0.75 MW. Full average RF power output was not attempted during the first series of tests, although the klystron was operated at up to 50 kW RF average, as efforts were concentrated on obtaining RF phase data during the pulse.

The diagnostic value of an accurate RF phase bridge cannot be overemphasized since it provides a sensitive and easily calibrated means of qualitatively and guantitatively analyzing the performance of both the RF system and the modulator. By progressive comparison of pulse signals across the driver and main klystrons (or with the "standard" arm of the bridge connected to the cw source of RF power), the various phase modulation contributions due to RF drive, modulator pulse voltage droop and ripple, klystron cathode heater hum, temperature drift, etc., can be readily isolated and measured. The modulator intrapulse voltage amplitude variations can be determined essentially in time domain, thus avoiding the errors (and perennial debates) associated with high voltage monitor corrections factors (compensation of capacitance dividers, droop of monitoring pulse transformers, ringing, etc)—especially when the variations being considered are small fractions of one percent.

For example, the transit phase angle ($\Phi$) through a klystron is related to the electron velocity ($\beta c$) and drift distance (S) between terminal cavity gaps by the simple expression, $\Phi = 2\pi S/(\beta\lambda_0)$. Differentiating this expresion with respect to the klystron cathode voltage (V) gives, $(\partial\Phi/\partial v) = (\partial/\partial v)\ [2\pi S\gamma(\gamma^2 - 1)^{-\frac{1}{2}}/\lambda_0]$, where $\lambda_0$ is the free space wavelength, and the electron energy in rest mass units ($\gamma$) is given

by, $\gamma = 1 + V(keV)/511 = 1/(1-\beta^2)^{1/2}$ This then gives the relativistically corrected phase shift $[\Delta\Phi)$ through the klystron for small fluctuations of cathode voltage $(\Delta V)$ as, $\Delta\Phi = -(\Delta V/V)\ [2\pi S\ (\gamma - 1(\gamma^2-1)^{-3/2}/\lambda_0]$. As an example, at a frequency of 2856 MHz and with a klystron drift distance of 35 cm, a cathode voltage variation of 0.1 percent will produce klystron phase variations of 0.73 and 0.96 degrees at cathode potentials of 122 kV and 80 kV, respectively. Additional cross-checks on the video performance, as determined from RF phase measurements, can be conducted by observing the associated intrapulse amplitude variation of the RF power and using the perveance relationship of a space charge limited beam, i. e., $(\Delta P/P) = (5/2)\ (\Delta V/V)$.

Typical RF phase pulse characteristics obtained during the preliminary tests are shown in Figures 7(a) and (b). Fugure 7(a) was obtained with the phase bridge connected across the input of the driver klystron and the output of the main klystron, i.e., measuring the combined phase shift of both klystrons. For this example, the main klystron was operated at the low end of the peak power range (80 kV, 44.9 amps) and therefore at the highest phase sensitivity, due to the low cathode potential. The trace shows a phase **advance** of approximately 2 degrees over 12 $\mu$ sec which is a somewhat unusual phenomenon since voltage droops and therefore lagging phase shifts usually characterize long pulse operation. In this case, however, the phase advance is consistent since a rising characteristic was discovered during video tests at low peak, power, as noted above. (A rising pulse voltage and advancing phase characteristic at low peak power is a desirable feature for low gradient linacs since it enables the bunch to be located slightly ahead of crest at entry to the waveguide, thereby providing compensation against space charge energy spread contributions while minimizing additional phase slippage due to reactive effects).

Figure 7(b) shows the results of an RF phase measurement made across the driver klystron only, to determine its contribution to the total phase variation of the RF output shown in Figure 7(a). This measurement indicated that the drive signal RF phase variation was maintained within a $\frac{1}{4}$ degree bin over a 33 $\mu$sec pulse length and was substantially in agreement with earlier data obtained under laboratory conditions.

A notable feature of the high power RF output pulses, regardless of peak power level or pulse length, was the absence of phase ripple of the type commonly observed with klystrons that are driven by line type modulators and pulse transformers. The high level of video pick-up encountered during the tests required careful shielding and grounding of the monitoring and diagnostic equipment and limited the RF phase bridge to relatively low gain operation. Work is currently in progress to improve the shielding and filtration of the RF phase bridge circuits to allow operation at maximum sensitivity in the video noise environment.

## Beam Break-up

The microwave design characteristics and electron beam specifications of the accelerator waveguides are listed in an earlier section of this report, and the layout configuration is shown in Figure 1. With the exception of the buncher section, each waveguide contains eleven uniform, $2\pi/3$ mode segments interconnected by transition regions of progressively increasing impedance. The MIT linac specification of 60 kW of beam power at 400 MeV and 1.8 percent duty requires the demonstration of a peak current of 8.4 mA with pulse lengths extending out to 14 or 15 μsec. Under the conditions of weak focusing intended for the initial phase of the MIT linac, an extrapolation made in 1966 based on the SLAC experience[5] suggested that a cumulative beam break-up threshold value of approximately 5 mA could be expected. As a consequence, several microwave design approaches were investigated with the aim of elevating the threshold value to a safe level. A design value of 50 mA was chosen as a goal since the low gradient waveguides at the end of the machine (four sections per klystron) have an $i_m$ value of 60 mA when the klystron is operated at the specified maximum RF peak power of 4 MW. Since, for a given field gradient and charge per pulse, the cumulative type of beam break-up is strongly dependent on the number of identical resonant elements which can interact with the beam and on the $HEM_{11}$ transverse shunt impedance, the investigations[11] were concentrated on means of reducing the coherency lengths and on $HEM_{11}$ Q-spoiling techniques.

The design finally adopted for the MIT linac made use of a progressive stop-band concept which required a specific relationship between different waveguide sections along the beam centerline. The eighteen long waveguide sections are comprised of four design groups, A through D, which are similar in external physical detail but differ in microwave design.

The $HEM_{11}$ dispersion characteristics for the group A waveguides are arranged so that the narrow bands of closely spaced undesirable resonances associated with the input coupler and several of the adjoining uniform impedance segments, in the vicinity of the $v_p=c$ intercept, are displaced outside and below the $HEM_{11}$ pass bands of all subsequently located structures, regardless of group affiliation. Similarly, the range of $HEM_{11}$ resonances associated with the critical initial regions of the group B waveguides are designed to fall below the $HEM_{11}$ pass band regions of all following waveguides in groups C and D. This stop-band procedure is applied progressively along the full length of the accelerator. In this manner, the displacement modulation information carried by the beam at low $HEM_{11}$ frequencies, due to transverse fields in the initial segments of waveguides in an upstream group, is excluded from interacting with downstream waveguides; and further deflection amplification at these frequencies is avoided. When using disc loaded waveguides of conven-

tional construction, this technique requires that the iris diameters in the initial region of waveguides in a given group be smaller than those in any preceding group but larger than those in subsequently located groups. This progressive stopband concept is illustrated diagrammatically in Figure 8. Curves $A_1$, $B_1$, $C_1$, and $D_1$ represents the $HEM_{11}$ $\omega$-$\beta$ diagrams for the input coupler and the first uniform impedance segment of the waveguides in groups A, B, C, and D, respectively. Similarly, the dashed curves $A_2$ through $D_2$ and $A_3$ through $D_3$ refer to the second and third uniform impedance segments, respectively. The curves show that undesirable resonances in the proximity of the $v_p$=c intercept are located below cut-off for the pass band of any following group and that these resonances are separated by approximately 30 MHz from those correspondi g segments in the waveguides of neighboring groups.

The measured $HEM_{11}$ resonances and field patterns for each of the 11 uniform segments of the prototype long waveguide, as obtained by excitation and detection through the cavity pumpout holes and RF couplers, were found to agree closely with the computed design data. (The maximum frequency discrepency was -1.4 MHz at 3946.6 MHz, and this was associated with the first uniform section which contains an off-set coupler and large iris discs. In all probability this discrepency is due to inaccurately estimating the exact $HEM_{11}$ terminal phase shift through the off-set coupler cavity). Figure 9 is a view of the prototype long waveguide section, after final nodal tuning, undergoing probe tests to evaluate the $HEM_{11}$ resonance and polarization characteristics.

In regard to the latter, it should be noted that during the normal nodal tuning procedure, the cavities were deformed in a specific orientation to provide a simple means of Q-spoiling the $HEM_{11}$ mode. With this technique, a normally large VSWR, due to the mismatch presented by the RF couplers at the higher frequency, is reduced by coupling the $HEM_{11}$ mode into the external system. Individual cavities are tuned (permanently deformed) in a radial plane at 45° to the plane of the rectangular waveguide feed; and for a given set of cavities, the deformation is applied in only one plane, i.e., the cavities of a given segment contain only two wall perturbations, and these are diametrically opposed. In this manner, partial coupling can be obtained for either of the orthogonal planes of polarization, and this results in a lowering of the $HEM_{11}$ loaded Q values and peak field strengths. As an example, the prototype long waveguide had input coupler VSWR maximum values of 2.9 and 2.2 for the two orthogonal $HEM_{11}$ modes at their respective dominant frequencies. The corresponding range of VSWR values for the output coupler extended from 2.2 down to the surprising low value of 1.14.

The second waveguide shown in the background of Figure 9 is used as a very sensitive phase reference in a system which automatically provides frequency correction[3] and tracking during the nodal tuning

of production waveguides, regardless of variations in air pressure, temperature or relative humidity.

## Injector Linac

Traditionally, the injection and RF systems have always played key roles in the ultimate limitation of beam spectra achieved, with conventional microwave accelerators. Now, however, with high duty factor operation, and with the advent of transmitters capable of demonstrating high quality video pulses ($<$0.1 percent droop and ripple) combined with phase stable RF drive systems, and even greater dependence must be placed on the injector if the inherent resolution of the linac system is to be fully realized. High stability of peak current is no longer as important an issue, owing to the low beam loading conditions and injected peak currents of reduced absolute value, and achieving large fractions of current in 1/10 percent energy bins is now primarily dependent on the attainment of bunches of narrow phase width and good phase stability.

The strong recommendations made here for a 1 or 2 degree bunch width, to improve beam spectra, are clearly not justifiable on the basis of direct contributions to energy spread alone, since a 5 degree bunch **continuously** located on crest (with negligible space charge forces) is equivalent to a 1/10 percent spread in beam energy. (From small angle approximation, $\Delta V/V^0/_0 \approx -(\Delta\theta^\circ)^2/260$). In practical reality, however, with high power RF operation, only after considerable effort is it possible to minimize phase shifts during the pulse, as well as phase drifts from one module to another, to approximately $\pm$ 2 degress. On this basis, and considering the effect of bunch width only, it is apparent that a 5 degree bunch, **if centered**, will time average over an effective 9 degrees of RF, leading to energy spread contriburions of $\frac{1}{4}$ percent. With a 1 degree bunch and identical RF conditions, however, the energy spread contribution will remain within a 1/10 percent bin. In practice, these energy dispersion effects are approximately doubled due to nonsynchronous operation and/or non-optimum initial phasing of the bunch at entry to the section. Nevertheless, in conducting an experiment with, say, 1/10 percent analyzing slits, it is clear that the time averaged target current can be increased appreciably as the bunch is reduced from 5 to 1 or 2 degrees.

For the injector linac, the concept chosen as the most likely to meet the bunch objectives, less than 2 degrees of longitudinal phase space for peak currents up to 25 mA at not less than 6 MeV beam energy, was based upon the use of a high potential electron source and two stages of bunch compression, bearing in mind the need to minimize both cost and number of components.

The first stage, designed to operate at beam energies within the range of 300 to 500 keV, utilizes a biased RF chopper prebuncher com-

bination[6] to compress a 120 degree chopped beam to $<10$ degress. A stabilized, gas insulated, HV dc power supply energizes the electron gun assembly which comprises a small indirectly heated cathode, a non-intercepting modulation extraction electrode, and an electrostatic focusing electrode followed by 13 intermediate accelerating electrodes designed for uniform gradient operation. The dc magnetically biased $TE_{102}$ chopper is followed by a slotted brebuncher cavity and a chopping aperture designed for 10 kW dissipation. A drift length of approximately 130 cm was chosen to limit phase modulation at injection to the buncher waveguide to $<1\frac{1}{2}$ degrees for a gun potential variation of 1/10 percent.

The second stage consists of a 1.2 meter long, 6 MeV disc loaded buncher waveguide, designed to provide approximately 5 to 1 compression of the injected bunch, connected in series to a 3.7 meter waveguide. Apart from the input coupler and several neighboring cavities which have phase velocities slightly less than c, the buncher waveguide is designed as a phase velocity of light, $2\pi/3$ mode circuit. The very high level of dissipation in the short buncher waveguide presented a difficult design problem since brazing cooling tubes directly onto the structure, the technique used for the longer sections, would not prevent dangerously high stresses from developing in the vicinity of the disc apertures. As a design compromise, to avoid the expense of using cooling ducts in the discs, the outer peripheries of the discs were fluted to form a high velocity, multiple channel, cooling jacket system. The buncher waveguide requires a flow of 100 GPM and an automatic temperature-phase control system[3] similar to that used for the other waveguide sections. Typical disc and spacer components for the buncher waveguide are shown in Figure 10, together with some of the electron gun components including the cathode assembly and several focusing electrodes.

## Linac Facility at Middleton, Massachusetts

A layout of the overall facility including the control and experimental areas is shown in Figure 11, and Figure 12 shows a view of the building construction nearing completion at the Middleton site, which is located 20 miles north of Boston. A brief summary of the construction schedule is listed below.

| | |
|---|---|
| Building Design Completed | July 1967 |
| Building construction contracted | Oct. 1967 |
| Partial occupancy | July 1969 |
| Full occupancy and completion of utilities (schedule) | Jan. 1970 |
| Electrical Utilities, Water and Vac System Design Concept | Aug. 1967 |
| Completion of electrical and water utilities (schedule) | Jan. 1970 |

| | |
|---|---|
| Transmitters Contracted | March 1967 |
| Prototypo transmitter: First RF tests | June 1969 |
| Master Driver Design Concept | Jan. 1968 |
| Completion of engineering design | Sept. 1968 |
| Completion of master driver unit | Feb. 1969 |
| Overall Drive System Design Concept | Sept. 1967 |
| Completion of engineering design | Aug. 1969 |
| Accelerator Waveguides Design Concept | Dec. 1966 |
| Completion detailed engineering microwave design | Dec. 1967 |
| Waveguide construction contracted | Feb. 1968 |
| Completion of overall engineering design | Aug. 1968 |
| Completion of prototype long waveguide | April 1969 |
| Commence installation of accelerator waveguides (schedule) | Jan. 1970 |
| Completion of injection Linac Design Concept | April 1968 |
| Completion of prototype HV electron gun | Sept. 1969 |
| Beam Switch Yard Design Concept | Jan. 1967 |
| Completion of engineering design (schedule) | Sept. 1969 |
| Energy Loss Spectrometer Design Concept | Jan. 1967 |
| Completion of engineering design (schedule) | Sept. 1969 |


## Acknowledgement

The author acknowledges the fine supporting efforts of a team of less than 40 MIT technicians, engineers and physicists, working under the restrictions of a very limited budget, to design and construct a relatively large facility. The cooperative efforts and diligence of our various contractors in the production manufacturing and testing of the major sub-systems,are aslo gratefully acknowledged.


## REFERENCES


1. **E. A. Knapp,** "Resonantly Coupled Standing Wave Accelerator Structures for Electron and Proton Linac Applications", IEEE Trans. Nucl. Sci. NS-16, № 3, June 1969, 329.

2. **H. Leboutet, G. Azam, F. Netter and C. Tzara,** "First Operation of the High Duty Cycle Saclay Electron Linac (ALS)", IEEE Trans. Nucl. Sci. NS-16. № 3, June 1969, 299.

3. **J. Haimson,** "High Duty Factor Electron Linear Accelerators", Chapter 3.2, **Linear Accelerators,** P. Lapostolle and A. Septier, (Eds.) (North-Holland Publishing Co., Amsterdam, 1969).

4. J. Weaver and R. Alvarez, IEEE Trans. MTT, MTT-14; № 12, Dec. 1966, 623.
5. R. B. Neal and W. K. H. Panofsky, Science 152, 1966, 1353.
6. J. Haimson, IEEE Trans. Nucl. Sci. NS-12, № 3. June 1965, 499.

## ДИСКУССИЯ

**Зыков:** Какого типа секция в вашем ускорителе с постоянным импедансом или с постоянным градиентом?

**Haimson:** Each waveguide section consists of 11 subsections each of constant but different impedance. The subsections are joined together by means of matched ransitions.

**Чижов:** Не могли бы Вы высказать свое мнение о возможности создания линейного электронного ускорителя на энергию 400 МеВ с коэффициентом заполнения 10% и более?

**Haimson:** When you go to linacs with duty factors more then 10% you will meet immediatly serious economical difficulties. There are klystrons with average power up to 80 kW now, and one may expect that we shall have soon klystrons with average power up to 150 kW now, If we take such klystrons and duty factor 20% then the peak power of a RF source will be of order of a few MW. and we shall be forced to use very long waveguides with high attenuation in order to get required energy of electrons. Such waveguides have several drawbacks, namely, very rapid decrease of energy. gradient. Surely linacs with energies of 400—500 MeV may have duty factor up to 4%, linacs with energies 150—300 Mev-to 10%. However further increase of the duty factor is not worthwill from the economical point of view.

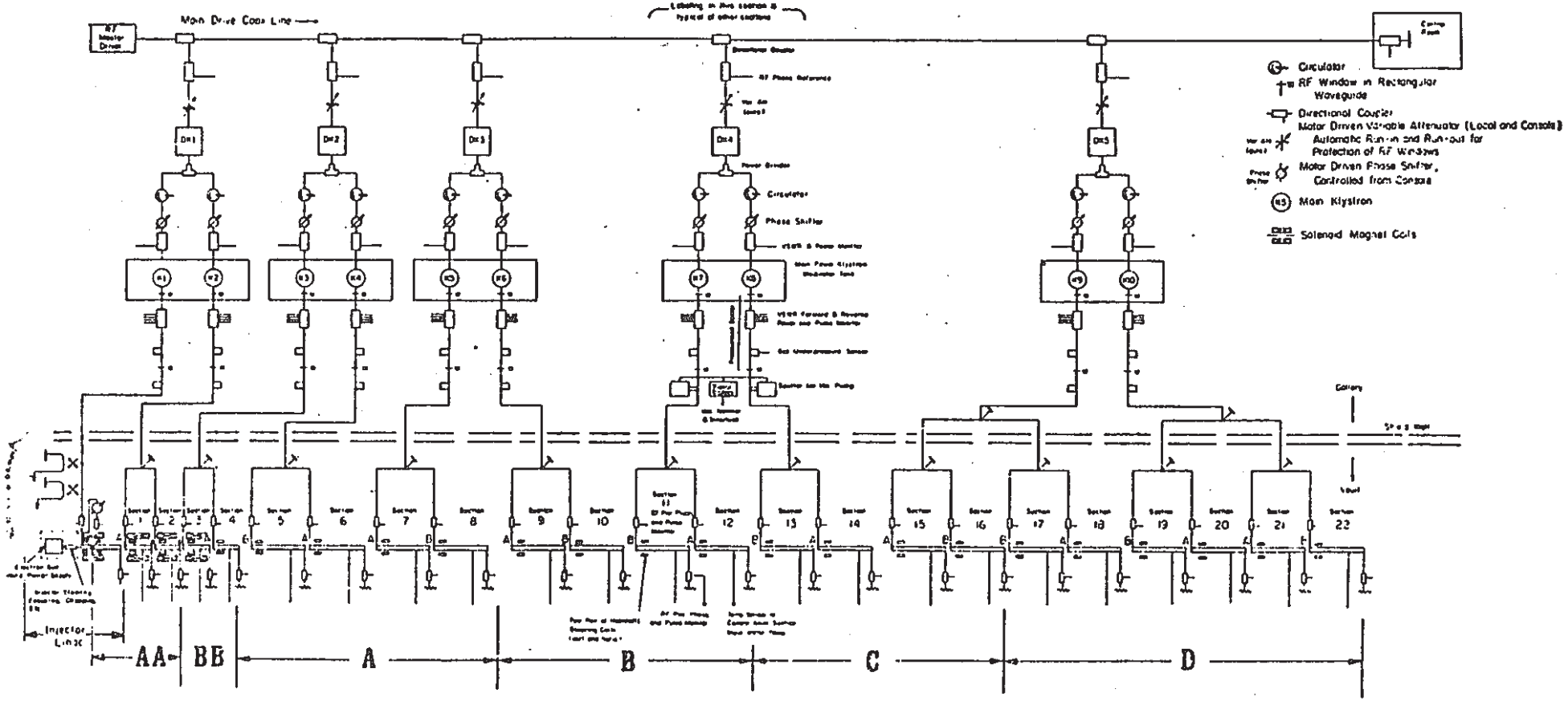
Main Drive Coax Line
Circulator
RF Window in Rectangular Waveguide
Directional Coupler
Motor Driven Variable Attenuator (Local and Console)
Automatic Run-in and Run-out for Protection of RF Windows
Motor Driven Phase Shifter, Controlled from Console
Main Klystron
Solenoid Magnet Coils
Injector Linac
AA
BB
A
B
C
D

Fig. 1.

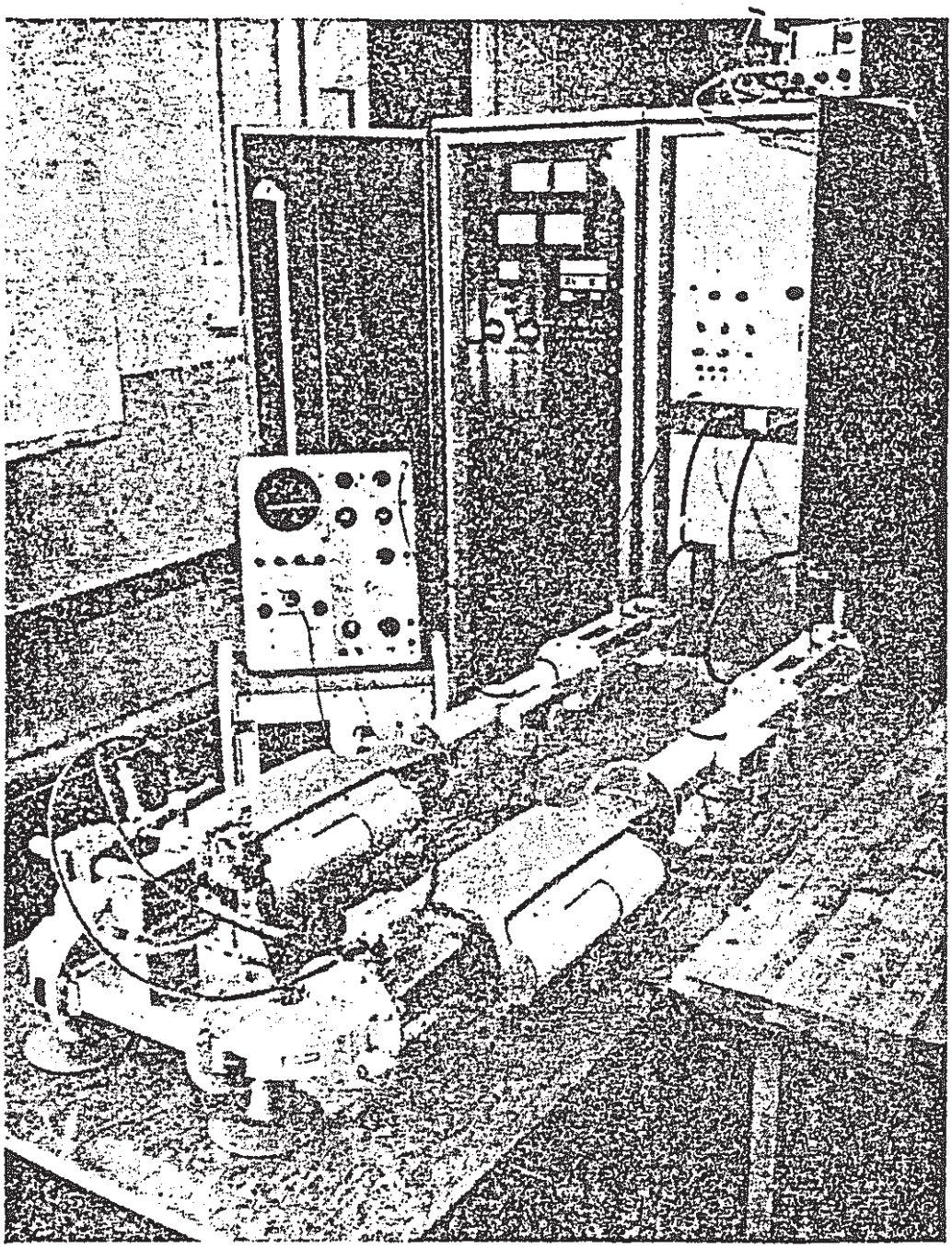

Fig. 2.

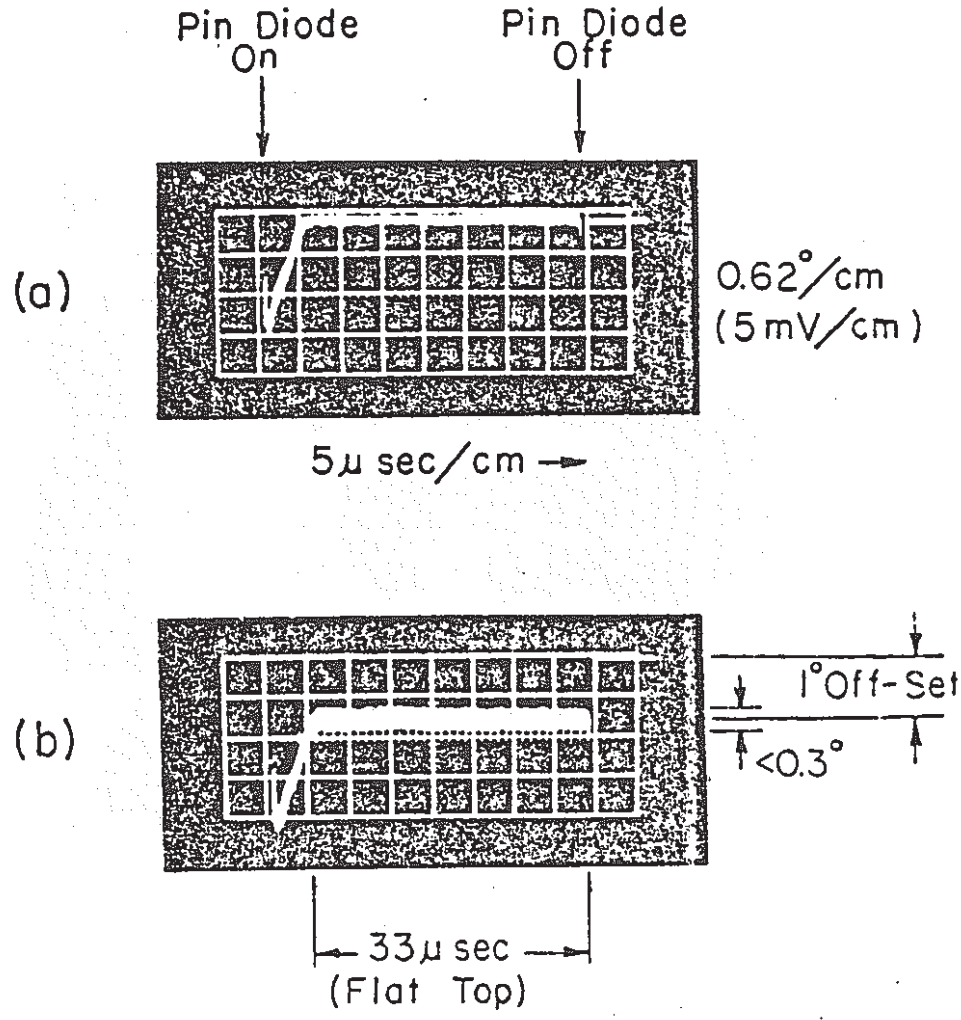
Pin Diode
On
Pin Diode
Off
(a)
0.62°/cm
(5 mV/cm)
5μ sec/cm →
(b)
1°Off-Set
<0.3°
33μ sec →
(Flat Top)

Fig. 3.

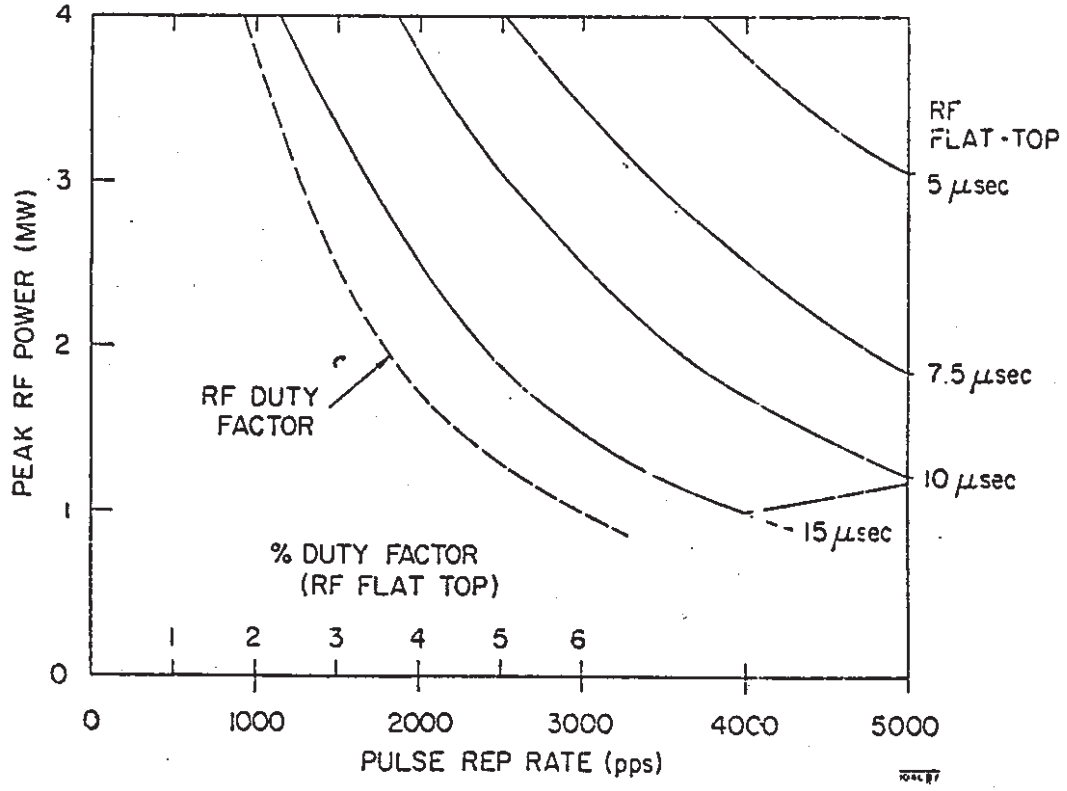
PEAK RF POWER (MW)
PULSE REP RATE (pps)
RF DUTY FACTOR
% DUTY FACTOR
(RF FLAT TOP)
RF
FLAT-TOP
5 μsec
7.5 μsec
10 μsec
15 μsec
0
1000
2000
3000
4000
5000
1
2
3
4
5
6

Fig. 4.

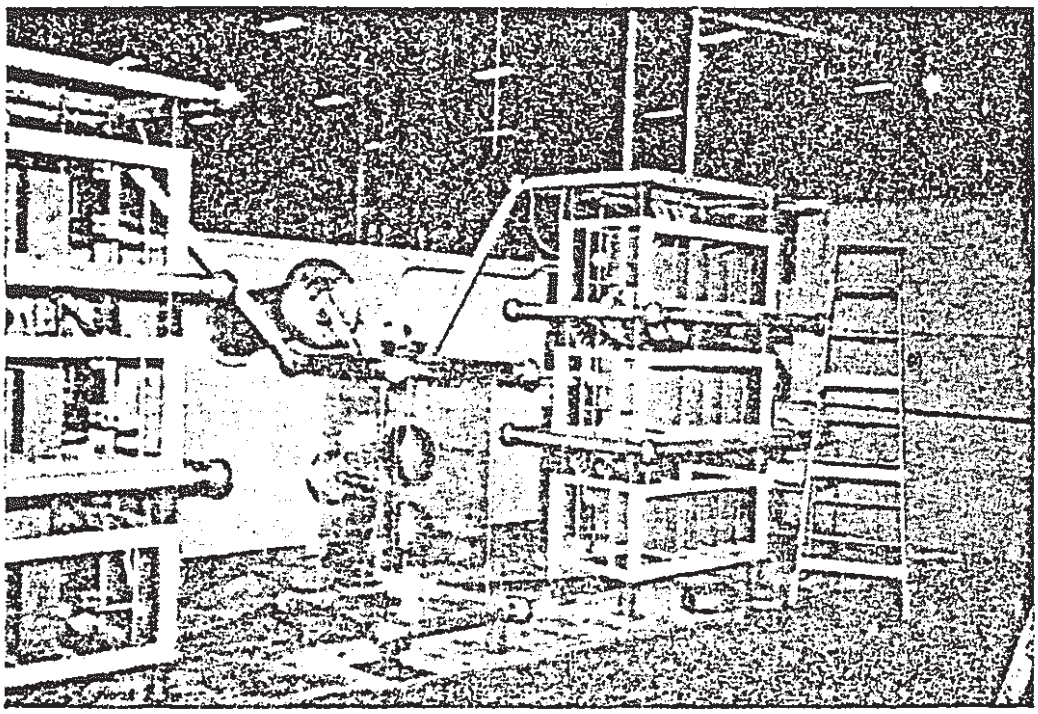

Fig. 5.

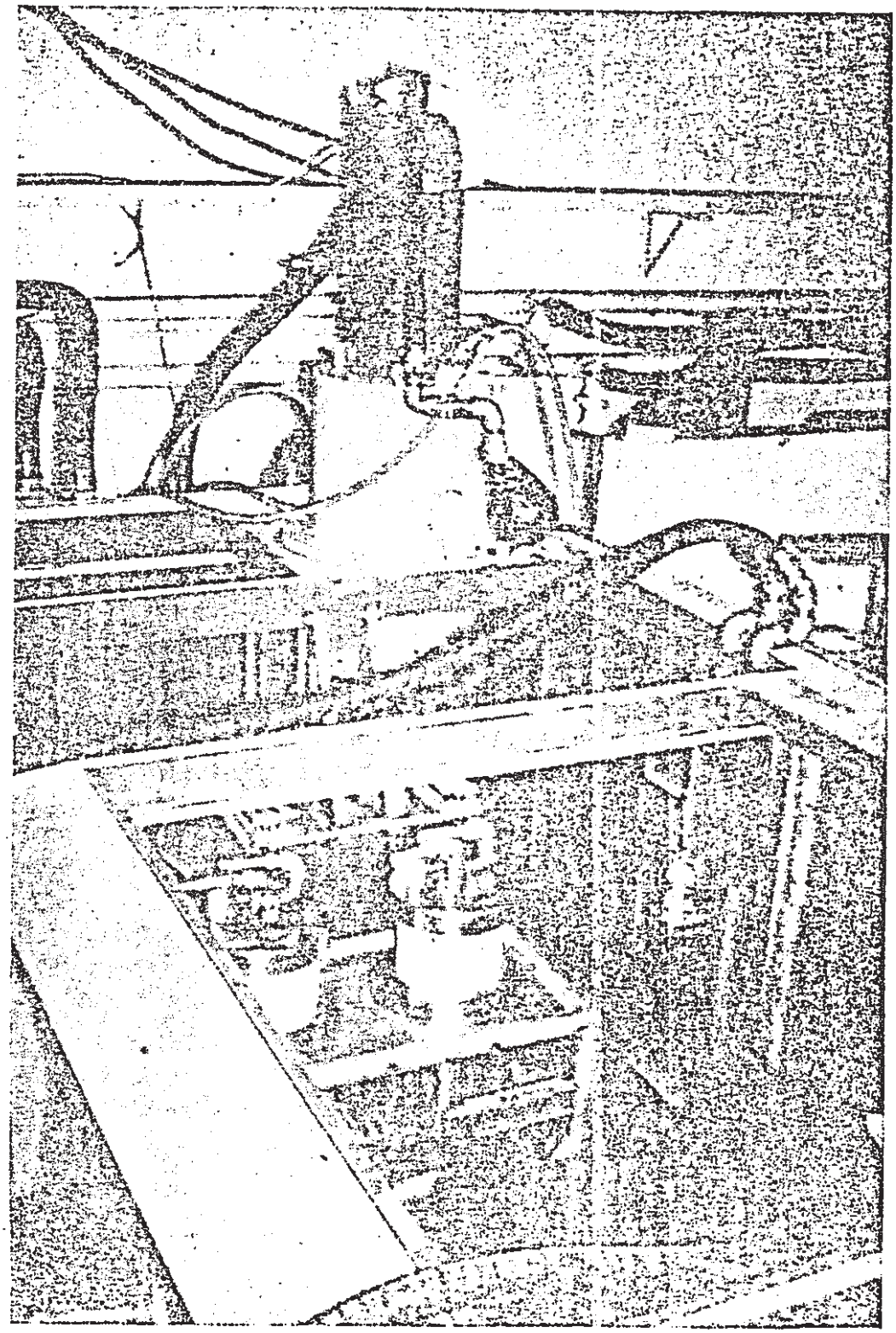

Fig. 6.

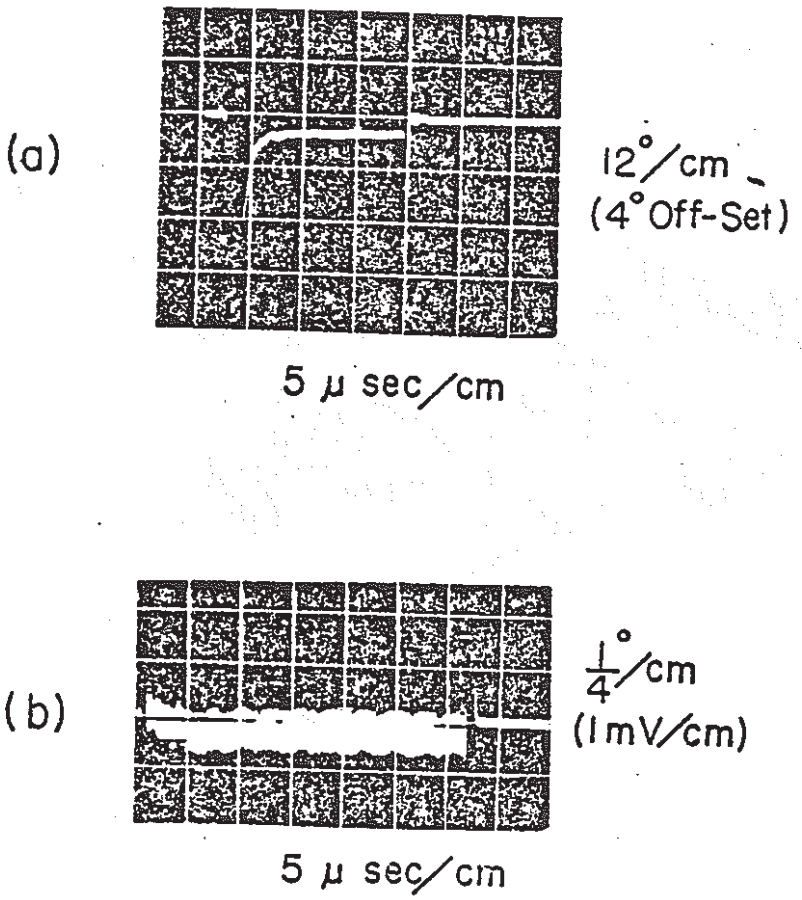
(a)
12°/cm
(4° Off-Set)
5 μ sec/cm
(b)
1/4°/cm
(1mV/cm)
5 μ sec/cm

Fig. 7.

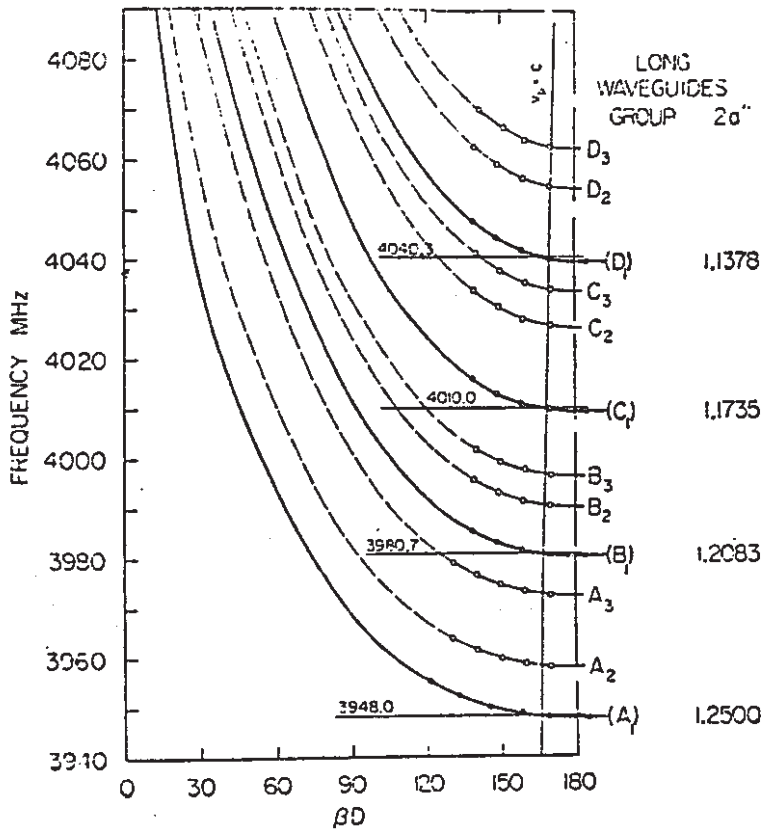
LONG
WAVEGUIDES
GROUP 2a"
D3
D2
(D1) 1.1378
C3
C2
(C1) 1.1735
B3
B2
(B1) 1.2083
A3
A2
(A1) 1.2500
4050.3
4010.0
3980.7
3948.0
FREQUENCY MHz
4080
4060
4040
4020
4000
3980
3960
3940
0
30
60
90
120
150
180
βD

Fig. 8.

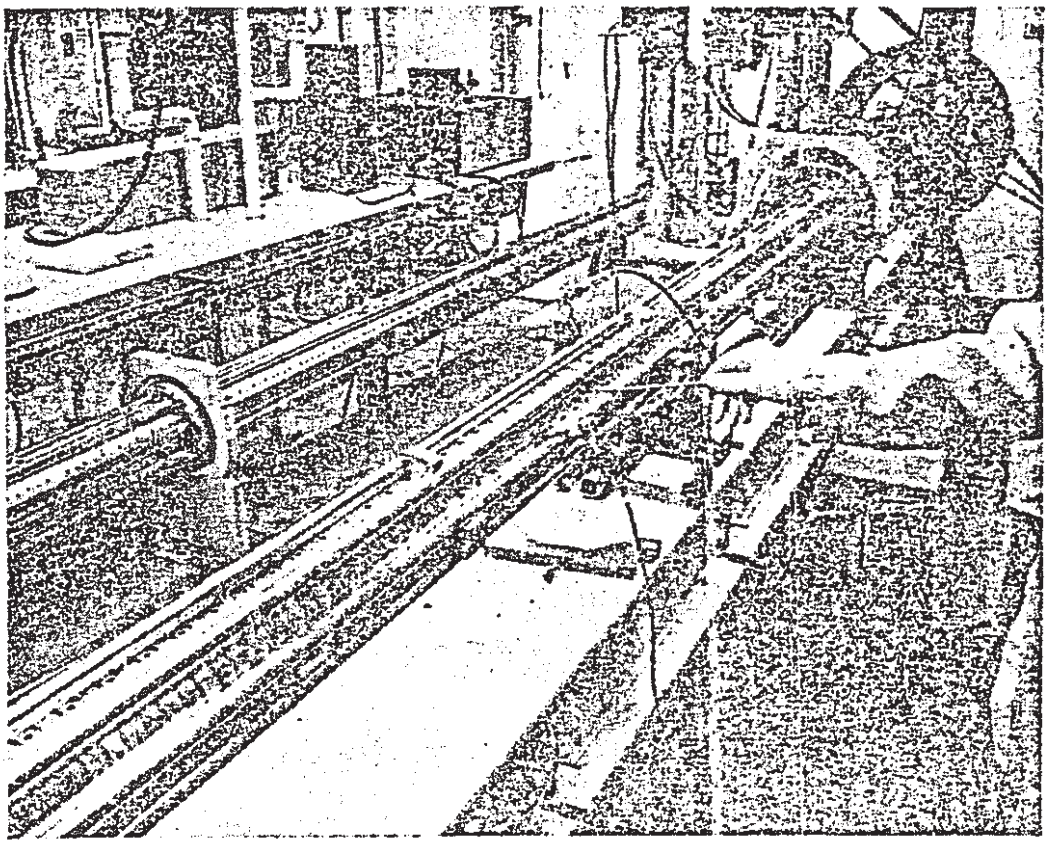

Fig. 9.

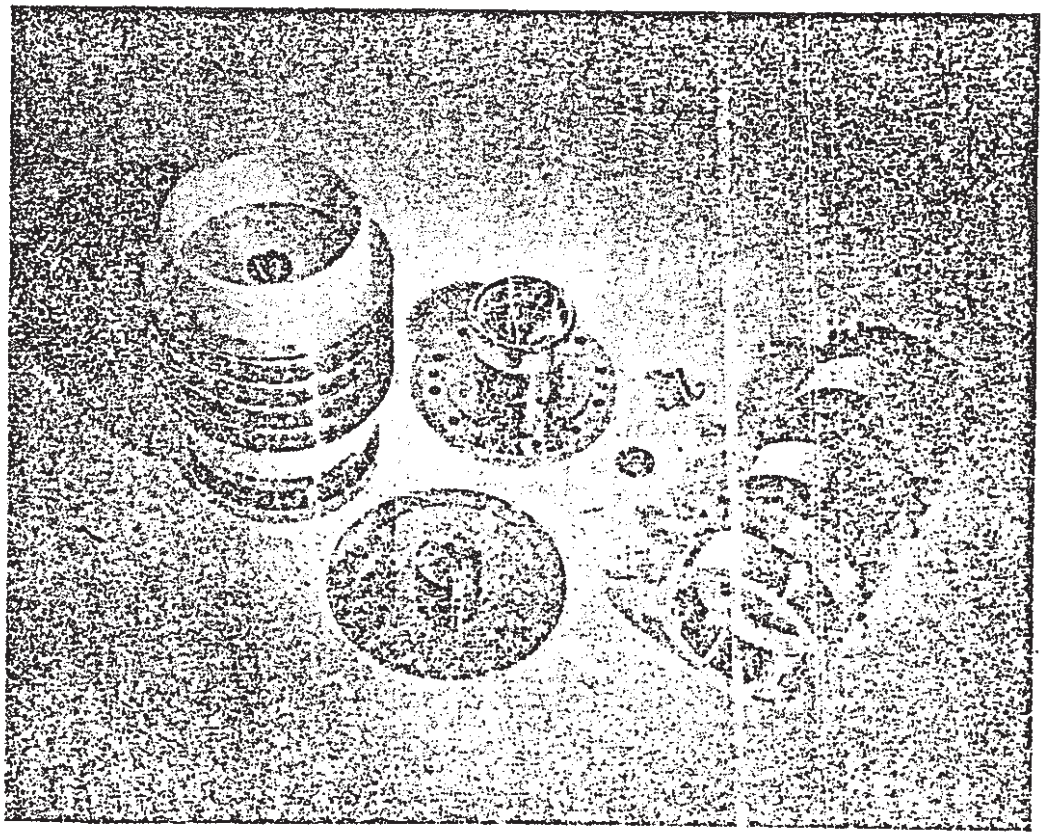

Fig. 10.

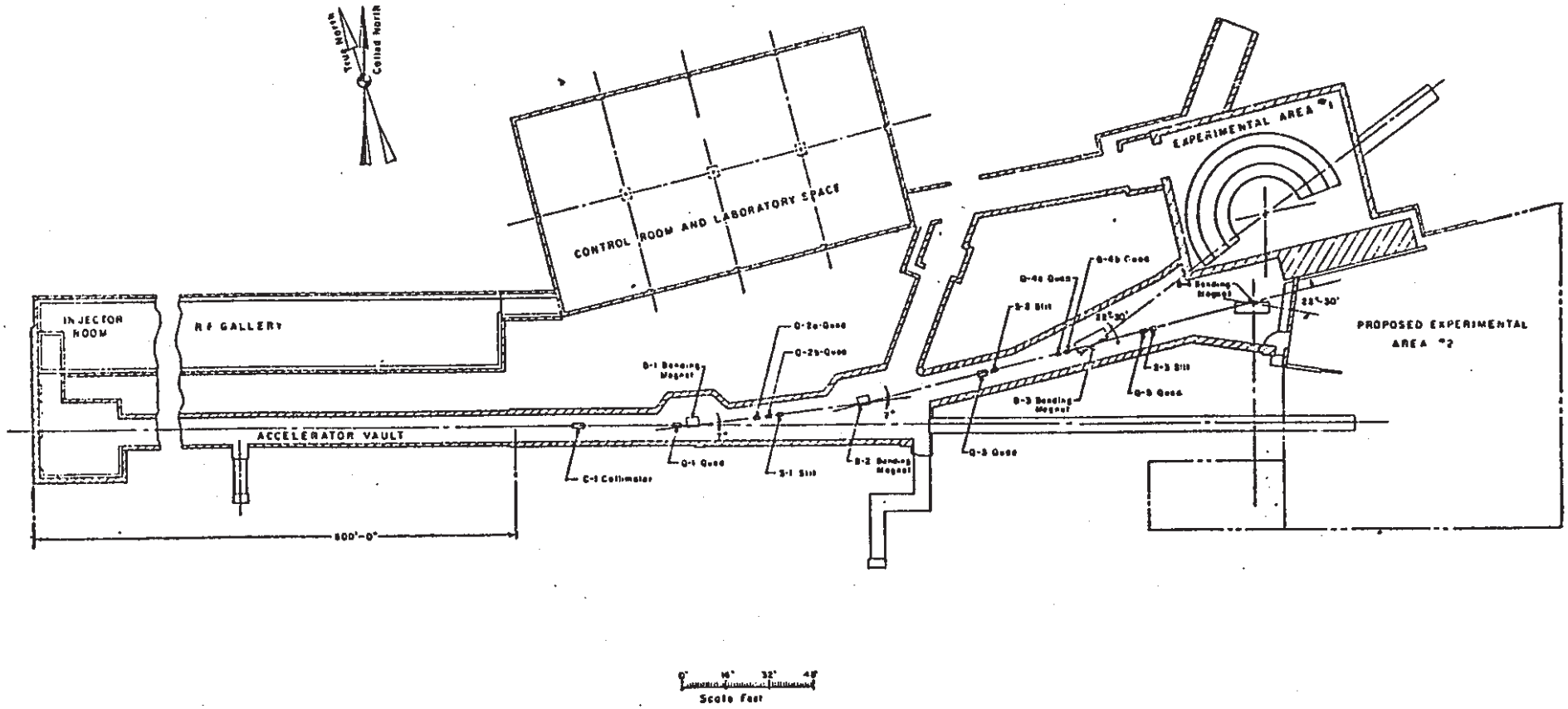
True North
Called North
CONTROL ROOM AND LABORATORY SPACE
EXPERIMENTAL AREA #1
INJECTOR ROOM
RF GALLERY
PROPOSED EXPERIMENTAL AREA #2
ACCELERATOR VAULT
800'-0"
Scale Feet

Fig. 11.

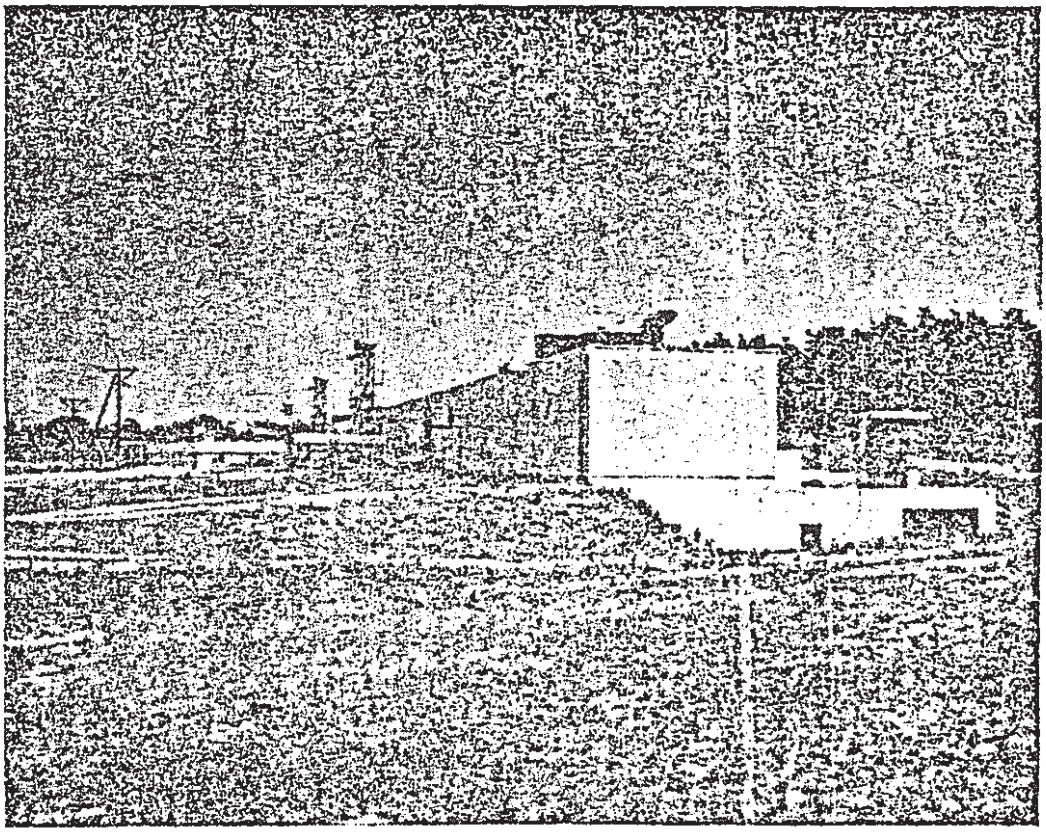

Fig. 12.

• 資料９－１

A Brieting on CEBAF

• 資料９－２

Project Overview

資料９－１

# A Briefing on CEBAF

## October 2, 1988

Continuous Electron Beam Accelerator Facility
Southeastern Universities Research Association
12000 Jefferson Avenue
Newport News, Virginia 23606

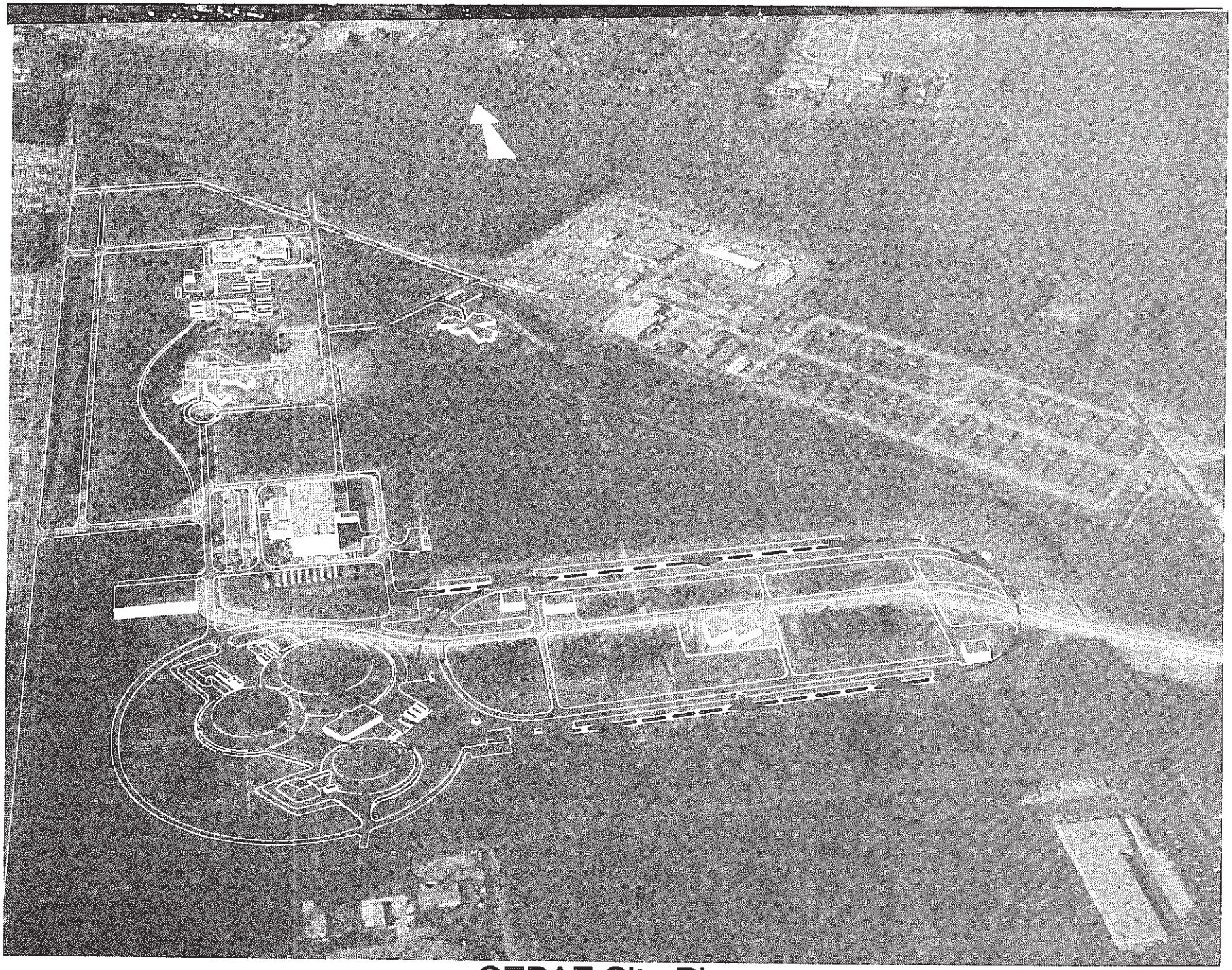

CEBAF Site Plan

# PROJECT HISTORY CEBAF

| | |
|---|---|
| 1976 | Friedlander Panel |
| 1977 | Livingston Panel |
| December 1979 | First NSAC Long Range Plan |
| Fall 1982 | Barnes Subcommittee recommends a 4 GeV electron accelerator |
| April 1983 | NSAC endorsement that SURA proposal be selected |
| December 1983 | Second NSAC Long Range Plan |
| September 1984 | Vogt Subcommittee Report |
| December 1984 | Reaffirmation of NSAC Long Range Plan |

Orien488:pas

# SURA CEBAF

**Southeastern Universities Research Association**

- Non profit consortium of 38 universities in southeast formed to manage large, cooperative state-of-the-art research facilities
  - CEBAF (DOE)
  - SURANet (NSF)

- SURA Leadership
  - President: William A. Wallenmeyer

  - Chairman of Council of Presidents: Chancellor Joe B. Wyatt (Vanderbilt University)

  - Chairman of Board of Trustees Provost George W. Wheeler (Univ. Tennessee)

- 48 Researchers at 12 SURA universities collaborating in CEBAF Experimental Program

Helms688:mbs

## ALABAMA

Auburn University
University of Alabama at Birmingham
The University of Alabama

## DELAWARE

University of Delaware

## DISTRICT OF COLUMBIA

American University
Catholic University
Georgetown University
George Washington University

## FLORIDA

Florida State University
Florida Institute of Technology
Florida International University
University of Florida

## GEORGIA

Georgia Institute of Technology
University of Georgia

## KENTUCKY

University of Kentucky

## LOUISIANA

Louisiana State University

## MARYLAND

University of Maryland College Park

## MISSISSIPPI

Mississippi State University

## NORTH CAROLINA

Duke University
North Carolina State University
University of North Carolina

## SOUTH CAROLINA

Clemson University
University of South Carolina

## TENNESSEE

University of Tennessee
Vanderbilt University

## VIRGINIA

College of William and Mary
Christopher Newport College
George Mason University
Hampton University
James Madison University
Norfolk State University
Old Dominion University
University of Richmond
University of Virginia
Virginia Commonwealth University
Virginia Polytechnic Institute & State University
Virginia State University

## WEST VIRGINIA

West Virginia University

# BEAM PERFORMANCE OBJECTIVES — CEBAF

- o High energy, current, and duty factor
  - Energy: 4 GeV
  - Current: 200 $\mu$A
  - Duty factor: CW
- o Excellent beam quality
  - Small emittance: $\epsilon < 2 \cdot 10^{-9}$ m $\quad (\sigma_x^2 = \frac{\epsilon\beta}{4})$
  - Low energy spread: $\sigma_E/E \sim 2.5 \cdot 10^{-5}$
- o High user multiplicity
  - Three simultaneous beams

LINAC88:yhs
10/88

# DESIGN APPROACH CEBAF

- o CW linac to generate a high-quality beam
- o RF superconductivity to overcome the power barrier
- o Beam recirculation to minimize cost
- o Extraction by rf separation for low-halo beam

# RECIRCULATED LINAC CONCEPT — CEBAF

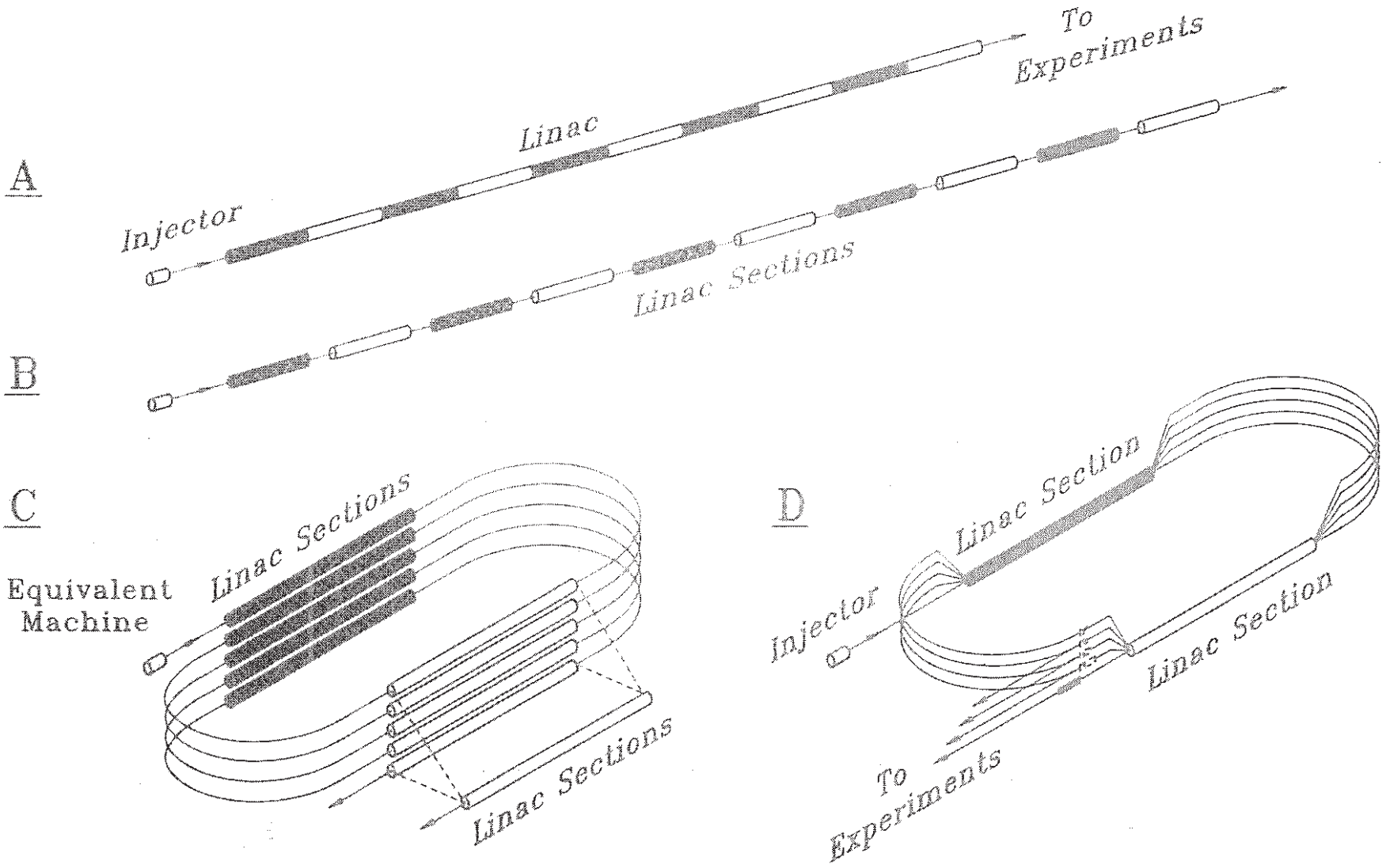

# MACHINE CONFIGURATION

CEBAF

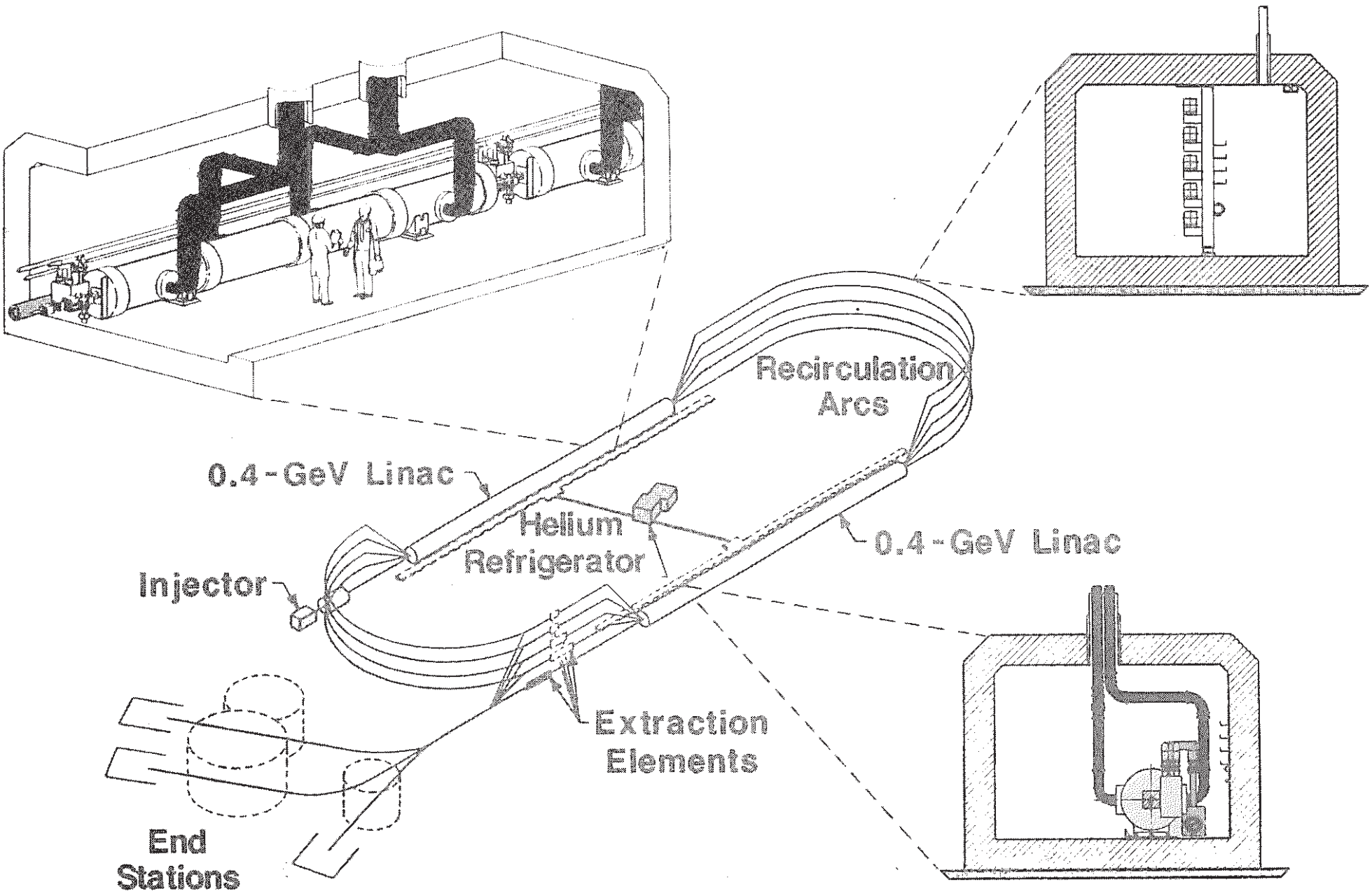

# ACCELERATOR & INJECTOR DESIGN PARAMETERS

CEBAF

| | |
|---|---|
| **o Accelerator** | |
| - Concept | Superconducting cw recirculating linac |
| - Number of linac segments | 2 |
| - Number of passes | 5 |
| - Maximum energy gain per pass | 0.8 GeV |
| - Focusing | FODO |
| - Phase advance per cell (pass 1) | $120^{o}$ |
| - Magnetic radii of recirculation arc beamlines | 5.1 to 30.6 m |
| **o Injector** | |
| - Injection energy | 45 MeV |
| - Transverse emittance (at 0.1 MeV) | 1 mm·mr |
| - Bunch length at 45 MeV | $<1.0^{o}$ |

LINAC88:yhs
10/88

# CAVITIES, RF, & CRYOGENICS
# DESIGN PARAMETERS

CEBAF

| | |
|---|---|
| **o Superconducting cavities** | |
| - Frequency | 1497 MHz |
| - Design gradient | 5.0 MV/m |
| - Design $Q_o$ at 2 K, 5 MV/m | $2.4 \times 10^9$ |
| - Shunt impedance $(r/Q)$ | 960.0 Ω/m |
| - Typical HOM $Q_{external}$ | $10^3$ to $10^5$ |
| **o RF** | |
| - Klystrons/cavity | 1/1 |
| - Klystron power rating | 5.0 kW |
| - Phase control | $<1^o$ |
| - Gradient regulation | $<10^{-4}$ |
| **o Cryogenic system** | |
| - System capacity (2.0 K) | 4800 W |
| - Heat shield helium (50 K) | 12,000 W |

LINAC88:yhs

10/88

# FIVE-PASS RECIRCULATION CEBAF

- Number of recirculations is a tradeoff between cost and operational complexity

  - Five-pass recirculation minimizes cost while keeping complexity and error sensitivity within state of the art

- Status of five-pass design:

  - Component layout and first-order redesign of optics completed
  - Beam breakup threshold ~ 100 times design current
  - Detailed error analysis in progress

LINAC88:yhs
10/88

# BEAM STABILITY SIMULATION CEBAF

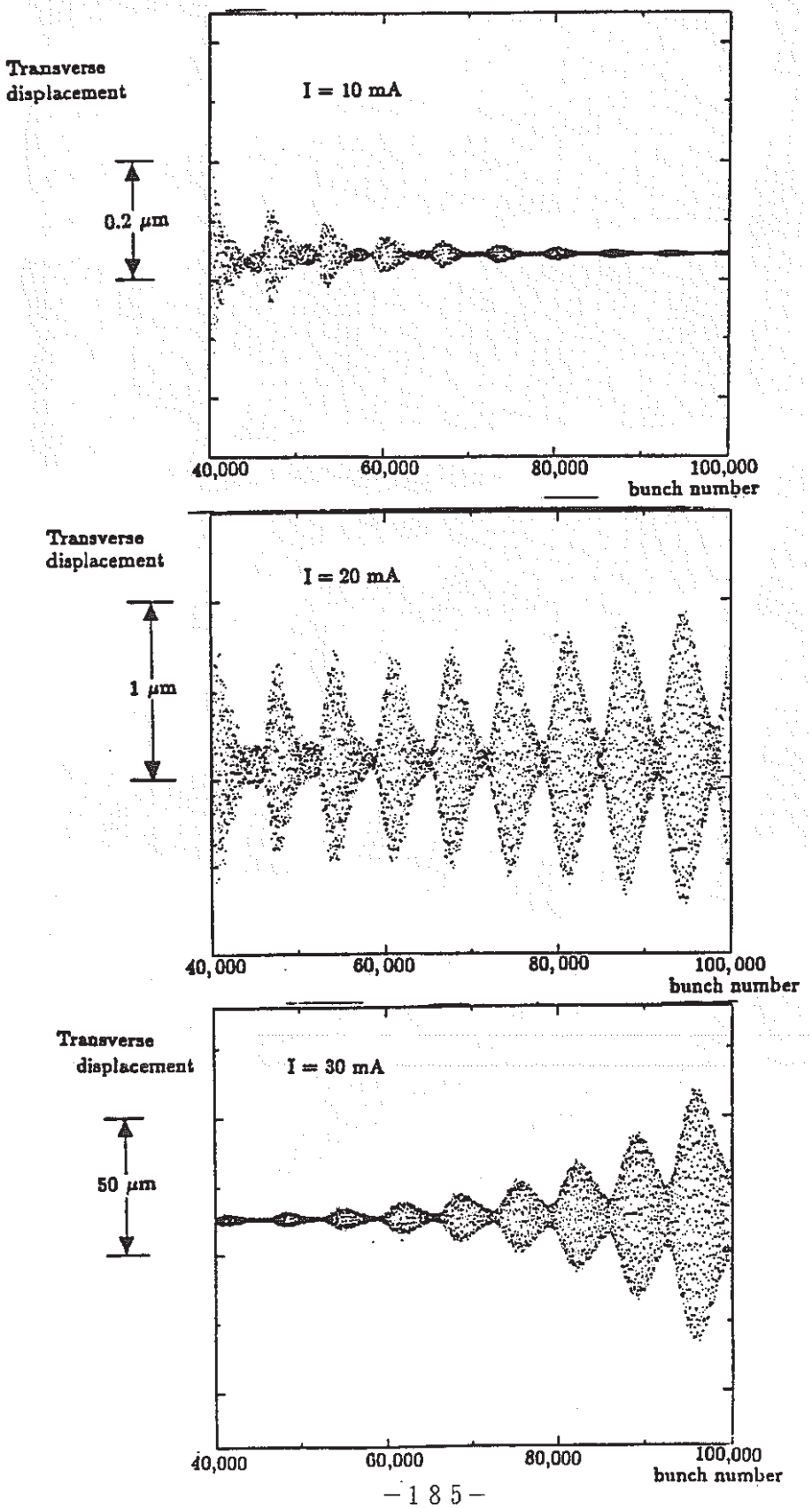

# CEBAF

**The Continuous Electron Beam Accelerator Facility**

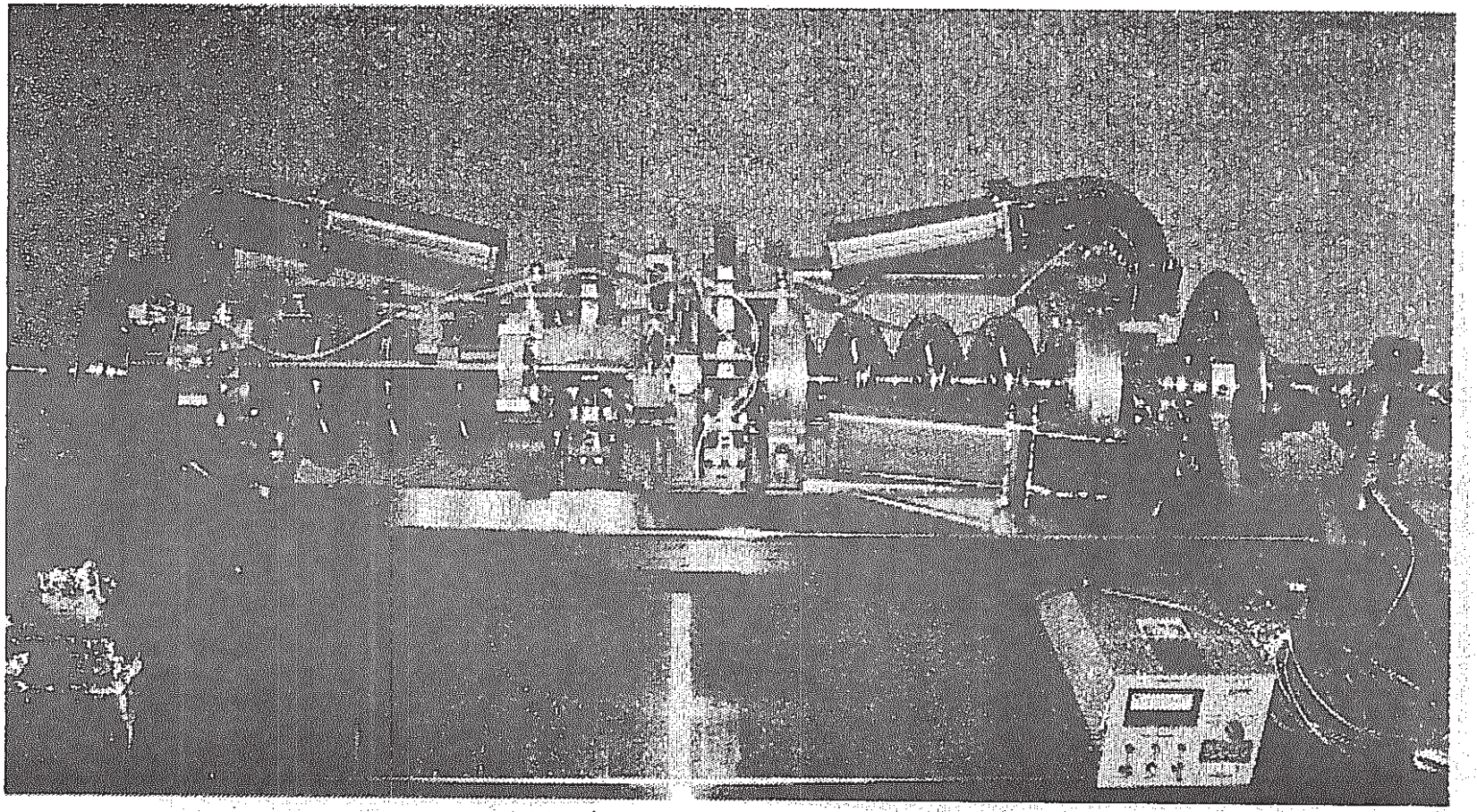

**SUPERCONDUCTING CAVITY PAIR**

CAVITY PAIR BEING INSERTED INTO HELIUM VESSEL

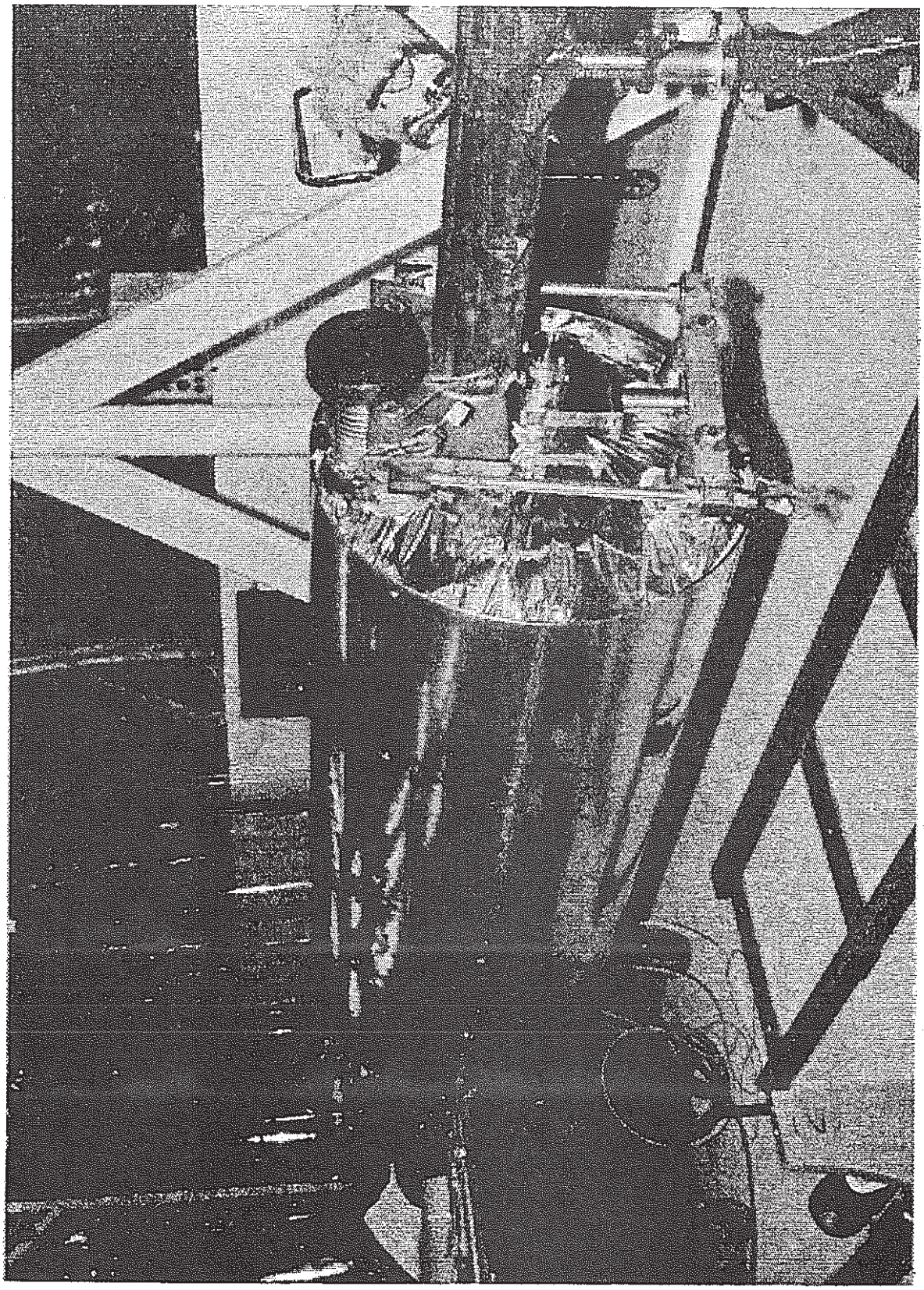

16

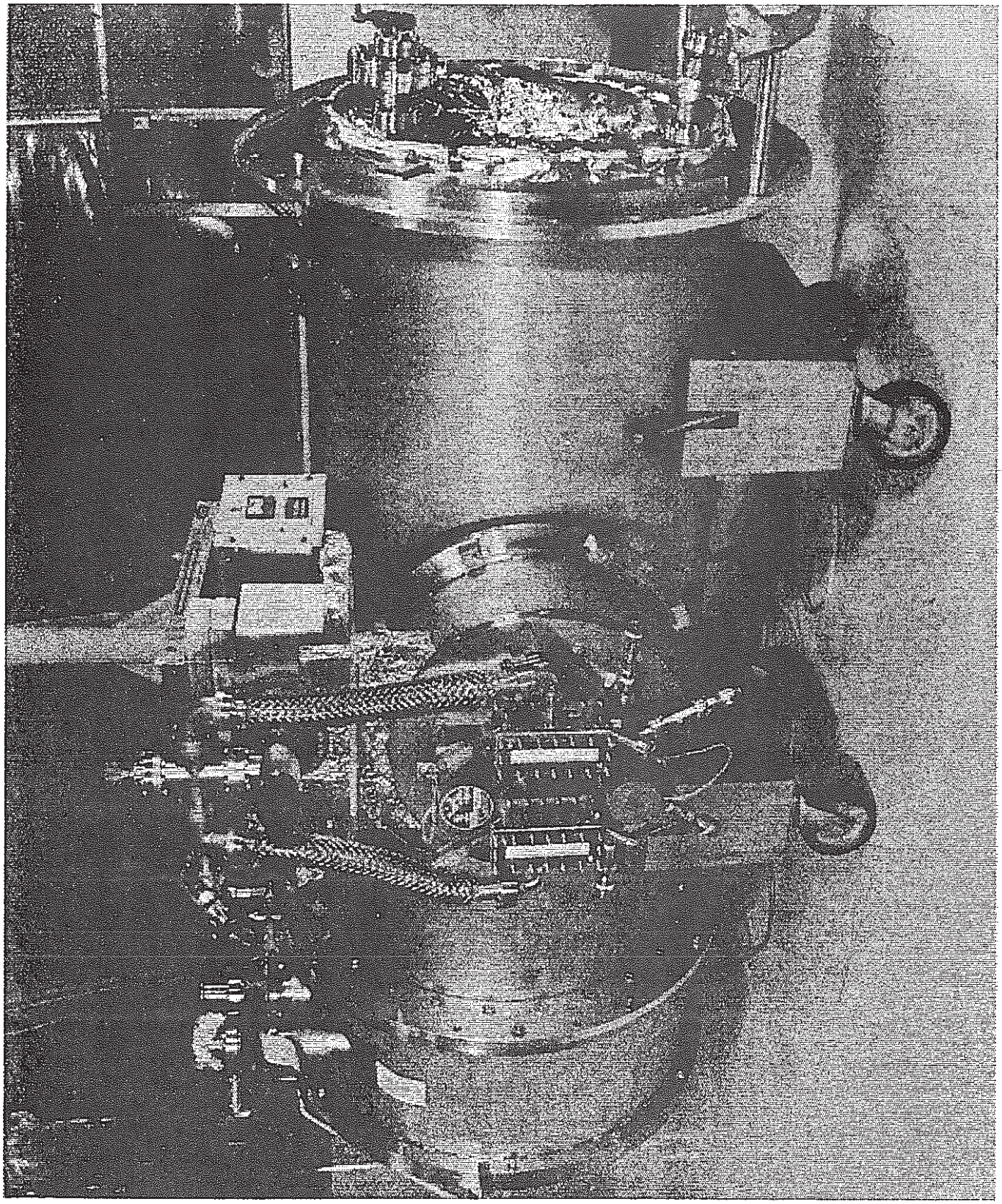

# I&C SYSTEM CEBAF

- Implement setpoints and/or read, analyze, display systems values for
  - Injector
  - RF system including cavity parameters
  - Beam transport and diagnostics
  - Cryogenics and vacuum
  - Safety systems

- Provide efficient human interface for system with ~ 20,000 I/O data points

- System features:
  - Off-the-shelf hardware and operating system (CAMAC, UNIX/C)
  - Hardware intensive
  - Two-level hierarchy (supervisory and local) with distributed control functions ("local intelligence")
  - Industry standards wherever feasible

# CONTROL SYSTEM ARCHITECTURE CEBAF

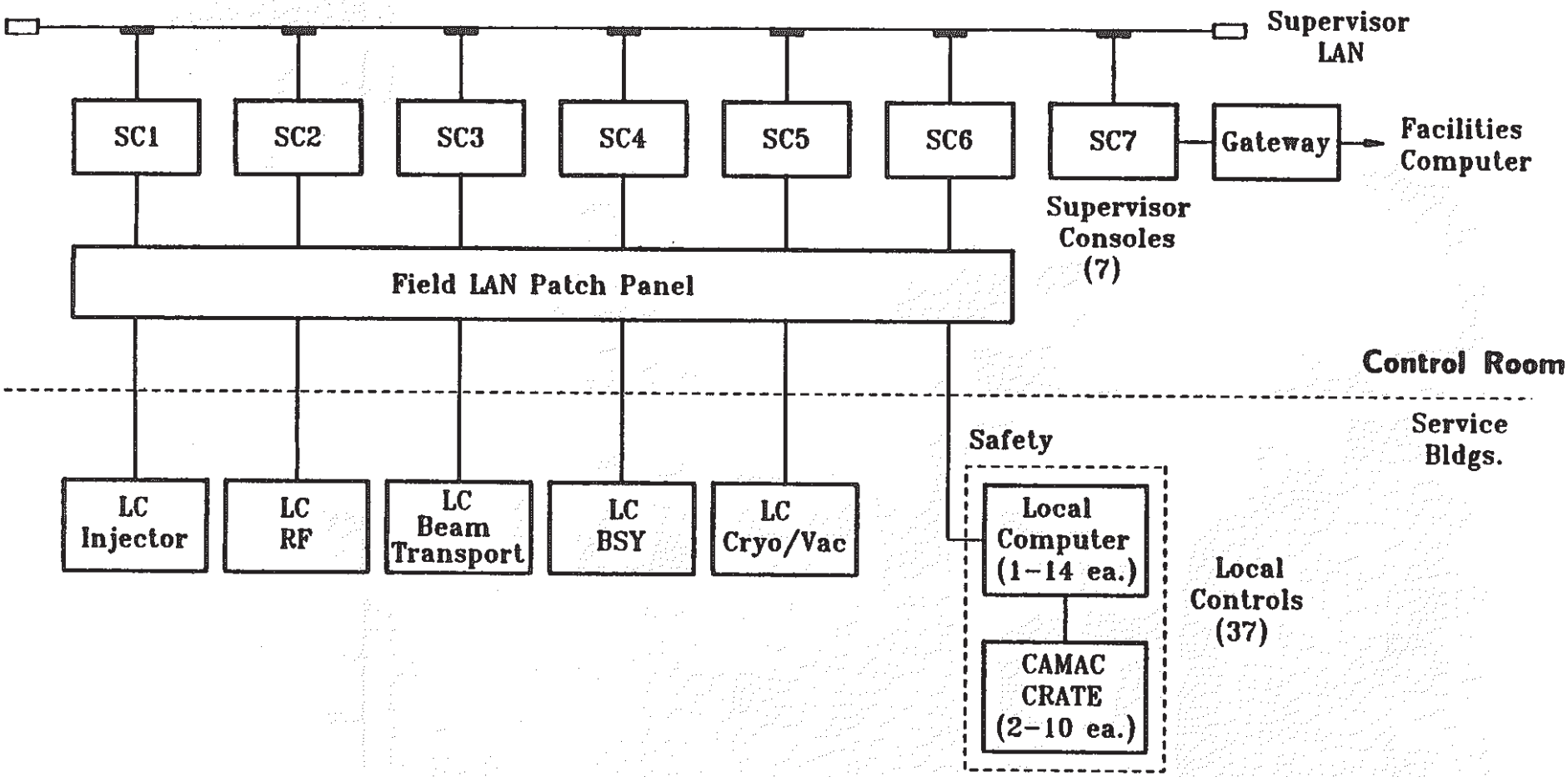


[soltys.sa88]wbs5.tex

14 July 1988

CEBAF CONTROL CONSOLE

# HIGHLIGHTS CEBAF

- o Accelerator tunnel under construction

- o Cryounit assembly and testing program ongoing

  - Tests on three initial cavity pairs exceeded specifications
  - Cryounit A tested and analysis completed
  - Subcryomodule A/B assembled, tested, and analysis completed
  - Cryostat design improvements finalized and in final prototyping
  - Job shop approach being explored for cavity fabrication

- o Machine control systems operational for cryounit testing, Cryogenic Test Facility, and Injector Test Facility

  - CEBAF machine control systems adopted for tandem facilities at LLNL and Yale

ACCELERATOR ENCLOSURE UNDER CONSTRUCTION

# PROTOTYPE CAVITIES PAIR TEST PERFORMANCE

CEBAF

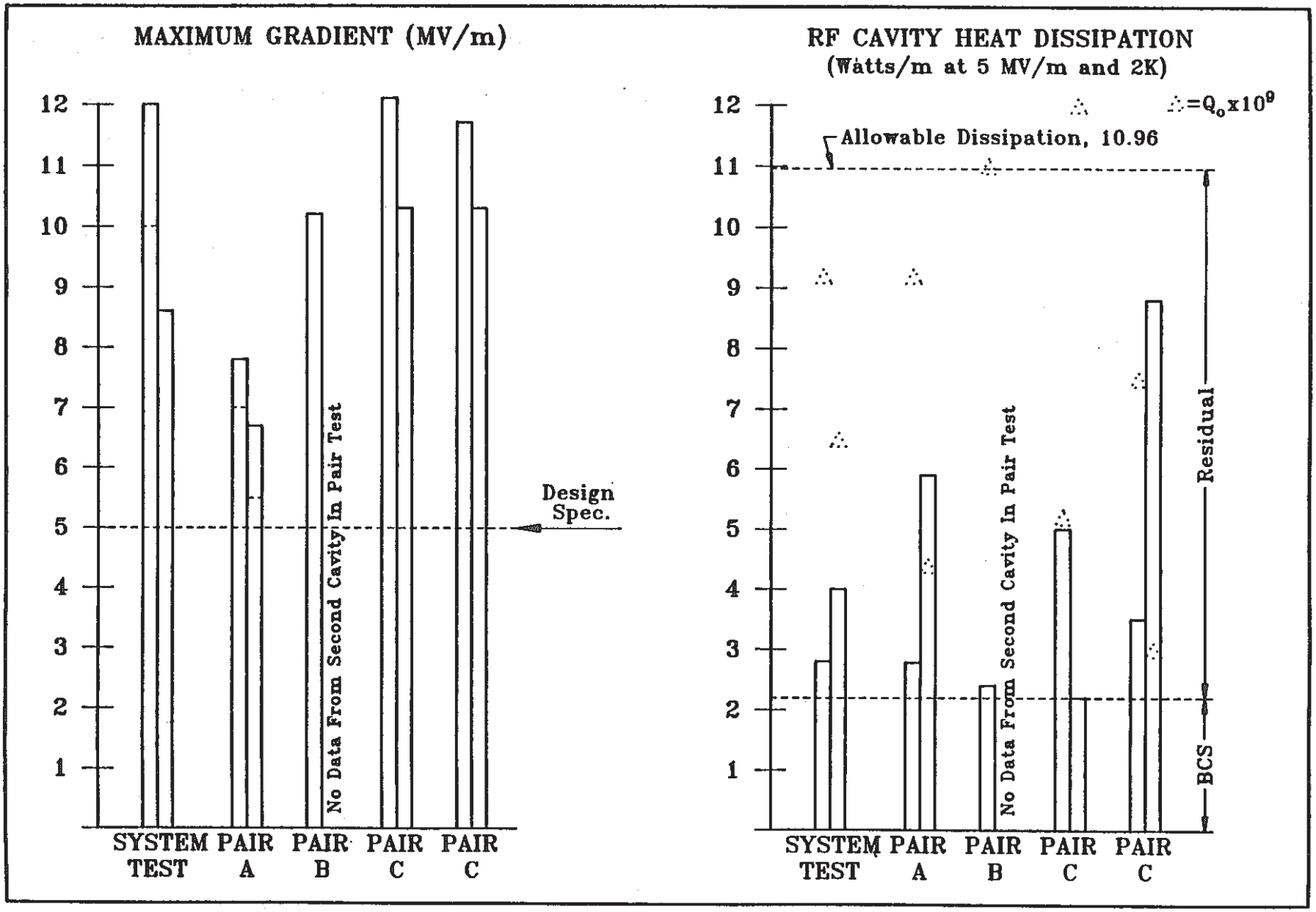


9/28/88

# HIGHLIGHTS CEBAF

- o Beam diagnostics
  - Profile and position monitors prototyped and bench tested
  - Installed on injector for beam tests
- o Injector assembled on final girder; 100-keV chopped and bunched beam has been produced
- o Test Lab
  - Two 25-ton cranes installed
  - Cryomodule test cave completed
  - CNC milling machine operational
  - R&D chemical room nearing completion
  - Production clean room and chemical room under construction
  - Vertical test area under construction
  - Electron beam welder arrives 10/88

CEBAF INJECTOR DEVELOPMENT

# HIGHLIGHTS — CEBAF

- o Central Helium Liquefier being fabricated by industry
- o Cryogenic Test Facility operational for liquid helium production
  - Generation capability on site
  - Transfer lines being assembled
- o Pre-production magnets (dipole)
  - Steel core and coil on site, assembly in progress
  - Initial measurement gear in place
  - Tests scheduled for Fall 1988
- o Order placed for eight pre-production klystrons from three vendors

LINAB88:yhs
10/88

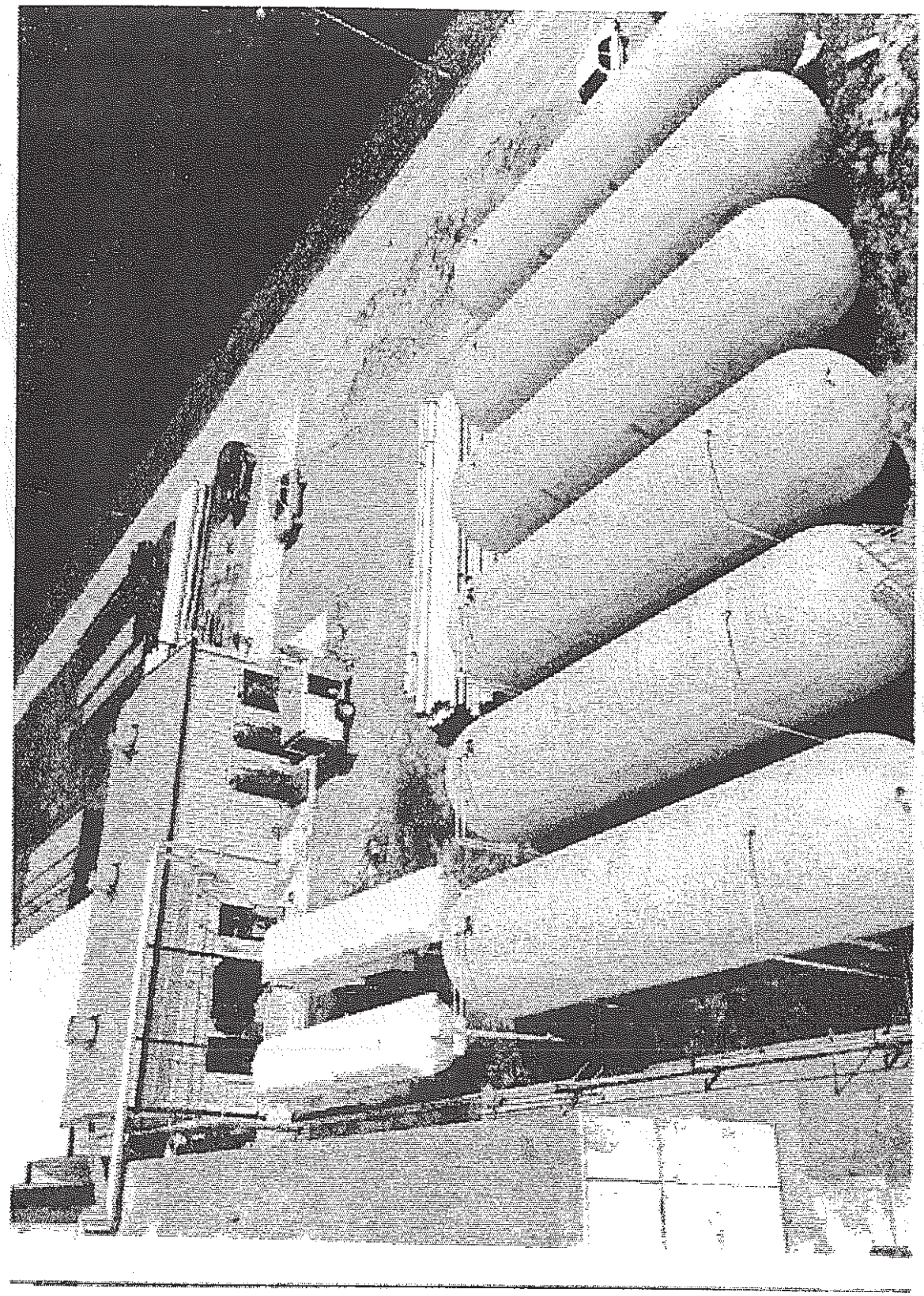

SCREW COMPRESSOR IN CRYO TEST FACILITY

# HIGHLIGHTS



- o RF separator prototype designed and low-power tested
- o Preliminary accelerator commissioning plan prepared
- o Experimental program
  - Extensive user collaborations and meetings held
  - Experimental Equipment Preliminary Conceptual Design to be presented to 3rd PAC - 2/89
- o CEBAF Center under construction
- o 248 staff on board (+ 4 commitments)

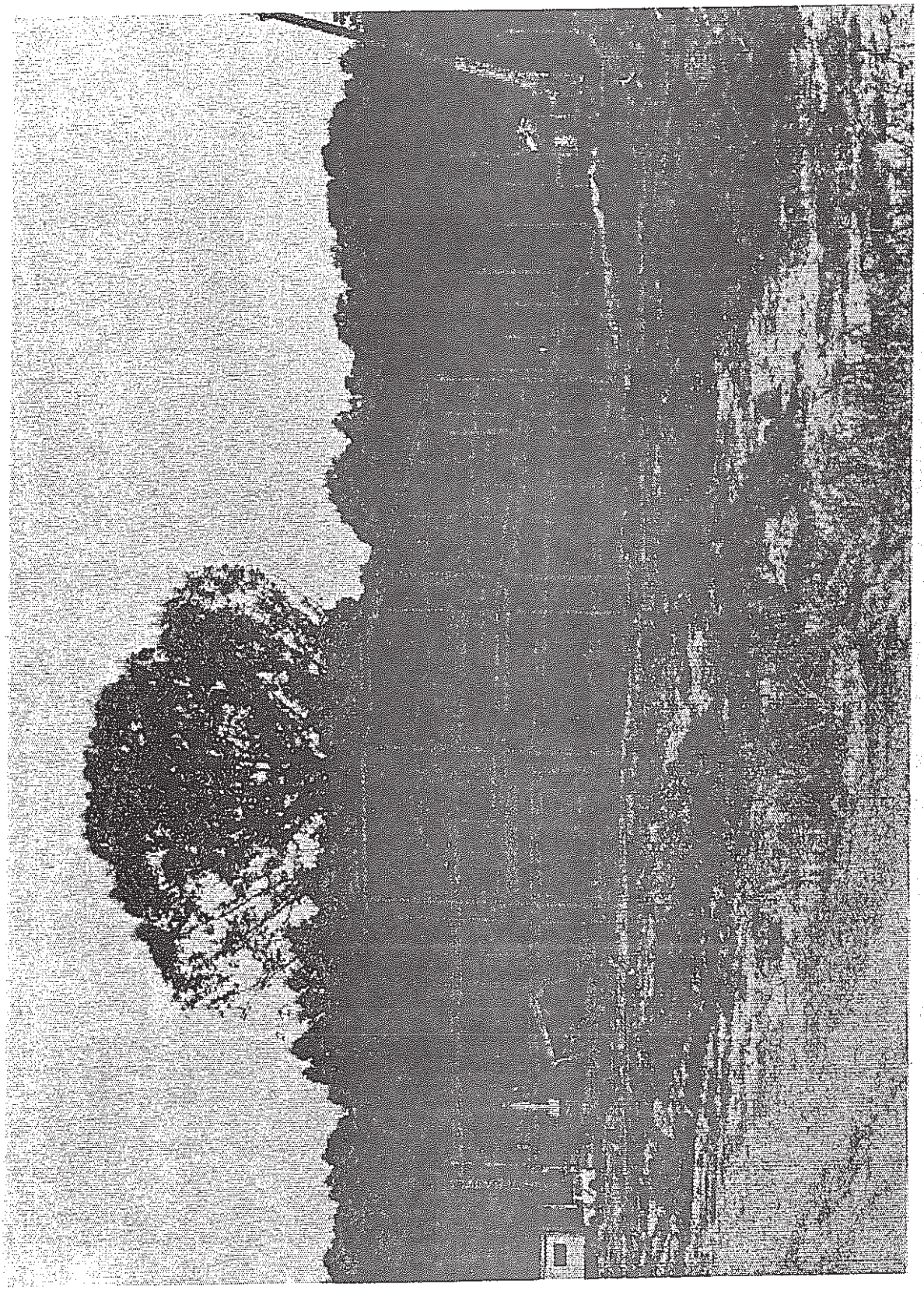

# OPERATIONAL CHALLENGES

CEBAF

- Complex machine in terms of size and component count
  - 2,284 magnets on 1,993 independent circuits
  - 338 cavities and rf drive units
  - 722 BPMs producing 1,444 position readings

- Need for clean, loss-free operation
  - To protect machine from effects of 1 MW, submillimeter size beam
  - To preserve beam quality
  - To maintain cryosystem reserve capacity

LINAC88:yhs
10/88

# PREOPERATIONS & COMMISSIONING CEBAF

- Theory and simulations
- Develop procedures, automated routines, and the supporting applications software
- Of central importance: front end test (FET)
  - Beam test with at least 1 1/4 cryomodules in tunnel
- Extend FET results to full linac length
- Arc tests followed by progression through 2, 3, 4, and then 5-pass operation

# EXPERIMENTAL HALL DESIGN CONCEPTS

CEBAF

- o Three experimental halls, three independent beams

  - Hall A (185 ft diameter)
    Pair of high resolution spectrometers

  - Hall B (100 ft diameter)
    Large Acceptance Spectrometer

  - Hall C (150 ft diameter)
    User-mounted experiments

- o CDR for end station civil construction: May 1988

- o CDR for experimental equipment: March 1989

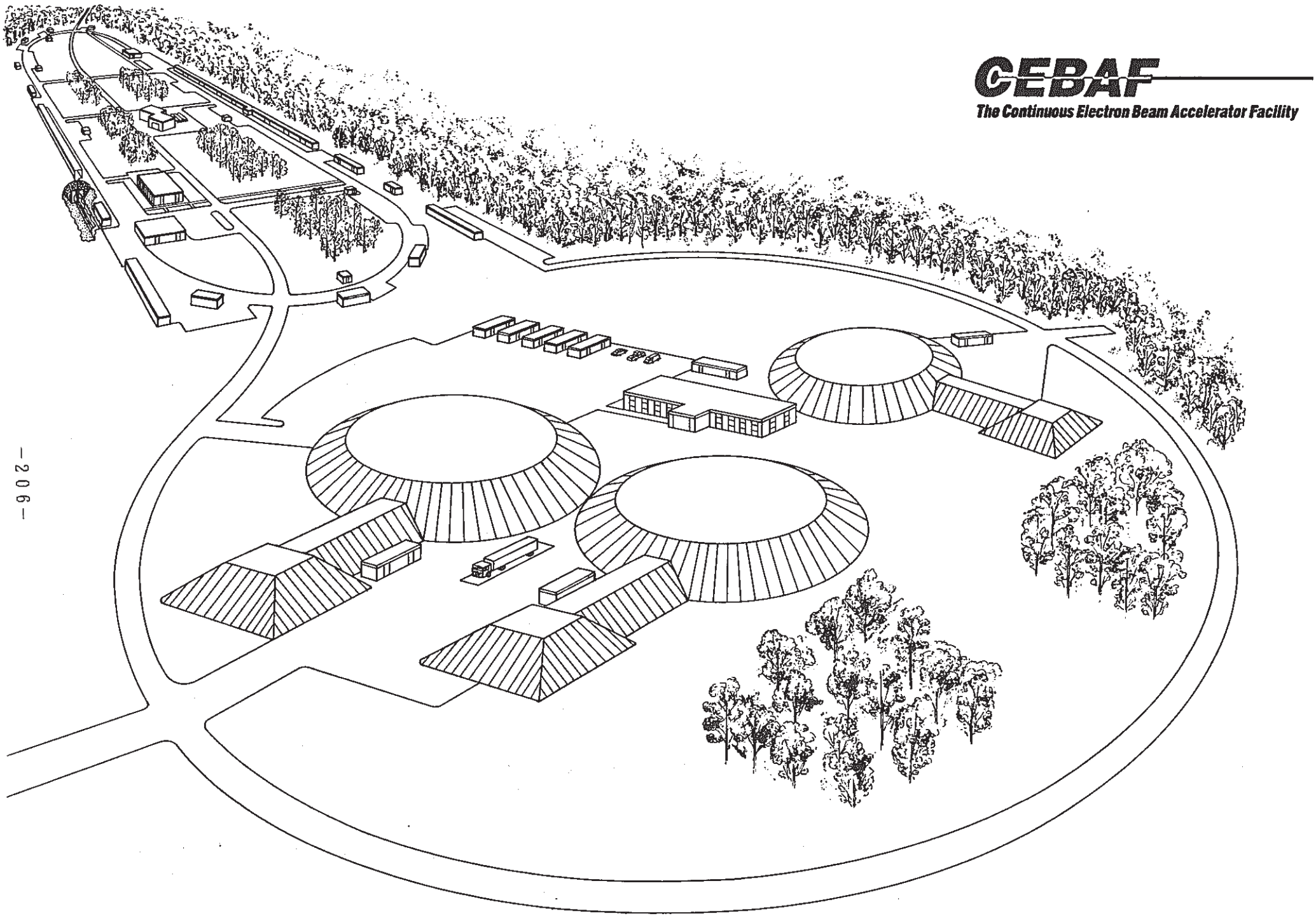
CEBAF
The Continuous Electron Beam Accelerator Facility

# WBS 8.5 End Station
## Grade Level Plan

CEBAF

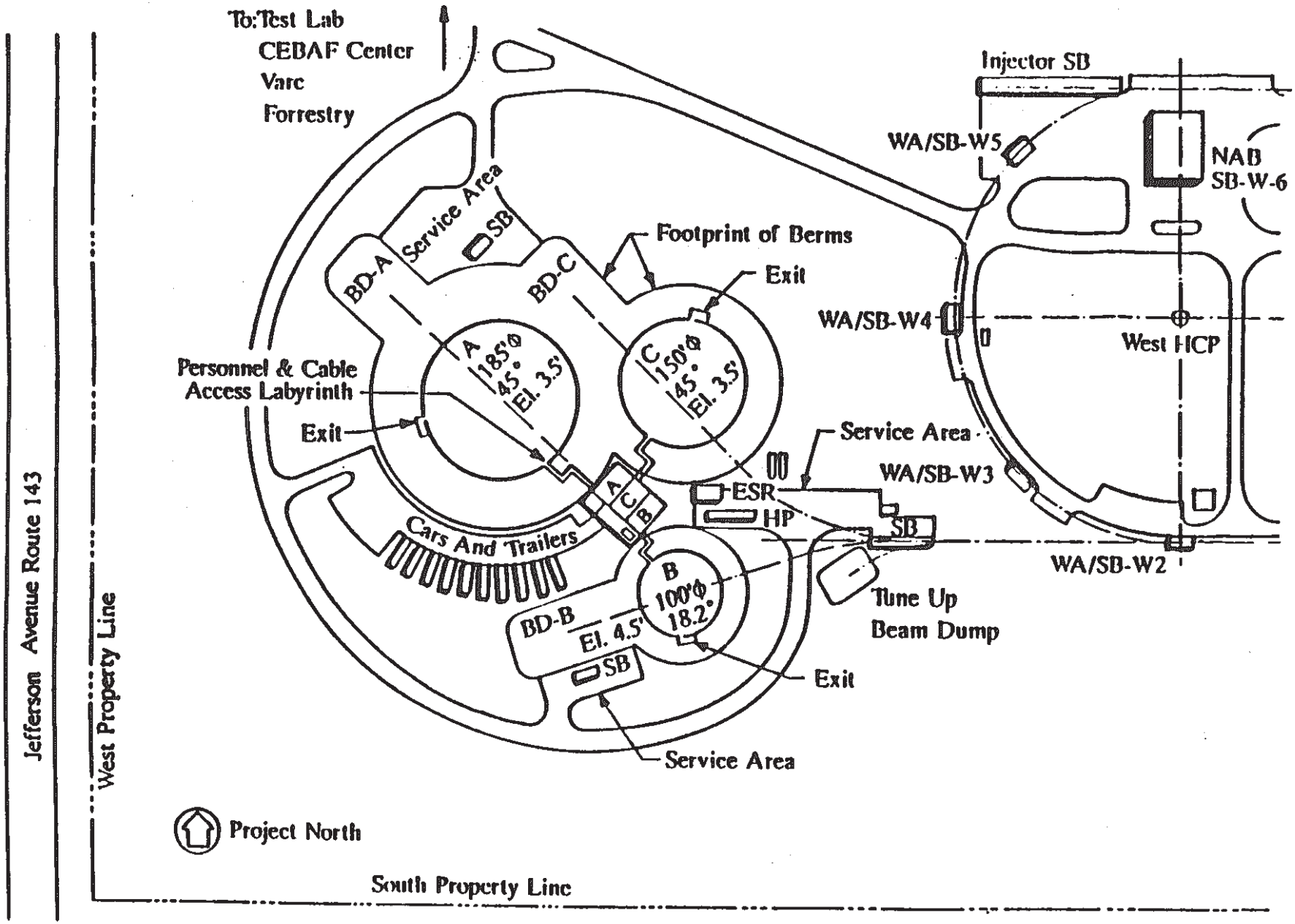

# END STATION A CEBAF

## High Resolution Spectrometers

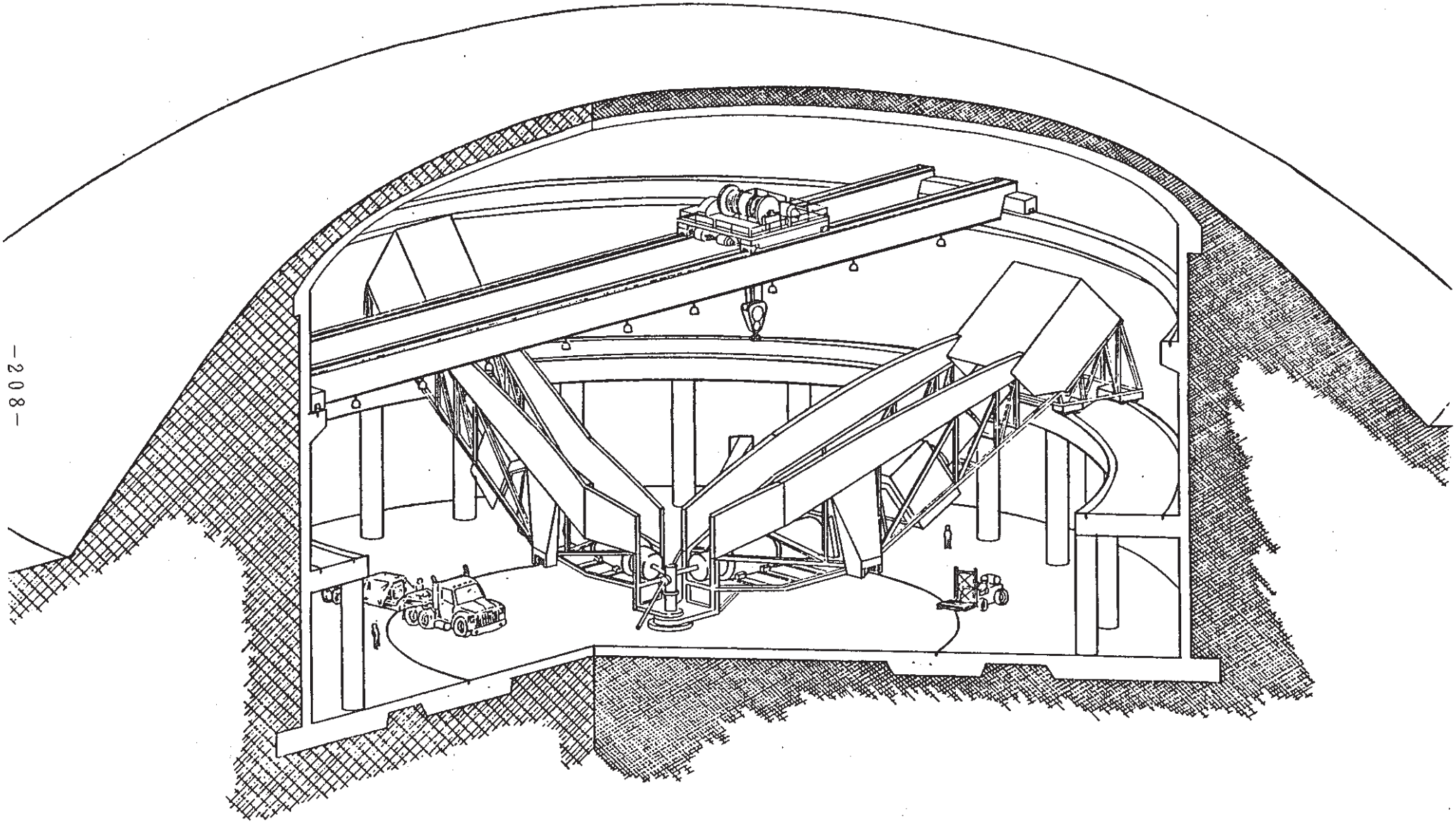

# Highlights of Physics Program — CEBAF

## High Resolution Spectrometers (Hall A)

- o Measurement of elastic and inelastic form factors

- o (e,e'N) reactions:
  - single nucleon density distributions
  - momentum distributions at high momenta

  electromagnetic structure of bound nucleons

- o (e,e'd), (e,e'$^3$He), (e,e'2N): reactions to specified final states: multinucleon correlations

- o (e,e'$\pi$) reactions: nucleon and nuclear pion fields

- o (e,e'K) reactions: hypernuclear physics (preliminary investigations)

# END STATION B

# CEBAF

## Large Acceptance Spectrometers

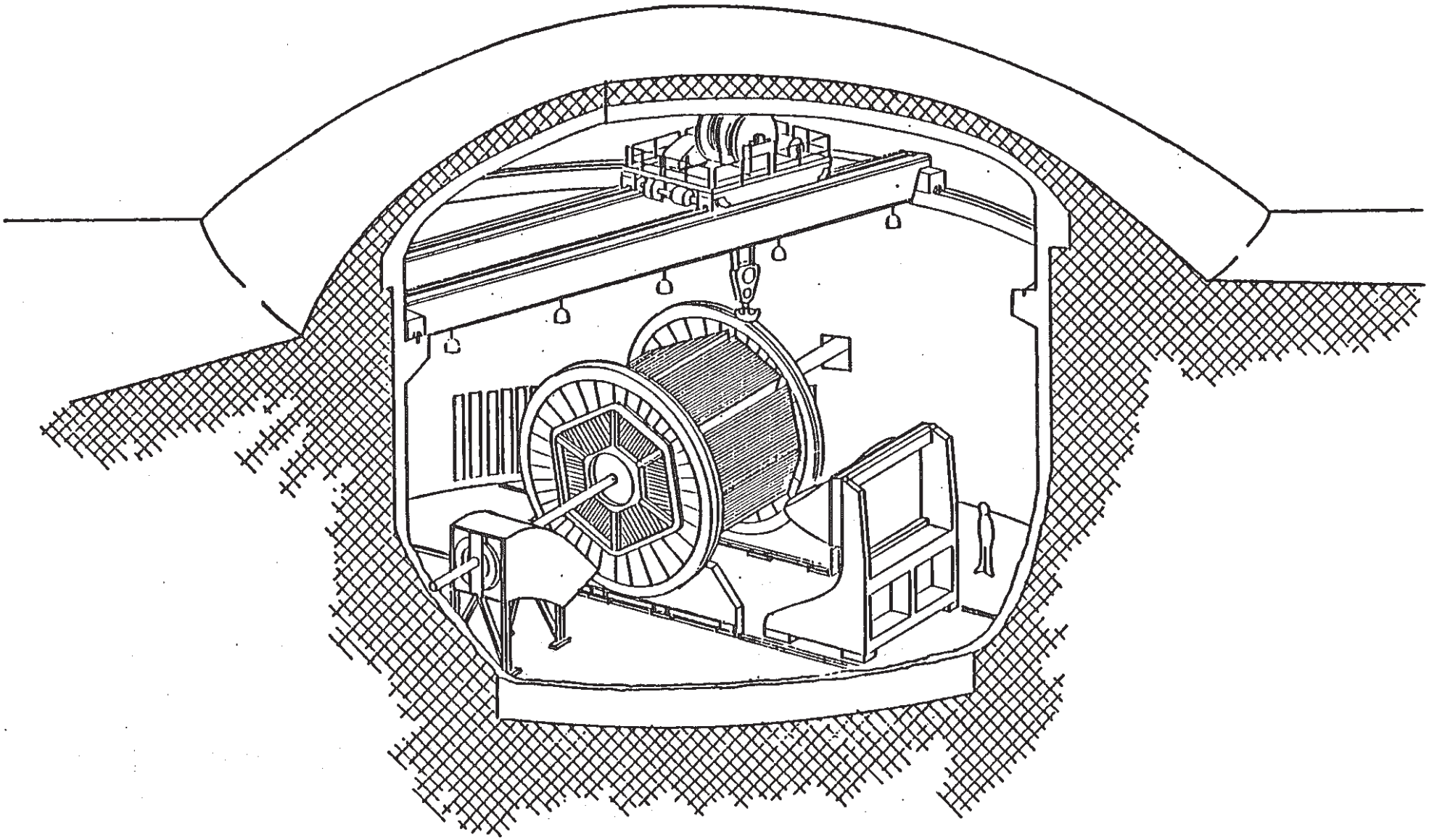

# Highlights of Physics Program CEBAF

## Large Acceptance Spectrometer (Hall B)

- Bias-free investigation of hadronic final states

  X in inelastic electron scattering

  (e,e'X) X=N, $\pi$, N + $\pi$, N+N

- Detection of multiple particle final states

  1. electromagnetic transition form factors of 3quark-systems

     $\gamma N \rightarrow N^* \rightarrow N\pi$, $N\pi\pi$..

     $K^+\Lambda$

  2. Resonance production and propagation in nuclei

     $\gamma A \rightarrow N^*X \rightarrow \pi NX$

     $\gamma A \rightarrow K^+\Lambda(1520) \rightarrow K^+Kp\ X$

  3. Multi-nucleon emission

     A(e,e'NN...)X

# END STATION C

CEBAF

## Moderate Resolution & Out of Plane

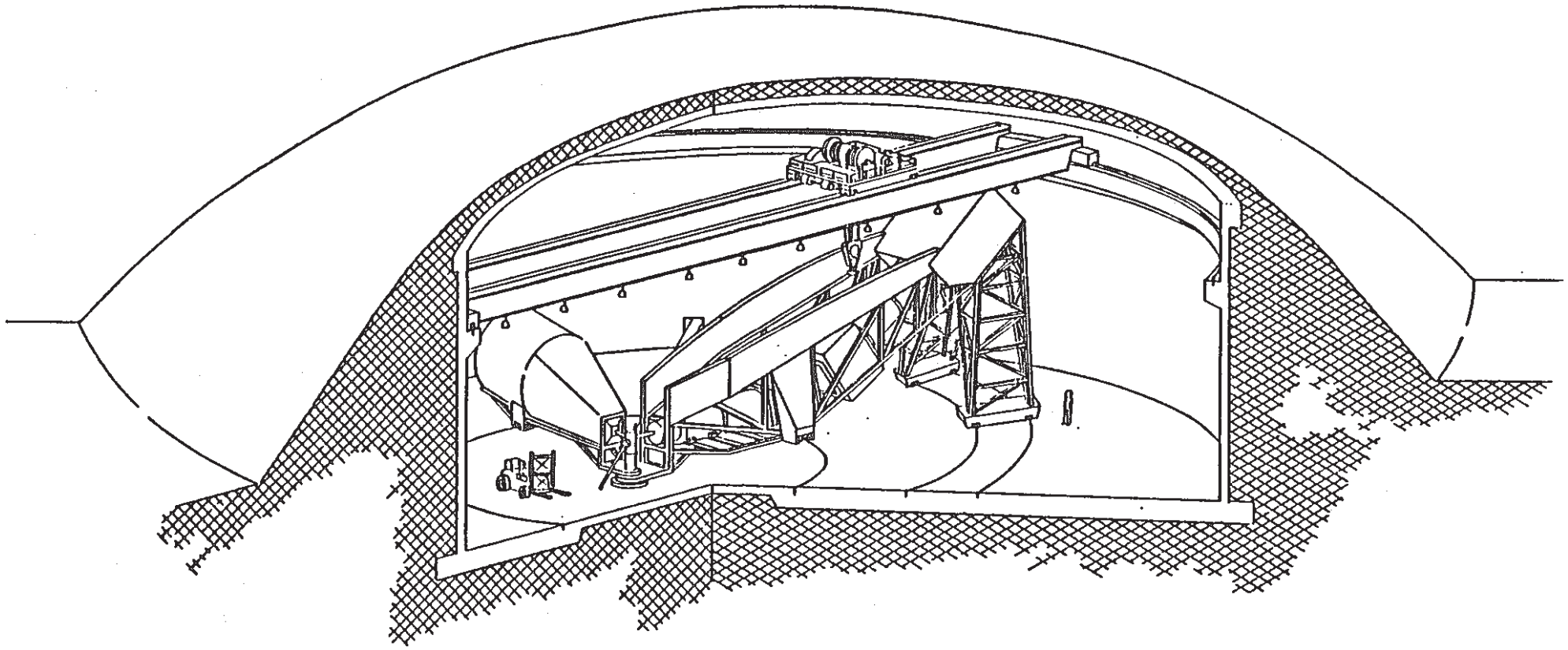

# Highlights of Physics Program — CEBAF
## Specialized Apparatus (Hall C)

- o Form Factor Measurements
  - Accurate Measurement of $G_E n$ as a function of $Q^2$.

- o Parity Violation
  - Precision tests of extensions to the standard model in the electron-quark sector.

- o High $Q^2$ Baryon Resonance Program

  - Test predictions of perturbative QCD.





Europe:rf
10/88

# SCIENTIFIC PROGRAM PLANNING — CEBAF

## Upcoming Activities

| | |
|---|---|
| o Technical Advisory Panel (2) for Large Acceptance Spectrometer | Nov. 17-19, 1988 |
| o Letters of Intent - 2nd Round | Nov. 29, 1988 |
| * o Experimental Equipment Preliminary Conceptual Design (PCDR) | Dec. 14, 1988 |
| o Program Advisory Panel (3) | Feb. 9-11, 1988 |
| * o Experimental Equipment Conceptual Design Complete (CDR) | March 89 |
| o Proposals | 1989 |

*DOE Milestone

misc:pas

COST CEBAF

Federal Budget FY 1989

Construction Budget: $265 M over 6 1/2 Years

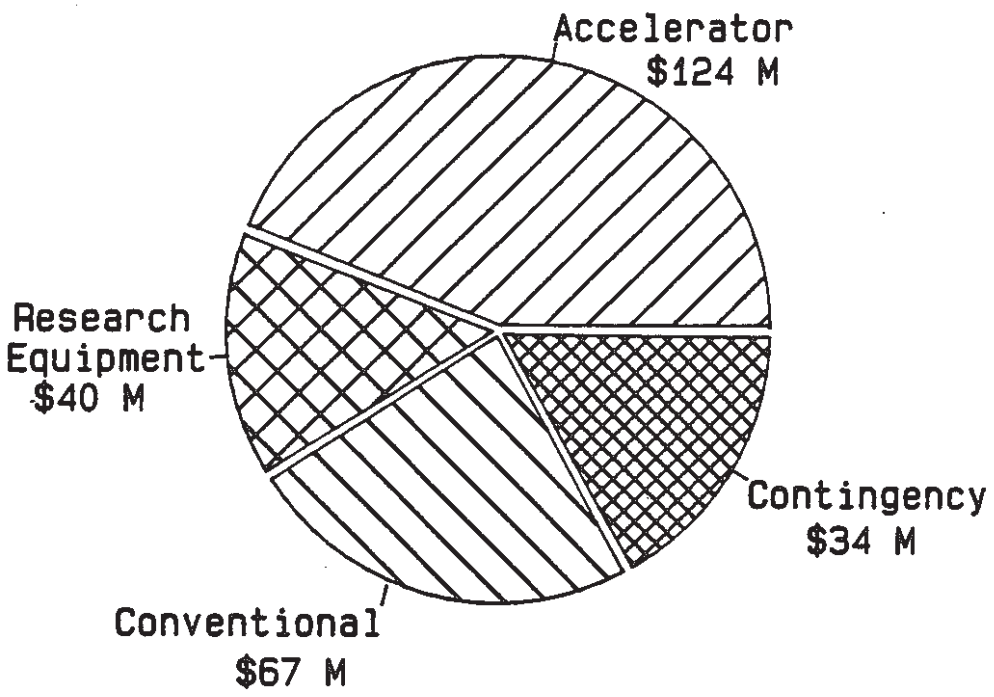


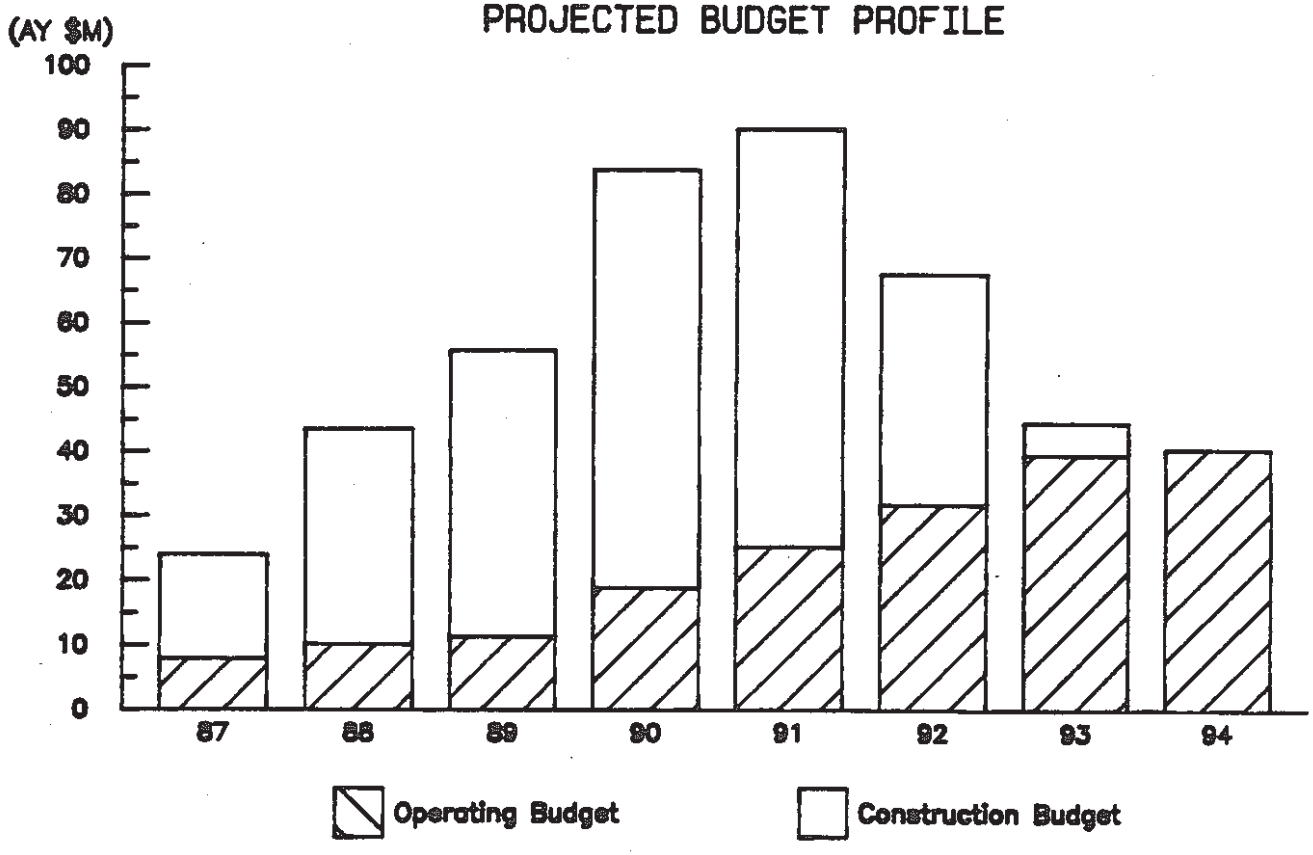


43

# MILESTONES — CEBAF

| | | |
|---|---|---|
| o | Start construction | Feb. 1987 |
| o | End station conceptual design | May 1988 |
| o | Start tunnel construction | Aug. 1988 |
| o | Place cavity contract | 2Q FY89 |
| o | Experimental equipment conceptual design | 2Q FY89 |
| o | Complete cryomodule R&D | 3Q FY89 |
| o | Start front end test (to 25 MeV) | 3Q FY90 |
| o | Start CHL operations | 1Q FY91 |
| o | Start north linac beam commissioning | 3Q FY92 |
| o | Construction project complete | 4Q FY93 |
| o | First beam to experiment | 2Q FY94 |

LINAC88:yhs
10/88

# 1. Project Overview

## 1.1 Project Scope

The Continuous Electron Beam Accelerator Facility (CEBAF) will be a high-intensity, continuous wave (CW) electron accelerator for nuclear physics. Its principal scientific goal is to understand the quark structure, behavior, and clustering of individual nucleons in the nuclear medium, and simultaneously to understand the forces governing this behavior.

To achieve this goal, the mission of CEBAF is to design, build, and operate a world-class electron accelerator facility to serve the nuclear physics community. Implicit in the mission is the support of facility users, the conduct of an in-house research program using CEBAF and complementary facilities, and continuous improvement of the accelerator and experimental areas to keep pace with the needs of the users.

Scientific requirements, summarized above and described in detail in Chapter 2, define the scope of CEBAF. It is to be an electron accelerator providing a continuous beam of electrons at any energy between 0.5 and 4.0 GeV to one or more of three equipped experimental stations. To serve more than one experimental station simultaneously, the current or intensity of the continuous electron beam is to be 200 μA.* The beam will have a duty factor of 100%. (See Table 1.1.) Finally, the accelerator is to be completed and available for physics research in 1992 for a total estimated cost of $236 million (actual year dollars).

**Table 1.1**
**CEBAF Project Scope**

| | |
|---|---|
| **Accelerator Specifications** | |
| Particle | electron |
| Energy | 0.5 to 4.0 GeV |
| Current | 200 μA |
| Duty factor | 100% |
| **Additional Features** | |
| Three equipped experimental areas | |
| Other buildings and facilities necessary to support the accelerator, users, and staff | |
| **Cost and Schedule** | |
| Total estimated cost (actual year dollars) | $236 M |
| Construction period | FY 1987–1992 |

*GeV=billion electron volts; μA = millionth of an ampere.

This conceptual *Design Report* describes the accelerator and its conventional facilities. Chapter 2 presents the scientific justification. Chapters 3 through 9 describe in detail the conceptual design for a superconducting CW electron linac meeting CEBAF's specifications. The report also includes a description of a possible initial complement of equipment for the experimental areas (Chapter 10).

The conventional facilities included within the project scope are described in Chapter 11. Chapter 12 summarizes plans for project management, Chapter 13 discusses cost, and Chapter 14 discusses schedule.

The remainder of Chapter 1 relates the history and context of the CEBAF project, introduces the CW linac design, and considers alternative designs.

## 1.2 Project History

The scientific need for a high-duty-factor, high-energy electron accelerator to explore the quark structure of the nucleus has been recognized for more than a decade. Such an accelerator was foreseen by the first *Long Range Plan for Nuclear Science* (1979) developed by the DOE/NSF Nuclear Science Advisory Committee (NSAC) and endorsed by subsequent panels. It would provide a capability not available elsewhere in the world (Figure 1.1).

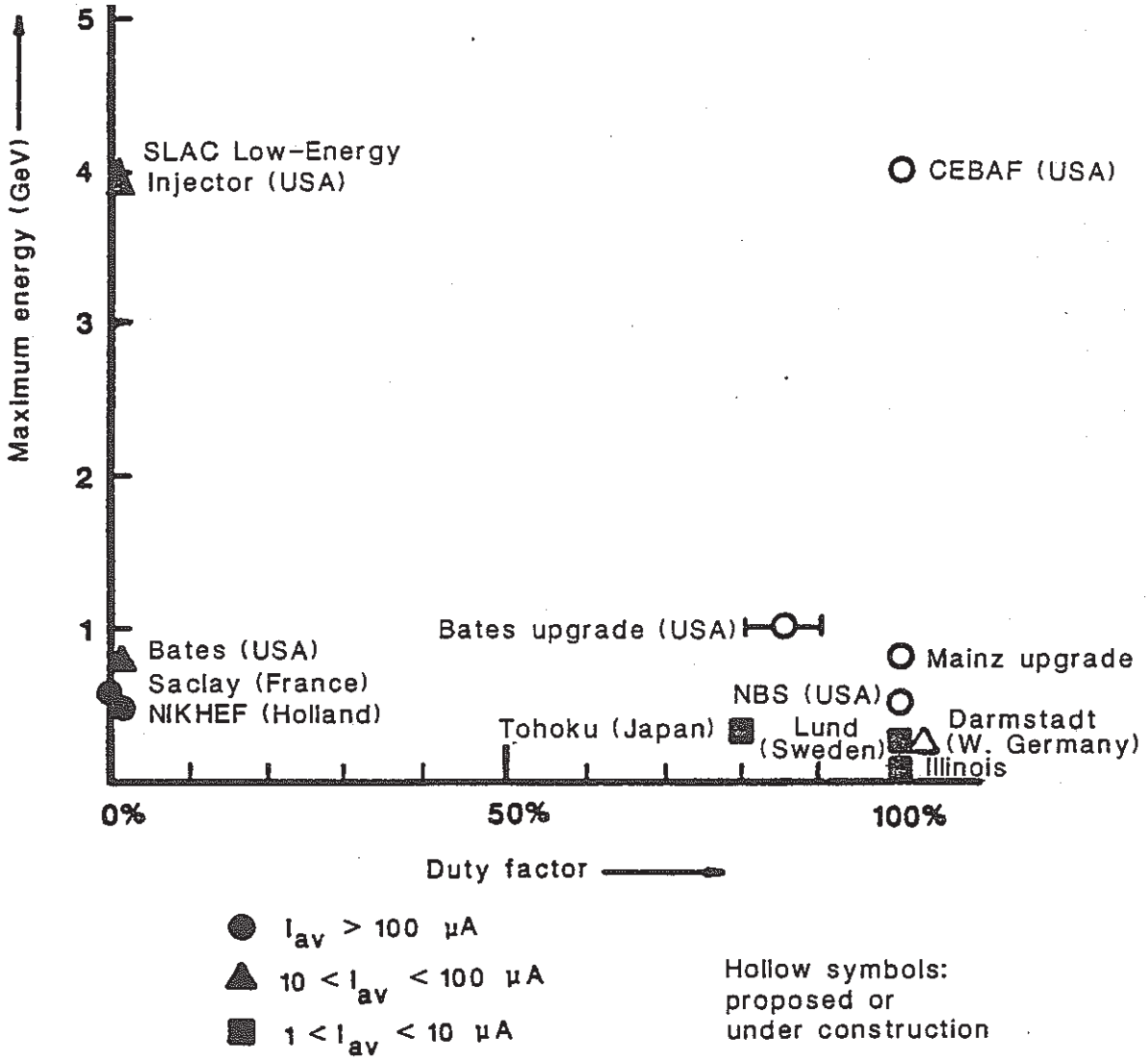


**Figure 1.1.** Electron accelerators from 0.1 to 5.0 GeV maximum energy and a current in excess of 1 μA. Hollow symbols indicate machines currently under construction or proposed.

Recognizing this need in the mid-1970s, Prof. James S. McCarthy of the University of Virginia became interested in designing and proposing a new electron accelerator for nuclear physics. He convened the First University of Virginia Conference on Electron Accelerators in 1979, and set in motion the collaborations that led to the incorporation of the Southeastern Universities Research Association (SURA) in August, 1980.

With a limited budget and staff, McCarthy designed an accelerator to produce continuous beams of 4-GeV electrons. In December 1980, SURA submitted a proposal for construction of this accelerator to the DOE. The design of the SURA accelerator relied primarily on well-proven technology. It was a pulsed linear accelerator (linac), of the same design as the Stanford Linear Accelerator Center's (SLAC), with a pulse stretcher ring (PSR) to stretch the pulses into a continuous beam (Figure 1.2). The circumference of the PSR would be exactly equal to the length of the electron pulse from the linac. Thus one linac pulse would fill the PSR completely with beam. As this loop of electrons would circulate around the PSR it would be extracted slowly and continuously, during the interval between linac pulses. The experimental stations would receive an essentially continuous beam. SURA called this accelerator proposal the National Electron Accelerator Laboratory (NEAL).

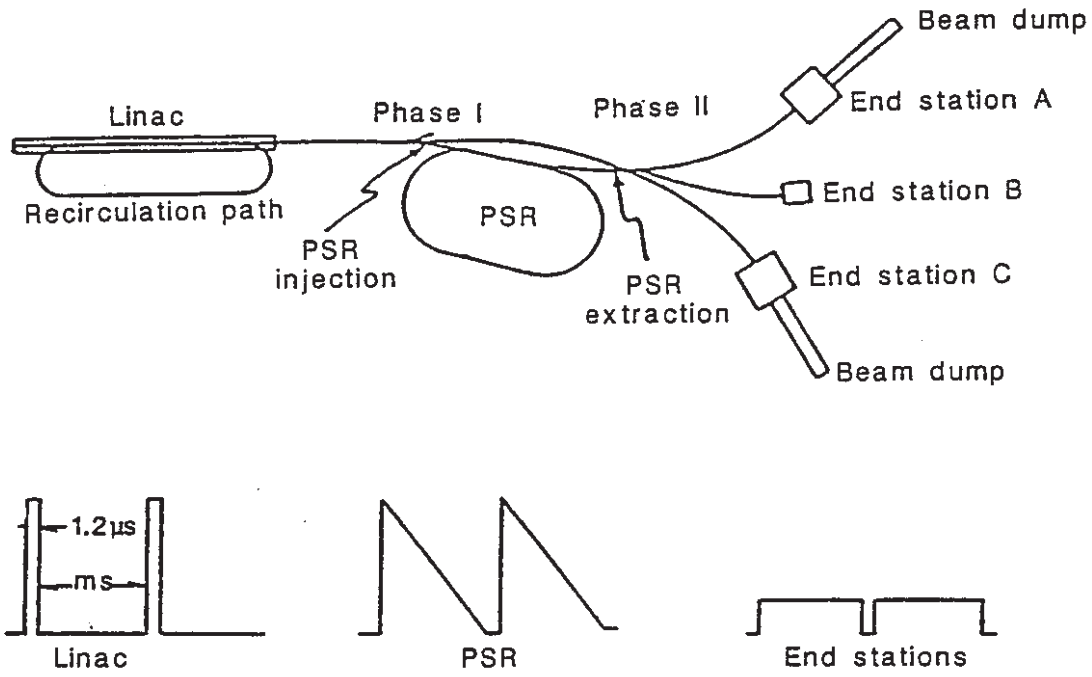


**Figure 1.2.** CEBAF conceptual design as of May, 1985—a pulsed linear accelerator with pulse stretcher ring. This design has since been superseded by the superconducting CW design.

The submission of the SURA proposal triggered significant activity with in the electromagnetic nuclear physics community, both to prepare a national scientific justification and to develop alternative designs. Much discussion centered on selecting the appropriate energy for the continuous electron beams. In the fall of 1982 an NSAC subcommittee, chaired by Prof. Peter D. Barnes of Carnegie-Mellon University, recommended 4 GeV. Shortly thereafter, SURA submitted the second NEAL proposal. Argonne National Laboratory, the University of Illinois, the Massachusetts Institute of Technology (MIT), and the National Bureau of Standards (NBS) also submitted proposals. Both Argonne's and SURA's proposals were for 4-GeV accelerators; the other institutions' designs were for lower energies.

During the winter of 1982/83 the NSAC Panel on Electron Accelerator Facilities (Prof. D. Allan Bromley, chairman) reviewed and evaluated the proposals at the request of the NSF and DOE. As part of the deliberations, the panel reconsidered the choice of energy and affirmed the selection of 4 GeV. NSAC endorsed the panel's recommendations to build a facility based on the SURA proposal. In May 1983, SURA submitted a proposal to DOE for preconstruction R&D.

Subsequently the agency and the nuclear physics community have reviewed and consistently reaffirmed the various decisions, including the choice of energy, the priority of an electron machine, and the selection of the SURA proposal. In this process, the name of the new facility was changed to Continuous Electron Beam Accelerator Facility (CEBAF). Fiscal Year 1987 was set as the year for construction authorization.

In May 1985, Dr. Hermann A. Grunder became director of CEBAF. In preparation for construction Dr. Grunder initiated a study to review the project's basic technology in light of innovations and technological progress made since the design was originally proposed in 1980 and refined in 1982.

The objectives of CEBAF's Technology Review were to identify the most appropriate and cost-effective technology choices for CEBAF commensurate with an FY 1987 construction start. At that point, superconducting RF technology emerged as a promising alternative to the pulsed linac with PSR. Its advantages are numerous: inherently continuous beam with 100% duty factor, improved beam quality, considerable power savings during operation, ability to deliver simultaneous continuous beams at three energies, conceptually simpler design (no PSR), and potential for significant upgrades in energy and operational flexibility.

The key component of a superconducting linac is the superconducting accelerating cavity. Since the early 1960s pioneering groups have been developing such cavities and the technology to support them. An early leader was Stanford University's High Energy Physics Laboratory (HEPL). Now there are many centers of superconducting RF research. Initial results were encouraging, but progress has been slow until recently, when several breakthroughs occurred. Within the past two years, improvements in niobium quality, cavity fabrication, and processing have allowed the performance of the cavities to more than double. Prototype cavities now consistently exceed generally accepted specifications for application in electron accelerators.

Within the past year, designers of two major accelerators under construction in Europe and one in Japan have elected to use this technology. These accelerators (Table 1.2) are expected to become operational when CEBAF does. Industrial capability (especially in Europe) has grown rapidly, and the companies working with the European accelerators have built and delivered components that exceed specifications.

**Table 1.2**
**Worldwide Plans for Cavities Produced by Industry**

| Lab | Machine | Number of cavities | Electrical length (m) | Date running |
|---|---|---|---|---|
| U. Darmstadt | Linac | 8 | 8 | 1986 |
| DESY | HERA (30 GeV) | 16 | 20 | 1987 |
| DESY | HERA (upgrade) | — | — | — |
| CERN | LEP | 16 | 27 | 1988 |
| CERN | LEP II | 200 | 340 | 1991/92 |
| KEK | Tristan | 130 | 200 | — |
| CEBAF | Linac | 400 | 200 | 1991 |

Reviews and workshops involving technical experts and nuclear physicists have confirmed that superconducting accelerator technology is ready and appropriate for CEBAF's construction start in FY 1987. In October and November 1985, CEBAF prepared a Scientific and Technological Assessment Report (STAR) on the superconducting CW linac. From November 20 to 22, 1985, DOE reviewed the STAR. On December 4, 1985, the Department directed CEBAF to complete the preconceptual and conceptual designs for this machine. This Conceptual Design Report was reviewed on February 11 and 12, 1986, by DOE.

## 1.3 Superconducting CW Linac

CEBAF's continuous wave (CW) linear accelerator (linac) is a straightforward way to produce continuous high-energy electron beams. One simply injects a steady beam from an electron gun, preaccelerates it in the injector to nearly the speed of light, accelerates it to the desired energy in the main accelerator, and sends it to an experimental area.

The acceleration is accomplished electromagnetically using a metal structure to establish the electric field gradient that accelerates the electrons. When this metal structure is copper, as is the case at existing electron linacs, the electric field produces enormous resistive heating in the copper. The resistive heating is so large that for practical reasons such a linac is operated only in a pulsed mode, with brief high-current pulses of electrons separated by long intervals between pulses. However, if the accelerating structure were superconducting—that is, with vanishing electrical resistanee—the resistive losses would be very small, and acceleration of a continuous beam would become feasible.

Some materials, for example niobium, become superconducting at temperatures close to absolute zero. For niobium this transition occurs at 9.2 K. Since no material is a perfect RF superconductor, there are small resistive losses in a superconducting niobium accelerating structure. The quality factor $Q$ is a measure of these losses. A superconducting structure has a very high $Q$; its losses are smaller by a factor of around a million than the losses in a room-temperature copper structure.

The prerequisites for a CW linac, then, are superconducting accelerating structures, known as cavities, and a cryogenic system to keep them below their transition temperature.

In two ways, the CEBAF design differs from the simple concept sketched earlier. First, the electron beam is passed through the accelerator four times in a process called recirculation. Second, the linac is split into two segments so that half of the acceleration during each pass occurs in one segment while the other half occurs along the return path (figures 1.3 and 1.4). Each linac segment can accelerate the beam

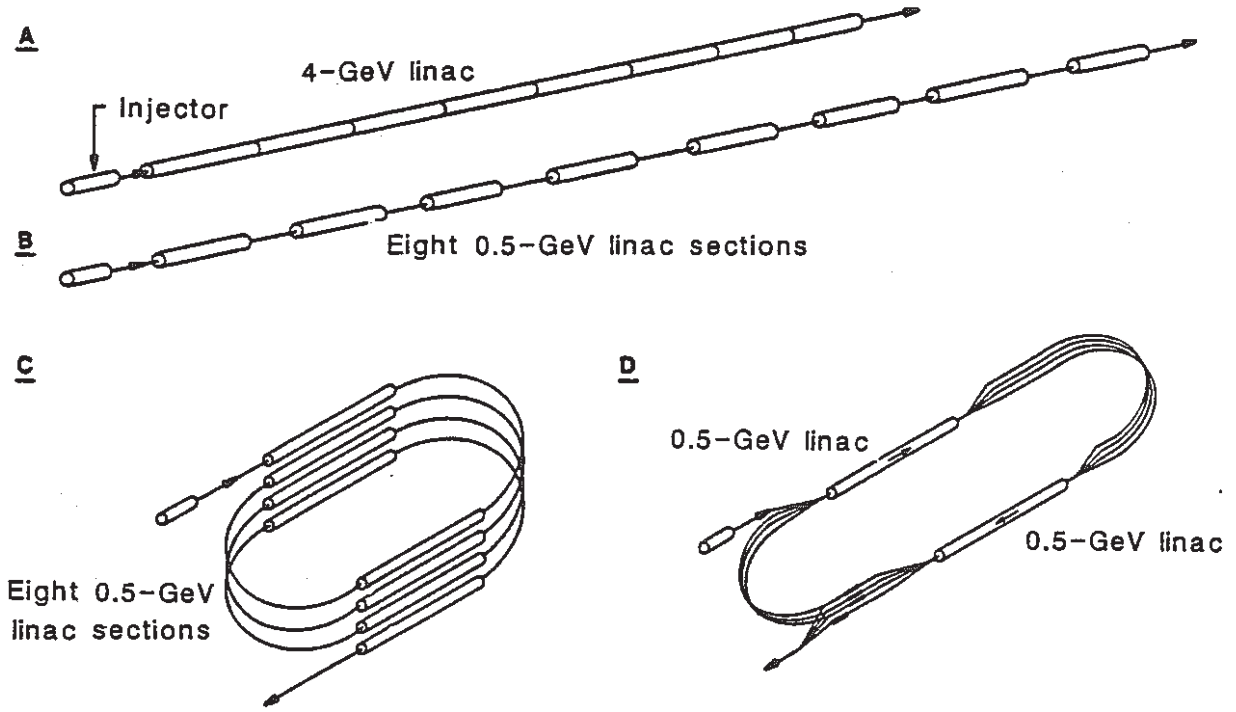


**Figure 1.3.** Recirculating linac concept. A 4-GeV linac (A) could be divided into eight 0.5-GeV sections (B) and wrapped into a compact spiral (C). With recirculation (D), the four sections on each side are merged into one that the beam passes through four times.

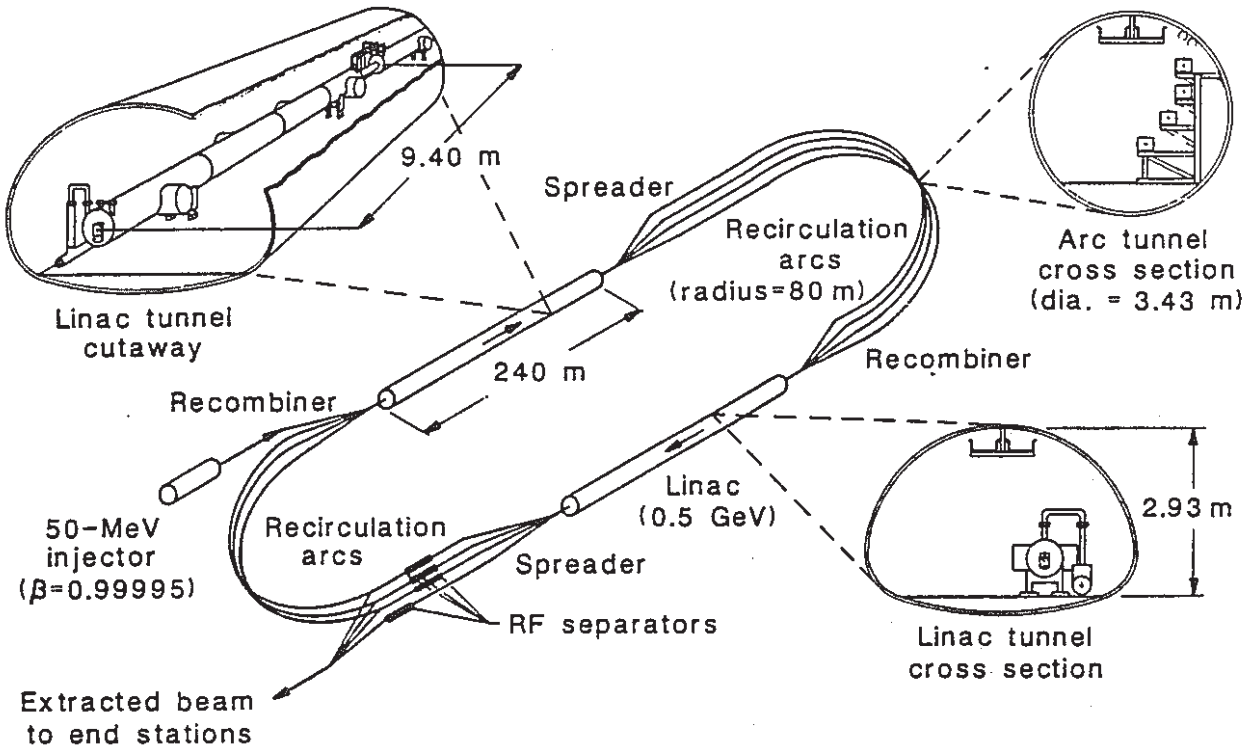


**Figure 1.4.** Schematic of CEBAF superconducting CW recirculating linac.

by 0.5 GeV. The paragraphs below describe how the linac works by following electrons through the machine from injection to the experimental areas.

In the injector, a CW electron gun produces a continuous stream of electrons which is bunched to the linac's RF frequency (1500 MHz) and preaccelerated to 50 MeV for injection into the first linac segment. As the beam passes through this linac segment it sees a repeating pattern of superconducting accelerating cavities and magnets. The cavities are the basic accelerating structures, and the magnets focus and steer the beam.

The CEBAF linac will use a superconducting cavity designed, developed, and tested at Cornell University (Figure 1.5). Four prototypes of this 1500-MHz cavity have been built by Cornell, and all have exceeded performance criteria now being specified for the CEBAF linac: they must support an accelerating gradient of at least 5 MV/m at a $Q$ of $3 \times 10^9$. The active length of each cavity is 0.5 m, so each cavity provides 2.5 MeV of energy gain.

During FY 1986 CEBAF is working with industry to fabricate and test additional prototypes, thereby qualifying industry for cavity fabrication. The first two cavities were completed and tested in February, and both exceeded these specifications (Table 1.3).

The cavities are paired and enclosed in a cryostat. Within the cryostat, the cavities are completely immersed in liquid helium to keep their temperature at 2 K. RF power from CW klystrons feeds through the cryostat into the cavities. Four cryostats are joined together in series within a cryogenic module containing eight cavities. The cryogenic modules are linked together in a cryogenic network supplied with liquid helium chilled at a central refrigeration plant. The magnets, beam instrumentation, and vacuum attachments are placed in the warm sections between cryogenic modules. In each of the two linac segments the beam passes through 25 cryogenic modules containing, in total, 200 superconducting cavities to accelerate the beam by 0.5 GeV.

At the end of the first linac segment, the beam enters a recirculation arc to transport it to the entrance of the linac segment on the return path. The second linac segment is identical to the first, and can accelerate the beam an additional 0.5 GeV to a second arc that carries it back to the beginning of the first linac segment for further acceleration.

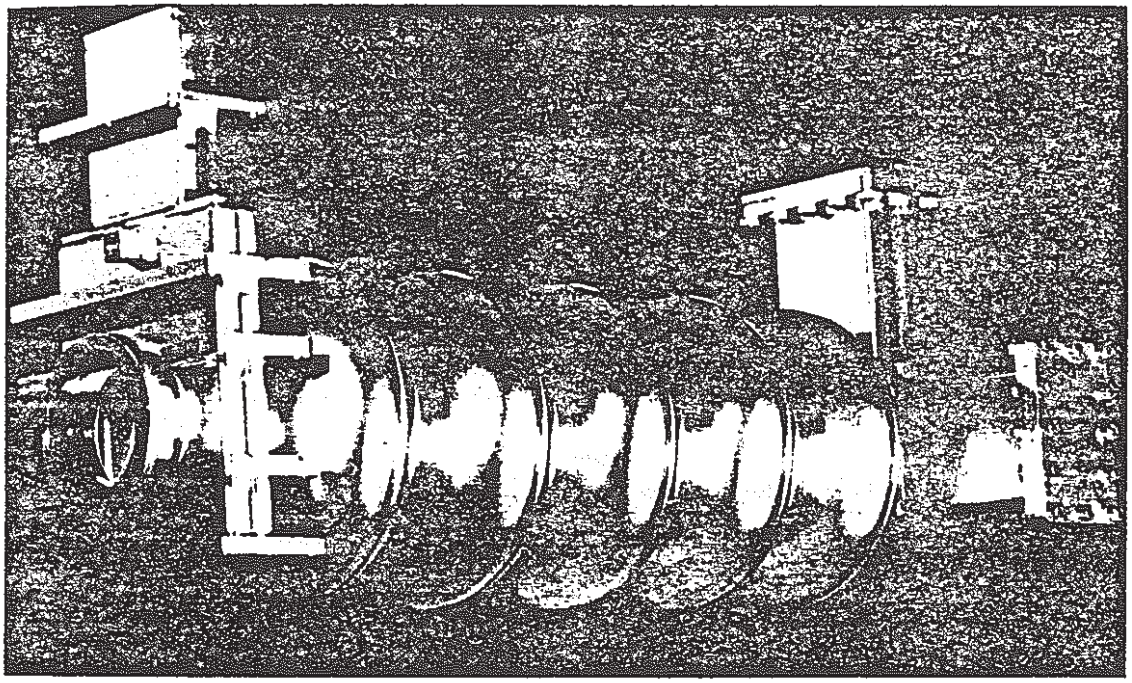

**Figure 1.5.** A CEBAF-Cornell accelerating cavity.

**Table 1.3**
**Performance of Prototype Cavities**

| | Gradient (MV/m) | Achieved gradient as percentage of design gradient | Quality factor ($Q$) | Achieved $Q$ as percentage of design $Q$ |
|---|---|---|---|---|
| CEBAF design specification | 5.0 | — | $3 \times 10^9$ | — |
| Cavity #1 (vendor 1) | 6.1 | 122% | $5 \times 10^9$ | 167% |
| Cavity #2 (vendor 2) | 7.9 | 158% | $6 \times 10^9$ | 200% |
| Cavity #3 (vendor 1) | 6.8 | 136% | $7 \times 10^9$ | 233% |

Electrons can make as many as four full circuits of the accelerator. Since the beam is continuous, there are simultaneously electrons at four discrete energies in each linac segment. For example, when the machine is set to produce a 4-GeV beam after four passes, halfway down the first segment there are electrons at 0.30 GeV, 1.30 GeV, 2.30 GeV, and 3.30 GeV. These four beamlets must be spread apart from each other and put into separate beam lines to negotiate the recirculation arcs connecting the two linac segments. In each beam line the field of the bend magnets controlling the beam's trajectory must be matched closely to the energy of the beam. Therefore a magnetic device, called a spreader, is located at the end of each linac segment to spread the beams vertically so that they can follow separate paths

through the arcs. Each path has a lattice of magnets to steer and focus the beam it contains. At the beginning of each linac segment, another magnetic device—a recombiner—recombines the beams so that they can travel as one through the linac segment (Figure 1.4).

Beams at three energies can be extracted from the linac and directed to the experimental areas. One or more of these beams may be the highest-energy beam, which has made four circuits of the linac. This beam is separated from the others by the spreader at the end of the second linac segment and sent toward the experimental areas. To extract a beam at any of the other three energies present at the end of the second linac segment, a device called an RF separator is installed in each beam line just downstream of the spreader. This device can deflect specific bunches of electrons so that one can be diverted to the experimental areas while the next two continue into the arc for further acceleration by the linac. The beams directed toward the experimental areas are sent through the beam switchyard for distribution to the appropriate experimental areas.

Table 1.4 summarizes the baseline specifications for the CEBAF linac design.

**Table 1.4**
**Baseline Specifications for the CEBAF Recirculating Superconducting CW Linac**

| | |
|---|---|
| **Beam characteristics** | |
| Electron energy $E$ [GeV] | $0.5 \leq E \leq 4.0$ |
| Average current [μA] | 200 |
| Transverse emittance [m-radians]* | $\leq 10^{-8}$ |
| Energy spread† | $\leq 2 \times 10^{-4}$ |
| Duty factor | 100% |
| Simultaneous beams | 3 |
| Simultaneous correlated energies | 3 |
| **Linac parameters** | |
| Concept | Recirculating CW linac |
| Structure type | Superconducting RF cavity |
| Number of linac segments | 2 |
| Number of beam passes | 4 |
| Energy gain per pass | 1.0 GeV |
| Frequency [GHz] | 1.5 |
| Design gradient [MV/m] | 5.0 |
| Design residual $Q$ | $3 \times 10^9$ |
| Nominal injection energy [MeV] | 50 |
| Arc average radius [m] | 80 |

*Emittance = phase space area containing 95% of beam, divided by π
†FWHM (full width at half maximum)

## 1.4 Summary of Alternatives

The CEBAF Preconstruction Technology Review evaluated alternative technological approaches for meeting the CEBAF Scope. The results of this review are described in the workshop report from the Technology Review. Three approaches were considered viable: the superconducting CW linac, the pulsed standing wave linac with pulse stretcher ring (PSR), and the pulsed traveling wave linac with PSR. Other accelerator designs are unable to deliver the current or the energy specified in the project scope.

The original design for CEBAF was a recirculated, pulsed traveling wave linac with PSR. The Technology Review judged this design to be sound and able to meet the specifications. However, it does not represent the latest design concept for high-average-current linacs. Conservative in most aspects,

this design has challenging RF requirements: klystrons with 40-MW peak power and 130-kW average power.

Technology Review participants (Appendix B) considered designs using alternative room-temperature structures. The most cost-effective solution uses a modern standing wave structure and 42 klystrons of 27 MW peak power and 60 kW average power.

The pulsed linac with PSR achieves a duty factor around 80%. Its upgrade potential is limited to 6 GeV by the size of the PSR; at higher energies quantum excitation destroys the beam quality by greatly increasing the emittance.

Table 1.5 shows the comparison between the pulsed linac with PSR and the CW linac. Both designs meet the original project requirements, of course; but as can be seen, the CW approach is superior in several ways. It provides a macroscopic duty factor of 100%; that is, it provides a truly continuous beam when the accelerator is on. It has better beam quality, as measured by emittance and energy spread. It offers experimenters simultaneous CW beams at different (but correlated) energies for each of the three experimental stations.

**Table 1.5**
**Comparison of Pulsed Linac/PSR and CW Linac**

| | Pulsed/PSR | CW Baseline |
|---|---|---|
| Duty factor | >80% | 100% |
| Emittance ($\pi$m) | $2 \times 10^{-7}$ | $<10^{-8}$ |
| Energy spread ($\Delta E/E$) | $2 \times 10^{-3}$ | $<2 \times 10^{-4}$ |
| Simultaneous CW beams at different energies | 1 | 3 |
| Design energy (GeV) | 0.5–4 | 0.5–4(6) |
| Possible upgrade energy (GeV) | ~6 | ~16 |
| Current ($\mu$A) | 200 | 200 |
| Amount of accelerating structure (GeV) | 2.0 | 1.0 |
| Number of recirculations | 1 | 3 |
| Passes through linac | 2 | 4 |

The superconducting CW linac is also superior to the pulsed linac with PSR in terms of maximum energy—both design energy and possible upgrade energy. With the conservative component specifications selected to ensure meeting the scope with superconducting technology, the CW linac may exceed the 4-GeV energy specification by as much as 50% shortly after commissioning. Moreover, it has substantially more potential for upgrade in energy. Whereas the pulsed linac with PSR was expected to be able to reach 6 GeV after upgrade (its energy is limited by the circumference of the pulse stretcher ring), the CW linac is expected to be able to reach significantly higher energies when accelerating cavities achieving higher gradients become available.

This upgrade potential is important. An accelerator facility is a major, long-term investment for a scientific field. Thus the scientific community and the accelerator designers must anticipate a desire to modify the facility to keep pace with future scientific interests of the community. In the case of CEBAF, nuclear physicists have already expressed an interest in using polarized beams, and one can foresee that they eventually may want to push to higher energy, increase the number and variety of end stations, and use positrons. The extent to which the CW linac permits cost-effective upgrades is a clear advantage in the selection of technological approach.

# 3. Superconducting CW Linac

## 3.1 Design Overview

The mission of CEBAF is to design, build, and operate a world-class electron accelerator facility to serve the nuclear physics community. The accelerator is to provide a continuous beam of electrons at any energy between 0.5 and 4.0 GeV. To serve more than one experimental station simultaneously, the current or intensity of the continuous electron beam is to be 200 μA. This chapter describes a recirculating superconducting CW electron linac which meets these needs.

The key component of a superconducting linac is the superconducting accelerating cavity, which allows for continuous acceleration of beam without excessive power loss in the cavity wall. The CEBAF linac will use a superconducting cavity designed, developed, and tested at Cornell University. Four prototypes of this 1500-MHz cavity have been built by Cornell, and all have exceeded performance criteria specified for the CEBAF linac, as have three prototypes that have been built by industry for CEBAF. Superconducting RF (SRF) technology is now sufficiently mature that construction of a high-efficiency CW superconducting linac is practical.

The remainder of this section of Chapter 3 introduces the conceptual design for a multiply recirculating superconducting CW electron linac for CEBAF. Later sections present an outline of the work breakdown structure for the construction of the accelerator, a discussion of beam stability, a discussion of radiation safety, and an analysis of the technology base for the linac design. The conceptual design for the systems and subsystems required for the linac is described in chapters 4 through 11.

**Multiply Recirculating Linac**

The most straightforward CW accelerator is a single linear accelerator which the beam traverses one time. With an accelerating gradient ($E_a$) of $E_a$ = 5 MeV/m, 800 m of active accelerating structure would be required to reach an energy of 4 GeV (Figure 3.1(a)). Even a cursory estimate shows this to be an economically inefficient approach. A more cost-effective solution is obtained by passing the beam repeatedly through a shorter linac structure by means of recirculation paths (Figure 3.1(b)).

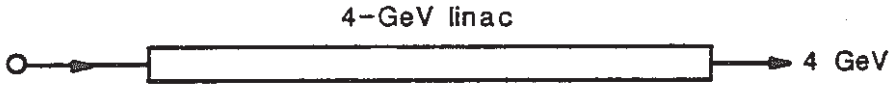


**Figure 3.1(a).** Single linear accelerator.

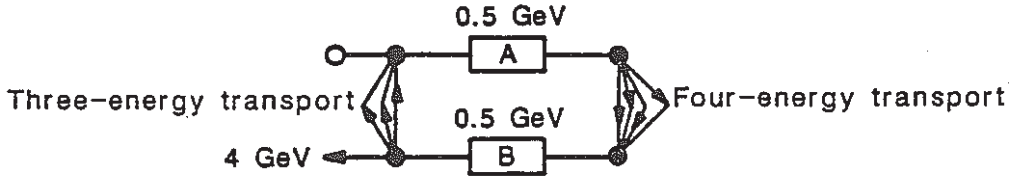


**Figure 3.1(b).** Multiply recirculating linac.

This approach is made possible by the fact that electrons are fully relativistic, i.e., move at very nearly the speed of light at quite modest energies. At only 50 MeV, for instance, the electron velocity is 0.99995*c*. Once fully relativistic, an electron's velocity is essentially independent of energy. Thus, beams at different energies pass together through the linac structure, all maintaining the proper phase relative to the accelerating RF field. The recirculating linac approach has been used successfully at both the HEPL superconducting linear accelerator and the MIT-Bates conventional pulsed linear accelerator, and will be employed at the Wuppertal-Darmstadt superconducting linac, currently under construction.

Since the electrons are fully relativistic, the cavities need not have the same accelerating gradient. One cavity can have a higher gradient than its neighbors without the bunch RF phase being degraded. Strongly performing cavities can make up for weaker ones since the RF design allows for individual control to excite each cavity to its maximum field. The total beam energy, therefore, reflects the average gradient of all the cavities and is not severely limited by the weakest unit.

The number of passes through the linac must be determined through cost optimization. More passes reduce the capital cost. Fewer passes reduce the operational complexity and enhance beam stability. Based on the cost of our cavity prototype (the CEBAF-Cornell five-cell cavity) and the design choices for the recirculation arcs, the optimum number of passes is four or five.

A four-pass system has been adopted for CEBAF. This accelerator will consist of two 0.5-GeV linac segments joined by recirculation arcs that bend the beam, transporting it from the exit of one linac to the entrance of the next (Figure 3.2). Beam will be injected at an energy of 50 MeV.

In this four-pass system, four electron beams, each at a different energy, are simultaneously present on the same trajectory in the linac segments. As each beam is at a different energy, each will require a separate recirculation path tuned to accommodate the particular energy of that beam. There are, there-

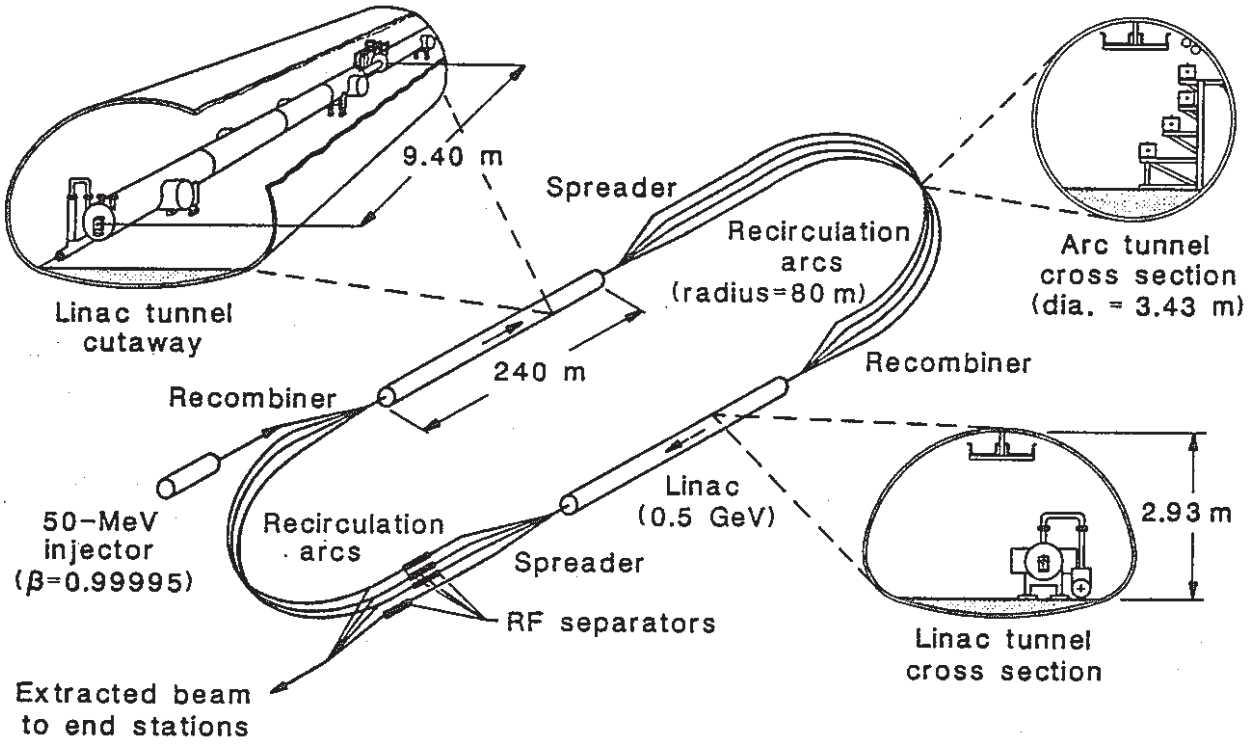


**Figure 3.2.** Schematic of the CEBAF recirculating superconducting CW linac.

fore, several recirculation beam lines within each recirculation arc. These beam lines are separated vertically. Upon exiting a linac, the beams at different energies are spread apart vertically and transported to the appropriate recirculation beam lines through use of a device we have termed a *spreader* (or, if at the required energy, extracted and transported to the experimental areas). At the end of the recirculation arc, the beams are transported from each recirculator beam line, recombined, and injected into the next linac through use of a device we have termed a *recombiner.*

The path of a single electron bunch from injector to experimental area therefore comprises four acceleration cycles, each of which is as follows:

1. injection into first linac segment,
2. acceleration by first linac segment (for 0.5 GeV additional energy),
3. "spreading" to the proper beam line in first recirculation arc,
4. transport through recirculator to recombiner for injection into second linac segment,
5. acceleration by second linac segment (for 0.5 GeV additional energy),
6. spreading to the proper beam line in second recirculation arc, and
7. transport through recirculator to recombiner for reinjection into first linac segment.

On the fourth (and final) cycle, this sequence is interrupted at step 6 where the beam, after spreading, enters an extraction beam line. Extraction elements in each of the recirculation arc beam lines allow extraction at step 6 on any of the preceding cycles as well.

Energies between 500 MeV and 4 GeV can be achieved by lowering the energy gains per linac and extracting bunches of the desired energy at step 6 after an appropriate number of cycles. For example, a beam of 1.6 GeV may be obtained by using an energy gain of 0.4 GeV per linac segment and by extracting the beam at step 6 of the second pass.

The extraction elements for beam extraction at cycles 1, 2, and 3 are *RF separators,* time-dependent deflecting devices that allow one out of every three passing bunches to be steered into the extracting beam line rather than into the recirculation arc beam line. On the fourth cycle the beam is directed to a fourth RF separator. As will be shown in subsequent chapters, this configuration makes it possible to serve all three experimental stations simultaneously with beams of up to three different energies and individually adjusted current levels.

**Key Beam Dynamics Issues**

The key beam dynamics issues for a recirculating linac are beam stability and beam quality. Both issues have been resolved in the conceptual design of CEBAF.

The first issue is the problem of insuring against beam breakup, which limits the amount of beam current a linac can accelerate. In a recirculating linac, the most likely cause of beam breakup is the growth of transverse deflecting fields in the RF cavities generated by repeated passes of beam bunches. This process is called multipass regenerative beam breakup. Analysis of multipass regenerative beam breakup in CEBAF predicts that the beam current required is below threshold by well more than an order of magnitude.

The second issue is the problem of conserving the emittance and momentum spread. In a recirculating linac two factors can degrade the beam: synchrotron radiation during bending in the recirculation arcs, and possible mismatch of the electron beams upon reinjection into the linac segments. Beam quality can be maintained and reinjection mismatches avoided through proper design of the recirculation arc beam lines. The features of CEBAF's beam lines are characteristic of approaches employed in the design of low-emittance storage rings. They include careful control of beam path length, isochronicity, achromaticity, and careful correction of chromatic effects to facilitate reinjection after each arc. Strong focusing minimizes emittance growth caused by quantum excitation due to synchrotron radiation.

**Accelerator Parameters**

The main parameters of the CW linac are summarized in Table 3.1. To describe the machine components, we follow the Work Breakdown Structure (WBS) (Table 3.2) that is described in greater detail in Section 3.2.

**Table 3.1**
**CEBAF SRF CW Linac Design Parameter List**

| | |
|---|---|
| **Beam characteristics** | |
| Electron energy $E$ [GeV] | $0.5 \leqslant E \leqslant 4.0$ |
| Average current [μA] | 200 |
| Transverse emittance (95%, 1 GeV) [m] | $2 \times 10^{-9}$ |
| Energy spread [95%] | $1 \times 10^{-4}$ |
| Duty factor | 100% |
| Simultaneous beams | 3 |
| Simultaneous energies | $\leqslant 3$ |
| **Linac parameters** | |
| Concept | Superconducting CW recirculating linac |
| Number of passes | 4 |
| Number of linac segments | 2 |
| Segment length [m] | 235 |
| Maximum energy gain per pass [GeV] | 1.0 |
| Recirculation time per pass [μs] | 4.2 |
| Focusing | FODO |
| Phase advance per cell (pass 1) | 120° |
| Half-cell length [m] | 9.4 |
| Number of cavities per half-cell | 8 |
| Number of half-cells per segment | 25 |
| Vacuum (before cooldown) [torr] | $10^{-9}$ |
| **Cavity parameters** | |
| Type | Superconducting |
| Frequency [MHz] | 1500 |
| Electric length [m] | 0.5 |
| Shunt impedance ($r/Q$) [ohm/m] | 960.0 |
| Design gradient [MV/m] | 5.0 |
| Design residual $Q$ | $3 \times 10^9$ |
| Typical HOM $Q_{external}$ | $10^3$ to $10^5$ |
| Clear aperture [mm] | 70 |
| Transverse HOM $Z^{\perp}/Q$ [ohms/m$^2$] | $\leqslant 16.4 \times 10^4$ |
| **RF system** | |
| Number of klystrons | 418 |
| Klystron RF power coupled to beam [kW] | 2.0 |
| **Injector parameters** | |
| Gun energy (MeV) | 0.10 |
| Injection energy [MeV] | 50 |
| Average current [μA] | 200 |
| Transverse emittance (at 0.1 MeV) [mm-mr] | 1 |
| Longitudinal emittance [keV-degrees] | $< 15\pi$ |
| Bunch length [degrees] | $< 1.5$ |
| Pulse capability [μs] | 0.05 to 10 |
| **Recirculation arcs** | |
| Number | 7 |
| Magnetic radii [m] | 11.5 to 28.6 |
| Phase advance per period | $2\pi(5/4)$ |
| Periods per arc | 4 |
| **Cryogenic system** | |
| Total RF load at 2.0 K [W] | 2400 |
| Total heat load at 2.0 K [W] | 3200 |
| Total heat load at 40–60 K [W] | 6000 |

**Table 3.2**
**Work Breakdown Structure by Level**

| | |
|---|---|
| Level 1 | CEBAF |
| Level 2 | 1. Machine Vacuum Components |
| | 2. Beam Transport |
| | 3. RF System |
| | 4. DC Power Systems |
| | 5. Instrumentation & Control |
| | 6. Experimental Stations |
| | 7. Cryogenics |
| | 8. Conventional Facilities |
| | 9. Project Services |
| Level 3 | .1 Linac |
| | .2 Recirculation Arcs |
| | .3 Switchyard |
| | .4 Injector |
| | .5 Experimental Station A |
| | .6 Experimental Station B |
| | .7 Experimental Station C |
| | .8 Distributed Systems |
| | .9 Conventional Facilities |

## 3.2 Work Breakdown Structure

CEBAF's Work Breakdown Structure (WBS) divides the accelerator facility into areas of functional responsibility (level 2) and machine sector (level 3) (Table 3.2). Deeper WBS levels break these areas down into assembly units and subunits and cost components (Table 3.3).

**Table 3.3**
**Work Breakdown Structure Levels**

| | |
|---|---|
| Level 1. | Project |
| Level 2. | Functional Responsibility |
| Level 3. | Machine Sector |
| Level 4. | Major Assembly |
| Level 5. | Assembly |
| Level 6. | Subassembly |
| Level 7. | Cost Components |

As reflected in the WBS, the main accelerator parts are machine vacuum components (WBS 1.0), beam transport elements (WBS 2.0), RF system (WBS 3.0), DC power (WBS 4.0), instrumentation and control (WBS 5.0), and cryogenics (WBS 7.0). WBS element 6.0 is experimental equipment, WBS 8.0 is conventional facilities, and WBS 9.0 is project services. The following subsections provide overviews of the nine WBS elements.

**Machine Vacuum Components (WBS 1.0)**

Machine vacuum components include the beam vacuum as well as insulating vacuum in cryostats. In particular, the SRF cavity is included here. The CEBAF CW linac will employ a 1500-MHz, 5-cell cavity with waveguide, beam pipe, fundamental power and higher order mode couplers that follow strictly the proven design of the Cornell cavity. Specifications call for a minimum accelerating gradient of 5 MV/m and a residual quality factor ($Q$) of at least $3 \times 10^9$. Recent experience shows these specifications to be conservative. Two cavities will be installed in a cryostat to form a *cryo-unit*, the smallest self-

contained modular unit of the linac. Four cryo-units containing a total of eight cavities form a *cryogenic module*, placed between warm linac sections containing linac quadrupoles, steering magnets, beam instrumentation, and vacuum equipment. Chapter 4 describes the machine vacuum components.

**Beam Transport (WBS 2.0)**

Beam transport elements (Chapter 5) include the dipole, quadrupole, and sextupole magnets required for beam steering and focusing in the linac and in the recirculation arcs, as well as the RF separators and septum magnets for extraction. The magnets are relatively small bore (typically with a 38-mm gap), and have low to medium field (< 1 T). They are of laminated steel construction with copper coils. RF separators at 2.5 GHz follow closely established designs (e.g., CERN-Karlsruhe S-band separator).

**RF System (WBS 3.0)**

The RF system (Chapter 6) powers the cavity. For maximum flexibility and control without mechanical devices, one klystron per cavity is envisaged. This will maximize machine availability and will allow each cavity to operate near its maximum capabilities in the most straightforward manner. Included in the RF system is the injector, whose key parts are the gun, subharmonic chopper, and a buncher. Beam quality depends on these components and their proper functioning. *Differential bunch loading*, i.e. the creation of beams of different current levels, is accomplished by the injector.

**DC Power Systems (WBS 4.0)**

DC power systems (Chapter 7) are the power supplies and their controls required to energize the magnets in the linac, recirculation arcs, and the beam switchyard.

**Instrumentation and Control (WBS 5.0)**

Instrumentation and control (Chapter 8) includes all diagnostic and control (computers, instrumentation, interfaces, and software) functions required to operate the accelerator. A key feature of CEBAF's control architecture will be heavy reliance on hardware vs. software, and on *distributed intelligence*. Most controlled components will be equipped with ILCs (intelligent local controllers), devices that will maintain proper operation with minimum flow of data to and from higher levels. Chapter 6, in which RF controls are described in greater detail, illustrates how this particular system could remain operational even if communications to the next higher level were temporarily interrupted.

**Experimental Stations (WBS 6.0)**

CEBAF will have three end stations (Chapter 10) for experiments. The major pieces of experimental equipment are the magnetic spectrometers, the Large Acceptance Detector (LAD), the Variable Acceptance Spectrometer (VAS), and targets.

**Cryogenic System (WBS 7.0)**

The cryogenic system, which is essential to operate the SRF cavities, is described in Chapter 9. The SRF cavities must operate at cryogenic temperature. An optimization has led to the choice of an operating temperature of 2 K. The cryogenic system includes a central helium refrigerator, storage vessels, and a distribution system to keep the cavities at 2 K and the heat shields in the cryostats below 60 K. The total cryogenic load in the linac is 3200 W at 2 K, and 600 W at 60 K. The AC power requirement of the cryogenic system is 5 MW. The experimental end stations may use superconducting magnets operating at 4.2 K. If supplied by the central refrigerator, their requirements will add another 0.5 MW of power, for a total of 5.5 MW cryosystem input power.

**Conventional Facilities (WBS 8.0)**

CEBAF's conventional facilities will include all of the buildings and structures for the accelerator, the three experimental areas, and the various support systems and utilities, as well as for the users and staff. Chapter 11 covers this element of the WBS.

**Project Services (WBS 9.0)**

CEBAF's management objectives are to design, build, and operate a facility meeting the project scope. Chapter 12 summarizes the project responsibilities and management tools and procedures planned to accomplish these objectives.

## 3.3 Beam Stability

**Introduction**

The beam current of RF linacs has been limited by beam breakup phenomena. In normal conducting linacs single-pass cumulative and regenerative beam breakup have threshold currents of tens to hundreds of milliamperes. Since higher-order-mode $Q$'s of the superconducting RF cavities of the CEBAF linac will be reduced by couplers to levels ($10^4$) characteristic of room-temperature cavities, these single-pass effects should not be of significance at the few-hundred-microampere-per-beamlet values of CEBAF. Computer modeling supports this conclusion. Multipass regenerative beam breakup, on the other hand, has limited the beam current of superconducting CW linacs such as the Stanford recyclotron to tens of microamperes. The damping achieved in the 55-cell cavities used at Stanford, however, reduced HOM $Q$'s to values still in excess of $10^7$. Considerably higher threshold currents, in excess of 10 mA, can be expected with the five-cell cavity considered here.

The following discussion presents a detailed investigation of multipass regenerative beam breakup for the CEBAF CW linac. Computer modeling of beam breakup has been developed, and includes accurate accounting for time delays, mode frequency spread, and lattice function variation. This simulation was found to agree with a more specific theoretical analysis which had successfully described beam breakup at the Stanford recyclotron. Application of this simulation to the long array of five-cell cavities of the CEBAF design indicates that beam breakup occurs only when currents exceed ten milliamps per beamlet—more than an order of magnitude above CEBAF's design current of 200 μA.

**Phenomenology of Beam Breakup**

Consider the excitation of a single parasitic mode of a cavity by a charge $q$ passing at transverse position $r$ off axis. A charge $e$ passing $\tau$ behind will experience a transverse momentum kick of

$$\frac{c}{e}\Delta p \equiv W(\tau) = \frac{Z''lc}{2Q}\, q\, r \sin(\omega\tau)\, e^{-\frac{\omega}{2Q}\tau} \tag{3.1}$$

where $Z''$ is the transverse coupling impedance (ohms/m$^3$) and $l$ is the active length of cavity structure. Consider now a series of bunches spaced by $f_b$ with average current $I_0$ and charge per bunch of $q = I_0/f_b$. Let $W_0\cos(\omega t + \phi)$ be some initial wakefield excitation of the cavity. A bunch will experience a momentum kick

$$\Delta p = \frac{e}{c}\, W_0 \cos(\omega t + \phi) \tag{3.2}$$

After recirculation, this bunch returns to the cavity with a transverse displacement

$$r_{12} = B_{12}\, \Delta p \tag{3.3}$$

where $B_{ij}$ is the transfer coefficient (momentum to transverse position) between the $i^{\text{th}}$ and $j^{\text{th}}$ passes. On traversing the cavity the second time, an additional wakefield

$$\Delta W = \frac{Z''}{2Q}\, lc\, q\, (B_{12}\, \Delta p)\, \sin(\omega\tau)\, e^{-\frac{\omega}{2Q}\tau} \tag{3.4}$$

is excited. Steady state is maintained if the bunch excitation compensates for losses in the cavity walls and HOM couplers. At higher current levels there will be instability. With the assumption of a most-pessimistic conspiracy of time delay, the steady-state condition yields the threshold condition

$$I_{\text{th}} = \frac{1}{e}\, \frac{2\omega}{Z''l\, |B_{12}|} \tag{3.5}$$

In an $n$-pass recirculation configuration, there are $n$ beamlets passing through the cavity. One beamlet has been kicked ($n$-1) times and has a perturbed transverse position described by the transfer coefficients $B_{1n}$ through $B_{(n-1)n}$. Another beamlet has been kicked ($n$-2) times with corresponding coefficients $B_{1(n-1)}$ through $B_{(n-2)(n-1)}$, and so forth. Thus, for an $n$-pass recirculating linac, the threshold current is (again, assuming a worst-case phase conspiracy)

$$I_{th} = \frac{1}{e} \frac{2\omega}{(Z''l) \sum_j \sum_{i<j} |B_{ij}|} \tag{3.6}$$

where the maximum values of the $B_{ij}$ are taken to obtain a most-pessimistic result.

Determination of the threshold current in CEBAF requires estimates of both the transfer functions $B_{ij}$ of the linac/recirculator and the expected transverse impedance of the RF cavities. The HOM impedance of the Cornell five-cell structure is well documented in the literature. The $Z''$ and $Q$ for the four worst modes are listed in Table 3.4.

**Table 3.4**
**Strongest Transverse Modes of 5-Cell Cavity**

| | | Frequency (MHz) | | | |
|---|---|---|---|---|---|
| | | **1888** | **1969** | **2086** | **2110** |
| $Q$ | ($10^4$) | 3.2 | 0.4 | 1.0 | 1.3 |
| $Z''/Q$ | ($10^4$ ohm/m$^3$) | 6.95 | 16.4 | 5.0 | 10.0 |
| $Z''l$ | ($10^9$ ohm/m$^2$) | 445.0 | 131.0 | 100.0 | 260.0 |
| $(Z''l)_{eff}$ | ($10^9$ ohm/m$^2$) | 89.0 | 94.3 | 47.0 | 104.0 |
| $l$ = 200 m for CEBAF CW linac | | | | | |

The linac will consist of some 400 of these five-cell (0.5-meter active length) cavities and have a total active length of 200 meters. Manufacturing tolerances will yield mode frequency variations of about 1 MHz full width. Thus, there will not be perfect coherence of 400 modes of a given type since mode widths are typically less than 1 MHz. In addition, cryo-units are separated by small-bore (38 mm) stainless steel beam pipes which limit cavity-to-cavity mode coupling. At threshold there exists a steady-state modulation of the linac beam at some frequency, and it will be the value of the impedance at this frequency (modulus the bunching frequency) that will drive the beam above threshold. In light of this, the total impedance offered by the RF cavities is

$$(Z''l)_{eff} = \frac{Z''}{Q} \cdot Q \cdot 200 \text{ m} \cdot F(Q) \tag{3.7}$$

where $F(Q)$ estimates the fraction of modes of a particular type acting coherently. Computation of the impedance sum of randomly distributed resonators gives $F(32000) = 0.2$ and $F(4000) = 0.72$ for a uniform distribution of modes centered at 2 GHz with full width of 1 MHz. The last two entries in Table 3.4 give the total $Z''l$ (assuming no manufacturing variations) and the effective $(Z''l)_{eff}$ (assuming 1-MHz variations) for the four modes listed.

The linac lattice is modeled by a 9.4-meter half-cell-length lattice with a phase advance per cell of 120° for the first-pass energy. The recirculator is assumed to offer an identity transformation. Without

any lattice optimization, a maximum value of $\Sigma|B| = 56.0$ cm/(MeV/$c$) was found. Insertion of this value and the effective $(Z''l)_{\text{eff}}$ of Table 3.4 into Equation (3.6) yields lower bounds on threshold currents, between 1.5 and 3.3 mA/beamlet for the four Cornell modes.

These values represent a worst-case analysis, with effectively all passes assumed to have time delays yielding maximal coherence and with the cavities localized on the largest value of $B_{ij}$. However, even these worst-case thresholds exceed the design current of 200μA by nearly an order of magnitude.

**Breakup at the Stanford Recyclotron**

A standing wave theory of multipass regenerative beam breakup of Vetter was confirmed by a series of experiments performed at the Stanford superconducting recyclotron. Although the theory contains both singlepass and multipass effects in the form of integrals over the cavity fields, it was found that an impulse approximation of the multipass effects alone was sufficient to describe the instability thresholds. This limit is consistent with the analysis of the previous section and the work of Herminghaus. The Stanford experiments were well described by the threshold condition

$$I_{\text{th}} = \frac{1}{KQ\ (R/\gamma_{\text{in}})}$$

$$R = \sum_j \sum_{i<j} R_{xx}^{ij}\ \frac{\gamma_{\text{in}}}{\gamma_{\text{in}} + (i-1)\gamma_0} \sin\ (\delta_{j-1} - \delta_{i-1}) \tag{3.8}$$

where $\delta_u$ is a phase shift for the $u^{\text{th}}$ recirculation, $\gamma_{\text{in}}$ is the injection energy (in units of rest mass), $\gamma_0$ is the energy gain per pass, $R_{xx}^{ij}$ is the transfer matrix element (in TRANSPORT notation), and $K$ summarizes the cavity field integrals. For the strongest mode at 1863 MHz

$$K = 4.0 \cdot 10^{-5} \frac{N^2}{L_s}\ (\text{A-m})^{-1} \tag{3.9}$$

where $N$ is the number of cells active for the mode and $L_s$ is the effective length of the mode. From the definition of $K$ in terms of field integrals as given by Vetter, we have

$$\frac{Z''l}{Q} = 2\left(\frac{mc^2}{e}\right) K \frac{\omega}{c} \tag{3.10}$$

and the equivalence of equations (3.6) and (3.8). Numerically,

$$Z''/Q = 11.7 \cdot 10^4\ \Omega/\text{m}^3 \tag{3.11}$$

is obtained for the 1863 MHz mode of the Stanford structure. This value is comparable to the values found for the Cornell structure itemized in Table 3.4. The damped HOM $Q$'s at Stanford, however, were at the $10^7$ level as compared to the $10^4$ level for the Cornell cavities, and are primarily responsible for observed threshold currents of about 10 μA.

In summary, the experience with multipass regenerative beam breakup at the Stanford recyclotron indicates that the phenomenon is described by conditions of the form of equations (3.6) or (3.8) with transverse impedances $Z''$ consistent with the values listed in Table 3.4. On the other hand, because of the high $Q$'s associated with the Stanford structures, there was not mode frequency overlap as would be the case for the proposed CEBAF cavities. Some uncertainty therefore remains concerning the effects of cavity-to-cavity mode frequency variations and the distribution of interacting cavities along the length of the linac in improving the threshold currents. These issues among others have been addressed with a computer simulation which is discussed in the next section.

**Computer Simulation of Beam Breakup**

From the Stanford experience it appears that the dominant mechanism for multipass regenerative beam breakup can be modeled by an impulse approximation. This is also the regime appropriate to single-pass cumulative beam breakup as observed in SLAC where extensive computer modeling has been

successful. The SLAC program (authored by R. Helm) has been modified at CEBAF to include multipass recirculation with both random and systematic bunch displacement as initial conditions. For the single-pass cumulative breakup the chief diagnostic is the final bunch position at the output of the linac. A threshold is determined by a scraping condition at the beam pipe wall. For multipass regenerative breakup, there will be exponential growth of cavity fields. For a particular amplitude of initial condition, beam displacement may remain small for the duration of the run even though cavity fields are growing exponentially. However, for CW operation these fields will eventually grow to the point of producing beam loss. Therefore, the chief diagnostic in determining threshold currents is the observation of exponential growth of the cavity wakefields.

The analytic work as presented above represents a worst-case analysis in that time delays were assumed to conspire for maximum effect and the largest values of the machine transverse transfer function were taken even though the cavities are uniformly distributed along the linac. The simulation offers the possibility to study more realistic distributions of time delays and lattice functions, and, in addition, allows for investigation of the effects of modal frequency spread.

The analysis summarized in Equation (3.6) is appropriate to a localized, single mode with no frequency spread. Since the threshold current for this case can be simply calculated including exact pass-to-pass time delays, it offers a clear test of the simulation. Both 2-pass and 4-pass threshold current values were calculated for a FODO linac lattice structure with a mode frequency of 1890.0 MHz. These configurations were also modeled with the simulation code. Simulation and analytic threshold current values were found to agree well within a factor of two. Figure 3.3 shows results for a four-pass configuration with a localized transverse impedance equivalent to 1 m of CEBAF structure with no mode frequency variation.

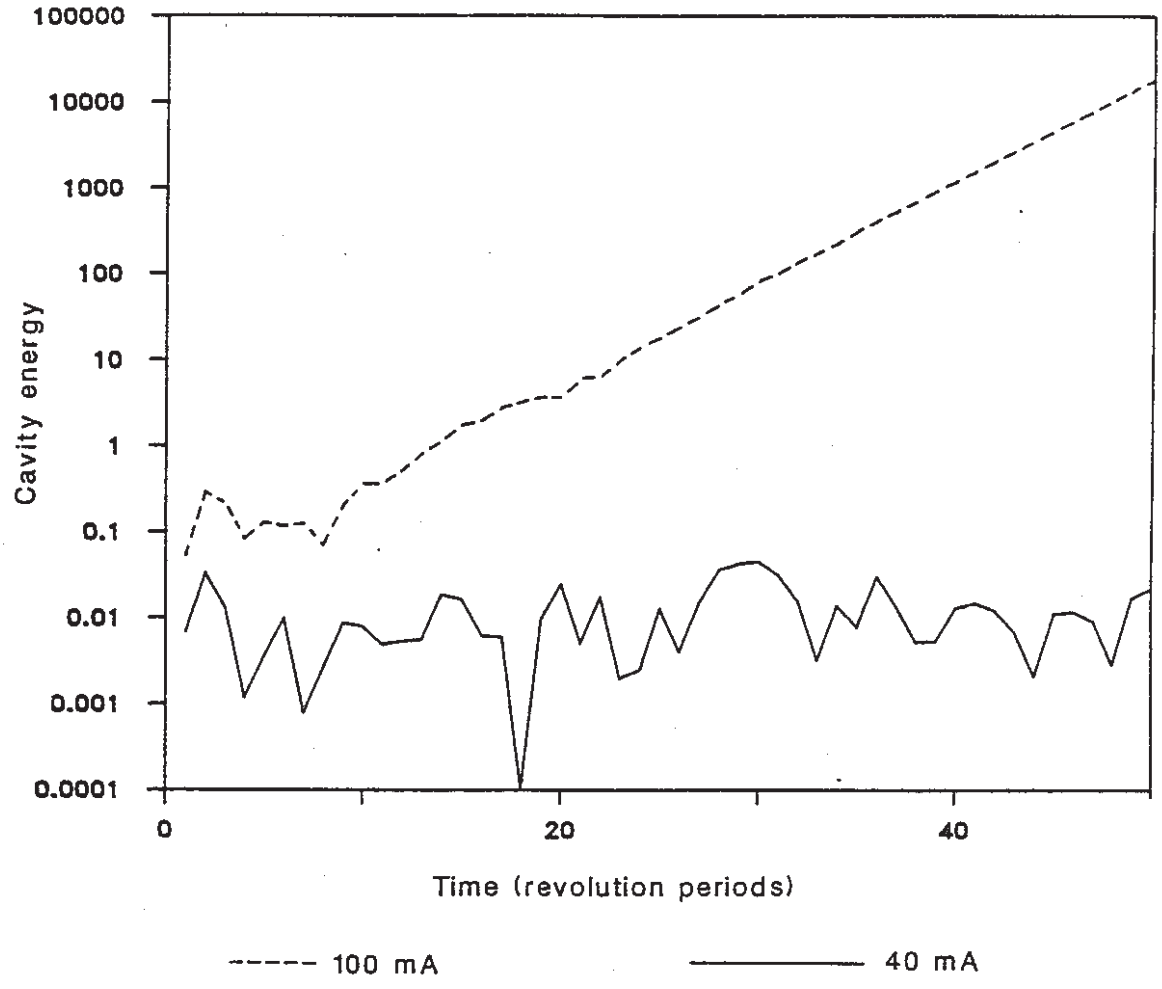


**Figure 3.3.** Simulation of beam breakup driven by localized structure. Analytic threshold current is 70 mA.

A second study compared the single 1890.0 MHz ($Q$ = 32000) threshold with that of 100 modes uniformly distributed between 1890.0 and 1891.0 MHz. Each mode was given 1% of the single-mode transverse impedance and all were localized at the same point on the lattice. The threshold current has been found to be a factor of 6 higher for the distributed modes and is in reasonable agreement with the factor-of-5 estimate included in the worst-case analysis presented earlier. This result firmly establishes the benefits of mode frequency spread in easing beam breakup.

Runs were performed to model the full CEBAF cavity array distributed along the linac with a FODO lattice. Run lengths corresponded to over 200 damping times of the cavity modes. Threshold currents for the four Cornell cavity modes are summarized in Table 3.5. All threshold currents are greater than 10mA/beamlet.

**Table 3.5**
**Computer Simulation Estimates of Beam Breakup Thresholds**

| | 1888 MHz | 1969 MHz | 2086 MHz | 2110 MHz |
|---|---|---|---|---|
| $I_{th}$ | 12 mA | 13 mA | 22 mA | 11 mA |

A final set of runs was performed to observe any interaction of modes of significantly different frequency. Each of fifty "supercavities" was allowed to have four modes at frequencies of 1890, 1969, 2108, and 2120 MHz with no cavity-to-cavity frequency spread. Each mode was given an impedance equal to the 1890 mode. The observed threshold current and growth rate were within 25% of single-mode values and do not indicate any significant mode interaction.

**Summary**

A computer model of multipass regenerative beam break up that includes mode frequency spread and lattice variation has been developed. For a single, localized mode, this simulation is found to be in agreement with analytic estimates which have been successful in describing beam breakup in existing recirculating linacs. For the CEBAF design, a threshold current for beam breakup in excess of 10 mA/beamlet is found. This estimate exceeds the design goal of 200 μA by more than an order of magnitude. In addition, further improvements in threshold behavior can be expected with optimization of recirculator design.

## 3.4 Radiation and Safety

**Overview**

Any electrons lost from the electron beams, normally confined within the accelerator beam pipes and cavities, will constitute a radiation source. A major source is the beam dump where the electron beams are finally deposited after passing through the experimental target. Electrons, when they strike something such as the sides of the beam pipe, magnets, the experimental target, the beam dump and so forth, produce penetrating radiation which must be shielded. Based on assumed electron losses, the facility is shielded so that levels of radiation external to the shield and hence the exposure of workers and members of the public is below accepted limits. In general, specifications for thick shielding against this radiation are dominated by the very penetrating high-energy neutron component. Although the dose equivalence for the high-energy neutron component is a relatively small fraction of the total yield, it requires greater thicknesses of shielding to reduce it to the low levels required in occupied areas.

In order to specify adequate shield thicknesses it is necessary to define certain basic parameters, which can be summarized as follows:

1. loss term,
2. source term for each contributing type of radiation (with high-energy neutrons dominating the specifications for thick shielding, as mentioned above),
3. external dose to be achieved, and
4. removal mean free path for the appropriate source term.

The loss term (1) is the most difficult to specify with any certainty in any location other than beam dumps, which are intended to cope with the full beam power in any given channel. The loss term will be discussed below under each of the accelerator component parts. The source term (2) is a complicated means of converting loss into radiation dose in such a way that it can be attenuated by a given quantity approximately defined in the case of high-energy neutrons by a constant inelastic cross section for the shield material. In actual practice the source term and relevant attenuation lengths are largely based on experimental measurements. Parameter (3) is the external dose to be achieved by the shielding. It is necessary to design shielding to achieve radiation levels in occupied areas lower than the limits for radiation doses to people laid down by appropriate authorities. For CEBAF we have designed to radiation dose levels of 1 rem/year just out-side shielding (compared with the limit for occupational personnel of 5 rem/year). We have not included any allowance for occupational factors, thus giving a further measure of safety. Radiation limits to individual members of the public are lower than for people who work with radiation, and dose limits for prolonged exposures of the population are lower still at 100 mrem/year. Therefore, CEBAF will be designed and operated so that dose rates at the property boundary will be less than 100 mrem/year.

We consider each part of the facility separately:

*Beam Dumps*

These, although requiring the most shielding, provide the simplest beam loss term—the total average beam power of the channel which the beam dump serves. The main beam dumps A and C will be adequately sized to cope with the *full* machine power. Beam dump B is sized to cope with 1% of the full beam power since end station B will only be used for low-intensity experiments. The beam dumps will incorporate specific safety features to overcome any problems of dump coolant failure or other malfunction. The assumed full accelerator capability is 1.2 MW corresponding to 6 GeV, but for shielding purposes we take an annual average of 600 kW or $2 \times 10^{22}$ electrons accelerated to 6 GeV per year.

*End Stations*

The major loss in the end stations arises from electrons scattered from the experimental targets. Furthermore, the end stations have to be large to accommodate the angular movement of the spectrometers. The two-meter-thick concrete walls and one-meter-thick roof are designed to achieve the required external radiation levels and yet permit experimenters reasonable freedom to perform a broad mix of experiments. Typical experiments require the insertion of a thin piece of material into the electron beam so that the various electron nucleus events may be studied. However, these thin targets will give rise to some scattering of the electrons so that not all the electron beam finally ends up on the beam dump. Instead, a small fraction of the beam is unavoidably lost in the end station itself. The amount of beam scattered depends on the thickness of the experimental target (the thicker the target, the greater the fraction scattered) and the energy of the incident electron beam (the lower the energy, the greater the fraction scattered). It is of interest that for a target of given thickness, the overall source terms get larger as the energy reduces since the fraction of electrons scattered increases faster than the reduction in total beam power. The average power loss in the end stations per mrem/year on the nearest property boundary is 4 watts for A and C. For end station B the power loss must be restricted to 0.05 watts to achieve the 1 rem/year just outside the shield wall with a resulting boundary dose less than 10 mrem/year. These calculated power losses permit a reasonable average mix of experimental conditions, while keeping boundary dose rates less than the limit of 100 mrem/year.

*The Linac*

It is not expected that the linac will suffer significant continuous loss of electrons. It has a large aperture and the beam has a very small emittance. The pressure in the superconducting cavities will be low. Thus there will be insignificant losses from gas scattering. Other possible mechanisms for beam loss are being studied, but it is thought that any continuous beam loss will be very small. On the basis of experience with other accelerators such as SLAC, and given the good beam and aperture of CEBAF, a loss term of 0.05% has been used for linac shielding. This is a very conservative assumption, in that it exceeds any conceivable estimate of *continuous* beam loss by several orders of magnitude. This aspect is considered in Section 5.3.

*Arcs and Beam Switchyard*

Again on the basis of the low beam emittance and good aperture, a continuous loss term of 0.5%, based on experience from SLAC, is considered to be highly conservative. A similar loss term is used for

the beam lines and switchyard. Again, the highest fractional beam loss would occur during tune-up (i.e., low-current operation) and would therefore lead to a low total loss.

In steady state lower relative loss terms are to be expected. Most of the loss would be forced to occur by judiciously placed halo scrapers placed in spreaders, halfway through recirculation arcs, and in recombiners. These would eliminate halos corresponding to less than $10^{-5}$ of the total beam, force these losses to occur locally (where they are most easily shielded), and prevent any further loss downstream.

**Shielding**

A description of the shielding structure is given in Chapter 11. A summary of the numbers used for shielding is given in Table 3.6.

**Table 3.6**
**Beam Loss and Shield Thickness**

| Component | Loss (%) | Energy (GeV) | Average annual loss (power) | Average annual loss (electrons/year) | Shield thickness (ft) |
|---|---|---|---|---|---|
| Beam dumps A & C | 100 | 6 | 600.0 kW | $2 \times 10^{22}$ | 31 (earth) |
| Beam dump B | 1 | 6 | 6.0 kW | $2 \times 10^{20}$ | 22 (earth) |
| Arcs & BSY | 0.5 | 6 | 3.0 kW | $1 \times 10^{20}$ | 21 (earth) |
| Linac | 0.05 | 6 | 0.3 kW | $1 \times 10^{19}$ | 17 (earth) |
| End stations A & C | | | 4.0 W* | | 6.6 (concrete) |
| End station B | | | 0.05 W | | 2 (concrete) |

*per mrem (boundary)

Note: These beam loss terms are averages assumed for shielding calculations only.

**Monitoring**

It must be stressed again that during commissioning, beam currents will be kept low and only increased slowly toward maximum after stable conditions have been fully established. Any major fault conditions or excessive beam loss will be detected by installed instrumentation. These fast-response instruments will rapidly cause the injector to be disabled and shut the beam off. Beam diagnostic and radiation loss instruments are described in Section 8.2.

In addition to the beam-loss monitors, other radiation monitors will be installed in occupied areas around the facility. These instruments are designed to measure radiation at the levels designated for the given area. They will not only operate as stand-alone instruments, but will also provide data to a central monitoring/recording location; they will also have level alarms to warn of any high external radiation conditions which might occur under exceptional conditions. Monitors at site boundary will also be provided. The combination of shielding and monitoring provides one layer of the total safety system. Other layers will involve the definition of categories of radiation areas and the necessary administrative procedures to control the entry of personnel. Where high radiation areas inside shielding are concerned, all access ways will be fitted with a high-reliability system of locked and interlocked closures.

## 3.5 Technology Base

**Introduction**

Radio-frequency superconductivity is an attractive technology for several types of accelerators, from heavy-ion machines to electron machines. The technology for low-beta acceleration (heavy ions) is sufficiently different from that for machines with $\beta = 1$ to allow this discussion to concentrate on the

latter. However, experience operating superconducting low-beta systems will be mentioned where it is applicable.

Superconducting accelerating structures with $\beta = 1$ have intrinsic advantages for several types of electron accelerators: storage rings, CW linacs, TeV-scale linear colliders, and free-electron lasers. The basic element of the accelerating structure for each of these applications is a superconducting cavity consisting of one to tens of cells, each half as long as the RF wavelength. For the past 20 years, R&D on such cavities has focused on bringing their performance to a useful level with regard to accelerating gradient and current-carrying capacity. Simultaneous efforts have aimed at developing a cavity fabrication process capable of producing cavities that consistently meet performance specifications.

**Electron/Positron Storage Rings**

The main recent motivation for the development of superconducting accelerating cavities has come from interest in high-energy electron/positron storage rings. For these machines, superconducting cavities offer a practical means of compensating for synchrotron radiation losses, which increase with the fourth power of the energy for a given machine. Several laboratories (CERN, DESY, Cornell, KEK) operating or planning high-energy electron storage rings have thus invested significant effort and funds in developing RF superconducting technology. Within the past two years, this effort has paid off, with all four laboratories fabricating cavities that have achieved accelerating gradients exceeding 5 MV/m. Table 3.7 summarizes the recent progress.

**Table 3.7**
**Laboratory Results on Multi-Cell Cavities Designed for Storage Ring Use**

| Lab | Year | MHz | Cells | $E_{max}$ (MeV/m) | $Q_0$ | $E_a$ (MeV/m) | Coupling holes | Couplers | Limitation |
|---|---|---|---|---|---|---|---|---|---|
| CERN | 1983 | 500 | 5 | 5.0 | $0.74 \times 10^9$ | 5.0 | Yes | No | Defect,* main coupling hole |
| CERN | 1985 | 352 | 4 | 6.0 | $3.3 \times 10^9$ | 5.0 | Yes | No | |
| Cornell | 1984 | 1500 | 5 | 8.9 | $7.0 \times 10^9$ | 8.9 | Yes | Yes | Defect, location undetermined |
| Cornell | 1984 | 1500 | 5 | 8.0 | $3.0 \times 10^9$ | 8.0 | Yes | Yes | Defect, cell 3, 2.5 cm from eq. |
| Cornell | 1984 | 1500 | 5 | 15.3 | $2.0 \times 10^9$ | 15.3 | Yes | Yes | Defect or field emission, cell 1 |
| DESY | 1983 | 1000 | 9 | 6.6 | $0.9 \times 10^9$ | 6.6 | No | No | Defect or electron loading |
| DESY | 1983 | 1000 | 9 | $> 6.7$ | $0.9 \times 10^9$ | 6.7 | No | No | Available power |
| KEK | 1983 | 508 | 3 | $> 5.2$ | $0.5 \times 10^9$ | 4.0 | Yes | No | Available power |

*Spots of high resistivity, such as weld imperfections, inclusions, impurities, or surface contamination.

Since August 1983, four superconducting cavities have been tested in storage ring beams at DESY, KEK, and Cornell. They have yielded accelerating gradients up to 6.5 MV/m, exceeding the goal of 5 MV/m, and have handled currents up to 22 mA. This progress is noteworthy, since achieved in-beam gradients were only around 2 MV/m just two years ago.

As a consequence, several laboratories now have definite plans to use superconducting cavities in electron storage rings on a large scale (Table 3.8). CERN and DESY expect to issue bid packages soon. European industry—Interatom (Siemens) and Dornier (Daimler-Benz)—is prepared to respond.

Table 3.8
Plans for the Application of SC Cavities to Storage Rings

| Lab | Storage ring | Energy (GeV) | Freq. (MHz) | Cells per cavity | Cavities | $E_a$ (MeV/m) | $Q$ |
|---|---|---|---|---|---|---|---|
| CERN | LEP I | 55–62 | 352 | 4 | 8–16 | 5–7 | $3 \times 10^9$ |
| CERN | LEP II | 95–104 | 352 | 4 | 384 | 5–7 | $3 \times 10^9$ |
| DESY | HERA | 30 | 500 | 4 | 16 | | |
| KEK | Tristan | 33–35 | 508 | 5 | 40 | | |
| KEK | Tristan | 40 | 508 | 5 | 120–144 | | |

**CW Electron Linacs**

Experience with superconducting CW linacs began about 21 years ago with a pioneering effort at Stanford's High Energy Physics Laboratory (HEPL). Because this machine never achieved its design specifications, the technology has been largely ignored in the United States. However, much has been learned from the development and operation of that facility, and its achievements are noteworthy. Specifically, HEPL demonstrated the successful operation of a large 1.8 K refrigeration system, it achieved recirculation, and it produced a beam of outstanding quality (with low emittance and momentum spread).

With its 34 meters of accelerating structure, HEPL is the largest superconducting electron linac operating to date. Since 1976 the University of Illinois has been operating a superconducting microtron using one 6-meter HEPL linac section. Currently, the Universities of Wuppertal and Darmstadt in West Germany are building a small recirculating CW linac. Cavities produced by industry for this machine within the past year consistently achieve gradients in excess of 5 MV/m.

HEPL's problems, namely low gradient and low current capacity, are both understood and solved today. The gradient was limited to just over 2 MV/m by multipactoring, a regenerative process caused by secondary emission. The current capacity was limited to 92 μA for two passes and 20 μA for three passes (confirmed well by theory) by transverse particle motion induced by inadequately damped higher order modes (beam breakup). Solutions to these problems are described below.

**Advances in Superconducting RF Technology**

The problems that plagued HEPL all relate to the design and processing of the superconducting cavities. Over the past few years there have been significant improvements in these areas:

*Optimization of Shape and Coupling*

- Spherical or elliptical cavity shape prevents serious multipactoring.
- RF coupling and higher-order-mode damping at the beam pipe prevent cell wall penetrations, which cause field enhancement and can also induce local multipactoring.

*Better Quality Superconductor*

- Improved niobium purity may reduce the density of defects and does improve thermal conductivity, which stabilizes remaining defects against driving the cavity normal.

*Better Manufacturing Procedures*

- "Rhombic raster" or defocused electron beam weld minimizes weld defects.
- Improved cleanliness in assembly reduces dust contamination.
- Better surface inspection and cavity testing with thermometry allow dirt and defects to be identified and repaired.
- Increased rinsing speed following acid cleaning reduces the formation of insoluble compounds.

*Understanding and Cure of Current Limitations*

- Deliberate heavy damping of higher order modes significantly decreases excitation of transverse deflecting modes of the beam, thereby allowing significantly increased currents to be accelerated.

**Cavity Performance**

To build a CW superconducting linac, the following major issues related to the cavity and its performance must be addressed:

1. accelerating field strength and $Q$ of the cavity,
2. long-term performance,
3. tuning of the cavity and RF coupling to the cavity,
4. RF frequency, and
5. damping of higher order modes and beam breakup.

*Accelerating Field Strength and Q of the Cavity*

Since the HEPL experience, it has been recognized that SC linac technology would become practical when accelerating gradients of 5 MV/m or higher could be achieved routinely. In a paper presented at the 1985 Accelerator Conference, H. Piel (Wuppertal) observed that groups working on RF superconductivity at various frequencies and at several laboratories all have achieved this goal (Table 3.9).

**Table 3.9**
**Performance of Superconducting RF Cavities**

| Laboratory | CERN | | | KEK | DESY | Cornell | Wuppertal-Darmstadt | |
|---|---|---|---|---|---|---|---|---|
| Accelerator | LEP | | | TRISTAN | PETRA/HERA | CESR | 130-MeV Recyclotron | |
| Material | Nb | Nb | Nb on Cu | Nb | Nb | Nb | Nb | $Nb_3Sn$ |
| Frequency in MHz | 350 | 500 | 500 | 500 | 1000 | 1500 | 3000 | 3000 |
| Operating temperature | 4.2 K | 4.2 K | 4.2 K | 4.2 K | 4.2 K | 1.8 K | 1.8 K | 4.2 K |
| *Single-cell cavities* | | | | | | | | |
| $E_a$ (MV/m)** | 10.8 | 13.0* | 10.8 | 7.6* | 5.5 | 22.8* | 23.1* | 7.2 |
| $Q$ at $E_a$ 1985 | $1.8 \times 10^9$ | $0.7 \times 10^9$ | $0.4 \times 10^9$ | $0.6 \times 10^9$ | $5 \times 10^8$ | $2.5 \times 10^9$ | $1.2 \times 10^9$ | $1.1 \times 10^9$ |
| $E_a$ (MV/m)* | 4.7 | 7.6 | — | 6.5 | 5.5 | 8.5 | 10.0 | — |
| $Q$ at $E_a$ 1983 | $5 \times 10^9$ | $3.6 \times 10^9$ | — | $4.1 \times 10^9$ | $5 \times 10^8$ | $7 \times 10^9$ | $4 \times 10^9$ | — |
| *Multicell results* | 4 cells | 5 cells | — | 3 cells | 9 cells | 5 cells | 5/20 cells | 5 cells |
| $E_a$ (MV/m) | 7.5* | 5.0 | — | 5.8 | 5.5 | 15.3* | 12.3/7.4 | 4 |
| $Q$ at $E_a$ 1985 | $2.2 \times 10^9$ | $0.7 \times 10^9$ | — | $0.6 \times 10^9$ | $0.5 \times 10^9$ | $2.2 \times 10^9$ | $3.5/1.2 \times 10^9$ | $4.5 \times 10^9$ |
| $E_a$ (MV/m)** | — | 2.8 | — | — | 2.5 | 5.4 | 3.7 | — |
| $Q$ at $E_a$ 1983 | — | $1 \times 10^9$ | — | — | $5 \times 10^8$ | $4.5 \times 10^9$ | $1 \times 10^9$ | — |

*Cavities fabricated from high-thermal-conductivity niobium **Under continuous wave operation
Source: H. Piel, Wuppertal.

He concluded, therefore, that it would be conservative to design a superconducting accelerator based on niobium cavities with a gradient of 5 MV/m and a $Q$ of a few times $10^9$. This advice is confirmed by recent results from Cornell, where the latest four 5-cell cavities (1500 MHz) all achieved gradients exceeding 6 MV/m (average: 8.3 MV/m).

*Long-Term Performance*

Experience shows that superconducting cavities perform for long periods without degradation of gradient or $Q$ (Table 3.10). Cavities have been kept in-beam for modest to long periods at DESY, Cornell, CERN, and HEPL, Illinois, and Argonne (low beta), without adverse effect other than due to

a few specific accidents. The most impressive test, however, was an accelerated lifetime test done at Cornell in 1974/75. The vacuum in the Cornell synchrotron was degraded deliberately to expose the cavity to the equivalent of 20 years of operation at $10^{-10}$ torr ($2 \times 10^{-9}$ torr-years of gas exposure). The performance of the cavity decreased by only about 10%. On one occasion this same cavity was accidentally exposed to titanium dust from a sputter ion pump. The 3 performance dropped drastically in gradient and $Q$. On examination, the inner surface of the cavity was found to be fully coated with titanium oxides and nitrides. After washing with detergents and rinsing with solvents, but without acid cleaning, the cavity regained its original gradient and $Q$.

**Table 3.10**
**In-Beam Experience with Multi-Cell SC Cavities**

| Lab | Machine | Number of cavities | Electrical length (m) | Date |
|---|---|---|---|---|
| **Routine Operation** | | | | |
| Stanford | HEPL-SCA | 7 | 34 | 1972–present |
| Illinois | Microtron | 1 | 6 | 1976–present |
| CERN | SPS (separator) | 2 | 5.5 | 1977–79 |
| Argonne | ATLAS | (low beta) | 7 to 13 | 1978–present |
| Stonybrook | Linac | (low beta) | 7 | 1984–present |
| **Lifetime and Performance Tests** | | | | |
| Cornell | Synchrotron | 1 | 0.6 | 1974–75 |
| Cornell | CESR | 4 (separate) | 0.5 (ea) | 1982, 1984 |
| Karlsruhe | DESY/PETRA | 1 | 0.3 | 1982 |
| CERN | DESY/PETRA | 1 | 1.5 | 1983 |
| DESY | PETRA | 1 | 1.5 | 1985 |

*Cavity Tuning and RF Coupling*

Superconducting accelerating cavities, properly coupled and loaded, are remarkably broad band. They can be tuned mechanically, simply by squeezing or stretching the structure. For RF coupling, it is essential not to disturb the symmetry of the cells; thus all coupling is done at the ends of the cavity, as close as possible to the beam axis. Waveguides are used on the 1500-MHz cavities, and broad-band coaxial couplers are being developed for lower frequencies at CERN and DESY.

*RF Frequency*

Cavities operating at RF frequencies between 350 MHz and 3000 MHz have been fabricated successfully (Table 3.9). For CEBAF, we have selected a frequency of 1500 MHz. This choice represents a satisfactory compromise between the combined criteria of fabrication ease, material costs, and quality, all of which improve with high-frequency (small) cavities, and operational issues, which favor low-frequency (large) cavities. Dominant operational issues are deflecting impedance, which causes beam breakup and increases as the cube of the frequency (for similar shapes of cavities), and the number of cavities and controls required per unit length of the accelerator. An additional factor favoring 1500 MHz is that Cornell has developed prototype cavities at this frequency that meet or exceed all specifications required for CEBAF. The Cornell group is willing to collaborate with CEBAF and assist in transferring their technology to industry.

*Damping of Higher Order Modes and Beam Breakup*

Engineering to suppress the $Q$ of all important HOMs has succeeded in obtaining typical loaded HOM $Q$'s of $10^4$ in cavities developed at Cornell. These $Q$'s are approximately 1000 times lower than those achieved in the HEPL structure. This is accomplished by using special couplers at one end of the

cavities to extract HOMs and by using the fundamental power coupler to extract HOMs at the other end. According to measured and computed HOM impedances and external $Q$'s, existing Cornell cavities with HOM couplers could support recirculating CW linac output currents around 10 mA or higher (after four passes), with no beam breakup (see Section 3.3). The CEBAF baseline output current is 200 μA.

**Future Developments**

As a result of ongoing and future R&D, improvements in achievable gradients are inevitable. Currently, gradients are limited by defects in the superconductor or by field emission; thus the achieved performance of 5 to 15 MV/m in multicell cavities is far below the theoretical limit (~50 MV/m for niobium; ~80 MV/m for niobium-tin). As superconductor quality improves, achieved gradients will rise.

Within the next decade, Nb (or $Nb_3Sn$, with its high critical temperature) promises to achieve gradients between 15 and 25 MV/m. Corresponding increases in residual $Q$ would be useful to minimize RF losses in the cavity, thereby avoiding increased need for refrigerator power. By replacing CEBAF's cavities when the technology is ready, the electron energy of the linac can be increased significantly.

# 4. Machine Vacuum Components

## 4.1 Introduction

This chapter includes an overall description of machine vacuum components: the accelerating cavity and cryostat, and the vacuum system for the injector, linac segments, recirculation arcs, and beam transport lines.

## 4.2 Accelerating Cavities

**Overview**

CEBAF uses superconducting radio-frequency (RF) cavities as the basic element for accelerating the beam to its final energy of 0.5 to 4.0 GeV. The principal characteristics of these cavities are that they operate continuous wave (CW) at $\geq$ 5 MV/m with a residual $Q \geq 3 \times 10^9$. The high $Q$ is required to minimize the heat dissipation that must be removed by the cooling system. For purposes of the work breakdown structure (WBS), the cavities include the welded cavity units and the reference probes that are installed on these cavities.

**Physical Description**

The niobium superconducting RF cavities are identical in design to cavities developed and tested at Newman Laboratory of Nuclear Studies at Cornell University. A pair of CEBAF-Cornell accelerating cavities is shown in Figure 4.1. These cavities have five cylindrically symmetrical accelerating cells, with a waveguide at one end of the cells which acts as the fundamental power input coupler and as a coupler for extracting some of the higher order modes (HOMs) generated by the beam current. At the other end of the cavity, two waveguides serve as couplers to extract higher order modes; these waveguides are

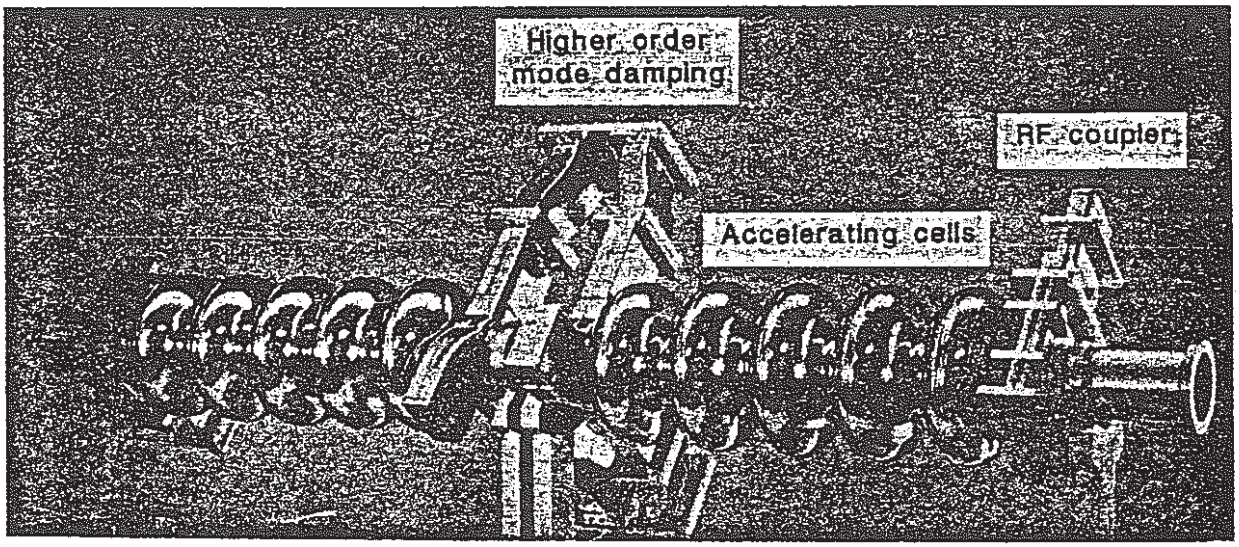


**Figure 4.1.** A pair of CEBAF-Cornell accelerating cavities in the configuration used at Cornell.

perpendicular to each other and to the beam axis. The cavities are referred to as "elliptical" because, in dorsal section, the inner surfaces of the cells comprise elliptical segments. The operating frequency is 1497 MHz, and each cell has a length of 0.1 m. CEBAF will use 200 of these cavities in each of two parallel linac segments, plus 18 cavities in the injector.

The functional characteristics of these cavities are described in the following section. Their fabrication, initial inelastic tuning, and processing are described in Section 4.8. Assembly and testing are described in Section 4.9. The heat dissipated in these cavities is described in Section 4.10.

**Functional Characteristics and Basis for Selection**

All research and development on the CEBAF-Cornell cavities necessary to meet all of CEBAF's requirements has been completed. Four prototypes of this cavity have been built at Cornell University, and all of these cavities have met or exceeded all requirements for CEBAF (Table 4.1). The final verification of the suitability of these cavities for use in CEBAF was provided by a beam test of a pair of these cavities in the CESR $e^+e^-$ storage ring at Cornell in November 1984.

**Table 4.1**
**Parameter Choices for CEBAF**

| Parameter | CEBAF Requirement | Demonstrated Capability CEBAF-Cornell Cavity |
|---|---|---|
| Frequency [MHz] | 900–3000 | 1500 |
| Gradient [MV/m] | 5.0 | 8.2 (avg.) |
| Residual $Q$ | $3 \times 10^9$ | $3.9 \times 10^9$ (avg.) |
| Cavity current transport [μA] | 800 | 22,000 |
| Output current, BBU limit [μA] | 200 | 10,000 |
| Power into beam [kW/m] | 4 | 26 |
| Input coupling, $Q_{ext}$ | $2.2 \times 10^6$ | 7,000 to $1 \times 10^8$ |
| HOM power extraction requirement [W/m] | < 0.5 | > 280 |

**Frequency**

Since the beam extraction system can remove every third microbunch for delivery to a particular end station, and since it is desired that the bunches arriving at a particular end station be not more than 3.3 ns apart, the CEBAF RF frequency must be at least 900 MHz. An upper limit of 3000 MHz was established because no developmental work has been done on practical superconducting accelerating structure above this frequency. Keeping the number of modules from becoming too large favors low frequencies, as does the fact that low frequencies permit the use of somewhat higher cryogenic temperatures. High frequencies are favored by the ease of handling individual modules and avoiding their contamination, and by the fact that the lower cavity surface area associated with higher frequencies reduces the probability that there will be a significant defect present on the surface. The Cornell prototypes operate at 1.5 GHz, and this has been selected as the frequency of the CEBAF-Cornell cavities.

**Gradient**

The accelerating gradient specified for the CEBAF-Cornell cavities is 5.0 MV/m. In a total of ten tests conducted at Cornell on the four prototypes, each with a separate surface treatment, the average gradient reached was 8.2 MV/m; these ten tests represent all (including the worst) tests conducted on these cavities following the removal of initial design defects. Among these ten tests, the first cooldown of each cavity met or exceeded the CEBAF gradient specification. The accelerating field achieved in each of the four prototypes was between 6.0 and 15.3 MV/m (Figure 4.2), all exceeding the CEBAF requirement of 5 MV/m. The beam test in CESR demonstrated the feasibility of reaching gradients in excess of 5 MV/m in the presence of substantial beam current. Since the gradient in each cavity at CEBAF will be controlled separately (see Chapter 6), the maximum capability of each cavity can be fully exploited.

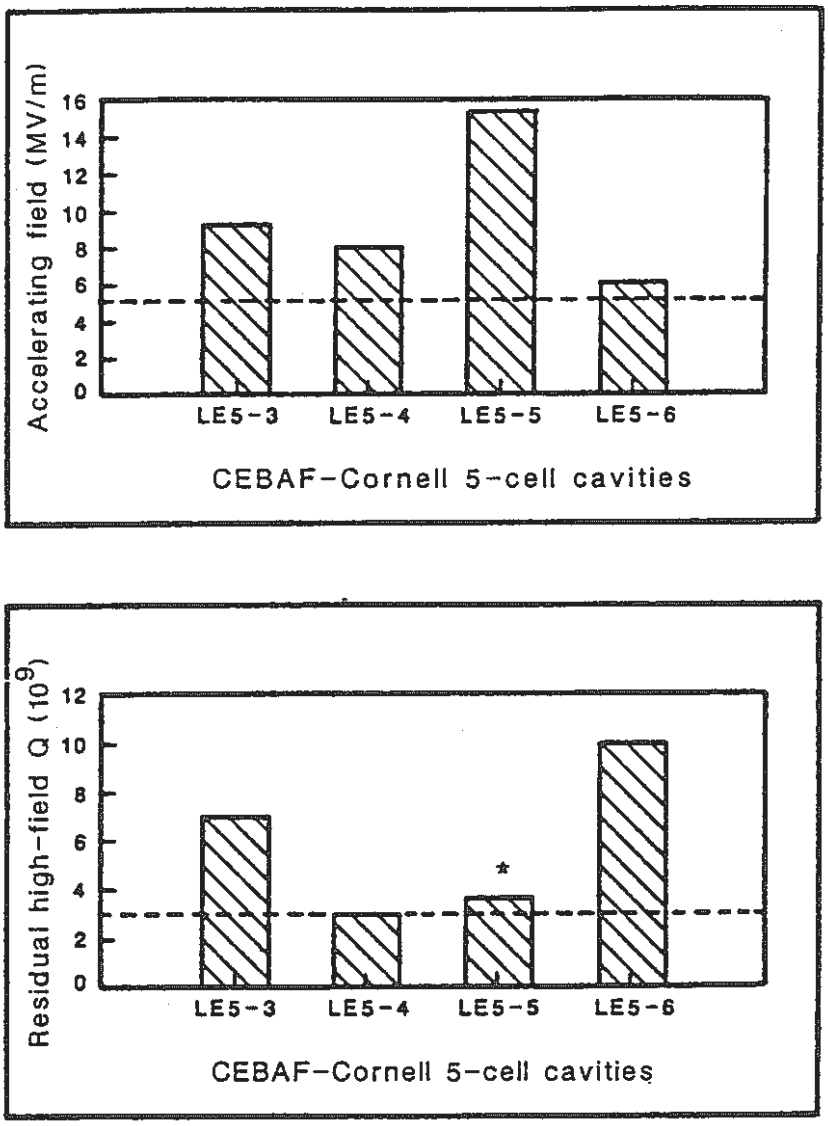


**Figure 4.2.** Residual high-field $Q$ and accelerating field. The dashed lines represent design goals. The residual $Q$ shown for LE5-5 (marked by an asterisk) was measured at 12.0 MV/m; all others were measured at the gradient shown.

**Residual $Q$**

The RF losses in a superconducting cavity consist of two components: residual losses and BCS (Bardeen, Cooper, and Schrieffer) losses, as discussed in Section 4.10. The CEBAF requirement for the residual $Q$ is $3.0 \times 10^9$. The average residual $Q$ obtained in the ten independent tests at Cornell was $3.9 \times 10^9$ at high field. The residual $Q$ obtained in each of the four prototype cavities, together with the corresponding gradient, is shown in Figure 4.2. These values range from $3 \times 10^9$ to $10 \times 10^9$, equaling or exceeding the CEBAF requirement of $3 \times 10^9$. The beam test in CESR also demonstrated the ability of these cavities to exceed the required $Q$ in the presence of the beam.

**Current Transport**

The current-handling capability (e.g., without cavity breakdown) required for CEBAF is 200 μA per beamlet times 4 beamlets, or 800 μA. The current sustained by the cavity in the CESR beam test was 22 mA.

The output current required without beam breakup in CEBAF is 200 μA. Based on the known impedances of the CEBAF-Cornell cavity, the beam breakup threshold exceeds 10 mA, as discussed in Section 3.3. The heavy damping achieved for the important higher order modes in this cavity was developed as follows.

**Higher Order Mode Suppression**

The HOM coupling on this cavity was designed to provide heavy damping of HOMs, with particular emphasis on those with high intrinsic impedances *(r/Q)*. The lengths of the shorted stubs on both the HOM coupler and the fundamental power coupler were determined on this basis, as were the dimensions and locations of the couplers. Intrinsic impedances and $Q_{ext}$ values were measured using bead pulls and probes on copper models, and computed using the programs SUPERFISH and URMEL. The accuracy of the $r/Q$ and $Q_{ext}$ values was confirmed by measuring instability thresholds in the beam test in CESR; resonance widths observed in the beam test provided further verification of the $Q_{ext}$ values of important HOMs.

All important HOMs are damped successfully to $5 \times 10^2 \leq Q \leq 1.7 \times 10^5$. The cavity threshold instability current was measured in the CESR beam test by mechanically sweeping the resonant frequencies of the cavity during the beam test in order to provide an indication of the instability probability one would encounter if the HOM frequencies were selected at random within a particular frequency range. This measured probability distribution was compared to one computed by a Monte Carlo program (written by Robert Siemann). The input to this program consisted of HOM impedances, frequencies, and external $Q$'s obtained by measurements and by computations using SUPERFISH and URMEL. The agreement between the beam measurement and calculation is shown in Figure 4.3. Note that the measured instability threshold current is within a factor of 2 of the computed current at all probability levels. This is evidence that no serious errors or omissions occurred in determining the cavity impedances.

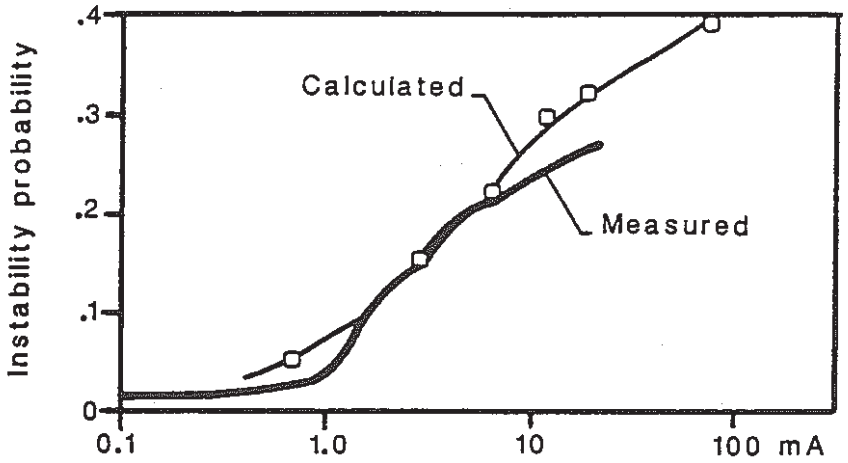


**Figure 4.3.** Comparison of instability probabilities measured in Cornell beam test with predictions based on bench measurements.

The HOM power extracted through the fundamental power coupler is absorbed by an HOM filter. The two arms of the HOM couplers are at right angles to each other to couple effectively to both polarizations of the deflecting modes. Quadrupole and sextupole modes are also adequately damped by these couplers. The waveguides leading out of the HOM couplers are cut off at 1900 MHz, so no separate filters are required on these couplers to reject the fundamental power (1500 MHz).

The HOM couplers on the CEBAF-Cornell cavity provide heavy coupling for both accelerating and deflecting HOMs. Only transverse instabilities are of concern in CEBAF, since the orbits are isochronous. However, the amount of HOM power generated in CEBAF is dependent on the $Q_{ext}$ values of the accelerating modes. Since the HOM power generated by the CEBAF beam is less than 0.5 W/m—sufficiently low to be absorbed at liquid helium temperature—the HOM waveguides are designed to be terminated in the liquid helium vessel within the cryostat, as described in Section 4.4.

**Fundamental Power Coupling**

At full beam current and an accelerating gradient of 5 MV/m, 4 kW/m (or 2 kW per cavity) of fundamental power must be coupled into the beam in CEBAF. The power coupled into the beam in the CESR beam test was 26 kW/m.

The input coupling (fundamental mode $Q$) required for CEBAF is $2.2 \times 10^6$. This value represents a factor of 3 overcoupling at 5 MV/m and 200 μA per beamlet, and was chosen because, at the design current, it requires only 20% added incident power, permits the cavity to be operated stably at as little as 0.83 MV/m, and triples the control bandwidth of the cavity. The input coupler of the CEBAF-Cornell cavity is designed in such a way that, by varying the location of the step between wide and narrow waveguides, the $Q_{ext}$ value can be varied from 7,000 to $1 \times 10^8$.

**Other Parameters**

As previously mentioned, the amount of HOM power induced by the CEBAF beam is less than 0.5 W/m. In the CESR beam test the cavity extracted more than 280 W/m of HOM power.

The minimum acceptable beam hole diameter in the cavity is 3.9 cm, to ensure that the cavity aperture is not the smallest aperture in the linac. The CEBAF-Cornell design has a beam hole diameter of 7.0 cm.

Other properties of the CEBAF-Cornell cavity are an intercell coupling of 3.3% and an $r/Q$ value of 960 ohms/meter.

In summary, all properties exhibited by the CEBAF-Cornell cavity meet or exceed the requirements of CEBAF.

## 4.3 Cryostats

Cryostats serve the function of providing a suitable environment for the cavities. The cryostats remove heat to maintain the cavities at a temperature of 2.0 K, and they provide the cavities with an ambient magnetic field of less than 5 milligauss. Other devices, such as waveguides and beam pipes, connecting the cavity to objects outside the cryostat are also considered to be part of the cryostat. For purposes of this report, a cryostat is considered to be the cryogenic housing for one pair of five-cell cavities, plus the auxiliary equipment just described. A cryostat with cavities installed, as discussed in Section 4.4, is defined as a cryo-unit. CEBAF requires 209 cryo-units: 200 for the two linac segments plus 9 for the injector.

The components and design of the cryostat are described in Section 4.4.

## 4.4 Cryo-Units

**Overview**

As stated in Section 4.3, a cryo-unit is a cryostat with two cavities installed (Figure 4.4). A cryo-unit, with the simple addition of a pair of end caps, is the smallest individually testable accelerating component in CEBAF; relatively small units have been chosen intentionally to maximize the probability that each unit will meet specifications when first assembled and to minimize the number of neighboring cavities subjected to the risk of contamination should an adjacent cavity require servicing. As discussed in Section 4.5, four cryo-units plus some other components comprise a cryomodule.

**Physical Description**

As previously stated, a cryo-unit is a cryostat with two installed cavities (Figure 4.4). All internal auxiliary components associated with both the cavity and the cryostat, with the exception of the reference probes on the cavities and their mounting hardware, are defined to be part of the cryostat. The principal components making up the cryostat are as follows.

The cryostat consists of an outer vacuum vessel, a 40 K to 60 K helium gas cooled radiation shield, a two-layer magnetic shield, inner and outer superinsulation blankets, a liquid helium vessel, radial and axial support rods for the helium vessel, a feedthrough tube for 2.2 K helium, two dynamic tuners for the cavities, three niobium beam-pipe extensions, two stainless steel bellows beam-pipe extensions, two beam-line gate valves, four niobium waveguide elbows for the HOM couplers, four waveguide loads for the HOM couplers, two stainless steel supports for the outboard ends of the cavities, two Kapton windows and short niobium waveguide extensions for the fundamental power couplers, two copper-plated stainless steel fundamental power waveguides with integral Kapton windows, two external copper-plated stainless steel fundamental power elbows with thin ceramic windows, infrared detectors, and arc detectors, instrumentation cabling and feedthroughs, two sets of bellows-sealed rotary feedthroughs and shafts for driving the tuners, one heater, two thermometers, and a complete set of assembly hardware.

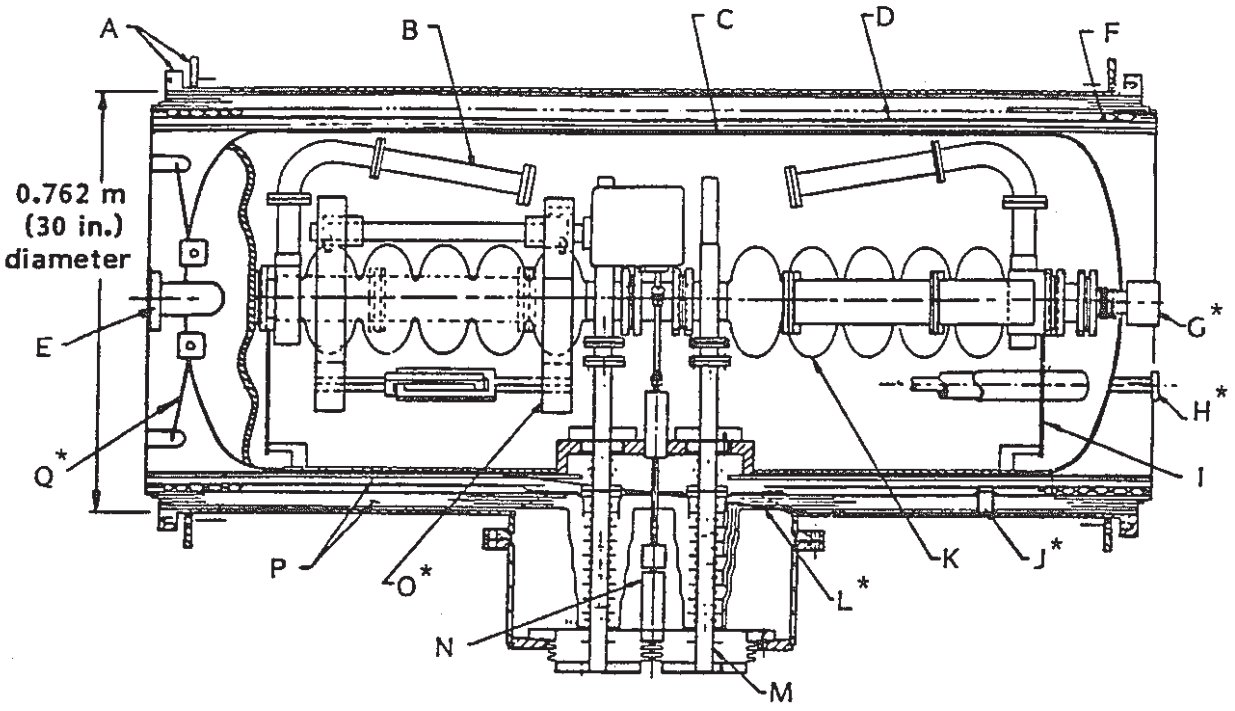


**Figure 4.4.** Top view of a CEBAF cryo-unit. Asterisked items shown only once. (A. Vacuum shell flange and captured seal ring; B. HOM load; C. Inner magnetic shield; D. Outer magnetic shield; E.* 2 K return helium connection and helium vessel; F. 40 to 60 K radiation shield; G.* Beam-pipe flange surface on end valve; H.* 2.2 K helium supply line; I. Outboard cavity support; J.* Shield support bumper; K. Cavity; L.* Axial support; M. Fundamental waveguide; N. Rotary feedthrough; O.* Tuning mechanism; P. Superinsulation; Q.* Helium vessel support rod.)

**Functional Characteristics**

With reference to Figure 4.4, the outer vacuum vessel, made of stainless steel, houses the insulation vacuum. The flanges at the ends of this vessel are machined after welding to permit alignment of successive cryo-units without the use of adjustable devices. A study of the manufacturing tolerances shows that a cryomodule can be assembled and installed within the tolerance specified in Section 5.2. The method of joining one cryo-unit to the next or to an end cap is described in Section 4.5. The vacuum vessel also has a "top hat" on the side to permit installation of waveguides and other instrumentation devices. The cylindrical cover of the top hat is O-ring sealed to the remainder of the top hat to facilitate access.

Thermal radiation from room temperature is intercepted by a radiation shield, cooled to 40 K to 60 K by helium gas supplied directly by the refrigerator. The shield is made of two layers of stainless steel sheet, spot-welded together in a quilted pattern, and hydraulically expanded to provide passages between the two sheets. The ends of the shields have the two sheets welded together to form a vacuum-tight seal. Tubulations are welded to the shield to permit cold helium gas to enter at one end of the shield and to exit from the other end. The opening in the shield at the top hat is closed by a copper cover plate.

Proper magnetic shielding is important during the cooldown of the cavity as it passes the critical temperature to guard against magnetic flux trapping within the niobium cavity that could cause a severe degradation in $Q$. Magnetic shielding can be accomplished either actively by a few wires, arranged to compensate for all exterior magnetic fields, or passively by adding magnetic shielding around the cryostat. The passive method has been chosen, because the active method requires that the counteracting field be present at all times. With the active method, turning off the bucking field, followed by an accidental warmup to a temperature above the superconducting transition temperature, followed by re-cooling, would cause flux to enter the cavity and be trapped. Two layers of an iron-nickel alloy such as Conetic are planned. The inner layer is wrapped on the helium vessel, and the outer layer lines the interior of the thermal radiation shield. The magnetic shielding is also continued through the top hat region by the use of separate pieces which have adequate overlap of the main shield.

A blanket of superinsulation consisting of 60 layers of aluminized mylar separated by nylon spun bonded cloth covers the outside of the shield. This blanket greatly reduces the thermal radiation load reaching the shield, and also reduces the thermal conductivity of any gases which may be present but not cryopumped. A blanket of 20 layers of superinsulation is installed on the inside of the thermal radiation shield and serves the same functions as the outer blanket, but does so with respect to the thermal load on the liquid helium vessel.

The liquid helium vessel contains a pair of cavities, and during operation is filled with liquid helium at 2.0 K to somewhat above the bottom edge of the end pipes at the top of the vessel. Helium vapor at 0.031 atmosphere is present above the liquid. A machined and accurately positioned plate is welded into the cryostat at the center of the side. A frame is welded around the perimeter of this plate, and a skirt is welded to the frame before the plate is machined to ensure that effects of weld warpage are negligible. During welding, a fixture holds this assembly in place in the main pipe forming the helium vessel. After the cavities and their associated equipment have been installed in the main pipe, the end domes and end-dome centers are welded in place.

The liquid helium vessel is supported at each end by four stainless steel rods mounted between the helium vessel end dome and the vacuum vessel flange. As shown in Figure 4.5, the rods are positioned

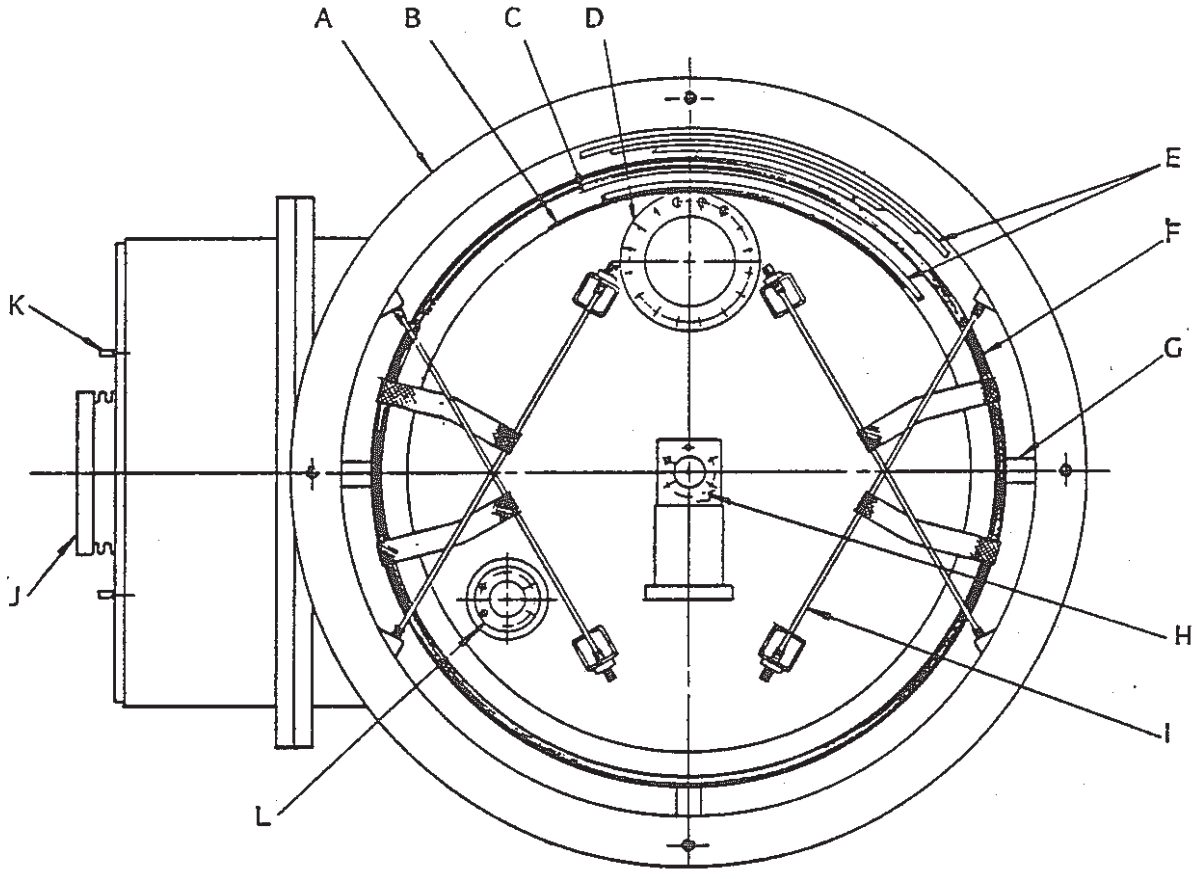


**Figure 4.5.** End view of a cryo-unit showing supports for the liquid helium vessel. (A. Vacuum shell flange; B. Inner magnetic shield; C. Outer magnetic shield; D. 2 K return helium connection and helium vessel; E. Superinsulation; F. 40 to 60 K radiation shield; G. Shield support bumper; H. Beam-pipe flange surface on end valve; I. Helium vessel support rod; J. Fundamental waveguide; K. Rotary feedthrough shaft; L. 2.2 K helium supply line.)

in a double-X (XX) pattern such that pitch, roll, yaw, and radial translations are constrained. The mounts at the end dome are beyond center such that the contraction of the vessel towards center is slightly less than the graded contraction of the entire rod upon cooldown. Thus the rods go into slight tension upon cooldown and the liquid helium vessel remains centered in the vacuum vessel. Two axial supports (item

L, Figure 4.4) are used to prevent axial ($z$) motion of the helium vessel; each of these supports lies in the same plane as the beam axis. All of these supports are tied to the 40 to 60 K heat shield by means of copper braids to reduce heat conduction into the 2.0 K bath.

The cryostat houses part of the transfer line for the 2.2 K supercritical helium supply circuit. The pipe for this line passes through the liquid helium vessel rather than around it. This is accomplished with negligible heat transfer during the cooldown cycle by isolating the tube within another internally super-insulated tube that tunnels through the helium vessel. Thus the vacuum vessel and 40 to 60 K heat shield need not be made larger in diameter. The tunnel-tube, welded to the helium vessel, has a hydroformed bellows at one end to accommodate dimensional change due to temperature differentials.

Figures 4.4 and 4.6 illustrate the tuning mechanism used on the cavity. Dynamic tuning of the cavity is supplied by a mechanical tuner which applies axial compression to the cavity between the centers of the first and fifth cells. A collar is fitted to each of these cells, and each collar is pinned to a yoke. On one side of each cavity, a differential ball screw is used to adjust the dimension between yokes. On the other side of each cavity, a piezoelectric stack provides fine adjustment of the same dimension between the yokes. The design is such that the piezoelectric stack is in compression when the linkage between the yokes is in tension. A stainless steel worm gear on a bronze spur gear provides torque multiplication to drive the differential ball screw. The worm gear is driven by shafts which are linked through bellows-sealed rotary feedthroughs to a stepping motor outside of the vacuum vessel. The reaction torque of the gear reducer is balanced by the off-center axial force provided by the drive linkage. The operational aspects of the tuner are described in Section 4.10.

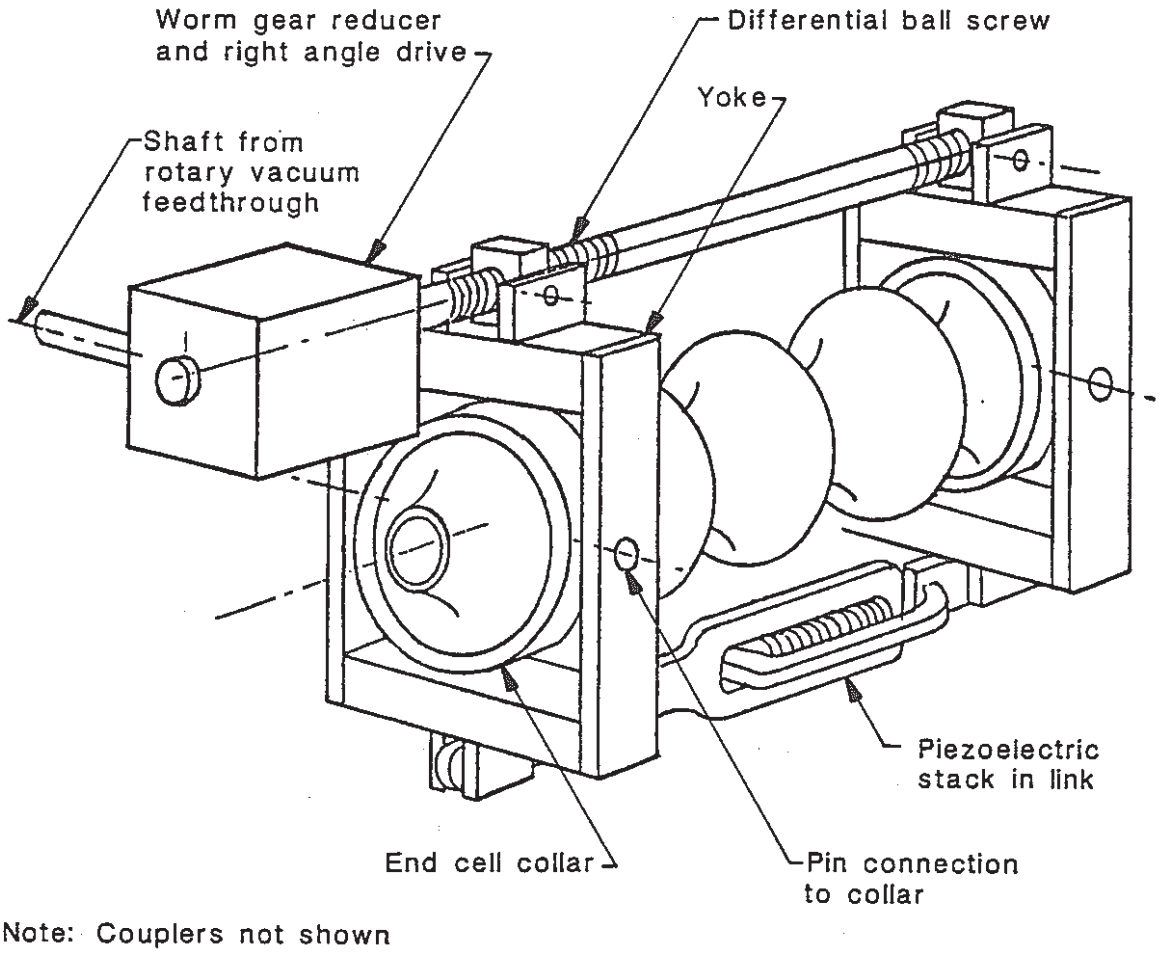


**Figure 4.6.** Frequency tuner for the CEBAF-Cornell cavity.

As shown in Figure 4.4, niobium beam-pipe extensions are used between the two cavities, and at the outboard end of each cavity. RF fringing fields from the cavities are cut off exponentially in the beam pipes, and the surface must be superconducting for 14 cm from the last cell iris at each end of each cavity in order to avoid excessive heat dissipation due to these fringing fields and their associated surface currents. The spacing between cavities within the cryo-unit is maintained at 1.25 wavelengths (2.5 cell lengths) to reduce cross talk between the cavities to a negligible level. This spacing also makes it possible to power a pair of cavities from a single power source, and to divert the reflected power into a dummy load, should this capability ever be needed.

Outboard of the outer niobium beam-pipe extensions, which are 7 cm in diameter, a pair of 3.8-cm (1.5″) ID stainless beam-pipe extensions is added. These beam pipes contain integral bellows to compensate for differential thermal contraction between the cavity and helium vessel, and to permit the cavities to change in length due to tuner operation. The relatively small diameter of these pipes reduces the amount of blackbody radiation which can enter the cavities at the ends of a cryomodule, and also protects the cavities in adjoining cryo-units from cross talk via those HOMs which are not cut off by the diameter of the niobium beam pipes. This cross talk is also severely inhibited since HOMs are not tuned to a controlled frequency, and the probability that two consecutive cavities will have HOM frequencies close enough to form an effective collective mode is very small. The stainless steel beam-pipe extensions are pre-welded to integral dished disks which match and are welded into the domes on the ends of the helium vessels. These disks have a larger diameter than the gate valves (described next) and are necessary to permit clean assembly (without disturbing the cavity vacuum).

A gate valve is installed at each end of each cryo-unit, and is used to keep the cavities under vacuum after initial testing of the cavity pair (described in Section 4.9). The gate valves also permit any cryo-unit to be removed from a cryomodule for servicing without destroying the vacuum in adjacent cryo-units. The gate valves have a 3.8-cm (1.5″) clear diameter, and are all-metal construction except for Viton O-ring gate seals. Viton O-rings are used because warm sealing is required but sealing along the beam line at cryogenic temperatures is not. These valves have manual actuation mechanisms. The valves are mounted such that the seals face the exterior of the cryo-unit.

Niobium elbows are used on each of the four HOM coupler waveguides in a cryo-unit. These elbows must be superconducting because the fundamental field amplitude is cut off slowly in these waveguides, and is too large at the location of the elbows to permit use of normal conducting waveguides. The elbows redirect the HOMs being extracted so that the required diameter of the liquid helium vessel is no larger than necessary. Copper braid straps connected to the one elbow which protrudes above the liquid helium level enhance cooling of this elbow.

Waveguide loads connect to the waveguide elbows just mentioned. These loads have a VSWR (voltage standing wave ratio) less than 1.5 between 1.9 GHz and 5.0 GHz, and are used to absorb part of the HOM power geneated by the CEBAF beam. This power is less than 0.5 W per active meter of cavity. These loads will be sufficiently clean that they can be connected directly to the cavity vacuum.

The outboard ends of the cavities are supported in the liquid helium vessel by stainless steel sheets which hold the ends of the cavities precisely in the center of the liquid helium vessel. These sheets provide considerable rigidity in the transverse direction (both vertically and horizontally), but are flexible in the longitudinal direction to permit motion due to differential thermal contraction and due to tuner operation.

Kapton windows are used on each of the fundamental power waveguides to permit the cavities to be sealed at an early stage of assembly. Kapton is chosen because of its small RF reflection, good vacuum properties, and excellent radiation resistance.

The Kapton windows in the fundamental power waveguides are followed immediately by short lengths of niobium waveguide so that seals at the ends of these extensions can be made and broken without disturbing the seals on the Kapton windows.

Additional lengths of niobium waveguide are used to connect the waveguide extensions to the plate at the side center of the liquid helium vessel. The waveguides are made of niobium because they are surrounded by helium at 2.0 K, and the use of superconducting material in this location minimizes heat losses due to RF power dissipated in the waveguide. This waveguide is annealed at $\leq 10^{-7}$ torr and 1800°C to render the niobium dead soft before welding to its flanges (which must remain hard). The flanges on the cavities and on the waveguides are all machined after welding to obtain flat, smooth sealing surfaces in the correct locations. Care must be taken not to introduce a bend in the cavity during inelastic tuning, described in Section 4.8. With all of the flange locations precisely determined, and with the location of

the plate in the side of the helium vessel precisely determined, the two cavities are attached to the helium vessel without the requirement for any flexibility other than the slight flexibility provided by the annealing of the waveguides. This procedure was used successfully in the beam test of a pair of cavities in CESR. The end of each cavity near the center of the helium vessel is thus supported by its fundamental waveguide, and the outboard end of each cavity is supported by the stainless steel sheets previously described. The niobium waveguide is made slightly short at room temperature to compensate for the fact that the stainless steel helium vessel contracts more than does the niobium waveguide; the cavity has sufficient flexibility to accommodate this differential contraction without inelastic deformation.

Stainless steel waveguides are used between the liquid helium vessel and the vacuum vessel. These waveguides are plated on the inside with several skin depths of copper (to minimize RF losses without causing too large a thermal conduction along the length of the waveguide). Each has an integral Kapton window with a 1-cm-diameter hole in it. This window is located at the waveguide flanges, which are maintained at 60 K, and serves to intercept most of the infrared radiation transmitted down the waveguide so that it does not get absorbed at 2.0 K. The hole in the window permits vacuum pumping on both sides of the window without use of an external pumping manifold to connect the two sides. These waveguides pass through the plate on the vacuum vessel's top hat, and are vacuum sealed to this plate employing hydroformed bellows which accommodate relative changes in length and transverse displacements.

The sum of the heat conducted through the waveguide from room temperature and of the heat generated by dissipation within the waveguides is minimized by placing the 60 K heat intercept 8 cm from the 2.0 K end of the waveguide.

Two copper-plated stainless steel fundamental power elbows are used outside the insulation vacuum vessel. Each of these elbows is equipped with a thin ceramic window which separates evacuated waveguide from air-filled waveguide. Ceramic is used here because Kapton has some permeability to most gases and a high permeability to helium gas. Each elbow is also equipped with an infrared detector and a visible arc detector to detect anomalous conditions at any of the windows, and also has a pumping port to permit the waveguide to be pumped as described in sections 4.5 and 4.7.

The stainless steel plate at the side of the liquid helium vessel and the flat plate at the side of the vacuum vessel are equipped with instrumentation feedthroughs. These feedthroughs include two coaxial SMA bulkhead feedthroughs (on each plate) for the semi-rigid cables leading from each of the reference probes on the HOM couplers. There are also feedthroughs for two sets of four leads for thermometers, two sets of two leads for the piezoelectric tuning adjusters, and one pair of leads for a heater. Also in this region are the two bellows-sealed rotary feedthroughs for operation of the tuner.

The heater in the cryo-unit is to calibrate the heat load measuring instrumentation (described in Section 4.10), and to accelerate warmup of the cryo-unit when desired.

A thermometer is attached to the cavity, and is used to determine the temperature. This is particularly useful during cooldown and warmup. Another thermometer, located at the bottom of the cryostat, provides temperature information during cooldown and warmup.

Assembly hardware includes nuts, bolts, and spring washers where required. Also included are the vacuum sealing materials. At room temperature, O-ring seals are used on the vacuum vessel. Indium is used to seal between niobium and niobium, or between niobium and stainless steel. It has been found that indium seals are reliable if the flange faces are flat and smooth, and if the flanges are at least 1.0 cm (0.375") thick so that they do not distort excessively. It is also required that spring loading of the seal be maintained. Cryogenic joints between stainless steel and stainless steel are made with knife-edge seals using copper gaskets. Any joints which do not require disassembly for servicing purposes are welded wherever possible.

## 4.5 Cryomodules

**Overview**

A cryomodule normally consists of four cryo-units connected together, with an end cap on each end (figures 4.7 and 4.8). One cryomodule is used between each set of magnetic focusing elements. CEBAF uses 50 cryomodules in the linac segments, and two standard cryomodules, together with a cryomodule containing only one cryo-unit, in the injector. It is planned that the first seven cryomodules will be pretested and installed in the linac. To service any particular cavity, its entire cryomodule would be removed from the linac and a spare unit installed in its place.

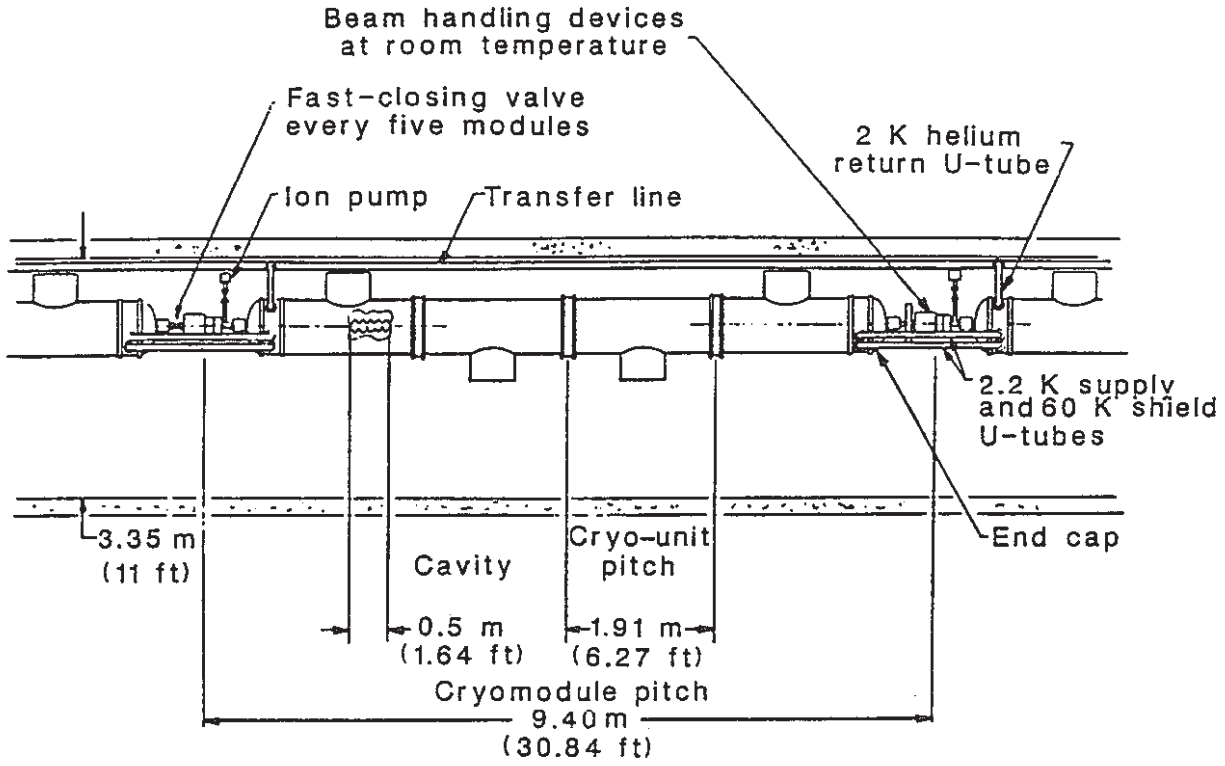


**Figure 4.7.** Schematic plan view of a cryomodule installed in the linac. (RF equipment not shown.)

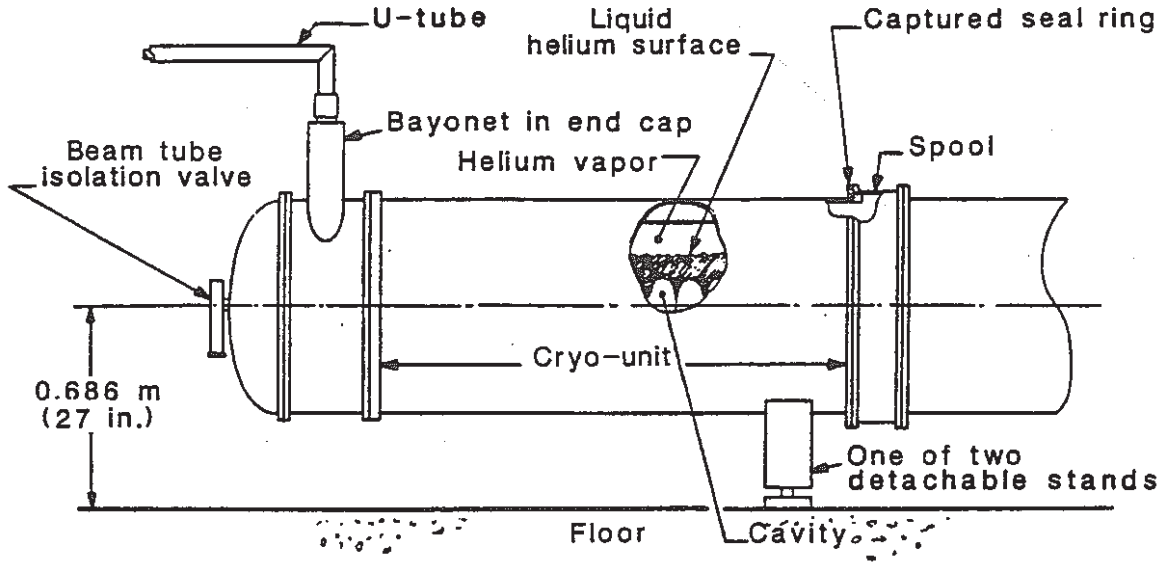


**Figure 4.8.** Side view of the end of a cryomodule.

**Physical Description**

In addition to four cryo-units, which are described in Section 4.4, each cryomodule includes three spool pieces which span a 15-cm space between cryo-units. Within each of these is installed a beam pipe with bellows to accommodate thermal contraction, a pinch-off pump-out tube, a pipe with bellows to connect the liquid helium vessels, a pipe with bellows to connect the 2.2 K supercritical feed lines, connections for joining the two 40–60 K thermal radiation shields, a set of thermal radiation shield bridge pieces, two sets of magnetic shielding bridge pieces, bridge wraps for the 60-layer superinsulation blanket, and a bridge wrap for the 20-layer superinsulation blanket. A 7.6-cm (3″) diameter pumping manifold runs along the outside of each cryomodule for pumping on the fundamental power feed waveguides; this apparatus is described in Section 4.7.

A supply end cap is bolted to the vacuum vessel on one end of the cryomodule, and contains the bayonet sockets for two U-tubes (Figure 4.9), one supplying 2.2 K supercritical gas and one supplying 40–60 K shield gas. The first is internally connected through a JT valve to the input of the helium vessel in the first cryo-unit, and also continues in parallel with the JT valve into the transfer line passing through the first cryo-unit. The 40–60 K gas input is connected through a thermal shield in the end cap into the shield in the first cryo-unit. This end cap also contains all the relief valves and rupture disks on both the helium circuits and the vacuum tank. A beam-pipe extension with thermal expansion bellows and a transition from 2.0 K to room temperature is also included in this piece, as are closures for both layers of magnetic shielding and closures for the superinsulation blankets. Vacuum vessel closure is provided by a dished cover which passes over a motorized gate valve located on the beam pipe.

At the other end of the cryomodule, a return end cap is similarly attached to the cryomodule, and contains bayonet sockets for three U-tubes. One of these sockets is for continuing the 2.2 K supercritical gas supply to the next cryomodule, one is for continuing the shield gas to the next cryomodule, and one is for connecting the 0.031-atmosphere helium gas exhaust line to the return transfer line. The components in this cap are similar to those in the supply end cap, except that the additional U-tube connection is connected into the pipe at the top of the helium vessel and contains the module's liquid-level gauge. Another exception is that the connection between the 2.2 K supply line and the liquid helium vessel is absent. Pumping on the insulation vacuum is provided at only one end, as discussed in Section 4.7.

Each cryomodule also has two detachable support stands cradling the vacuum vessel at the inner end of the first and fourth cryo-unit. Each stand's feet contain the adjustment mechanisms necessary to position the module on the beam-line axis.

**Functional Characteristics**

The principal characteristics of the cryomodules are the same as those described in Section 4.4; only the features not characteristic of individual cryo-units are described here.

As shown in Figure 4.7, the cryo-units are assembled with the top hats in a left-right-right-left pattern. The purpose of this pattern is to reduce to a negligible value the effect of small transverse beam kicks caused by the asymmetric fields in the fundamental power couplers.

The thermal radiation shields and magnetic shields between cryo-units are attached to one cryo-unit and are free to slide with respect to the other one to accommodate thermal contraction. With the inclusion of the end caps, a nearly closed volume is provided with respect to thermal radiation shielding and magnetic shielding.

The spool pieces, which slide over one of the adjacent cryo-units during assembly, have their ends machined to provide accurate alignment of the cryo-units within the cryomodule without adjustable alignment devices. The spool pieces are mounted in compression between seal rings bolted to the back face of the vacuum vessel flanges. Connection is provided by a series of threaded rods between seal rings. These seal rings each contain two O-rings, with one sealing to the cryo-unit vacuum vessel flange and the other to the spool piece.

The JT valves are adjusted to maintain the level of liquid helium above the bottom of the pipes connecting the helium vessels of the cryo-units, and below the center of these pipes. Upon passing through the JT valves, the supercritical 2.2 K helium is expanded to become 2.0 K liquid. Additional details are included in Section 4.10.

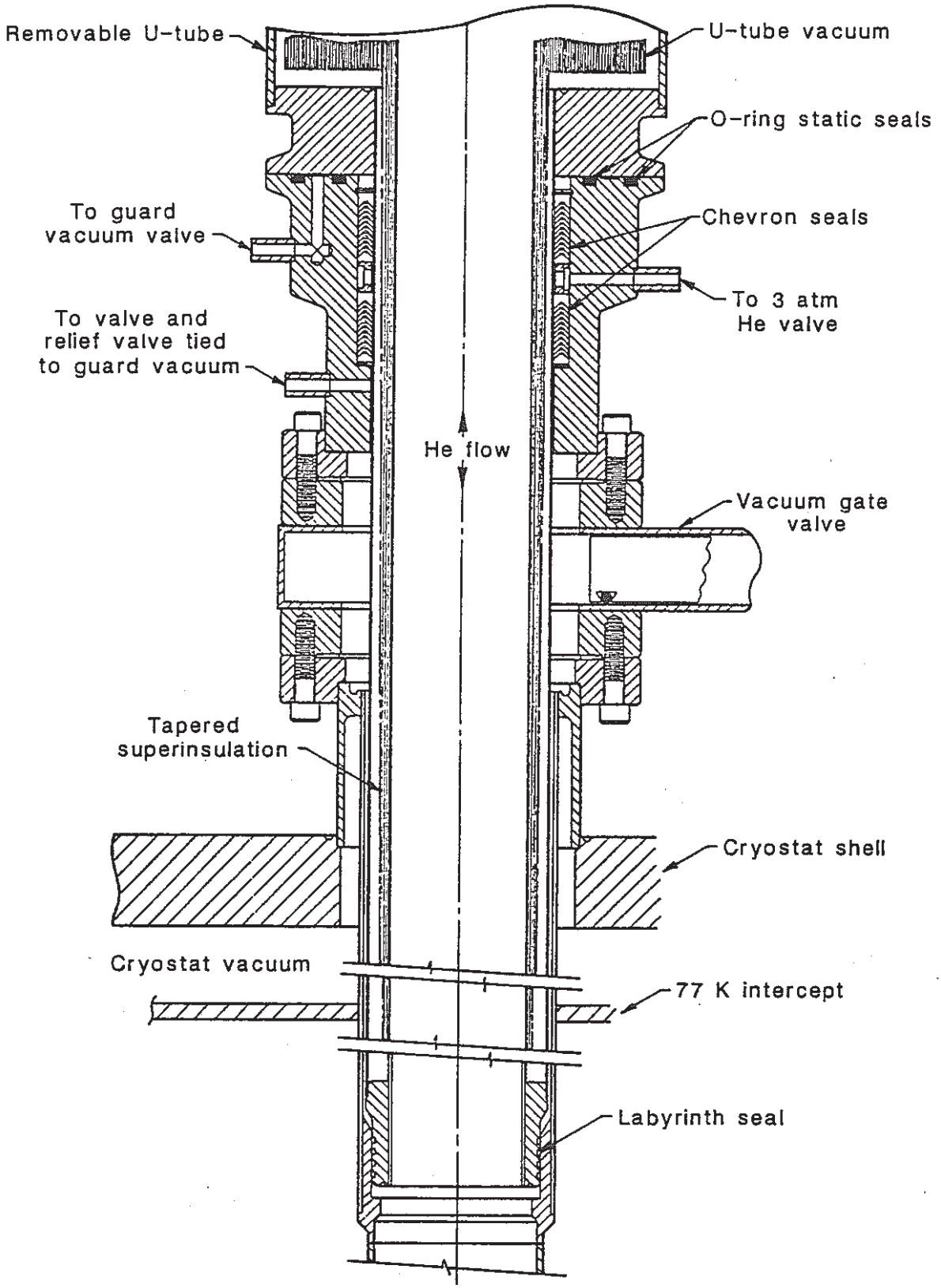


**Figure 4.9.** Subatmospheric cryogenic transfer bayonet with guard vacuum.

## 4.6 Cryomodule Interconnection

**Overview**

CEBAF uses two antiparallel linac segments, each containing 25 cryomodules and therefore 100 cryo-units, or 200 five-cell cavities. Each of the two linac segments is designed to produce an energy gain of at least 0.5 GeV per pass. The linac segments are connected via warm recirculation beam lines. Along each linac segment the beam pipe is warm between cryomodules.

**Physical Description**

In addition to elements previously described, the linac segments include warm 3.8-cm-diameter beam pipes passing through the magnetic elements and connected between cryomodules. These room-temperature beam pipes have pump-out provisions and bakeout provisions, and are continuously pumped by 60 liter/sec ion pumps. They have 2.5-cm-diameter collimators to provide the smallest apertures formed in the vicinity of the cryomodules; these apertures are many times the diameter of the beam. This portion of the vacuum system is further described in Section 4.7.

The linac segments also contain fast-closing valves every five cryomodules.

At each end of each linac segment, there is an additional 1 m of beam pipe which is maintained at 2.0 K.

**Functional Characteristics**

Condensable gases from warm sections must be prevented from entering and contaminating the cavities. This is accomplished by baking out and pumping out the warm sections prior to cooling down the cavities. In addition, the sections are pumped continuously by 60 liter/sec ion pumps. For further protection, there are fast-closing gate valves every five cryomodules. The vacuum system and bakeout process are described further in Section 4.7.

The shield gas temperature increases from 40 K to 60 K as it passes through either 12 or 13 cryomodules in series. (The 25 cryomodules of a linac segment are split 12 and 13 for this particular purpose.)

The additional one-meter beam pipes maintained at 2.0 K at both ends of each linac segment adsorb condensable gases which could otherwise enter the linac segments and contaminate the cavities. These pipes must be cooled down before the cryomodules are, and warmed up after the cryomodules are.

## 4.7 Vacuum System

**Overview**

A high vacuum is required in an accelerator to minimize the amount the beam is scattered by collisions with gas particles. In a superconducting accelerator the vacuum also protects the cavities, by minimizing the rate at which material accumulates on the superconducting surface, thereby degrading the $Q$. An additional function of the vacuum system in a cyrogenic machine is to maintain the insulating vacuum in the cryomodules. Figure 4.10 is a schematic diagram of CEBAF's beam-pipe vacuum system.

**Vacuum System: Linac Segment**

*Physical Description*

The beam-line pumping of the linac segment is described in Section 4.6. Pumping on the fundamental power waveguides is provided by a 7.6-cm (3") diameter manifold that runs the length of each cryomodule. This manifold is equipped with a valve for initial pumpdown. There is also a 60 liter/sec ion pump mounted near the center of the manifold. Jumper lines connect the manifold to each of the eight fundamental power elbows.

Each cryomodule has a valved port for initial pumpdown of the insulation vacuum. Also included is a thermocouple gauge to monitor vacuum quality. In case of a small helium leak to the vacuum space, this port acts as a connection point for a 50 liter/sec turbomolecular pump with backing roughing pump which would be installed. Provision has been made to purchase five pump systems for this use.

*Functional Characteristics*

It has been empirically determined that the pressure in a superconducting cavity should be $\leq 10^{-7}$ torr at the time the cavity is cooled down in order not to suffer degradation of performance due to the adsorbed gas layer. Once the cavity is cold, the surfaces which were contributing to this pressure by outgassing will no longer outgas at a significant rate. However, any surface which remains warm and

# 6. RF Power System

## 6.1 Injector

**Background of the CEBAF Design**

Any of several existing high-quality injectors for CW electron accelerators could serve as a model for the CEBAF accelerator. The injectors used at the superconducting linear accelerator at the High Energy Physics Laboratory (HEPL) at Stanford and at the room-temperature microtrons at the National Bureau of Standards (NBS) and the Nuclear Physics Laboratory (NPL) of Illinois have many common features that will be used in the CEBAF design. The 100-kV section of the NPL injector (which, in turn, was modeled on the NBS injector) is the closest in design to the CEBAF injector and serves as a good model.

**Overview of Design**

There are four different sections of the injector that have to be considered in the design: a 100-keV line to produce, collimate, and bunch the electrons; a region to capture the electrons and accelerate them to nearly the velocity of light; a preaccelerator; and an acceleration section to increase the energy to a nominal 50 MeV before injection into the rest of the linac. The main features of the injector are outlined schematically in figures 6.1 and 6.2. The 100-keV section consists of an electron gun, a compensated RF subharmonic chopper, and a buncher. The other elements of this line are solenoidal lenses, steering coils, and apertures to control the transport of the low-energy electron beam into the first accelerating section. The RF elements of the injector up to and including the capture section are room-temperature components operating at 1500 MHz, or subharmonics for the RF chopper. The 100-keV line produces an electron beam with a velocity of 0.55 $c$, bunched into 10-degree bunches for injection into the capture section.

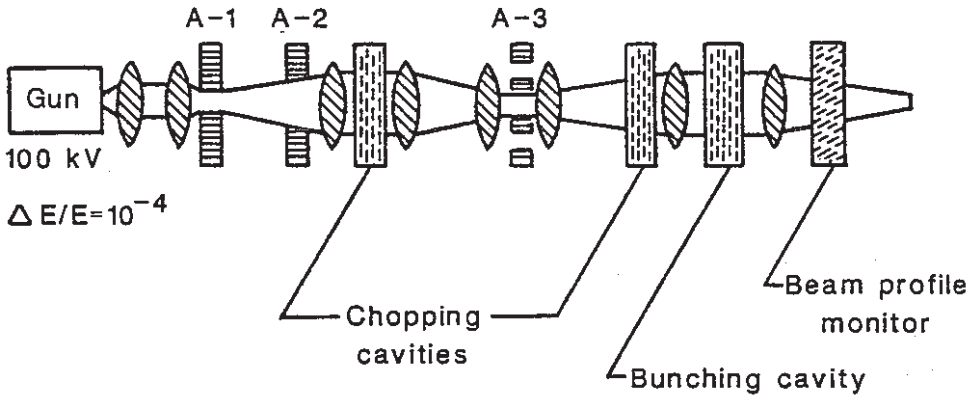


**Figure 6.1.** Schematic view of the 100-keV section of the CEBAF injector. This section produces a chopped and bunched beam for further acceleration in the rest of the injector.

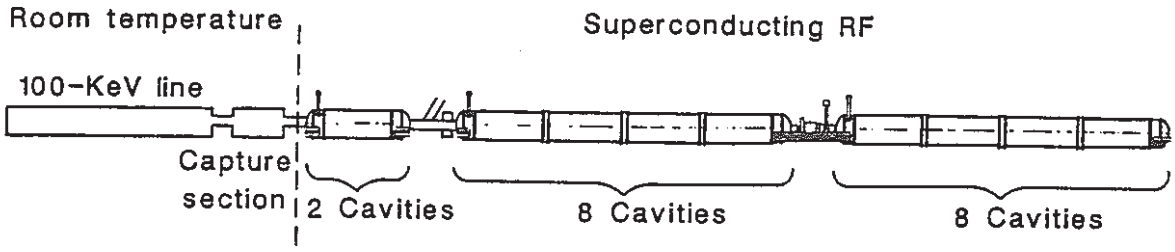


**Figure 6.2.** The CEBAF injector.

The capture section increases the velocity of the electrons to nearly the velocity of light and further reduces the width of the bunch. Experience at the Darmstadt superconducting linac has shown that injection from a 100-keV line into a $\beta = 1$ superconducting capture section did not work well. Therefore, a room-temperature capture section will be used to increase the energy of the electrons before injection into a cryogenic preaccelerator. Two sections of room-temperature accelerator will be used, graded in beta, and each powered by 5 kW of RF. This would produce an electron beam energy of about 950 KeV ($\beta = 0.937$) that will be injected into two standard CEBAF-Cornell cavities used as a preaccelerator in a dedicated cryostat. A small analyzing magnet will be used after the first injector cryostat to deflect the electron beam into a diagnostic region for beam tests and to set up the injector before sending the beam into the rest of the linac. A lens is used after the injector cryostat to refocus the electron beam into the next section of the injector line. Two cryogenic modules are used as an injector accelerator, as shown in Figure 6.2. These will increase the energy of the electron beam to a nominal 50 MeV before it is injected into the main part of the linac.

**Electron Gun**

The electron gun produces a high-quality DC electron beam at an energy of 100 keV. The basic details of the gun are shown in Figure 6.3. The gun has a Pierce geometry with a 1-mm-diameter dispenser

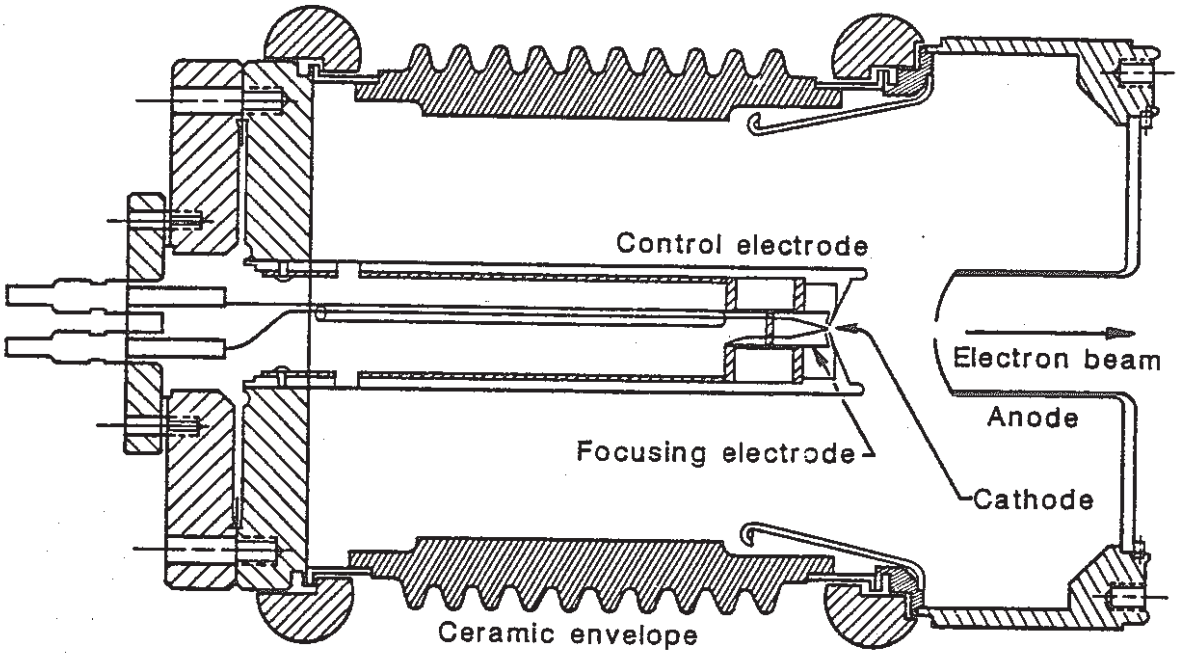


**Figure 6.3.** Details of the 100-keV electron gun for the CEBAF injector.

cathode that will produce 2 mA of electron beam current at a reasonable current density. A modulating nonintercepting electrode is used to add fast pulsing capabilities to the gun; this is a useful feature for setup, other beam diagnostic experiments, and some experimental programs. The emittance of a Pierce geometry electron gun at this low perveance and small cathode diameter should be about 1 mm-mrad at 100 kV. The cathode and anode radii are designed for a 2:1 ratio. The beam is focused by a lens to pass through aperture A-1 (Figure 6.1), a 1-mm-diameter aperture built as shown in Figure 6.4. This is

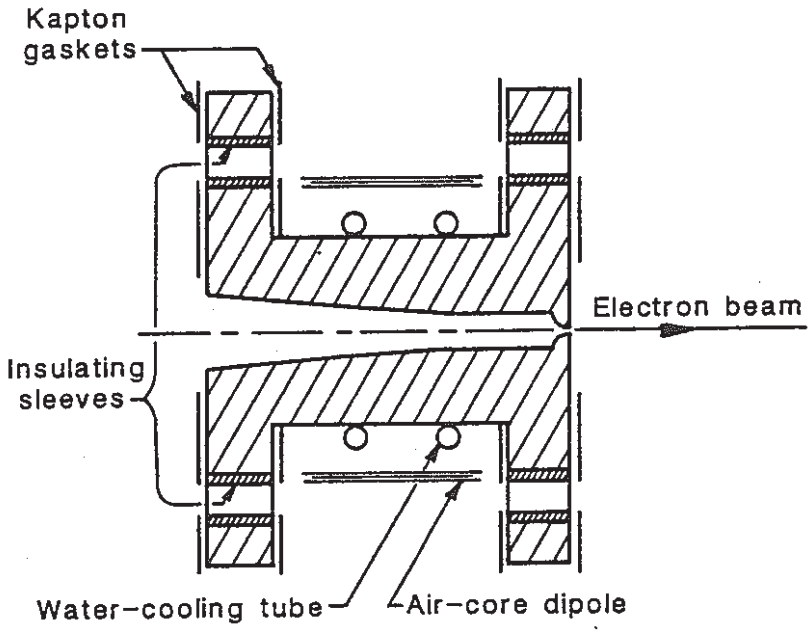


**Figure 6.4.** Water-cooled apertures for the 100-keV injector line. The shallow impact angle that the electron beam makes with the aperture surface has been found to reduce cathode poisoning.

insulated from the beam line using the Kapton insulated conflats developed at Chalk River Nuclear Laboratories, and water-cooled with an external cooling coil as shown. These apertures are simple to construct and were found to produce very little poisoning of the dispenser cathode when used on the higher-current ETA injector at Chalk River. The second aperture, A-2, is 4 mm in diameter, and located 0.5 m downstream. This combination of apertures limits the emittance to about 1 mm-mrad. Although the electron gun is capable of about the same emittance, the apertures actually define the transverse emittance of the injector. A simple air-core dipole is used around A-1 to provide an in-line beam dump for conditioning the gun cathode.

**RF Chopper**

The beam is then focused through the RF chopper to an image at the chopper slit, A-3. The CEBAF injector will use the NPL injector's technique to chop the beam at subharmonic frequencies in order to load different bunches at different levels. The RF chopper is a rectangular cavity driven at $f_0/2$ in the vertical direction and $f_0/3$ in the horizontal direction. Figure 6.5 shows the details of the chopper cavity. The RF inputs shown on the figure will produce the scanning pattern shown in Figure 6.6 at the chopper aperture, A-3. Variable slits at the chopping aperture can be used to reduce the bunch length from 60 degrees to 0 degrees for each of the three succeeding bunches. These differentially loaded bunches are separated at the end of the accelerator to produce up to three different beams of different currents that can be delivered to the end stations. A compensating lens similar to that used at the NPL injector will be used to avoid rotation of the scanning pattern. The second chopper is used to compensate for the radial momentum introduced by the first chopper, and completes the chopping system. Tests at the NPL injector have shown that the beam current transmitted by this system can be controlled over a range of greater than 100:1.

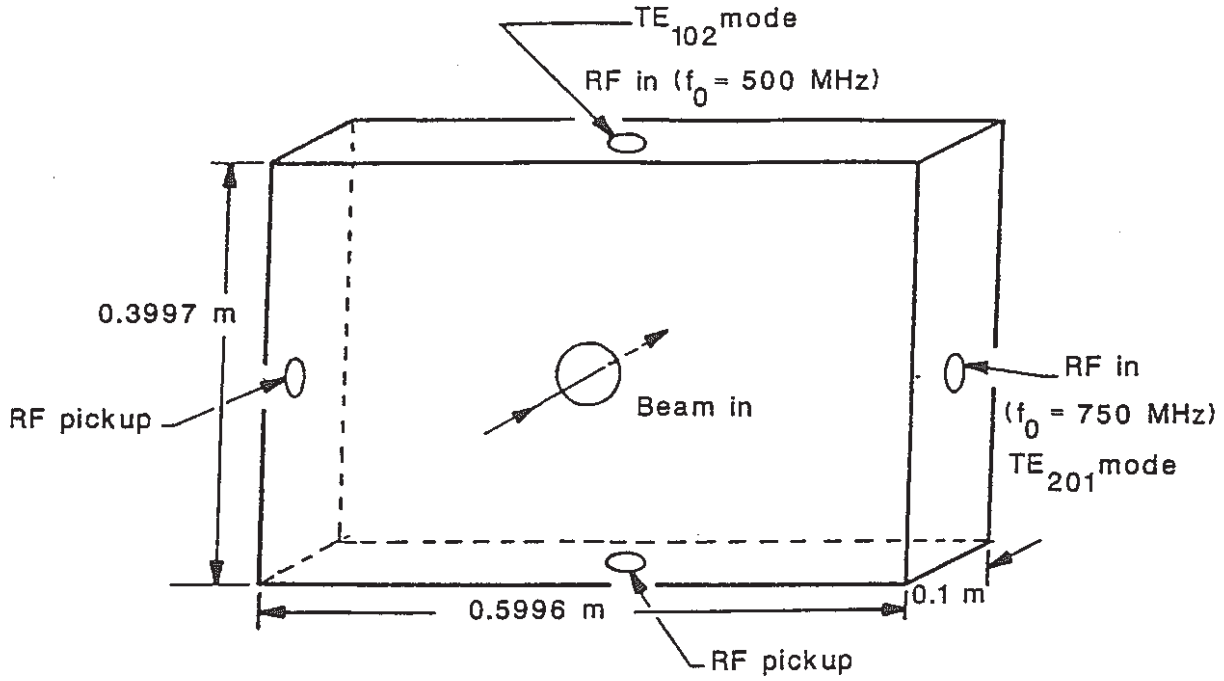


**Figure 6.5.** Details of the rectangular subharmonic chopper cavity.

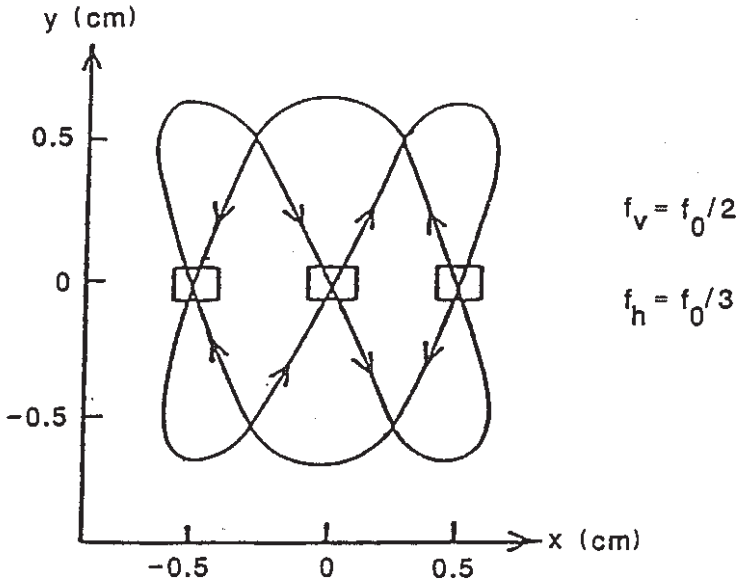


**Figure 6.6.** The beam pattern produced by the chopping cavity at the aperture A-3.

**Buncher**

The electron beam is then transmitted into a bunching cavity that uses the same principle as a klystron buncher to further bunch the beam from the 60 degrees to 10 degrees before it enters the capture section. The buncher is a $TM_{010}$ room-temperature cavity at the same frequency (1500 MHz) as the fundamental of the accelerator. The electrons are accelerated or decelerated depending on their phase with respect to the buncher RF field. After a drift distance, the higher-energy electrons reach the lower-energy electrons, producing a compression of the longitudinal phase of the beam.

**Capture Section**

The bunched beam is then injected into an RF cavity that acts as a capture section. Ideally, this section should have a $\beta < 1$ and be graded in beta. Experience at the Darmstadt superconducting electron linac has shown that injection from the 100-keV line into a $\beta = 1$ superconducting capture section does not work well. Therefore a room-temperature capture section will be utilized. In order to use the same low-power klystrons and RF control systems that are used for the rest of the accelerator, short, five-cell standing wave accelerator cavities similar in design to the NBS capture section will be used. The injector has been modeled with the code PARMELA, and it was found that two 5-cell room-temperature cavities, graded in beta, produced a good match into the first superconducting cavity. The beam energy is 0.95 MeV ($\beta = 0.94$) after the two 5-cell cavities, with an energy and phase spread of 16 keV and 1.7 degrees. The beam is then focused with a solenoid and injected into a cryogenic preaccelerator.

**Preaccelerator**

The preaccelerator uses two 5-cell CEBAF-Cornell cavities in a dedicated cryostat. The beam energy is 5.8 MeV ($\beta = 0.997$) with an energy and phase spread of 26 keV and 1.2 degrees after the preaccelerator. A bending magnet will be used after the preaccelerator to bend the beam into a diagnostic region for beam tests and tune-up before injection into the rest of the linac. A lens will be used after the preaccelerator to refocus the beam before injection into the injector accelerator. Figure 6.7 shows the results

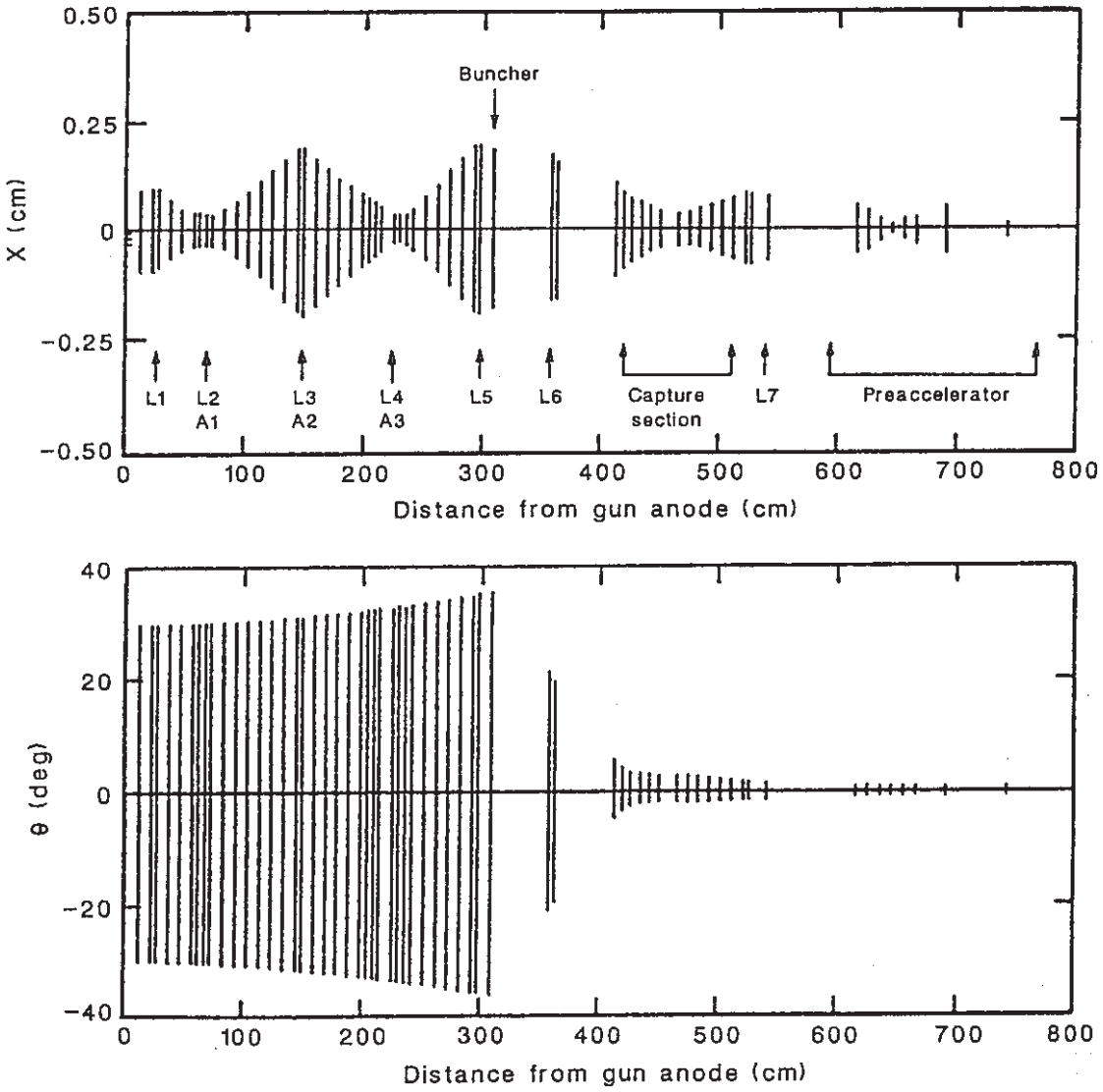


**Figure 6.7.** Calculated transverse beam profile and longitudinal phase of the beam as it passes through the injector.

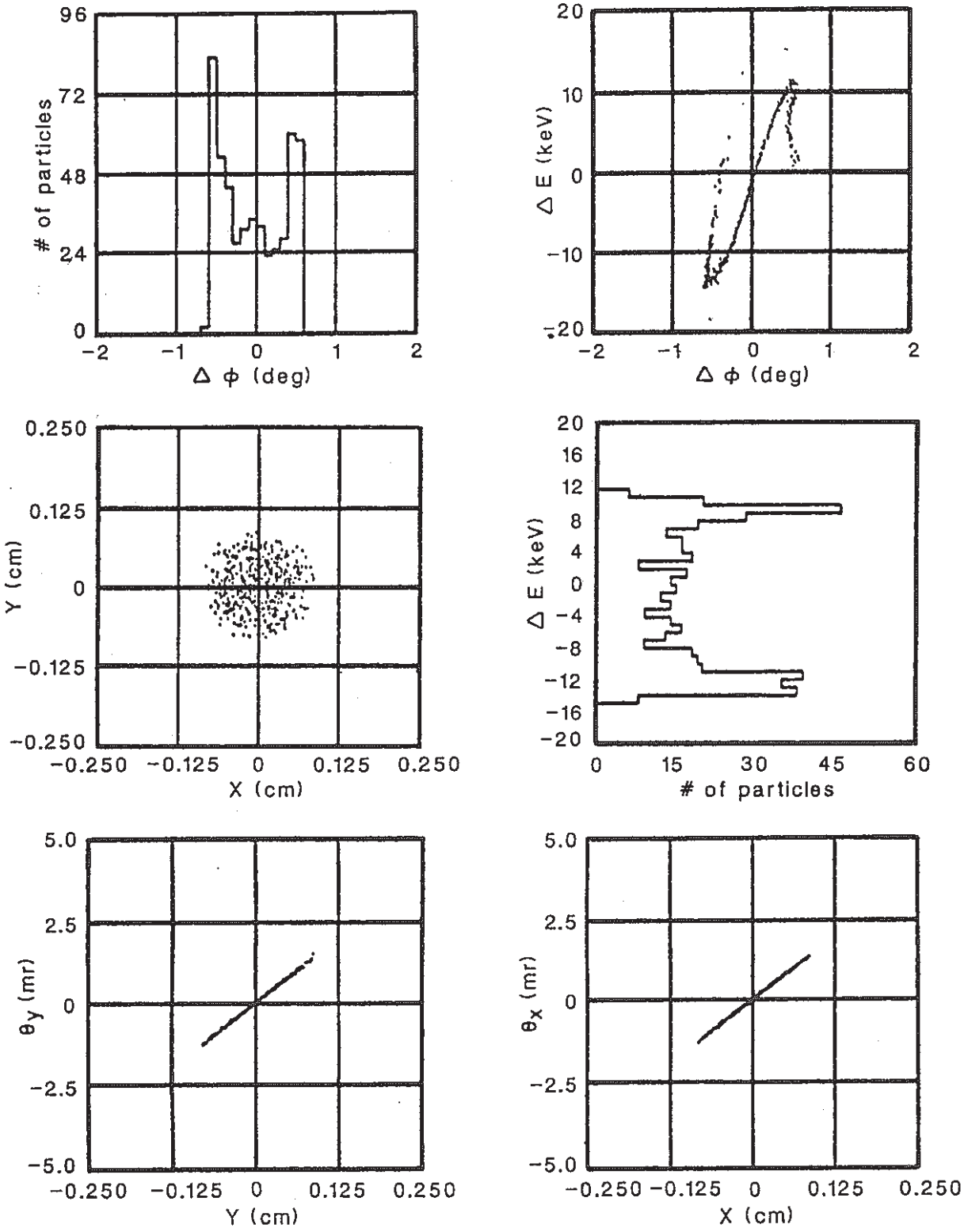


**Figure 6.8.** Calculations of the phase and energy spectrum of the electron beam at the end of the preaccelerator.

of PARMELA calculations performed at Los Alamos for the 100-keV line and the capture and preaccelerator sections. The beam current was 200 μA and calculations were performed both with and without space charge, which produced only a small effect. Figure 6.7 shows the transverse dimensions of the beam, and also shows the phase, as a function of distance from the gun anode. The position of the

elements is shown on Figure 6.7(a). A 60-degree beam was started from the gun to simulate the chopper to avoid starting a large number of particles that would be lost at the chopper. Figure 6.8 shows the calculated phase and energy spectra at the exit of the preaccelerator. A bunch of less than 1.5 degrees and 26 keV has been prepared for injection into the rest of the accelerator.

**Injector Accelerator**

The rest of the injector will consist of two cryogenic modules to increase the energy of the electron beam up to about 50 MeV before injection into the main accelerator. These will be identical to the cryogenic modules used in the rest of the linac. The injector line will be built in-line with the rest of the linac, and a chicane of dipole magnets will be used to bend the beam around the recombining dipole at the end of the recirculator. Small correction dipoles will be used on each of the recirculation paths to correct for the small deflections produced by the last injection dipole.

## 6.2 Linac RF System

The fundamental objective of the linac RF system is to provide the energy necessary to accelerate an electron beam. In order to accomplish this, precise power and phase control of the cavity is required. Additionally the RF system must protect itself, and the accelerator, from the effects of various failures. Finally, the RF system must provide information for determining the proper tune and operation of the superconducting cavities and must report cavity parameters to the higher-level control hierarchy for operator evaluation. Generically, the system consists of individual RF systems driving each of the cavities installed in the linac. Each system is autonomous in function and is coordinated through a hierarchy of control computers, RF frequency references, and real-time monitors and diagnostics. Each system consists of the waveguide and coaxial cable connections to the cavity, a 5-kW output klystron, a higher order mode (HOM) absorber, a dual-directional coupler, and an RF control module (Figure 6.9).

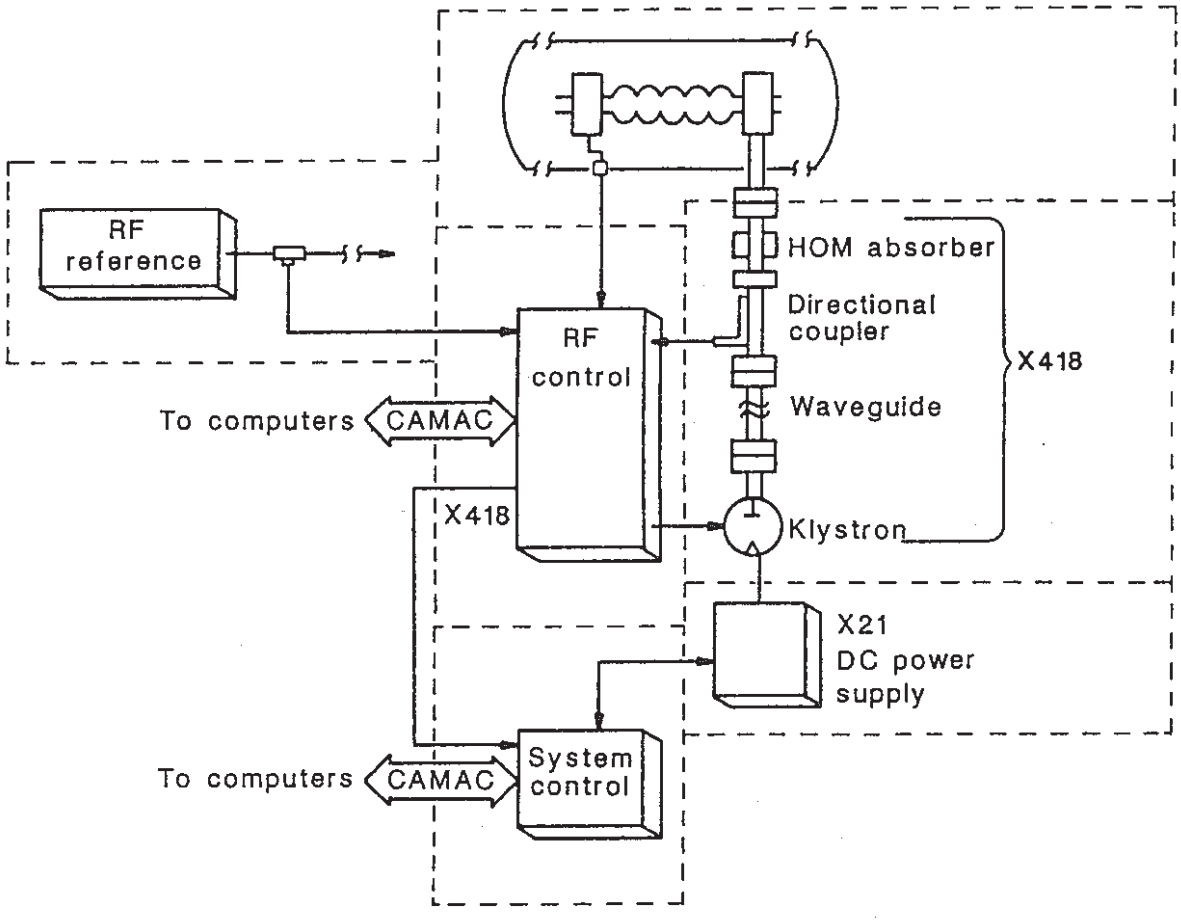


**Figure 6.9.** RF drive system.

An important requirement of the linac RF system is the ability to control the accelerating field gradient and phase of each cavity individually. This allows utilization of each cavity's maximum gradient performance to achieve the desired machine energy. Individual cavity controls allow precise set-point control of gradient and phase; they also simplify the structure of the control system while maintaining maximum flexibility in the operation of the RF system. Installation, maintenance, and initial turn-on are facilitated by having this flexibility.

The RF power required to drive each cavity is given by the formula:

$$RF_{input} = \frac{(\Delta V_{cavity})(4\, I_{beam}) + 2\,(\Delta V_{cavity})^2/\,(960\, Q)}{\beta} + P_{ext\ losses}$$

The first term of the equation represents the power coupled to the electron beam with four passes. The second term represents the RF losses in the cavity due to the cavity intrinsic $Q$. The last term represents the power losses in waveguide components. The $\beta$ is the coupling coefficient of the coupler. Thus, for a cavity accelerating potential of 2.5 MV, a delivered current of 200 $\mu$A, a $\beta$ of .75, and external losses of 20 W, the input RF power required is:

$$RF_{input} = \frac{(2.5 \times 10^6)\cdot 4\cdot(200 \times 10^{-6}) + 2\,(2.5 \times 10^6)^2/\,(960 \times 3 \times 10^9)}{.75} + 20$$

$$= 2693\ \text{W}$$

The klystron will be capable of delivering 5-kW RF output at 1500 MHz. This power level meets the minimum requirements for the accelerating gradients plus some design margin for losses and growth. It is anticipated this unit will be a permanent magnet-focused device, eliminating the need for an electromagnet and associated power supply. The high-voltage DC will be supplied from central supplies. Each DC power supply will service 20 klystrons, isolated by power conditioning and high-voltage switching circuitry to minimize ground loops and cross talk and allow the removal of defective or unwanted klystrons from the system (Figure 6.10).

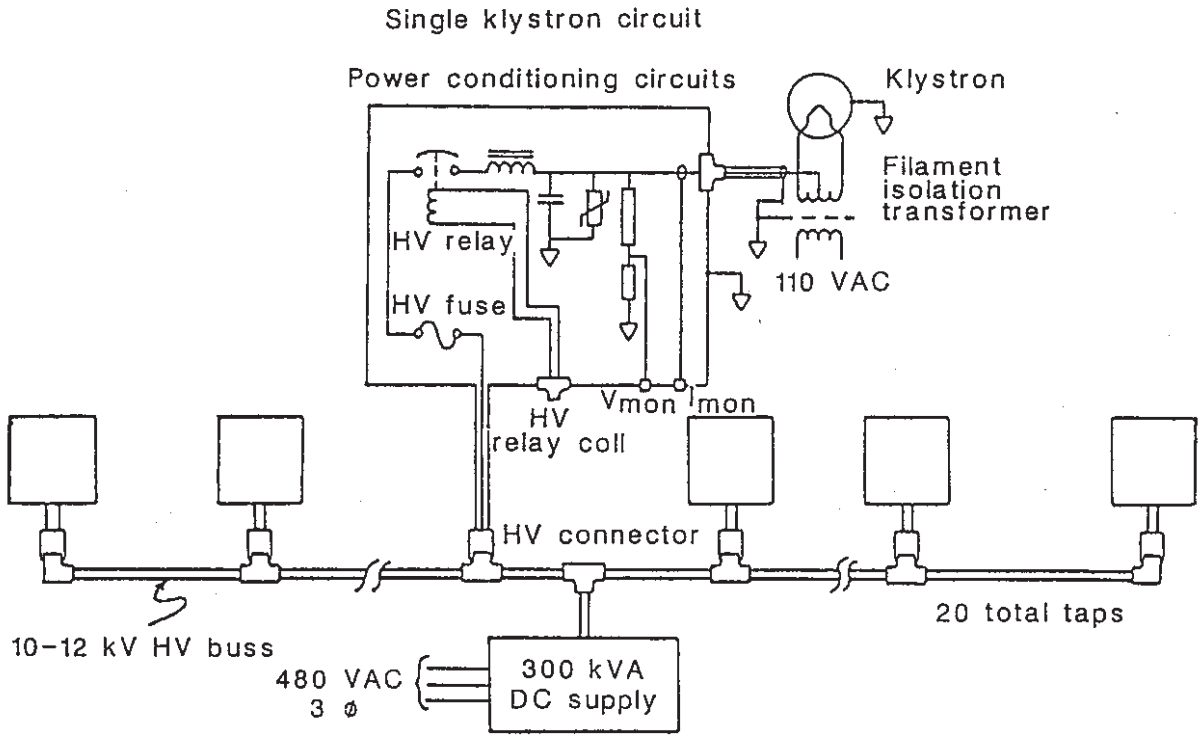


**Figure 6.10.** Typical klystron DC distribution (with one klystron circuit shown).

The key to the overall system is the RF control module, which has all of the circuitry required to control the entire RF chain. It provides set-point control, gradient leveling, phase control and stability, quench detection, reflected power foldback, and drive for the klystron. It also provides outputs proportional to field gradient, forward klystron power, reflected klystron power, and phase. It will be built in CAMAC (IEEE-583) format using a 3-wide module. Utilizing this format, the control hierarchy need only deal with this one module to control any of the parameters of the cavity. This structure simplifies the control software and allows replication of software routines throughout the system (Figure 6.11).

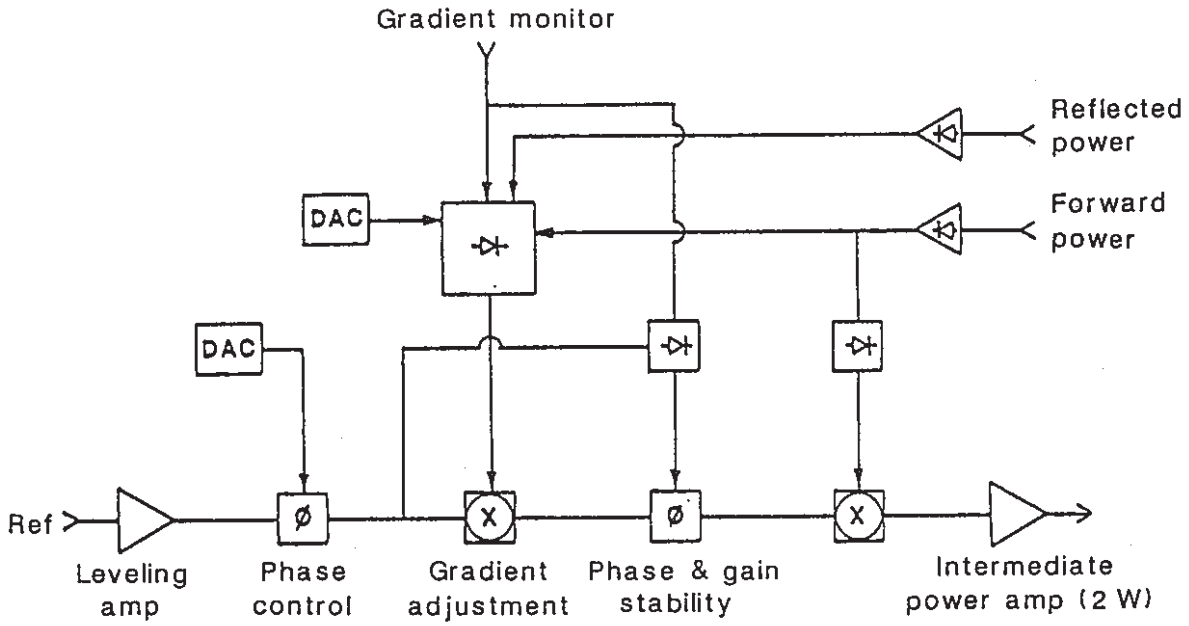


**Figure 6.11.** RF control module.

The advantage of individual control lies in the ability to operate each cavity at any power level up to its maximum operable field gradient. In the case of high performing cavities this means operating at energies above the specified 5 MV/m gradient. For cavities operating below 5 MV/m, this means operating at the maximum possible gradient without breakdown. Since each cavity can be set individually, stronger performing cavities can make up for weaker ones with individual cavities able to operate at greater than the lowest-common-denominator gradient.

System availability is always an operational concern. For a system composed of 400 RF drive chains, each with an estimated MTBF (mean time between failures) of 4000 hours, the probability of failure during an operating cycle of 160 hours (6⅔ days) running and 8 hours (1 shift) of maintenance with no intervening maintenance is .039. Assuming an operating energy of 4 GeV, and assuming that the total system can compensate for a 6.5% loss in RF drive, then 26 drive systems can be lost before the accelerator will be down. Using a POISSON distribution, the probability of 26 or more systems going down in the operating cycle described above is .013. Therefore, there is a probability of .987 of successfully completing an operational cycle as described above without having to stop for maintenance on the RF system.

Table 13.4

CEBAF Budget Projection

(Actual Year M $)

Construction-Related Budget (Obligations)

| | Prior Years | 87 | 88 | 89 | 90 | 91 | TOTAL to 1991 | 92 |
|---|---|---|---|---|---|---|---|---|
| Construction | | | | | | | | |
| Line Item, TEC | 0.3 | 25.0 | 65.0 | 65.0 | 55.0 | 26.0 | 236.3 | - |
| Pre-Construction | | | | | | | | |
| R&D | 9.5 | 6.2 | 6.0 | 4.5 | - | - | 26.2 | - |
| Total Project Cost | | | | | | | 262.5 | |

Operation-Related Budget

| | | | | | | | | |
|---|---|---|---|---|---|---|---|---|
| Pre-Ops/Ops | - | - | 1.1 | 7.1 | 11.9 | 18.6 | 38.7 | 29.1 (20.5*) |
| Physics Research | - | ** | 2.0 | 3.3 | 6.0 | 7.3 | 18.6 | 9.2 (6.5*) |
| Capital Equipment | - | - | - | - | 1.2 | 2.0 | | 5.7 (4.0*) |
| GSO & Mgmt. Fee | ** | ** | 1.4 | 2.8 | 2.0 | 3.5 | | |
| TOTAL | | 31.2 | 75.5 | 82.7 | 76.1 | 57.4 | | 44.0 |

*FY 1986 Dollars

**Included in Pre-Construction R&D

## 13.2 Cost Estimate

All cost estimates include EDIA and hardware deliverables. FY 1985 dollars are used throughout, except where indicated. Escalation is added after the budget profile is applied. Contingency is addressed at the estimating level and will be discussed in a later section.

The Level 2 WBS elements consist of hardware deliverables, except for Element 9 which is a service function. They are defined below:

1.0 Machine vacuum components consist of all accelerator components that hold vacuum, including RF cavities, cryostats, valves, and vacuum accessories.

2.0 Beam transport system consists of magnets, RF beam switches, magnetic septa, and beam position monitors.

3.0 RF system consists of components required to accelerate the beam such as the electron gun, klystrons, waveguides and power supplies. It also includes the local control module, the master oscillator, analog-to-digital modules, and control power systems.

4.0 DC power system consists of components required to deliver DC power to the magnets in the linac, the recirculating arcs, and the beam switchyard.

5.0 Instrumentation and control system consists of components required to provide master control hardware and software to all the facility systems. The local control hardware is included within each individual system; however, all of the integrating software is in WBS element #5.

6.0 End stations system consists of experimental equipment used for physics research, such as spectrometers, targets, large acceptance detector, scintillation counter array, and beam dumps.

7.0 Cryogenic system consists of the central helium refrigerator and helium distribution system for the linac and the end stations.

8.0 Conventional facilities system consists of tunnels for the accelerator, end station buildings for the experiments, support facilities for the whole project, utilities, and site preparation. CEBAF construction management and A/E management services are also included here. This WBS element includes the purchase and renovation of the SREL building.

9.0 Project services system consists of costs associated with the functions of project management, cost monitoring, schedule monitoring, systems integration (including overall physics support), clerical services, reporting, and procurement. The quality assurance and safety issues directly relating to project construction activities are costed in this WBS element.

Input data for the cost estimates come from several sources, for example: vendor catalogs, discussions with appropriate vendors, CEBAF staff experience, and accelerator construction experience at other laboratories. For non-standard items--the superconducting RF cavity is the major example--CEBAF double-checked vendor estimates by considering material cost and fabrication labor.

Tables 13.5(a) and (b) show the details of the cost estimate.

Table 13.5(a)

Project Cost Detail (K$)

| | | | Item Cost* | Total Cost* |
|---|---|---|---|---|
| a. | Engineering, Design, Inspection & Admin | | | 38,300 |
| | 1. Conventional Construction (at 21.6%) | | 10,800 | |
| | 2. Accelerator Components (at 28.5%) | | 19,100 | |
| | 3. Research equipment (at 27.6%) | | 8,400 | |
| b. | Construction Costs | | | 148,900 |
| | 1. Land & land rights (SREL) | | 1,700 | |
| | 2. Conventional construction | | 49,800 | |
| | a. Accelerator facilities | 8,600 | | |
| | b. Experimental facilities | 15,300 | | |
| | c. Support facilities | 10,200 | | |
| | d. Utilities and site preparation | 15,700 | | |
| | 3. Technical components | | 97,400 | |
| | a. Accelerator components | 67,000 | | |
| | b. Research equipment | 30,400 | | |
| c. | Standard Equipment | | | 1,900 |
| d. | Contingency (at 25%) | | | 46,900 |
| | Subtotal | | | 236,000 |
| c. | PE&D | | | 300 |
| | TOTAL | | | 236,300 |

Table 13.5(b)

Project Cost Profile by Major Cost Components ($M)

| | | |
|---|---|---|
| Accelerator Components | 67.0 | |
| Accelerator EDIA | 19.1 | |
| Subtotal | | 86.1 |
| Research Equipment | 30.4 | |
| Research EDIA | 8.4 | |
| Subtotal | | 38.8 |
| Conventional Facilities | 49.8 | |
| Conv. Fac. EDIA | 10.8 | |
| Subtotal | | 60.6 |
| SREL Purchase | | 1.7 |
| Standard Equipment | | 1.9 |
| Contingency | | 46.9 |
| Subtotal TEC | | 236.0 |
| PE&D | | 0.3 |
| TOTAL | | 236.3 |

Table 13.6 shows the cost breakdown from Level 1 through Level 3 in FY 1985 dollars, before contingency and escalation have been applied. The highest valued item in the table is the conventional facilities (WBS9.9). The estimate is $53.1 M, which was derived after extensive design and cost estimating studies by the A/E firm DMJM. Considerable documentation exists to back up the estimate. Chapter 11 describes all of the conventional facilities.

Table 13.6

Cost Breakdown Summary to Level 3

| | | MACHINE VACUUM | BEAM TRANS | RF SYS | DC POWER | CTRLS | END STATION | CRYO | CONV FAC | PROJ SERV | TOTALS |
|---|---|---|---|---|---|---|---|---|---|---|---|
| | | 1. | 2. | 3. | 4. | 5. | 6. | 7. | 8. | 9. | |
| Linacs | .1 | 23.2 | 0.6 | 12.1 | 0.1 | 1.4 | | 9.4 | | | 46.7 |
| Recirculators | .2 | 2.2 | 7.0 | | 2.8 | 1.0 | | | | | 13.0 |
| Beam Switch Yard | .3 | 0.6 | 1.2 | | 0.5 | 0.5 | | | | | 2.9 |
| Injector | .4 | 1.0 | | 1.5 | | 0.2 | | | | | 2.8 |
| End Station A | .5 | | | | | | 11.5 | 1.9 | | | 13.3 |
| End Station B | .6 | | | | | | 8.8 | | | | 8.8 |
| End Station C | .7 | | | | | | 7.0 | | | | 7.0 |
| Distrib. Systems | .8 | | | | | 1.7 | 0.8 | | | 5.3 | 7.9 |
| Conv. Facilities | .9 | | | | | | | | 53.1 | | 53.1 |
| Totals | | 27.0 | 8.8 | 13.6 | 3.4 | 4.9 | 28.1 | 11.3 | 53.1 | 5.3 | 155.4 |

Table entries are in rounded M$ and in FY1985$

The highest-valued linac components are machine vacuum components (WBS 1.1), RF power system (WBS 3.1) and the cryogenic system (WBS 7.1). These items are discussed below.

WBS 1.1 Machine Vacuum Components - Linac, estimate is $23.2 M. We have completed the detailed design layouts of this element, which includes the RF cavity and the cryostats. The superconducting RF cavity has been fabricated at Cornell University Newman Laboratory. Manpower time estimates for cavity fabrication are extrapolated from Cornell experience to production. These estimates have been confirmed with four interested vendors, who have studied the cavity drawings, and are involved in CEBAF's FY 1986 cavity prototyping program. The estimate of the RF cavities' cost is based on CEBAF analysis of part-by-part fabrication cost, Cornell experience, and the cumulative input from all four prototype vendors. The detailed fabrication drawings for the cryostat replacement units, which will contain the RF cavities, completely identify the cryostat components and their design shapes, for estimating purposes.

WBS 3.1 RF System & Injector, estimate is $12.1 M. All of the components within this system are within the capability of conventional RF technology. Many vendors and other large laboratories were contacted to contribute data for the cost estimate.

WBS 7.1 Cryogenic System - Linac, estimate is $9.4 M. All of the components designed into this system have been fabricated to date; however, the operating experience with cold pumps is limited. Cold compressor testing is underway at Fermi Lab, Brookhaven National Lab, and vendors.

Table 13.7 shows the construction budget profile by fiscal year. This Table indicates the derivation of the escalation amounts, using escalation factors provided to the project by DOE/DCES staff. The SREL purchase price of $1.66M, determined by the GSA, does not have contingency or escalation applied to it. The construction budget profile is graphed in Figure 13.2. The plot of the cumulative budget distribution is shown in Figure 13.3.

Table 13.7 CEBAF Construction Budget Profile

| | Prior Years | FY 1987 | FY 1988 | FY 1989 | FY 1990 | FY 1991 | Total |
|---|---|---|---|---|---|---|---|
| Construction Budget in FY 1985 $'s (w/o SREL Purchase) | | 18.59 | 45.06 | 42.45 | 33.79 | 13.83 | 153.72 |
| Escalation each year with respect to FY 1985 | | 1.69 (9.1%) | 6.94 (15.4%) | 9.55 (22.5%) | 10.21 (30.2%) | 5.33 (13.85%) | 33.72 (21.9%) |
| Contingency | | 3.06 | 13.0 | 13.0 | 11.0 | 6.84 | 46.90 (25.0%) |
| SREL Purchase | | 1.66 | | | | | 1.66 |
| Total Budget, in actual year $'s | | 25.0 | 65.0 | 65.0 | 55.0 | 26.0 | 236.0 |
| PE&D | | | | | | | .3 |
| TOTAL | | | | | | | 236.3 |

Table entries are in M$

Figure 13.2 Obligation Budget Profile.

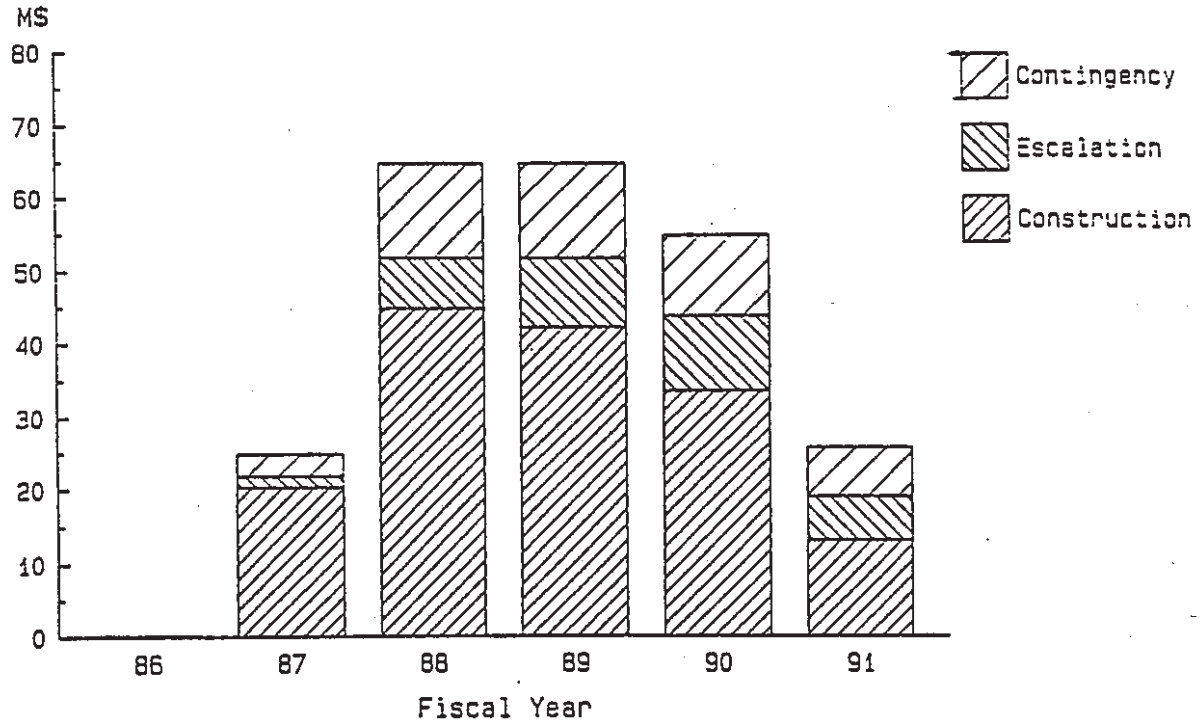


Figure 13.3 Cumulative Obligation Budget Distribution.

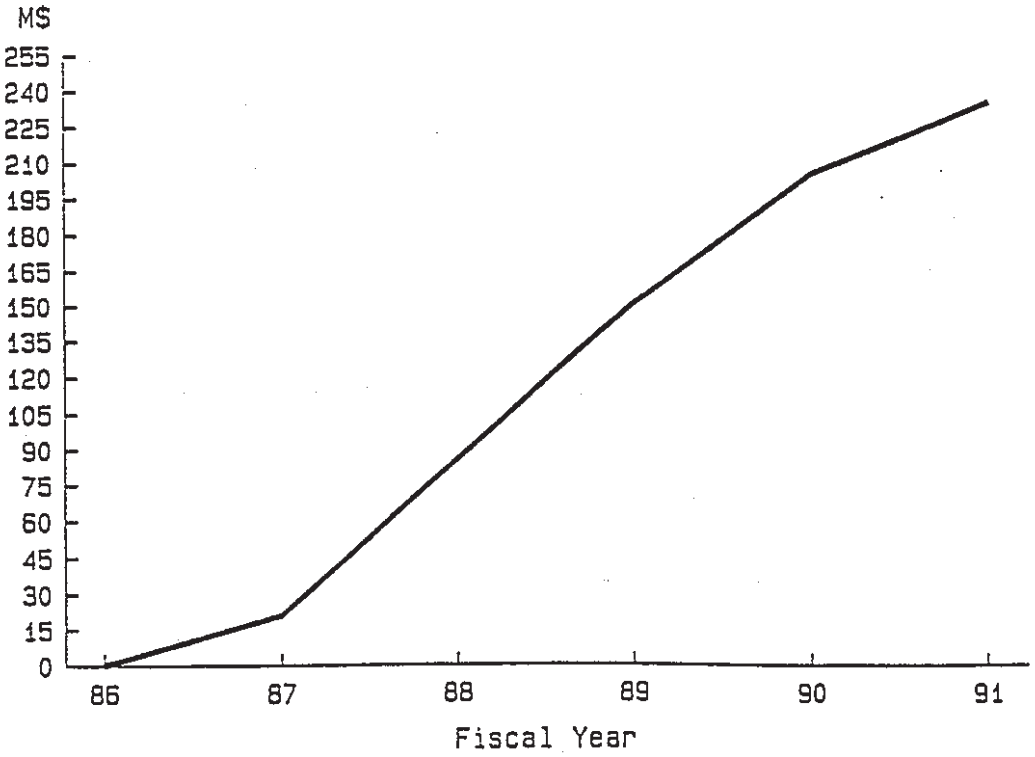

## 13.3 Contingency Analysis

Following the format of Table 13.6, Table 13.8 shows the contingency allowance at WBS Level 3. The contingency allowance was estimated after evaluating four factors: 1) design completeness, 2) unforeseen and unpredictable conditions, 3) uncertainties and risks, and 4) market conditions--prices and competition. Contingency factors are considered on each input data sheet (Figure 13.2), and assigned as a cost component at that level.

Table 13.8 Contingency Breakdown Summary to Level 3

| | | MACHINE | MAVACUUM | BEAM TRANS | RF SYS | DECR POWER | CTRLS | END STATION | CRYO | CONV FAC | PROJ SERV | TOTALS |
|---|---|---|---|---|---|---|---|---|---|---|---|---|
| | | 1. | | 2. | | 3. | 4. | 5. | 6. | 7. | 8. | 9. | |
| Linacs | .1 | 30 | 6.96 | 20 | .11 | 30 3.62 | 15 .01 | 25 .35 | | 30 2.81 | | | 30 13.86 |
| Recirculators | .2 | 20 | .43 | 20 | 1.40 | | 15 .43 | 25 .24 | | | | | 19 2.50 |
| Beam Switch Yard | .3 | 20 | .12 | 20 | .24 | | 15 .07 | 25 .13 | | | | | 20 .57 |
| Injector | .4 | 30 | .31 | | | 30 .45 | | 25 .06 | | | | | 30 .82 |
| End Station A | .5 | | | | | | | | 19 2.18 | 30 .57 | | | 21 2.74 |
| End Station B | .6 | | | | | | | | 19 1.67 | | | | 19 1.67 |
| End Station C | .7 | | | | | | | | 19 1.34 | | | | 19 1.34 |
| Distributed Sys. | .8 | | | | | | | 25 .44 | 20 .16 | | | 20 1.07 | 21 1.66 |
| Conv. Fac. | .9 | | | | | | | | | | 25 12.86 | | 25 12.86 |
| Totals, in %<br>Totals, in M$ | | 29 | 7.82 | 20 | 1.76 | 30 4.07 | 15 .51 | 25 1.21 | 19 5.34 | 30 3.38 | 25 12.86 | 20 1.0 | 25 |

Table entries on left of column are in percent and on right of column in rounded M$ (in FY 1985$).

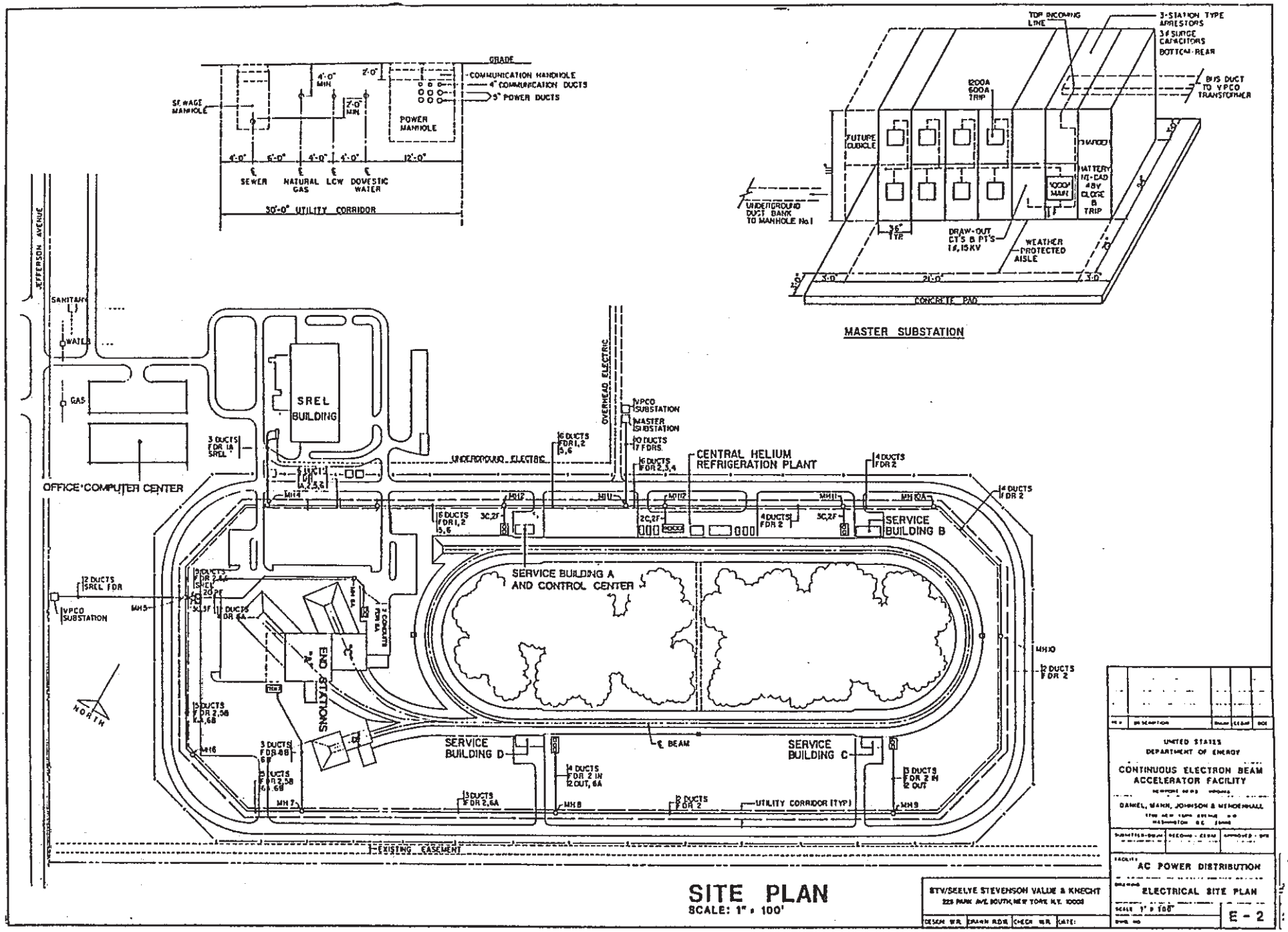
GRADE
COMMUNICATION HANDHOLE
4" COMMUNICATION DUCTS
5" POWER DUCTS
SEWAGE MANHOLE
POWER MANHOLE
4'-0" MIN
7'-0" MIN
2'-0"
4'-0"
5'-0"
4'-0"
4'-0"
12'-0"
SEWER
NATURAL GAS
LOW DOMESTIC WATER
30'-0" UTILITY CORRIDOR
TDP INCOMING LINE
3-STATION TYPE ARRESTORS
3¢ SURGE CAPACITORS
BOTTOM-REAR
BUS DUCT TO VPCO TRANSFORMER
1200A 600A TRIP
FUTURE CUBICLE
METER
BATTERY NI-CAD 48V CLOSE & TRIP
1000A MAIN
UNDERGROUND DUCT BANK TO MANHOLE No.1
3'6" TYP
DRAW-OUT CT'S & PT'S 14.15KV
WEATHER PROTECTED AISLE
3'-0"
21'-0"
3'-0"
CONCRETE PAD
MASTER SUBSTATION
JEFFERSON AVENUE
SANITARY
WATER
GAS
SREL BUILDING
OFFICE-COMPUTER CENTER
3 DUCTS FDR 1A SREL
OVERHEAD ELECTRIC
VPCO SUBSTATION
MASTER SUBSTATION
10 DUCTS 17 FDRS.
6 DUCTS FDR 1,2 5,6
6 DUCTS FDR 2,3,4
UNDERGROUND ELECTRIC
CENTRAL HELIUM REFRIGERATION PLANT
4 DUCTS FDR 2
SERVICE BUILDING B
SERVICE BUILDING A AND CONTROL CENTER
12 DUCTS SREL FDR
VPCO SUBSTATION
MH5
MH6
MH7
MH8
MH9
MH10
MH11
MH12
MH13
MH14
MH15
MH16
MH17
MH18
MH19
MH20
MH21
MH22
MH23
MH24
MH25
MH26
MH27
MH28
MH29
MH30
MH31
MH32
MH33
MH34
MH35
MH36
MH37
MH38
MH39
MH40
MH41
MH42
MH43
MH44

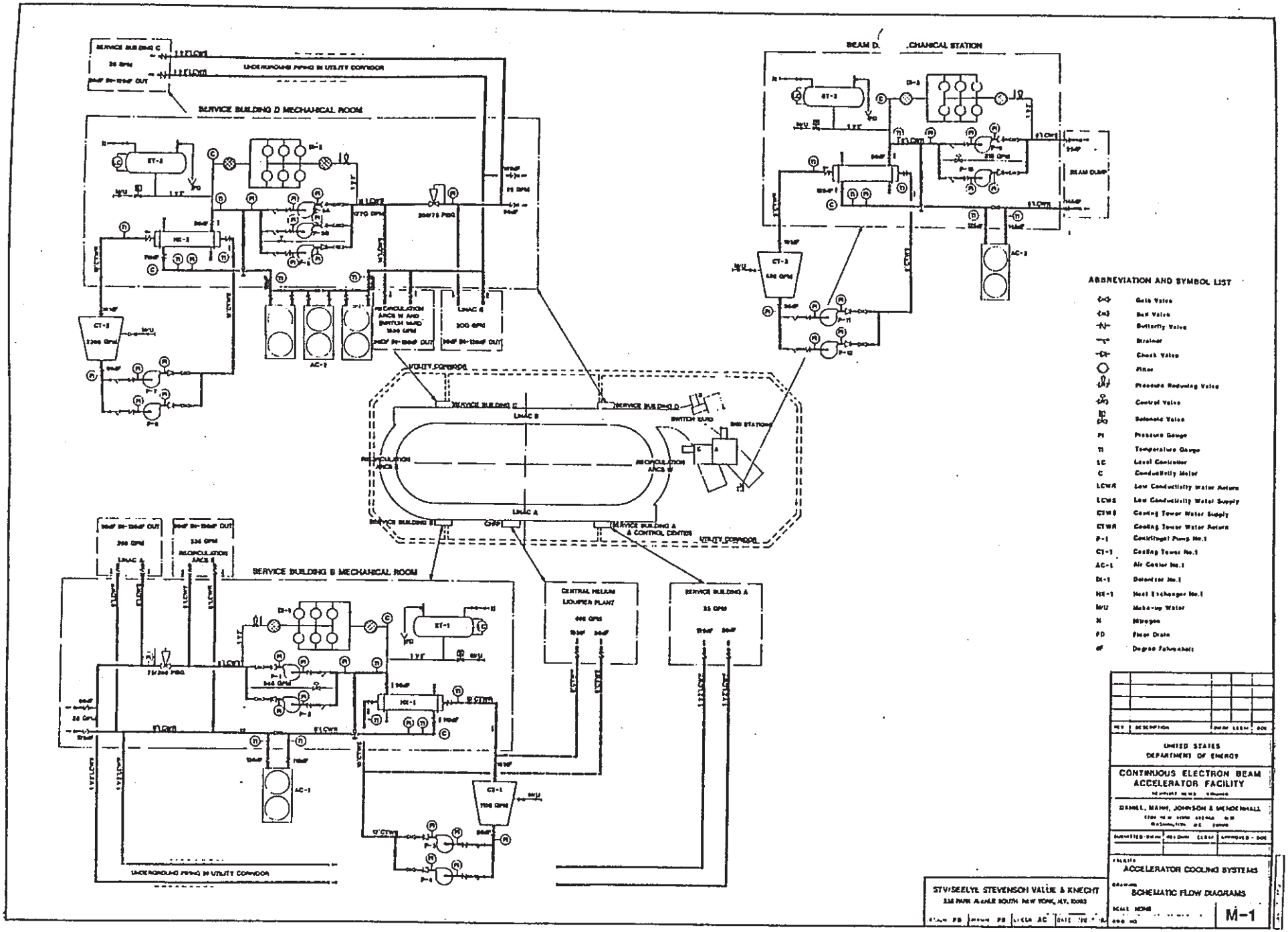
SERVICE BUILDING D MECHANICAL ROOM
BEAM D.
CHANICAL STATION
BEAM DUMP
UTILITY CORRIDOR
SERVICE BUILDING C
SERVICE BUILDING D
LINAC B
LINAC A
SERVICE BUILDING B
SERVICE BUILDING A
& CONTROL CENTER
SERVICE BUILDING B MECHANICAL ROOM
CENTRAL HELIUM LIQUEFIER PLANT
SERVICE BUILDING A
UNDERGROUND PIPING IN UTILITY CORRIDOR
ABBREVIATION AND SYMBOL LIST
Gate Valve
Ball Valve
Butterfly Valve
Strainer
Check Valve
Flow
Pressure Reducing Valve
Control Valve
Solenoid Valve
Pressure Gauge
Temperature Gauge
Level Controller
Conductivity Meter
Low Conductivity Water Return
Low Conductivity Water Supply
Cooling Tower Water Supply
Cooling Tower Water Return
Centrifugal Pump No.1
Cooling Tower No.1
Air Cooler No.1
Deionizer No.1
Heat Exchanger No.1
Make-up Water
Nitrogen
Floor Drain
Degree Fahrenheit
UNITED STATES DEPARTMENT OF ENERGY
CONTINUOUS ELECTRON BEAM ACCELERATOR FACILITY
DANIEL, MANN, JOHNSON & MENDENHALL
ACCELERATOR COOLING SYSTEMS
SCHEMATIC FLOW DIAGRAMS
M-1
STV/SEELYE STEVENSON VALUE & KNECHT



Figure 11.16

資料10－1

1. NONLINEAR BEAM DYNAMICS IN A FUNNEL FOR COMBINING TWO INTENSE ION BEAMS
2. BEAM BREAK-UP AND RESISTIVE WALL INSTABILITY IN A STEADY-STATE FREE ELECTRON LASER IN THE MICROWAVE REGIME
3. RELATIVISTIC KLYSTRON RESEARCH FOR HIGH GRADIENT A CCELERATORS
4. LABORATORY PERFORMANCE OF THE BEAR RFQ
5. HIGH-POWER MICROWAVE SOURCE DEVELOPMENT AT LOS ALAMOS
6. STUDYING THE END REGIONS OF RFQs USING THE MAFIA CODES
7. PROGRESS OF ELECTRON GUN SYSTEMS FOR THE $e^-/e^+$LINAC AT KEK
8. A FLIGHT-QUALIFIED RFQ FOR THE BEAR PROJECT
9. HIGH POWER L-BAND KLYSTRONS FOR LINEAR ACCELERATOR

10. A Compact Proton RFQ Injector for the Bevalac

11. TRANSIENT ANALYSIS OF MULTICAVITY KLYSTORNS

12. BEAM DETERMINATION OF QUADRUPOLE MISALIGNMENTS AND BEAM POSITION MONITOR BIASES IN THE SLC LINAC

13. THE ROLES OF FREQUENCY AND APERTURE IN LINAC ACCELERATOR DESIGN

14. DESIGN CONSIDERATIONS OF HIGH PEAK POWER GYROKLYSTRONS FOR LINEAR COLLIDERS

15. ENGINEERING DESIGN OF THE INJECTOR LINAC FOR THE ADVANCED LIGHT SOURCE(ALS)

16. RF POWER SOURCES

17. High-Brightness, High-Current Density Cathode For Induction Linac FELs

18. A LOW BETA RF LINAC-STRUCTURE OF THE IH-TYPE WITH IMPROVED RADIAL ACCEPTANCE

# NONLINEAR BEAM DYNAMICS IN A FUNNEL FOR COMBINING TWO INTENSE ION BEAMS*

J.H. Whealton, R.J. Raridon, K.E. Rothe,
W. R. Becraft,† and T.L. Owens,‡

Oak Ridge National Laboratory, P.O. Box 2009, Oak Ridge, Tennessee 37831-8071 USA

## 1. Abstract and Introduction

The concept of funnels was introduced over the last few years with an endeavor to increase the beam intensity by combining two beams in the following fashion:

The beam is, in each case, produced by an rf accelerator and thereby composed of bunches. The beam bunches are made to occupy relatively small fractions of the longitudinal phase in these cases. The bunches from each of the two beams are made to interlace and enter an rf deflector which produces the interlacing of the beams into one beam with twice as many bunches occupying twice the phase. The funnel itself, in one embodiment called the magnetic funnel, is composed of many transport elements with strong transverse focusing produced by quadrupole permanent magnetic fields. An occasional rf rebuncher is introduced to recompress the beam longitudinally so the beam occupies the appropriate small fraction of velocity space in the parallel direction. Crucial elements of the funnel are the beam dynamics in the rf rebuncher and in the deflector. Beam dynamics in either case must be assessed using an analysis which we are going to describe below.

Several components in a magnetic[1] funnel have been examined by dint of a full three-dimensional solution to the time-dependent Vlasov-Poisson equations with all image charges included.[2] Specifically, the rms emittance growth of subsystems is examined in detail. For the systems considered, a significant parallel emittance growth occurs. Details of the cause and ephemerality of this emittance growth are studied. These systems[1] were originally designed using the 2-1/2-D PARMILA-type analysis[3] which does not account for image charges and neglects azimuthal nonlinear space charge forces. Designs based on PARMILA are referenced for the subject evaluation. A highly resolved, accurate assessment of rms emittance growth has not been obtained with such analysis. However, for the subject analysis at least the precision is significant as will be shown. First, we will consider the simple rebuncher; second, the rf deflector; and third, we will introduce a nonlinear longitudinal emittance reducing "optical" element. The rms parallel emittance growth is due to the longitudinal velocity kick being dependent on a transverse dimension as well as the longitudinal dimension forming an oblique surface of zero volume, for example, in the three-dimensional phase; $z$, $V_z$, and $x$. A plane surface parallel to $x$ in this space has zero rms emittance. A curved surface or a plane not parallel to $x$ in this space has finite rms emittance under the conventional definition:

$$\varepsilon_{z,rms} = \frac{\beta\gamma}{n}\left\{\sum_j (z_j^2)\sum_j (z_j'^2) - \left(\sum_j (z_j^2 z_j')\right)^2\right\}^{1/2}.$$

*Research sponsored by the Office of Fusion Energy, U.S. Department of Energy, under contract DE-AC05-84OR21400 with Martin Marietta Energy Systems, Inc.

†Consultant, Grumman Space Systems, P.O. Box 3056, Oak Ridge, TN 37831.

‡Now at Fermilab

This is considered conventional, because of the protocol suggested by Los Alamos National Laboratory (LANL), and practical, because the occupation in phase space of an uncontrolled surface, even for a moment, eventually makes that surface uncontrollable. To effect control would require two identical particles seeing a different force even when they are in the same position at the same time. Control must be exerted as soon as possible upon the deviant. Having the longitudinal velocity depend differently on both transverse positions does not help matters as this is what happens in an rf deflector as presently considered.

## 2. Nonlinear Beam Dynamics in a RF Rebuncher (2-D)

The dynamic systems which we will consider are:

$$\nabla^2 \phi(\mathbf{x},t) = \int f_{-}(\mathbf{v}_{-}, \mathbf{x}, t)d\mathbf{v} - exp[-\phi(\mathbf{x},t)/T_e] \tag{1}$$

$$\frac{\partial f_{-}(\mathbf{v}_{-},\mathbf{x},t)}{\partial t} + (v_{-} \bullet \nabla_x) f_{-}(\mathbf{v}_{-},\mathbf{x},t) + [\nabla\phi(\mathbf{x},t) \bullet \nabla_{v_{-}}] f_{-}(\mathbf{v}_{-},\mathbf{x},t) = f_o(\mathbf{v}_{-},\mathbf{x},t) \tag{2}$$

The subject analysis can best be understood with reference to Figure 1, which shows the path of the calculation. First, the Poisson equation is considered. For this first pass, the source terms are set equal to zero and a Laplace equation is solved by SOR, finite difference, and boundary interpolation within a cell, using a Gauss-Seidel implicit method.[4] Considering the attributes A1, resource utilization, and A2, accuracy, iteration reduces memory requirements (A1), and boundary interpolation contributes to the accuracy per cell (A2). Generally, individual convergence of the solutions is not warranted on each pass (contributes to A1), since the iteration procedure lends itself to incomplete convergence of the intermediate solutions. As noted before, the finite difference method compared with the finite element method has in our experience reduced A1 by a factor of 20 for the Poisson solution (Reference 5 vs Reference 6) for the same accuracy. Boundary conditions for arbitrarily shaped metal surfaces can be specified as time-dependent Dirichlet or ramped Dirichlet conditions (contributes to A2). Neumann boundary conditions can also be specified.

Second, the Vlasov equation is solved for an arbitrary initial condition using the solution to the Laplace equation above for a time step $\Delta t$. The technique is described in References 7 and 6 where significant advances in A1 and A2 are reported. Reference 7 speeds up the Vlasov solver by a factor of 10 (contributes to A1) from that in References 8 or 9 while at the same time improving the accuracy by over a factor of 10 (contributes to A2). Reference 6 decreases resource utilization (A1) over Reference 5 by a factor of 400 with the same accuracy. The trivial relationship between the coordinates inside an element and the global elements for the uniform Cartesian grid used in this algorithm allows a factor of 20 (of the 400) savings in the Vlasov solver (A1) over that employed in the irregular elements of Reference 5. As mentioned in Reference 7, the Vlasov solver is made self-regulating in accuracy; trajectory refinement is undertaken only in those places that need it (A2).

Third, charge deposition is done in three dimensions by interpolation over the grid and is "exact" in the sense that as the three-dimensional grid is made more fine and the number of trajectories is increased, a result as accurate as desired can be obtained (A2). Notice that nowhere is any paraxial-like assumption made, and the fields "to all orders" are directly calculated (attribute A3, nonlinear effects). Therefore, aberrations (to all

orders) are also directly computed. Other nonlinear optics effects (A3) computed include space charge "to all orders" caused by nonuniform beam density and/or boundaries. (Boundaries cause nonlinear space charge forces also because they alter the delicate dependence of $\phi$ on r required to keep it linear.)

Fourth, the beam charge and the exponential plasma term (A3) are taken as inhomogeneous terms to the Laplace equation solved in step 1 above. Now the two inhomogeneous terms are, in many cases, large, of opposite sign, extremely nonlinear, and three dimensional. This is the cause of numerical difficulties that were first surmounted (in two-dimensional steady state) in Reference 8. The technique used, accelerated under-relaxation, improved the prior art[10] by a factor of 1000 (A1) in the beam perveance of interest and by a greater factor for higher perveance. Another factor of 10 (A1) increase in speed was achieved, while at the same time the accuracy was increased by more than a factor of 100 (A2) in Reference 9. This technique was extended to three dimensions in References 5 and 6. Essentially the best technique we have found is to use an unconverged Newton SOR outside its established range of validity.[11]

Fifth, the time is moved back by $\Delta t$, the ions are moved back to their phase space positions a time $\Delta t$ ago, and the Vlasov equation is resolved with the new fields computed from the Poisson equation solution of step 4. The trajectories are different from those computed in step 2 because of the presence of the space-charge terms (steps 3 and 4).

Sixth, since the trajectories of step 5 are different from those of step 2, steps 3, 4, and 5 are repeated (Vlasov-Poisson iteration) until no change obtains. This completes the convergence procedure (A2), and it is time to proceed to the next time step. However, one should note the implication of the iteration consisting of steps 5 and 6.

Seventh, the time is advanced by $\Delta t$ and steps 2 through 6 are repeated. This performs the beam evolution through the device under consideration.

The attributes A1 through A3 provide orbit accuracies of up to $10^{-8}$ radians in speedy calculations with significant nonlinearities. Six items contributing to a decrease in resource utilization (A1) total about $2 \times 10^9$ in the product of memory saved and CPU time (however, the accounting procedure leading to this figure is somewhat ambiguous). Five items contributing to increased accuracy (A2) make an improvement of about $10^6$ for a significantly nonlinear problem.

We turn now to a preliminary examination of a 425 MHz rebuncher. A rebuncher is generally a cylindrically symmetric affair as illustrated in Fig. 2. An emittanceless beam bunch of constant density (waterbag) is shown entering the fringe fields of an rf rebuncher. The fields are near the maximum and the nonlinear forces are evident in the accompanying phase space occupation diagrams.

When the center of the bunch is in the center of the rebuncher, the rf fields are at a null and only the space charge and image charge fields are present. At the end of the rebuncher, the longitudinal phase space occupation is supposed to have a negative slope. Nonlinear shear aberrations are also shown. Longitudinal emittance as a function of time is shown in Fig. 3 for both zero and 100 mA beam current. The double lumped structure represents partial canceling of aberrational shear forces on both sides of the null field (denoted as $\phi$=0 on Fig. 3). The partial cancellation occurs because of the extreme fringe fields such as shown in Fig. 2(a). The radial center of the bunch is molested much more than the edges. As the bunch proceeds, the edge catches up, partially mitigating the aberrations. Immediately after the null, the edge gets more action than the center (overshoots) and the emittance climbs again. Near the trailing edge of the fringe fields, the center catches up again. The net result, at least in the case of zero beam current is that most of the aberrations cancel (90 percent). The reason the rms emittance, at zero current, does not completely round out is that some ion relative motion occurs during traversal of the rebuncher. However, in the high

current case in Fig. 3, there is a noticeable space charge/image charge component which is superimposed on the above described shear aberrational phenomena.

The effect of waterbag bunch shape on longitudinal emittance is shown in Fig. 4 (for a somewhat different beam radius). The emittance growth for the hard (square) beam (S0) is significantly greater than the softer (elliptical) beams (S1 and S2); however, there is not much difference between S1 an S2 over the region considered. Numerical noise is 11 orders of magnitude lower than emittance values of interest.

A parallel normalized rms emittance growth on the order of 0.003 πcm. mr. is expected on the "simple" rebuncher. This is in contrast to the negligible growth predicted by PARMILA. Since there are several rebunchers, the total emittance growth due to rebunchers is expected to be higher than 0.003. The complex double rebunchers, necessary near the rf deflector, will probably add more than this because of the possible degradation of mode purity; the smoothness of the phase space distribution will possibly half this. For the whole funnel the estimated total parallel emittance growth due to the rebunchers is greater than 0.005.

## 3. Nonlinear Beam Dynamics in an RF Deflector (2-D)

Visualization of emittance growth in the rf deflector is aided by reference to a three-dimensional isometric which is shown in Fig. 5. For openers, we are going to consider a two-dimension variant of the deflector by considering strictly slot geometry. This produces some errors which will be checked later.

Three bunches in an rf deflector are shown at a particular instant of time in the lower part of Fig. 6, labeled B1, B2 and B3. The dashed lines are electric potentials at that instant of time. For this figure, the beam space charge is zero. The potential contours are at linear increments: a coarse increment for extreme potentials, and a finer linear increment near the center of the potential range where the beam bunch is located. Also shown in Fig. 6 are the transverse phase space occupation (upper left-hand side) and longitudinal phase space occupation (middle upper side and expanded on right-hand upper side).

Fringe fields due to the boundary conditions are clearly shown in Fig. 6. The part of the beam bunch nearest the deflector gets kicks in both the transverse and longitudinal directions. The bunches begin with zero emittance. Bunch number 1, as indicated on the $x$–$x'$ phase space diagram, is steered approximately into place (aberrations are noticeable); bunch number 2 is approximately 1/3 steered into place also with much aberrations; bunch number 3 shows very little change at this time (as indicated on both the phase space occupation diagrams shown). Longitudinal emittance of bunch number 2 is relatively large as indicated by the B2 $z$–$z'$ phase diagram while the first bunch parallel emittance is decreasing since the aberrational shear fields in the second gap, G2, are canceling out some of the rms emittance produced by the shear fields in the first gap, G1. At a later time, as illustrated in Fig. 8 taken near a null in the rf driving frequency, bunch number 1 has completed its emittance reduction and B3 is at a maximum in emittance because almost no cancellation has taken place. For 50 mA average beam current, the corresponding cases are shown in Figs. 8 and 9, respectively. Space charge fields interact with the fringe fields in the case of bunch numbers 1 and 3, respectively, in Fig. 8, whereas the main steering force is bent visibly for bunch number 2. The longitudinal emittance is even qualitatively different. The null field illustrated in Fig. 7 for zero current is now dominated by interacting bunches in Fig. 9.

Now we will consider the effect of a 425 MHz deflector on a 50 mA beam composed of bunches occupying 28 degrees out of 360 degrees longitudinal phase and 2.5 mm transverse width (see Fig. 10). The longitudinal emittance growth of this bunch is shown in Fig. 11. Both 50 mA and 0 mA are shown in Fig. 11. To get an idea of the properties of such a deflector, we consider first the time reversed deflector in slot geometry. This is done to expedite the calculation. Time reversal is not seriously inhibiting. Similar

results apply either way when correctly interpreted. Slot geometry probably shows the emittance growth to within a factor of two in either the parallel or transverse direction. An azimuthal nonlinear space charge issue is neglected by such a representation. The main point of the computation is to get a clear idea of the space charge, image charge and applied field aberration issues as quickly as possible, so we can focus on the relevant causes.

In Fig. 10(a), a bunch is entering (leaving) the fringe fields of the deflector. The space charge fields and image charge fields are clearly interacting with the fringe fields. In Fig. 10(b) and 10(c), the time is near an rf null [as is Fig. 10(f)] and the space charge fields dominate the applied rf fields. In Fig. 10(d)-(e), the applied fields dominate, but are clearly perturbed by the space charge fields.

The shear fields are partially canceled by having the field reversed in the gap. This is one of the advantages of having the field reversed in the gap. Another advantage is that the nonlinear shear fields will on the average be smaller in the gap since the rf fields are nearer zero. A major disadvantage is that the steering is mitigated as a result (see Fig. 12 for $T_D=1\beta\lambda/2$). As the bunch enters the gap, the steering is initially in the wrong direction; exiting the second gap also produces wrong direction steering. Therefore, the intended steering has to compensate for this. The steering will be less than intended. In this instance, where the thickness of the deflector is $\beta\lambda/2$, the actual steering is 1.36 degrees instead of the 1.50 degrees as planned. Incidentally, the computations agree exactly with the simple calculations (it was only tested to one part in 1000) for the steering in a configuration with no fringe fields. Such a deficit in steering may appear at first sight to be an issue; however, to produce higher steering, say 10 percent higher, requires higher fields in the deflection section which impact reliability and higher heat loading since the rf power to the device is proportional to $E^2$, so the rf power/heat loading must go up to 20 percent. There may be a heat dissipation problem even without this inconvenience.

The effect of changing the deflector thickness on the longitudinal emittance growth and steering angle are shown for four values of L: $\beta\lambda/2$, 1.2 $\beta\lambda/2$, 0.7 $\beta\lambda/2$, and 0.8 $\beta\lambda/2$. Emittance growth is shown in Fig. 13 and steering is shown in Fig. 12. A thickness somewhat smaller than $\beta\lambda/2$ appears desirable since the steering increases a few percent with no reverse fringes to counter and the emittance decreases.

Also shown in Fig. 13, is the situation without deflector fields (therefore no field aberrations). The parallel emittance grows, even in this case, about the same as for the thin plate $T_D$ ~0.7 $\beta\lambda/2$ case, indicating that virtually all of this emittance growth is due to nonlinear space charge and image charges.

An important feature of Fig. 11 is a qualitative difference between the emittance growth in the high current case and the low current case. The low current case, when not molested by fringe fields, shows no rms emittance growth. However, the high current case seems to suggest a prevailing emittance growth with time, or distance traversed, on which the shear aberrational fields are only a perturbation. This prevailing emittance growth is caused by nonlinear space charge forces and nonlinear image charge forces and is denoted by the line L2.

Results for a 100 mA deflector whose pulse width is 4 mm and longitudinal phase occupation is 28.30 is shown in Fig. 14. The convergence of the solution as a function of axial resolution is shown in Fig. 15 for an order of magnitude variation.

## 4. Three-Dimensional Calculations on RF Deflector

The heart of the deflector in full three-dimension is shown in Fig. 16. Fig. 16(b) is rescaled and the three axes are not the same. The beam is chosen to be a square bunch and is seen drifting approximately in the middle of the device in Fig. 16. Because of the scale of the figure the fact that the rf deflector plates are much longer than the space between them is not evident from the drawing. However, the spacing was indicated

previously in the two-dimensional section; for example, Fig. 10 actually reflects the situation. In Fig. 17 is shown again unscaled coordinates of the rf deflector in full three-dimension showing the entrance aperture, the rf parallel plate deflector itself. In this case, in part A of this figure, potential contours on the symmetry axis occur at an instant of time when the pulse happens to be in the middle of the deflector and these fields, at a maximum, are shown. The fringe fields can easily be seen. The contours of the fringe fields are compressed over the contours of the fields in the normal deflection region so as to show the extent of the fringe fields. In part B, the same situation is shown except the 100 mA pulse is being deflected. The pulse happens to be at this time in the middle of the rf deflector plates. On the symmetry axis one can see an indentation. A depression of this equal potential contour is due to this pulse. This is similar to the findings in the two dimensional situation.

The situation in Fig. 18 is rather similar to Fig. 17, except that here is exhibited explicitly the fringe fields near the aperture. This is the situation shown for both 0 mA and 100 mA current in Fig. 18(a) and 18(b), respectively. The issue is these fringe fields coming from the parallel plate deflector and entering and impinging upon a circular hole at the entrance of the exit aperture. The effect of these fringe fields is a principle result of these three-dimensional calculations.

The parallel emittance growth for these three-dimensional deflectors is shown as a function of time for a particular pulse in Fig. 19. Here we see the characteristic emittance growth at the beginning for either 0 mA or 100 mA current. We see a gradual but slower emittance growth in the region of the rf deflector itself for the case of the 100 mA beam and no growth for the case of the 0 current beam. The various bunches given to the beam at the fringe field upon exiting the deflecting region are shown in both the 100 mA and the 0 mA cases by the twitches thereof, and finally, the post emittance variation is shown. There is no increase of emittance above a certain level for the 0 current beam, which is expected since no nominal space charge forces are present and nothing else would be existing in this region to increase the emittance of the beam. However, as was shown in other cases previously, for the 100 mA beam there is the characteristic nonlinear space charge induced longitudinal emittance growth.

In this case, as in so many cases, the initial distribution of the beam has zero emittance, which corresponds to a shoebox waterbag model. If the emittance was larger to begin with, then the emittance growth fortunately would be presumably less than is shown here. All the emittance growth that we see here is obtained in the funnel itself for a 0 emittance. If the beam, for example, has an initial emittance of 0.005 and a current of 100 mA, then instead of the final emittance being 0.0085 as is shown here at the final time, the final emittance would probably be approximately 0.01, reflecting the quadratics zoning of the emittance growth with the initial emittance of the beam.

The transverse component of the emittance transfers both to the beam direction and transverse to the surface of the deflector electrodes is shown in Fig. 19 as a function of time. Again we have the usual twitches on both as the beam bunch passes both ends of the deflection plate and we have in both cases a significant emittance contributed by non-cancellation of these fringe fields from one end to the other.

The emittance growth calculation here for the rf deflector are approximately 0.008 $\varepsilon_z$, or $\varepsilon_x$, and slightly less for $\varepsilon_y$, These values are significantly in excess of the PARMILA projection (Reference 3).

## 5. New Parallel RMS Emittance Reducing Lens

For a typical rebuncher, the parallel emittance growth for a hard (square in r-z space) and soft (elliptical) beam as a function of distance traveled by the bunch is shown by the upper curves in Figs. 20 and 21. Suitable phasing of the rebuncher, as determined by the subject analysis, with respect to the bunch produces a deliberate smashing of the

beam to counteract the natural nonlinear space charge/image charge forces. The successful use of this technique is indicated by the bottom curves of Figs. 20-21, showing significant improvements in parallel emittance growth (factor of ~2). Further development of this, and similar techniques, have the prospect of enhancing beam quality significantly.

A look at Fig. 22, which is the same as Fig. 20 for the symmetry rebuncher but is continued for twice the time or distance, will show that the peak of the parallel emittance as a function of the time for a bunch increases after the region of the rebuncher starting at the point labeled A. The parallel emittance continues to increase in the drift rather strongly to point B, continues to increase, after a while starts to level off, reaching a maximum at point C, then levels off for a significant time, finally dips a little bit (approximately 10 percent at point D), and then starts increasing. An examination of the beam properties in these four cases will show why the emittance has this property. Fig. 23 is a simple rebuncher with a beam pulse. This corresponds to point A of the curve in Fig. 22. The rebuncher is joined by a transport channel with no fields connected but a Dirichlet metal boundary condition as indicated. The beam simply drifts along this channel and the emittance is examined. The top diagram in Fig. 21 is the transverse emittance where the transverse philosophy is plotted versus the transverse distance. There is a finite emittance which can be seen. The bottom right hand diagram is the longitudinal emittance with the longitudinal velocity as the vertical axis and the longitudinal position of the beam as the horizontal axis. The points approximately fall along a straight line with relatively low emittance (point A in Fig. 22). Slight aberrations occur on the ends. The velocity is characteristic of a rebuncher, which means the beam is compressing. Fig. 24 is after the beam has drifted a significant distance, as shown. This corresponds to point B on Fig. 22. The transverse emittance has increased significantly and the parallel has obviously increased. Enormous aberrations, basically from nonlinear space charge forces between points A and B, can be seen on the longitudinal emittance diagram on the lower right hand side. This is consistent with the curve in point B of Fig. 22. As the beam drifts still further, as indicated in Fig. 25 (corresponding to point C of Fig. 22), it covers an enormous distance. The longitudinal emittance is very high and very different from that presented in Fig. 24. Here the beam is essentially crossing over from a rebunch case to a debunched case. Figure 26, corresponding to point D of Fig. 22, shows the beam transported still further. The beam is now debunching. Space charge forces have caused the beam to expand instead of compress, and the emittance growth is slowing down for the moment, but will increase again as the beam simply expands in a very nonlinear fashion. This kind of growth is a significant concern for intense beams drifting in long, unneutralized transport systems where there is a requirement for very low longitudinal emittance growth.

## 6. Conclusions

One embodiment of a funnel will probably contribute to a parallel emittance growth, end to end, of about 0.015 πcm mr, assuming perfect alignment according to calculations performed thus far. The transverse emittance growth is expected to be slightly less, but still on the order of 0.010πcm mr. The value for the parallel emittance may be halved with the deployment of the lens discussed in Section 5.

## References


1. K. Bongardt et al., Proc. Symp. Accel. Aspects of Heavy Ion Fusion, GSI-82-8, 224 (1982), also GSI-84-11, 389 (1984); F.W.Guy, AIP Conf. Proc. 139, 207 (1985); F.W. Guy and T.P. Wangler, ibid, p. 185.
2. "Ab Initio Calculation of Nonlinear Transient Beam Dynamics for Ion LINAC and Injectors," J.H. Whealton, R.J. Raridon, M.A. Bell, K.E. Rothe, B.D. Murphy, and P.M. Ryan, Workshop on Space Charge Effects in Beam Dynamics, ORNL (1986); "Ion Beam Dynamics in High Intensity RFQ LINAC," J.H. Whealton, R.J. Raridon, M.A. Bell, K.E. Rothe, B.D. Murphy, Twenty-Eighth Annual Meeting of the Division of Plasma Physics of the American Physical Society, Baltimore, Maryland, November 3-7, 1986; 1987 Particle Accelerator Conference, Washington, D.C. March 16-19, 1988, Bull. APS 32, 189 (1987); "3D, Full Implicitly, Ion Time Scale, Self-Consistent Plasma Edge Calculations Near ICRH Antenna/Faraday Shield," J.H. Whealton, P.M. Ryan, and R.J. Raridon, ICRF/Edge Physics Workshop, Boulder, Colorado, March 30, 1988.
3. T.L. Owens, private communications (1987). Some of the PARMILA calculations were done by K. Crandall of AccSys Inc.
4. G. D. Smith, Numerical Solution of Partial Difference Equations: Finite Difference Methods, 2nd ed. (Oxford Univ. Press, Oxford, 1978).
5. J. W. Wooten, J. H. Whealton, D. H. McCollough, R. W. McGaffey, J. E. Akin, and L. J. Drooks, J. Comput. Phys. **43**, 95 (1981); K. Ota, N. Inone, H. Hikei, J. Marikawoo, S. Ishida, and T. Uchida, J. Appl. Phys. **23**, 1241 (1984);J. W. Wooten, J. H. Whealton, and D. H. McCollough, J. Appl. Phys. **52**, 6418 (1981).
6. J. H. Whealton, R. W. McGaffey, and P. S. Meszaros, J. Comput. Phys. **63**, 20 (1986).
7. J. H. Whealton, J. Comput. Phys. **40**, 491 (1981); J. H. Whealton, Nucl. Instrum. Methods **189**, 55 (1981); J. H. Whealton, IEEE Trans. Nucl. Sci. **NS28**, 1358 (1981).
8. J. H. Whealton, E. J. Jaeger, and J. C. Whitson, J. Comput. Phys. **27**, 32 (1978).
9. J. C. Whitson, J. Smith, and J. H. Whealton, J. Comput. Phys. **28**, 408 (1978); J. H. Whealton and J. C. Whitson, Part. Accel. **10**, 235 (1980).
10. E. F. Jaeger and J. C. Whitson, ORNL/TM-4990, 1975.
11. J. M. Ortega and W. D. Rheinboldt, Iterative Solution of Nonlinear Equations in Several Variables (Academic Press, N.Y., 1970).

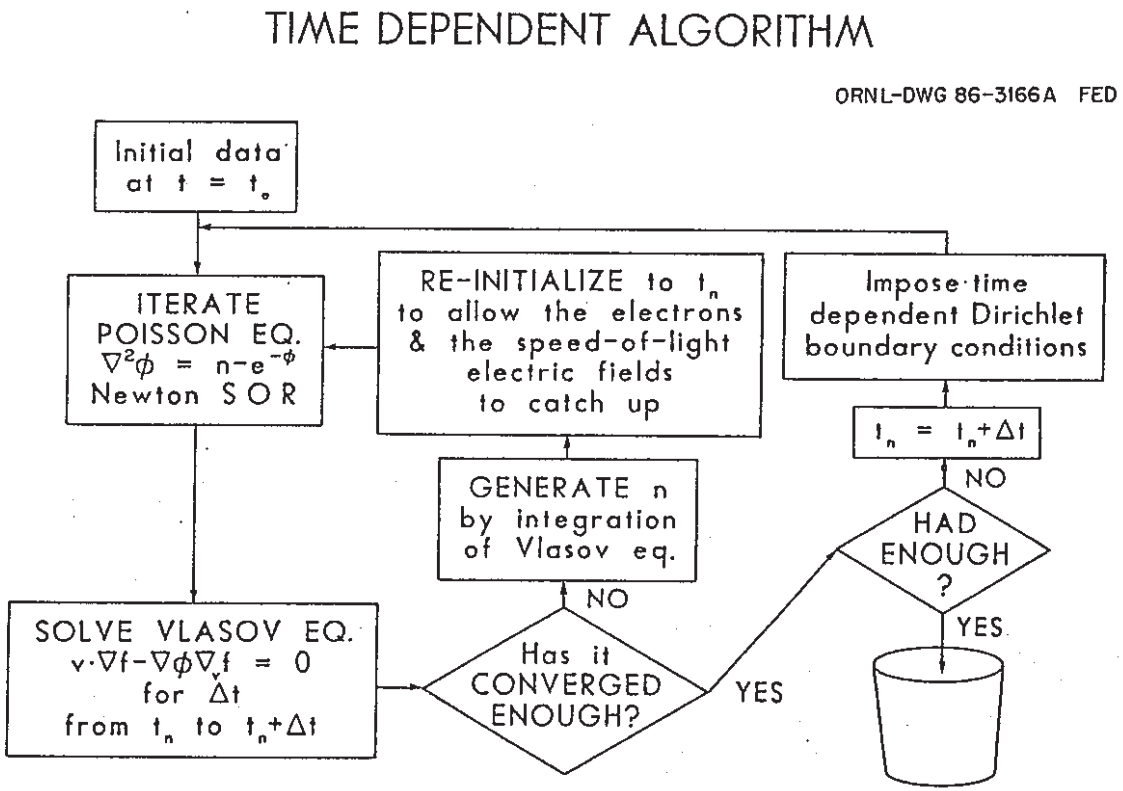


Fig. 1. Path of calculation for 3-D, time-dependant Vlasov-Poisson analysis.

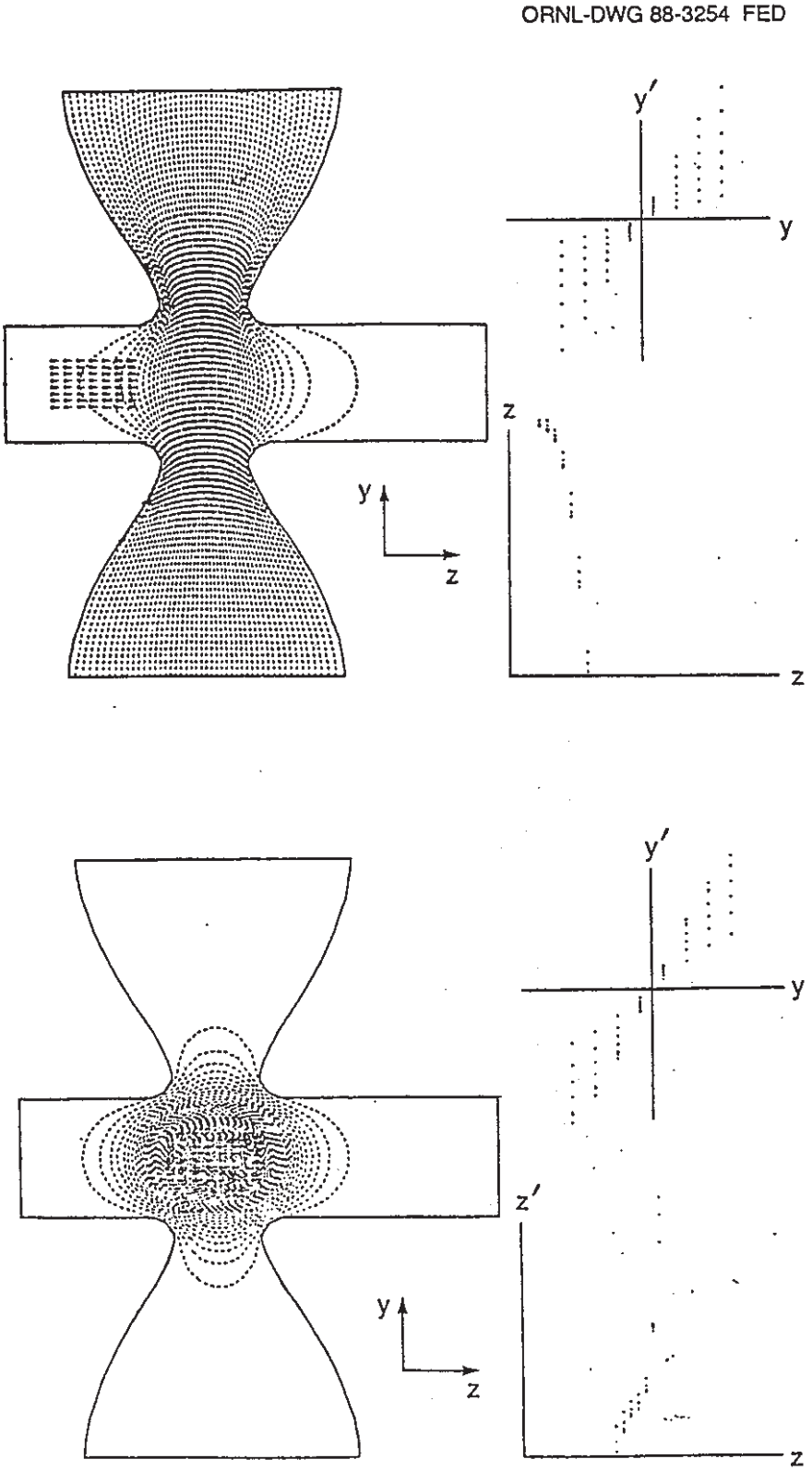


Fig. 2. Rebuncher at two different times.

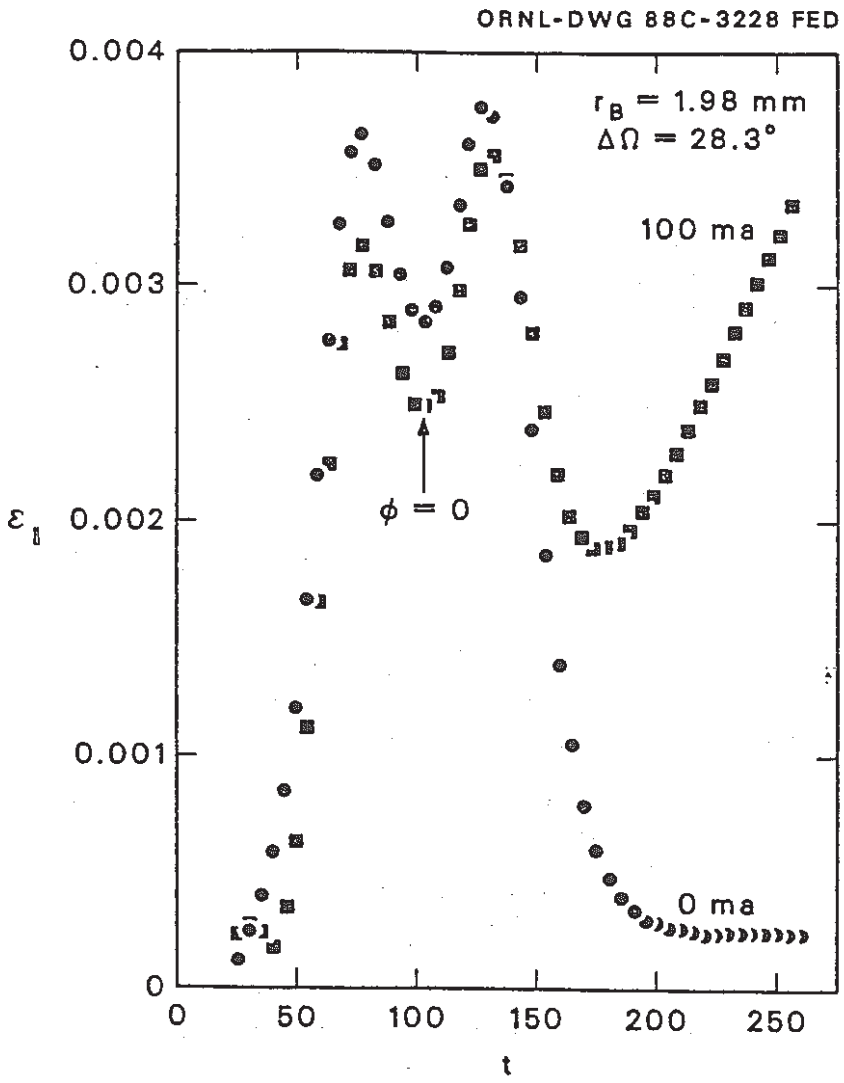


Fig. 3. Longitudinal emittance as a function of time.

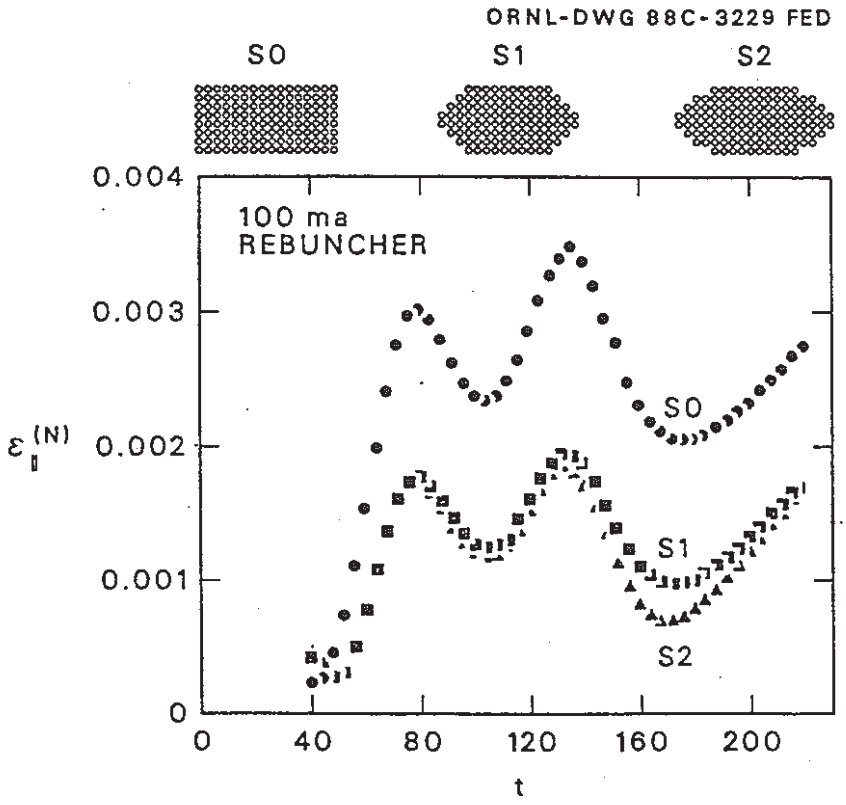


Fig. 4. Effect of beam shape on longitudinal emittance.

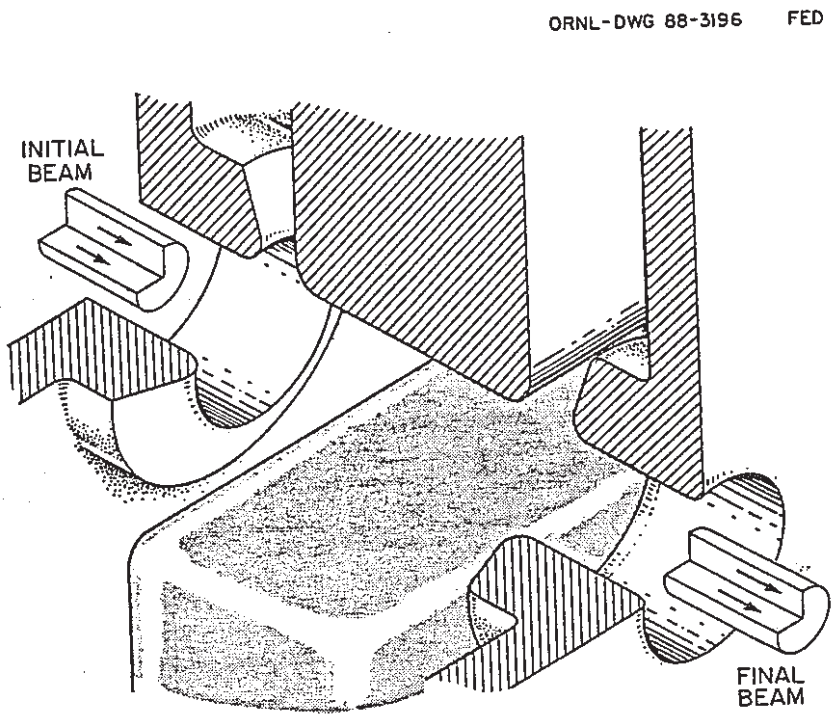


Fig. 5. Isometric of an rf deflector.

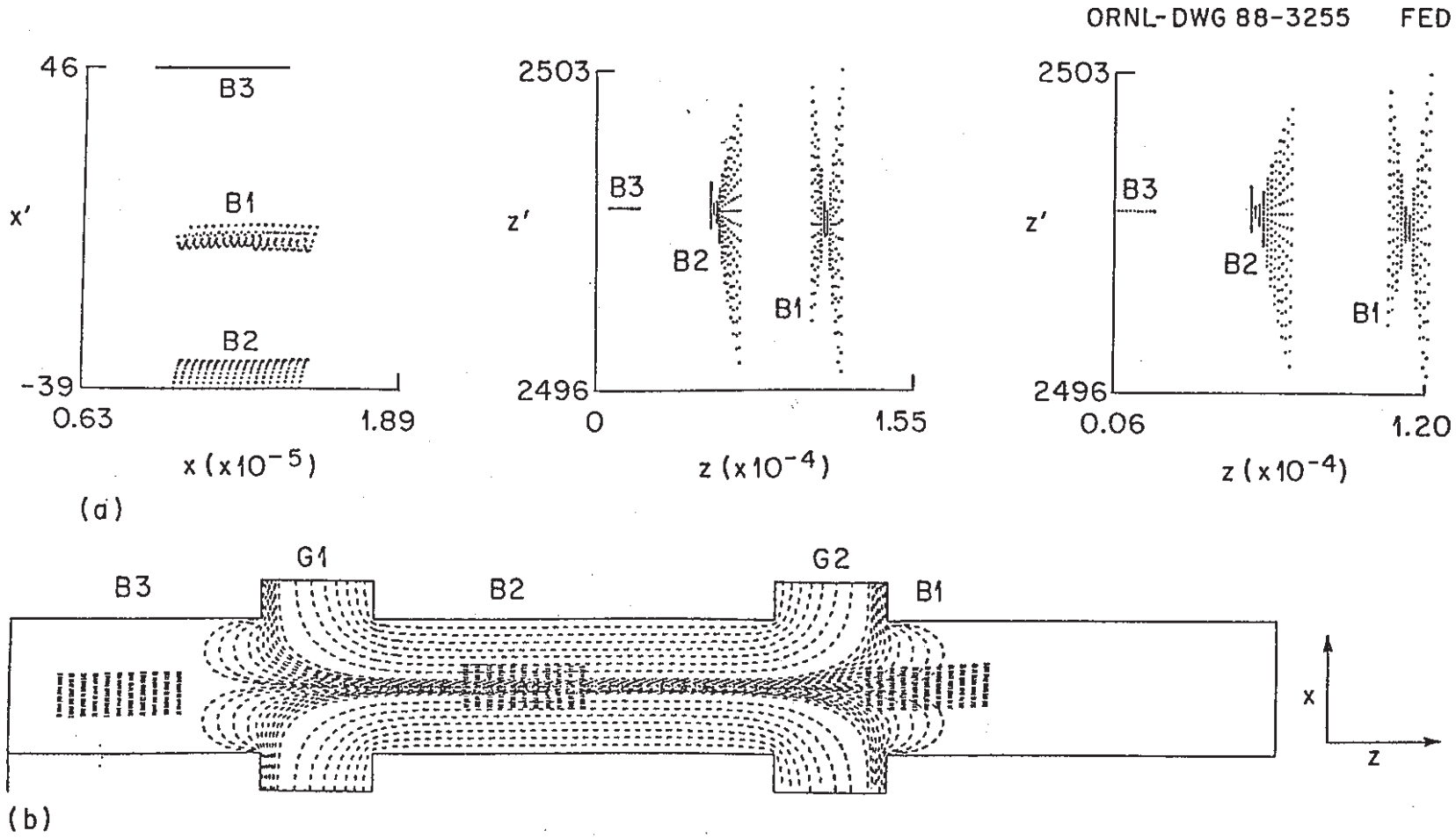


Fig. 6. Phase space occupation and deflector.

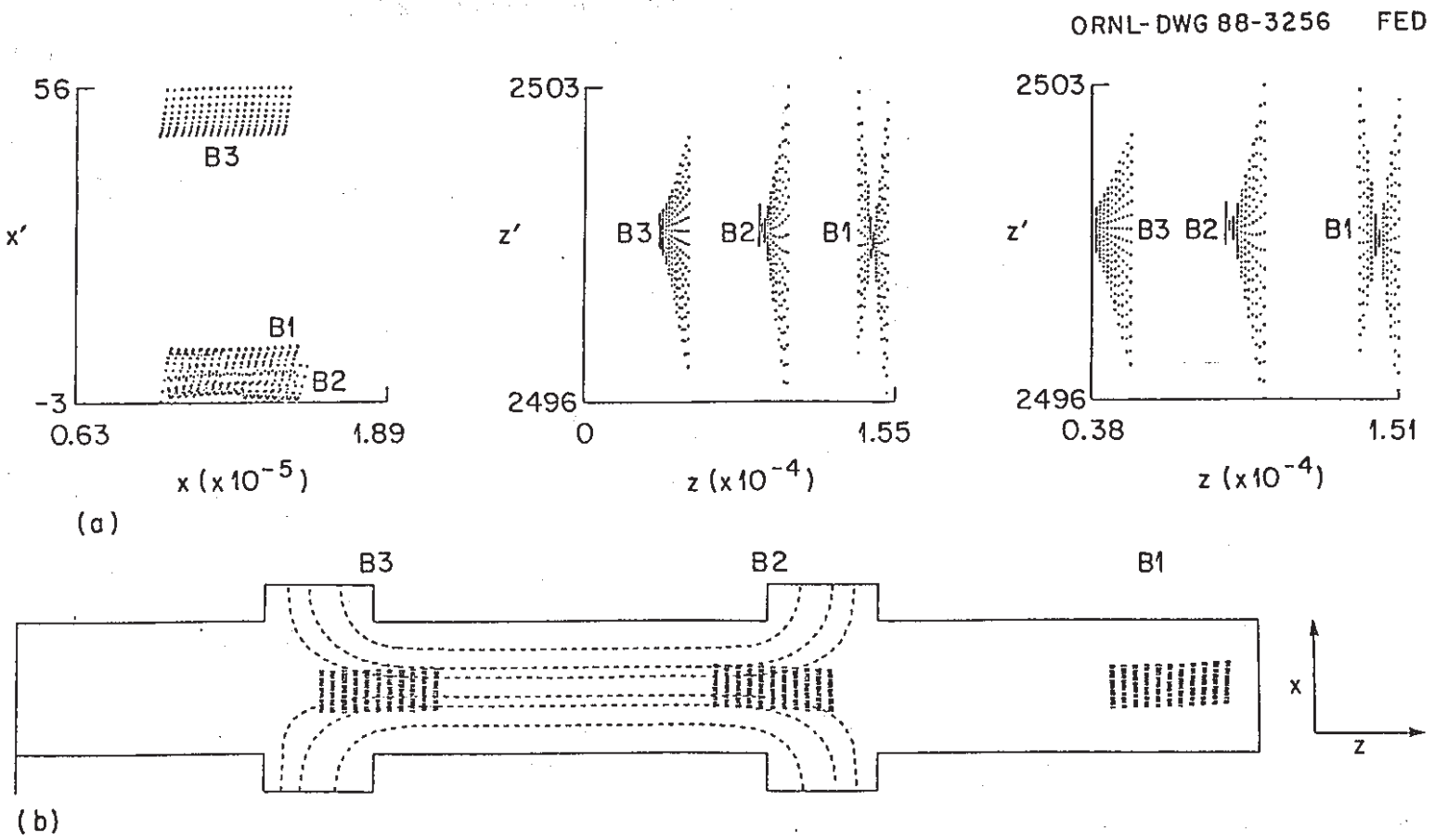


Fig. 7. Phase space occupation and deflector near a null.

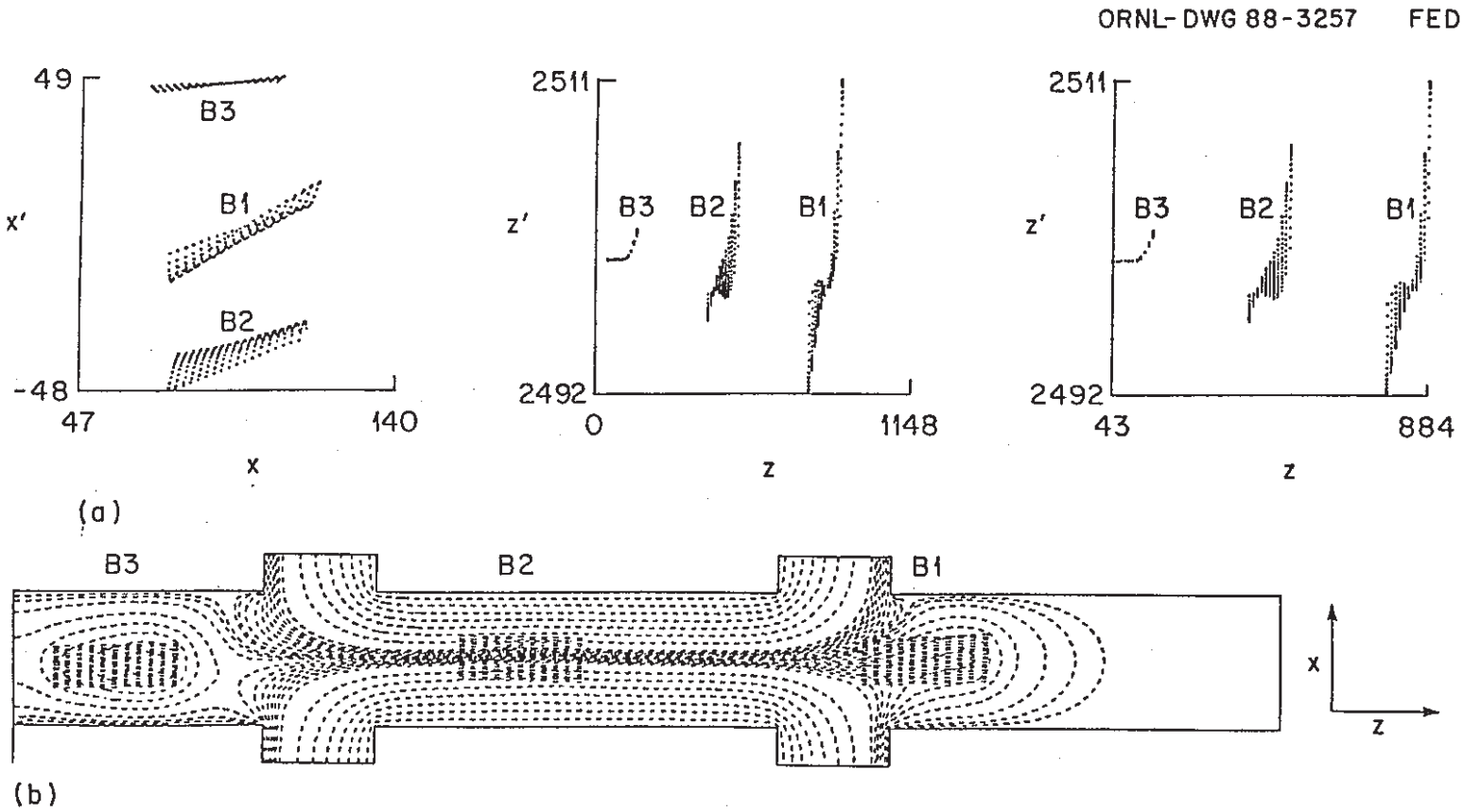


Fig. 8. Phase space occupation and deflector for $I_B$ = 50 ma.

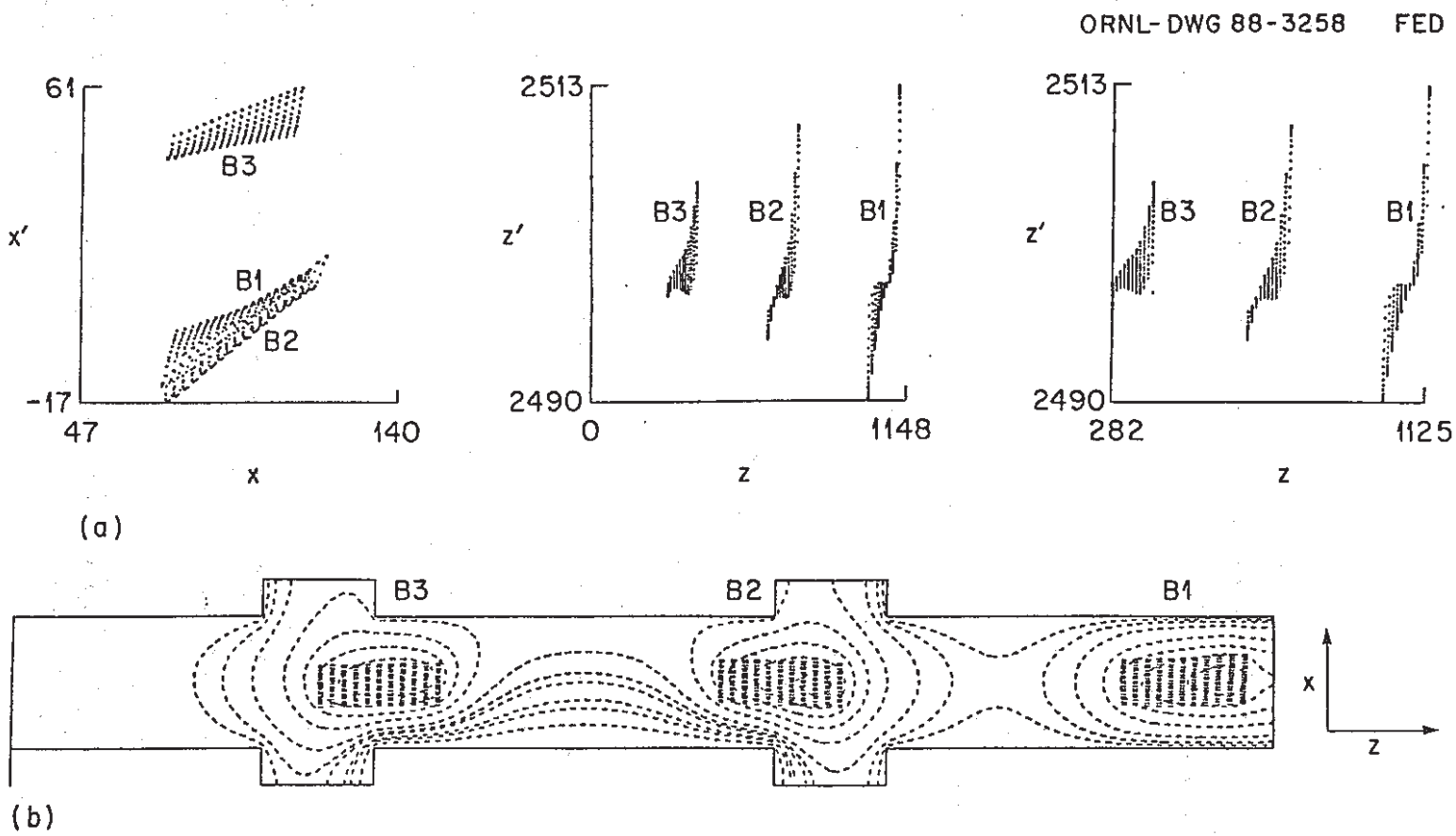


Fig. 9. Phase space occupation and deflector near a null for $I_B$ = 50 ma.

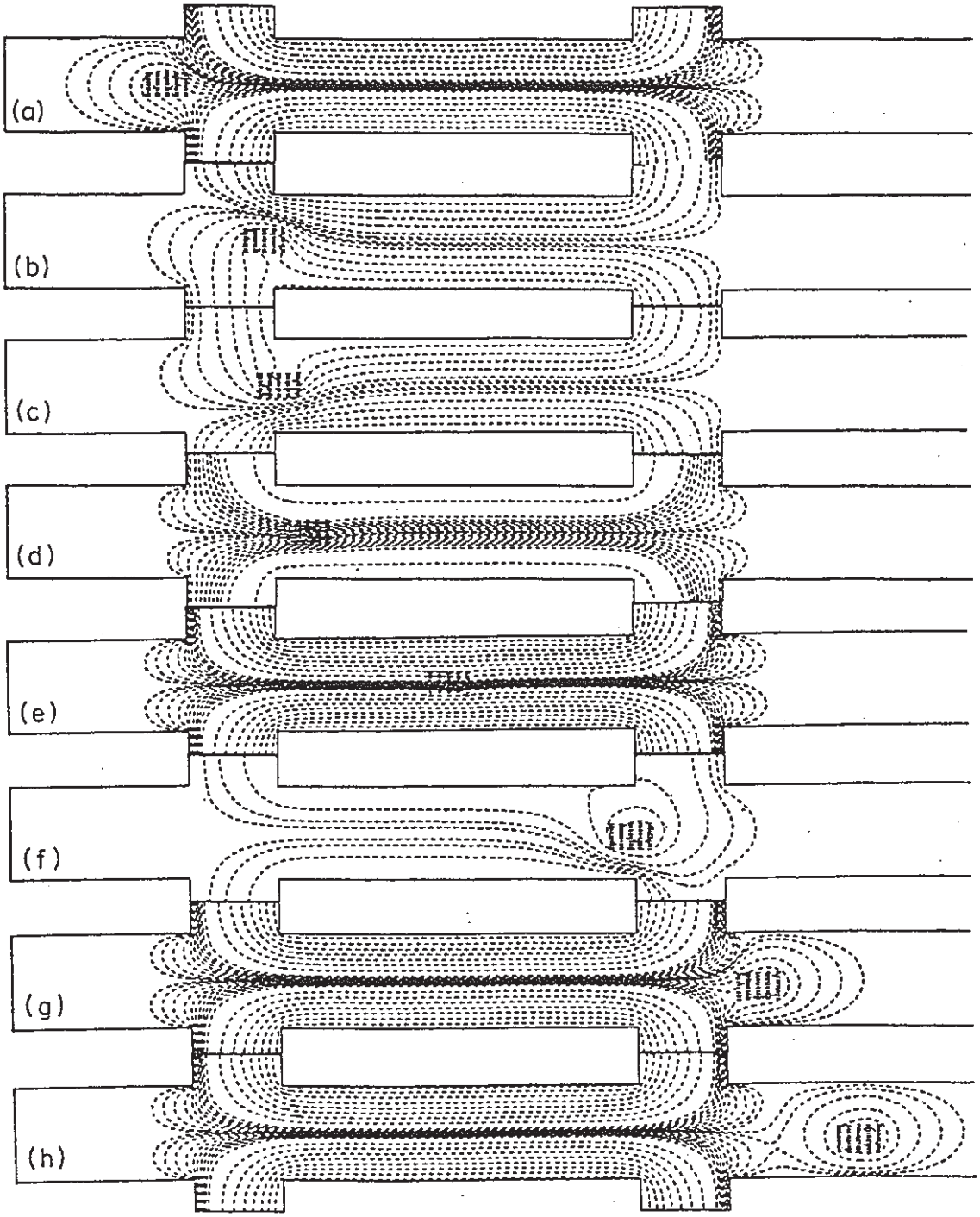


Fig. 10. Bunches occupying 28 degrees out of 360 degrees longitudinal emittance.

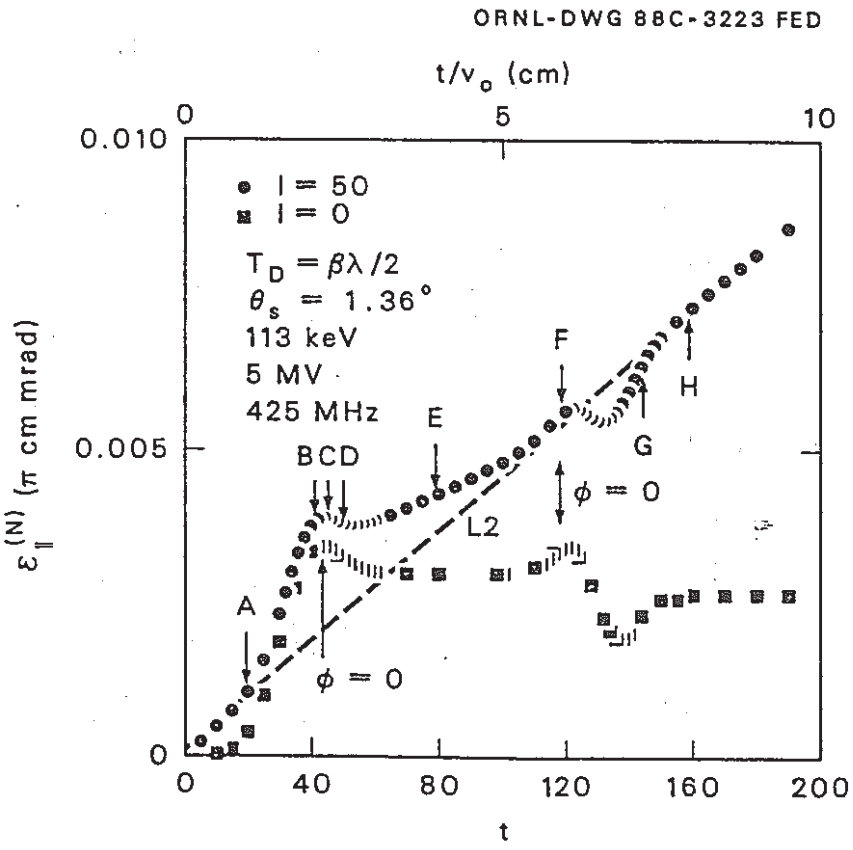


Fig. 11. Longitudinal emittance growth of bunches in Figure 10.

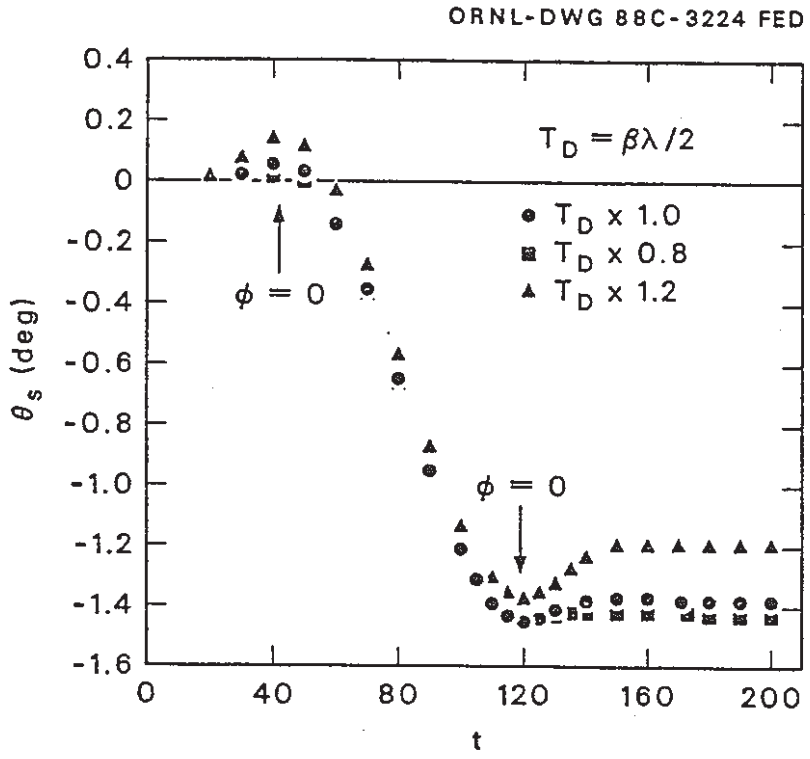


Fig. 12. Rf deflector steering showing mitigation by fringe fields.

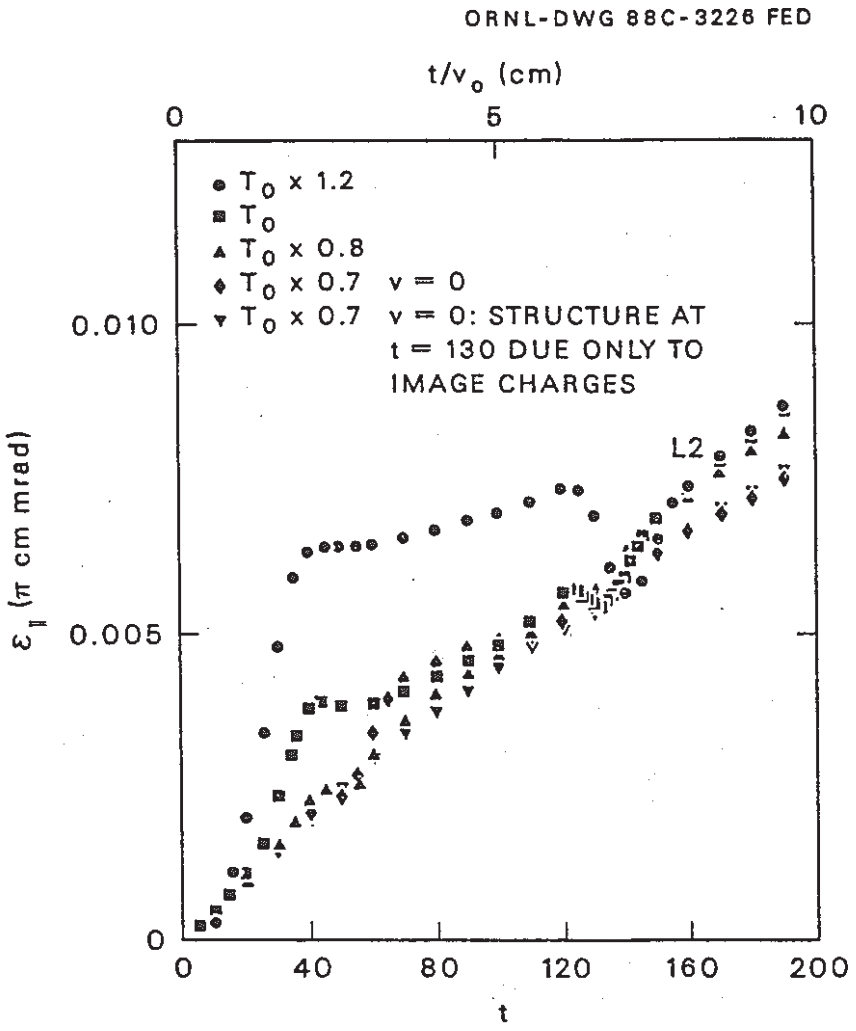


Fig. 13. Effect of deflector thickness on longitudinal emittance growth.

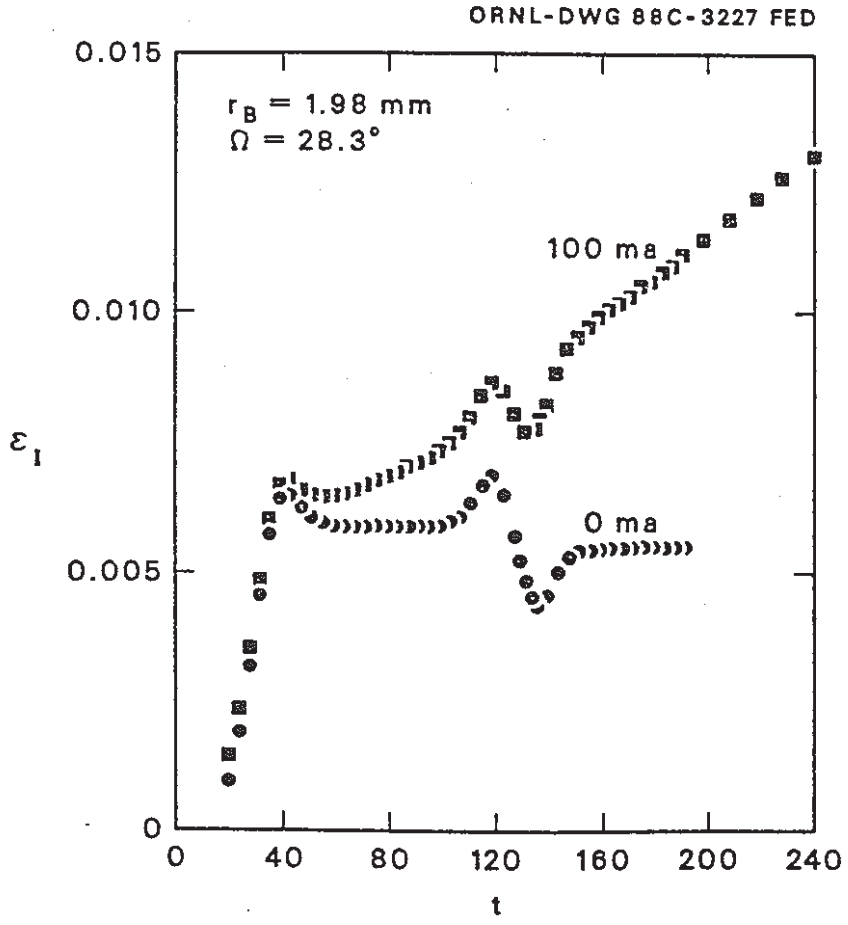


Fig. 14. 100 ma deflector.

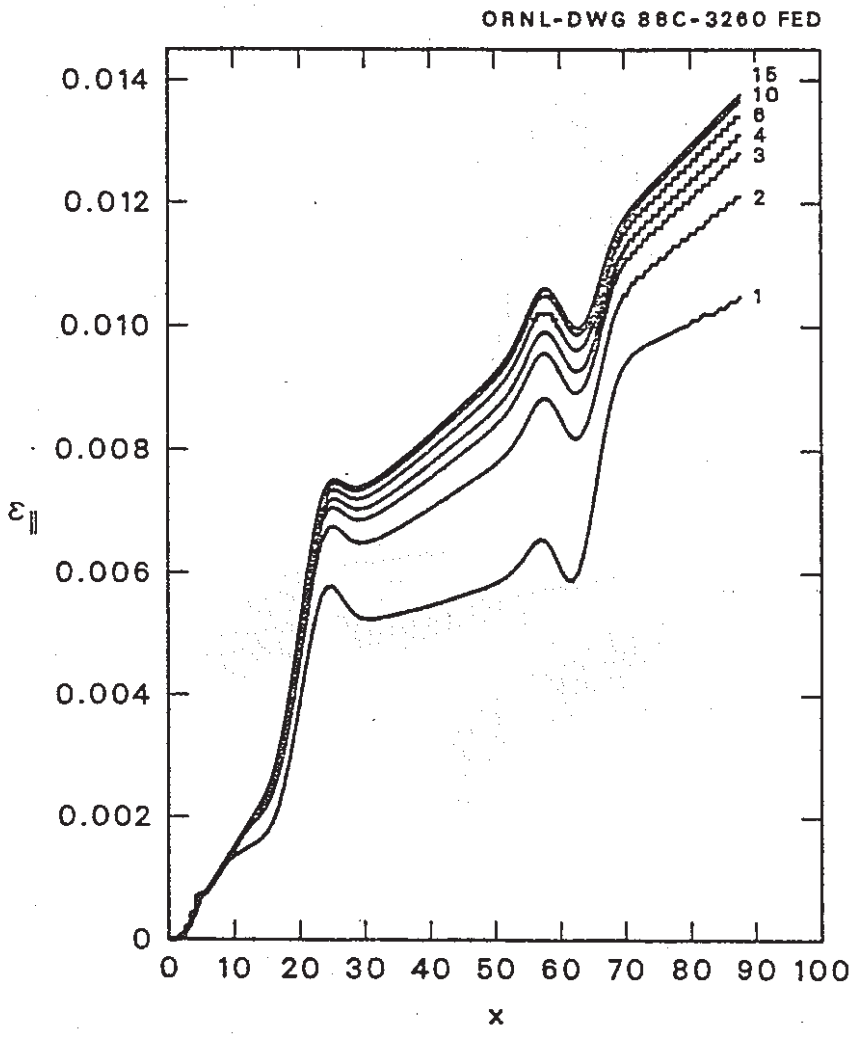


Fig. 15. Convergence as a function of axial resolution.

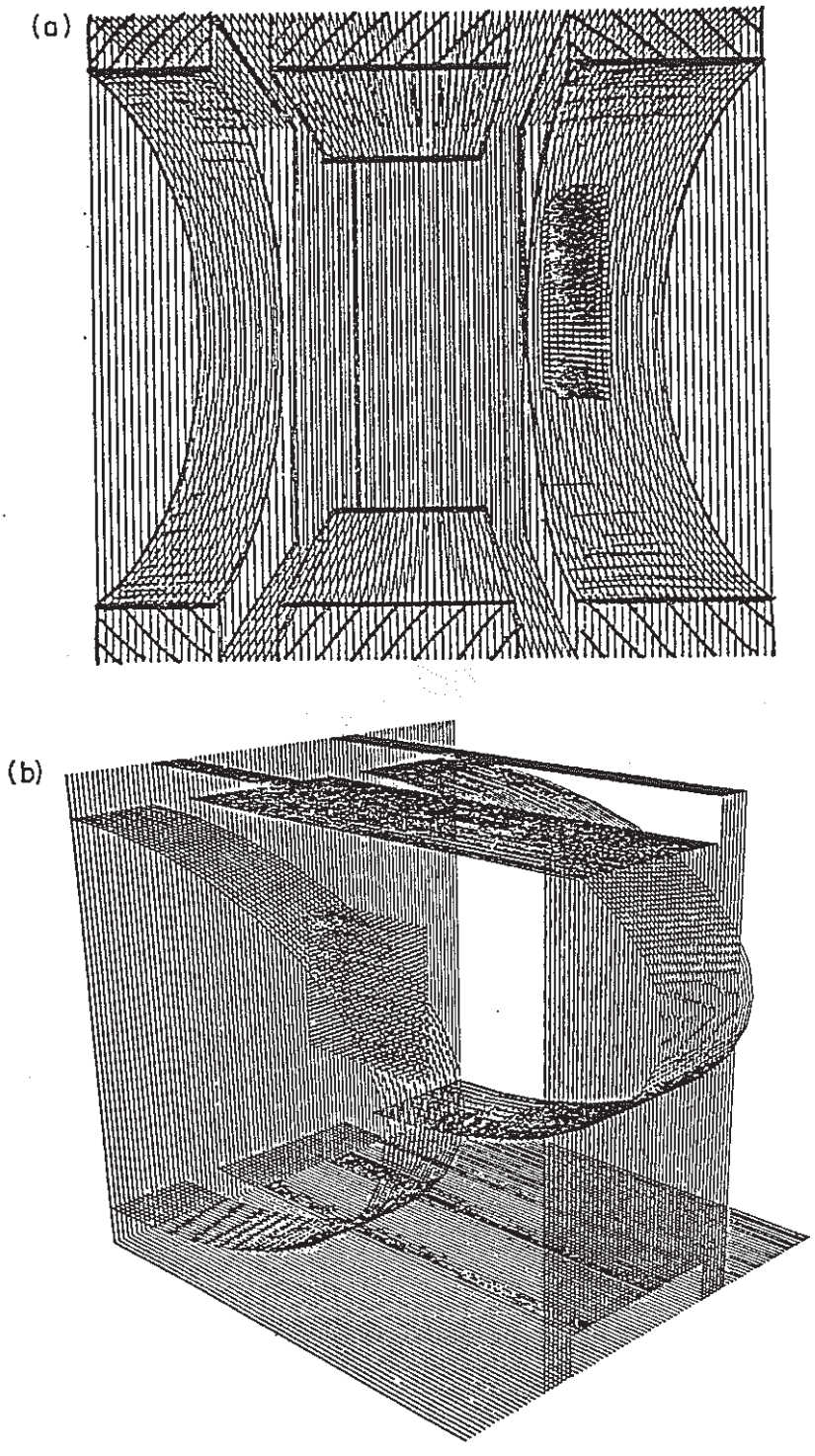


Fig. 16. A deflector in two views.

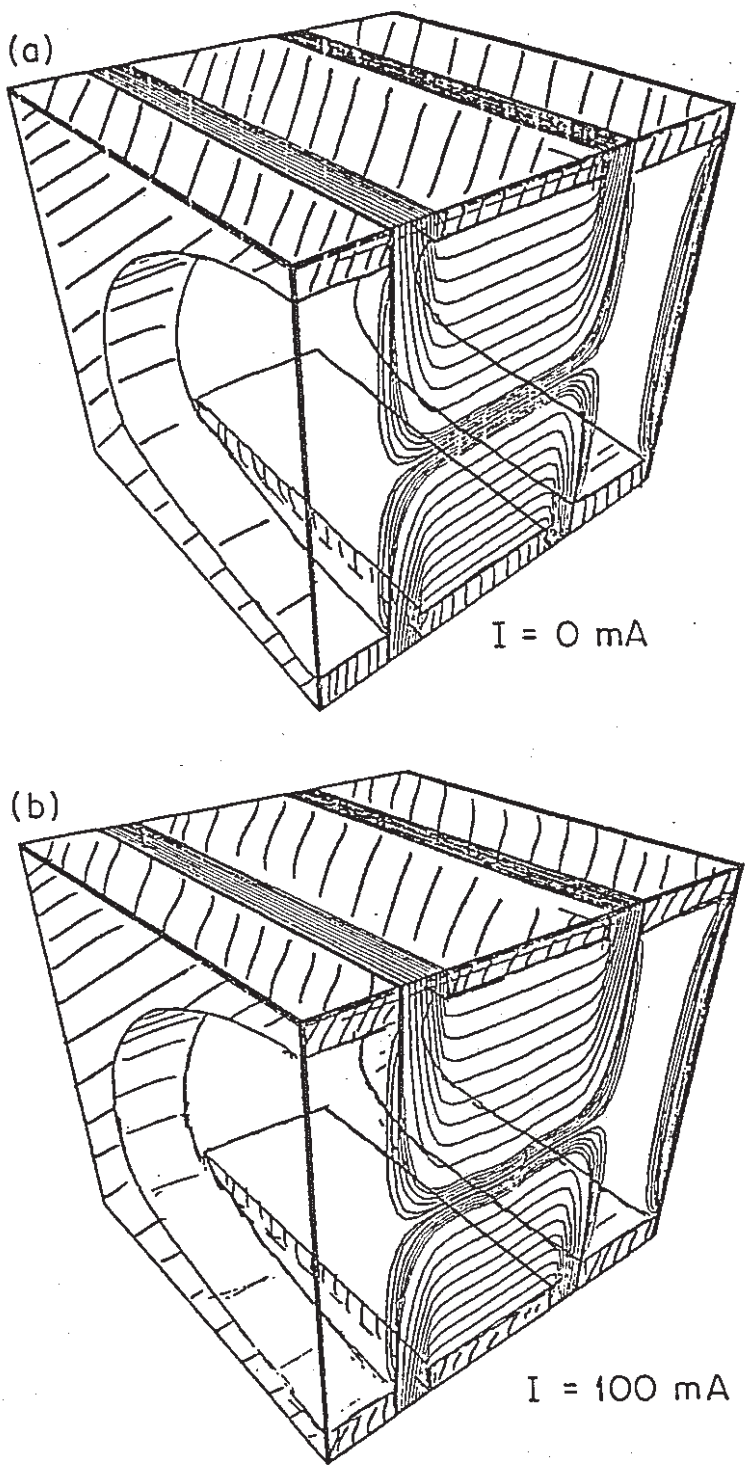


Fig. 17. Rf deflector potentials in 3 dimensions.

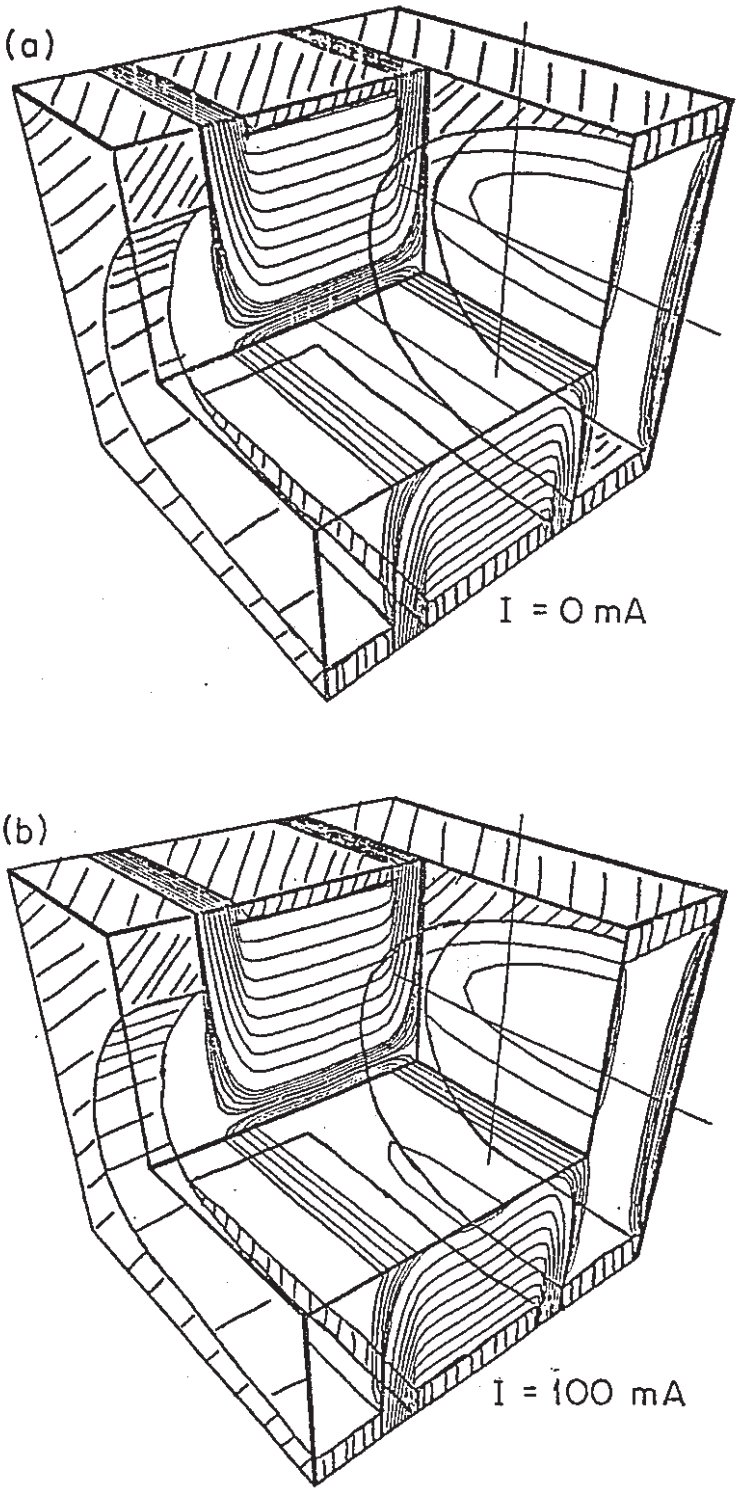


Fig. 18. Rf deflector with fringe fields.

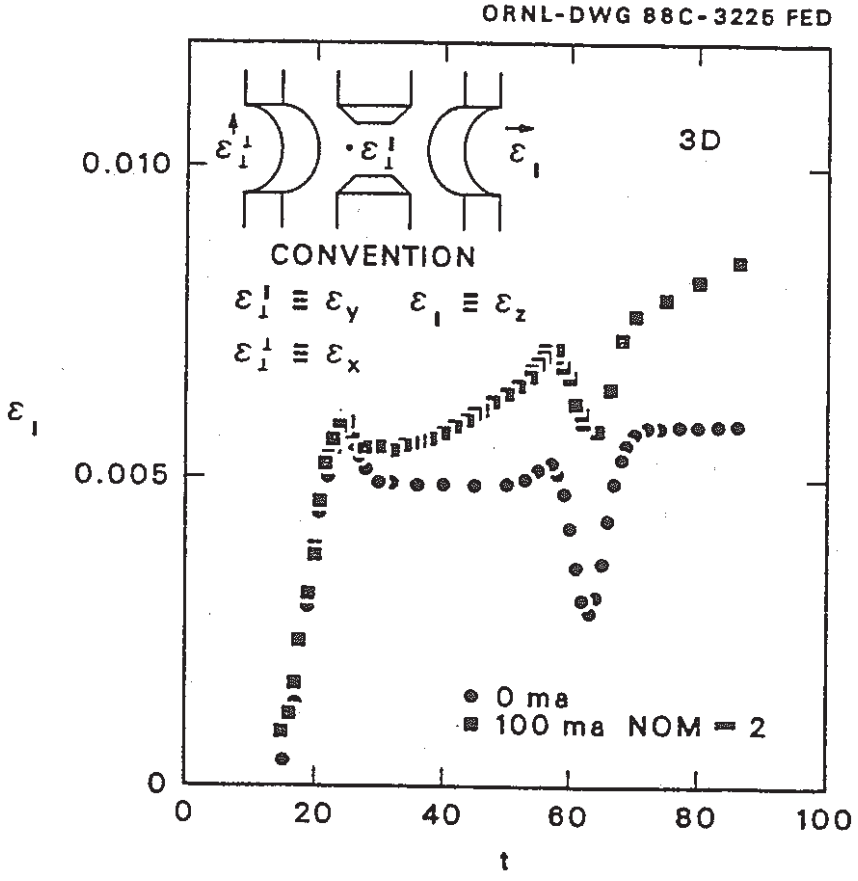


Fig. 19(a). Emittance growth as a function of time.

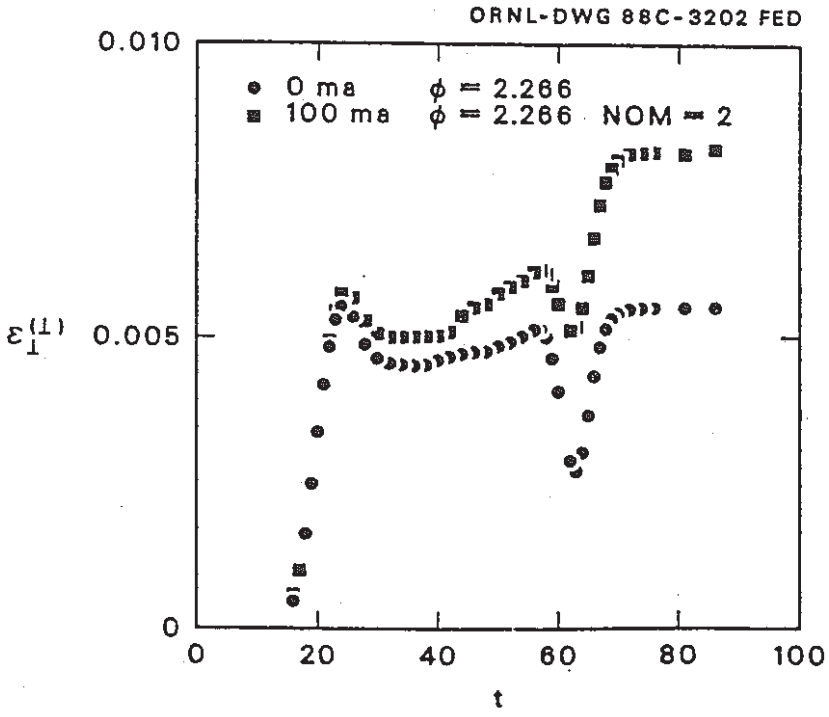


Fig. 19(b). Emittance growth as a function of time.

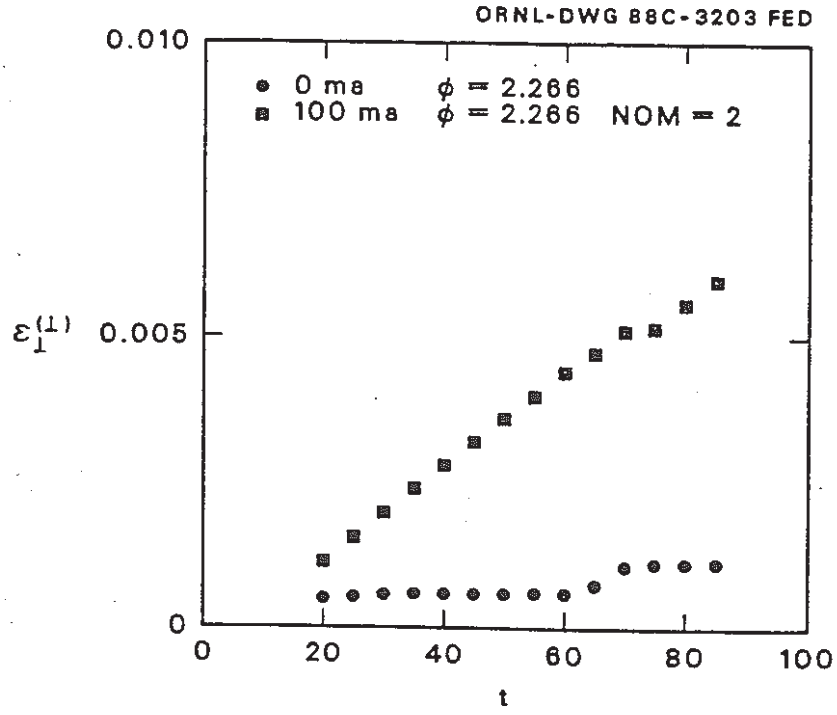


Fig. 19(c). Emittance growth as a function of time.

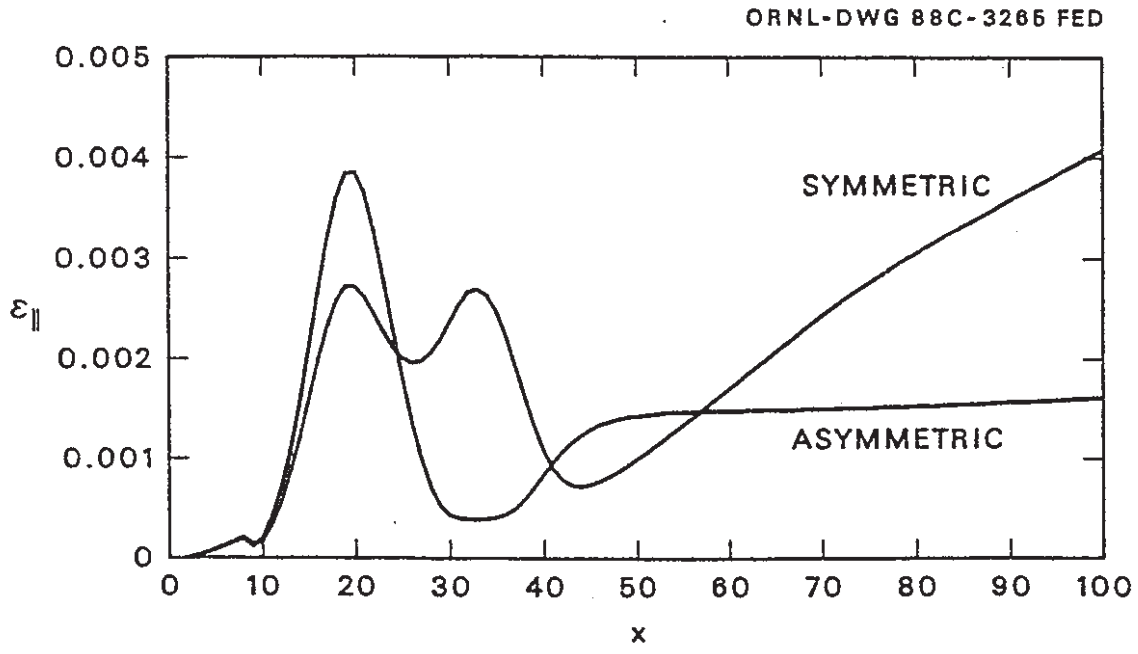


Fig. 20. Parallel emittance growth vs distance traveled for a soft beam.

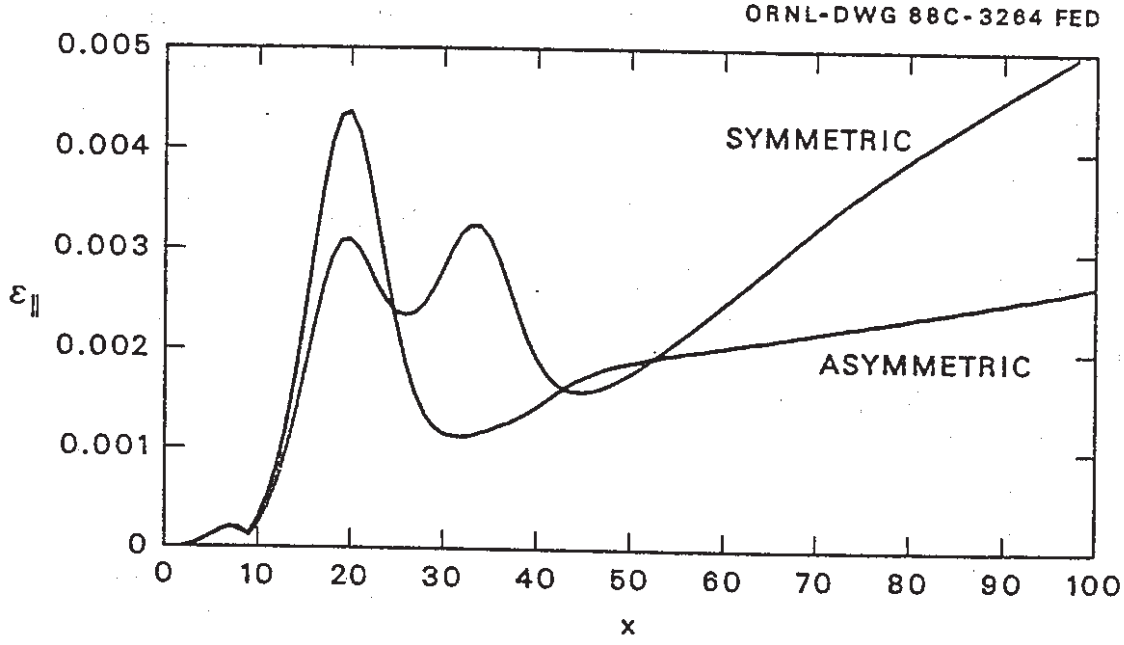


Fig. 21. Parallel emittance growth vs distance traveled for a hard beam.

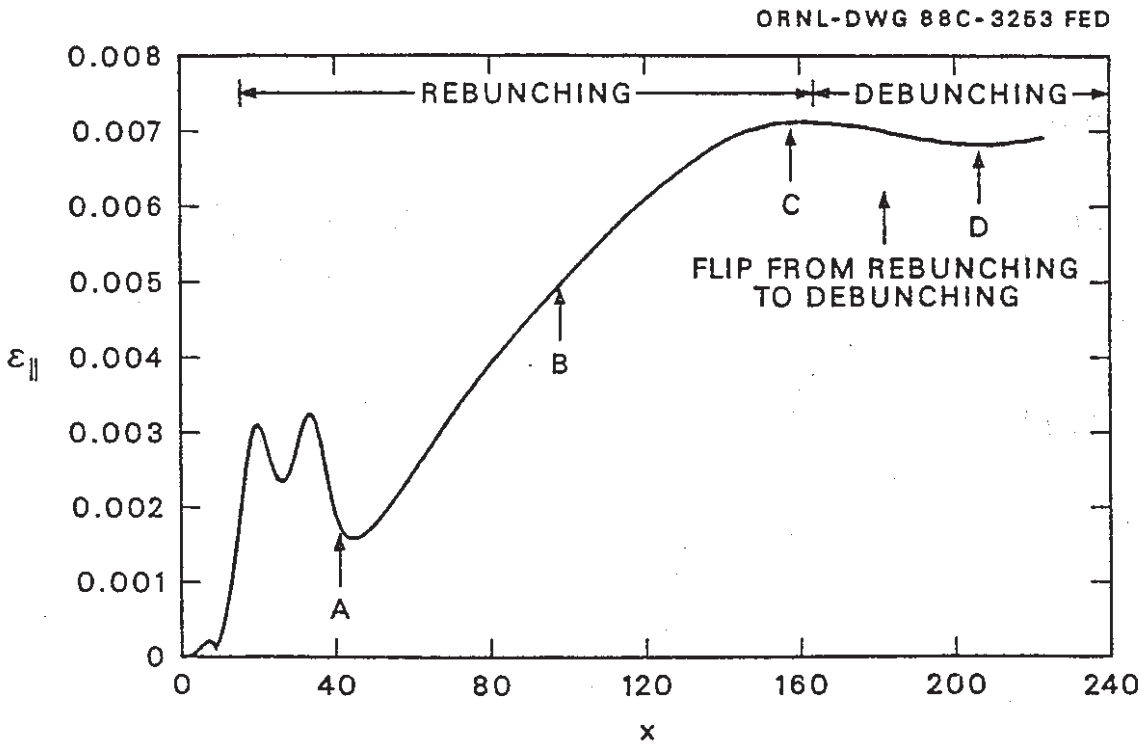


Fig. 22. Hard beam parallel emittance growth for a longer distance.

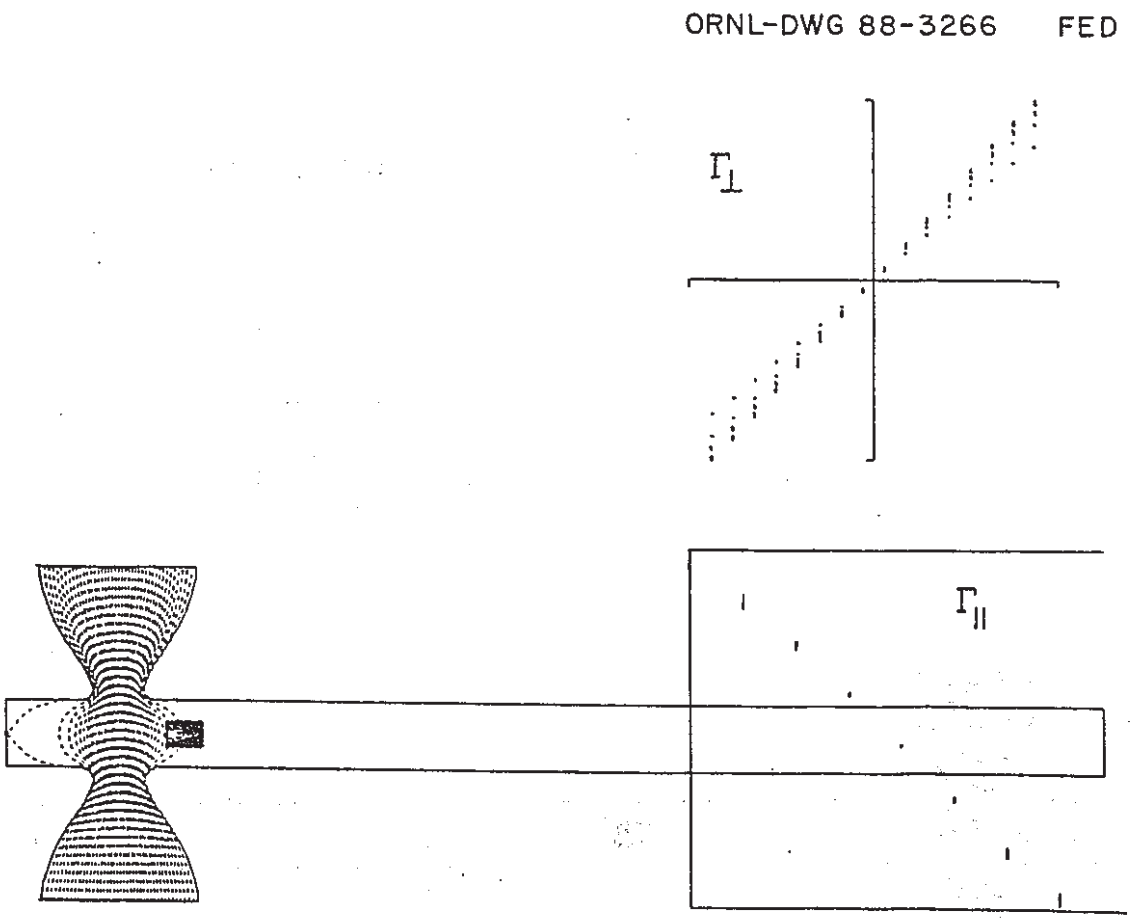


Fig. 23. Simple rebuncher with a beam pulse.

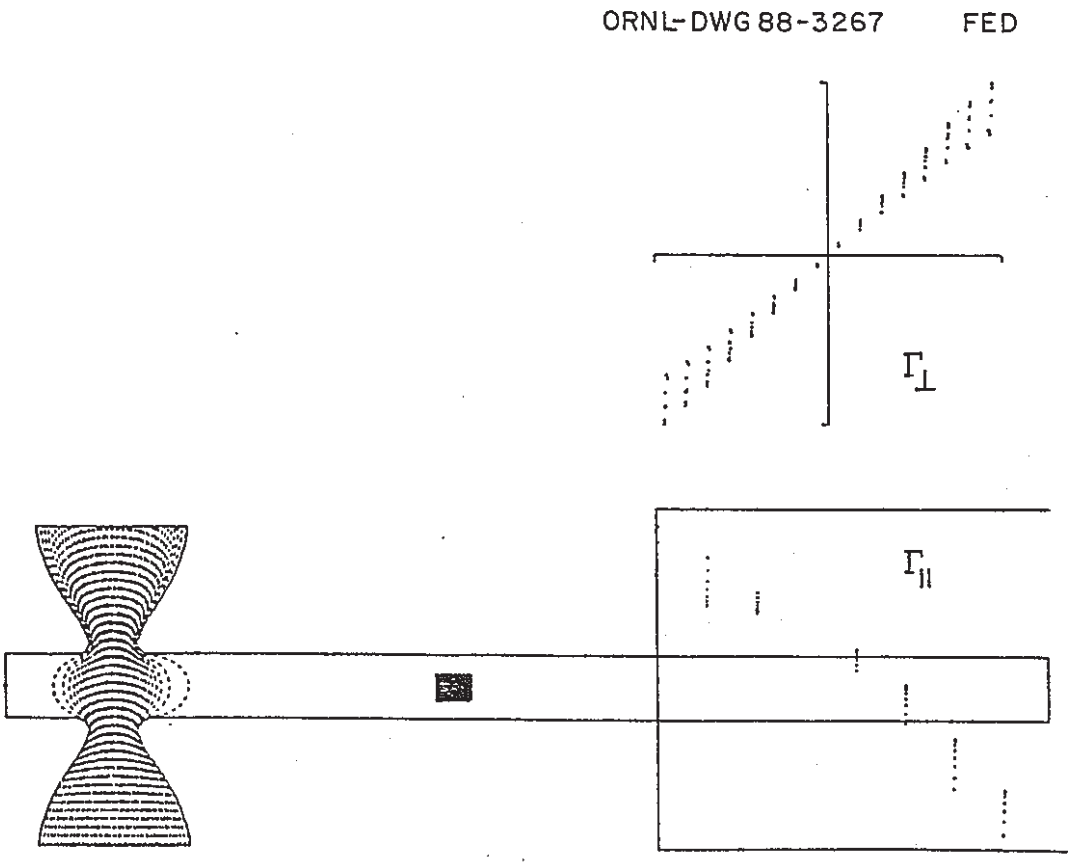


Fig. 24. Same as Figure 23 but at a later time.

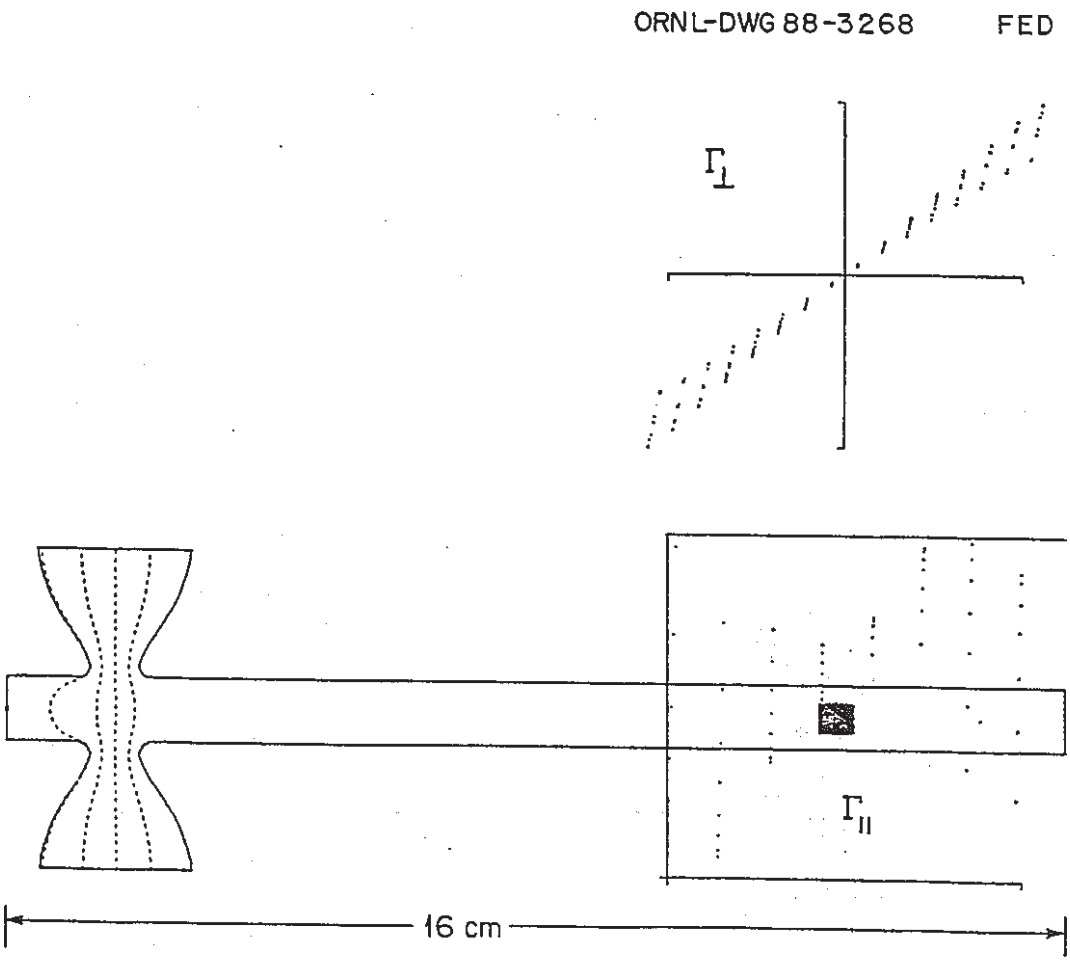


Fig. 25. Yet later.

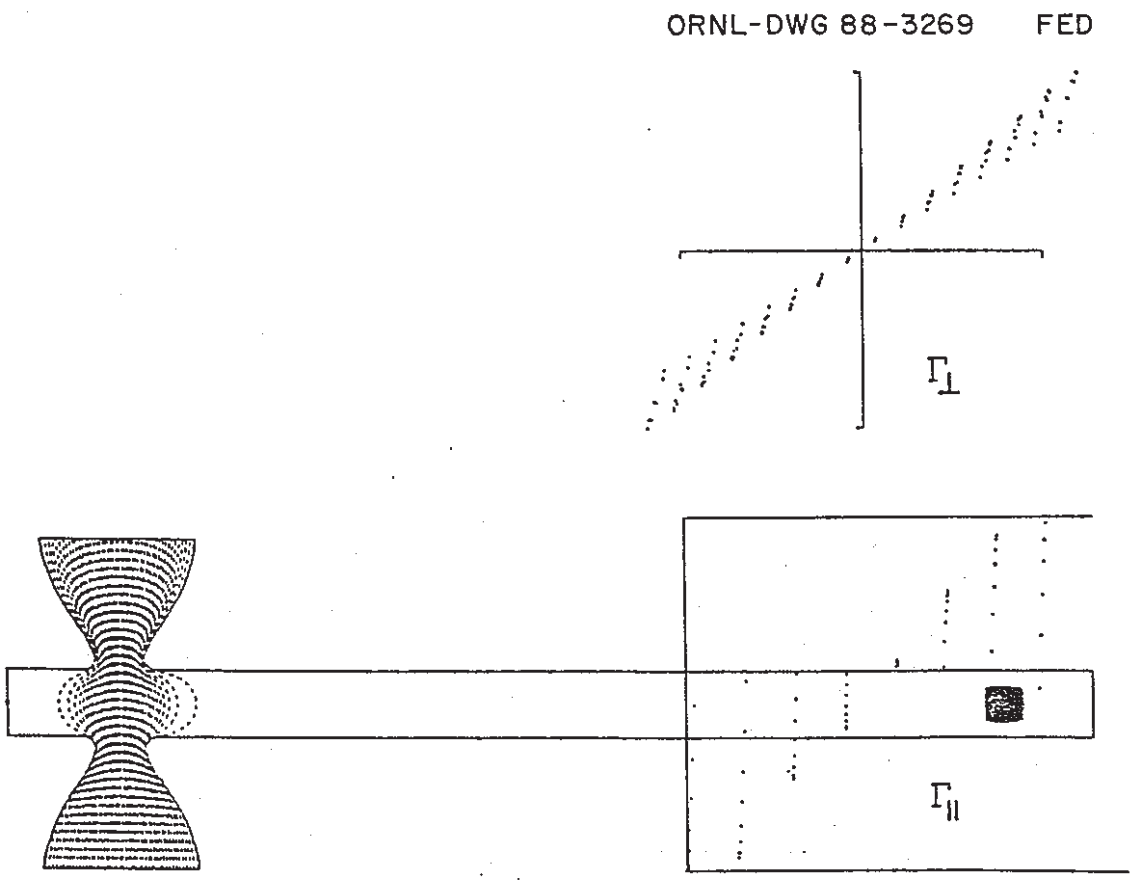


Fig. 26. Yet later: the beam debunching.

# BEAM BREAK-UP AND RESISTIVE WALL INSTABILITY IN A STEADY-STATE FREE ELECTRON LASER IN THE MICROWAVE REGIME

Ken Takayama
National Laboratory for High Energy Physics (KEK)
Tsukuba, Ibaraki, 305 JAPAN

## *Abstract*

The beam break-up instability and resistive wall instability caused by interaction between beam and induction gap, vacuum chamber wall, in a steady-state free electron laser in the microwave regime are considered. The large energy spread induced by free electron laser performance is theoretically proved not to lead to Landau damping of both instabilities when the synchrotron frequency is of order or larger than the betatron frequency(This is an intrinsic nature of a steady-state free elctron laser).

## *Introduction*

A microwave FEL is regarded as a possible candidate of high power microwave sources in the frequency region of 6~30 GHz for which the high energy accelerator society gets tired of waiting. In fact, the collaboration of LLNL and LBL has dramatically demonstrated the successful single-stage experiment of 35 GHz and 1 GW [1]. However this single-stage experiment is not straightforwardly extrapolated to a multi-stage level which is motivated by its use in a two-beam accelerator[2], because there are still unsolved many basic problems of microwave's extraction without RF breakdown[3], phasing of output RF[4], or the stability of a driving beam itself over a long distance[5]. From an accelerator physics point of view, an essential issue of the two-beam accelerator concept is how far a kiloamp electron beam in a steady-state FEL can be propagated with tolerable loss of beam quality. Major obstacles to long distance transport of kiloamp beams are the so-called BBU and transverse resistive wall instability. The former arises as a result of interaction between beams and induction gap, and the existance of wall charges and currents induced on the waveguide surface of finite conductivity by the displacement of beam centroid gives rise to the latter instability. So far the synchrotron oscillation in a large bucket of steady-state FEL has been supposed to induce a relatively large energy spread associated with a large spread in the betatron wave number $k_\beta$, eventually resulting in Landau damping of both instabilities. This hypothesis seems not true in the case of a steady-state FEL where the synchrotron frequency $\nu$ is in general the same order of magnitude as the betatron frequency, as described in Appendix. Recently it has been theoretically proved by the present author[5] that Landau damping of BBU due to a large energy spread is not expected in a steady-state FEL; in addition Whittum[6] has demonstrated the same result for the resistive wall instability by computer simulations.

Main purposes of the present paper are to summarize the analysis of BBU in a steady-state FEL, to extend the techniqe used there to the resistive wall instability, and to find the characteristic distance formulas: $L_{BBU}$ and $L_R$. Based on these formulas, the possible limit of multi-stage for a proposed FEL is given.

## *BBU and Resistive Wall Instability*

### BBU

The analysis is based on the BBU model provided in Ref. 7 where the induction gaps are treated as discretely distributed along the structure with spacing of $L_g$ and the BBU cavity mode is characterized by its angular frequency $\omega_\perp$, quality factor Q, and transverse shunt impedance $Z_\perp/Q$. The mode is excited by a dipole current source term which is proportional to the product of the beam current $I_B$ and transverse displacement $\langle\xi\rangle$. The transverse position of the beam centroid is determined by the linear focusing, the cavity fields, and the planar wiggler field. Now, introducing the variable $\tau=t-z/c$ which measures the time-delay behind the beam pulse head and averaging the perturbed betatron oscillation over a wiggler period and over one period of induction module, the BBU equations become

$$\left(\frac{\partial^2}{\partial\tau^2}+\frac{\omega_\perp}{Q}\frac{\partial}{\partial\tau}+\omega_\perp^2\right)\Delta(\tau,z)=\frac{I_B}{I_0}\omega_\perp^2\frac{Z_\perp}{Q}\langle\xi(\tau,z)\rangle \qquad (1a)$$

$$\left[\frac{\partial}{\partial z}(1+\varepsilon\cos\nu\zeta)\frac{\partial}{\partial z}+k_\beta^2\right]\xi_{\varepsilon,\varphi}(\tau,z)=\frac{\Delta(\tau,z)}{L_g\gamma_0} \qquad (1b)$$

$$(\zeta=z+\varphi/\nu)$$

where $\Delta$ the z-averaged normalized transverse momentum change of the beam centroid, $\xi_{\varepsilon,\varphi}$ the transverse position of each particle, $\varepsilon$ and $\varphi$ the maximum relative energy deviation and the initial phase for each particle, $I_0$ the Alfven current, $\nu$ and $k_\beta$ the synchrotron and betatron frequency, respectively, $\gamma_0$ the synchronous energy assumed to be constant in the following discussion. Here we assume a clude relation among characteristic distance: $L_{BBU}>\frac{2\pi}{k_\beta}, \frac{2\pi}{\nu}>L_g>\lambda_\gamma$(wiggler wave-length). Eq. (1a) represents the time-evolution of momentum gain proportional to magnetic wake fields in the induction gap located at z after pulse head arrival and Eq. (1b) represents the orbital-evolution of transverse position of i-th particle in the slice at pulse position $\tau$ behind the pulse head.

Introducing a new variable $\eta_{\pm,\varphi}=(1+\varepsilon\cos\nu\zeta)^{1/2}\xi_{\pm,\varphi}$ instead of $\xi_{\pm,\varphi}$ and performing Fourier transform of Eqs. (1a), (1b) in the variable $\tau$ to $\omega$, we have

$$(\omega_\lambda^2-\omega^2+i\frac{\omega\omega_\lambda}{Q})\bar{\mathcal{I}} = \omega_\lambda^2\frac{I_B Z_\perp}{I_0 Q}\langle\bar{\xi}\rangle \qquad (2a)$$

$$\frac{\partial^2\tilde{\eta}_{\pm,\varphi}}{\partial z^2}+\left[k_\beta^2+\varepsilon(\frac{\nu^2}{2}-k_\beta^2)\cos\nu\zeta\right]\tilde{\eta}_{\pm,\varphi} = \frac{\bar{\mathcal{I}}}{L_g\gamma_0} \qquad (2b)$$

where transformed quantities are denoted by tildes. Nonlinearization of the Mathieu coefficient in a Mathieu-like equation is known to admit exact solutions[5]; the homogeneous solutions of Eq. (2b) are approximately written by

$$x_\pm(Z)=(1+G\cos 2Z)^{1/2}\exp[\pm i\frac{\sqrt{1+\lambda}}{2}\times\sin^{-1}\left[(1-G^2)^{1/2}\frac{\sin 2Z}{1+G\cos 2Z}\right]]$$

where $Z=\nu\zeta/2$, $G=\varepsilon\frac{\nu^2-2k_\beta^2}{\nu^2-4k_\beta^2}=\varepsilon\varrho$, $\lambda=-\frac{1-4(k_\beta^2/\nu^2)}{1-\varrho^2\varepsilon^2}$

Since $G<1$ for $k_\beta\sim\nu$, $\sin\phi=(1-G^2)^{1/2}\sin\nu\zeta/(1+G\cos\nu\zeta)\simeq\sin\nu\zeta/(1+G\cos\nu\zeta)$, then $\phi=\nu\zeta-G\sin\nu\zeta$. From this result and $\sqrt{\lambda+1}/2\simeq k_\beta/\nu$, we have

$$\eta^{\pm}_{\pm,\varphi}(z)=(1+\frac{G}{2}\cos\nu\zeta)\sum_{n=-\infty}^{\infty}J_n(\frac{k_\beta}{\nu}G)e^{\pm i(k_\beta-n\nu)\zeta} \qquad (3)$$

, employing terms of the Bessel function. Using the Green function $G(z,z')$ evaluated from Eq. (3), the solution to Eq. (2b) is given by

$$\bar{\eta}_{\pm,\varphi}(\omega,z)=\bar{\mathcal{J}}(\omega,z)+\frac{1}{L_g\gamma_0}\int_{-\infty}^{z}G(z,z')\bar{\mathcal{I}}(\omega,z')dz' \qquad (4)$$

where $\bar{\mathcal{J}}$ is the initial value term. Multiplying both sides by $(1+\varepsilon\cos\nu\zeta)^{1/2}$, substituting the expression $\bar{\mathcal{I}}=h(\omega)\langle\bar{\xi}\rangle$ where

$$h(\omega) = \frac{\omega_\lambda^2}{\omega_\lambda^2-\omega^2+i\omega\omega_\lambda/Q}\frac{I_B}{I_0}\left(\frac{Z_\perp}{Q}\right)$$

derived from (2b), into Eq. (4), and averaging its both sides over the distribution of energy spread and initial phase, we have a Volterra equation of the 2-nd kind for $X(z)=\langle\bar{\xi}(\omega,z)\rangle$.

$$X(z)=Q(z)+\frac{h(\omega)}{L_g\gamma_0 k_\beta}\sum_{m=-\infty}^{\infty}a_{mm}\int_{-\infty}^{z}dz'X(z')\times\sin[(k_\beta-\nu m)(z-z')]$$

where the abbreviations: $X(z)=\langle\bar{\xi}\rangle$, $Q(z)=\langle(1+\varepsilon\cos\nu\zeta)^{1/2}\bar{\mathcal{J}}\rangle$, and $a_{mm}=\frac{1}{\sigma}\int_0^\sigma J_m^2(\frac{k_\beta}{\nu}\varrho\varepsilon)d\varepsilon$ are used. Here a flat distribution for $\varepsilon$ ($\sigma$: maximum deviation) is assumed. Utilizing a Faltung theorem, the equation is solved by the Laplace transformation in the variable z to p. The inverse Laplace transformation of $X(p)$ gives

$$\langle\bar{\xi}(\omega,z)\rangle=\frac{1}{2\pi i}\int_{\sigma-i\infty}^{\sigma+i\infty}\frac{Q(p)e^{pz}}{1-\frac{h(\omega)}{L_g\gamma_0 k_\beta}\sum_{m=-\infty}^{\infty}\frac{a_{mm}(k_\beta-\nu m)}{p^2+(k_\beta-\nu m)^2}}dp \qquad (5)$$

From the theory of residue, the integral is evaluated in the form $X(z)=\sum_j A_j(\omega)e^{p_0^j(\omega)z}$ where $p_0^j(\omega)$ is the zero-point of the denominator in the integrand. The Fourier inverse transformation of X(z) gives

$$\langle\xi(z)\rangle = \sum_j\frac{1}{\sqrt{2\pi}}\int_{-\infty}^{\infty}A_j(\omega)e^{p_0^j(\omega)z}e^{+i\omega\tau}d\omega \qquad (6)$$

An assymptotic form of the integral may be evaluated by the method of steepest descents to become $\langle\xi(z)\rangle\propto A_j(\omega_s)e^{p_0^j(\omega_s)z+i\omega_s\tau}$ where the saddle point $\omega_s$ satisfies

$$\frac{dp_0(\omega_s)}{d\omega}+i\tau=0.$$

The problem finally reduces to a mathematical problem of solving the dispersion relation

$$1-\frac{h(\omega)}{L_g\gamma_0 k_\beta}\sum_{m=-\infty}^{\infty}\frac{a_{mm}(k_\beta-\nu m)}{p^2+(k_\beta-\nu m)^2}=0 \qquad (7)$$

where $k_\beta\sim\nu$, the summation is dominated by three terms of $m=0,\pm1$ : $a_{00}=1-\delta^2/6$, $a_{11}=a_{-1-1}=\delta^2/12$ ($\delta\equiv k_\beta\varrho\sigma/\nu$), then an assumption of strong focusing ($h/L_g\gamma_0 k_\beta^2$, $h/L_g\gamma_0 k_\beta^2<1$) leads to

$$p_0(\omega) = -ik_\beta+\frac{ih(\omega)}{2k_\beta L_g\gamma_0}(1-\frac{\delta^2}{6})$$

After tedious mathematical calculation for seeking the saddle point[6], the asymptotic form

$$\langle\xi(\tau,z)\rangle\propto e^{-ik_\beta z+i\omega_\lambda\tau}e^{-\alpha\tau+\sqrt{2|B|\omega_\lambda\tau(1-\delta^2/6)z}} \qquad (8)$$

where $\alpha=\omega_\lambda/2Q$ and $|B|=\frac{\omega_\lambda}{2L_g k_\beta\gamma_0}\frac{I_B}{I_0}\frac{Z_\perp}{Q}$

is obtained. The real part of index, $\Psi(\tau)$, takes its maximum value

$$\Psi(\tau_{max}) = \frac{|B|\omega_\lambda}{2\alpha}(1-\frac{\delta^2}{6})z$$

for $$\tau_{max}=\frac{1}{2\alpha^2}\left[|B|\omega_\lambda(1-\frac{\delta^2}{6})z\right]$$

Eventually, we can arrive at the BBU growth distance as follows.

$$L_{BBU} = z/\Psi(\tau_{max}) = \frac{2L_g k_\beta\gamma_0}{\omega_\lambda Z_\perp}\left(\frac{I_0}{I_B}\right)\frac{1}{1-\delta^2/6} \qquad (9)$$

For the present case, the BBU growth distance falls in the below range.

$$L_{BBU}(\sigma=0) < L_{BBU}(\sigma) \le \frac{6}{5}L_{BBU}(\sigma=0)$$

because of $\left(\frac{k_\beta}{\nu}\varrho\right)^2\sigma^2\sim1$ at most.

Eq. (3) indicates that the frequency modulated betatron oscillation involves the infinite number of eigenmodes with the frequency $|k_\beta \pm n\nu|$ and the relative strength of these modes is determined by the Bessel function term which is a function of the betatron and synchrotron frequencies, and the energy spread. This discrete spectrum of oscillation mode tends to localize at $k_\beta(1-\varepsilon/2)$ in the limit of $k_\beta/\nu\to\infty$, yielding an effective spread in the betatron frequency of the beam. The spread leads to Landau damping of BBU. When $k_\beta/\nu\sim 1$, on the other hand, there are only three dominant modes of $k_\beta$, $|k_\beta\pm\nu|$ as above derived. It is easily supposed that interference among different spectra consisting of three lines is quite weak.

Resistive wall instability

The analysis is based on the equation formulated by Caporaso et al. [8] which describes the resistive wall instability. Their equation is modified in the orbital form

$$\left[\frac{\partial}{\partial z}\left(1+\varepsilon\cos\nu\zeta\right)\frac{\partial}{\partial z}+k_\beta^2\right]\xi_{\varepsilon,\phi}(\tau,z)=\frac{\beta}{\sqrt{\pi}}\int_0^\tau\frac{\langle\xi(\tau',z)\rangle}{\sqrt{\tau-\tau'}}d\tau'$$

$$\beta=\left(\frac{e}{mc}\right)\frac{I_B}{\pi\gamma_0 b^3}\sqrt{\frac{\mu_0}{\sigma}} \qquad (10)$$

where $1/\sqrt{\tau-\tau'}$ of the right-hand side indicates the resistive wall wake function. b is the vacuum chamber radius, $\sigma$ is the conductivity of chamber wall material, and $\mu_0$ is the magnetic permeability in vacuum. Solutions of Eq. (10) are written by the term of Green function in the similar way to the previous discussion.

$$\xi_{\varepsilon,\phi}(\tau,z)=f_{\varepsilon,\phi}+\left(1+\frac{\varepsilon}{2}\cos\nu\zeta\right)^{1/2}\int_0^z dz'G(z,z')$$

$$\times\int_0^\tau d\tau' K(\tau-\tau')\langle\xi(\tau',z')\rangle$$

where $f_{\varepsilon,\phi}$ is the initial value term and the abbreviation $K(\tau-\tau')=\beta/\sqrt{\pi(\tau-\tau')}$ is used. Averaging both sides over the distribution of energy spread and initial phase, we have a Volterra equation again.

$$\langle\xi\rangle=\langle f\rangle+\frac{1}{k_\beta}\sum_{m=-\infty}^{\infty}a_m\int_0^z dz'\sin[(k_\beta-\nu m)(z-z')]$$

$$\times\int_0^\tau d\tau' K(\tau-\tau')\langle\xi\rangle \qquad (11)$$

Utilizing a Faltung theorem, Eq. (11) is solved by two-stages of Laplace transformation: in the variable $\tau$ to $q$,

$$\langle\xi(q,z)\rangle=F(q,z)+\frac{1}{k_\beta}\sum_{m=-\infty}^{\infty}a_m\int_0^z dz'\sin[(k_\beta-\nu m)$$

$$\times(z-z')]K(q)\langle\xi(q,z')\rangle,\quad (K(q)=\beta/\sqrt{q})$$

and in the variable $z$ to $p$,

$$\langle\xi(q,p)\rangle=H(q,p)+\frac{\beta}{k_\beta}\sum_{m=-\infty}^{\infty}\frac{a_m(k_\beta-\nu m)}{p^2+(k_\beta-\nu m)^2}\frac{\langle\xi(q,p)\rangle}{\sqrt{q}} \qquad (12)$$

After algebraic calculation, the double inverse Fourier transformation leads to

$$\langle\xi(\tau,z)\rangle=\frac{1}{4\pi^2}\int_{\sigma'-i\infty}^{\sigma'+i\infty}dq\int_{\sigma-i\infty}^{\sigma+i\infty}dp\frac{H(q,p)e^{zp+\tau q}}{1-\frac{\beta}{k_\beta\sqrt{q}}\sum_{m=-\infty}^{\infty}\frac{a_m(k_\beta-\nu m)}{p^2+(k_\beta-\nu m)^2}} \qquad (13)$$

From the assumption of strong focusing, the pole of the integrand is evaluated as follows,

$$p_0(q)=-ik_\beta+\frac{i\beta}{2k_\beta\sqrt{q}}\left(1-\frac{\delta^2}{6}\right) \qquad (14)$$

Thus,

$$\langle\xi(\tau,z)\rangle=\frac{1}{4\pi^2}\int_{\sigma'-i\infty}^{\sigma'+i\infty}dqH(q,p_0)e^{zp_0(q)+\tau q}$$

The saddle point of the above integrand, $q_s$, is calculated from $zdp_0(q_s)/dq+\tau=0$, then

$$q_s=(\pm i)^{2/3}\left[\frac{4k_\beta\tau}{\beta z(1-\delta^2/6)}\right]^{-2/3}$$

Thus, the asymptotic form of the integral becomes

$$\langle\xi(\tau,z)\rangle\propto e^{\frac{3}{2}\left[\frac{\beta z(1-\delta^2/6)}{4k_\beta}\right]^{2/3}\tau^{1/3}} \qquad (15)$$

Finally, we have the growth distance formula,

$$L_R=2\pi\left(\frac{2}{3}\right)^{3/2}\sqrt{\sigma\mu_0}\left(\frac{I_0}{I_B}\right)\frac{\gamma_0 b^3}{\lambda_\beta}/\sqrt{\tau}\left(1-\frac{\delta^2}{6}\right) \qquad (16)$$

where $I_0=4\pi(mc/e)/\mu_0$ is the Alfven current.

## Summary

The integral equations for the BBU and resistive wall instability have been evaluated in compact forms, introducing a novel technique of nonlinearization of the Mathieu coefficient and the dispersion relations have been derived from these integral equations. In the region of $k_\beta\sim\nu$ of particular interest, we have calculated the poles from the dispersion relations and finally arrived at the formulas for the BBU growth and resistive wall instability growth distances, $L_{BBU}$ and $L_R$ which are functions of the synchrotron and betatron frequencies, and the energy spread. From the expressions of $L_{BBU}$ and $L_R$, we realize that enlargement in $L_{BBU}$ and $L_R$ due to the energy spread is quite small. Accordingly we conclude that a large energy spread particular for an FEL in the microwave regime doesn't contribute to Landau damping of BBU and the resistive wall instability.

The growth formulas give $L_{BBU}=71m$ and $L_R=1.47km$ with typical parameters (10), $I_b=2kA$, $k_\beta=2\pi/3m^{-1}$, $\sigma(sus)=3.64\times10^7(\Omega\cdot m)^{-1}$, $L_g=2m$, $\gamma_0=40$, $\omega_1 Z_\perp=0.4cm^{-1}$, b(chamber radius)=5cm, $\tau(pulse\ length)=50nsec$. The value of $L_{BBU}$ is crucial for a steady-state FEL employed in a two-beam accelerator. One would have hoped beam transport over a greater distance for higher conversion efficiency from beam power to microwave power. This requirement may be satisfied in two possible ways. One of those is to use induction gaps with the same accelerating voltage but slightly different deflecting mode frequencies; Landau damping of BBU can be expected because of dephasing by the frequency spread. The other is to introduce a sufficient spread in the betatron number caused by nonlinearity as seen in the ion focusing regime(9). The latter has been proposed in Ref. 10 where a possibility of ion channel guiding is theoretically anticipated.

The present theory is general for the beam break-up instability in a frequency modulated system. For instance, the present conclusion can be applied to the case of a relativistic klystron(11) (RK) which also is motivated by its use in a two-beam accelerator, if it is driven with a low energy. Unlike a steady-state free electron laser, however, $k_\beta/\nu$ in a relativistic klystron is proportional to $\gamma^{1/2}$; therefore, Landau damping will be expected when an RK is operated with a sufficient large $\gamma$. $L_{BBU}(\sigma)$ and $L_R(\sigma)$ in such a case must be analytically derived by solving the original dispersion relation or obtained by computer simulations. However, both are out of the present scope.

## *Acknowledgements*

The author would like to thank Dr. A. M. Sessler for valuable comments on the present work. A critical comment of Prof. I. Satoh has reminded him of the clear dependence of the asymptotic form (8) on the pulse length. He also enjoyed discussions of the present topic with the KEK FEL group members.

## *References*

(1) T. J. Orzechowski et al., Phys. Rev. Lett 57, 2172 (1986).
(2) A. M. Sessler, AIP Conf. Proc. 91, 163 (1982).
(3) D. B. Hopkins et al., Proc. of 1987 Particle Accel. Conf., 80 (1987).
(4) R. W. Kuenning et al., AIP Conf. Proc. 15 371 (1986).
(5) K. Takayama, KEK Preprint 88-11 (1988) to be published in Phys. Rev. A
(6) D. Whittum, private communication
(7) V. K. Neil et al., Particle Accelerators 9, 123 (1979).
(8) G. J. Caporaso et al., Particle Accel. 11, 71 (1980).
(9) G. J. Caporaso et al., Phys. Rev. Lett. 5 1951 (1986).
(10) K. Takayama and S. Hiramatsu, Phys. Rev. A 37, 173 (1988).
(11) A. M. Sessler and S. S. Yu, Phys. Rev. Let' 58, 2439 (1987).
(12) D. B. Hopkins and R. W. Kuenning, Proc. of 1985 Particle Accel. Conf., 3476 (1985)

## *Appendix*

The ratio of the betatron frequency to the synchrotron is described by

$$\frac{k_\beta}{\nu}=\frac{1}{2}\sqrt{\frac{cB_\gamma}{E_s}}\left(1+\frac{\lambda_\gamma\lambda_s}{18b^2}\right)$$

where c is the velocity of light, $B_\gamma$ and $E_s$ are the magnetic and signal field amplitudes, respectively, $\lambda_\gamma$ and $\lambda_s$ are the wiggler period and the signal wave length in vacuum, respectively, and b the vertical dimension of waveguide. The second term on the right-hand side is normally much smaller than unity. The power density requirement (~ GW/m) in the proposed scheme(12) where permanent wiggler magnets with the nominal surface field of ~1 Tesla are employed yield $0<k_\beta/\nu<2$.

SLAC – PUB – 4650
UCRL – 98843
June 1988
(A, E)

# RELATIVISTIC KLYSTRON RESEARCH FOR HIGH GRADIENT ACCELERATORS[†]

M. A. ALLEN, R. S. CALLIN, H. DERUYTER, K. R. EPPLEY, W. R. FOWKES, W. B. HERRMANNSFELDT, T. HIGO,[*] H. A. HOAG, T. L. LAVINE, T. G. LEE, G. A. LOEW, R. H. MILLER, P. L. MORTON, R. B. PALMER, J. M. PATERSON, R. D. RUTH, H. D. SCHWARZ, Y. TAKEUCHI,[*] A. E. VLIEKS, J. W. WANG, AND P. B. WILSON

*Stanford University, Stanford Linear Accelerator Center, Stanford, California 94309*

D. B. HOPKINS AND A. M. SESSLER

*University of California, Lawrence Berkeley Laboratory, Berkeley, California 94720*

W. A. BARLETTA, D. L. BIRX, J. K. BOYD, T. HOUCK, G. A. WESTENSKOW, AND S. S. YU

*University of California, Lawrence Livermore National Laboratory, Livermore, California 94550*

## ABSTRACT

Relativistic klystrons are being developed as a power source for high gradient accelerator applications which include large linear electron-positron colliders, compact accelerators, and FEL sources. We have attained 200 MW peak power at 11.4 GHz from a relativistic klystron, and 140 MV/m longitudinal gradient in a short 11.4 GHz accelerator section. We report here on the design of our first klystrons, the results of our experiments so far, and some of our plans for the near future.

## 1. INTRODUCTION

Large linear electron-positron colliders, compact accelerators, and FEL sources require a new generation of high gradient accelerators. Conceptual designs for large linear electron colliders for research at the frontier of particle physics, for example, call for center-of-mass energies of 1–2 TeV and luminosities of $10^{33}$–$10^{34}$ $cm^{-2}sec^{-1}$. Accelerating gradients of 150–200 MV/m are desired in order to keep the accelerator length within acceptable limits. Frequencies of 11–17 GHz are desired in order to keep peak power requirements and beam loading reasonably small. The peak power necessary to drive a traveling wave structure in the desired frequency range with the desired gradient is of order 1 GW/m with a pulse length of 50–100 ns.

Pulsed beams of such high peak power can be obtained using the technologies of magnetic pulse compression and induction acceleration.[1] Beam pulses of 1 kA current and 50–100 nsec duration are routinely accelerated to several MeV at Lawrence Livermore National Laboratory (LLNL). These beams contain several gigawatts of peak power.

The first demonstration of RF power extraction from such a beam yielded an impressive 1 GW at 35 GHz, using a free electron laser.[2] A. M. Sessler and S. S. Yu, following a suggestion by W. K. H. Panofsky, proposed a more direct method for energy extraction by bunching a relativistic beam and passing it through extraction cavities.[3] Sessler and Yu suggested that if only part of the beam energy were extracted, the beam could be reaccelerated and energy again could be extracted. Repeated reacceleration and extraction was the concept they called a "relativistic klystron two-beam accelerator."[3] The idea of a relativistic klystron, however, is not limited to the two-beam accelerator concept. Relativistic klystrons can be imagined which span the range from a 1 GW device powering 1 m of accelerator, to a 10 GW device powering 10 m, to a two-beam device extending several kilometers.

These ideas have led to a collaboration between Stanford Linear Accelerator Center (SLAC), Lawrence Berkeley Laboratory (LBL), and LLNL to study the combination of the klystron concept with induction accelerator and magnetic pulse compression technology. The first experiments have been done at the Accelerator Research Center (ARC) at LLNL using as a gun an induction accelerator designed to produce 1 kA currents with 1.2 MeV kinetic energy for up to 75 nsec duration. Three klystrons have been tested with this injector. They are, in chronological order as tested,

(1) SL3, a multicavity klystron with a conventional gun designed to operate at 8.6 GHz (three times the frequency of the SLAC linac),

(2) SHARK, a sub-harmonic drive relativistic klystron with relatively low gain,

(3) SL4, a high gain relativistic klystron at 11.4 GHz (four times SLAC frequency) designed specifically for the high power pulsed beam.

In this paper we discuss the design of these klystrons, report on the results of our experiments so far, and discuss some of our plans for the near future.

## 2. KLYSTRON SCALING

To motivate the increase in energy of the beam in an otherwise conventional klystron, it is useful to discuss the physics of the klystron interaction. In a klystron, the beam is velocity modulated by an RF drive cavity and allowed to drift until the velocity modulation bunches the beam. The bunched beam then is passed through another cavity which may be used to extract RF power. In practice, such a two cavity device has low gain. In most klystrons, there are several intermediate "idler" cavities. The first cavity bunches the beam. The bunched beam drives the second cavity to an RF voltage an order of magnitude greater than the first, which in turn bunches the beam more strongly. This process continues until the final idler cavity of the "linear gain region" of the klystron. The bunching is determined primarily by the voltage on the final idler cavity. After this cavity the bunches are allowed to drift until the RF current is maximum. At this point the beam is passed through two more cavities: a highly detuned "penultimate" cavity which sweeps still unbunched electrons into the bunch, and an output cavity which extracts energy by decelerating the beam. The output cavity could be replaced by a series of cavities or by a traveling wave structure.

An important parameter in klystron scaling is the beam plasma wavelength. Velocity modulation bunches a DC beam. However, space charge repulsion (modified by the drift tube) causes the beam to debunch. In the linear region, this process produces oscillations. The distances between cavities in a klystron are chosen to be approximately one-quarter of a plasma wavelength for optimal bunching. For a long relativistic beam of current $I$ and radius $a$ in a narrow tube of radius $b$ the plasma wavelength on axis is

[†] Work supported by the U.S. Department of Energy under contracts DE-AC03-76SF00515 (SLAC), DE-AC03-76SF00098 (LBL), and W-7405-ENG-48 (LLNL), and by the U.S.-Japan Collaboration on High Energy Physics.

[*] Visitor from KEK, National Laboratory for High Energy Physics, Oho, Tsukuba, Ibaraki 305, Japan.

*Presented at the European Particle Accelerator Conference, Rome, Italy, June 7–11, 1988*

$$\lambda_p \simeq \lambda_{RF}\sqrt{\frac{17\,\mathrm{kA}}{I}\frac{(\beta\gamma)^5}{1+2\ln(b/a)}}$$

where $\beta = v/c$ and $\gamma = 1/\sqrt{1-\beta^2}$. Increasing the beam energy ameliorates longitudinal space charge effects but increases the bunching distance. Increasing the frequency reduces the bunching distance. Our choice of 2.6 cm RF wavelength makes possible a multicavity klystron design that can bunch a 1 MV, 1 kA beam efficiently and extract power from it in a total distance of 1 m. For higher energy beams, bending magnets can be used to create differences in path length for particles of different energies. This permits bunching of higher energy beams even though their velocity is nearly independent of energy.

Another important parameter in klystron scaling is the magnetic field necessary to focus the beam. For a space charge dominated beam of uniform cross section the solenoid field $B$ necessary to confine the beam current $I$ to radius $a$ is

$$B = \frac{2m_e c^2}{ea}\sqrt{\frac{2I}{17\,\mathrm{kA}}\frac{1}{\beta\gamma}} = \frac{3.4\,\mathrm{kG\,cm}}{a}\sqrt{\frac{2I}{17\,\mathrm{kA}}\frac{1}{\beta\gamma}}.$$

In the relativistic klystrons discussed here both $\gamma$ and $I$ are greater than in conventional klystrons. At shorter wavelengths higher magnetic fields are needed to focus the beam since the radius of the drift tube scales with the wavelength. An estimate of the required field must include the effects of beam bunching. The peak current in the bunched beam typically is about four times the initial DC current. Thus the magnetic field required is typically twice that calculated for focusing a DC beam.

## 3. EXPERIMENTAL APPARATUS

### 3.1 Induction Accelerator

Most of the experimental studies described here were performed using the SNOWTRON injector at the ARC facility at LLNL. SNOWTRON is a linear induction injector composed of ten 150 kV induction cells driven by pulsed magnetics.[1] For klystron experiments, a triode electrode configuration was used with a cathode of 12.5 cm diameter and 35.6 cm spherical radius. The inner diameter of the anode drift tube was 8.8 cm. The cathode was placed 35 cm from the downstream end of the injector. Accelerating voltages up to 1.2 MV, beam currents up to 1.4 kA, and pulse widths up to 75 nsec have been obtained for the klystron experiments. The greatest stress on the injector is 260 kV/cm on the cathode shroud at peak voltage. The DPC computer code, which was used to design SNOWTRON, predicts peak currents of 2.3 kA at 1.2 MV.[4] However, the operating pressure of the injector led to cathode contamination which precluded uniform space charge limited emission.

### 3.2 Beam Transport

The distance from cathode to klystron was 4 m for the SL3 test and is 1.5 m for the SHARK and SL4 tests. Just downstream from the injector is a 30 cm taper where the beam pipe narrows from 8.8 to 1.9 cm diameter. The pipe diameter is narrowed further to 9.2 mm in the SHARK and SL4 klystrons. Nine 2.5 kG solenoid coils powered by five separate power supplies focus the beam between the cathode and the klystron. Three independently controlled 5 kG solenoids focus the beam in the relativistic klystron. Four sets of dipole magnets for horizontal and vertical steering are used to correct for beamline misalignments.

Beam transport calculations with the ST code have been used to estimate the required strengths of the focusing fields for 100% transmission of current through the klystron.[4] The result of such a calculation is shown in Figure 1.

### 3.3 Klystrons

Parameters of the three relativistic klystrons tested are summarized in Table 1. Further descriptions are given below.

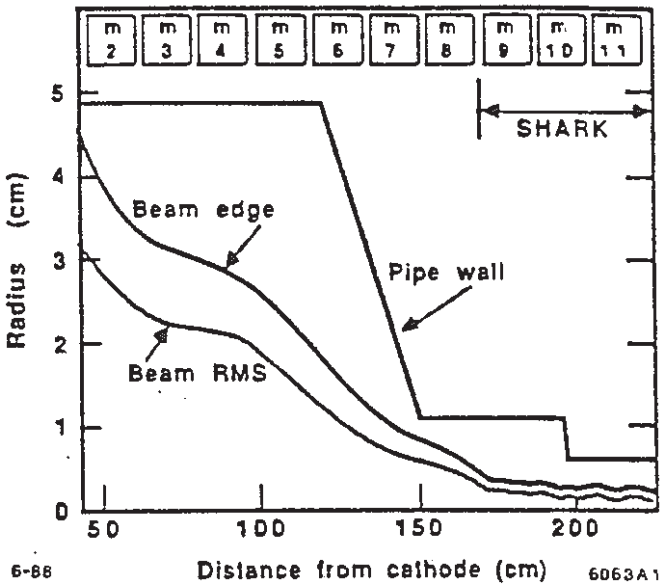


FIG. 1. Beam size calculated through SHARK.

| Klystron | SL3 | SHARK | SL4 |
|---|---|---|---|
| Output freq. (GHz) | 8.57 | 11.4 | 11.4 |
| Drive freq. (GHz) | 8.57 | 5.7 | 11.4 |
| Output power (MW) | | | |
| Peak (max.) | 75 | 47 | 200 |
| Flat pulse (max.) | 75 | 47 | 68 |
| Design gain (dB) | 54 | 20 | 65 |
| Efficiency (%) | | | |
| Design | 60 | 20 | 40 |
| Operation (max.) | 55 | 25 | 50 |
| Beam Voltage (kV) | | | |
| Design | 330 | 1200 | 1200 |
| Operation (max.) | 1000 | 1200 | 1000 |
| Beam Current (A) | | | |
| Design | 300 | 1000 | 1000 |
| Operation (max.) | 350 | 750 | 750 |
| Number of cavities | 5 | 2 | 6 |
| Total length (cm) | 31 | 25 | 98 |
| Beam-off loaded $Q$ | | | |
| Input cavity | 250 | 725 | 280 |
| Idler cavities | 4000 | — | 120 |
| Penultimate cavity | 4000 | — | 3800 |
| Output cavity | 44 | 40 | 20 |
| Drift tube diam. (mm) | 11 | 19, 9.2 | 14, 9.2 |

TABLE 1. Parameters of relativistic klystrons tested.

SL3 is a conventional high gain klystron designed to operate at 8.6 GHz with a conventional gun. With its design gun replaced by an induction accelerator, it served as an expedient first demonstration of a relativistic klystron. SL3 was driven by a 1 kW X-band TWT amplifier.

SHARK is a two cavity sub-harmonic drive relativistic klystron. The input cavity is driven by an RF source of several MW at 5.7 GHz which modulates the beam velocity. After drifting, the beam current has large Fourier components at 5.7, 11.4, and 17.2 GHz. Resonant cavities tuned to the higher harmonics can be used to extract power and measure breakdown fields at the higher frequencies. The 11.4 GHz output cavity is positioned after a 25 cm drift for optimal bunching at that harmonic. With only two high $Q$ resonant structures in this klystron, problems with beam breakup instabilities are minimized. However, the gain of a two cavity tube is low. Therefore, in order to achieve beam-to-RF power conversion

comparable to that in multicavity tubes, a conventional 5 MW, 5.7 GHz klystron is used to drive SHARK. The RF fields in the input and output cavities are comparable for 2 MW of drive and 50 MW of output because of the different $Q$'s.

SHARK was designed to serve as a testbed for cavity design to be used in relativistic klystron research. Its design allows study of a wide range of beam parameters and minimizes difficulties with beam propagation. The drift pipe and output cavity are easy to replace, making it possible to use SHARK to study different output cavities at several frequencies.

SL4 is a high gain, six cavity, relativistic klystron at 11.4 GHz which was designed specifically for the 50 nsec pulsed 1.2 MV, 1 kA SNOWTRON beam. Therefore, unlike most klystrons, it was designed without an integral gun assembly. In order to make the RF filling time of the SL4 cavities much shorter than the 50 nsec beam pulses, three of the gain cavities are coupled by irises and waveguides to absorptive ceramic wedges. This results in loaded $Q$'s of 120, and filling times of 2–3 nsec for these cavities.

To reduce the difficulty of maintaining a well-focused electron beam over a 1 m drift length, the SL4 drift tube was tapered. The drift tube diameter in the first four cavities is rather wide, 14 mm. The tube then is tapered to 9.2 mm just upstream of the penultimate cavity. Tapering permits the use of solenoid magnets with axial field of 2.7 kG for most of the length of the klystron. A 5 kG solenoid surrounds the region of the penultimate and output cavities.

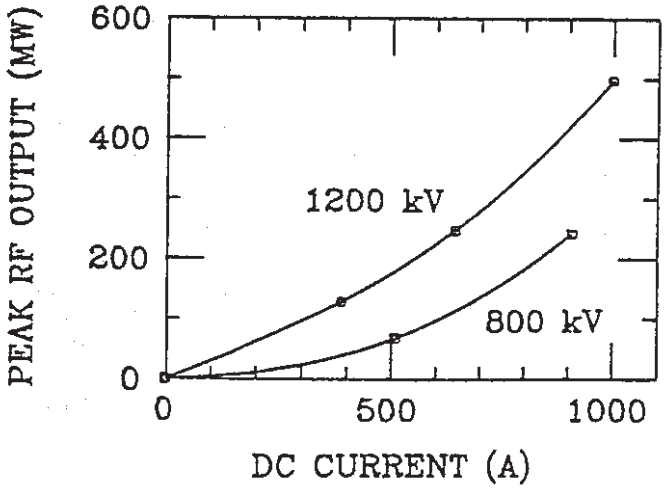


FIG. 2. MASK simulations of SL4 output power.

The design gain and efficiency for SL4, 65 dB and 40%, respectively, are obtained using the MASK computer code.[5] MASK simulations were used to optimize the SL4 design parameters and to predict the efficiency and gain at several different beam currents and voltages. Some simulation results are shown in Figure 2. The saturation RF drive power is approximately 200 W, which is supplied by a 1 kW X-band TWT amplifier.

Because of the high peak electric fields in the penultimate and output cavities good vacuum is necessary to prevent cavity breakdown. Consequently, a 500 liter/sec cryopump evacuates the klystron collector section and two 8 liter/sec vac-ion pumps evacuate the output waveguide. In this configuration waveguide and collector pressures can be maintained at $10^{-8}$ Torr.

### 3.4 Diagnostics

**Current Monitors:** The pulsed DC beam current is monitored in three places: at the injector, upstream from the input cavity, and downstream from the output cavity. The DC current monitors measure image currents in the beam pipe wall. An RF current monitor is placed downstream from the SHARK output cavity. The RF current diagnostic is a pickup loop, recessed azimuthally in the beam pipe wall, which measures $\dot{B}_\phi$.

**RF Power Diagnostics:** Forward and reflected RF drive signals are sampled using 20 dB broadband waveguide directional couplers. Relativistic klystron output power and, in the SL4 experiment, the RF reflected back from the high gradient accelerator test section, were sampled using 56 dB waveguide directional couplers. The sampled RF signals are transported on individually calibrated, 25 m long, high quality heliax cables from the couplers to the control room where they are measured with calibrated HP 8470B crystal diode detectors. Calorimetric measurement methods so far have been precluded by a 1 Hz pulse repetition rate necessitated by inadequate shielding.

### 3.5 High Gradient Accelerator

To complement the SL4 experiment, a 26 cm long section of 11.4 GHz accelerator structure operating in the $2\pi/3$ traveling wave mode has been built. The constant impedance structure consists of 30 cells and has $r/Q = 14.2\,\mathrm{k}\Omega/\mathrm{m}$. The attenuation parameter is 0.136 nepers. The group velocity is $0.031c$, giving a filling time of 28.4 nsec. The iris diameter was chosen to be 7.5 mm. Parameters were calculated by the SUPERFISH code and confirmed by cold test measurements. Coupler dimensions were approximated by extrapolation from S-band data, and finalized by cold test. The accelerator was fabricated from machined "cups" which were stacked and brazed. A special tool permitted each cavity to be tuned up or down in frequency in order to obtain the correct phase advance per cell.

## 4. EXPERIMENTAL RESULTS

### 4.1 Beam Transmission

The design goal of 100% beam transmission through the klystrons has not been achieved experimentally, even after focusing adjustments were performed by empirical optimization using a diagnostic such as transmitted current or output RF. The maximum current transported through SHARK is 750 A, only 65% of the maximum current entering the klystron. Up to 80% transmission has been achieved at 400 A. Transmission achieved through SL4 (which is four times longer than SHARK) is 55% at 800 A, and is 65% at 500 A. Transmission is observed to be independent of RF drive for SHARK. However, for SL4, a slight decrease in transmission was noted at high RF output levels. (There was no downstream current monitor in the SL3 tests; transmission through SL3 was not measured.)

### 4.2 SL3 Demonstration

The SL3 test was designed to be a demonstration of the effects of putting a conventional klystron tube (stripped of its gun) in a high power pulsed beam. No unusual or unexpected phenomena were observed. No evidence of multipactor, breakdown, parasitic oscillations, nor other instabilities was observed. RF pulse risetimes were 5–10 nsec. RF pulses reproduced the shape of the beam current pulses quite well. SL3 performance at beam energies much greater than design is illustrated in Figure 3. Peak power of 75 MW was attained with an 800 kV, approximately 250 A beam. Output power observed agreed well with the predictions of the MASK simulation code.

### 4.3 SHARK and SL4

Peak output power of 200 MW at 11.4 GHz was attained with the SL4 relativistic klystron design using a 930 kV, 420 A beam. SL4 has not yet operated at its 1000 A design current.

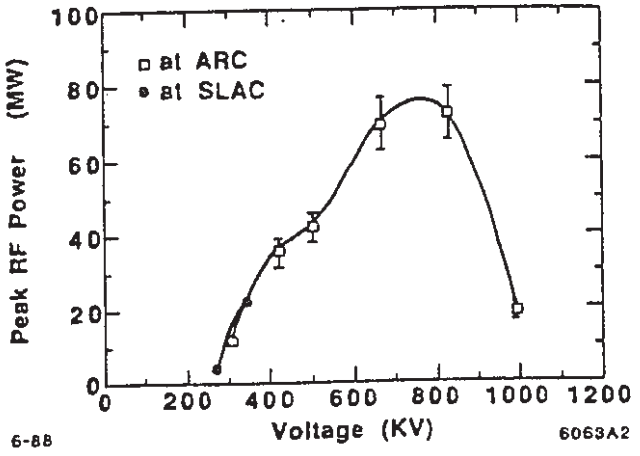


FIG. 3. SL3 performance.

However, agreement is excellent between output power measured at lower currents and the MASK predictions (Figure 2) for operation at these currents. The 200 MW peak power delivered by SL4 to the 11.4 GHz accelerator corresponds to a longitudinal accelerating gradient of 140 MV/m. Early indications are that there is appreciable dark current in the accelerator when the accelerating gradient exceeds 90 MV/m.

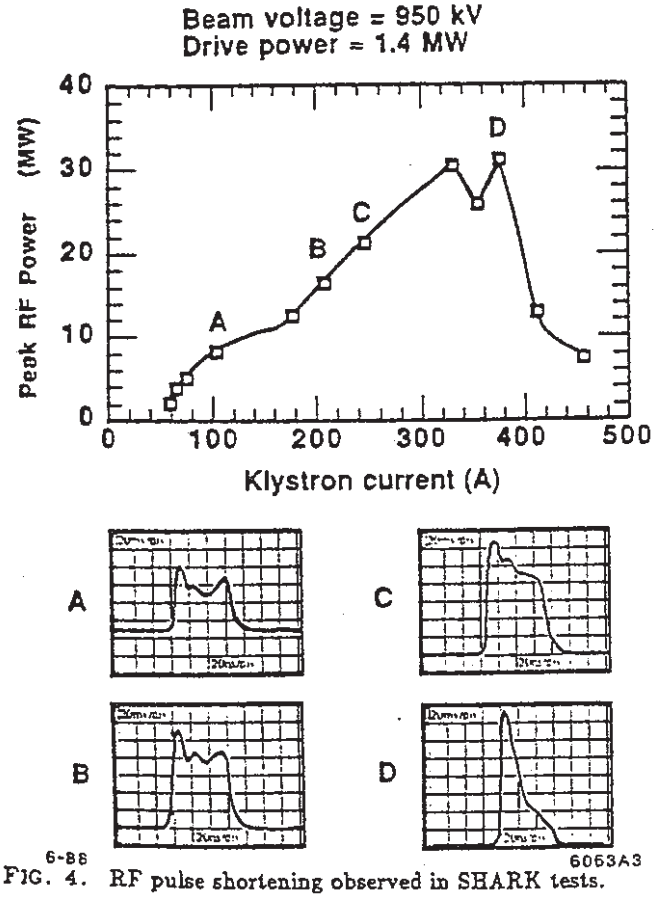


FIG. 4. RF pulse shortening observed in SHARK tests.

In our tests of both SHARK and SL4, we observe that as the beam current through the klystron is increased up to a certain level, the output power pulses remain relatively flat. However, if the beam current is increased beyond this level, the trailing edges of the output power pulses diminish in amplitude, while the leading edges continue to grow with the beam current. This behavior in SHARK tests is illustrated in Figure 4. We have demonstrated that our ability to obtain flat output power pulses is affected by beam current, RF drive level, and focusing magnetic field strength. The practical importance of these observations is that even though 200 MW of RF was produced with SL4, the maximum reasonably flat RF pulse achieved was only 60 MW. Low and high peak power SL4 pulses are illustrated in Figure 5. The pulse shortening phenomenon is a serious impediment to making flat high power RF pulses. It is not beam breakup because the transmitted DC beam current pulse does not shorten with the RF pulse. Two possible pulse shortening mechanisms, (a) "anomalous" beam loading and (b) transient effects, are described below.

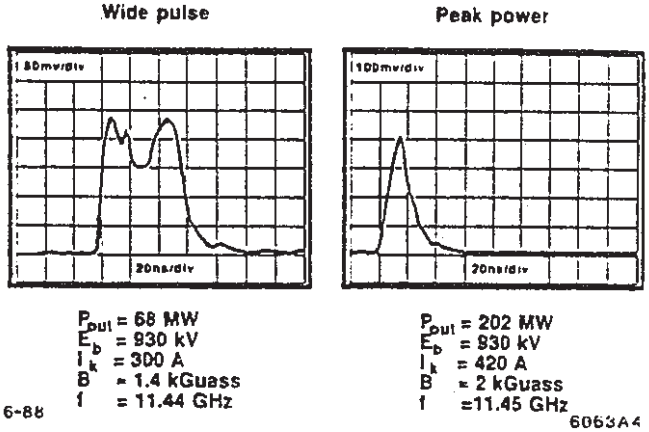


FIG. 5. Low and high peak power pulses in SL4 tests.

### (a) Pulse Shortening by Anomalous Beam Loading:

To understand the mechanism for the limited power output and pulse shortening in SHARK, an experiment was performed in which simultaneous data on reflected power from the input cavity and on output power were recorded at a critical point for the onset of the shortening phenomenon. With no external changes in the beam condition and/or input power, the output alternates from pulse to pulse between the rectangular pulse and the triangular pulse.

When the beam turns on, there is a significant dip in the drive power reflected from the SHARK input cavity. Two distinctly different states have been observed in the reflected drive, as shown in Figure 6, one having a much greater reflection during the beam-on time. Furthermore, the state with large reflection is correlated repeatably with the narrow output pulse.

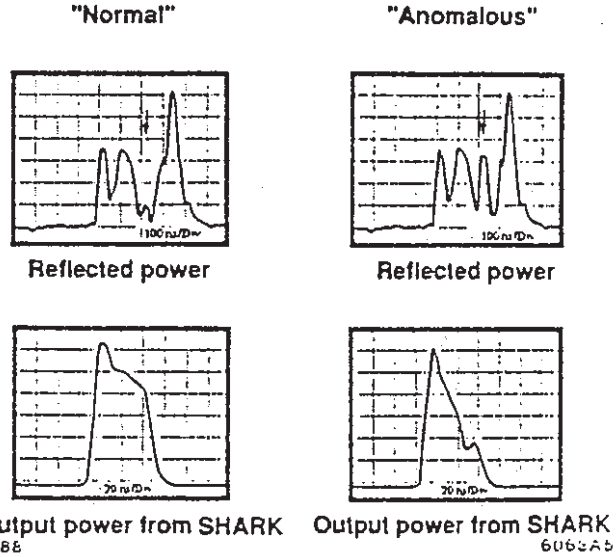


FIG. 6. SHARK reflected drive and output power. Arrows indicate the 50 nsec beam time in the reflected power.

This observation can be reproduced with our computer code for transient analysis. In the code, we use a circuit model to compute the time varying voltage across the input gap. The reflected power is calculated from the time-varying voltage by power balance.

Results of the transient calculation are shown in Figure 7 where the relatively flat output pulse with the low beam-on reflected power was obtained by using a beam loading generally consistent with MASK calculations and measurements. The narrow output pulse and increased reflection were obtained by arbitrarily increasing beam loading by a factor of 2.5.

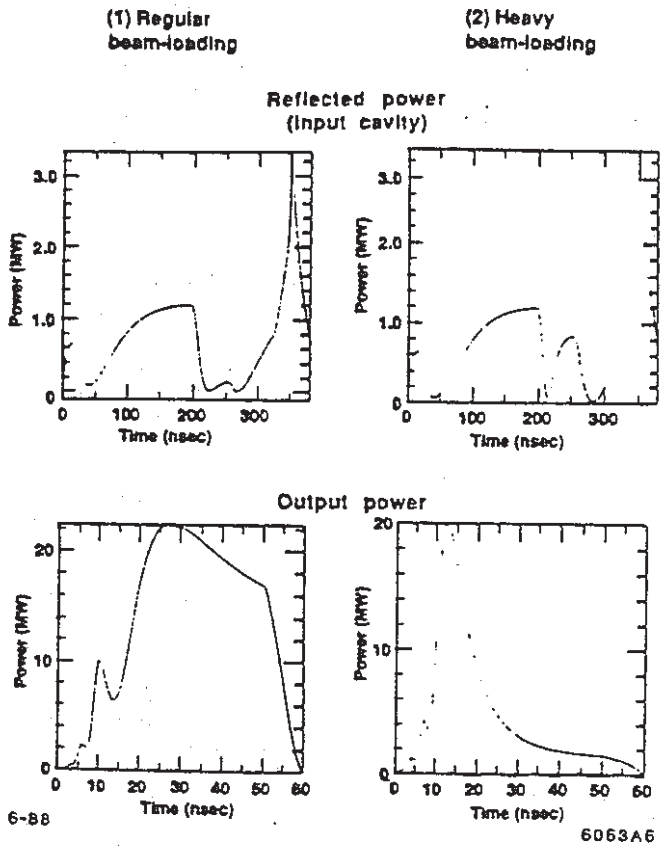


FIG. 7. Calculations of the effect of anomalous beam loading on SHARK reflected drive and output power.

A proposed mechanism follows. During the beam-on time, secondary electrons produced by impinging x-rays are emitted from the high field regions around the cavities. When the cavity field is low, these secondaries oscillate in trajectories close to the cavity walls with no net absorption of energy. At higher field gradients, the secondary electrons have longer path lengths. Above a critical field value, the path lengths are long enough for secondaries to hit the opposite nose cone, depositing their kinetic energy in the walls in the process, which constitutes a loading phenomenon.

The proposed mechanism is qualitatively consistent with several observations: Pulse shortening does not occur below an input power of 500 kW. The voltage across the gap at this critical drive power level is 360 kV. If secondary electrons move in straight lines, the path length during half a period is approximately 1 cm. This is consistent with the gap length being 8 mm at the neck. As the focusing field is reduced, the secondary electrons have curved paths, and require higher field gradients to hit the opposite wall. This is consistent with the observed increase in threshold power with reduced solenoid $B$ field.

The secondary electrons in the anomalous beam loading mechanism may be caused by x-rays from the beam. Hence, they turn on and off with the beam. Note that during the experiment, roughly 200 A of current was lost in traversing the taper-klystron system. Preliminary calculations indicate that the x-rays produced are consistent with secondary electron currents required to account for the additional loading (5–10 A). This hypothesis is also consistent with the observation of reduced power output with increasing beam current, since the x-ray dosage is generally increased with beam current.

### (b) Pulse Shortening by Transient Effects:

In addition to anomalous beam loading, transient effects due to normal resistive loading and reactive detuning of cavities by a high power pulsed beam influence the output power pulse shapes in relativistic klystrons. The transient nature of the pulsed beam energy and current make the loading and detuning time dependent. The beam-cavity coupling is sensitive to the radial charge density distribution in the beam. Since this distribution is unknown and sensitive to focusing, it is desirable to measure, rather than to calculate, the beam loading and detuning.

Measurements made on the SL4 input cavity so far indicate a beam loading $Q$ of 670 and detuning by +22 MHz at 500 A beam current and 950 kV beam voltage. These measurements differ from the predictions of MASK simulations, most likely due to the sensitivity of the calculation to the true radial distribution of charge in the beam.

The beam pulses from the induction accelerator have a "rounded" energy distribution, dominated by the rise and fall times of the accelerating voltage (which are comparable to the switching time of the magnetic energy compressor that drives the induction cells). Consequently, transient effects of beam loading and detuning are expected to be more significant near the beginning and end of the pulse, where beam energy and current are reduced and are changing rapidly. In the SL4 klystron, for which we have begun to measure the input cavity beam loading and detuning, the minimum beam loading $Q$ is comparable to the external $Q$ values of the drive and idler cavities, and the maximum detuning is comparable to the stagger tuning differences between cavities.

We analyze the effect of transient beam loading and detuning on the shape of the output power pulse in the following way. Using a resonant circuit model, we calculate the time-development of the voltage on a driven cavity. Then, by calculating the beam velocity modulation produced by the calculated cavity voltage, we estimate the RF current that drives another cavity downstream. Following this analysis through all six cavities of the SL4 klystron, we can study how the shape of the output power pulse develops as a function of the different time dependent $Q$'s and detunings of the individual klystron cavities.

The output pulse shapes we have calculated look strikingly similar to some of the pulses we have observed. The shapes may be described qualitatively as being composed of transient precursors followed by a flat pulses. The precursor primarily is due to the transient detuning that results from reactive beam loading and, in some cases, may be of much larger amplitude than the trailing flat part of the RF pulse. The precursor peak power level has broad bandwidth and is minimized by appropriate choice of driving frequency. High power flat-top RF pulses have emerged in our calculations with a driving frequency bandwidth narrower than, and shifted upward from, the bandwidth of the large precursor phenomenon. The shift in driving frequency necessary to obtain rectangular pulses in our calculations is the typical cavity detuning. We have not observed these rectangular pulses from SL4 yet at any frequency, presumably due to the "anomalous" beam loading described in the previous section.

### 4.4 Other Observations

**SHARK Input Cavity Breakdown:** The drive cavity of SHARK was afflicted with breakdown problems. When first installed the cavity would operate at drive levels as high as 2 MW without arcing. As testing progressed the arcing threshold gradually decreased to about 1 MW. The arcing was evidenced by the input cavity reflection coefficient suddenly jumping to unity and staying there until the end of the RF drive pulse. At threshold the arcs were initiated apparently at random times during the pulse. At drive levels well above threshold the arcs would occur on every pulse and start early in the drive pulse. It was possible to raise the threshold from 1 MW to about 1.5 MW by RF processing at 15–20 pps with the beam off. The cavity was processed in this way for 1–2 hours. However, when the repetition rate was reduced to 1 pps and the beam was turned on (inadequate radiation shielding limited the repetition rate to 1 pps with beam on) the threshold would quickly decrease again to about 1 MW. The arcing was a serious limitation for the klystron tests and limited the maximum output power which could be obtained.

**SHARK Input Cavity Cyclotron Resonance:** There was also evidence of multipactoring or some other electronic activity in the SHARK input cavity. The pressure in the SHARK vacuum system was monitored while the solenoid field was varied with the RF drive on and the beam off. A sharp rise in pressure was observed at a field strength of about 1035 G. The cyclotron dipole resonance for the 5.7 GHz drive occurs at 2041 G. However, the linear dependence of the radial electric field produces a quadrupole resonance at half that field.

**SL4 Input Cavity Multipactoring:** The reflection coefficient of the SL4 input cavity is a function of drive power even when the beam is off. At low drive levels, less than 40 W, the reflection coefficient is constant and equal to that measured during cold testing. Above 40 W drive, the reflection coefficient drops rather abruptly. Since the cavity is heavily over-coupled (9.5 standing wave ratio) this reflection coefficient means that something is absorbing power from the cavity. The threshold for the onset is sensitive to the solenoid $B$ field. We feel this is evidence of multipactor. Nevertheless, stable output power was observed.

**SL4 Parasitic Oscillations:** Under certain focusing and steering conditions a large RF pulse at 13.2 GHz is radiated from the SL4 input cavity, coincident with the beam pulse. This can occur with or without RF drive. The 13.2 GHz pulse appears to be much larger than the RF drive pulse, but since the RF components have not been calibrated at 13.2 GHz, we do not know how much power the pulse contains. The 13.2 GHz signal probably arises from dipole mode resonance in the input and one of the downstream cavities. Since 13.2 GHz will propagate (in the $TE_{11}$ mode) through the 14 mm drift tube of the klystron, a signal can feed back from the idler cavities to the input cavity. Consequently, the system can oscillate. The phenomenon does not appear to affect the gain of the klystron. The 13.2 GHz signal has not been observed in the klystron output.

In addition to the 11.4 GHz drive frequency, a spurious 11.8 GHz frequency has been observed in the output from SL4 in the presence of drive. Power at this frequency was detected by measuring the distance between nulls on a sliding stub tuner placed in the output path. This parasitic oscillation can be eliminated by adjusting the beam focusing and steering.

## 5. FUTURE PLANS

At present, SL4 and the high gradient accelerator section are in the experimental area and tests are continuing. To further understand transient effects measurements of input cavity beam loading and detuning as discussed in Section 4.3(b), will be continued on SL4. Similar studies will be initiated on the high-field SHARK input cavity when it is reinstalled. We hope to study correlations between input cavity beam loading and output pulse shapes as functions of beam energy, current, and focusing on both SL4 and SHARK. Studies of high gradient accelerator breakdown at high frequencies, and measurement of accelerating gradients, also are anticipated.

To reduce anomalous beam loading in SHARK, we plan to apply techniques which have reduced multipactoring in other RF systems to the SHARK input cavity. These include (1) collimating the beam aperture upstream of the klystron, (2) RF conditioning at higher rep-rate with better shielding, (3) slotting the noses of the drive cavity to reduce secondary electron emission, and (4) locally perturbing the focusing magnetic field at the cavity with a magnetic shunt.

Several modifications to the current SHARK 11.4 GHz output cavity are planned. The SHARK output cavity will be replaced by the penultimate and ouput cavities of SL4 (which were designed as a modular section). The addition of a penultimate cavity to SHARK in this way should improve bunching and increase output power. A traveling wave output structure which has been fabricated will also be used to replace the SHARK output cavity. New output cavities at the 5.7 and 17 GHz harmonics may be built and tested.

## 6. SUMMARY

We have been working to develop a high power (500 MW) short wavelength (2.6 cm) relativistic klystron with beam kinetic energy greater than 1 MeV. Three different klystrons have been tested. Two parasitic oscillations (at 11.8 and 13.2 GHz) have been observed but do not appear to be debilitating and have been avoided by suitable choice of operating parameters. Peak RF power of 200 MW has been achieved, but only with an RF flat top much shorter than the beam current pulse. This pulse shortening phenomenon is by far the most serious problem encountered. It is clearly not beam breakup since it does not correlate with shortening of the DC current pulse. Experimental evidence from one of the klystrons (SHARK) indicates that pulse shortening is caused by loading of the input cavity by anomalous charged particle currents. Since this loading occurs only when the beam is on, it is believed to be due to either secondary electrons or to photoelectrons produced by the copious supply of x-rays caused by beam interception. A second and perhaps related problem is rather poor beam transmission through the klystrons, which has not exceeded 65%. Finally, the 200 MW peak RF pulses have been transmitted into a 26 cm long high gradient accelerator structure. This power corresponds to an accelerating gradient of 140 MV/m.

## ACKNOWLEDGEMENTS

We thank R. J. Briggs, G. J. Caporaso, M. Chodorow, Y. Goren, E. W. Hoyt, K. V. Niel, A. C. Paul, C. Pearson, D. S. Prono, T. O. Raubenheimer, L. L. Reginato, A. C. Smith, K. Whitham, D. Yu, and L. Zitelli for their assistance. The authors from SLAC thank LLNL for its continuing hospitality.

## REFERENCES

1. L. L. Reginato and D. L. Birx, "Pulsed High Power Beams" and "Recent Advances in Magnetically Driven Induction Linacs" in these proceedings.
2. T. J. Orzechowski *et al.*, "High Efficiency Extraction of Microwave Radiation from a Tapered Wiggler Free Electron Laser," *Phys. Rev. Lett. 54*, 889 (1985).
3. A. M. Sessler and S. S. Yu, "Relativistic Klystron Two-Beam Accelerator," *Phys. Rev. Lett. 58*, 2439 (1987).
4. J. K. Boyd, "SNOWTRON Numerical Calculations," LLNL-RM-87-48 (November 1987).
5. K. Eppley, "Algorithms for the Self-Consistent Simulation of High Power Klystrons," SLAC-PUB-4622 (May 1988), to be published in the proceedings of the Linear Accelerator and Beam Optics Codes Workshop, San Diego, California, January 19–21, 1988.

LA-UR-88-3236

Los Alamos National Laboratory is operated by the University of California for the United States Department of Energy under contract W-7405-ENG-36

TITLE: # LABORATORY PERFORMANCE OF THE BEAR RFQ

AUTHOR(S): P. G. O'Shea, D. L. Schrage, L. M. Young, T. J. Zaugg, M. T. Lynch, L. D. Hansborough, K. F. McKenna

SUBMITTED TO: 10th Conference on the Application of Accelerators in Research & Industry, Denton TX, November 7-9, 1988



Los Alamos
Los Alamos National Laboratory
Los Alamos, New Mexico 87545

FORM NO. 836 R4
ST NO 2629 5/81

# LABORATORY PERFORMANCE OF THE BEAR RFQ*

P. G. O'Shea, D. L. Schrage, L. M. Young, and T. J. Zaugg, M. T. Lynch,
K. F. McKenna, and L. D. Hansborough
Los Alamos National Laboratory, MS H817, Los Alamos, NM 87545

The BEAR (Beam Experiment Aboard Rocket) accelerator will be part of an experiment to demonstrate the operation of an ion accelerator in space and to characterize the exoatmospheric propagation of a neutral particle beam. The RFQ (radio-frequency quadrupole) has been designed to produce a 25-mA $H^-$ beam with an emittance of 0.01 π cm-mrad (rms normalized) at an energy of 1 MeV. Because of the rigors of spaceflight, the accelerator design has been constrained by factors not normally applicable to conventional terrestrial accelerators. These factors and the mechanical features are described in a companion paper in these proceedings. The design techniques developed for BEAR would be applicable whenever rugged, lightweight, or power-efficient systems are required. The BEAR RFQ has been operated under power with beam in the laboratory. This paper presents details of measured beam transport, emittance, and energy spectra.

## 1. Introduction

The BEAR accelerator will be the first complete rf particle accelerator to be tested in space [1]. The exigencies of launch and space flight require that many novel techniques be developed to fabricate a lightweight, reliable, and rugged system. Details of the design considerations, fabrication, mechanical testing, and

*Work supported by the US Department of Defense, Strategic Defense Initiative Office, under the auspices of the US Department of Energy.

tuning are reported elsewhere in these proceedings [2]. This paper will report the results of laboratory beam transport studies on the BEAR Test Stand.

The main components of the BEAR accelerator are as follows: an $H^-$ ion source [3], with 30-keV extraction, a low-energy beam transport (LEBT) quadrupole system, radio-frequency quadrupole (RFQ) accelerator that takes the beam to 1 MeV, a high-energy beam transport (HEBT) quadrupole system, and a gas neutralizer. Design parameters of the BEAR RFQ are given in table 1.

The RFQ body is an electroformed aluminum/copper structure, with no rf or mechanical joints. The cavity walls are copper plated on aluminum, with the vane tips being bare aluminum.

The RFQ was designed to have a copper power requirement of 70 kW and 1 kW/mA of accelerated beam. The low duty factor of 0.025%, along with the frequency control of the rf amplifier, precluded the need for cooling.

The rf power for the RFQ [4] is provided by two solid-state amplifiers, capable of producing 60-kW pulses, 60 μs long, at 5 Hz with a frequency of $425 \pm 0.5$ MHz. The amplifiers are capable of tracking the RFQ resonant frequency to within 0.02 MHz, which eliminates the need for temperature stabilization of the RFQ. The amplifiers have a specific power output of 0.9 W/g.

The LEBT, which focuses the $H^-$ beam from the source to the RFQ, consists of a quadrupole triplet made of NdFe permanent-magnet blocks. This was designed to be a fixed focus system with no on-line adjustment of quadrupole strength or position. The match into the RFQ is adjusted by varying the extraction voltage from the ion source and by controlling the plasma neutralization in the LEBT region through the addition of Xenon gas [3]. This has resulted in a less than ideal, but stable and reliable, match in to the RFQ.

The vacuum system for the LEBT region consists of two specially modified Sorbac™ getter pumps, which have a pumping speed of 600 ℓ/s for hydrogen and zero

for xenon. The only xenon pumping from the LEBT is 0.6 ℓ/s through the RFQ orifice to a cryo trap in the HEBT region. This provides a means of allowing a high partial pressure of xenon and a low partial pressure of hydrogen, which is desirable for optimum operation.

The HEBT, which collimates the output beam from the RFQ, is similar in design to the LEBT. The HEBT was not installed while the measurements reported here were being made. An overview of the test-stand configuration is shown in fig. 1.

The RFQ has produced currents up to 27 mA at the design energy of 1 MeV. Details of the RFQ performance are given below.

## 2. LEBT output and match into the RFQ

The typical current output from the LEBT was 60 mA at a source extraction voltage of 34 kV. Extraction from the source was through a 4- by 1-mm slit. This extraction voltage was found to be the one that produced the best transverse match into the RFQ and, therefore, the highest current out of the RFQ. The match was found to be strongly dependent on the degree of space-charge neutralization. This neutralization was controlled by adding xenon to the LEBT vacuum chamber through a piezoelectric bleed valve.

The emittance of the beam near the RFQ entrance was measured using 30-keV electric sweep scanners [5]. Because of the tight spacing between the LEBT and the RFQ, emittances could only be measured with the RFQ removed. The scanners were configured to measure in two perpendicular planes, and the entrance slits were positioned 1 cm downstream of the RFQ entrance plane. Fig. 2 shows the transverse phase space (emittance) of the beam in the direction parallel to the short axis of the source slit. Without the addition of Xe, the base pressure in the LEBT was $3 \times 10^{-5}$ torr or lower, and the match to the RFQ was extremely poor. In this situation, the

current exiting the RFQ ($I_{rfq}$) was typically no more than 5-10 mA. The addition of Xe had a dramatic effect on the match into the RFQ, resulting in an increase in $I_{rfq}$ to 24-27 mA. The optimum partial pressure of Xe was found to be approximately $4 \times 10^{-5}$ torr. The emittance (rms normalized) of the beam (50 mA) at the RFQ entrance in directions parallel to the short and long axes of the source slit are 0.008 and 0.015 π cm·mrad, respectively. Without xenon, the emittances are typically twice these values. The mismatch factor of the beam into the RFQ is 1.6 at best, which would be expected to result in approximately 50% of the beam in the LEBT being accelerated through the RFQ.

## 3. RFQ output

The $I_{rfq}$ was measured at the design intervane voltage as the injection energy was varied. The peak $I_{rfq}$ was found to be at 34 keV, which was in agreement with estimates of the optimum match based on LEBT phase-space measurements.

The RFQ output emittance was measured using newly designed compact 1-MeV electric sweep scanners. The angular resolution of the scanners is approximately 2 mrad. An RFQ output emittance plot is shown in fig. 3, the measured emittance being 0.014 π cm·mrad normalized rms at a current of 24 mA. The measurements were made at a distance of 134 mm from the end of the RFQ vanes.

The energy spectrum of the beam was measured using a magnetic spectrometer. The bending magnet was a 45°, stigmatic, homogeneous-field electromagnet with rotated poles. The resolution of the spectrometer was 5 keV at 1 MeV. Apart from resolution-related broadening, the measured spectrum is ~20 keV broader than that at the exit of the RFQ because of space-charge effects. A spectrum measured with $I_{rfq}$ = 26 mA, and an intervane voltage close to 100% of the design

value is shown in fig. 4. A single peak was found at 1 Mev and no other peaks were detected. At lower current levels (20 mA), the 1-MeV peak was split in two with peaks at 0.96 and 1.02 MeV with a shallow valley in between. This splitting of the peak has been observed previously for RFQ output [6].

Spectra were also taken at lower intervane voltages. At voltages above 75% of design, the peak energy remains close to 1 MeV. At lower field levels, the accelerating buckets collapse and so does the energy spectrum, resulting in a broad low level spectrum at 70%. Between 60 and 70%, a spectrum with a single peak at 0.25 MeV was found. This corresponds to particles being accelerated to half the design velocity in the RFQ.

## 4. Conclusion

The BEAR RFQ has met or exceeded all of its design requirements. It is the lightest operational RFQ in the world. Over 600 hrs of operation with beam have been logged, and there has been no discernable damage to the aluminum vane tips, nor has there been any degradation in performance. Many of the techniques developed for the BEAR project will have applications in ground-based accelerators where weight, size, and reliability are important. These will be described in future publications.

The definitive test will be during the spaceflight, which is planned for spring of 1989.

## Acknowledgment

The authors would like to acknowledge all the members of the BEAR Accelerator Team who assisted with this work, particularly R. Maggs, P. Schafstall, L. Catlin, J. Dyson, J. Plato, J. Devenport, and J. Martinez.

## References

[1] T. M. Foley, Aviation Week & Space Review, March 21, 1988.

[2] D. Schrage, et al., these proceedings.

[3] P. Allison and J. Sherman, Proc. 3rd Symp. on Production and Neutralization of Negative Ions and Beams, AIP Proc # 111, p. 511 (1983).

[4] C. D. Davis, M. T. Lynch, and D. W Reid, to be published Proc. 1989 Particle Accelerator Conf., Chicago, Illinois.

[5] P. W. Allison, J. D. Sherman and D. B. Holtkamp, IEEE Trans. 30 (4), 2204 (1983).

[6] James E. Stovall, K.R. Crandall, and R.W. Hamm, "Performance Characteristics of a 425-MHz RFQ Linac," IEEE Trans. Nucl. Sci., 28, (2), 1508 (1981).

Table 1

BEAR RFQ Design Paramaters

| | |
|---|---|
| Particle | $H^-$ |
| Resonant frequency | 425 MHz |
| Injection energy | 0.03 MeV |
| Final energy | 1 MeV |
| Output current | 25 mA |
| Output emittance (rms norm.) | 0.01 π cm·mrad |
| Pulse width | 50 μs |
| Rep. rate | 5 Hz |
| Copper power | 71 kW |
| Beam power | 26 kW |
| Intervane voltage | 0.044 MV |

## Figures

Fig. 1. BEAR test stand viewed from above.

Fig. 2. LEBT output emittance diagrams, (a) without xenon and (b) with a partial pressure of xenon of $3 \times 10^{-5}$ torr. Contour levels are 0.01, 0.05, 0.1, 0.2, 0.3, 0.4, 0.5 of peak signal, measured parallel to the short axis of the source slit (x axis).

Fig. 3. RFQ output emittance diagram, measured parallel to the vertical vane at 134 mm from the RFQ at a current of 24 mA.

Fig. 4. RFQ output energy spectrum, measured at a current of 26 mA.

## BEAR TEST STAND

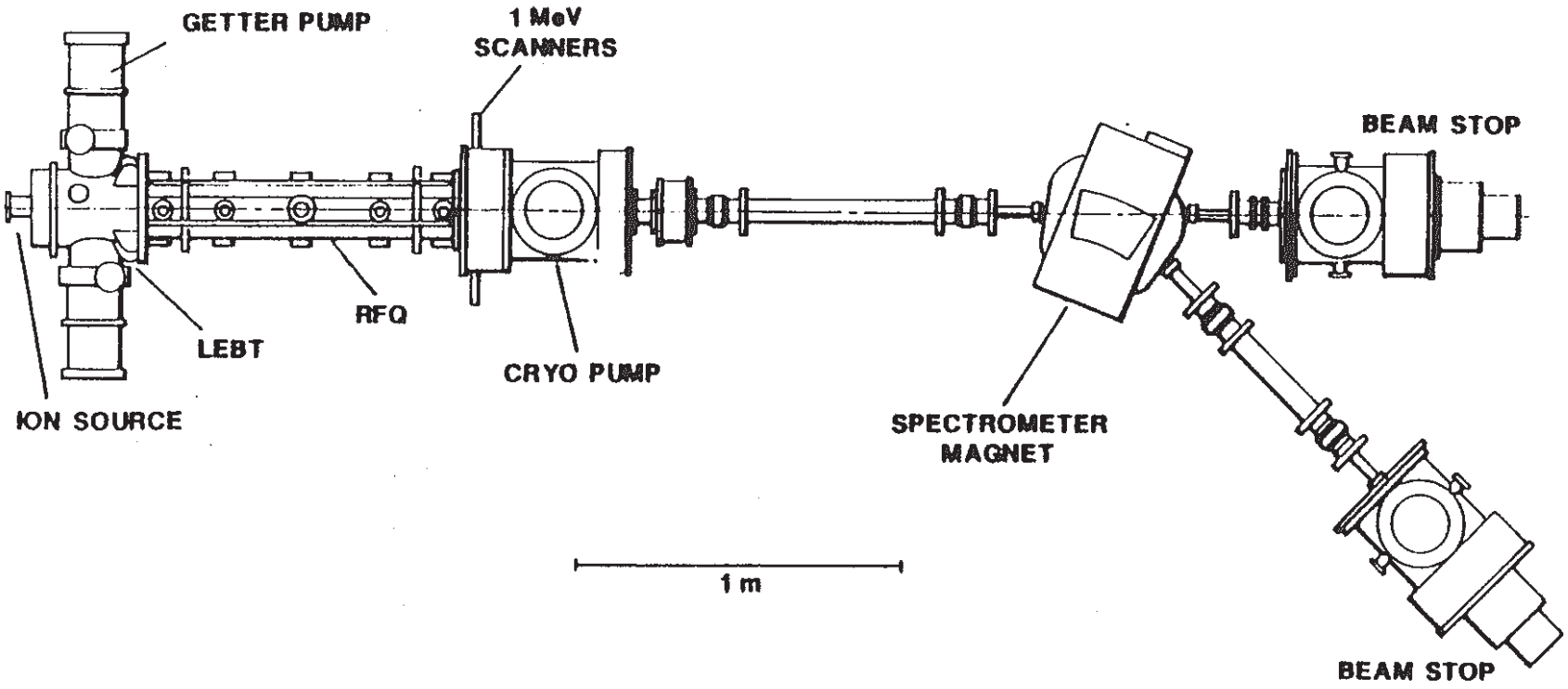

# LEBT OUTPUT EMITTANCE DIAGRAMS
# X PLANE

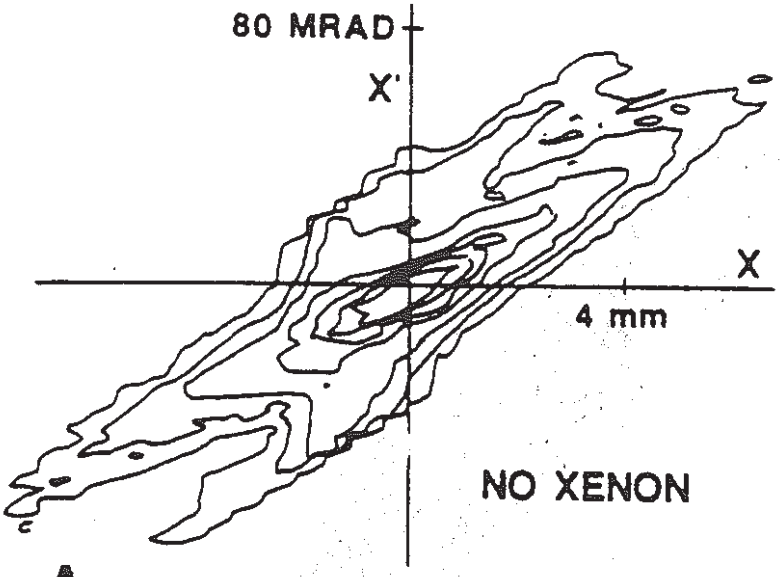


A

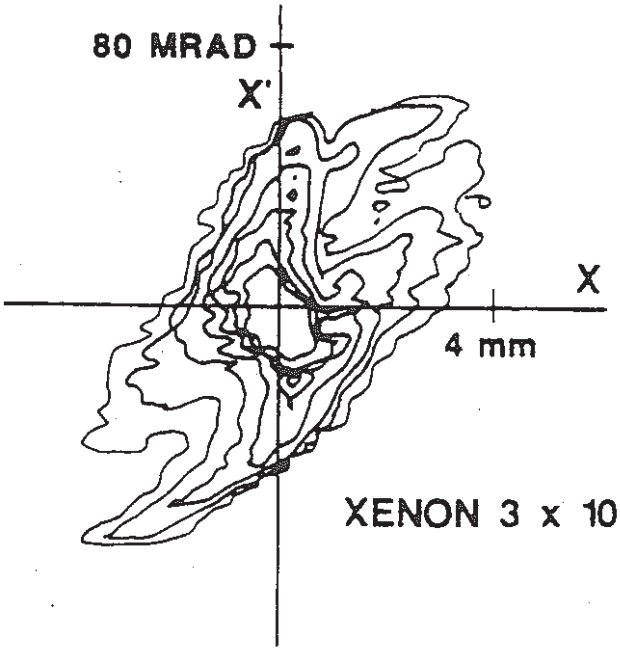


B

# RFQ OUTPUT EMITTANCE
# VERTICAL

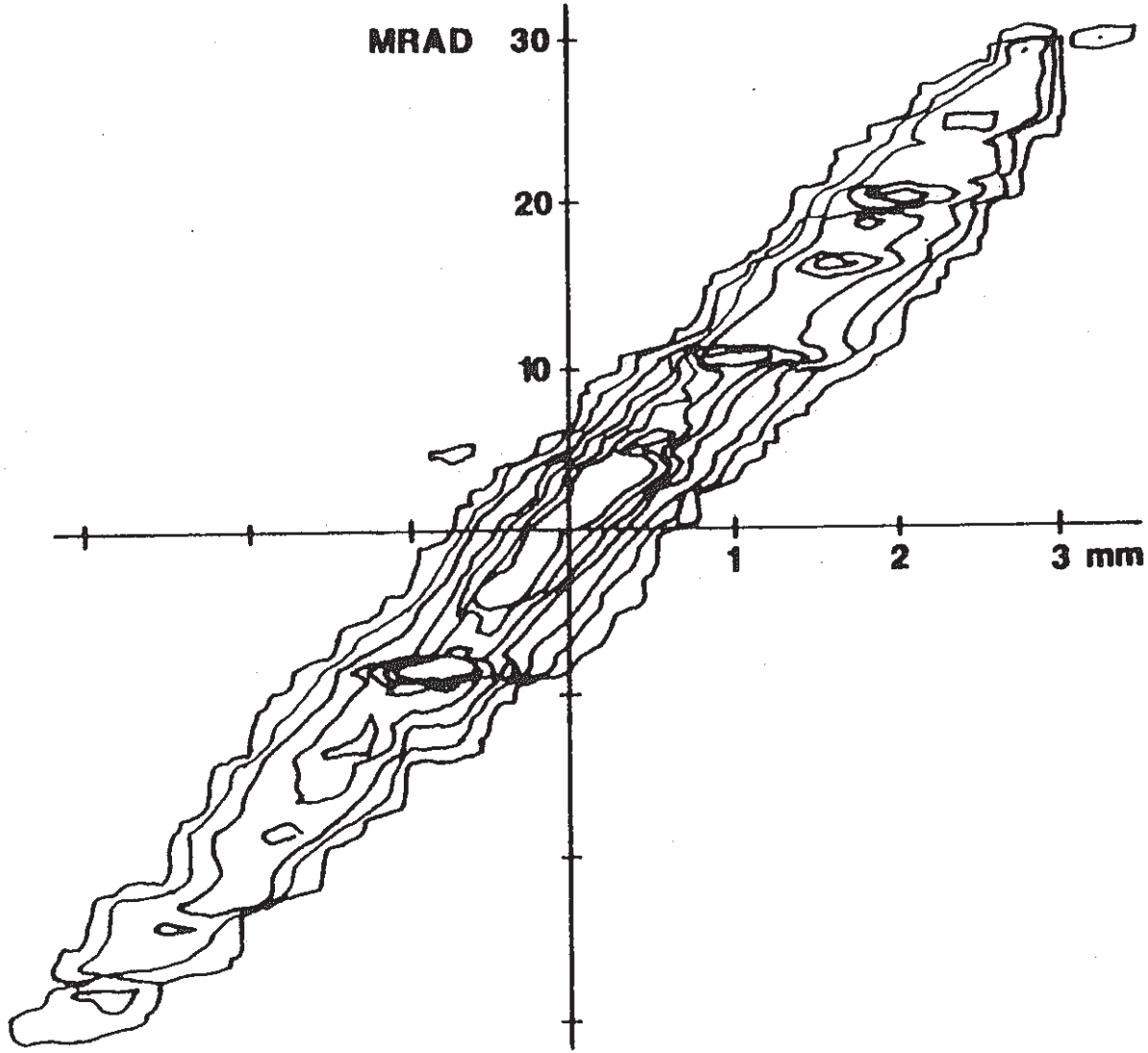

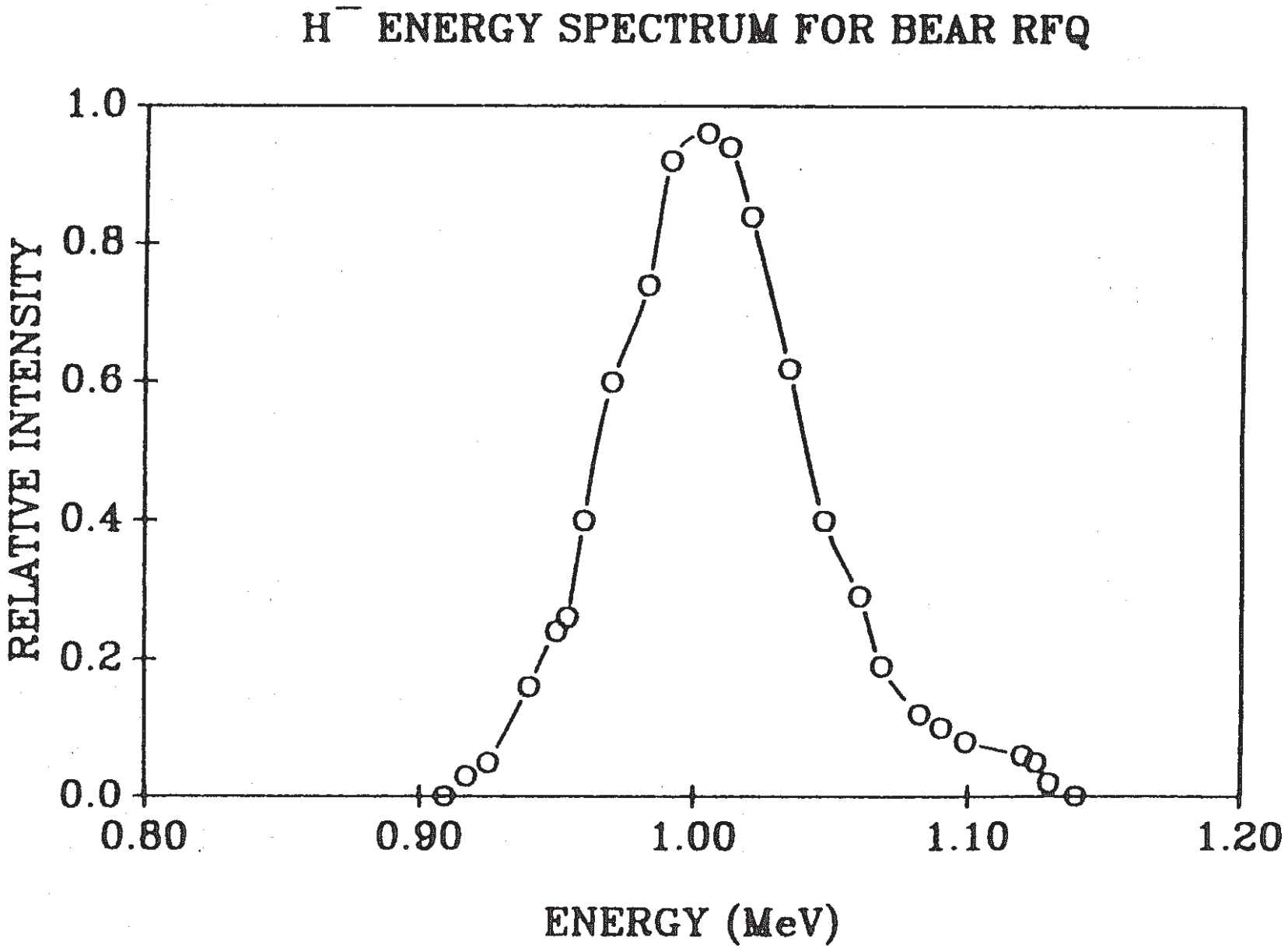
H⁻ ENERGY SPECTRUM FOR BEAR RFQ
RELATIVE INTENSITY
1.0
0.8
0.6
0.4
0.2
0.0
0.80
0.90
1.00
1.10
1.20
ENERGY (MeV)

LA-UR-88-3278

Los Alamos National Laboratory is operated by the University of California for the United States Department of Energy under contract W-7405-ENG-36

TITLE: # HIGH-POWER MICROWAVE SOURCE DEVELOPMENT AT LOS ALAMOS

AUTHOR(S): M. V. Fazio
J. Kinross-Wright
R. F. Hoeberling
F. VanHaaften

SUBMITTED TO: 1988 Linear Accelerator Conference, Williamsburg, VA, October 3-7, 1988



Los Alamos
Los Alamos National Laboratory
Los Alamos, New Mexico 87545

FORM NO. 836 R4
ST NO 2629 5/81

# HIGH-POWER MICROWAVE SOURCE DEVELOPMENT AT LOS ALAMOS*

M. V. Fazio, J. Kinross-Wright, R. F. Hoeberling, and F. VanHaaften
MS-H827, Los Alamos National Laboratory, Los Alamos, NM 87545

## Abstract

Experimental research is under way at Los Alamos to develop the large-orbit gyrotron and the resonant-cavity virtual cathode oscillator as very high power microwave sources. These sources, though still in an early stage of development, have demonstrated power outputs from the several hundred megawatt to the gigawatt level at various Laboratories. These devices exhibit very narrow band output, making them candidates for future accelerator drivers. Our efforts are directed toward achieving repetitively pulsed operation at pulse lengths in the microsecond regime. To provide the pulsed power for these experiments, a 1-MV, 10-kA modulator with a 1-μs pulse length and a 5-Hz pulse-repetition frequency has been developed and is currently being assembled. The resonant-cavity virtual cathode source has achieved very narrow band output compared to the conventional free-running virtual cathode oscillator. Techniques are being developed for extracting the microwave power from both sources into the rectangular waveguide. The experimental effort is described and current experimental results are discussed.

## Summary

The development of new types of high-microwave sources capable of generating power levels as high as 1 GW is being pursued at Los Alamos and a number of other Laboratories around the world. These very high power sources include the virtual cathode oscillator, relativistic klystron, gyrotron, large-orbit gyrotron, lasertron, and several others. At Los Alamos the source development effort is concentrated on the resonant-cavity virtual cathode source, the large-orbit gyrotron, and the lasertron. This paper will discuss the research effort on the first two.

For many applications, coupled with the desire for high power is the need for narrow bandwidth and repetitively pulsed operation at pulse widths ranging from 100 ns to several microseconds. Because of its characteristic single mode, very narrow band output, the large-orbit gyrotron may be particularly useful as the microwave driver for future linear colliders. Several Laboratories have demonstrated that the large-orbit gyrotron is capable of producing 200-500 MW of power and efficiencies of 40%.[1]

Researchers working on the virtual cathode oscillator (VCO) have routinely reported power levels in excess of 1 GW with the highest being ~ 30 GW (Ref. 2). Although its high power output and simplicity make the VCO attractive as a microwave source, it is inherently a wideband source, which makes it unsuitable as an accelerator power source in its simplest configuration. At Los Alamos, an approach has been developed that uses a resonant structure surrounding the oscillating virtual cathode to achieve a very narrow band output operating as a mode-locked oscillator. This concept has been further developed, and experiments are under way to operate the VCO as a source that is frequency and phase locked to a microwave signal injected from an external source.

These high-power sources have, in general, only been operated in a single-shot mode for pulse lengths of 100 ns or less. This is a limitation imposed primarily by the capabilities of the pulsed power sources that are used to drive these microwave devices. These devices require power sources capable of producing voltages as high as 1 MV and electron currents as high as tens of kiloamperes. In the past this power has been usually generated using Marx-Blumlein technology. To reach pulse lengths of a microsecond, and to achieve repetitively pulsed operation, Los Alamos is pushing conventional modulator technology into the megavolt-kiloampere-microsecond regime. These expanded capabilities are made possible by new improvements in thyratron technology.

## Resonant Cavity Virtual Cathode

The free-running virtual cathode oscillator, which is produced by an electron beam whose current exceeds the space-charge limiting value, has an oscillation frequency that is roughly the beam plasma frequency $\omega_p$, where

$$\omega_p = \left(\frac{4\pi n e^2}{\gamma m}\right)^{1/2},$$

and
n = electron density,
γ = Lorentz factor, and
m = electron rest mass.

Virtual cathode devices operating in this free-running mode exhibit considerable frequency instability, which makes them unsuitable for most applications. Los Alamos has developed a technique for achieving frequency stabilization[3] that uses a cavity resonator surrounding the oscillating virtual cathode. The basic approach is to tune the frequency of the oscillating virtual cathode by varying the beam current density so that its free-running oscillation frequency is near the passband of a suitable mode in the microwave cavity resonator. Creating a strong electron beam/cavity interaction allows the field induced in the cavity by the oscillating virtual cathode to feed back on the virtual cathode, forcing it to oscillate at the resonant frequency of the cavity mode.

Experiments were performed using a cylindrical cavity operating in the $TM_{020}$ and $TM_{012}$ modes. The electron beam was produced by a diode consisting of a field emission cathode and an aluminum-wire-screen anode located at the upstream end wall of the cavity. Microwave power was extracted through three L-band waveguide ports located around the cavity at 90° intervals. This configuration is shown in Fig. 1. The frequency of the microwave output was measured as a function of diode current. These data are plotted in Fig. 2, which shows the measured output frequency as a function of peak injected beam current. For comparison, the free-running virtual cathode oscillation frequency is also plotted. The mode spectrum for the cold

*Work supported by the US Department of Energy, Assistant Secretary for Defense Programs.

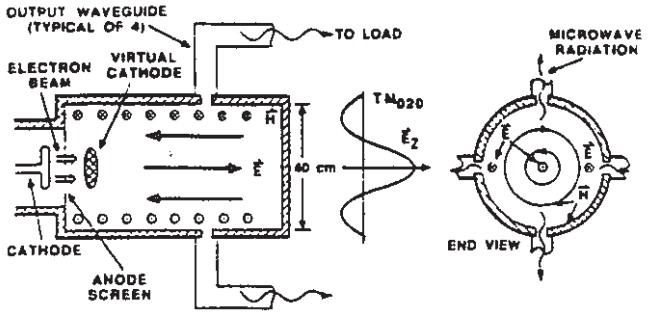


Fig. 1. Cylindrical resonator configuration.

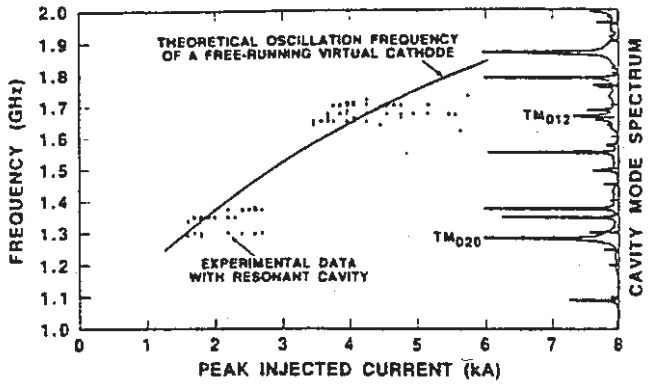


Fig. 2. Measured microwave frequency as a function of peak injected beam current.

cavity is plotted along the right axis. Nominal diode voltage was 300-400 kV. These data clearly indicate that the virtual cathode will oscillate at a single frequency when feedback is provided by a resonant structure.

The oscillation frequency of the virtual cathode locks to the $TM_{020}$ and the $TM_{012}$ modes over as much as a 70% change in electron beam current. This virtual cathode resonant-cavity configuration results in a 3-dB bandwidth of less than 1% (~17 MHz at 1.66 GHz). The bandwidth appears to be limited by the finite temporal width of the microwave pulse, which is ~100 ns.

An experiment is currently under way to injection lock the frequency and phase of the injection signal from a high-power klystron. The basic idea is to excite the cavity with the klystron before firing the electron beam, which gives the cavity fields a chance to build up in the desired mode. Then when the electron beam is injected, the virtual cathode oscillations build up from the injected field in the cavity instead of building up in intensity from noise voltage present on the beam. In this way, the virtual cathode is locked in frequency and phase to the klystron injection signal.

## Large-Orbit Gyrotron

The attractive features of the large-orbit gyrotron include high power and efficiency, as well as long-pulse (>1 μs) repetitive operation. The large-orbit gyrotron converts the kinetic energy from an axis-encircling rotating electron beam into microwave energy by a resonant interaction between the negative mass instability on the beam and a surrounding magnetron-like resonant structure. In the present experiment the electron beam is produced by a circular, knife-edged field-emission cathode. This hollow beam is accelerated toward the anode, which contains a circular slit through which the beam can pass. A magnetic cusp is provided at the anode plane that converts the linear beam into a rotating beam. The downstream solenoidal field then maintains the cyclotron motion of the beam as it travels downstream interacting with the resonant structure. The resonator has been designed for operation at 2 GHz, the third harmonic of the electron cyclotron frequency.

The Los Alamos program is focusing on three major areas: microwave source development including techniques for extracting the microwave energy into dominant mode waveguide, repetitively pulsed operation, and thermionic electron gun injection. All of these areas are being addressed in order to realize the goals of high-power, long-pulse, repetitive operation with reasonable reliability and lifetime.

The 2-GHz large-orbit gyrotron is currently operational using an existing single-shot pulser with a pulse length of 100 ns. The device operates at the third harmonic of the electron cyclotron frequency with a solenoidal magnetic field strength of 500 G. Typical operation is at 600-keV electron energy and a beam current of several kiloamperes. Power output is estimated at 100 MW for 50-100 ns. The current effort is focusing on coupling the power from the three-vane resonator into rectangular waveguide through longitudinal slots in the resonator wall. A second large-orbit gyrotron is being designed for operation at 8 GHz, 600 kV, 100 ns, with a 10-Hz pulse repetition frequency.

## Pulsed-Power Technology Development

Crucial to the microwave source development is the availability of pulsed power sources with adequate performance characteristics compatible with the microwave source requirements. Thyratron-switched, line-type modulator technology is being extended to the megavolt level to power this new generation of high-power microwave sources. Los Alamos has two modulators under development. The first is a 1-MV, 10-kA, 1-μs flat-top, 5-Hz unit that is expected to be operational by December 1988. The second is a 600-kV, 3-kA, 100-ns, 10-Hz unit. The key technical issues are the thyratron tubes, minimizing system rise time and achieving reasonable component lifetimes. The microsecond pulser is described below.

The modulator is designed to supply up to 1-MV pulses of 1-μs duration (flat top) with a rise time of ~0.5 μs to diode impedances of ~100 Ω. The design uses two newly developed 100-kV hollow anode thyratrons to discharge four, parallel, lumped-constant Blumleins composed of 1- to 2-Ω PFNs. The Blumleins are command resonantly charged to 100 kV from a capacitor bank. The Blumleins are then discharged through a 10:1 step-up iron-core transformer to 1 MV.

A system block diagram is shown in Fig. 3. The primary switches in the modulator must be able to hold off 100 kV and conduct currents up to 200 kA with a di/dt approaching $10^{12}$ A/s total. This is almost a factor of 2 in voltage and a factor of 4 in peak current over the best demonstrated performance of a single thyratron.

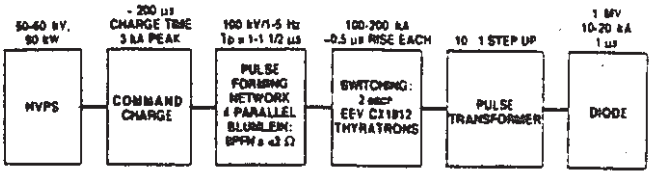


Fig. 3. System block diagram of 1-MV, 1-µs, 10-kA, 5-Hz pulser.

Initial tests have been conducted using one thyratron in conjunction with one or two Blumleins. A level of 50 kV across the tube has been attained with a resistive load instead of the pulse transformer.

The pulse transformer unit has a 10:1 step-up ratio, a pulse rise time of 0.5 µs, and tolerates an output level of 1 MV for 1 µs.

## Conclusions

The resonant-cavity virtual cathode source has demonstrated narrow band single-mode operation. An experiment is currently under way to demonstrate frequency and phase locking of the oscillating virtual cathode to an injected klystron signal. The achievement of injection locking opens up the possibility of coherently operating several virtual cathode sources in parallel to reach very high microwave power levels because all the sources could be pumped by the same injection signal and would consequently be frequency and phase locked to each other.

Large-orbit gyrotron development is being pursued because of its single frequency, high efficiency, high power output that make it a candidate for future accelerator applications. To complement the microwave work, pulsed power sources are under construction to drive the microwave sources in a repetitive mode at useful pulse lengths.

## References

1. W. W. Destler, E. Chojnacki, R. F. Hoeberling, W. Lawson, A. Singh, C. D. Striffler, "High-Power Microwave Generation from Large-Orbit Devices," IEEE Trans on Plasma Science, 16 (2), 71-89, April 1988.

2. A. Brombrosky, G. A. Huttlen, R. A. Kehs, G. W. Still, S. E. Graybill, F. J. Agee, M. C. Clark, "High-Power Microwave Radiation From a Reflex Diode Driven by the Aurora Intense Relativistic Electron Beam Generator," Proc. Third Nat. Conf. on High Power Microwave Technology for Defense Applications (Kirtland Air Force Base, Albuquerque, New Mexico, December 1-5, 124-126, (1986).

3. M. V. Fazio, R. F. Hoeberling, "A Coherent Very High Power Microwave Source Using a Virtual Cathode Oscillator," Proc. 1986 Linear Accelerator Conference, SLAC Report No. 303, 157-159, September 1986.

Preprint LA-UR-88-3276

Title: # STUDYING THE END REGIONS OF RFQs USING THE MAFIA CODES

Author(s): M. J. Browman, G. Spalek, and T. C. Barts

Submitted to: 1988 Linear Accelerator Conference, Williamsburg, VA, October 3-7, 1988

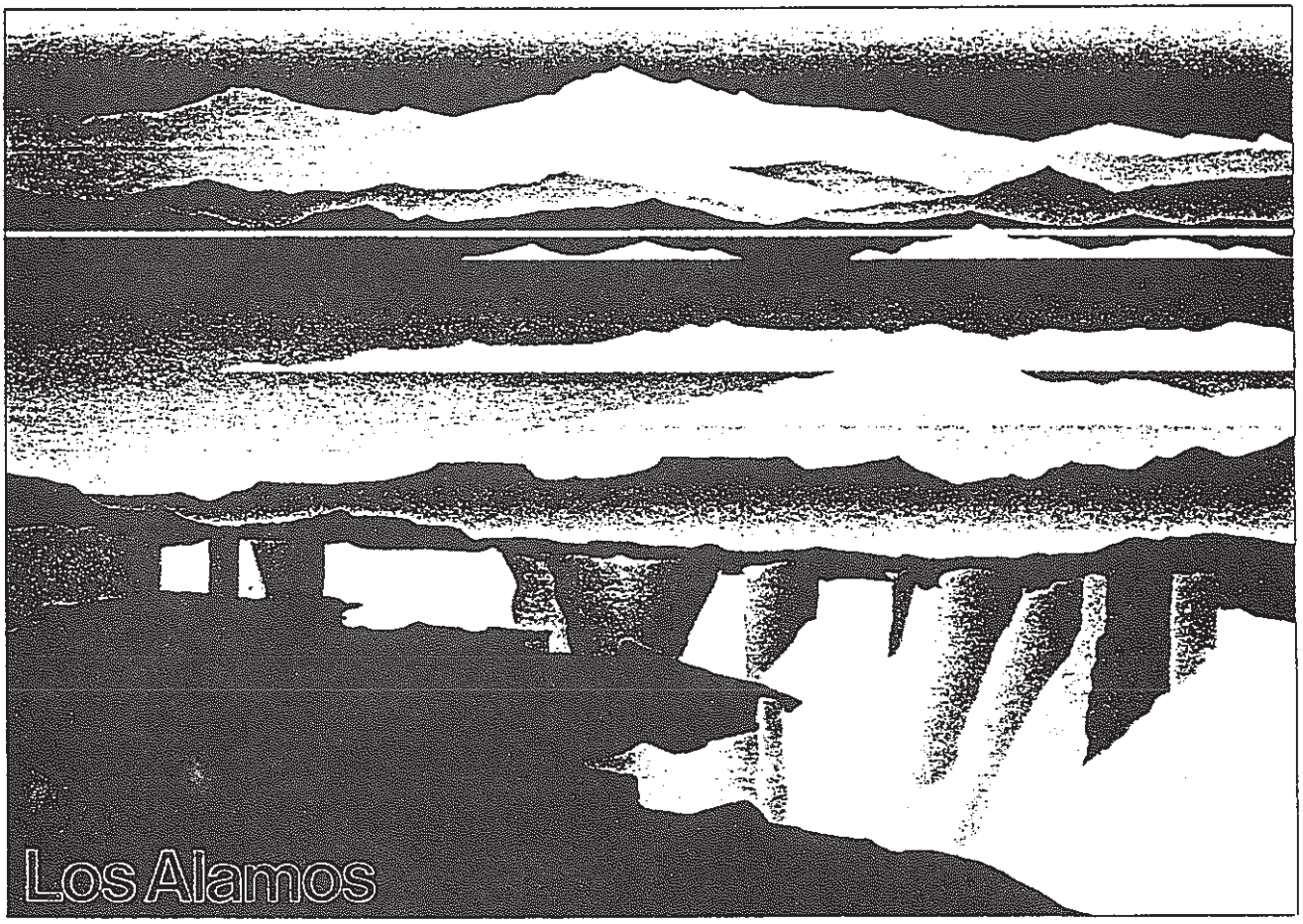

# STUDYING THE END REGIONS OF RFQS USING THE MAFIA CODES *

M. J. Browman, G. Spalek and T. C. Barts
MS H829, Los Alamos National Laboratory, Los Alamos, NM 87545

## Abstract

The three-dimensional MAFIA codes[1] were used to study the end regions of a radio-frequency quadrupole (RFQ). The following determinations were made:

- Undercutting the vane is essential.[2]
- To a point, increasing the distance between the vanes and the end plate decreases the power loss at the ends of the vanes: this effect (assuming we begin with an end gap slightly larger than the distance between the vanes) decreases with distance and eventually reaches a limit.[3]
- The slope of the undercut affects the peak current flow and the power dissipation at the ends of the vanes; in particular it was found that in designing such an end region a tradeoff must be made between minimizing the peak power loss density and reducing the total power loss[4].

This paper gives the details of the calculations leading to the above conclusions.

## Modeling the Structure

An RFQ is essentially a waveguide operated at the cutoff frequency, terminated by an end region whose fields must be matched to those of the waveguide. In practice this matched condition is met if the frequency of the end region is tuned to the cutoff frequency of the waveguide.

The cutoff frequency of the waveguide was found by generating a finite length of the structure (Fig. 1), requiring that the magnetic fields be perpendicular to each end, and solving for the lowest resonant frequency (425.9 MHz). Because of symmetry, only one-quarter of the structure need be generated.

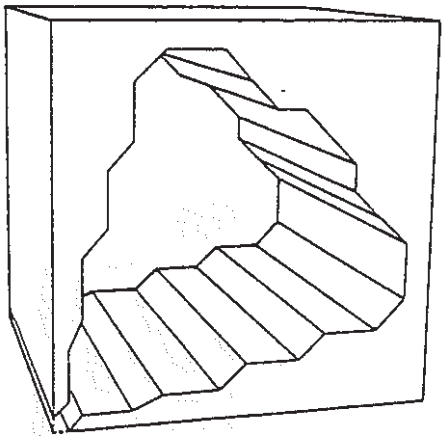

Fig. 1. Three-dimensional computer plot of the structure (one quadrant) used to compute the cutoff frequency of the model RFQ .

Next, the end region was generated by extending the walls of the structure (Fig. 2) and by requiring that the tangential electric field be zero at the position of the end plate. The boundary condition at the waveguide end, of course, remained unchanged.

## The Need for Vane Undercutting

Figure 3 shows a plot of the frequency of the structure shown in Fig. 2 as a function of the distance between the ends of the vanes and the end plate. The dotted line indicates the tuned frequency of the end region, i.e., 425.9 MHz. Clearly, the end region cannot be tuned by varying only this distance.

* Work supported and funded by Los Alamos National Laboratory Institutional Supporting Research, under the auspices of the US Department of Energy.

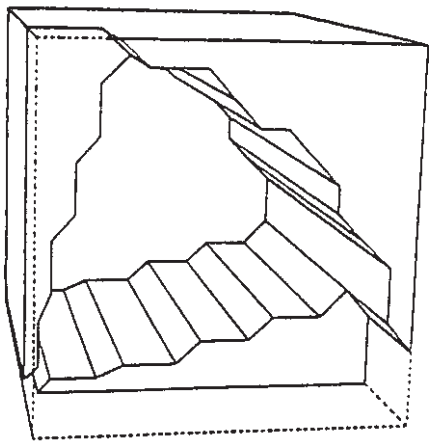

Fig. 2. Three-dimensional plot of one of the geometries of the end region used in this study.

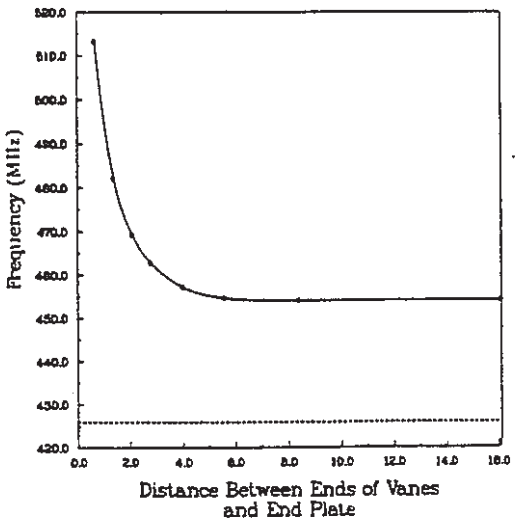


Fig. 3. Plot of the frequency of the end region shown in Fig. 2 as a function of the distance between the ends of the vanes and the end plate. The curve is drawn to guide the eye, and the dotted line indicates the tuned frequency of the end region.

In another tuning experiment, the end plate was placed 8.4 cm from the end of the vanes and a nose cone was added to the end plate. Figure 4 shows a plot of the frequency of the structure as a function of the distance between the nose cone and the end of the vanes. Notice that even when the distance is as small as 0.35 cm (less than the distance between the vanes), the frequency has dropped to only 445.8 MHz. Thus for a reasonable gap between the end of the vanes and the nose cone, the end region cannot be tuned using only a nose cone.

On the other hand, the structure was easily tuned by undercutting the vane, or, equivalently, by adding an overhang (Fig. 5). An overhang of 2.45 cm tuned the end region to the desired 425.9 MHz.

## The Effect of the End-Gap Distance on Power Dissipation

Figure 6 shows a cross section of the model RFQ (with undercutting) taken along the center of the vanes. An ample 9.2 cm was allowed between the waveguide end and the beginning of the overhang to guarantee that the fields had stabilized at the waveguide end. The end-gap distance was varied, and the model structure was tuned to 425.9±0.1 MHz by varying the length of

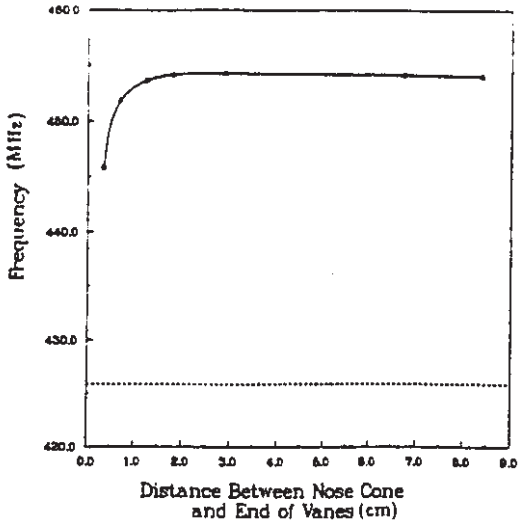


Fig. 4. Plot of the frequency of the end region with nose cone as a function of the distance between the nose cone and the end of the vanes. The curve is drawn to guide the eye, and the dotted line indicates the tuned frequency of the end region.

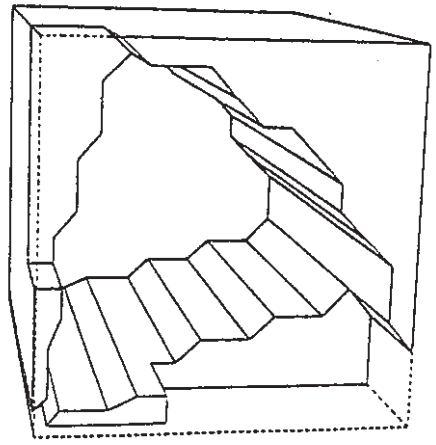

Fig. 5. Three-dimensional computer plot of an end region tuned by vane undercutting.

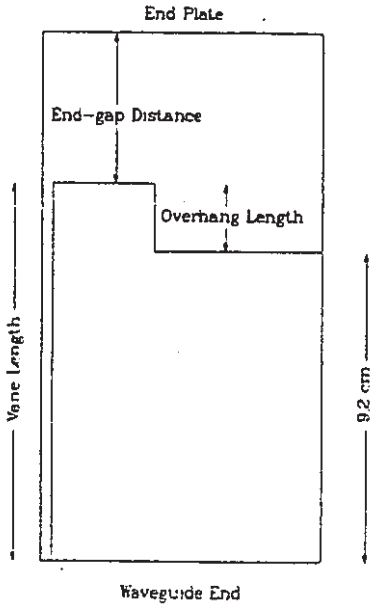


Fig. 6. Cross section of the RFQ end region used to study the effect of the end-gap distance.

the overhang. The relative overhang length, the peak current density, and the power dissipation caused by the end region were plotted as a function of end-gap distance (Fig. 7). All values are normalized so that the maximum value is 1. The "power loss caused by the end region" was calculated by computing the total power loss of the model structure and subtracting the power loss of an equivalent length of the RFQ waveguide. Figure 7 shows that all three quantities decrease at first, but eventually reach a limit. Figure 8, a plot of the magnetic field lines along the center of one of the vanes for an end gap of 5.6 cm, indicates why this limit is reached. The magnetic field is almost zero at the end wall, so further increasing the end-gap distance will have little effect. In Fig. 8 the circles with dots indicate that the field lines are directed out of the paper, and the radii of the circles are proportional to the magnetic field strength.

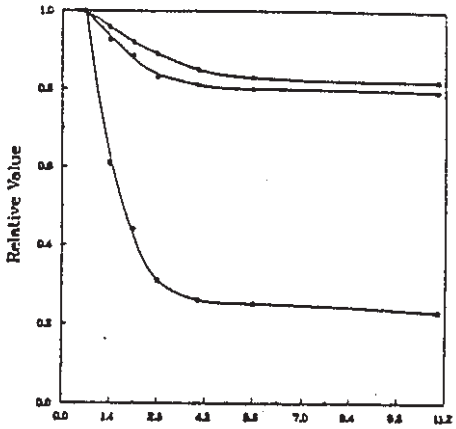


Fig. 7. Plots of the relative overhang length (top curve), the peak current density (middle curve), and the power loss caused by the end region (bottom curve) as a function of end gap distance. The curves are drawn to guide the eye.

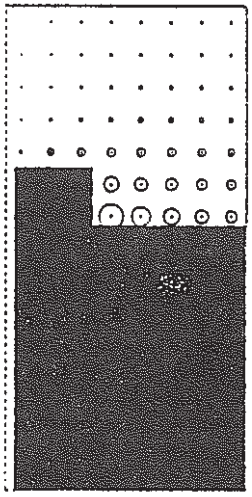

Fig. 8. Plot of computed magnetic field lines for an end gap of 5.6 cm. The cut is taken along the center of one of the vanes. The circles indicate that the field lines are perpendicular to the plane of the paper.

### The Effect of the Shape of Vane Undercutting

Next, the power loss in the end region was studied as a function of the slope of the undercut (Figs. 9 and 10). Four slopes were used: 0°, 22.5°, 30.2° and 39.2°. In each case the length of the overhang was varied until the frequency of the model structure was tuned to 425.9±0.1 MHz. Table 1 shows that the overhang length and the power loss on the overhang decreases as the slope increases.

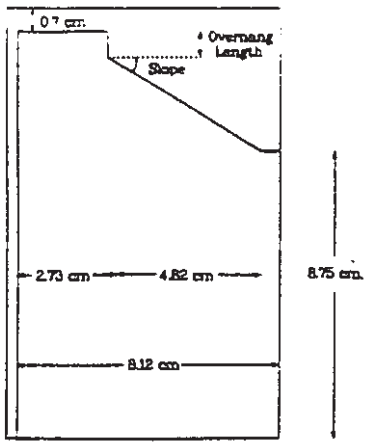


Fig. 9. Cross section of the RFQ end region used in studying the effect of the slope of the vane undercut.

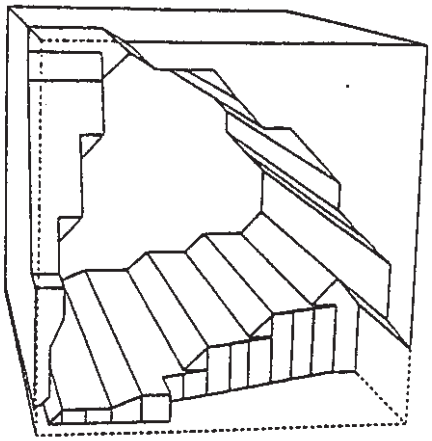

Fig. 10. Three-dimensional computer plot of the end region with a sloped undercut. The strips of surface area shown on the sloped cut and on the end of the overhang were used in computing the average power loss plotted below in Fig. 11.

TABLE I
OVERHANG LENGTH AND RELATIVE POWER LOSS AS A FUNCTION OF SLOPE

| Slope (deg.) | Length of Overhang (cm) | Relative Power Loss on Overhang |
|---|---|---|
| 0.0 | 2.45 | 1.00 |
| 22.5 | 1.30 | 0.54 |
| 30.2 | 0.79 | 0.41 |
| 39.2 | 0.00 | 0.18 |

Figure 11, which plots the the average power loss density as a function of distance from the RFQ axis for each of the four slopes, shows that the average power loss at the base of the overhang also decreases with increasing slope. Because the surfaces and base of the overhang are the hardest regions to cool, the ease of cooling increases with the slope of the overhang.

In Fig. 11 the power loss densities at the top of the overhang and on the sloped undercut were averaged over the strips of surface shown in Fig. 10. The multiple points at the boundary between these two regions represent the average power-loss density along the sides of the overhang, which are not visible in Fig. 10. Notice that as the slope increases, the power-loss density becomes more evenly distributed in the sloped region. In other words, as the slope increases, the power-loss density increases in the region where the vanes are the widest (see Fig. 10), and thus it is not surprising that the total power loss in the end region also increases. (See Table II below.)

In Table II, power losses are normalized so that the value corresponding to 0.0° slope is 1. Because increasing the slope

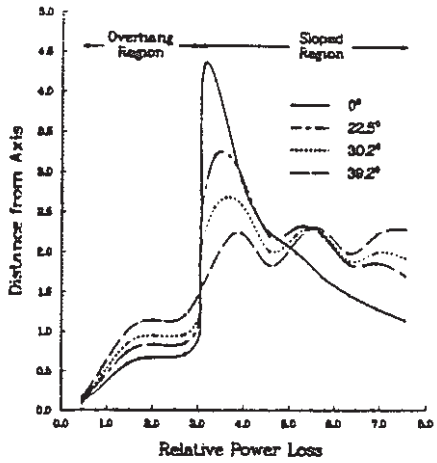


Fig. 11. Plots of the average power loss density, for four different slopes, as a function of distance from the the RFQ axis. The curves are drawn to guide the eye.

TABLE II
RELATIVE POWER LOSS IN END REGION AS A FUNCTION OF SLOPE

| Slope (deg.) | Relative Power Loss in End Region |
|---|---|
| 0.0 | 1.00 |
| 22.5 | 1.13 |
| 30.2 | 1.17 |
| 39.2 | 1.23 |

makes the structure easier to cool but increases the total power loss, a tradeoff must be made when designing the end region of an RFQ.

## Conclusions

The study of the model end regions showed the following:

- Undercutting the vane is essential.
- To a point, increasing the distance between the vanes and the end plate decreases the power loss at the ends of the vanes; this effect (assuming we begin with an end gap slightly larger than the distance between the vanes) decreases with distance and eventually reaches a limit.
- The slope of the undercut affects the peak current flow and the power dissipation at the ends of the vanes; in particular it was found that in designing such an end region, a tradeoff must be made between minimizing the peak power-loss density and reducing the total power loss.

## Acknowlegment

We would like to thank Richard K. Cooper for his encouragement and helpful suggestions.

## References

1. R. Klatt, F. Krawczyk, W.-R. Novender, C. Palm, T. Weiland, B. Steffen, T. Barts, M. J. Browman, R. Cooper, C. T. Mottershead, G. Rodenz, S. G. Wipf, "MAFIA—A Three-Dimensional Electromagnetic CAD System for Magnets, RF Structures, and Transient Wakefield Calculations," *1986 Linear Accelerator Conference Proc.*, Stanford Linear Accelerator Center report SLAC-303, 276-278 (1986).
2. M. J. Browman and G. Spalek, "Tuning the End Regions of RFQ's—the Need for Vane Undercutting," Los Alamos National Laboratory internal report, AT6-ATN-87-19.
3. M. J. Browman and G. Spalek, "The Effect of the End-gap Distance on Power Dissipation in the End Regions of RFQ's," Los Alamos National Laboratory internal report, AT6-ATN-87-14.
4. M. J. Browman and G. Spalek, "The Effect of the Shape of Vane Undercutting on Power Loss in the End Regions of RFQ's," Los Alamos National Laboratory internal report, AT6-ATN-87-14.

# PROGRESS OF ELECTRON GUN SYSTEMS FOR THE e⁻/e⁺ LINAC AT KEK

S. Ohsawa, Y. Ogawa, Y. Otake, M. Yokota, S. Fukuda, Y. Saito,
A. Enomoto, O. Azuma*, H. Iwata* and A. Asami
*National Laboratory for High Energy Physics(KEK)*
*1-1 Oho, Tsukuba-shi, Ibaraki-ken, 305 Japan*
** Ishikawajima-harima Heavy Industries Co., Ltd.*

**Abstract:** Several improvements have been made in the electron gun systems of the 2.5 GeV PF linac and the Positron Generator. In the electron gun system of the PF linac, the vacuum system and the focusing system have been modified, and the anode current was increased. In the case of a short pulse beam with a width of 2 ns, the anode current has been more than 200 mA for about a year with a constant pulse voltage output of a grid pulser. Injection time of the electron beam into the Accumulation Ring of TRISTAN has been normally less than 10 s. Meanwhile in the electron gun system of the Positron Generator, improvements have been made mainly in the following two points: (1) a raise of injection voltage of the gun from 115 kV to 150 kV, which was made possible by using a newly designed insulator, and (2) an increase of pulse voltage output of a grid pulser by use of new transistors with a high slew rate. As a result of these improvements, a maximum anode peak current of 12 A with a pulse width of 4 ns can be obtained, which satisfies the design parameters of the gun system.

## Introduction

In the electron linacs at KEK, two electron guns are now in operation. One is the gun for a 2 ns / 0.7 μs electron beam which is injected into the colliding ring of TRISTAN / the Photon Factory storage ring.[1] The other is the gun for a high intensity electron beam in the Positron Generator. In the gun of the PF linac, there was a problem that anode current was affected by residual gases in the gun chamber and changed with pressure. This situation has been improved by modifying the vacuum system. The focusing system and beam monitors were also modified. Meanwhile in the gun of the Positron Generator, some improvements have been made to increase the anode current and to obtain a beam suitable for easy operation. Positrons had been used only in the colliding ring of TRISTAN, but recently it has started to use positrons also in the PF ring.[3] It has been confirmed that a positron beam with a width of tens ns is suitable for the PF ring to decrease the injection time. Therefore, it is necessary to prepare two kinds of positron beams of which pulse widths are 2 ns and tens ns. A beam width selection system has been developed to remotely switch over the beams.[4]

## Electron Gun System for the 2.5 GeV PF Linac

Overall modifications have been made in the electron gun system in 1987: the vacuum system, the focusing system, and beam monitors. Improvement of the vacuum system, however, was main in these modifications. As a result, the anode current became considerably stable over a long range of time especially in the long pulse mode operation, and in the short pulse mode operation anode current noticeably increased.

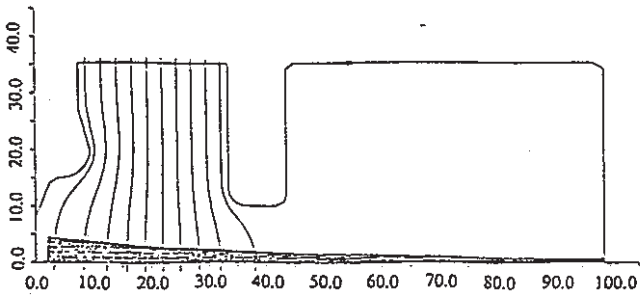


Fig. 1. Computer plot of the gun optics at 100 kV showing equipotential surface and beam focusing pattern. Shaded area denotes the electron beam. The emission current assumed to be 573 mA.

## Electron Gun

In our electron guns, a grid-cathode assembly of a planar triode is used. The cathode is an oxide-coated type.[1,2] In addition to merits of its compact size and very low cost, it has an advantage that the relatively low grid pulse voltage makes possible to draw a high current because of a short grid-cathode distance (0.18 mm). This feature is important especially in obtaining a beam as short as 2 ns from the gun, meanwhile it has a disadvantage that the emission current is sensitive to residual gases in the vacuum.

Figure 1 shows the electron trajectory calculated by the program of W. B. Hermannsfeldt.[5] In the calculation,the current is limited in the range of an actual value of a short pulse beam, that is 573 mA. The calculations predict a perviance of 0.12 $\mu A/V^{3/2}$ and an emittance of $1.1 \times 10^{-3}$ π (mc·cm). When the gun is operated in the space charge limited region, the maximum anode current is expected to be 3.8 A at the injection voltage of 100 kV.

## Vacuum system

Major modification has been made in the vacuum system in order to decrease residual gas pressure in the gun chamber. Figures 2(a) and 2(b) show the layout of the new gun system for the 2.5 GeV

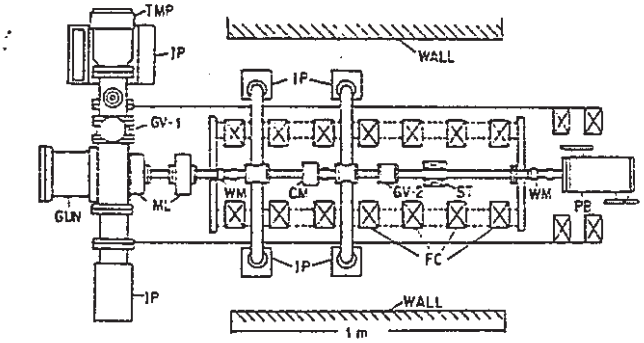


Fig. 2a. Top viewed layout of the new electron gun system for the 2.5 GeV linac. GV: Gate valve, IP:Ion pump, TMP: Turbo molecular pump, ML: Magnetic lens, WM: Wall current monitor, CM: Core monitor, ST: Steering coil, FC: Focusing coil, PB: Prebuncher, B-A G: B-A gauge, CCG: Cold cathode gauge

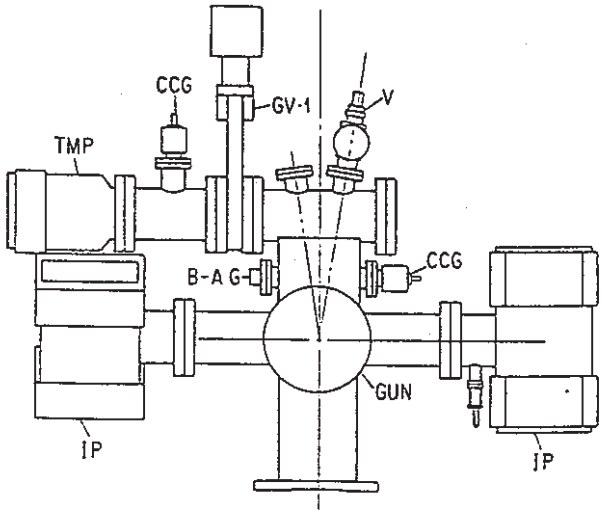


Fig. 2b. Layout of the new vacuum system for the 2.5 GeV linac.

linac. The same differential-pumping method was adopted as in the positron generator, and the gun chamber was isolated from the prebuncher.[2] The gun and the prebuncher are connected with 30 mm diameter small pipes to give low conductance. The pipes are differentially pumped with 4 ion pumps of which pump speed is 10 l/s each. The gun chamber is pumped by 2 ion pumps (60 l/s) and a turbo-molecular pump (300 l/s) as a roughing pump.

After baking out the vacuum system in the temperature range between 120 to 150 °C, the pressure in the gun chamber is kept as low as in the range of $10^{-7}$ Pa.

### Control and Monitoring System of Vacuum

The control and monitoring system of vacuum was also improved. It controls on/off switches of vacuum valves, vacuum gauges and a rotary pump locally or remotely. It makes possible to keep the cathode safe by closing a vacuum valve (GV1) when accidents happen such as a failure or an emergency in the turbo-molecular pump, etc. The circuit has also a logic as the following: if an electric power supply stops, all auto-valves are closed, and even if a power supply recovers, all valves remain in the states before recovery of a power supply.

### Focusing System and Beam Monitors

Although the improvement of the vacuum system is the main purpose of this modification, it was necessary to replace magnetic coils, focusing lenses and beam monitors with new ones, since the beam pipe connecting the gun and prebuncher should be smaller and longer than before in order to realize differential pumping.

The focusing system consists of 2 magnetic lenses and 7 focusing coils. A two-magnetic-lens system is adopted to be able to adjust both of size and divergence of the beam at the entrance of the first focusing coil. An end plate of the focusing coil's support is made of iron so as to decrease the leakage magnetic field and to shield the cathode from magnetic fields. There are three beam monitors between the gun and the prebuncher. Two of them are located between the gun and the first gate valve (GV2), that enables one to measure anode current even when the valve is closed: One is a wall current monitor for measuring a short pulse beam and the second is a core monitor for a long pulse beam. The third one is also a wall current monitor and is located at the entrance of the prebuncher .

### Time Variation of Emission Characteristics in a Long Term

After the modifications mentioned above, the anode current became more stable and did not decrease rapidly over a long term, compared with the state before. Consequently available beam current increased considerably. Figure 3 shows time variation of the emission characteristics of the gun for the 2.5 GeV linac. Data were measured during a year.from September in 1987 to August in 1988. In the long pulse ( ~ 0.7 μs) mode operation, the anode current required was usually in the range of 30 ~ 50 mA, and was controlled by the grid pulse voltage. Since the maximum current obtainable was high enough

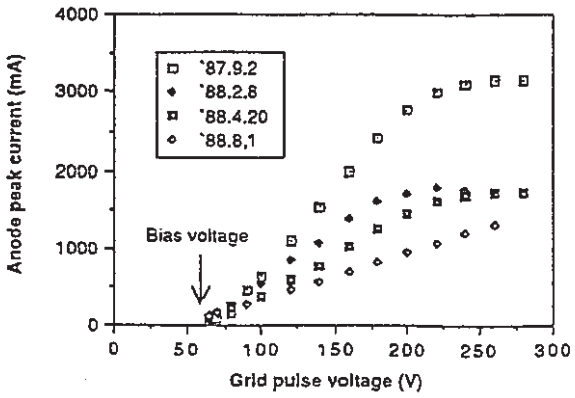


Fig. 3. Time variation of the emission characteristics of the oxide gun for the 2.5 GeV linac. Data were measured in the long pulse (~0.7 μs) mode operation. The anode current was usually 30 ~ 50 mA.

compared with the current needed, the influence of the time variation of the emission characteristics were negligibly small. And there were no problems in practical use during the period although maximum current decreased gradually from about 3 A to 1 A. In the short pulse mode operation, however, anode current was affected by deterioration of the cathode and actually decreased gradually during the same period as illustrated in Fig. 4. In this case, the output voltage of the grid pulser was not controlled and constant (~ 110 V ). Anyhow the anode current has been more than 200 mA for the period, and the injection time of the beam into the Accumulation Ring of TRISTAN has been normally less than 10 seconds even when the anode current was the lowest one. This indicates that the practical life time of the oxide cathode is at least a year in high vacuum.

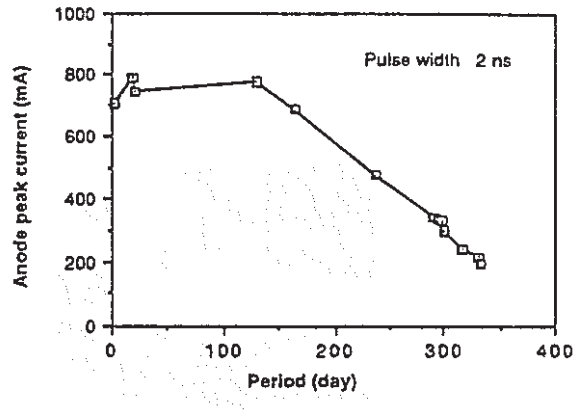


Fig. 4. Time variation in the anode peak current of the 2-ns beam. The grid pulse voltage was not controlled and constant. (~ 110 V.)

## Electron Gun System for the $e^+$ Linac

### New Ceramic Insulator

The injection voltage of the positron generator gun was designed to be 150 kV, however, it had been 115 kV owing to the short ceramic insulator. The insulator was enclosed for a while by an $SF_6$-gas-filled capsule in order to supply a cathode-anode voltage of 150 kV to the gun. The maintenance of the $SF_6$ gas, however , was troublesome so that the ceramic insulator was replaced by a new large one illustrated in Fig 5, which worked at higher voltage. The injection voltage was raised to 150 kV, that enabled the injection current to increase appreciably and made it much easier to transport the beam.

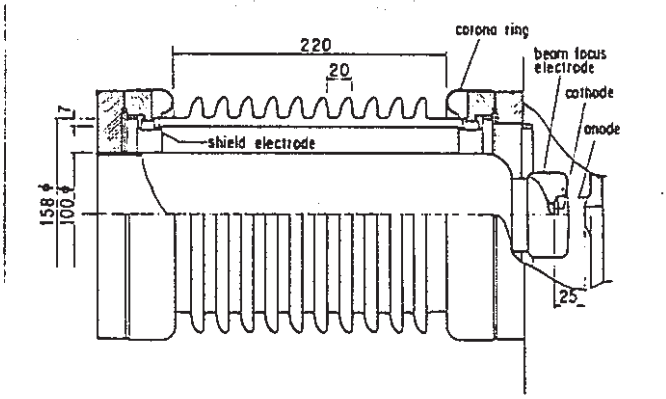


Fig. 5. New ceramic insulator of the gun for the Positron Generator. Size is shown in unit of mm.

### Development of a Grid Pulser Utilizing a Hybrid IC

A grid pulser for a high-intensity and short pulse electron gun has been under development for several years. A grid pulser utilizing a hybrid IC made of transistors 2N2222A or 2N5551 was manufactured and a good characteristic was obtained.[6] Figure 6 shows a hybrid IC

with 2N2222A's for the pulser which is one fourth of the can-type transistor circuit in size and has small stray capacitance and inductance, which is important especially for a high speed short pulse grid pulser. The output voltage waveform of the pulser with a hybrid IC with 2N5551's is given in Fig. 7, and the resulting electron beam current is 12 A at 150 kV as shown in Fig.8..

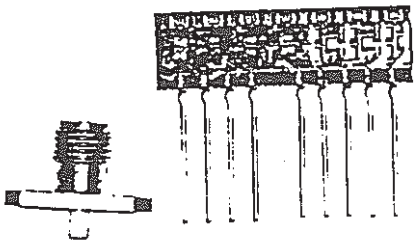

Fig. 6 Hybrid IC made of transistors 2N2222A for the short pulse grid pulser.

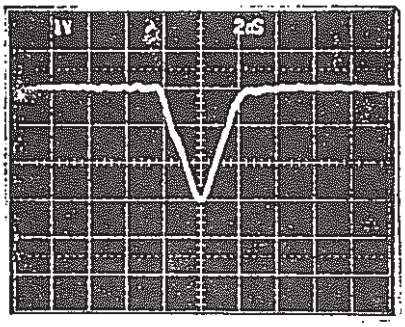

Fig. 7. Output waveform of the grid pulser with a hybrid IC (2N5551). Peak voltage of 300 V is obtained with 16.6 Ω input impedance.

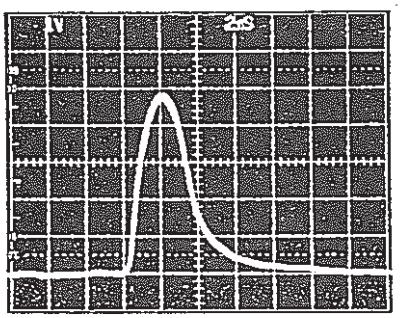

Fig. 8. Electron beam pulse obtained using the grid pulser of the hybrid IC with 2N5551 at 150 kV. Peak current is 12 A.

## Control and Interlock System

A vacuum interlock system was developed utilizing a programmable sequencer. It is connected with vacuum gauges and pumps, etc. and controls gate valves and vacuum gauges for preventing deterioration of the electron gun vacuum. Another sequencer is intended to be connected with power supplies on the high voltage station of the gun. Both of the sequencers will be controlled by a microcomputer which is connected to the linac control system.

The anode current of a short pulse beam can be controlled by varying a pulsed bias voltage applied between the cathode and grid.[7]

## Beam Width Selection System

Recently there was a request to inject positrons into the PF storage ring instead of electrons, and actually positrons were accumulated in the ring using the 2-ns beam and were put to practical use. The problem was the injection time, and a study has been made to obtain a suitable positron beam for the ring. As a result of the study, it was confirmed that the beam with a width of tens ns was suitable for the ring in order to decrease the injection time because much more charge could be contained in the longer beam than the shorter one.[7] On the other hand, for TRISTAN, the pulse width of the beam from the gun should be less than 4 ns, which is finally reduced to less than 2 ns by a subharmonic buncher. Therefore it is necessary to select one of the two beams remotely. A long pulse pulser was prepared in addition to the short one used so far. A beam width selection system has been made to exchange the beams by selecting one of the pulsers with a coaxial switch which is located between the electron gun and the pulsers as shown in Fig. 9. Selection signals are transferred through optical fibers which are also used to isolate the gun at high voltage from the ground potential .

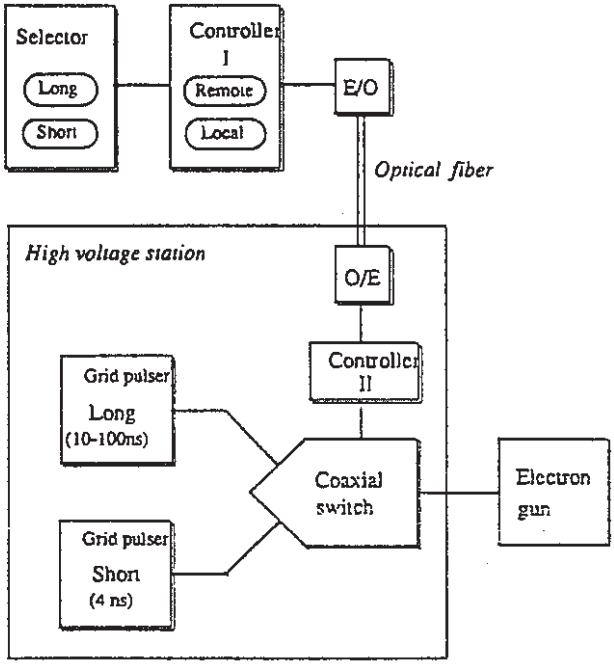


Fig. 9. Block diagram of the beam width selection system.

## References


1. J. Tanaka, "Operation of the 2.5 GeV electron linac," in Proceedings of the 1984 Linac Accelerator Conference, Darmstadt,1984, p. 475-479.

2. S. Fukuda et al.,"Electron gun for the Positron Generator," in Proceedings of the 1986 Linac Accelerator Conference, SLAC, Stanford, U.S.A., 1986, p. 487-489

3. A. Asami et al.,"Progress of the positron generator at KEK," presented at this Conference.

4. S.Ohsawa et al., "Positron production and acceleration," Presented at the Symposium on the Acceleration Technology for the High Brilliance Synchrotron Radiation Sources, Tokyo, Japan, Sept. 5-6, 1988.

5. W.B. Herrmannsfeldt, "Electron Trajectory Program," SLAC Report 226, November 1979.

6. Y. Otake et al., "Short pulse grid pulser for an electron gun of the KEK positron generator," in Proceedings of the 6th Symposium on Accelerator Science and Technology, Tokyo, Japan, October 27-29, 1987. p. 65-67.

7. Y. Ogawa et al. ,"Remote control of an emission current of a high-current, short-pulse electron gun," in Proceeding of the 6th Symposium on Accelerator Science and Technology, Tokyo, Japan, October 27-29, p. 62-64.

# A FLIGHT-QUALIFIED RFQ FOR THE BEAR PROJECT*

D. Schrage, L. Young, B. Campbell, J. H. Billen, T. Wangler,
J. Stovall, F. Martinez, W. Clark, S. Gibbs, G. Bolme,
P. O'Shea, M. Lynch, and J. Devenport
Los Alamos National Laboratory, Los Alamos, NM 87545

J. Rathke, R. Micich, and J. Rose
Grumman Space Systems, Bethpage, NY 11174

R. Richter and G. Rosato
GAR Electroformers, Danbury, CT 06810

## Abstract

A 1-MeV, 30-mA, low-duty factor, 425-MHz RFQ has been designed and constructed for the BEAR (Beam Experiments Aboard a Rocket) Project by Los Alamos National Laboratory, Grumman Space Systems Division, and GAR Electroformers. The design of this 1-m-long, lightweight (<55-kg) accelerator is unique in that it was constructed of four copper-plated aluminum quadrants joined longitudinally by a room-temperature electroforming process to produce a monolithic structure. There are no rf, vacuum, or mechanical joints in the vane/cavity region of the accelerator. As part of the design/fabrication process, spark-test, cold, and engineering model RFQs were constructed and tested. The completed flight unit has successfully passed static structural and thermal tests as well as dynamic structural (shake) tests according to the launch, separation, and flight specifications. In addition, the rf field distributions and beam-transport characteristics have been measured and found to satisfy the design requirements.

## Introduction

The BEAR[1] project will be the earliest opportunity for testing a neutral particle beam (NPB) accelerator in space. An NPB accelerator is one of the directed energy technologies being developed under the Strategic Defense Initiative Organization (SDIO). The BEAR Project, which began in 1985, is a suborbital flight of a 1-MeV NPB accelerator and diagnostic payload to be launched on an ARIES booster. The flight is scheduled for March 1989 at the White Sands Missile Range. The 1200-kg payload will be launched to an apogee of 200 km, and the accelerator experiments will be carried out during a period of 400 s. The usual space-borne hardware requirements regarding minimal size and weight along with environmental conditions must be met by the equipment used in the BEAR flight.

## Design Requirements

The BEAR accelerator payload consists of an $H^-$ ion injector (small-angle source[2] and low-energy beam transport), the RFQ accelerator, a high-energy beam transport, and a gas neutralizer. The fundamental requirement is to produce a minimum of 10 mA of neutral beam at the output of the neutralizer. This effected a specification of a 30-mA beam current for the RFQ. Payload weight restrictions limited vacuum pumping capacity, prohibited cooling of the accelerator structure, and dictated minimum weight for the rf power system. These, as well as other considerations, led to the selection of a resonant frequency of 425 MHz along with a very low duty factor, 0.025%.

*Work supported and funded by the US Department of Defense, Strategic Defense Initiative Office, under the auspices of the US Department of Energy.

The flight requirements dictated that all components and subassemblies pass environmental tests associated with operation under prelaunch ground support as well as under flight conditions.[3,4] Furthermore, even though the BEAR project involves a very low duty factor, it was required that the RFQ utilize technology and materials that were extendible to higher duty-factor (including CW) operation for future programs.

The beam dynamics design[5] was optimized to a short accelerator, 1 m long (1.42λ). The shorter length was achieved in part by using a varying transverse radius on the vane tips. Although this increased the complexity of the manufacture of the vane tips, it resulted in a 10% reduction in the length of the RFQ and a proportionate reduction in the copper power, along with similar reductions in the weight of both the RFQ and the rf power system. The final specifications and design parameters are given in Table I.

Table I. BEAR RFQ Design Parameters

| | |
|---|---|
| Particle | $H^-$ |
| Resonant frequency | 425 MHz |
| Injection energy | 0.03 MeV |
| Energy at end of buncher | 0.19 MeV |
| Final energy | 1 MeV |
| Synchronous phase at end of buncher | -40° |
| Final synchronous phase | -34° |
| Transmission | 87% |
| Final emittance | 0.01-cm·mrad rms |
| | |
| Beam current | 30 mA |
| Beam pulse width | 50 μs |
| Beam pulse repetition rate | 5 Hz |
| Beam power requirement | 30 kW |
| Copper power requirement | 70 kW |
| Total power requirement | 100 kW |
| Duty factor | 0.025 % |
| | |
| Intervane voltage | 0.044 MV |
| Peak surface field | 37.3 MV/m |
| | |
| Minimum aperture radius | 1.20 mm |
| Final aperture radius | 1.20 mm |
| Length | 1 m (1.42λ) |
| Outside diameter | 0.18 m |
| Weight | 55 kg |

## Conceptual Design

The project began with a conceptual design competition. One of the two competing concepts was a conventional structure consisting of a set of vanes bolted into a core tank that was to be enclosed in a vacuum vessel. In one variation of this, the core tank also functioned as the vacuum vessel.[6] The alternative proposal was an unconventional, novel concept that consisted of four independent vanes with the cavity walls, supporting structure, and vacuum vessel fabricated as an electroformed, copper cavity wall. A variant of this concept involved joining four vane/cavity quadrants by electroforming a joint. These concepts are shown in Fig. 1.

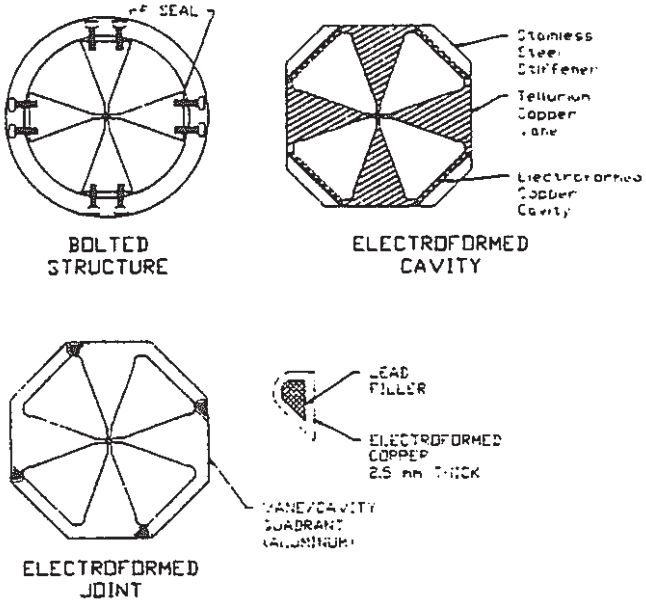


Fig. 1. BEAR RFQ options

### Bolted Structure

The bolted structure is one of proven performance, dating back to the proof-of-principle (POP) RFQ.[7] The unit is simple to fabricate, and many of the fabrication tolerances can be relaxed because the vanes are adjustable. However, it is that adjustability that contributes to its major deficiencies. The vane adjustability basically necessitates mechanical rf joints. The possibility of using welded-in rf joints per the CERN 201-MHz RFQ[8] was deemed to be remote because of the small dimensions of the 425-MHz cavity. Experience with the POP had shown that a design with a significant amount of stored mechanical energy in adjustment mechanisms would likely not maintain vane-tip alignment over a period of months, particularly during any thermal cycling. For flight-qualified hardware, with shake tests, launch vibrations, plus launch and separation shock loads, the possibility of vane-tip misalignment was a major concern. This concept would also have many more vacuum joints than would the electroformed concepts. Lastly, given that the vanes should not carry structural loads, additional weight would be added to the tank structure.

### Electroformed Cavity

The electroformed cavity has significant advantages over the bolted structure in that there are no longitudinal rf joints. The only rf and vacuum joints would be those associated with tuners and rf drive loops. Such an RFQ would be a monolithic copper structure with tellurium copper vanes and Type II (high-strength) copper cavity walls. Stainless steel flanges for the drive loops, rf pickup loops, and slug tuners would be joined to the cavity walls by electroformed copper. In addition, stainless steel stiffeners would be attached by electroformed copper. There were two identified disadvantages of this concept. The first was that the copper has a lower stiffness-to-weight ratio than aluminum and, therefore, for a structure subjected to equivalent dynamic loads, would weigh more. The second, now believed to have been an incorrect assumption, was that the lack of a capability for measurement of the rf field distribution before electroforming might result in a structure that could not be tuned. Experience with the BEAR RFQ has led to reconsideration of this assumption. Careful mechanical alignment of the vanes before electroforming does produce a structure that is tunable with slug tuners. This concept was considered a backup to the selected design, and a one-half length, full cross-section engineering model was fabricated.

### Electroformed Joints

The concept that was selected and fabricated involved four copper-plated aluminum (Type 6061-T651) vane/cavity quadrants that were joined by electroforming. As in the case of the other electroformed concept, this one had no longitudinal rf or vacuum joints. Its main advantages were that measurement of the rf field distribution before electroforming was possible and the structure had the benefit of the stiffness-to-weight ratio of the aluminum. It was primarily on the basis of the provision to make pre-electroforming measurements of the rf field distribution that this concept was selected. A comparison of the concepts is summarized in Table II. The final design of the BEAR RFQ is shown in Fig. 2.

Table II. BEAR RFQ Concepts

| Parameter | Bolted Structure | Electroformed Cavity | Electroformed Joints |
|---|---|---|---|
| Vacuum vessel | Separate or integral | Integral | Integral |
| Longitudinal rf joints | 8 | None | None |
| Vacuum joints | Yes | None | None |
| Mechanical joints | Yes | None | None |
| rf tuning stability | Poor | Excellent | Excellent |
| Premanufacturing rf tuning | No | No | Yes |
| Extension to CW | Poor | Good | Good |

## Spark Testing

A spark test cavity was constructed and tested with both bare aluminum as well as copper-plated (~0.01 mm thick) aluminum vane tips. The cavity walls were copper plated (~0.1 mm thick) in both cases. The 45-cm-long cavity was of rigid construction and the 15-cm-long vanes were not adjustable. The design relied upon the accuracy of manufacture for alignment of the vane tips. The cavity

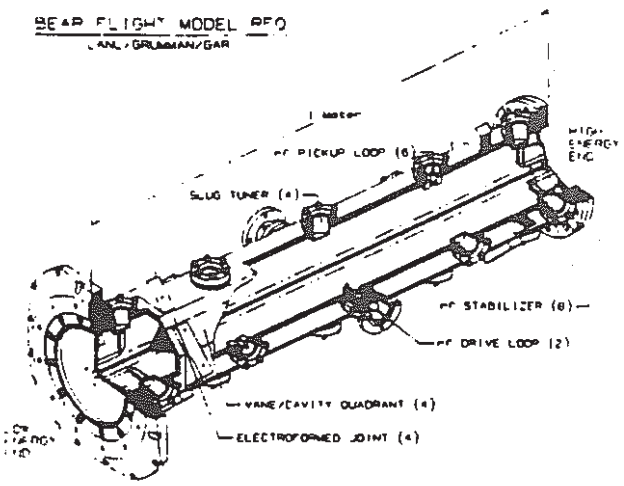


Fig. 2. BEAR flight model RFQ

was tested at Los Alamos, and in both configurations peak surface fields of 60 MV/m were achieved, corresponding to three times the Kilpatrick limit for 60-ms pulses at 5 Hz.

## Cold Model RFQ Testing

A number of calculations using the code SUPERFISH were made to predict the frequency sensitivity and mechanical fabrication tolerances for the RFQ. A full-length, full cross-section, cold (low-power) model RFQ with unmodulated vane tips verified the SUPERFISH predictions of tuning sensitivity It was also used for experimental design of the end plates, for verifying the planned pre-electroforming alignment procedures, and for verifying the decision to use end stabilizers rather than vane coupling rings. These are similar in design to dipole suppressors[9] but are mounted directly to the end plates on both ends of the RFQ, and the capacitive gap is to the radial slug tuner.

The cold model RFQ consisted of four vane/cavity quadrants that were adjusted as rigid bodies on the basis of displacements and rotations determined by software[10] that was developed at Los Alamos for this purpose. The positions of tooling holes, whose locations relative to the vanes tips were known to a high degree of accuracy (0.008 mm), were used to determine the rigid body motions of the quadrants.

## Engineering Model RFQ Testing

The one-half length, full cross-section engineering model RFQ with unmodulated vane tips was fabricated for the purpose of developing the electroforming technique and verifying the structural analysis performed by Grumman. This unit was fabricated jointly by Los Alamos and Grumman, with the electroforming being carried out by GAR. The alignment of the vane/cavity quadrants used software[10] that was developed as part of the cold model studies. The electroformed joint consisted of a 2.5-mm-thick layer of high-strength copper, a lead filler, and a 2.5-mm-thick layer of high-strength copper deposited over the lead. After completion of the electroforming, this unit was subjected to thermal testing as well as to the static equivalent of the flight dynamic loads. Comparison of pre- and post-test rf field distribution measurements (beadpulls) demonstrated that there had been no change in the vane tip alignment as a result of the thermal and structural loads.

## Flight Model RFQ Fabrication

The vane/cavity quadrants were fabricated in the Grumman shops. The manufacture of RFQ vane tips had been a concern at Los Alamos since the POP unit. A technique that utilized a ball end mill was developed for the POP[11] and had been successful, but it had the fundamental deficiency of having zero cutting speed at the top of the vane tip, which resulted in a poor surface finish. A method developed at the Brookhaven National Laboratory[12] that utilizes a cylindrical tool bit overcomes this deficiency, but it was not suitable for the small size of the BEAR RFQ cavity. A variation of the POP method, which involved mounting the ball end mill at an angle relative to the axis of the vane, was developed for this project. This method resulted in an rms surface finish of better than 32 microinches on the entirety of the vane tip.

The experience gained in the electroforming of the engineering model RFQ allowed the flight model electroforming to be completed in 10 weeks. Throughout the electroforming process, witness tensile test and adhesion test coupons were electroformed and tested. In all cases both the strength of adhesion to the aluminum as well as the yield strength of the copper exceeded the design specifications. The original design called for the RFQ to be operated with a thin copper strike (~0.01 mm thick) on the vane tips with the cavity and the remainder of the vanes copper plated to a thickness of 0.08 mm. However, reaction with the plating solution caused the strike on the tips to peel in a few places; therefore, the strike was removed by an acid dip and the RFQ was operated with bare aluminum vane tips.

## Testing of the Flight Model RFQ

After the completion of the electroforming by GAR, the RFQ was returned to the Grumman shops for final machining of the end flanges and penetrations for the tuners and rf drive loops. It was then delivered to Los Alamos for rf tuning. The assembled RFQ is shown in Fig. 2. Power is supplied to the cavity by two drive loops inserted into opposite cavities at midlength. Longitudinal rf field stabilization is achieved by eight end stabilizers mounted in the ports at the ends of the RFQ. These, along with ten slug tuners (six of which mount rf pickup loops) were used to tune the rf fields. After final adjustment of the tuners, the longitudinal field tilts were reduced to less than 2% and the dipole mode contributions were reduced to less than 2% of the quadrupole field strength.

The RFQ was installed on the BEAR test stand and rf conditioned to 120% of the design power level within 24 hours of operating time. The outgassing rate of the RFQ was $1.0 \times 10^{-9}$ torr-liter/cm$^2$-s. The beam transport properties at 1 MeV were verified by testing with the prototype BEAR injector. The unit was then subjected to a random vibration shake test and to a shock test at levels corresponding to the ARIES specification.[3,4] Post-test rf field distribution measurements verified that there had been no change in the rf field distribution; i.e., vane-tip alignment had not changed as a result of operation on the test stand or because of the shake test. The measured performance parameters are given in Table III.

## Present Status

At the present time the BEAR RFQ is installed on the BEAR test stand and is in use in the testing of the downstream components, such as the neutralizer and the flight beam diagnostics. In December of 1988 the entire rocket payload will be assembled and subjected to environmental and shock tests. The BEAR flight is scheduled for March 1989.

Table III. BEAR RFQ Performance Parameters

| Parameter | Design Requirement | Achieved Value |
|---|---|---|
| Resonant frequency | 425 ±0.5 MHz | 425 ±0.5 MHz |
| rf fields | <5% dipole<br><5% tilt | <2% dipole<br><2% tilt |
| Cavity Q | 6300 | 6330 |
| Weight | 55 kg | 55 kg |
| Peak surface fields | 37 MV/m<br>1.8 Kilpatrick | 60 MV/m<br>3.0 Kilpatrick |
| Thermal loads | 33° C temp rise | >33° C temp rise |
| Structural loads | | |
| External pressure | 117 000 Pa | Exceeded |
| Launch/separation | 5 g's lateral<br>50 g's axial | Exceeded |
| Random vibration | AFGL[a] ARIES spec | Tested<br>Tested |
| Material properties | | |
| Copper yield str | ≥ $1.47 \times 10^8$ Pa | ≥ $1.69 \times 10^8$ Pa |
| Adhesion to Al | ≥ $1.47 \times 10^8$ Pa | ≥ $1.69 \times 10^8$ Pa |
| Outgassing rate torr-liter/cm²-s | $3.0 \times 10^{-9}$ | $1.0 \times 10^{-9}$ |

[a]Air Force Geophysics Laboratory.


## Acknowledgment

The authors acknowledge E. Boltezar of CERN for his contributions to the design concepts of the cold model and flight model.


## References


1. T. M. Foley, "SDIO Moves Up Launch Date for Particle Beam Space Test," Aviation Week & Space Technology, 70-71, March 21, 1988.
2. Paul Allison, and Joseph Sherman, "Operating Experience with a 100 keV, 100 mA $H^-$ Injector," Proc. 3rd Symp. on Production and Neutralization of Ions and Beams, AIP Proc., #111, 511 (1983).
3. R. D. Arritt and C. S. Dugan, "ARIES Controlled Sounding Rocket: Past-Present-Future," U.S. Naval Research Laboratory report (1983).
4. R. G. Steeves, "ARIES Rocket Flight Vibration Environment Multispectral Measurements Program," Air Force Geophysics Laboratory report AFGL-TR-79-0514 (1979).
5. T. P. Wangler and C. E. Griffin, "An RFQ Beam Dynamics Study for BEAR," Los Alamos National Laboratory memorandum AT-1:85-348 (October 1985).
6. A. Abbott, R. MacGill, and R. Yourd, "Mechanical Design of a Heavy Ion RFQ," IEEE Trans. Nucl. Sci. 30 (3), 3004 (1983).
7. J. E. Stovall, K. R. Crandall, and R.W. Hamm, "Performance Characteristics of a 425-MHz RFQ," IEEE Trans. Nucl. Sci. 28 (2), 1501 (1981).
8. E. Boltezar, et al., "Experimental RFQ as Injector to the CERN Linac I," Proc. of the 1981 Linear Accelerator Conf., Los Alamos National Laboratory report LA-9234-C, 302 February 1982).
9. M. Vretenar, "RFQ Field Stabilization Using Dipole Suppressors," Proc. First Workshop on the INFN Eliosatron Project, Erice, Sicily, 271 (1986).
10. J. H. Billen, "Alignment of RFQ Vanes for BEAR," Los Alamos National Laboratory memorandum AT-1:87-21 (January 1987).
11. S. W. Williams and J. M. Potter, "Vane Fabrication for the Proof-Of-Principle Radio Frequency Quadrupole Accelerator," IEEE Trans. Nucl. Sci. 28 (3), 2967 (1981).
12. R. B. McKenzie-Wilson, "Design & Fabrication of the BNL Radio Frequency Quadrupole," IEEE Trans. Nucl. Sci. 30 (4), 2998 (1983).

LINAC 88
5-7/10 - WILLIAMSBURG

# HIGH POWER L-BAND KLYSTRONS FOR LINEAR ACCELERATOR

G. Faillon - E. Boghossian - Ph. Guidée

THOMSON-CSF Division Tubes Electroniques
38 rue Vauthier BP 305
92102 Boulogne-Billancourt Cedex, France

ABSTRACT

The use of L-band Linear Accelerators for a large range of applications has become very widespread during the past years ; these Linacs operate at 1.3 GHz, usually in a medium energy range, which allows to drive a high electron beam for appropriate industrial applications, such as irradiation, sterilisation and hardening of solid state devices.

In addition to these still-active application areas, a renewal of the L-band Linacs has arisen lately with the fast growth of the Free Electron lasers.

---

Usually the RF sources are multimegawatt pulsed klystrons. The characteristics of these high power tubes are basically the same, that means they work at a fixed frequency of 1.3 GHz with a 1 % (-1 dB) bandwidth and a peak output power in the order of several MW peak up to 30 or 40 MW peak. But because ea accelerator has its own pecularities as regards the required average power, pulsed lengths, maximum available high voltages ... it appeared very soon that the klystrons had to be optimized for each user and at the same time to keep the advantages of an important number of similar klystrons already built and to be built.

These ascertainments have led Thomson-CSF to design the L-band klystrons in a modular structure. To define a tube, the designer has the following basic subassemblies available :

- Three guns : the first one is cathode pulsed, with a perveance adjustable between 1.7 µperv. and 2.4 µperv. The high voltage capabilities are 320 kV - 7 µs with a cathode load of 12 A/cm$^2$ max.

  The second gun differs from the previous one, just by the ceramic insulator which is larger, in order to increase the pulse length capabilities (300 µs - 10 MW peak).

  The third gun has a modulating anode and two ameter ceramic insulators. The perveance is 2.5 µperv. when the anode is grounded. The characteristics of this gun are 135 kV DC/1.7 µperv. - 2.5 µperv. with a cathode load not greater than 4 A/cm$^2$ on the edge (see figure 1). Pulses of ms duration can be delivered easily.

- The cavities are parallelepipedic and made of copper. Their lengths are chosen in order to resonate at the design frequencies. However each has a standardized inductive tuning system to adjust the frequency on the field. All the klystrons have five cavities, including the output circuit.

The cathodes are made of impregnated tungsten with an osmium coating (M-type) for the third gun model. The figure 2 gives examples of normal and M cathode thermoemission curves :

- The total length of the body between the two polepieces is always the same. The cavities can be placed within this length. The drift tubes lengths can be chosen according the small and large signal calculations.

- The distance between the pole pieces being always the same, we don't need many electromagnets. Only two are manufactured : the TH 20100 with a small internal diameter, designed for the TV 2022 which is equipped with the first gun type, and the TH 20277 with a larger internal diameter fitted to the 2$^{nd}$ and the 3$^{rd}$ gun types. Usually a cathode trim coil allows to adjust the electrode beam transmission and thus the gain and the efficiency.

- The output cavities differ from one another by the coupling iris and the cooling circuits. Especially for the TH 2104U which delivers 250 kW average, the cooling subassemblies are critical parts.

- The output waveguide WR650 is horizontal and two pill box type windows are available, one with an AL300 Ø 19 cm usual ceramic and a second one with a low loss and same diameter AL995 ceramic. These windows can also be used for the accelerator itself (TH 20141).

- Four collectors are available, depending on the average power and the electrons energies. The dimensions are given on Figure 3. All of them are cooled by the hypervapotron(R) technique, allowing low water flow and low pressure drop. The total beam power (without any RF signal) can be accepted in any case by the collectors. The design has also taken into account reflected and secondary electrons originating in the collector region, which could give oscillations and instabilities problems.

Special features and characteristics which have been illustrated on the attached drawings need some comments :

- The large size third gun type with a modulating anode is mounted on the klystron TH 2095A used on a FEL injector. The dimensions and the design are chosen in such a way that everywhere the pulsed and DC electric fields on the dielectric and metallic surface are never greater than 10 kV/mm at 130 kV (figure 1) ; also a M-type low temperature cathode also prevents any contamination of the electrode and allows a good vacuum. During this process the Fowler-Nordheim diagram is drawn and the operating voltage is increased to stay in the transition region between the conduction and the field emission regions (figure 4).

- According our 1 and 2D large signal codes the efficiencies are always greater than 55 %, even with a 2.4 µperv. beam. Figure 5 gives examples of such calculations.

- We can obtain in any case a -1 dB bandwidth around 12 MHz - 15 MHz. The 2$^{nd}$ harmonic level is low, but can increase strongly if a resonance at such frequencies is presented to the klystron output with a defined phase. For example a circulator must be matched not only at 1.3 GHz (< 1.3:1) but also at 2.6 GHz perhaps within more flexible constraints (VSWR < 2:1). Also it is the same thing to say that the maximum acceptable VSWR all phases is 1.5:1, or to say that 4 % of reflected power is allowable. At a lower output power, the reflected power can be the same - at least - and therefore the acceptable VSWR be greater.

The sensitivities of the output power and of the phase variation as regards the cathode voltage (V) and the anode ($V_A$) are roughly given by :

- pulsed cathode : $\Delta P/\Delta V \simeq 3P/V$ and $\Delta\phi/\Delta V \simeq 1000$ °/V

- modulating anode : $\Delta P/\Delta V \simeq P/V$ and $\Delta\phi/\Delta V \simeq 1000$ °/V

$$\Delta P/\Delta V_A \simeq 1.5\ P/V_A \text{ and } \Delta\phi/\Delta V_A \simeq 172\ °/V_A$$

- The X rays radiation pattern is needed to evaluate the shielding or the protection inside the building (figure 6). Because the X rays are mainly created in the collector, it can be strange to observe a larger amount when the power in the collector becomes smaller by turning on the RF. This can be explained by some very high velocity electrons entering the collector when the RF is on.

Obviously in all cases the gain is high and around 50 dB. Taking into account usual RF losses between the driver and the high power klystron, the driver must be able to deliver at least 500 W peak. The medium power permanent magnet klystrons TH 2437 and TH 2437A have been designed for this purpose : 1 kW CW and 10 kW pulsed - 1.3 GHz.

The characteristics of all klystrons of this L-band family are summarized in Table I.

Beside the klystrons we have also presented, the TH 2086A is a totally different tube, specially designed for plasma heating and fusion experiment. Its main characteristics are the pulse length and the close CW operation around 1 MW. At the same time, the frequency can be adjusted by the user between 1.25 GHz and 1.35 GHz.

Other klystrons exist around 1.3 GHz ; however they are radar klystrons where the instantaneous -1 dB bandwidths and the frequency tuning capabilities are of special importance.

Usually the noise figure, related mainly to the current is around 60 dB, according to measurements on similar beam radar tubes. Therefore the signal to noise ratio is about 110 dB/kHz. But in some cases, spurious emerge from this low level 1/f noise. Such spurious can be explained by electrons oscillating within a gap or accross the tube between two cavities or the first one and the collector. Low frequency oscillations are sometimes related to a mismatch on the output side or to a feedback loop through external leakage. The multipactoring effects are sometimes involved in these parasitic phenomena.

In conclusion, we have described the present 1.3 GHz klystrons family of Thomson-CSF, designed for scientific and especially for accelerators applications. The modular technology is very flexible and quite adapted to many users, whose requirements differ slightly from one another. Special care is taken to eliminate any defect on all the character-istics curves, and any parasitic oscillation. At the same time, because of the growing number of sockets, the reliability is improved.

TABLE I

| TYPE | F (GHz) | Ppeak(MW) | Paverage | tp (µs) | BW(MHz)1dB | η(%) | Pd(W) | V (KV) | I (A) | SOL | Isol(A) | Vf(V)xIf(A) |
|---|---|---|---|---|---|---|---|---|---|---|---|---|
| | SCIENTIFIC | | | | | | | | | | | |
| TV 2022 | 1.3 | 20 MW | 40 KW | 8 µs | 10 MHz | 44 % | 160 W. | 235 KV | 194 A | TH 20100 | 53 | $28^{V}_{24^{A}}$ |
| TV 2022A | 1.3 | 20 | 50 | 8 | 10 | 44 | 160 | 235 | 194 | TH 20100 | 57 | 28-24 |
| TV 2022B | 1.3 | 20 | 60 | 10 | 10 | 44 | 160 | 235 | 194 | TH 20100 | 59 | 28-24 |
| TV 2022C | 1.3 | 20 | 10 | 20 | 10 | 44 | 160 | 235 | 194 | TH 20100 | 59 | 28-24 |
| TV 2022D | 1.3 | 30 | 60 | 7 | 10 | 43 | 160 | 279 | 251 | TH 20100 | 69 | 28-24 |
| TH 2095 (2) | 1.3 | 6 | 45 | 275 | 10 | 46 | 150 | 126 | 97 | TH 20277 | 62 | 18-19 |
| TH 2095A(2) | 1.3 | 6.5 | 45 | 275 | 10 | 46 | 150 | 132 | 107 | TH 20277 | 66 | 18-19 |
| TH 2104 | 1.3 | 15 | 50 | 100 | 10 | 47 | 120 | 200 | 165 | TH 20277A | 61 | 21-21 |
| | 1.3 | 10 | 100 | 200 | 10 | 45 | 160 | 163 | 134 | TH 20277A | 54 | 21-21 |
| TH 2104A | 1.3 | 5 | 150 | 600 | 10 | 44 | 160 | 124 | 92 | TH 20277A | 48 | 21-21 |
| TH 2104U | 1.3 | 10 | 250 | 250 | 10 | 48 | 160 | 160 | 132 | TH 20277A | 51 | 21-21 |
| TH 2115 (2) | 1.3 | 2 | 150 | 1.1msec | 8 | 46 | 140 | 82 | 54 | TH 20277 | 59 | 20-20.5 |
| TH 2437 | 1.3 | - | 1 | CW | 1 | 30 | 0.1 | 6 | 0.55 | P.M. | - | 6-4.7 |
| TH 2437P | 1.3 | 10(KW) | 15(W) | 10 | 1 | 25 | 0.1 | 16 | 2.50 | P.M. | - | 6-4.7 |
| | RADAR | | | | | | | | | | | |
| TH 2068 (1) | 1.25-1.35 | 4.5 | 11 | 7 | 15 | 46 | 50 | 122 | 81 | TH 20108 | 16 | 12.5-21.5 |
| TH 2068A(1) | 1.25-1.35 | 4 | 8.5 | 7 | 15 | 46 | 30 | 116 | 75 | TH 20108 | 15 | 12.5-21.5 |
| TH 2068B(1) | 1.25-1.35 | 4 | 8.5 | 7 | 30 | 46 | 30 | 116 | 75 | TH 20108 | 15 | 12.5-21.5 |
| TH 2068S(1) | 1.25-1.35 | 1.5 | 2 | 4 | 40 | 35 | 50 | 87 | 49 | TH 20108 | 13 | 12.5-21.5 |
| | FUSION | | | | | | | | | | | |
| TH 2086 (1&3) | 1.25-1.35 | 1.5 | - | 100msec | 6 | 40 | 20 | 80 | 46 | TH 20108 | 13.5 | 18-21 |
| TH 2086A(1&3) | 1.25-1.35 | 1.0 | - | 250msec | 6 | 38 | 20 | 70 | 38 | TH 20108 | 12 | 18-21 |
| | 1.25-1.35 | 0.6 | - | 500msec | 6 | 35 | 20 | 58 | 30 | TH 20108 | 11 | 18-21 |

(1)= TUNABLE WITHIN THE INDICATED BANDWIDTH
(2)= WITH A MODULATION ANODE
(3)= TIME BETWEEN PULSES,20 sec min.

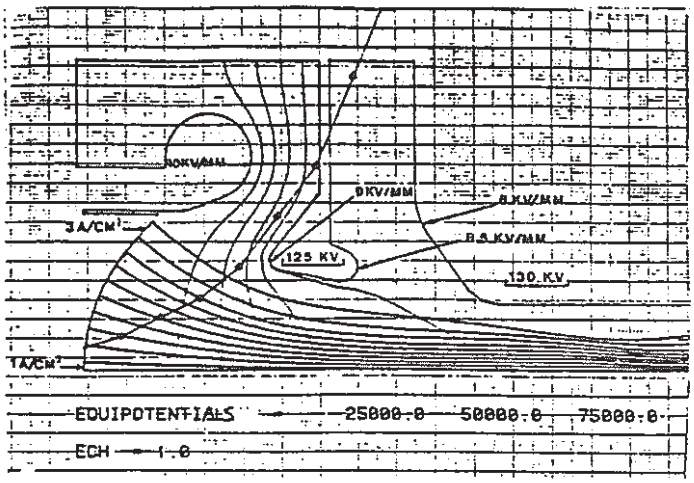


Figure 1 : TH 2095 computer calculations

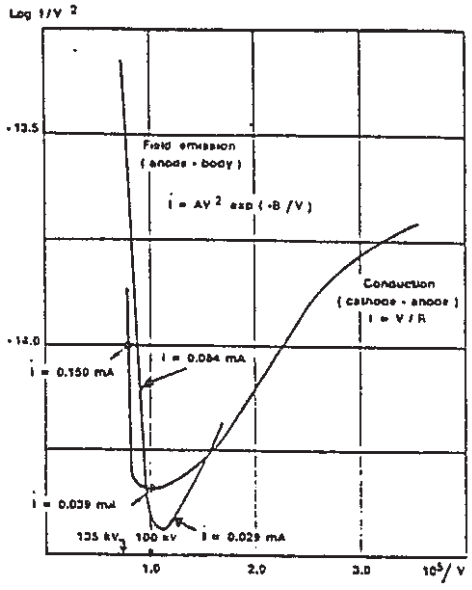


Figure 4 : TH 2095 Fowler-Nordheim diagram

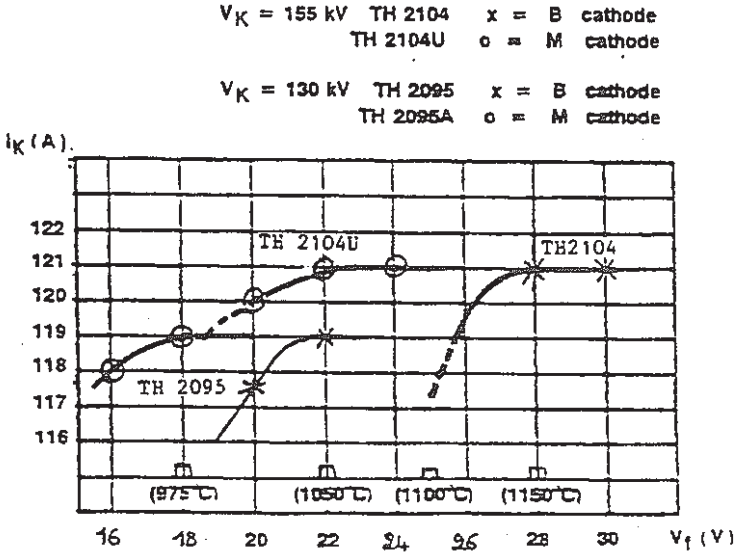


Figure 2 : Cathode behaviour curves


Figure 3 - L-band klystron collectors

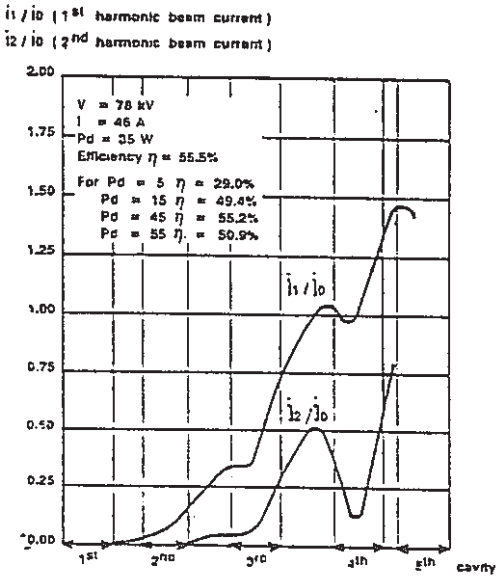


Figure 5 : TH 2115 efficiency calculation

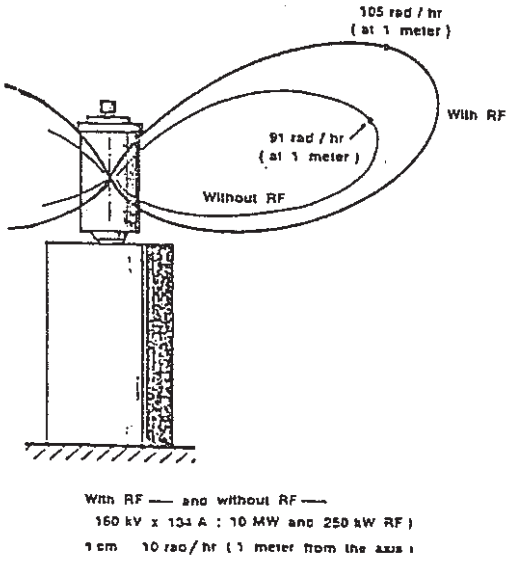


Figure 6 : TH 2104U X rays radiation pattern

# A Compact Proton RFQ Injector for the Bevalac†

J. W. Staples, S. R. Abbott, R. J. Caylor, R. A. Gough, D. R. Howard, R. A. MacGill
*Lawrence Berkeley Laboratory, Berkeley, California 94720*

## Abstract

A compact 800 keV 410 MHz RFQ using new construction techniques has been fabricated at LBL. It comprises four integrated vane-cavity sections, with end caps and vane coupling rings. The RFQ will inject protons into the present heavy-ion linac by drifting the protons through a heavy ion RFQ into the two $2\beta\lambda$ Alvarez tanks which will be operated in the $\beta\lambda$ mode, producing 20 MeV protons. Along with a new third ion source, the Bevatron injector systems will comprise two RFQ's and two Alvarez tanks, offering rapid particle selection from 20 MeV protons to 5 MeV/n argon. The mechanical characteristics of the RFQ and the drift-through process in the second RFQ will be emphasized.

## Background

The LBL Bevatron complex, used since 1971 to accelerate heavy ions, has two injector systems, the SuperHILAC and the Local Injector (LI). The SuperHILAC is used to inject ions to mass 238. The LI, used to provide 5 MeV/n ions up to mass 40, consists of a $q/A \geq 1/7$ RFQ followed by two $2\beta\lambda$ Alvarez tanks, all operating at 200 MHz[1]. A duoplasmatron provides $He^{1+}$ ions and a sputter PIG provides both gas and metallic ions through $Ar^{6+}$.

Unlike the original configuration of the LI, this arrangement is unable to provide 20 MeV protons for injection into the Bevatron. Because of uncorrectable closed orbit error at low fields, 5 MeV protons cannot be accepted. The Alvarez tanks can be run in the $\beta\lambda$ mode, but then must be injected with 800 keV protons, which the present heavy ion RFQ cannot provide. Additionally, the heavy ion RFQ is located immediately upstream of the first Alvarez tank to simplify matching into the DTL with no space for an inflection magnet to introduce an 800 keV proton beam.

## New RFQ Injector

The problem of providing 20 MeV protons to the Bevatron can be solved by providing a source of 800 keV protons with a new RFQ and drifting the protons through the present heavy ion RFQ which functions as a transport channel. The proposed configuration is shown in Figure 1. It has been experimentally established that a 400 keV proton beam with $\beta \approx 0.029$ is efficiently transported through the heavy ion RFQ[1], which has a synchronous velocity range from input to output of $\beta = 0.0043$ to $\beta = 0.021$. The proton beam is not synchronous with the accelerating wave in the heavy ion RFQ, which provides only transverse focusing throughout its length. The transverse matching of the proton beam into the DTL will be the same as is presently used for heavy ions, with a slight decrease in the r.f. defocusing strength. The energy spread of the proton beam is slightly increased, and will be discussed quantitatively below.

## Proton RFQ Characteristics

LBL has produced three 200 MHz RFQ's operating at LBL[1], CERN[2] and BNL[3]. The new 800 keV proton RFQ, shown in Figure 2, is a departure from the previous 200 MHz technology; it is a lightweight, compact copper plated aluminum structure which operates at 410 MHz. This structure incorporates new concepts in mechanical design, vacuum practice and assembly techniques. The beam dynamics design is derived from the proton RFQ made for BNL[3] and from the BEAR[4] design and makes use of a relatively long shaper section and a shorter gentle buncher. This configuration results in a shorter structure with a smaller longitudinal output emittance but with the characteristic that the output energy spread tends to increase with decreasing input current. The RFQ parameters are tabulated below.

| | | |
|---|---|---|
| Ion | proton | |
| Frequency | 410 | MHz |
| Input Energy | 40 | keV |
| Output Energy | 800 | keV |
| Vane Length | 101.7 | cm |
| Vane Voltage | 72 | kV |
| Measured Q | 6300 | |
| Cavity Power | 135 | kW |
| Choke Current | 108 | mA |
| Foc Parameter B | 4.77 | |
| Surface field | 1.9 | Kilpatrick |
| $r_0$ | 0.303 | cm |
| Final $\phi_s$ | -32° | |
| Acceptance | $0.05\pi$ | cm-mrad, normalized |
| No. of cells | 160 | |
| No. of RM cells | 8 | |

The shaper section is 31 cm long, accelerating the beam from 40 to 80.7 keV with a final $\phi_s$ of -60°. The gentle buncher is 17.5 cm long, accelerating to 195 keV with a final $\phi_s$ of -40° with a constant $\Delta_{gap}$ of -0.12. The accelerator section is 50.9 cm long, with $\phi_s$ tapering to -32°.

A constant $\rho_\perp = 0.75 r_0 = 0.227$ cm design is used with a minimum value of $\rho_{\parallel min} = 0.48$cm. This small $\rho_{\parallel min}$ requires a tight cutter design, described below.

Parmteq simulations show a 91% transmission of a 30 mA input beam with a 38% transverse emittance increase and a longitudinal emittance of $\pm 16$ keV $\times \pm 29°$ at the 90% contour.

This structure was originally to be a mechanical and vacuum test model, and the 1 meter length was arbitrarily chosen. Later when this use was discovered for this structure, the specific beam dynamics design was constrained by the 1 meter length. A satisfactory solution was found.

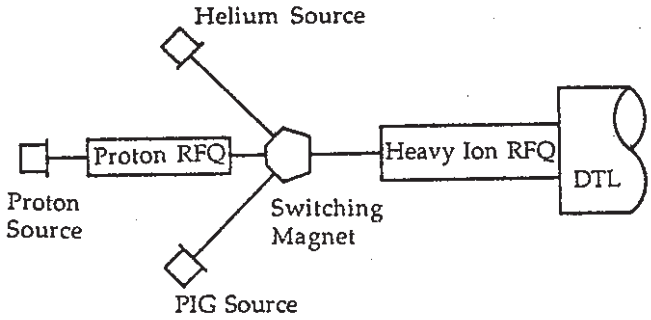


Figure 1
Injector configuration with existing PIG heavy ion source and duoplasmatron helium source, and new duoplasmatron proton source and 410 MHz RFQ.

## Mechanical Design

The mechanical design of this RFQ departs significantly from the previous RFQ's designed and built at LBL. The goal was to produce an economical, lightweight and compact structure that is easily assembled without precision tooling or highly skilled person-

† This work was supported by the Director, Office of Energy Research, Office of High Energy and Nuclear Physics, Nuclear Science Division, U.S. Department of Energy under contract number DE-AC03-76SF00098.

nel. The techniques developed are applicable to large scale production of RFQ structures. Patent proceedings are presently underway regarding the mechanical design.

The structure consists of even and odd vane pieces, as shown in Figure 2, which bolt together to form a strong and integral assembly. The mating surfaces serve as fiducials for the machining of the vane tips, so no adjustments are necessary at assembly. Measurements verifying the intervane spacings after assembly indicate that the ±0.5 mil (0.0005 inch = 13 microns) accuracy is readily achieved. The average machining error of the vane tip before plating was 0.3, 0.2, 0.5 and 0.2 mils from specification for each of the four vanes.

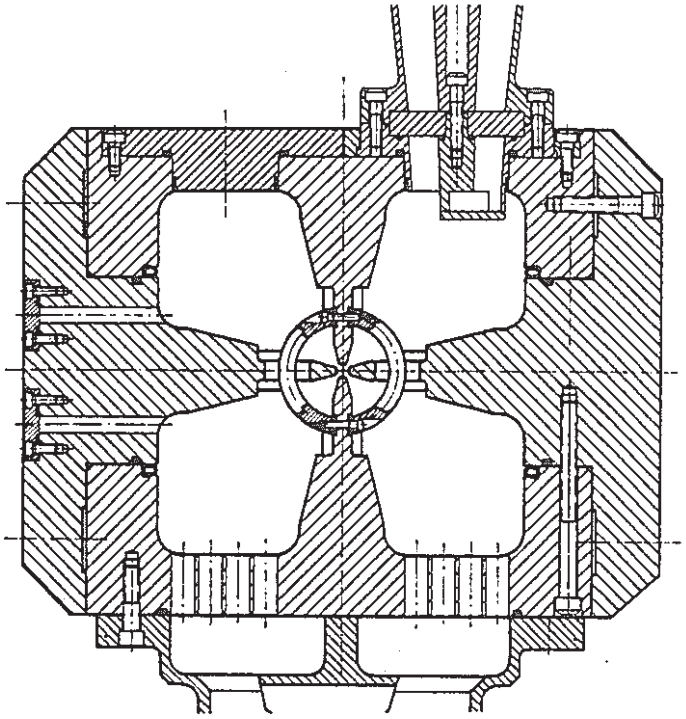

Figure 2
Cross section of RFQ showing both drive loop (top) and pump port (bottom), actually existing at differing longitudinal locations. The outside cavity dimensions are 9.8 by 7.5 inches.

As the precise frequency of the structure is not important in this case, no provision for tuning is included; however, tuning is readily added. In addition, as the duty factor is less than 0.2% and the thermal resistance from the vanes to the outside of the structure is very low, only ambient cooling is used. Cooling channels, if needed for other applications, are bolted onto the outside of the structure. The r.f. surface current crosses only four joints, rather than up to 24 as in previous designs.

A single tool steel cutter was used to machine all four vane tips. The cutter consists of a single plate with the proper shape, rotated along its axis as shown in Figure 3. As $\rho_{11\,min} = 0.48$ cm the distance from the axis of rotation to the cutter is 0.158 inches = 0.40 cm.

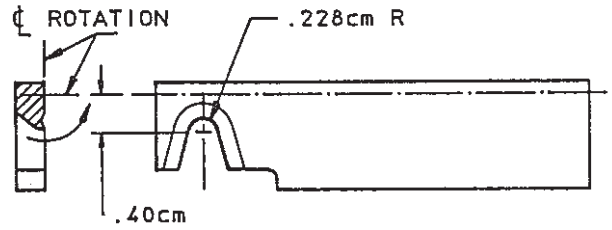


Figure 3
Tool used to cut the vane tip modulation. The small value of $\rho_{11\,min}$ of 0.48 cm requires the axis of rotation to be near the upper edge of the cutting surface.

The cavity sections were copper plated in the LBL shop. Three treatments were applied to the sections: cyanide and acid copper on the r.f. surfaces, and black anodizing on the exterior surfaces for hardness. No treatment was given to the fiducial (mating) and vacuum sealing surfaces. Three different masking operations were required, one each for the cyanide and the acid copper plating, and one for the anodizing. Several auxiliary electrodes surrounded the structure during the plating process to insure even thickness.

The copper plate consists of 0.3 mil thick cyanide strike on all r.f. surfaces, followed by 2 mil acid copper away from the vane tips. The aluminum surface is first prepared by a caustic etch followed by a hydrofluoric acid etch and a zincate surface preparation. The thickness of copper plate over aluminum cannot be measured by standard magnetic thickness gauges. The thickness away from the vane tips is not critical, and the thin cyanide strike on the tips is well controlled during the plating process.

## R.F. Characteristics

Two pairs of vane coupling rings, each near the end of the vane, and one drive loop in the physical center of the cavity are used. The measured Q is 6300, 65% of the pure copper Q. With 30 mA of beam loading, 160 kW of r.f. power is required. The measured quadrant unbalance is <2% at the rings, and about 10% in the center where the drive loop is located. The quadrupole field component varies no more than ±4% along the structure. The only electrical adjustment required after assembly is the positioning of the end walls. Temporary movable end walls were fitted during bead perturbation tests. The final end walls are then machined of 6061-T6 aluminum which is copper plated.

The high power tests were carried out by AccSys Technologies, Inc., under contract to LBL. The structure conditioned to over the 1.9 kilpatrick design gradient in 5 hours, producing X-ray emission which was stopped by an eighth inch lead shield. The r.f. amplifier uses multiple planar triodes and was designed and built by AccSys for the Boeing Aerospace cryogenic RFQ accelerator development program.

## Vacuum

Each quadrant of the RFQ is provided with a vacuum port of hexagonally packed 0.375 inch diameter holes with a center spacing of 0.435 inches in wall material 0.9 inches thick. Only one pump is fitted, directly evacuating two adjacent quadrants and pumping the two opposing quadrants through the gap and end regions. The opposing pump port is blanked off, and all four quadrants contain the same inductive perturbation at the port. An 8 inch cryopump is used for the initial test. After r.f. conditioning the base pressure is less than $10^{-7}$ Torr with the r.f. off.

The O-ring has a cubical topology which extends around the ends of the structure with segments connecting the ends extending along the mating surfaces of the vanes, as shown in Figure 4. The longitudinal segments join the end segments in "T" sections with glued joints. The assembly of the structure with the O-ring in place is straightforward and no failures have occurred over many assemblies. Using an integral O-ring, rather than enclosing the RFQ in a tank, results in a small, light and accessible structure. The outside surfaces of the RFQ provide a direct reference to the beam axis.

## Integration into Local Injector System

The RFQ will be located upstream of the switching magnet in the LEBT for the present heavy ion RFQ, sharing the LEBT with two other ion sources, as shown in Figure 1. The proton beam from a duoplasmatron source will be accelerated to 800 keV by the 410 MHz RFQ and then will be drifted through the heavy ion RFQ into the DTL tank operated in the $\beta\lambda$ mode.

During the commissioning of the heavy ion RFQ in 1983, a 400 keV proton beam was drifted through with vane voltages of 4,

12.9 and 38.1 kV, corresponding to focusing parameter $B$ values of 1.5, 4.8 and 14.1[5]. The output energy spectrum is a bimodal distribution with peaks separated by about 17 keV for $B$ = 14.1. Beam transmission was typically 50% with no great effort at optimizing the input match.

To model the drift through beam dynamics a simple simulation program was written which integrates an ensemble of particles of arbitrary input energy along the axial field of the RFQ. (Parmteq cannot be used as the equations of motion assume near synchronous energy in each cell.) Transverse motion is ignored which is acceptable as the gap defocusing term averages to zero.

Simulations with a 400 keV d.c. beam agree fairly well with the distributions measured during commissioning of the heavy ion RFQ. In the case of the 800 keV beam drifting through the heavy ion RFQ with $B$ = 2.7, the same value presently used for heavy ions, the output energy spread is ±0.2%, well within the longitudinal acceptance of the DTL.

The proton beam leaving the 410 MHz RFQ will debunch in about 1.5 meters, less than the distance to the entrance to the DTL. Any 410 MHz bunch structure is irrelevant anyway, as it is not synchronous with the second harmonic of the 200 MHz DTL. The ±0.2% energy spread introduced by the heavy ion RFQ will not cause appreciable rebunching of the beam at the DTL frequency, so the DTL acceptance is expected to be about 25%, with the overall acceptance about 10% from the ion source. This is completely adequate for our application.

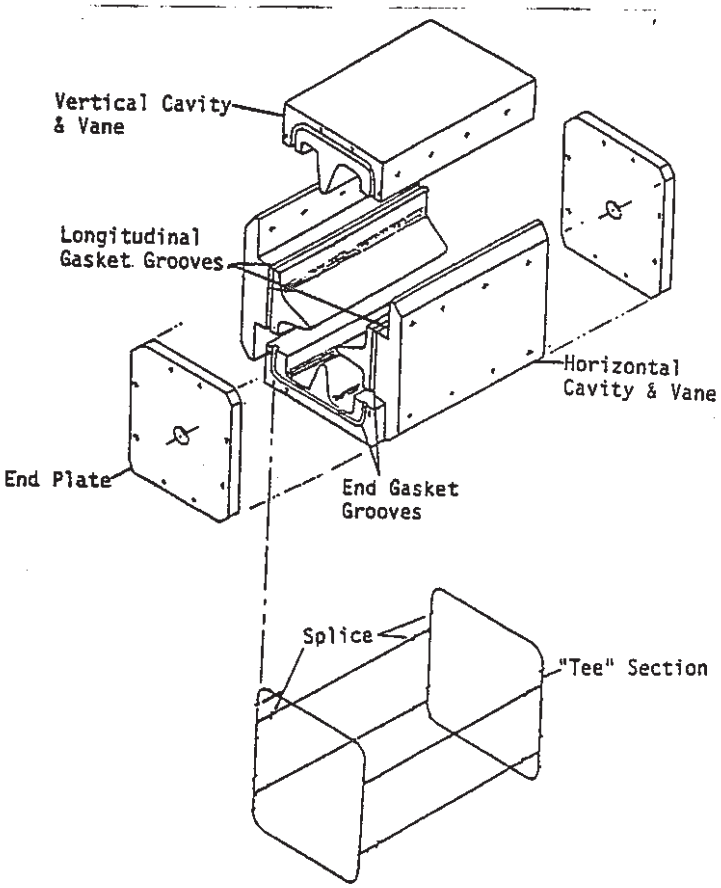


Figure 4
Exploded view of the the RFQ showing the even and odd vane pieces, the end caps and the O-ring configuration.

## Costs

The cost of producing this RFQ in aluminum are less than half the cost of a steel 4-vane RFQ using individual vanes in a cylindrical cavity. These savings are due to the simplicity and reduced number of parts, the reduced machining time, and the substantially reduced time required for assembly and alignment. Because of the self-aligning features of the basic mechanical design, the alignment tolerances are attained on the first assembly with no shimming required, and the time and effort required for this assembly is reduced by over a factor of 4. The total time required to produce an RFQ with this design is about one-half that required for a steel 4-vane structures. Furthermore, the fabrication techniques are particularly advantageous for multiple units or for large-scale production.

## Acknowledgements

Al Harcourt and Peter Sanchez did the outstanding plating job on the cavity.

## References

1. J. Staples et al, Heavy Ion Upgrade of the Bevatron Local Injector, 1984 Linear Accelerator Conference, Seeheim, 1984, p. 377.
2. H. Haseroth et al, Ion Acceleration in the CERN Linac 1, 1986 Linear Accelerator Conference, Stanford, 1986, p. 355.
3. R. A. Gough, Design of an RFQ-Based, $H^-$ Injector for the BNL/FNAL 200 MeV Proton Linacs, ibid, p. 260.
4. D. Schrage et al, A Flight-Qualified RFQ for the BEAR Project, paper M03-8, this proceedings.
5. J. Staples et al, Initial Operation of the LBL Heavy Ion RFQ, 12th International High-Energy Accelerator Conference, FNAL, 1983, p. 516.

SLAC – PUB – 4715
September 1988
(A)

# TRANSIENT ANALYSIS OF MULTICAVITY KLYSTRONS*

T. L. LAVINE, R. H. MILLER, P. L. MORTON, AND R. D. RUTH
*Stanford Linear Accelerator Center, Stanford University, Stanford, California 94309*

## ABSTRACT

We describe a model for analytic analysis of transients in multicavity klystron output power and phase. Cavities are modeled as resonant circuits, while bunching of the beam is modeled using linear space-charge wave theory. Our analysis has been implemented in a computer program which we use in designing multicavity klystrons with stable output power and phase. We present as examples transient analyses of a relativistic klystron using a magnetic pulse compression modulator, and of a conventional klystron designed to use phase shifting techniques for RF pulse compression.

## INTRODUCTION

Large linear electron colliders require high power short pulsed RF sources in order to attain accelerating gradients of 100–200 MV/m. Two techniques being developed to supply this RF are relativistic klystrons with modulators using magnetic pulse compression, and conventional klystrons using phase shifting techniques for RF pulse compression. The RF power and frequency range being explored is 100–500 MW at 11–17 GHz. The RF output pulse length desired is 50–100 nsec, making the transient behavior of the multicavity klystrons employed in both approaches important. This paper describes a model for analytic analysis of transients in multicavity klystron output power and phase. Cavities are modeled as resonant circuits, while bunching of the beam is modeled using linear space-charge wave theory. The model has been implemented in a computer program which is used in designing multicavity klystrons with stable output power and phase.

## RF CAVITIES

Each beam loaded klystron cavity is modeled as a parallel network of cavity and beam loading impedances as shown in Fig. 1. External resistance $R_e$ includes additional resistive loading by iris-coupled waveguides. The RF driver connected to the input cavity typically consists of a power source, isolator, waveguide, and coupling iris. The driver is modeled as a generator of alternating current $I_g = \hat{I}_g e^{i\omega t}$ with shunt resistance $R_e$ attached to the beam loaded input cavity (Fig. 1). Downstream cavities are driven by the bunched beam current.

The RF voltage on a cavity is $V(t) = \hat{V}(t)e^{i\omega t}$ where $\hat{V}(t)$ is the transient modulation of the RF oscillation $e^{i\omega t}$. The transient behavior of $V(t)$ is calculated from the circuit equation

$$\frac{d^2}{dt^2}CV + \frac{d}{dt}\frac{V}{R} + \frac{V}{L} = \dot{I}$$

which can be rewritten as

$$\ddot{V} + \left(\frac{1}{RC} + 2\frac{\dot{C}}{C}\right)\dot{V} + \left(\frac{1}{LC} - \frac{1}{RC}\frac{\dot{R}}{R} + \frac{\ddot{C}}{C}\right)V = \frac{\dot{I}}{C} \qquad (1)$$

where $L$, $R$, and $C$ are the beam loaded cavity inductance, resistance, and capacitance, respectively. $L$, $R$, and $C$ may be time dependent due to resistive and reactive loading of the cavity by beam pulses with finite risetime. The current $I$ flowing in the circuit model is the sum of generator current $I_g$ for the input cavity, RF beam current $I_1$ for intermediate and output cavities, and DC beam current $I_0$ for all cavities. Time dependence of $I_g$ (for the input cavity) is $e^{i\omega t}$ where $\omega$ is the RF angular frequency. Time dependence of $I_1$ (for intermediate and output cavities) is $\hat{I}_1(t)e^{i\omega t}$ where $\hat{I}_1(t)$ is the transient modulation of the RF oscillation $e^{i\omega t}$. Time dependence of $I_0$ is due to finite risetime.

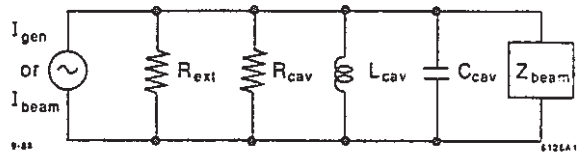


FIG. 1. Each beam loaded klystron cavity is modeled as a parallel network of cavity and beam impedances. External resistance includes additional resistive loading by iris coupled waveguides. The input cavity is driven by an RF generator current. Downstream cavities are driven by the bunched beam current.

The lumped circuit elements in Eq. (1) can be expressed in terms of measurable quantities through the definitions

$$\omega_r{}^2 = \frac{1}{LC}, \quad Q = \omega_r \frac{\frac{1}{2}CV^2}{\frac{1}{2}V^2/R} = \omega_r RC, \quad \tau = \frac{2Q}{\omega_r} = 2RC \qquad (2)$$

where $R/Q$ is constant. Inserting definitions (2) into Eq. (1) gives

$$\ddot{V} + 2\left(\frac{1}{\tau} - \frac{\dot{\omega}_r}{\omega_r}\right)\dot{V} + \left[\omega_r{}^2 - \frac{2}{\tau}\left(\frac{\dot{\tau}}{\tau} + \frac{\dot{\omega}_r}{\omega_r} + 2\frac{\dot{\omega_r}{}^2}{\omega_r{}^2} - \frac{\ddot{\omega}_r}{\omega_r}\right)\right]V = \omega_r \frac{R}{Q}\dot{I} \qquad (3)$$

which we solve for the transient behavior of $V(t)$.

The total quality factor $Q$ for resistive beam loading of the cavity is composed of contributions from cavity walls ($Q_0$), from beam loading ($Q_b$), and from coupling to external waveguides ($Q_e$). Total $Q$ is given by

$$Q = (Q_0^{-1} + Q_b^{-1} + Q_e^{-1})^{-1} \quad .$$

Beam loading $Q_b$ is related to the beam parameters by

$$Q_b = \gamma_0(\gamma_0{}^2 - 1)K_1/I_0 \qquad (4)$$

where $K_1$ depends on the spatial distribution of the beam. $\gamma_0 = 1 + eV_0/m_e c^2$, and $V_0$ is the accelerating voltage. The resonance angular frequency of the cavity is

$$\omega_r = \omega_0 + \delta$$

where $\omega_0$ is the resonance frequency without beam, and $\delta$ is the detuning by reactive beam loading. The detuning is related to beam parameters by

$$\omega_0/2\delta = \gamma_0(\gamma_0{}^2 - 1)K_2/I_0 \qquad (5)$$

where $K_2$ depends on the spatial distribution of the beam. Time dependence of $Q_b$ and $\delta$ results from finite risetime of the beam current $I_0$ and of the beam energy $\gamma_0 m_e c^2$ in Eqs. (4) and (5).

* Work supported by the Department of Energy under contract DE–AC03–76SF00515.

*Presented at the Linear Accelerator Conference, Williamsburg, Virginia, October 3–7, 1988*

### Initial Conditions

Velocity modulation is initiated by an external RF driver coupled by a waveguide to the klystron input cavity. The driver in general is not matched perfectly to the input cavity impedance which is time dependent due to the transient beam loading. If the driver is switched on long before the beam enters the input cavity, the input cavity voltage builds up to an asymptotic value which can be determined from the available drive power and the impedance mismatch as follows: The driver is modeled as a generator of alternating current $I_g = \hat{I}_g e^{i\omega t}$ with shunt resistance $R_e = (R/Q)Q_e$ attached to the beam loaded input cavity (Fig. 1). The beam loaded input cavity has impedance

$$Z_L = (R/Q)[{Q_0}^{-1} + {Q_b}^{-1} + i(\omega/\omega_r - \omega_r/\omega)]^{-1} \quad .$$

The fraction of available drive power that enters the input cavity is $1 - |\Gamma|^2$ where $\Gamma = (Z_L - R_e)/(Z_L + R_e)$ is the voltage wave reflection coefficient. The asymptotic peak voltage on the input cavity produced by available rms drive power $P$ has the same phase (relative to $\hat{I}_g$) as the total impedance through which $I_g$ flows. The total impedance is $Z_T = ({Z_L}^{-1} + {R_e}^{-1})^{-1}$. The phase of the asymptotic peak voltage on the input cavity produced by the generator then is

$$\phi = \tan^{-1}\frac{\mathrm{Im}Z_T}{\mathrm{Re}Z_T} = \tan^{-1}\frac{-(\omega/\omega_r - \omega_r/\omega)}{1/Q_0 + 1/Q_b + 1/Q_e} \quad .$$

The asymptotic peak voltage on the input cavity then is

$$V_d = \sqrt{2P(1-|\Gamma|^2)(R/Q)(Q_0^{-1} + Q_b^{-1})^{-1}}\, e^{i\phi} \quad .$$

Assuming the fields produced in the input cavity by the RF generator have reached equilibrium before the beam turns on, the voltage $V(t)$ on the input cavity at $t = 0$ just before the beam enters is $V(0) = V_d$ and $\dot{V}(0) = i\omega V_d$.

Alternatively, the transient due to switching on the generator is analyzed using the input cavity initial condition $V(0) = \dot{V}(0) = 0$.

Each downstream cavity is driven only by the beam and has $V = 0$ and $\dot{V} = 0$ before the beam enters.

### Driving Term

The rate of change in current $\dot{I}$ that drives the voltage on a cavity appears on the right side of Eq. (3). For the input cavity, which is driven by $I_g$ and by the risetime of $I_0$, $\dot{I} = i\omega I_g + \dot{I}_0$. Maximum rms drive power $P$ is transferred when the input cavity is matched to the driver. In this case, $P = \frac{1}{2}(\frac{1}{2}I_g)^2 R_e$ so $I_g = \sqrt{8P/R_e}$. For the intermediate and output cavities, which are driven by $I_1$ and by the risetime of $I_0$, $\dot{I} = i\omega I_1 + \dot{I}_0$. Calculation of $I_1$ from linear space-charge wave theory is discussed below.

## LINEAR SPACE-CHARGE WAVE THEORY OF BUNCHING

Bunching of the beam is modeled by linear space-charge wave theory. The transient cavity voltage $\dot{V}(t)e^{i\omega t}$ modulates the velocity of the beam. Longitudinal space-charge forces then produce space-charge waves which bunch the beam downstream.

### Space-Charge Force

The space-charge potential of a long bunch of charge density $\rho$ and radius $a$ in a beam tube of radius $b$ is

$$V(r < a < b) = -\frac{\rho a^2}{4\epsilon_0}\left(1 + 2\ln\frac{b}{a} - \frac{r^2}{a^2}\right)$$

assuming the longitudinal dimension ($z$) of the bunch is long compared to the radial dimension ($r$) so that end effects can be neglected. The longitudinal space-charge force in the frame moving with the beam at velocity $v_0 = \beta_0 c$ is

$$F_z(r) = -e\frac{\partial V(r)}{\partial z} = \frac{ea^2}{4\epsilon_0{\gamma_0}^2}\left(1 + 2\ln\frac{b}{a} - \frac{r^2}{a^2}\right)\frac{\partial \rho}{\partial z} \qquad (6)$$

where $\gamma_0 = (1 - {\beta_0}^2)^{-1/2}$. Note that when averaged over a uniform radial current distribution

$$\langle F_z \rangle = \frac{\int_0^a F_z(r)\, r\, dr}{\int_0^a r\, dr} = \frac{1}{2}\left[\frac{1 + 4\ln(b/a)}{1 + 2\ln(b/a)}\right] F_z(0). \qquad (7)$$

### Wave Equation

The longitudinal space-charge force produces space-charge waves on the beam. The space-charge wave equation can be derived from the linearized continuity equation in the coordinate frame moving with the beam at velocity $v_0$ with respect to the klystron,

$$\rho_0 \partial v_1/\partial z = -\partial \rho_1/\partial t \quad , \qquad (8)$$

where the charge density $\rho$ and the velocity $v$ are both sums of a constant term and a small modulation: $\rho(z,t) = \rho_0 + \rho_1(z,t)$ and $v(z,t) = v_0 + v_1(z,t)$. In the beam frame, the beam velocity is $v_1(z,t)$.

For small velocity modulation, $v_1 = c(\gamma - \gamma_0)/\beta_0{\gamma_0}^3$ where $\gamma = (1 - \beta^2)^{1/2}$. The acceleration is

$$\dot{v}_1 = \dot{\gamma} c/\beta_0{\gamma_0}^3 = F_z(r)/m{\gamma_0}^3 \qquad (9)$$

because $\dot{\gamma} = F_z \beta_0 c/m_e c^2$. Substituting $\dot{v}_1$ from Eq. (9) into the time derivative of Eq. (8) and using $F_z$ from Eq. (6), gives the wave equation

$$\frac{\partial^2 \rho_1}{\partial z^2} = \frac{1}{{v_\phi}^2}\frac{\partial^2 \rho_1}{\partial t^2}$$

where the phase velocity $v_\phi$ of space-charge waves is given by

$$\left(\frac{v_\phi}{c}\right)^2 = \frac{I_0}{17\,\mathrm{kA}}\frac{1}{\beta_0{\gamma_0}^5}\left(1 + 2\ln\frac{b}{a} - \frac{r^2}{a^2}\right) \quad . \qquad (10)$$

The beam current is $I_0 = \rho_0 \beta_0 c \pi a^2$.

### Space-Charge Wavelength

Space-charge wavenumber and wavelength are computed from the phase velocity (10) by averaging, as in Eq. (7), over a uniform radial beam current distribution. The average space-charge wavenumber is

$$\begin{aligned}\langle k_p \rangle &= \omega \langle v_\phi \rangle / {v_0}^2 \\ &= \frac{2}{3}\left[(1+g)^{3/2} - g^{3/2}\right]\left[\frac{I_0}{17\,\mathrm{kA}}\frac{1}{(\beta_0\gamma_0)^5}\right]^{1/2}\frac{\omega}{c}\end{aligned} \qquad (11)$$

where $g = 2\ln(b/a)$. The average space-charge wavelength is

$$\begin{aligned}\langle \lambda_p \rangle &= \frac{2\pi {v_0}^2}{\omega}\left\langle \frac{1}{v_\phi} \right\rangle \\ &= 2\left[(1+g)^{1/2} - g^{1/2}\right]\left[\frac{17\,\mathrm{kA}}{I_0(t)}(\beta_0\gamma_0)^5\right]^{1/2}\frac{2\pi c}{\omega} \quad .\end{aligned} \qquad (12)$$

For beam energy $eV_0 = (\gamma_0 - 1)m_e c^2 = 1.2\,\mathrm{MeV}$, current $I_0 = 1\,\mathrm{kA}$, and filling factor $a/b = 0.7$, the space-charge wavelength calculated from Eq. (12) is $\langle \lambda_p \rangle = 184\,\mathrm{cm}$, in good agreement with simulations by the electromagnetic particle-in-cell code, Mask.[1]

### RF Current

Velocity modulation by a cavity produces RF modulation of the beam current downstream. We approximate each klystron cavity as a narrow gap with voltage $\dot{V}(t)e^{i\omega t}$. After drifting a distance $d$, the beam develops an RF current given in the linear approximation by

$$\hat{I}_1(t) = -\frac{4\pi i V(t)}{Z_0}\sqrt{\frac{I_0(t)}{17\,\mathrm{kA}}\frac{1}{(1+g)\beta\gamma}}\sin(\langle k_p \rangle d)\, e^{i\omega d/\beta c} \qquad (13)$$

where $Z_0 = 377\Omega$ and $\langle k_p \rangle$ is computed from Eq. (11).

In the drift downstream from a cavity, space-charge waves evolve on the beam according to Eq. (13) with boundary conditions given by the cavity voltage. Bunching evolves on the scale of $\lambda_p/4$. In klystron designs, intercavity spacings are somewhat less than $\lambda_p/4$, making the overall lengths of klystrons scale with $\lambda_p$ times the number of cavities.

## MULTICAVITY KLYSTRONS

The transient calculation for a multicavity klystron is outlined in Fig. 2. For each cavity in sequence from input to output, the time dependent RF cavity voltage produced by the RF generator (for the input cavity) or the bunched beam (for the intermediate and output cavities) is calculated from Eq. (3) using the appropriate initial condition and driving term as discussed above. The voltage solution is used to compute from Eq. (13) the resulting RF modulation of the beam current at the downstream cavities. The RF current used to drive each cavity in the calculation is the phasor sum of RF currents from all cavities upstream. The output RF power is computed from the output cavity RF voltage as $|V(t)|^2/2R_e$. The output RF phase relative to the RF generator is $\tan^{-1}(\mathrm{Im}V(t)/\mathrm{Re}V(t))$.

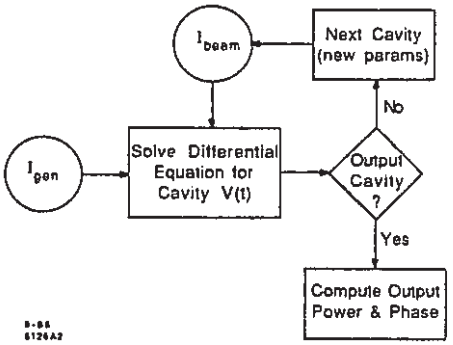


FIG. 2. Flowchart for klystron transient calculations.

## EXAMPLES

Relativistic klystrons under development at the Stanford Linear Accelerator Center (SLAC) and Lawrence Livermore National Laboratory (LLNL) are designed to extract hundreds of megawatts of RF power at 11.4 GHz from electron beam pulses of 1 kA current, 1 MeV kinetic energy, and 50 nsec duration.[2] These beams are produced by a linear induction accelerator driven by modulators using magnetic pulse compression at LLNL. One relativistic klystron, known as SL4,[2] is a six cavity tube designed to operate at 11.4 GHz with 1 kA beam current and 1.2 MV beam kinetic energy. Figure 3 shows our analysis of transients in klystron output power and phase due to a pulsed relativistic beam entering the SL4 klystron after the fields produced in the input cavity by the RF generator have reached equilibrium.

Phase shifting techniques for RF pulse compression are under development at the SLAC.[3] A 100 MW conventional klystron at 11.424 GHz has been designed for use in these experiments.[4] Figure 4 shows our analysis of the transients due to switching on the RF generator in the presence of a DC beam, and then due to reversing the generator phase after the switch-on transient has subsided.

## SUMMARY

We have described a model for analytic linear analysis of transients in multicavity klystron output power and phase. We have presented as examples our transient analyses of two multicavity klystrons designed for applications in which fast risetime and stable output power and phase are important.

## ACKNOWLEDGEMENTS

We thank K. R. Eppley, Z. D. Farkas, W. R. Fowkes, W. E. Gabella, W. B. Herrmannsfeldt, T. G. Lee, A. E. Vlieks, P. B. Wilson, and S. S. Yu for interesting and useful discussions.

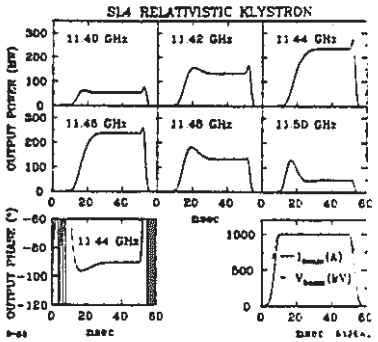


FIG. 3. Transient analysis of SL4, an 11.4 GHz six-cavity relativistic klystron. In this linear calculation, the fields produced in the input cavity by the RF generator have reached equilibrium before the beam turns on. The klystron cavity frequencies without beam are tuned to 0, 31, 23, 45, 425, and 6 MHz, respectively, above 11424 MHz. The pulsed beam detunes the cavities by 25 MHz and loads them with $Q_{beam} = 230$ when beam current and voltage are at their maximum values, 1 kA and 1 MV. The gain cavities are loaded externally with $Q_e = 120$ for faster risetime. Input $Q_e = 300$. Output $Q_e = 20$. For the six cavities, $R/Q = 27$, 27, 27, 27, 60, and 51Ω, respectively. Intercavity spacings are 28, 14, 21, 21, and 14 cm.

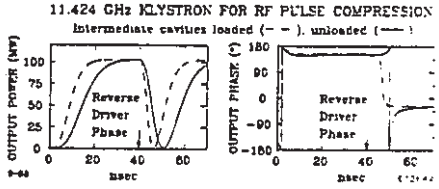


FIG. 4. Transient analysis of a 100 MW, 11.424 GHz five-cavity conventional klystron design for RF pulse compression. In this linear calculation, the RF generator is switched on at 0 nsec in the presence of a DC beam. The generator phase is reversed at 40 nsec, after the switch-on transient has subsided. Dashed curves show that improved risetime is obtained by adding external loads with $Q_e = 150$ to the gain cavities. Input $Q_e = 190$. Output $Q_e = 26$. The klystron cavity frequencies without beam are tuned to 21, 18, 40, 500, and 20 MHz, respectively, above 11424 MHz. The DC, 511 A, 440 kV beam detunes the cavities by −21 MHz and loads them with $Q_b = 210$. For the five cavities, $R/Q = 36$, 36, 36, 39, and 20Ω, respectively. Intercavity spacings are 6, 6, 8, 3 cm.

## REFERENCES

1. K. R. Eppley, private communication.
2. M. A. Allen *et al.* (SLAC-LBL-LLNL Relativistic Klystron Collaboration), "Relativistic Klystrons for Linear Colliders" (SLAC-PUB-4733, September 1988), presented by Roger H. Miller at this conference; and "Relativistic Klystron Research for High Gradient Accelerators" (SLAC-PUB-4650, June 1988), in the proceedings of the European Particle Accelerator Conference, Rome, Italy, June 7–11, 1988.
3. Z. D. Farkas, "Binary Peak Power Multiplier and its Application to Linear Accelerator Design," *IEEE Trans. MTT-34*, 1036 (1986).
4. T. G. Lee, private communication.

September 1988
(A)

# BEAM DETERMINATION OF QUADRUPOLE MISALIGNMENTS AND BEAM POSITION MONITOR BIASES IN THE SLC LINAC*

T. L. LAVINE, J. T. SEEMAN, W. B. ATWOOD, T. M. HIMEL, AND A. PETERSEN†

*Stanford Linear Accelerator Center, Stanford University, Stanford, California 94309*

C. E. ADOLPHSEN

*University of California at Santa Cruz, Santa Cruz, California 95064*

## ABSTRACT

Misalignments of magnetic quadrupoles and biases in beam position monitors (BPMs) in the Stanford Linear Collider (SLC) linac can lead to a situation in which the beam is off-center in the disk-loaded waveguide accelerator structure. The off-center beam produces wakefields which can limit SLC performance by causing unacceptably large emittance growth. We present a general method for determining quadrupole misalignments and BPM biases in the SLC linac by using beam trajectory measurements. The method utilizes both electron and positron beams on opposite RF cycles in the same linac lattice to determine simultaneously magnetic quadrupole misalignments and BPM biases. The two-beam trajectory data may be acquired without interrupting SLC colliding beam operations.

## INTRODUCTION

The lattice of the SLC linac in the region traversed by both electron and positron beams consists of many sets of quadrupole magnets for focusing, dipole magnets for steering correction, and stripline BPMs for measuring both horizontal and vertical beam positions.[1] In each set the BPM is mounted in the bore of the quadrupole and these elements are positioned 35–65 cm upstream from the dipole. The sets are separated from one another by spaces of between three and 12 meters containing RF sections. Misalignments of quadrupoles relative to the beam trajectories steer the beams. The BPMs are used to measure the trajectories and dipoles are used to correct the steering. The quadrupole misalignments and biases in the BPMs (due to both electronics and BPM misalignment) can lead to a situation in which the beam is off-center in the disk-loaded waveguide accelerator structure. The off-center beam produces wakefields which can limit SLC performance by causing unacceptably large emittance growth and beam breakup at currents below the design value. In the past, an optical system has been used to align the linac quadrupoles to high precision.[2] Beam-based surveying techniques such as the one described here provide a complimentary alignment tool which we are using to improve the mechanical alignment of the SLC linac.

## THEORY

Figure 1 illustrates schematically a linac lattice segment containing a biased BPM and a misaligned quadrupole. Beam transport equations in a lattice with quadrupole misalignments and BPM biases can be formulated using the following definitions. We denote by $0, \ldots, N+1$ the $N+2$ sets of BPMs, quadrupoles, and dipoles in a linac lattice segment. The accelerator axis is defined to pass through the centers of the endpoint BPMs (0 and $N+1$). For either transverse coordinate (labeled $x$) let

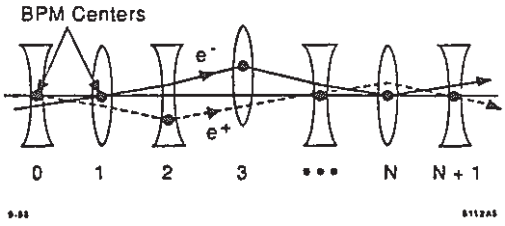


FIG. 1. Linac lattice containing a biased BPM (2) and a misaligned quadrupole (3). The electron and positron beams have been steered using correctors near each quadrupole to minimize the BPM measurements.

$d_i$ = misalignment of $i$th quadrupole relative to the axis

$b_i$ = bias of $i$th BPM relative to center of $i$th quadrupole

$m_i^{\pm}$ = measured displacement of the $e^{\pm}$ bunch at $i$th BPM

$x_i^{\pm}$ = $e^{\pm}$ trajectory displacement off axis at $i$th quadrupole

$\theta_i^{\pm}$ = $e^{\pm}$ trajectory slope relative to axis at $i$th quadrupole

$l_i$ = drift length preceding the $i$th quadrupole

$D_i$ = integrated kick angle of the $i$th dipole

($D > 0$ kicks $e^-$ in the direction of increasing $x$)

$Q_i$ = integrated gradient of the $i$th quadrupole

($Q > 0$ focuses $e^-$ in the horizontal plane)

Trajectory displacement off axis at a quadrupole is $d + b + m$ as shown in Fig. 2. The integrated dipole kicks $D_i$ and quadrupole gradients $Q_i$ are inversely proportional to the beam momentum. which is modified at each RF section of the linac.

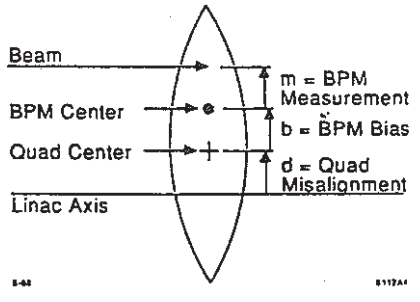


FIG. 2. Trajectory displacement off axis at a quadrupole is $d + b + m$.

In the approximation that all lenses are thin and that the BPM, quadrupole, and dipole of each set are superimposed at the same axial position, the beam transport equations are

* Work supported by the Department of Energy under contracts DE-AC03-76SF00515 and DE-AA03-76SF00010.

† Present address: SCS, Hamburg, Federal Republic of Germany.

*Presented at the 1988 Linear Accelerator Conference (LINAC '88), Williamsburg, Virginia, October 2–7, 1988*

$$
\begin{aligned}
x_i^{\pm} &= m_i^{\pm}, \quad i = 0 \text{ and } N+1, \\
x_i^{\pm} - b_i - d_i &= m_i^{\pm}, \quad i = 1, \ldots, N, \\
\theta_i^{\pm} - \theta_{i-1}^{\pm} \mp (x_i^{\pm} - d_i)Q_i &= \mp D_i, \quad i = 1, \ldots, N, \\
x_i^{\pm} - x_{i-1}^{\pm} - l_i\theta_{i-1}^{\pm} &= 0, \quad i = 1, \ldots, N+1.
\end{aligned} \tag{1}
$$

These equations can be rewritten in matrix form as

$$
\begin{pmatrix}
A_{1,1} & \cdots & A_{1,6N+6} \\
 & & \\
 & & \\
 & & \\
 & & \\
 & & \\
 & & \\
 & & \\
 & & \\
 & & \\
A_{6N+6,1} & \cdots & A_{6N+6,6N+6}
\end{pmatrix}
\begin{pmatrix} d_1 \\ \vdots \\ d_N \\ b_1 \\ \vdots \\ b_N \\ x_0^+ \\ \vdots \\ x_{N+1}^- \\ \theta_0^+ \\ \vdots \\ \theta_N^- \end{pmatrix}
=
\begin{pmatrix} m_0^+ \\ \vdots \\ m_{N+1}^+ \\ m_0^- \\ \vdots \\ m_{N+1}^- \\ D_1 \\ \vdots \\ D_N \\ 0 \\ \vdots \\ 0 \end{pmatrix} \tag{2}
$$

where $A$ matrix elements are the coefficients of the $d_i$, $b_i$, $x_i$, and $\theta_i$ in Eq. (1). These $6N+6$ equations may be solved for the quadrupole misalignments ($d_1, \ldots, d_N$), BPM biases ($b_1, \ldots, b_N$), trajectory displacements ($x_0^{\pm}, \ldots, x_{N+1}^{\pm}$), and trajectory slopes ($\theta_0^{\pm}, \ldots, \theta_N^{\pm}$). Calculated values of $d_i$, $b_i$, $x_i$, and $\theta_i$ at any lattice point $i$ are linear combinations of BPM measurements and dipole kicks. Schematically, the solution for the $j$th unknown in the column vector on the left side of Eq. (2) is

$$
\sum_{k=1}^{N+2} A_{jk}^{-1} m_k^+ + \sum_{k=N+3}^{2N+4} A_{jk}^{-1} m_k^- + \sum_{k=2N+5}^{3N+4} A_{jk}^{-1} D_k \, .
$$

The square of the statistical error in the calculated value of the $j$th unknown therefore is approximately

$$
\sum_{k=1}^{2N+4} (A_{jk}^{-1})^2 \sigma^2 \tag{3}
$$

where $A_{jk}^{-1}$ is the $k$th element of the $j$th row of the inverse of matrix $A$ in Eq. (2) and $\sigma$ is the BPM resolution, which typically is 50 $\mu$m for single-pulse measurements and can be reduced by averaging measurements made on several consecutive pulses. Uncertainties in the dipole kicks $D_k$ and in the quadrupole gradients $Q_k$ are neglected in Eq. (3) because their effect is small compared to the BPM resolution.

## ANALYSIS

A computer program has been written to implement the two-beam method. The program acquires BPM measurements $m_i^{\pm}$, quadrupole gradients $Q_i$, and dipole kicks $D_i$ from previously acquired data files, solves Eq. (2) numerically, and computes statistical errors using Eq. (3). The program may be applied to any segment of the SLC linac for which BPM measurements exist for electrons and positrons at all $N$ quadrupoles and at both endpoints.

The precision of the two-beam method as an alignment tool depends on statistical and systematic errors. Statistical errors have been studied by applying the method to segments of varying length at different regions of the SLC linac. Systematic errors have been studied by testing the reproducibility of the method for different endpoints and different beam trajectories. These studies are described below.

The statistical error of a calculated quadrupole misalignment $d$, calculated using Eq. (3), grows with the number of quadrupoles $N$. We observe that the error in the calculated $d_i$ values in the segment range from a maximum of $\Delta d_i \approx N^{3/2}\sigma$ near the center of the segment to a minimum of $\Delta d_i \approx N^{1/2}\sigma$ near the endpoints. The error in a calculated BPM bias $b$ is $\Delta b \approx 2\sigma$, independent of $N$.

Systematic errors result from the assumption that the endpoint BPMs (0 and $N+1$) define the accelerator axis. The effect of these systematic errors can be observed in the sensitivity of the calculated misalignments to the particular choice of endpoints. Each quadrupole misalignment $d_j$ is related to all BPM measurements $m_k^{\pm}$ ($k = 0, \ldots, N+1$) because all the $A^{-1}$ matrix elements relating $d_j$ to $m_k^{\pm}$ are non-zero. Therefore, calculated quadrupole misalignments are sensitive to the particular choice of endpoints and to $N$. In contrast, each BPM bias $b_j$ is determined only from measurements $m_j^{\pm}$ by that BPM, and by measurements $m_{j\pm1}^{\pm}$ by its immediate neighbors, because the $A^{-1}$ matrix elements relating $b_j$ to all non-neighboring BPM measurements are zero. Therefore, calculated BPM biases are insensitive to the endpoints and to $N$.

Additional systematic errors result from energy errors, from transverse RF kicks, and from the BPM readout electronics which permits BPM biases to be different for electrons than for positrons. From the data, we can check the magnitude of these systematic effects.

The magnitude of systematic effects have been checked by calculating quadrupole misalignments and BPM biases separately for two overlapping sets of 16 quadrupoles each, with eight quadrupoles in the overlap region. One set of calculated quadrupole misalignments in the overlap region, $d_i(1)$, and the differences between the two sets, $d_i(1) - d_i(2)$, are shown in Fig. 3. The distribution of differences is approximately 200 $\mu$m wide, consistent with the statistical variation expected due to the BPM resolution. The variation between sets expected for each $d_i$ is

$$
\Delta\big(d_i(1) - d_i(2)\big)^2 = \Delta d_i(1)^2 + \Delta d_i(2)^2 - 2\sum_{j'} A_{ij'}^{-1}(1) A_{ij'}^{-1}(2)\sigma^2
$$

where $\Delta d_i(1)$ and $\Delta d_i(2)$ are calculated using Eq. (3), and the $j'$ sum includes only coefficients of BPM measurements in the overlap region where the same BPM data are used in both analyses. The calculated BPM biases $b_i$, also shown in Fig. 3, are identical in both sets, consistent with the fact that the calculation of $b_i$ involves only measurements by the associated BPM and its immediate neighbors.

Another check of the magnitude of systematic effects has been performed by calculating quadrupole misalignments and BPM biases separately for two different two-beam trajectories recorded at different times through the same set of eight quadrupoles. One set of calculated quadrupole misalignments and BPM biases, $d_i(1)$ and $b_i(1)$, and the differences between the two sets, $d_i(1) - d_i(2)$ and $b_i(1) - b_i(2)$, are shown in Fig. 4. The distributions of differences in Fig. 4 are approximately 200 $\mu$m wide, consistent with the statistical variation expected due to the BPM resolution. The variation between sets expected for each $d_i$ is

$$
\Delta\big(d_i(1) - d_i(2)\big)^2 = \Delta d_i(1)^2 + \Delta d_i(2)^2 \tag{4}
$$

where $\Delta d_i(1)$ and $\Delta d_i(2)$ are calculated using Eq. (3), and no correlation terms are present because the two trajectories have independent BPM measurements. The variation between sets expected for each $b_i$ is expressed as in Eq. (4) with $d$ replaced by $b$.

Figure 5 shows the distribution of quadrupole misalignments and BPM biases calculated in the horizontal and vertical planes of SLC Linac Sector 27.

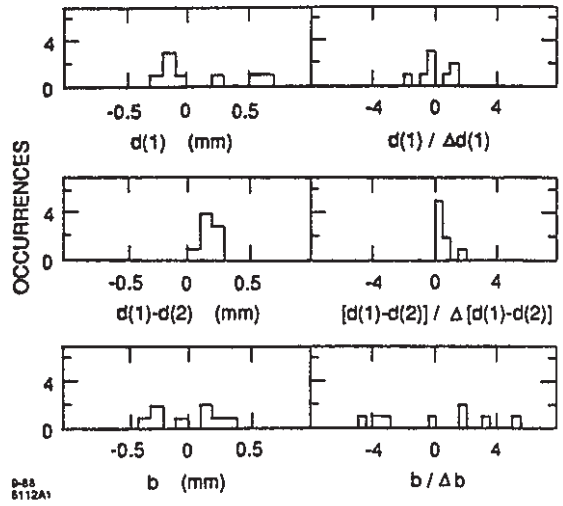


FIG. 3. Quadrupole misalignments $d$ and BPM biases $b$ calculated for eight quadrupoles in the overlap region between two overlapping sets, (1) and (2), of 16 quadrupoles each. The data plotted are from the vertical plane of SLC Linac Sector 2.

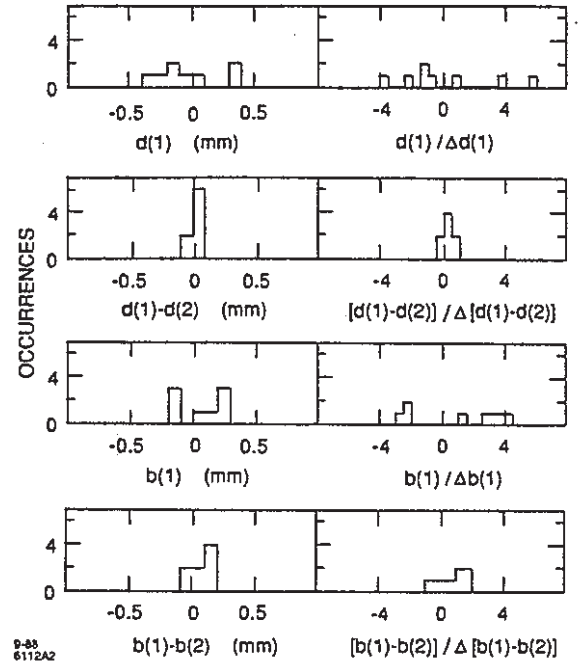


FIG. 4. Quadrupole misalignments $d$ and BPM biases $b$ calculated from two different two-beam trajectories, (1) and (2), through the same eight quadrupoles in the vertical plane of SLC Linac Sector 2.

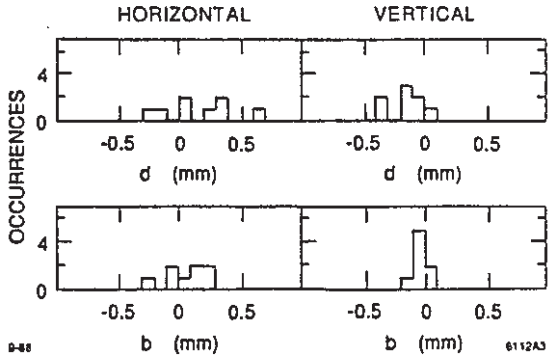


FIG. 5. Quadrupole misalignments $d$ and BPM biases $b$ calculated in SLC Linac Sector 27.

## CONCLUSION

Figures 3–5 demonstrate that the two-beam method as described is not sensitive to systematic errors in quadrupole misalignments and BPM biases at approximately the 200 $\mu$m level. We have calculated some misalignments significantly greater than this level and are using this information to improve the mechanical alignment of the SLC linac.

The sensitivity of the method can be improved by reducing the BPM measurement resolution by averaging measurements over many beam pulses. The two-beam method may be improved to include two biases for each BPM, different for electrons than for positrons due to differences between different BPM electronics channels. This modification requires additional constraints which may be obtained by introducing a third trajectory measurement for an electron beam coasting without focusing or steering correction. This three-beam modification interferes with normal accelerator operations, but may provide a better measure of quadrupole misalignments than the two-beam method by modeling BPM biases more realistically.

## ACKNOWLEDGEMENTS

We thank J. C. Sheppard, M. J. Lee, and T. S. Mattison for interesting and useful discussions.

## REFERENCES

1. J. T. Seeman and J. C. Sheppard, *Special SLC Linac Developments* (SLAC-PUB-3944, April 1986), published in *Proceedings of the Linear Accelerator Conference*, Stanford, California, June 2-6, 1986 (SLAC Report 303, September 1986), p. 214.
2. W. B. Herrmannsfeldt *et al.*, *Precision Alignment Using a System of Large Rectangular Fresnel Lenses*, *Appl. Opt.* 7, 995 (1968).

SLAC - PUB - 4722
September 1988
(A)

# THE ROLES OF FREQUENCY AND APERTURE IN LINAC ACCELERATOR DESIGN*

Z. D. FARKAS
*Stanford Linear Accelerator Center, Stanford University, Stanford, CA 94309*

## ABSTRACT

Expressions for accelerating structure parameters, including those that determine the peak and average power inputs required to attain a given gradient, are given as functions of aperture to wavelength ratio for a $2\pi/3$ mode disk-loaded guide. The value of the wavelength to aperture ratio varies over a large range, corresponding to group velocities that vary from nearly zero to nearly the speed of light. The parameters exhibit proper asymptotic behavior in both limits. These parameters are benchmark values to which parameters for other modes and for other structure shapes can be compared. For example, it will be shown that the increased peak surface field to accelerating field ratio due to increased aperture to wavelength ratio can be reduced by shaping the iris profile. Structure shapes are varied not only to show possible improvement of structure parameters, but also to improve ease of mechanical fabrication and temperature control.

## ACCELERATING STRUCTURE LOCAL PARAMETERS

In this section the local accelerating structure parmeters are defined and then expressed in terms of aperture to wavelength ratio, $a_\lambda \equiv a/\lambda$: Assume a SLAC-type $2\pi/3$ mode disk-loaded structure with an aperture $a$, cavity radius $b$ at operating wavelength $\lambda$. Define the structure parameters that depend only on $a_\lambda$:

$$\beta_g = \frac{v_g}{c} = \frac{P_t/w}{c}\,, \qquad b_a = \frac{b}{a}\,, \qquad E_{rl} = \frac{E_p}{E}\,. \tag{1}$$

Here $v_g$ is the group velocity, $P_t$ the power flow, $w$ the energy stored per unit length, $E_p$ the local peak surface field, and $E$ is the local accelerating gradient.

Define structure parameters that also depend on wavelength:

$$s = \frac{E^2}{w}\,, \qquad z_s = \frac{E^2}{P_t} = \frac{s}{v_g}\,,$$

$$T_0 = \frac{2w}{p_d} = \frac{Q}{\pi f}\,, \qquad r = \frac{E^2}{p_d} = \frac{sT_0}{2}\,. \tag{2}$$

Here $s$ is the elastance per unit length, $z_s$ is the serial impedance, $T_0$ the attenuation time, $p_d$ the power dissipated per unit length, and $r$ is the shunt resistance per unit length. Multiplying by the appropriate power of wavelength yields the wavelength independent shunt reactance, serial impedance, and attenuation time are:

$$x_l \equiv \frac{s\lambda}{\omega} \equiv \frac{r}{Q}\lambda \equiv x_l\lambda \equiv \frac{s\lambda^2}{2\pi c}\,,$$

$$z_{sl} \equiv z_s\lambda^2, \quad T_\lambda \equiv \frac{T_0}{\lambda^{3/2}}\,. \tag{3}$$

For a zero aperture $TM_{01}$ cavity, $x_l = 967T^2\ \Omega$, where $T$ is the transit time factor. If the cavity is a half wavelength long it is 392 $\Omega$. For the SLAC section middle cavity it is 440 $\Omega$.

Values of these parameters as a function of $a_\lambda$, for a $2\pi/3$ mode disk-loaded structure with a disk thickness of 0.0556 $\lambda$, were obtained using the computer code TWAP.[1] These data are fit by expressions developed by the author and R. Palmer.[2] Either $\beta_g$ or $a_\lambda$ can be specified.

*Work supported by the Department of Energy, contract DE–AC03–76SF00515.

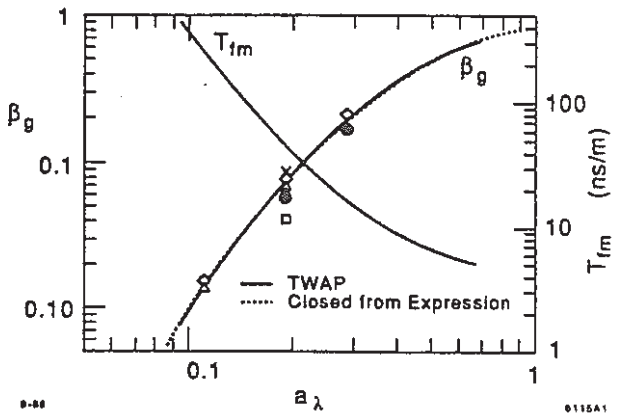


Fig. 1. Relative group velocity $\beta_g$ and fill time per meter $T_{fm}$ versus normalized aperture $a_\lambda$ for $2\pi/3$ disk-loaded structure.

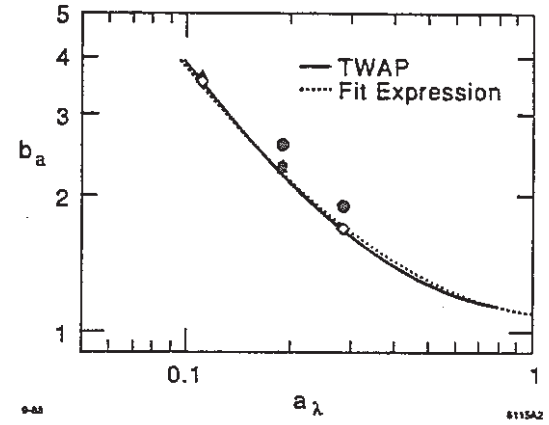


Fig. 2. Maximum radius to aperture radius ratio $b_a$ versus normalized aperture $a_\lambda$ for $2\pi/3$ disk-loaded structure.

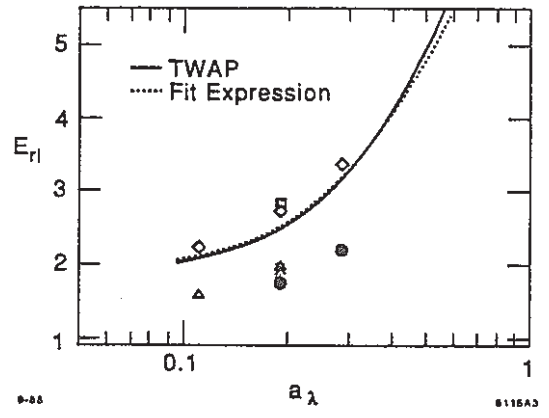


Fig. 3. Local peak to accelerating gradient ratio $E_{rl}$ versus normalized aperture $a_\lambda$ for $2\pi/3$ disk-loaded structure.

$$\beta_g = \exp\left\{3.1 - \frac{2.4}{\sqrt{a_\lambda}} - 0.9\,a_\lambda\right\}\,,$$

$$a_\lambda = \frac{0.31\,\beta_g^{1/4}}{(1-\beta_g)^{1/2}} + 0.3\,\beta_g\,. \tag{4}$$

$$b_a = 1.05\,\beta_g^{-0.28}\,, \qquad E_{rl} = 2 + 6\,\beta_g\,. \tag{5}$$

*Contributed to the 1988 Linear Accelerator Conference (LINAC 88), Williamsburg, VA, October 3–7, 1988*

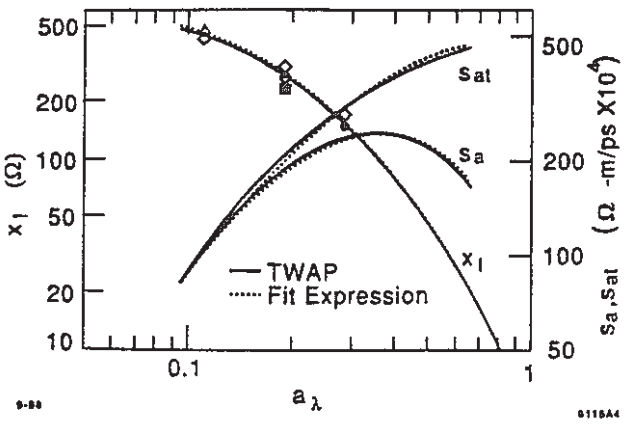


Fig. 4. Wavelength invariant elastance $x_l$ and aperture invariant elastances $s_a$, $s_{at}$ versus normalized aperture $a_\lambda$ for $2\pi/3$ disk-loaded structure.

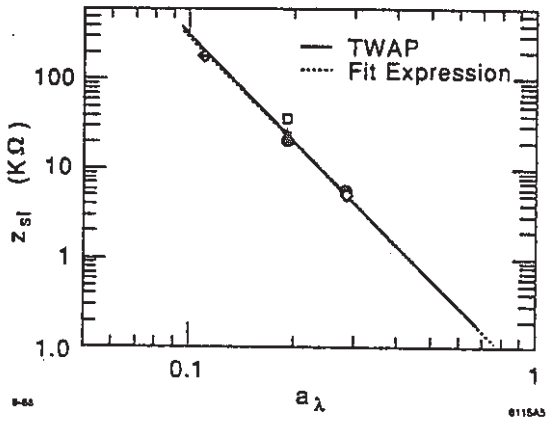


Fig. 5. Wavelength invariant serial impedance $z_{sl}$ versus normalized aperture size $a_\lambda$ for $2\pi/3$ disk-loaded structure.

$$x_l = \frac{30.24\,\beta_g^{0.4}(1-\beta_g)}{a_\lambda^2}, \qquad z_{sl} = 0.0413\,a_\lambda^{-3.836},$$
$$T_\lambda = 45.5(1+1.25\,\beta_g^{3/2}) - 3\,\beta_g\,. \tag{6}$$

These expressions show proper asymptotic behavior as $\beta_g$ approaches either zero or one.

The expressions for $\beta_g$, $b_a$, $E_{rl}$, $x_l$ and $s_{sl}$ versus $a_\lambda$ are plotted in Figures 1 to 5. Also plotted in these figures are the points obtained directly from TWAP. These expressions have been plotted as function of relative group velocity.[3] The advantage of the plots here is that they can be compared with a large aperture SW structure and with $\pi$ and zero mode cavities.

## ACCELERATING SECTION PARAMETERS

The section parameters, the fill time, attenuation, efficiency and filling factor are:

$$T_f = \frac{L}{v_g}, \qquad \tau = \frac{T_f}{T_o},$$
$$\eta_s = \frac{(1-e^{-\tau})^2}{\tau^2}, \qquad F_f \equiv 1-\beta_g\,. \tag{7}$$

Here, $L$ is the section length. We can specify $\tau$ and $L$ and obtain the wavelength and aperture from

$$\lambda = \left[\frac{T_f}{\tau T_\lambda}\right]^{2/3}, \qquad a = a_\lambda\lambda\,. \tag{8}$$

Define the section input serial impedance and section input elastance:

$$z_{ss} \equiv \eta_s z_s, \qquad s_s \equiv \eta_s s\,. \tag{9}$$

From Eq. (3) we obtain the local parameters at any frequency and aperture

$$s = \frac{x_l\omega}{\lambda} = \frac{x_l 2\pi c}{\lambda^2}, \quad z_s = \frac{z_{sl}}{\lambda^2}, \quad T_0 = T_\lambda\lambda^{3/2}\,. \tag{10}$$

The peak and average power inputs required to produce an average gradient $E_a$ in a section[4]

$$P_p = \frac{E_a^2}{z_{ss}}, \quad P_a = \frac{f_r E_a^2 L F_f}{s_s}\,. \tag{11}$$

## PEAK AND AVERAGE POWERS

Our choice of wavelength and aperture can be guided by plots of frequency, aperture, peak power and average power as a function of $a_\lambda$. Frequency and aperture vs $a_\lambda$ for several combinations of $\tau$ and L are plotted in Figure 6. Peak and average powers per meter, for the same combinations of $\tau$ and L as in Figure 6, are plotted in Figure 7. (Because we are interested how much peak and average power is needed at a given gradient, it is more meaningful to plot the quantities $P_p/L = E_a^2/Lz_{ss}$ and $P_a/L = f_f E_a^2 F_f/s_s$ rather than $z_{ss}$ and $s_s$.) These plots show how to trade increased frequency and decreased aperture for reduced peak and average powers. The fill time can be obtained from Figure 1.

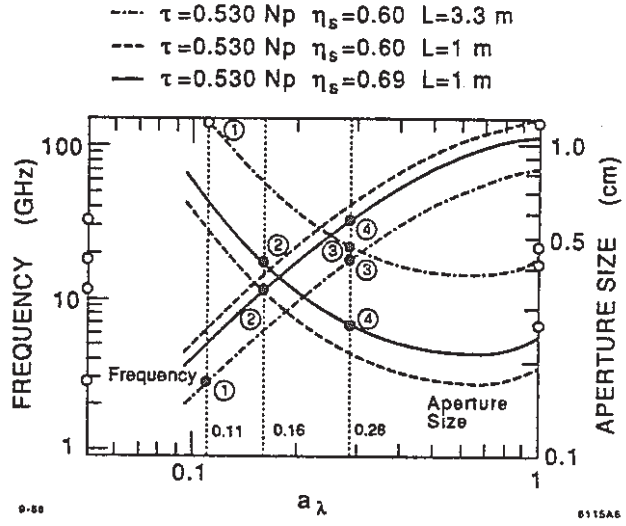


Fig. 6. Frequency and aperture size versus normalized aperture $a_\lambda$.

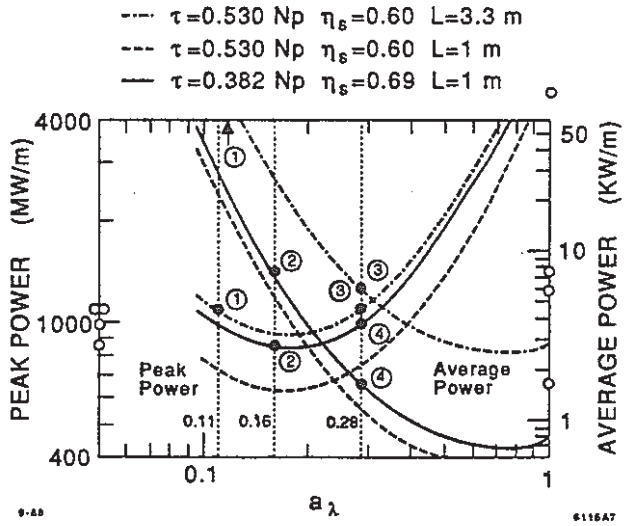


Fig. 7. Average and peak powers per meter versus normalized aperture $a_\lambda$ with $E_a = 200$ MV/m and $f_r = 120$ Hz.

Table 1. LINAC DESIGNS

| Frequency (MHz) | 2856 | 11424 | 17320 | 30000 |
|---|---|---|---|---|
| $a$ (cm) | 1.16 | 0.42 | .484 | 0.28 |
| $b$ (cm) | 4.06 | 1.03 | .816 | 0.417 |
| $a/\lambda$ | 0.11 | 0.16 | 0.28 | 0.28 |
| $\beta_g$ | 0.0134 | 0.048 | 0.184 | 0.184 |
| $E_{rl}$ | 2.10 | 2.3 | 3.1 | 3.1 |
| $T_0$ ($\mu$s) | 1.55 | 0.196 | 0.114 | 0.05 |
| $s$ ($\Omega$/ps-m) | 75 | 911 | 1009 | 3017 |
| $z_s$ (M$\Omega$/m$^2$) | 17.8 | 67.2 | 18.2 | 54.3 |
| $r$ (M$\Omega$) | 60 | 89 | 56 | 75 |
| $z,r/Q$ ($\Omega$/m) | 4180 | 12692 | 9272 | 16000 |
| $L$ (m) | 3.3 | 1 | 3.3 | 1 |
| $T_f$ (ns) | 760 | 70 | 60 | 18 |
| $\tau$ | 0.53 | .357 | 0.524 | 0.36 |
| $\eta_s$ | 0.632 | .707 | 0.60 | 0.705 |
| $E_a$ = 200 MV/m , $f_r$ = 120 Hz | | | | |
| $P_p$ (MW) | 3594 | 888 | 3620 | 1045 |
| $P_a$ (KW) | 323 | 7.08 | 21.1 | 1.84 |
| $p_p$ (MW/m) | 1089 | 888 | 1097 | 1045 |
| $p_a$ (KW/m) | 98 | 7.08 | 6.4 | 1.84 |

Using Figures 6 and 7 as a guide, we choose the four designs of Table 1. The first is the 2.856 MHz benchmark design, the present SLC structure, except that here a constant impedance structure is assumed and the gradient is about 10 times the SLC gradient. Design 2 increases the frequency to 11.4 GHz and decreases the aperture to 0.42 cm. Consequently, the average power is reduced from 98 to 7 kW, the peak power remains essentially at 1 GW.

Design 3 increases the frequency to 17.3 GHz. It requires the same number of feeds as Design 1 (1/3 of Design 2). The peak and average powers per meter are about the same as for Design 2. The peak power per feed is the same as for SLC which at 20 MV/m gradient is 36 MW. The average power is reduced from 32 KW to 2 KW. Thus replacing the accelerator sections and the high power amplifiers, with that of Design 3, but keeping the same modulators with the same peak and average powers, would result in 16-fold increase in luminosity. The aperture is smaller, but $a_\lambda$ is larger. Also, we may take advantage of the reduced $b$, from 4.06 cm to 0.82 cm, to place focusing coils along the accelerator sections.

Design 4 increases the frequency to 30 GHz. The peak power remains about the same, but the average power is reduced 50 fold. The peak powers are about the same for all four designs. The average power, however decreases sharply with decreased wavelength.

The dash curves in Figures 6 and 7 illustrate that increasing the section attenuation decreases both the peak and average powers at the expense of decreased wavelength and aperture.

## OPERATION AT HIGH WAVELENGTH TO APERTURE RATIO

Increasing $a_\lambda$ above 0.3 decreases the average power but it increases the peak power, even though the wavelength and aperture are both decreasing. This is desirable if high peak power is available, say by means of pulse compression. This can also be inferred from Figure 4, which shows that the aperture invariant elastance $s_a = sa^2$ has a maximum about $a_\lambda = 0.38$. This is the cutoff conditon for the $TM_{01}$ mode in a circular waveguide with a radius to wavelength ratio $a_\lambda$. Thus, if at any aperture in the neighborhood of $a_\lambda = 0.38$, the elastance decreases as the frequency increases. As the $TM_{11}$ beam breakup mode is at a higher frequency we expect that its elastance relative to the fundamental elastance is less than when we operate at lower $a_\lambda$. If $a_\lambda = 0.48$, the $TM_{01}$ mode is attenuated at 26% below cutoff and the $TM_{11}$ mode propagates at 26% above cutoff.

## OTHER STRUCTURES

To determine whether we can do better than the bench-mark $2\pi/3$ disk-loaded guide, parameters for several additional structure shapes are plotted in Figures 1 to 5, superimposed on plots for the $2\pi/3$ structure. The structure shapes and the symbol used for plotting the parameters of each shape are shown in Figure 8. We note that their behavior with $a_\lambda$ is similar to that of the disk-loaded guide and therefore they can be compared at any aperture, frequency, and section length. For the circular tip $2\pi/3$ mode at $a_\lambda = 0.11$, bench-mark design $E_{rl} = 2.1$. As $a_\lambda$ increases to 0.19, $E_{rl}$ increases to 2.5. If the tip changes from circular to elliptical, $E_{rl}$ remains about the same. For the circular tip $\pi/2$ mode at $a_\lambda = 0.19$, $E_{rl} = 2.7$. Changing the tip from circular to elliptical reduces $E_{rl}$ to 1.97. $E_{rl}$ is less than the bench-mark value for the structure shapes shown in Figure 8, except for circular tip and the square-wall structures.

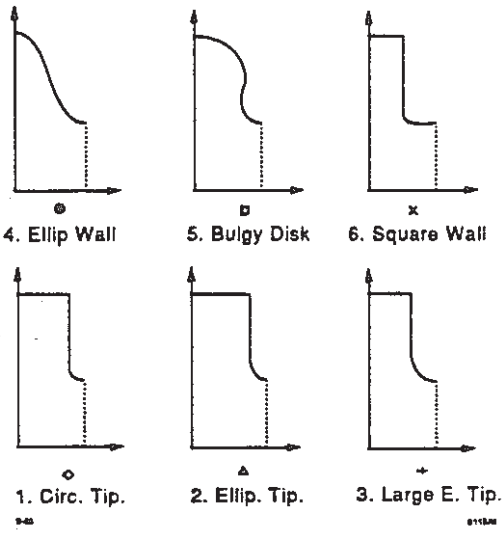


Fig. 8. Structure shapes.

As $a_\lambda$ changes from 0.11 to 0.19, the resulting increase in $b$ is a small fraction of the nearly two to one increase in $a$. The elastance is halved and the serial impedance decreases about nine-fold. This is, possibly, compensated by lowered wakefields, especially long-range wakefields. The elastance and attenuation time decrease for some shapes, and their use is indicated only if they result in ease of mechanical fabrication and lower wake fields.

## ACKNOWLEDGMENTS

I am grateful to P. Wilson for his help and to R. Helm for his unstinting help in running his program TWAP.

## REFERENCES

1. R. Helm, *"Computation of Properties of Traveling-Wave Linac Structures,"* SLAC-PUB-813, October 1970.
2. R. Palmer, *"The Interdependence of Parameters for TeV Linear Colliders,"* SLAC-PUB-4295, April 1987.
3. Z. D. Farkas, *"The Roles of Group Velocity, Frequency and Aperture in Traveling Wave Linear Accelerator Design,"* AAS Note 33, August 1987.
4. Z. D. Farkas, *"New Formulation for Linear Accelerator Design,"* IEEE Trans. of Nucl. Sci., NS-32, 2738 (1985).

# DESIGN CONSIDERATIONS OF HIGH PEAK POWER GYROKLYSTRONS FOR LINEAR COLLIDERS*

W. Lawson, P.E. Latham, J. Calame, M. Skopec, D. Welsh, B. Hogan, W. Wang, M.E. Read†,
C.D. Striffler, M. Reiser, and V.L. Granatstein

Laboratory for Plasma Research
University Maryland, College Park, MD 20742

## ABSTRACT

In this paper, the final preparations for bringing the University of Maryland's 10 GHz, 30 MW gyroklystron experiment on-line are discussed. We explain the enhanced circuit modelling and present a two cavity design which predicts an efficiency of 33% and a gain of 27 dB with the simulated beam parameters. We describe initial operation of the modulator and electron gun and detail the experimental design of the system. Finally, we present plans for a high gain gyroklystron circuit and discuss scaling considerations for producing powers in excess of 100 MW in the frequency range 10-30 GHz.

## INTRODUCTION

The results of scaling studies for the next generation of linear electron-positron colliders have demonstrated a need for high pulse power, high efficiency, high gain microwave (8-30 GHz) amplifiers.[1] As part of our investigation into the suitability of gyrotron amplifiers for this application, we are constructing an X-band gyroklystron which is predicted to achieve a peak power of 30-50 MW.[2] Successful operation of this device will increase the state-of-the-art in gyroklystron power capability by three orders of magnitude and will establish the gyroklystron as a viable candidate to drive high-energy linear colliders.

A schematic of the major subsystems of the initial two-cavity gyroklystron is shown in Fig. 1. The modulator supplies a 500 kV, 200 A, 1.5 $\mu$s pulse with an intermediate voltage to a double-anode Magnetron Injection Gun (MIG). The MIG generates a rotating beam which passes through the circuit after being adiabatically compressed. The beam's phase-space distribution is modulated by a microwave signal which is injected into the first cavity. Energy is extracted axially through a coupling aperture in the second cavity and travels through a nonlinear waveguide to a half-wavelength output window. The beam expands in the decreasing magnetic field and impinges on a 35 cm section of the output waveguide. A directional coupler and water calorimeter (not shown) measure the peak and average microwave power. The nominal parameters of this configuration are listed in Table I and details of these subsystems are discussed below.

## ELECTRON BEAM GENERATION

The 500 kV voltage pulse is generated by an 8–12 stage line-type modulator. Four pulse-forming networks (PFNs) in parallel are resonantly charged on command to 46 kV and are switched through two thyratrons into a 1:22 pulse transformer which provides the required potential of 500 kV. The electron gun is in the double anode MIG configuration.[3] Key dimensions of the gun design are listed in Table II and the simulated beam properties at 160 A are listed in Table I. The gun has been constructed by Varian Associates[4] and has passed its acceptance test. A 1 $\mu$s, 500 kV pulse was applied to the MIG when the cathode was cold. The voltage pulse and charging current are shown in Fig. 2. Without the axial magnetic field, a 143 kV pulse was applied with the cathode hot ($\sim 950°C$) and the control anode grounded. The resulting 120 A pulse represents a current density of 4.2 A/cm$^2$ and is shown in Fig. 3. The current was limited by the impedance of the modulator. Preparations are being made to draw the full power beam.

## MICROWAVE CIRCUIT

To design the microwave circuits, we use a partially self-consistent steady state, numerical code[5] that has evolved considerably during the past three years. The cold cavity field profiles are found from a scattering matrix formulation.[6] The effect of ac space-charge waves has been incorporated both as a frequency shift and a pertubation on the perpendicular field profile. The parameters of the two cavity design are listed in Table I along with the simulated results. The low Q of the input cavity is realized by two thin, carbon-impregnated aluminosilicate annuli located on either cavity end at the outer radius. Cold tests have revealed that we can achieve the required frequency and Q with such absorbers. The scattering matrix code was modified to include lossy dielectrics and was successfully compared to analytic results in simple geometries with lossy dielectrics and numeric codes (mafia and urmel-t) for complex geometries with loss-free dielectrics. This code also predicts the viability of the lossy rings.

A linear start oscillation code based on the scattering matrix formulation predicts that an all metal drift tube will have no stable region of operation. To suppress the unwanted modes, a drift tube consisting of alternate washers of metal and lossy dielectric will be used. Again, both experimental and analytic results indicate the viability of this technique. Our first tube will utilize six rings of MgO with a 1% concentration of SiC. The dielectric rings are 22% wider than the alternating metal rings and have a depth of 1.6 cm. The drift tube provides 117 dB isolation for the $TE_{01}$ mode and more than 16 dB isolation for the uncutoff modes at 10 GHz.

The output cavity Q is essentially diffractive and is sufficiently larger than the minimum Q so that a simple coupling iris can be used for the endfire system. Cold testing has confirmed both the frequency and Q predicted by the scattering matrix code for a variety of configurations.

The vacuum vessel between the output cavity and the output window doubles as the microwave and beam transport system and is shown in Fig. 6. A nonlinear taper brings the waveguide radius from 2.60 cm to the beam dump radius of 3.57 cm in 19.5 cm. The smaller radius can support only the lowest circular electric mode ($TE_{01}$) at 10 GHz while the larger radius can support the lowest two circular modes. To minimize mode conversion, a raised cosine radius is used. An approximate analytic solution predicts the mode conversion to be less than $1.1 \times 10^4$ percent in power.

Computer simulations of the beam with and without microwave interaction show that the beam is dumped fairly uni-

*Work supported by U.S. Department of Energy.
† Physical Sciences, Inc., Alexandria, VA.

formly by the decaying magnetic field over a 35 cm distance in the beam dump. This keeps the instantaneous temperature rise below 20° and the average temperature rise sufficiently low to allow modest water cooling. A dumping magnet prevents the few high energy electrons from reaching the output window. The vacuum port consists of a stainless steel tube with 150 holes distributed uniformly in angle and axial position to provide sufficient conductance with minimal microwave interference.

A second nonlinear taper is used after the beam dump to bring the radius to 6.35 cm. At that radius, four circular electric modes can propagate, but the ideal mode conversion to all other modes is still less than 0.002 percent in power. A half wavelength BeO window, brazed to a stainless steel flange via a Kovar ring, provides the vacuum-to-air interface.

## DIAGNOSTICS

There will be several standard external current transformers in conjunction with current breaks to measure the instantaneous beam current at several locations along the system. Capacitive probes, which consist of four 90° sections and a sapphire insulator, will be used at several locations in an initial beam test to measure total beam density and relative location. The two diagnostics jointly will give and estimate of the average axial velocity and (along with the beam voltage) will provide information about the average velocity ratio.

The microwave diagnostics consist of both peak and average power measurements. The peak power measurement involves a mode selective directional coupler combined with a crystal detector. Because the circular guide is highly overmoded and the rectangular guide is not, the phase velocity of the two waves cannot be the same and two sets of coupling holes are required. The 50 dB, $TE^0_{01} \rightarrow TE^{\square}_{10}$ coupler is designed to maximize $TE^0_{01}$ directivity (-83 dB) and minimize $TE^0_{11}$ coupling (-75 dB). The detector will provide the signal envelope and, with proper calibration, and estimate of the peak power. A non-resonant water calorimeter will provide the average power measurement and a check of the peak power measurement. Water is circulated between two 19.5 cm long stycast cones to maximize sensitivity. The thickness is adjusted to guarantee a minimum attenuation of 28 dB.

## SCALED DESIGNS

To achieve high gain, high efficiency gyroklystrons, multicavity circuits will be utilized. Simulations of a four cavity design with 4.5 cm long drift tubes and two buncher cavities with the approximate dimensions of the input cavity indicate that an efficiency of 45% and a large signal gain of 63 dB is achievable with the simulated beam parameters.

To achieve significantly higher power levels, the circuit will have to be modified considerably. The current limitation is the peak power capability of the magnetron injection gun. Scaling laws have been derived[7] which predict the dependence of the beam power on beam voltage, peak applied electric field, and the beam radius (related to cavity mode). If $\gamma_0 = 1 + V_0/(mc^2)$ is the normalized beam energy, $E_m$ is the maximum electric field, and $r_g$ is the average beam radius, then the peak power $P_0$ scales as follows:

$$P_0 \, \alpha \, (\gamma_0 - 1)^2 (1 + \gamma_0^{-1}) E_m r_g. \qquad (1)$$

From this relation we have designed a gun for a coaxial cavity (with twice the beam radius) at an energy of 800 keV which should be capable of producing 180 MW of 10 GHz microwave power.[1] Further power increases would be possible if we were to relax the constraint on maximum electric field which is currently $E_m < 90$ kV/cm.

To achieve high frequencies, again the trade-off between power and frequency in the gun is fundamental. The MIG frequency scaling is $P_0 \alpha f^{-1}$, which is superior to pierce gun scaling when considering high frequencies. This scaling has been confirmed with numerical simulations and should make the gyroklystron an even stronger contender to power the linear supercollider if the proposed operating frequency exceeds 10 GHz.

## REFERENCES


1. M. Reiser, D. Chernin, W. Lawson, and A. Mondelli, 3rd Workshop of the INFN Eloisatron Project, Erice, Italy, May 1987.

2. K.R. Chu, V.L. Granatstein, P.E. Latham, W. Lawson, and C.D. Striffler, IEEE Trans. Plasma Sci., PS-13, pp. 424-434, 1985.

3. W. Lawson, J. Calame, V.L. Granatstein, G.S. Park, C.D. Striffler, and J. Neilson, Int. J. Electronics, 61, pp. 969-984, 1986.

4. R.F. Garcia, K.L Felch, Y.M. Mizuhara, S.T. Spang, and W. Lawson, 1987 IEDM Tech. Digest, p. 821.

5. K.R. Chu, V.L. Granatstein, P.E. Latham, W. Lawson, and C.D. Striffler, IEEE Trans. Plasma Sci., PS-13, p. 424 (1985).

6. J. Neilson, P.E. Latham, M. Caplan, W. Lawson, submitted to IEEE Trans. Microwave Theory Tech., August, 1988.

7. W. Lawson, IEEE Trans. Plasma Sci. 16, pp. 290-295 (1988).


Table I.
The Two Cavity Gyroklystron Parameters.

| | | |
|---|---|---|
| Beam | Power $P_0$ | 80 MW |
| | Voltage $V_0$ | 500 kV |
| | Velocity ratio $v_\perp/v_z$ | 1.5 |
| | Velocity spread $\Delta v_z$ | 7.0% |
| | Larmor radius $r_L$ | 0.43 cm |
| | Center radius $r_g$ | 0.79 cm |
| | Guiding spread $\Delta r_g$ | 0.20 cm |
| | Axial field $B_0$ | 0.565 T |
| Circuit | Mode (both cavities) | $TE_{011}$ |
| | Peak Efficiency | 33% |
| | Gain | 27 dB |
| Input Cavity | Radius | 4.50 cm |
| | Length | 1.53 cm |
| | Q | 225 |
| | Injected Power | 50 kW |
| Drift Tube | Radius | 1.50 cm |
| | Length | 9.00 cm |
| Output Cavity | Radius | 2.11 cm |
| | Length | 2.38 cm |
| | Q | 165 |
| Aperture | Radius | 1.50 cm |
| | Length | 0.33 cm |
| Output Guide | Radius | 2.60 cm |

Table II.
80 MW MIG Electrode Specifications.

| | |
|---|---|
| Cathode Radius $r_c$ | 0.0228 m |
| Emitter Strip Width $\ell_s$ | 0.020 m |
| Cathode-Control Anode Gap $d_{ac}$ | 0.0613 m |
| Cathode Half Angle $\phi_c$ | 20° |
| Compression Ratio $f_m$ | 12 |
| Control Anode Voltage $V_a$ | 143 kV |
| Emission Current Density $J_c$ (Uniform) | 5.61 A/cm$^2$ |

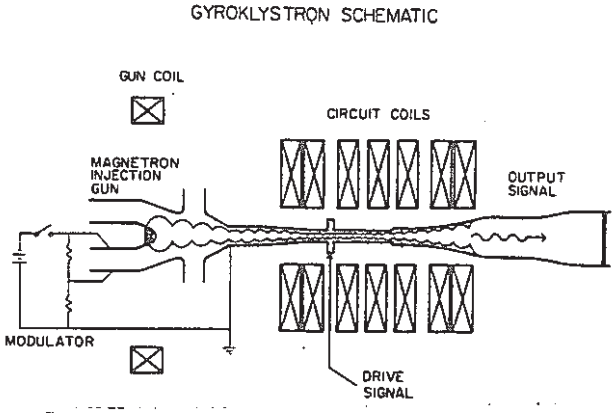


Figure 1.
The University of Maryland 30 MW Gyroklystron.

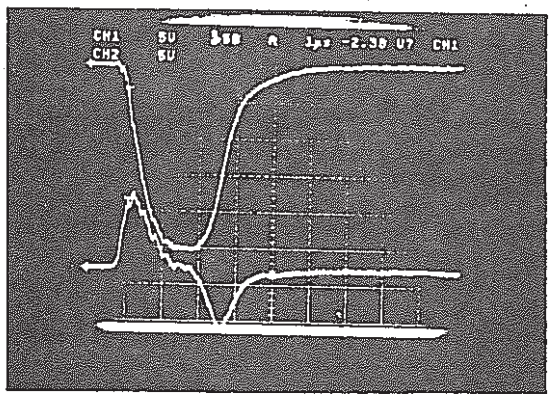


Figure 2.
A typical modulator pulse. The upper trace shows the voltage pulse with 100 kV/div. The lower trace shows the charging current with 50 A/div. The sweep rate is 1 $\mu$s/div.

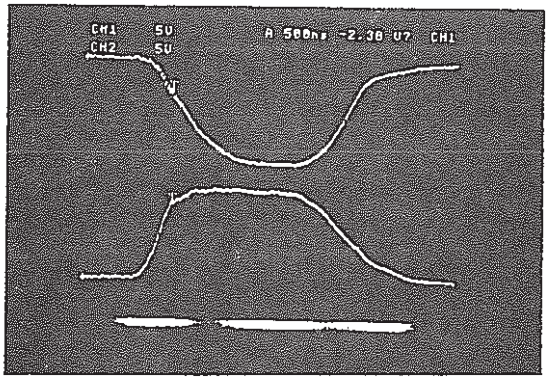


Figure 3.
The current pulse. The upper trace shows the voltage pulse in 50 kV/div and the lower trace shows the current pulse in 50 A/div. The sweep rate is 500 ns/div.

# ENGINEERING DESIGN OF THE INJECTOR LINAC FOR THE ADVANCED LIGHT SOURCE (ALS)*

B. Taylor and H. Lancaster
Lawrence Berkeley Laboratory
University of California, Berkeley, CA 97420
and
H. Hoag
Stanford Linear Accelerator Center
Stanford University, Stanford, CA 94305

## Introduction

The injection system for the ALS is designed to provide an electron beam of up to 400 mA at 1.5 GeV to the storage ring in a filling time of less than five minutes.[1] The 328 RF buckets in the storage ring can be filled with electrons in an arbitrary pattern. The injection system begins with an S-Band linac that provides 50 MeV electrons to the booster synchrotron for further acceleration to 1.5 GeV. The electron gun can be pulsed to give single and multi-bunch formats. An efficient subharmonic bunching system is used to compress the electron gun pulse to fit in a single S-Band bucket, thereby conserving charge and making the diagnostics of booster injection unambiguous.[2] A by-product of this bunching is flexibility for future FEL injection. Two disk-loaded accelerating waveguides that are independently powered complete the acceleration with modest field gradients. These two sections are fabricated using self-aligning precision-machined cups. Energy spread due to beam loading is compensated by a fast differential phase shift between the two accelerating sections.

TABLE 1. Performance Requirements of Linac

| | | |
|---|---|---|
| ELECTRON GUN | | |
| Energy | [keV] | 120 |
| Single bunch mode | | |
| Current | [A] | 2.4 |
| Pulse length | [ns] | 2.5 |
| Multi-bunch mode | | |
| Current | [A] | 1.0 |
| Pulse length | [ns] | 100 |
| LINAC | | |
| Energy | [MeV] | 50 |
| Repetition rate (max.) | [Hz] | 10 |
| Frequency | [MHz] | 2997.924 |
| Single bunch mode | | |
| Intensity | [e] | $1.3 \times 10^{10}$ |
| Bunch length (rms) | [ps] | 15 |
| Multi-bunch mode | | |
| Average current | [mA] | 125 |
| Pulse length | [ns] | 100 |
| Emittance (rms) | [π m-rad] | $0.4 \times 10^{-6}$ |
| Energy spread (rms) | [%] | 0.4 |

## Linac Construction and Layout

The layout, construction, and component complement of the linear accelerator are shown in Figure 1. The support girder structure is split into three parts. The first girder will be assembled well in advance of the S-Band sections to provide a Faraday Cup terminated test stand. The test stand will be used to evaluate the performance of the gun, subharmonic bunchers and diagnostics.

## The Electron Gun Source

The triode gun of the linac employs a 1.0 $cm^2$ dispenser cathode which operates at a dc potential of -120 kV. Pulses with an intensity of 6.0 nC (i.e. $3.8 \times 10^{10}$ electrons) and an emittance of less than $10 \times 10^{-6}$ π m-rad can be delivered.

* This work was supported by the Director, Office of Energy Research, Office of Basic Energy Sciences, Material Sciences Division, of the U.S. Department of Energy under Contract No. DEAC03-76SF00098.

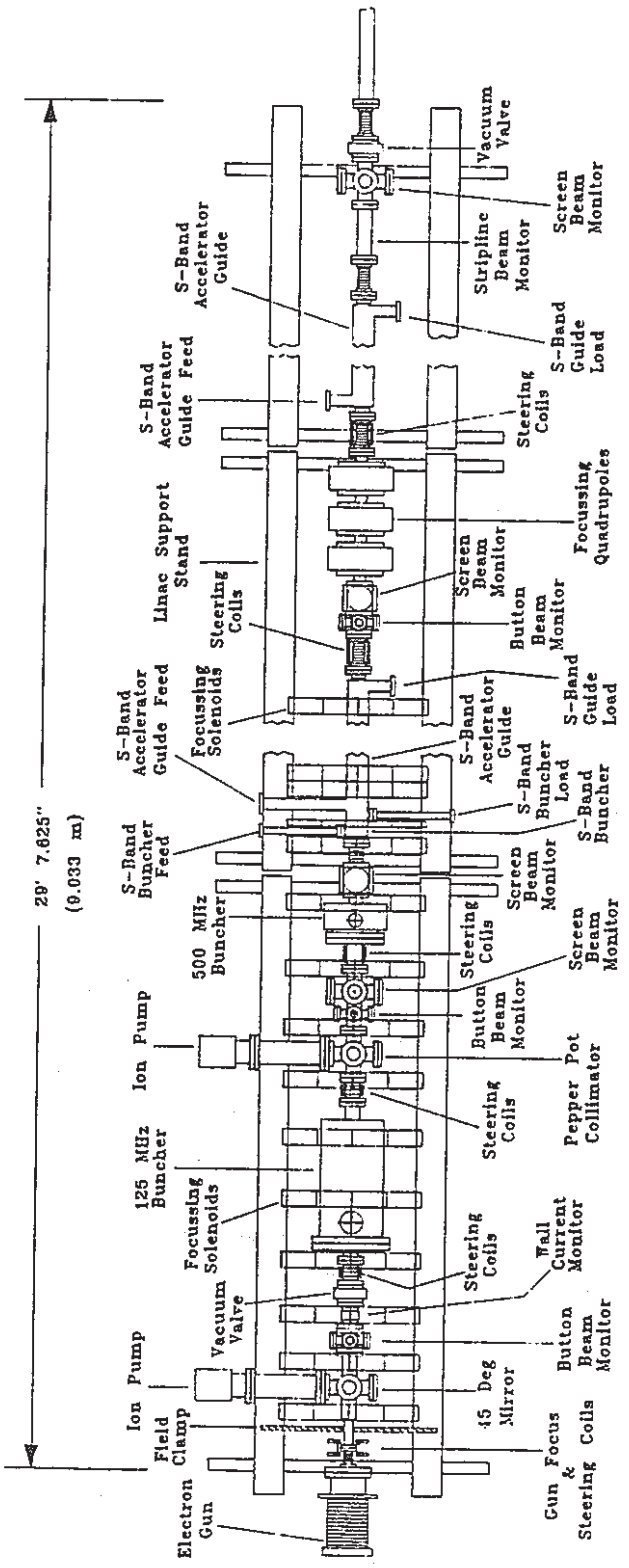


Figure 1. Linac Layout

A 125 MHz sine wave, divided down from the 500 MHz ALS master oscillator, is biased and clipped to form a continuous chain of 2.5 ns negative going pulses that are applied to the gun cathode. By applying a positive going gate pulse of from 12 ns to 150 ns to the grid any number of 2.5 ns beam pulses from 1 to 19 may be emitted at will.

## The Subharmonic Bunchers

Each buncher employs quarter-wave stainless steel resonant cavities; in both cases the nose cone gap is 2 cm. The shunt impedance of the 125 MHz cavity is 186 kΩ and of the 500 MHz cavity 248 kΩ. The required gap voltage in both cases is 60 kV.

Amplifiers using commercial modules hybrided together and using 3 CPX 800 A7 tubes are employed for both systems. Pulse power levels up to 24 kW at 100 μs and 10 Hz are obtained giving an ample power margin. The design of the amplifier systems also provides for several hundred watts of long pulse or cw power. This feature allows for outgassing and multipactor conditioning of the cavities.

Provision has been made for temperature stabilization of the cavities to minimize phase drift of the gap RF voltage.

## The S-Band Buncher

The buncher comprises four cavities (including the coupler) tuned to 2997.924 MHz in the $2\pi/3$ mode. The period is 25 mm, making the phase velocity equal to 0.75 times the velocity of light. A shunt impedance of approximately 38 MΩ/m indicates an axial field of 4.8 MV/m for an RF input power of 1 MW.

In order to minimize beam expansion and debunching, the buncher will be brazed directly to the first accelerator section, so that the intervening drift tube length is held to 22 mm.

Low-impedance waveguide feeds and special high-vacuum flanges are employed to allow close spacing of magnetic focussing coils in the buncher region.

The completed buncher is shown in Fig. 2.

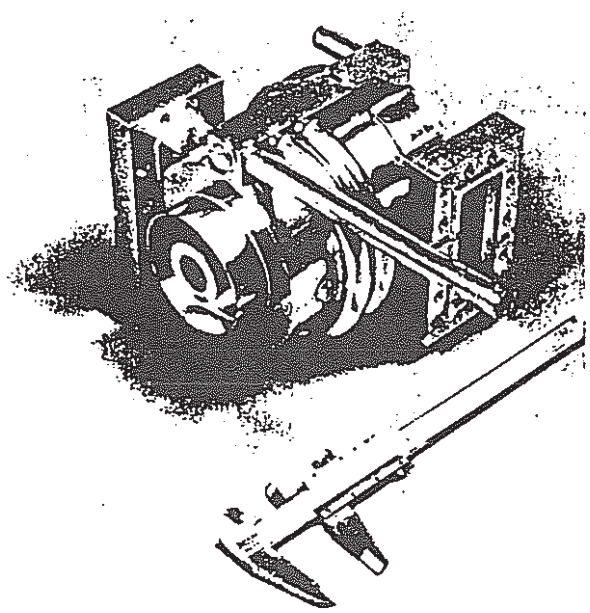

Figure 2. S-Band Buncher

## The S-Band Accelerator Sections

There are two disk-loaded waveguide accelerator sections, each 60 cavities (2m) long. A constant-impedance design was selected for economy and simplicity. The principal parameters are given in Table 2.

TABLE 2. Accelerator Section Parameters

| | | |
|---|---|---|
| Iris aperture | [mm] | 24 |
| Cavity diameter | [mm] | 79.25 |
| Period | [mm] | 33.33 |
| Shunt impedance | [MΩ/m] | 55.9 |
| Normalized group velocity | | 0.0173 |
| Attenuation constant | [Np] | 0.262 |
| Filling time | [ns] | 325 |
| Energy per section with 20 MW klystron power | [MeV] | 28.7 |
| Axial field in input cavity | [MV/m] | 16.3 |
| Beam loading at 125 mA | [MeV] | 1.7 |

The accelerator sections are fabricated from precision-machined copper cups, which are stacked and brazed. Initially, sub-sections are brazed as shown in Fig. 3 (which also shows the buncher and a single cup). At this stage, the coupler matching is checked and pre-tuning is done on the cavities in the coupler sections. After this, the sub-sections are brazed together and the water cooling circuits are added, and the completed section is tuned.

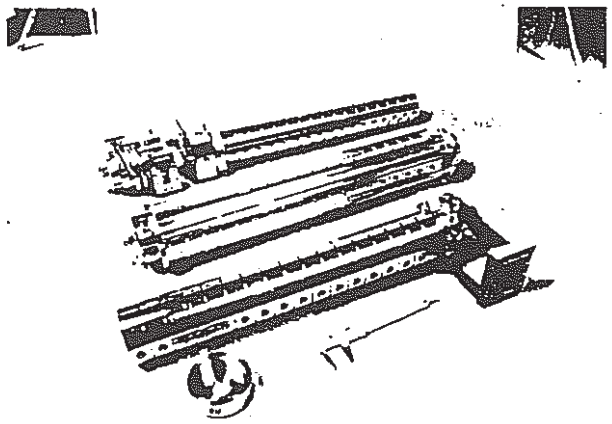

Figure 3. S-Band Buncher, Guide Sub-sections, and a Single Cup.

## Diagnostics

Immediately following the electron gun output spool a 45° double sided optical mirror may be inserted into the beam tube. The mirror allows for visual and optical pyrometer inspections of the cathode surface. A laser beam may also be injected via the mirror for alignment checks.

Following the mirror facility, a wall current monitor displays the gun intensity pulse.

Situated between the subharmonic bunchers, a pepper pot collimator and fluorescent screen allow for emittance measurements.

Button type RF beam position monitors and further screens are strategically placed for beam position and size monitoring.

The final output monitor of the accelerator is a strip line device monitoring position, intensity, and pulse shape.

## The Control System

The control system for the linac is integrated into the larger ALS system which uses a large number of small modules called intelligent local controllers (ILCs), multi-dropped on serial links. The linac uses 25 ILCs for controlling and monitoring all linac variables. Several are used as essential elements of feedback systems for the steering coil power supplies, the S-Band buncher high power phase and amplitude motor controllers, the beam loading compensation system, and the accelerating guide temperature controller.

Using a small portable control station the ILCs can be fully exercised, either in concert on the serial link or individually, for local control of the linac.

## The Focus and Steering System

The main water cooled solenoid focus system is comprised of 22 identical 55 turn coils and one 22 turn coil. The coils have large internal diameters to facilitate access to enclosed components and to give clearance for longitudinal coil movements.

Commercial dc power supplies feed the coils in groups of three or four, thereby allowing further field shaping adjustments.

Focussing at 25 MeV between the accelerator guides is by means of three quadrupole magnets.

The steering coil power supplies are high quality stereo amplifiers with dc response. They will provide typically ±7 A at 30 V. the amplifiers are converted to stable constant current devices by feedback involving ILCs that are part of the control system. This approach which provides horizontal and vertical steering from each amplifier unit is more economic than normal commercial bipolar supplies.

## The S-Band RF Drive System

A simplified schematic of the RF drive system is shown in Fig. 4. A 2997.924 MHz CW signal, derived from the ALS master oscillator and a x6 multiplier, passes through a phase-shifter and is divided into two drive paths, one for each klystron. Additional phase-shifters allow for beam loading compensation and phase adjustment between the two accelerator sections. Phase and amplitude detectors provide inputs to ILCs which control phase-shifters and attenuators to stabilize the operating parameters. Preamplification is provided by 800 W solid-state amplifiers. These amplifiers drive the input cavities of the klystrons. The two 25 MW klystrons provisioned are of established design.

A low duty cycle (1 μs at 1-10 Hz) allows considerable simplification of the klystron modulator design. A ten section transmission line with decoupled and individually variable inductors is used. The line is dc charged using a highly stable high voltage switching supply. Switching into the klystron pulse transformer is via the usual hydrogen thyratron. However, in this low duty case, a glass envelope tube can be used with economic advantage.

The klystron RF outputs are transmitted to the accelerator sections via temperature controlled evacuated waveguide. Power is coupled off the first klystron to drive the buncher. This power is transmitted through waveguide filled with pressurized nitrogen. The path contains a high-power attenuator and phase-shifter. Windows at each end isolate the nitrogen and vacuum systems.

## Beam Loading Compensation

The beam loading on the accelerating waveguides for the longest (100 ns) linac pulse will result in an energy spread of about 4 percent between the beginning and end of the beam pulse if left uncorrected. This must be reduced so the energy spread lies within the acceptance (±1%) of the Booster.

To compensate for the energy spread a fast step phase change is made between the klystron drive chains for the two accelerating waveguides at the beginning of the beam pulse. This results in a power increase to the accelerating waveguides that reduces the energy spread to within acceptable limits. The phase step method allows the klystrons to be operated in a more stable saturated mode.[3]

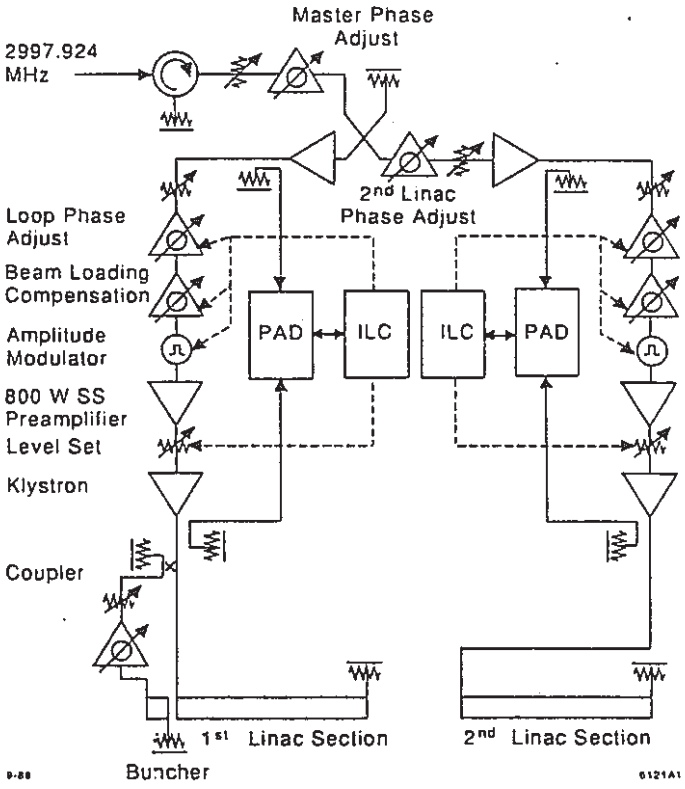


Figure 4. S-Band RF Drive System, Simplified Schematic.


## Acknowledgement

The authors wish to thank H. Deruyter (SLAC) for testing and tuning the S-Band components, and for assisting with design and coordination, J. Guigli (LBL) for mechanical design and coordination, C. C. Lo (LBL) for design of the subharmonic buncher system, J. Hinkson (LBL) for beam instrumentation design, and K. Baptiste for electrical coordination. Colleagues in the ALS Mechanical Engineering Group and the Accelerator Systems Group, especially K. Kennedy, F. Selph, and C. Kim, are acknowledged for their contributions to the linac design.


## References


1 F. Selph, A. Jackson, and M. S. Zisman, "Injection System Design for the LBL 1-2 GeV Synchrotron Radiation Source", IEEE Particle Accelerator Conference, Washington, D. C., March 1987.

2 R. H. Miller, C. H. Kim, and F. B. Selph, "Design of a Bunching System for a High-Intensity Electron Linac", European Particle Accelerator Conference, Rome, Italy, June 1988.

3 Frank Selph, "Compensation of Beam Loading in the ALS Injector Linac", This Conference.

SLAC - PUB - 4646
May 1988
(A)

# RF POWER SOURCES*

MATTHEW A. ALLEN
*Stanford Linear Accelerator Center*
*Stanford University, Stanford, CA 94309*

## INTRODUCTION

I am going to talk about RF power sources for accelerator applications. My approach will be with particular customers in mind. These customers are high energy physicists who use accelerators as experimental tools in the study of the nucleus of the atom, and synchrotron light sources derived from electron or positron storage rings. I will generally confine myself to electron-positron linear accelerators since the RF sources have always defined what is possible to achieve with these accelerators. A striking example of this is the development at Stanford immediately after World War II when Chodorow and Ginzton[1] set the stage for GeV electron accelerators with the development of the multi-megawatt klystron which at that time represented orders of magnitude of power capabilities above that which was available in klystron amplifiers.

Circular machines, cyclotrons, synchrotrons, etc. have usually not been limited by the RF power available and the machine builders have usually had their RF power source requirements met "off the shelf." The main challenge for the RF scientist has been then in the areas of controls. An interesting example of this is in the Conceptual Design Report of the Superconducting Super Collider (SSC) where the RF system is described in six pages of text in a 700-page report. Also, the cost of that RF system is about one-third of a percent of the project's total cost. The RF system is well within the state of the art and no new power sources need to be developed. All the intellectual effort of the system designer would be devoted to the feedback systems necessary to stabilize beams during storage and acceleration, with the main engineering challenges (and costs) being in the superconducting magnet lattice.

In sharp contrast, the next electron accelerator for high energy physics applications is the TeV linear collider. Studies of these machines are proceeding in many laboratories in the USA, Europe, the Soviet Union and Japan. All of these studies reveal that a key system which will determine the feasibility of these colliders is the RF system and, in particular, the RF power sources. In fact, many parameter studies and cost optimizations are being carried out and still it is difficult to keep the RF system cost below 50% of the total project cost.

In my presentation to this conference, I will focus on RF power sources for the next generation of linear colliders, demonstrating how the power sources developed for electron linear accelerators over the past forty years point the way to suitable sources for that application. Not surprisingly I will deal with the klystron and klystron-type interactions since Stanford University is where the klystron was invented in 1937 with the fiftieth anniversary being celebrated last year.

## PRESENT STATUS

### Storage Rings

Electron-positron storage rings require continuous power generally in the frequency range 50–1000 MHz. Klystrons producing over one megawatt are available for purchase from manufacturing companies at both 350 MHz and 500 MHz. These power amplifiers are high efficiency klystrons (65%) and high gain (greater than 50 dB) and are catalogue items of klystron manufacturers around the world.

The frequency of choice for storage rings dedicated to synchrotron light applications are 500 MHz and klystrons in the range 100 kW to 1200 kW are readily available for the individual requirements of these RF systems. The present day storage rings are not limited by the availability of RF power sources.

### Linear Accelerators

The way of life of accelerator builders is to respond to the demands of high energy physicists for higher and higher electron and positron energies and at lower and lower costs per GeV. After World War II the chosen frequency for electron accelerators was in the S-band frequency range where significant radar developments had taken place. The klystron eventually developed for the Stanford Linear Accelerator Center was permanently magnet-focused and produced 21 MW at 250 keV beam voltage for 2.5 $\mu$sec at 360 Hz repetition rate. This served very well to produce 20 GeV beams but then, responding to the demands for higher energy, a scheme was proposed to increase the energy by compression of the RF pulse coming out of the klystron. In SLED the power from the klystron is stored in a high $Q$ (greater than 100,000) cavity over part of the pulse and then, for the remaining part of the pulse, the power is rapidly fed into the accelerating sections for a high effective peak power level.[2] This, together with an upgrading of the SLAC klystron to above 30 MW, enabled SLAC to run close to 30 GeV for short pulses. This type of 30 MW klystrons are now readily available from tube manufacturers around the world.

The SLC program at SLAC then required a tube redesign in order to bring SLAC to greater than 50 GeV. The resulting tube which was designed and built at SLAC ran with a pulse width of 3.5 $\mu$sec giving 67 MW at 350 keV beam voltage at 180 Hz repetition rate.[3] The measured characteristics of the 5045 klystron is shown in Fig. 1 and represents the highest power, S-band, klystron for accelerator applications in large production at present. Over 300 of these klystrons have been built at SLAC with a greater of 75% production yield and lifetimes in excess of 20,000 hours.

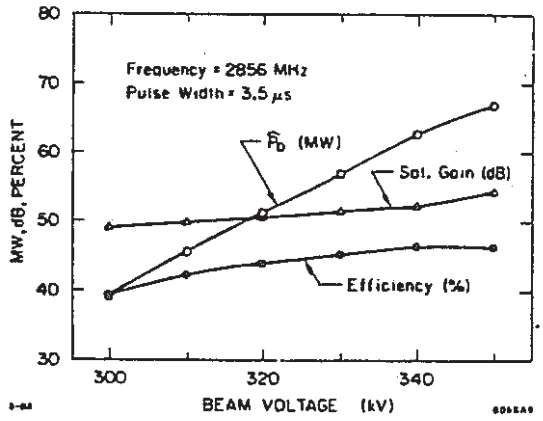


Fig. 1. Typical characteristics of production SLC klystron.

*Work supported by the Department of Energy, contract DE-AC03-76SF00515.

Invited Presentation to the European Particle Accelerator Conference
Rome, Italy June 7–11, 1988

At SLAC the limitations of these klystrons at 1 μsec pulse width (for use without SLED) was also studied. The measured characteristics of the 5045 klystron run up to higher voltages at 1 μsec is shown in Fig. 2. It was found that this production tube could operate at 415 kV at 100 MW peak power at 48% efficiency. No extensive lifetime data was taken but one tube did run for over 500 hours uninterrupted on a test stand.

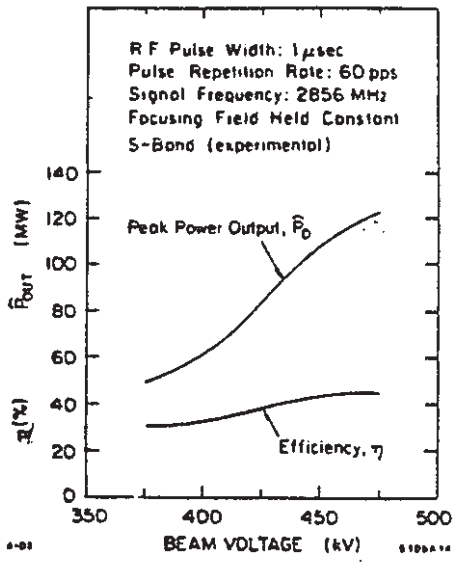


Fig. 2. Performance of production SLC klystron at beam voltages above the initial design beam voltage.

In parallel with the development of the 5045 tube for SLC, work was started for a tube to operate at 150 MW with 1 μsec.[4] The measured characteristics of this tube are shown in Fig. 3. In order to achieve the higher powers and for efficiency improvement, this tube employed a double gap in the output cavity. Although this tube was not put into production, it is likely that a successful production could have been made based on this experimental tube.

The 5045 klystron and the 150 MW klystron essentially represent the present state of the art for S-band accelerators. The next generation of linear accelerators for high energy physics looks towards higher frequencies and this is considered next.

## POWER SOURCES FOR LINEAR COLLIDERS

The next generation of electron machines beyond the SLC is a linear collider in the center of mass range of the order of 1 TeV (TLC). Designs for this class of accelerator have evolved over the past few years and, since the early days of these designs, all parameters[5] and cost optimization studies have indicated that the frequency must be higher than the well-established S-band frequencies heretofore used in electron linear accelerators. The accelerating field as related to the energy dissipated in the wall losses, is more favorable as the length decreases and wavelengths between 3 cm (X-band region) and 1.5 cm are necessary to achieve reasonable "wall plug" power for the total accelerator. Because of this, about two years ago, it was decided to develop at SLAC a conventional X-band klystron to explore the peak power capabilities in that frequency range. It was decided, initially, to build a tube to operate at 330 kV and designed to achieve 30 MW at that voltage level. If that was successful, the next stage would be to proceed to 100 MW which was estimated to be the limit

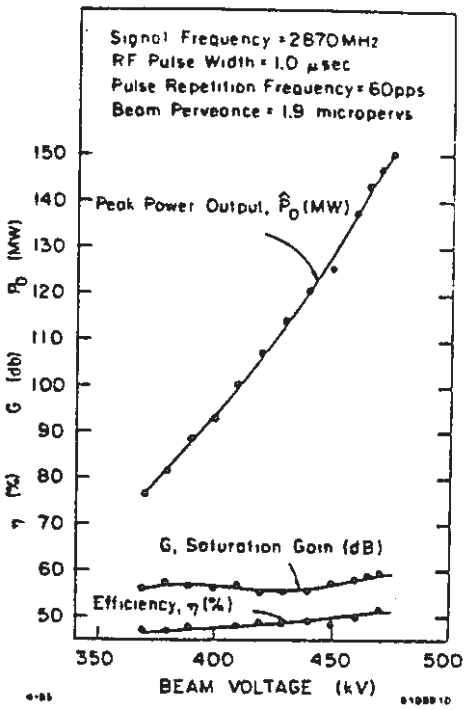


Fig. 3. Measured characteristics of experimental 150 MW klystron.

possible at 1 μsec pulse width. Figure 4 shows the performance of that tube as measured and 24 MW was achieved at 340 keV for an efficiency of 43%.

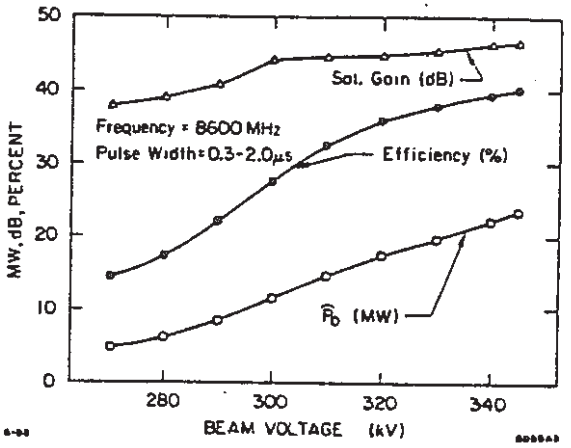


Fig. 4. Measured characteristics of experimental X-band klystron.

At about that time design studies on a TLC yielded power requirements per meter of 500 MW and higher in the frequency range 10–17 GHz with pulse widths of about 50 nsec. Short pulse widths brought us into a hitherto unexplored region of klystron performance where higher peak power might be possible. Two general approaches are possible as illustrated in Fig. 5. A long RF output pulse from a conventional klystron modulator combination could be compressed into a high peak power pulse by SLED-type techniques. A method of Z. D. Farkas utilizing a series of delay lines to store slices of the RF pulse and combine them into a single high power short

pulse is an innovative extension of this SLED principle.[6] This is illustrated in Fig. 5(a). An alternate scheme is compressing the modulator pulse before it is applied to the klystron and for 50 nsec forming a megavolt-kiloampere beam in a so-called "relativistic klystron." The relativistic klystron will be considered in greater detail, but it must be emphasized other approaches are being investigated in other laboratories. Two in particular show promise: the gyroklystron at the University of Maryland[7] and work on undulating structures at Cornell University.[8]

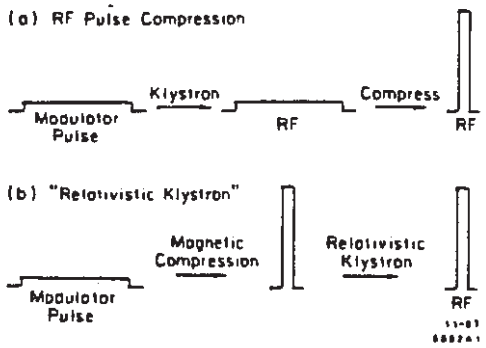


Fig. 5. a) Illustration of RF pulse compression.
b) Illustration of magnetic compression.

## RELATIVISTIC KLYSTRONS

A klystron is defined as a device using cavity resonators to convert an unmodulated electron beam to a bunched beam by use of velocity modulation and then to extract RF energy from that modulated beam. A relativistic klystron operates at energies where relativistic effects become significant in the bunching process. A broader definition of the relativistic klystron encompasses two-beam accelerators in which a bunched "low" energy, "high-current" beam transfers power at regular intervals to a high energy low current accelerator. Also, at regular intervals the low energy beam is reaccelerated by low frequency accelerator cavities. A significant example of this type of device is the RF power source for CLIC at CERN.[9] This proposed device would use superconducting cavities for the low energy beam. We will confine our comments to velocity modulated klystrons.

At the Lawrence Livermore National Laboratory (LLNL) there is an ongoing program using induction linear accelerators to produce high voltage high current beams.[10] Some of this work is done in collaboration with the Lawrence Berkeley Laboratory (LBL). A collaboration was started between these two laboratories and SLAC to operate a klystron with the beam of an induction linear accelerator at Livermore. As a first experiment, the X-band klystron described earlier in this paper was run with an induction accelerator beam and the experiment was designated SL-3. Essentially the cathode of this conventional X-band klystron was replaced with the induction linear accelerator. Although this klystron was designed for optimum performance at 330 keV, the experiment was performed with that klystron to confirm the fact that, at short pulse lengths, it might be impossible to achieve breakdown voltages in the klystron cavities well in excess of the 2 MV/cm which is thought to be about the limit of microsecond pulse width klystrons.

A summary of the performance of this klystron is shown in Fig. 6. Breakdown voltages well in excess of the previous limits were obtained. Since instrumentation is far from perfect at Livermore, the measured peak power outputs are ±10% in accuracy. Another difficulty in measurements at Livermore had to do with the measurement of klystron current. Since an isolated collector was not used, no measurement of body intercepted current as the beam passed through the klystron was made. Improvements are being made on future experiments and these are described in greater detail in another paper at this conference.[11] About 80 MW of peak power was obtained in 30 nsec pulses. In Fig. 7 the maximum RF field at the output gap before breakdown is calculated for this experimental tube. As expected, there is a steep rise in breakdown field as a pulse width is decreased. This confirms the expectation that much higher peak powers can be obtained from short pulse width relativistic klystrons and that peak powers in the hundreds of megawatts might be possible from a single klystron operating at the frequencies required for linear colliders.

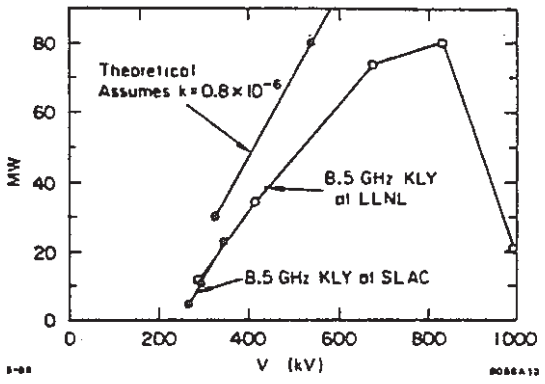


Fig. 6. Measured characteristics of relativistic X-band klystron with results with conventional cathode for comparison.

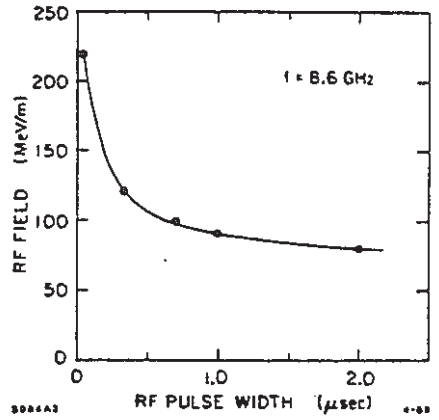


Fig. 7. Peak RF field in output cavity of X-band klystron as function of pulse width.

Two other experiments were carried out at LLNL. These are called SHARK and SL-4. SHARK is a subharmonic drive experiment shown in Fig. 8. It is a two-cavity klystron with a drive cavity at 5.7 GHz and the extraction cavity at 11.4 GHz. A summary of the output powers obtained from this experiment is shown in Fig. 9. At the highest power of 30 MW, there was a shortening of the output pulse which was due to

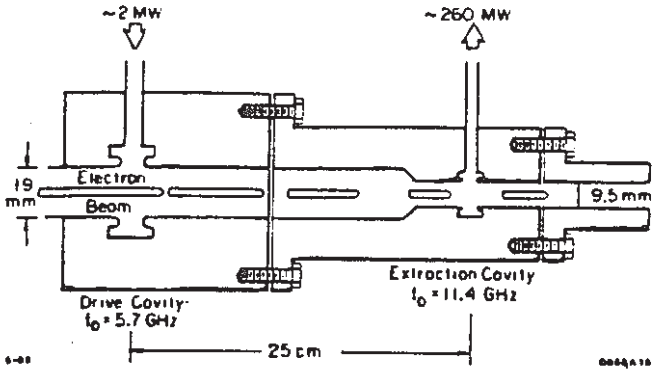


Fig. 8. Schematic of subharmonic drive experiment, SHARK.

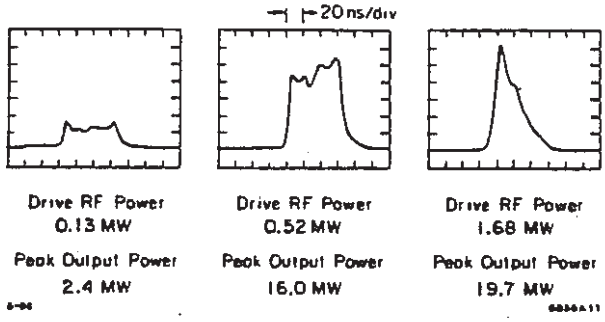


Fig. 9. SHARK RF output pulse shape for various drive powers.

some anomalous beam loading which is discussed in another paper.[11]

The next experiment consisted of a direct klystron amplifier similar to the first one, SL-3, but designed to operate with a beam voltage of 1.2 MV at 1 kA. This experiment is designated SL-4. Figure 10 shows a schematic cross section of the tube with its basic design parameters. There is high loading of the gain cavities by using lossy ceramics to decrease the rise time to less than 10 nsec. Also, because of the difficulty of focusing the 1 kA beam over long distances, it was decided to use a large drift tube diameter for the gain section and taper it down to a smaller diameter for the penultimate in output cavities, thus requiring only a short length of high-field solenoid. Figure 11 shows the typical power output pulse shape. Results from this tube is discussed in detail in the other paper at this conference.[11] The experiment produced a power output of 200 MW. The pulse shape does not follow the pulse shape of the beam current at its highest power and shows signs of anomalous loading possibly due to multipactor after 10–20 nsec. Using the values at the output cavity the maximum field at the output gap can be calculated and the value comes out to be about 300 MV/m at 200 MW. The transfer characteristics of power output versus drive is shown in Fig. 12 and it follows quite standard klystron characteristics. The gain peaks at between 300 and 600 W drive.

In an additional experiment, the output of SL-4 was fed to 25 cells (30 cm) of disk-loaded waveguide at 11.4 GHz. The 200 MW pulse was passed through the accelerator without breakdown. If this pulse could be maintained over the number of nanoseconds necessary to completely fill the structure for beam acceleration, this would correspond to accelerating fields of over 125 MV/m.

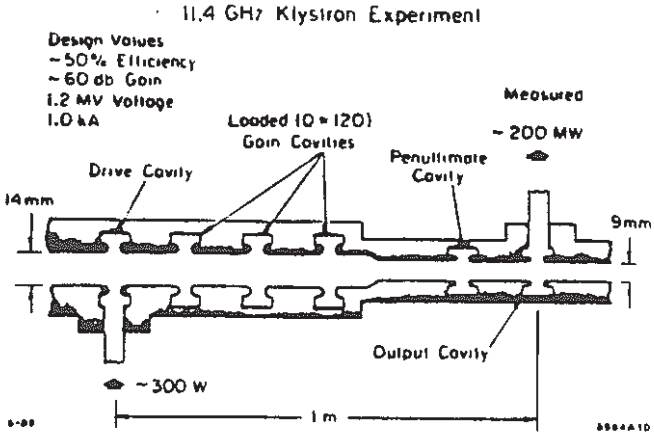


Fig. 10. Schematic of relativistic klystron, SL-4.

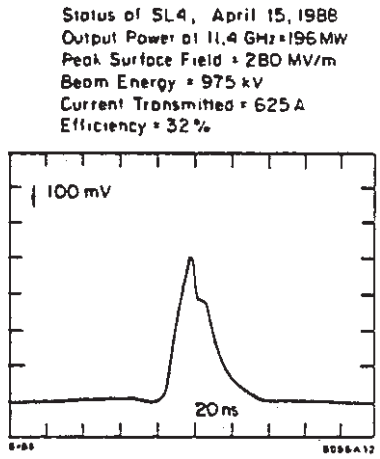


Fig. 11. Output power pulse of SL-4.

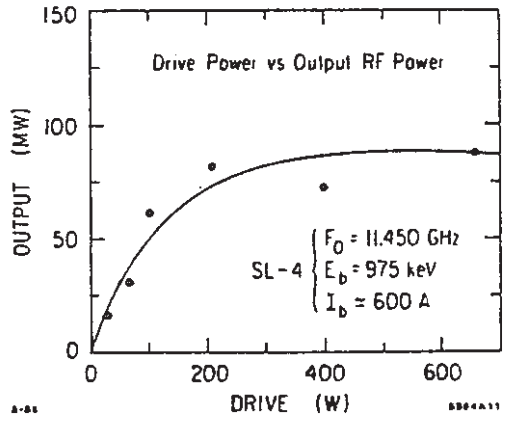


Fig. 12. Drive power versus output power of SL-4.

A summary of results is given in Fig. 13. It is possible to achieve 150 MW at S-band with 1 μsec pulses in an engineering tube and 200 MW has been achieved at X-band in very narrow pulse, but this is in a very preliminary, experimental, type of tube and the results are far from being amenable yet to tube production but are encouraging. Together with developing the relativistic klystron concept, it is necessary to

carry out a program of research and development of megavolt/kiloampere beam sources that can supply suitable beams for these new type of microwave sources suitable for linear colliders. Clearly it is not practical to use these very large linear accelerators as a beam source for each of the many thousands of relativistic klystrons that would be needed for the TLC. Much effort has to go into development of suitable beam sources with this specific application in mind.

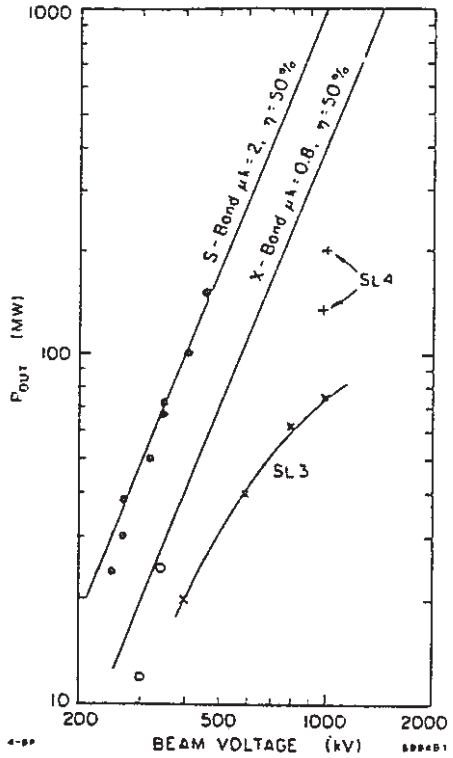


Fig. 13. Klystron power output versus beam voltages for klystrons described.

In conclusion, it has been demonstrated that the relativistic klystron is a promising RF power source for the next generation of linear colliders.

## REFERENCES


1. M. Chodorow, E. L. Ginzton, I. R. Neilsen and S. Sonkin, Proc. Inst. Radio Engrs. 41, 1584 (1953).
2. Z. D. Farkas et al., "SLED: A Method of Doubling SLAC's Energy," Proceedings of the 9th International Conference on High Energy Accelerators, p. 576, May 1976.
3. M. A. Allen, W. R. Fowkes, R. F. Koontz, H. D. Schwarz, J. T. Seeman and A. E. Vlieks, "Performance of the SLAC Linear Collider Klystrons," Proceedings of the 1987 IEEE Particle Accelerator Conference, pp. 1713–1715.
4. T. G. Lee, G. T. Konrad, Y. Okazaki, M. Watanabe and H. Yonezawa, "The Design and Performance of a 150 MW Klystron at S-band," IEEE Trans. on Plasma Science, Vol. Ps-13, No. 6, pp. 545–552 (1985).
5. R. Ruth, "Linear Collider Research at SLAC," SLAC-PUB-4446. ICFA Seminar on Future Perspectives in High Energy Physics, Upton, New York, October 5–10, 1987.
6. Z. D. Farkas, "Binary Peak Power Multiplier and its Application to Linear Accelerator Design," IEEE TRAN. MTT-34, p. 1036, October 1986.
7. W. Lawson, et al., "The Design of High Power Gyroklystron for Super Collider Applications," Proceedings of the 1987 IEEE Particle Accelerator Conference, pp. 1696–1700.
8. J. Nation, Private Communication, 1988.
9. W. Schnell, Advanced Accelerator Concepts, Madison, WI, AIP Conference Proceedings 156, 1987, p. 12 and CERN-LEP-RF/86-06 1986 (CLIC Note 13) Feb. 1986.
10. D. L. Birx, E. G. Cook, S. A. Hawkins, M. A. Newton, S. E. Poor, L. L. Reginato, J. A. Schmidt and M. W. Smith, "The Use of Induction Linacs with Nonlinear Magnetic Drive as High Average Power Accelerators," Lawrence Livermore National Laboratory, Report No. UCRL-90898, 1984.
11. SLAC/LLNL/LBL Collaboration, "Relativistic Klystrons Research and Development," These Proceedings.


## ACKNOWLEDGEMENTS


I am grateful to the following people for supplying me with the illustrations for this paper: Z. D. Farkas, J. V. Lebacqz, T. G. Lee, R. H. Miller, R. D. Ruth and G. Westenskow.

Preprint

# High-Brightness, High-Current Density Cathode for Induction Linac FELs

W. C. Turner, Y.-J. Chen,
and W. E. Nexsen
Lawrence Livermore
National Laboratory

G. Miram, M. C. Green,
and A. V. Nordquist
Varian Associates

Prepared for presentation at the
1988 Linear Accelerator Conference
Williamsburg, Virginia
October 2–7, 1988

September 28, 1988

**Beam Research Program**

*Lawrence Livermore National Laboratory*

# HIGH-BRIGHTNESS, HIGH-CURRENT-DENSITY CATHODE FOR INDUCTION LINAC FELS*

W. C. Turner, Y.-J. Chen, and W. E. Nexsen
Lawrence Livermore National Laboratory
Livermore, California 94550

G. Miram, M. C. Green, and A. V. Nordquist
Varian Associates
Palo Alto, California 94303

We have recently initiated an investigation to determine the intrinsic operating limits of an osmium coated dispenser cathode for use in free-electron lasers (FELs) driven by an induction linear accelerator. The experimental apparatus consists of a 5.1-cm-diam osmium coated dispenser cathode driven by a 250-kV, 10-Ω, 35-ns Blumlein pulse line. The pepper pot technique is used to measure intrinsic cathode brightness and uniformity. Recent measurements have yielded brightness values exceeding $1 \times 10^{10}$ A/m$^2$rad$^2$ for current densities up to 140 A/cm$^2$. We have also obtained quantitative data on cathode poisoning caused by a number of chemical agents of interest in the induction linac environment.

## Introduction

High-power, short-wavelength free-electron lasers (FELs) require high brightness, kiloampere electron beams. Consequently, we have initiated an experimental program to characterize the current density, brightness, and voltage gradient limits of an osmium alloy coated dispenser cathode (a derivative of the M cathode). We are also interested in the vacuum conditions required for high current density operation and the cathode lifetime. This type of cathode has been in use for many years in high power microwave tubes. However, their use in the pulsed environment of an induction linac FEL and the emphasis on brightness are relatively new. In this paper we report the extension of our earlier brightness measurements[1] from a current density of 44 A/cm$^2$ to 137 A/cm$^2$ and also give some initial results of our cathode poisoning tests.

## Experimental Setup

A diagram of the experimental setup is shown in Fig. 1. The cathode is a 5.1-cm-diam sintered tungsten disk that has been impregnated with 6BaO-CaO-2$Al_2O_3$ and coated with approximately 4000°A of osmium alloy. The cathode is directly heated with a bifilar spiral-wound filament and is recessed 0.25 cm behind a surrounding water-cooled electrode to supress edge emission. The anode is a 0.15-cm-thick water-cooled copper plate 2 cm in front of the cathode. The anode has been perforated with a pepper pot pattern of 0.1-mm-diam holes. Beamlets defined by the holes drift 23.5 cm to a 25-μm aluminum foil that is back coated with ZnO(Ga) phosphor (decay time 0.4 ns). The pepper pot holes lie on 45° radial lines from the center with the first set spaced 1 cm from the center hole and the rest spaced at 0.5-cm intervals. The phosphor is viewed with a gated-image intensifier CCD camera, and the images are recorded digitally for analysis (0.0174-cm/pixel $x$ direction, 0.0148-cm/pixel $y$ direction). The gate pulse width applied to the microchannel plate is 5 ns. The timing of the gate pulse is adjusted for the peak of the diode voltage and current. An optical pyrometer determines the cathode temperature. Diode voltage and current are measured with a capacitive probe and resistive current monitors, respectively. The diode is driven with a 250-kV, 10-Ω, 35-ns Blumlein pulse line. Vacuum pressure with the cathode hot is $1.0 \times 10^{-7}$ Torr, and residual gases consist almost entirely of water vapor. For quantitative poisoning experiments we have added a variable leak valve for admitting controlled partial pressures of selected vapors. Partial pressure of a selected vapor is determined by monitoring the current output of a quadrupole residual gas analyzer set on a characteristic mass peak. The absolute sensitivity of the gas analyzer is established by comparison with a capacitance manometer.

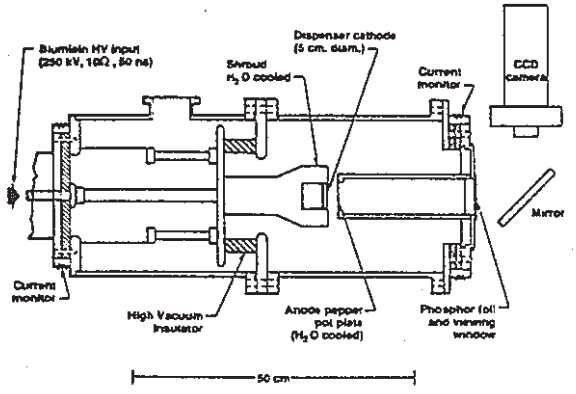


Figure 1. Schematic of the experimental apparatus.

## Experimental Results

Figure 2 shows a photograph of a recorded pepper pot image redisplayed on a video monitor. The diode voltage for these data was 106 kV and the space charge limited current 436 A. The images of the individual holes are well separated, and there is no apparent elongation in the radial direction from energy variations since the camera gate pulse is short (5 ns) and timed to occur at peak voltage, where variation in beam energy is small. The regular pattern is also characteristic of space-charge-limited current. For currents below the space-charge limit the image pattern of the anode holes becomes quite distorted. Because the anode plate shorts out the radial space charge electric field at the anode, the beam magnetic field causes the beam to pinch inward. This is evident in Fig. 3, where we have plotted beamlet direction (mean $x'$) versus $x$ at $y = 0$ projected back to the anode. The $S$ shape of this curve also indicates some nonlinearity in the focusing force. Because of this inward pinching the hole images get too close together for their radii to be measured easily at beam energies much above 106 keV. For this reason brightness data above 106 keV are taken with a single central hole in the anode. In the future we may move the phosphor closer to the anode to obtain multi-hole images for energies greater than 106 keV.

A profile of image intensity versus radial position of pepper pot holes in the anode is shown in Fig. 4(a) for a beam voltage $V = 106$ kV. Both the raw data and the data corrected for beam scrape off due to noncollinearity of the hole axis and beamlet direction are shown in Fig. 4(a). Similarly a profile of beamlet intensity versus azimuth at 1-cm radius is shown in Fig. 4(b). Azimuthally the beamlet intensity appears uniform to ±15%. The edge of the beam is not particularly well resolved since the spacing between holes is 0.5 cm and the measurements at $r = 2.5$ cm are sensitive to small misalignments. Since we have not independently verified the uniformity of the phosphor and cathode we can only say that the cathode current density is at least as uniform as the intensity plotted in Fig. 4.

For each beamlet image on the phosphor we define an image radius $a$ equal to the radius of a circle that encloses 90% of the electrons. Beamlet divergence angle is then calculated as $\theta = a/l$, where $l = 23.5$ cm, the distance between the anode and phosphor. The procedure is indicated in Fig. 5, where we give intensity scans through a single spot in two orthogonal directions. A background intensity $I_{bkg}$ is subtracted from the data and the full width of the curves read off at an intensity $I = 0.135(I_{max} - I_{bkg})$ and set equal to $2a$. This corresponds to the $2\sigma$ level of a Gaussian, which fits the data quite well and which encloses 90% of the electrons.

Figure 6 shows beamlet divergence angle versus anode radius for the data used for Fig. 4. Within ±10%, the divergence angle is constant and independent of radius. We have also verified that the

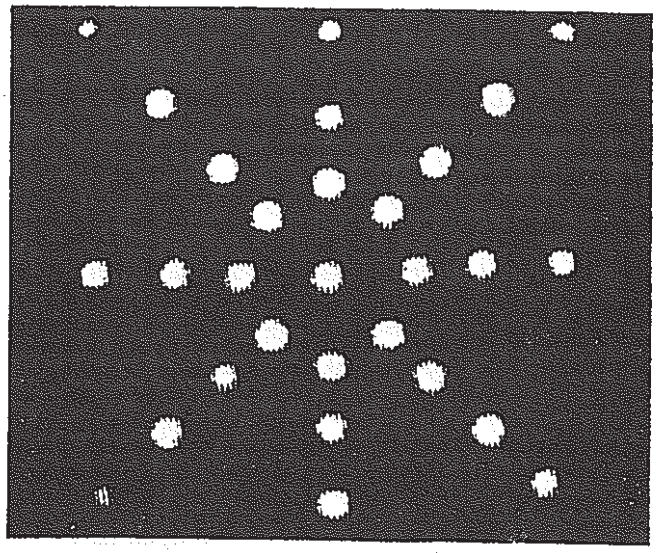

Figure 2. Photograph of digitally recorded pepper pot image.

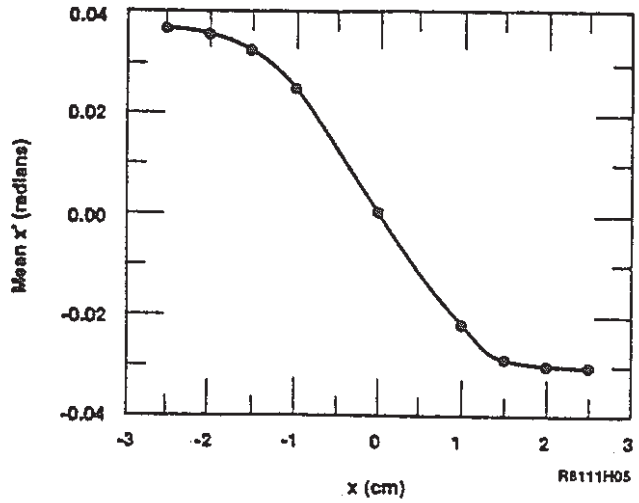


Figure 3. Mean $x'$ versus $x$ at $y = 0$.

beamlet images are circular by comparing radial widths of intensity profiles in orthogonal directions.

In addition to the divergence caused by random perpendicular velocity spread, which is the object of our measurement, a number of other effects contribute to the divergence angles measured in Fig. 6. These include camera resolution ($\theta_{cam}$), defocusing by field penetration into the anode holes defining the beamlets ($\theta_{hole}$), and space charge ($\theta_{sc}$). Estimates of each effect are given in Table 1 together with the raw data ($\theta_{meas}$) and the corrected divergence angle ($\theta_b$) we used to estimate brightness. Additional contributions from finite source size and change of mean beamlet steering angle across the anode holes are negligible. We measured the angular spread arising from finite camera spatial resolution ($\theta_{cam}$) by fitting a Gaussian function to the intensity distribution at the edge of a uniformly illuminated white spot. The divergence angle from hole defocusing ($a_o$) is calculated from the hole size and anode cathode separation ($d$) for the space-charge-limited case: $\theta_{hole} = 2/3[\gamma/(\gamma + 1)]a_o/d$. Using a method similar to that of Oettinger et al.,[2] we determine the space charge contribution from the first integral of a beam envelope equation for a beamlet passing from the anode to the phosphor. The final result for the corrected beam divergence angle is then obtained

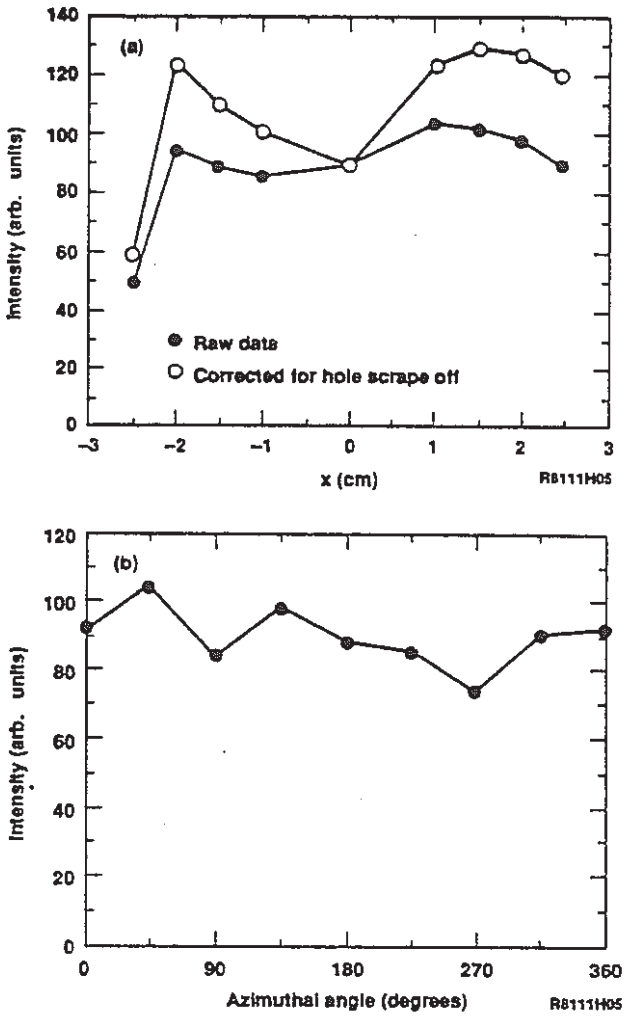


Figure 4. (a) Beamlet image intensity versus $x$. (b) Beamlet image intensity versus azimuthal angle at $R = 1$ cm.

from $\theta_b = (\theta_{meas}^2 - \theta_{cam}^2 - \theta_{hole}^2 - \theta_{sc}^2)^{1/2}$. As seen from Table 1 the corrected divergence is about 25% less than the measured value.

To estimate cathode brightness from our data we use the definition[3]

$$J = I/(\beta\gamma)^2 V_4 \quad ,$$

where $V_4$ is the four-dimensional phase space volume occupied by the electrons. Since the beam divergence angle is independent of radius, as shown in Fig. 6, to good approximation $V_4 = \pi R_c^2 \times \pi\theta_b^2$ and

$$J = I/\pi^2(R_c\beta\gamma\theta_b)^2 \quad ,$$

where $R_c = 2.54$ cm is the cathode radius.

Estimates of brightness are summarized in Table 2 for five sets of data obtained from a diode voltage of 106 kV to 407 kV and corresponding current densities varying from 21.5 A/cm$^2$ to 137 A/cm$^2$. When gathering these data we took care to assure operation above the knee of the transition from temperature to space-charge-limited flow. The perveance ($12.6 \times 10^{-6}$ A/V$^{3/2}$) is within 5% of the Child-Langmuir equation. The cathode temperature was 1100°C$_B$ for the 106-kV data and 1300°C$_B$ for 407 kV. Although the current density varies by a factor of 6.4 in Tables 1 and 2 the brightness lies in a relatively narrow range $1.14–1.6 \times 10^{10}$ A/m$^2$rad$^2$. This result is a consequence of the weak variation of $\theta_b$ with diode voltage. If there were a single transverse thermal energy characteristic

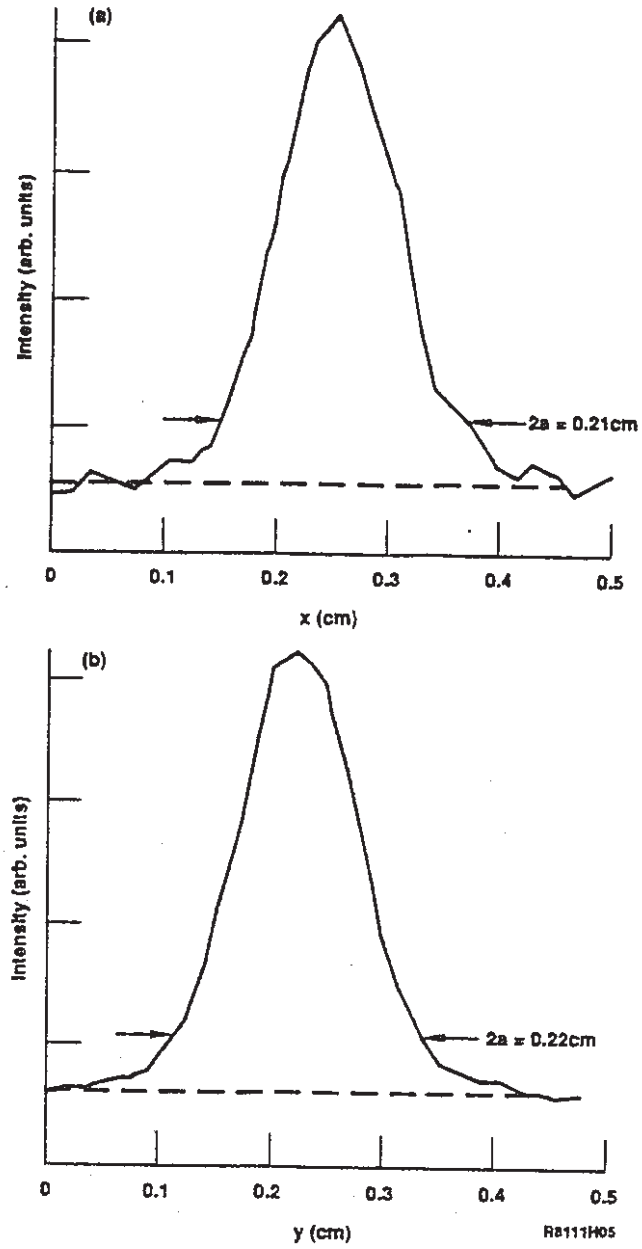


Figure 5. Intensity profiles of a single beamlet image (a) versus $x$ at $y = 0$ and (b) versus $y$ at $x = 0$.

of the cathode, then one would expect $\beta\gamma\theta_b$ to be a constant that is independent of diode voltage. However it is apparent from the third column of Table 2 that this is not what is observed. The transverse thermal energy of the beam, defined to be $E_\perp = 1/2mc^2(\beta\gamma\theta_b)^2$, is 1.5 eV for $V = 106$ kV and increases to 9.2 eV for $V = 407$ kV. For this initial set of data we have not yet identified the origin of this transverse energy nor have we established the upper bound of practically attainable high-brightness, high-current-density operation.

We have begun to look at the sensitivity of the cathode to poisoning by various chemical compounds. In this paper we report results obtained on poisoning by the dominant constituents of a leak-tight, unbaked vacuum system—water vapor, carbon monoxide, and methane. Typically the background partial pressure for water vapor is $1 \times 10^{-7}$ Torr and considerably less for carbon monoxide and methane. What we found was that the cathode emission current begins to decrease with only a slight increase in the partial pressure of water vapor, whereas such a decrease is not observed until a partial pressure of $1 \times 10^{-5}$ Torr is reached for carbon monoxide, and no decrease was observed for methane up to $1 \times 10^{-4}$ Torr. The poisoning curve for water vapor is shown in Fig. 7. The cathode emission current recovers when water vapor pressure is reduced to its background level. If we increase the cathode temperature, then the partial pressure at which the emission current decreases is observed to increase. What this implies is that the background water vapor pressure in our system is causing an effective increase of work function, and therefore we need to operate the cathode somewhat hotter (approximately 40°C) than if the water vapor pressure were reduced by about an order of magnitude. We note, however, from the data of Table 2 that quite good emission current densities and brightnesses are obtainable with this type of cathode in an unbaked vacuum system.

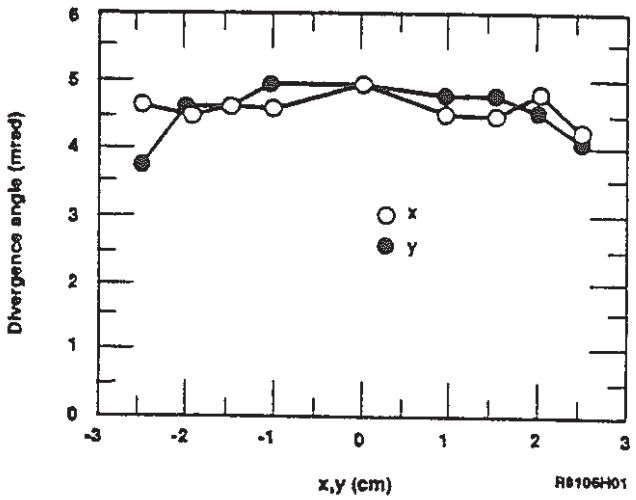


Figure 6. Beamlet divergence angle versus $x$, $y$.

Table 1. Summary of beamlet divergence angles.

| W (keV) | $\gamma\beta$ | $\theta_{meas}$ (mrad) | $\theta_{cam}$ (mrad) | $\theta_{hole}$ (mrad) | $\theta_{sc}$ (mrad) | $\theta_b$ (mrad) |
|---|---|---|---|---|---|---|
| 106 | 0.676 | 4.68 | 2.38 | 0.92 | 1.51 | 3.62 |
| 172 | 0.888 | 4.47 | 2.38 | 0.95 | 1.60 | 3.29 |
| 269 | 1.15 | 4.94 | 2.38 | 1.00 | 1.69 | 3.86 |
| 384 | 1.44 | 5.11 | 2.38 | 1.07 | 1.75 | 4.03 |
| 407 | 1.49 | 5.11 | 2.38 | 1.07 | 1.75 | 4.03 |

Table 2. Summary of brightness results.

| W (keV) | I (A) | $\gamma\beta\theta_b$ (rad) | $R_c\gamma\beta\theta_b$ (m-rad) | J (A/m$^2$rad$^2$) |
|---|---|---|---|---|
| 106 | 436 | 2.45 E-3 | 6.22 E-5 | 1.14 E10 |
| 172 | 889 | 2.92 E-3 | 7.42 E-5 | 1.64 E10 |
| 269 | 1564 | 4.44 E-3 | 1.13 E-4 | 1.24 E10 |
| 384 | 2594 | 5.80 E-3 | 1.47 E-4 | 1.22 E10 |
| 407 | 2780 | 6.00 E-3 | 1.52 E-4 | 1.22 E10 |

## Discussion

In Fig. 8 we plot cathode brightness versus current for the data obtained in this paper and for several other cathodes recently examined in the FEL context—graphite and velvet field emission cathodes,[4,5] a $Cs_3Sb$ photocathode,[2,6] and a $LaB_6$ thermionic cathode.[7]

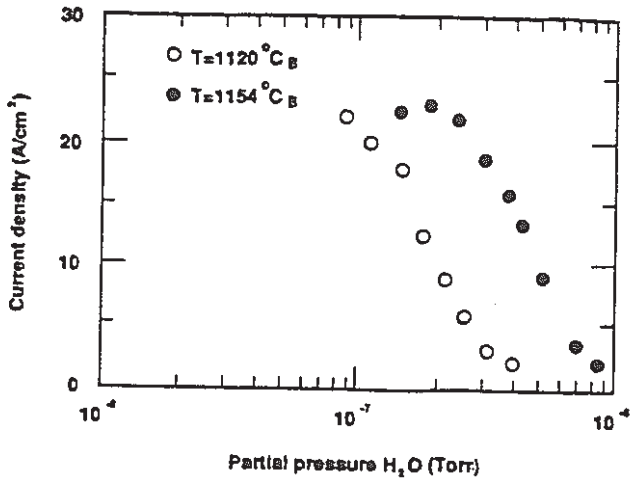


Figure 7. Cathode current density versus partial pressure of water vapor.

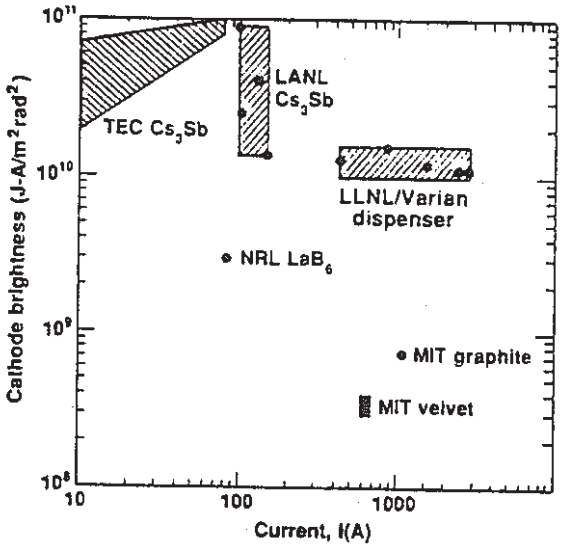


Figure 8. Cathode brightness versus current for various cathodes.

Of course, many other factors enter into the choice of cathode for a particular application. For instance, graphite and velvet field emission cathodes cannot be operated at high repetition frequencies, whereas the others can. Only the $Cs_3Sb$ cathode is easily gated after application of a high voltage pulse to the diode. Graphite and velvet can operate in poor vacuum conditions, $Cs_3Sb$ requires the best vacuum conditions ($10^{-10}$ Torr), $La_6B$ is relatively insensitive to poisoning and can operate at $10^{-6}$ Torr, and the osmium coated dispenser cathode can operate at $10^{-7}$ Torr.

So far we have not identified the practical upper limit on current density for the osmium-coated dispenser cathode in the induction linac environment. Ultimately, high current density operation will be limited by too short cathode lifetime at high temperature or by undesirable field emission from the cold electrode that surrounds the cathode. For data in this paper the maximum field stress on the cold electrode was 200 kV/cm, and field emission was not evident in surface damage or pulses with a cold cathode. The data in this paper were limited by the maximum operating voltage of the Blumlein pulse line. In the future we will increase the voltage stress by decreasing the diode gap from 2 cm to 1.0 cm.

To use the cathode studied here in an injector we will need to modify the electrode structure to permit the beam to be extracted through a hollow anode. This will necessitate decreasing the perveance from approximately 11 to 1.5 μpervs. Since for constant cathode current and radius the electric field stress is proportional to the inverse one-sixth power of perveance this will result in a 37% increase in field stress on the cold electrode surrounding the cathode. A second crucial issue is how much the beam brightness will be degraded by extraction through the hollow anode.

## References

1. W. C. Turner, Y.-J. Chen, M. C. Green, G. V. Miram, and A. L. Nordquist, *Proc. Beams '88 Seventh Intl Conf High Power Particle Beams*, Karlsruhe, Federal Republic of Germany, July 4–8, 1988 (in press).
2. P. E. Oettinger, I. Bursac, R. E. Sheffer, and E.Pugh, *Proc. 1987 IEEE Particle Accelerator Conf.*, Washington, DC., 286–288.
3. C. Lejeune and J. Aubert,in *Applied Charged Particle Optics*, A. Septier, Ed. (Academic Press, New York, 1980), Part A, 159–259.
4. D. A. Kirkpatrick, R. E. Shefer, and G. Bekefi, *J. Appl. Phys.* 57(11), 5011 (1985).
5. F. Hartmann, G. Bekefi, D. A. Kirkpatrick, R. E. Klinkowstein, and R. E. Shefer, *Proc. 1987 IEEE Particle Accelerator Conf.*, Washington, D.C., pp. 385–387.
6. J. S. Fraser, R. L. Sheffield, E. R. Gray, P. M. Giles, R. W. Springer, and V. A. Loebs, ibid., pp. 1705–1709.
7. P. Loschialpo and C. A. Kapetanakos, *High-Current Density, High Brightness Electron Beams from Large-Area Lanthanum Hexaboride Cathodes*, NRL Memorandum 6119, Naval Research Laboratory, December 13, 1987.

*Performed jointly under the auspices of the US DOE by LLNL under W-7405-ENG-48 and for the DOD under SDIO/SDC-ATC MIPR No. W31RPD-8-D5005.

# LOW BETA RF LINAC-STRUCTURE OF THE IH-TYPE WITH IMPROVED RADIAL ACCEPTANCE

U. Ratzinger

GSI, Gesellschaft für Schwerionenforschung mbH
Postfach 11 05 52, D-6100 Darmstadt
Federal Republic of Germany

## Summary

Recent injector plans at GSI asked for an RF structure to continue the acceleration behind an ECR-RFQ-combination up to $W_f$ = 1,4 MeV/u which is the injection energy of the Alvarez section of Unilac.

The interdigital H-type structure is very well suited to provide an efficient acceleration at that energy range. The beam dynamics and construction of an IH-type cavity for the energy range from $W_i$ = 0,3 MeV/u to $W_f$ = 1,4 MeV/u is described. The duty factor can be adjusted up to 60 %. A calculation is presented which demonstrates that by this kind of beam dynamics also heavy ion beams with substantial space charge forces can be handled.

## Introduction

The multi-gap cavity of the Munich SchweIN-type,[1,2,3] is used in several Tandem laboratories to postaccelerate heavy ion beams with injection energies above 2 MeV/u. This structure is characterized by its simple construction and its very high shuntimpedance. Our goal is to keep these advantages but to enlarge the radial acceptance by one order of magnitude as well as to increase the effective average voltage gain along the tank up to 3 MV/m and to lower the injection energy down to $W_i$ = 0,3 MeV/u.

We decided to do the acceleration from 0,3 MeV/u to 1,4 MeV/u with one cavity as the needs for RF equipment are minimized and the operating becomes more easy. One RF amplifier of the type which usually drives a GSI single-gap resonator cavity is sufficient to drive the IH-structure at a duty factor up to 0,6. In the following the combination of accelerating and rebunching sections - consisting of slim drifttubes - together with magnetic quadrupole tripletts is described. Experimental results from the investigations at our 1:2,5-scaled RF model are shown.

Finally, beam dynamics calculations with LORASR demonstrate the capability of that kind of structure to transport high beam intensities at $W_i$ ~ 0,6 MeV/u.

## The IH-cavity for the new 1,4 MeV/u-injector at GSI

### Beam Dynamics

The new injector,[4] consisting of an ECR-source with $W_1$ = 2,5 keV/u, an RFQ with $W_2$ = 300 keV/u and an IH-cavity will be operated at the Alvarez RF frequency of 108 MHz. The design particle for the cavities is $^{238}U^{28+}$. The design acceptances of the IH-structure are $\varepsilon_{norm}$ = 1,5 π mm mrad, $\varepsilon_{long}$ = 150 π keV/u deg. These numbers are bigger than the expected emittances out of the RFQ by a factor 2-6. The transformation of the phase space ellipses between RFQ and IH will be done by quadrupole lenses and a quarterwave coaxial resonator with 4 gaps.

A sketch of the drifttube structure of the cavity is shown in fig. 1a. Behind each quadrupole housing follows a three gap section with negative synchronous phase $\phi_s$ = - 30° to rebunch the particles. The beam dynamics principle along the $\phi_s$ = 0° sections follows the scheme described in ref. 3.

The figs. 1 bcde show results of the program LORAS in x/z-, y/z-, ΔE/E-, and Δφ/z-planes using the raytracing method. The injected ellipse areas are $\varepsilon_{ntr.}$ = 0,8 π mm mrad, $\varepsilon_{long}$ = 54 π keV/u deg.

The synchronous phase along the last 6 gaps is shifted in five degree steps from $\phi_s$ = -15° to $\phi_s$ = - 40° in order to rotate the phase ellipse in the longitudinal phase space. By that the debunching at a position about 4 m behind the IH cavity is more efficient.

### RF-model measurements

The IH-structure uses the TE 111 mode. The distribution of the capacity along the tank must be tuned accurately to get a flat accelerating electric field distribution. The question is how to install big quadrupole lenses inside the cavity at positions shown in fig. 1a without disturbing the TE111 mode.

By keeping the lense housing at zero RF potential as shown in fig. 2b, the TE111 mode is transmitted in that region. The resonance frequency can be adjusted to the resonance frequency of the neighbouring drifttube sections by changing the distance between quadrupole housing and tank, which defines the effective capacity.

In figs. 3 abc the connection between the electric gap field distribution along the tank and the capacitive coupling of the lense housings is demonstrated. When the bars with quadratic cross section in fig. 2b were dismantled we got the field distribution shown in fig. 3a; only the drifttube section between the lense housings is excited. Fig. 3b shows the distribution with the bars mounted. A further increase of capacitive coupling at the HE lense housing and a change in gap numbers per section resulted in fig. 3c. These measurements demonstrate that a combination of drifttube sections and big lenses inside one IH-type cavity is possible. For the array of fig. 3b with $f_r$ = 284 MHz we measured a Q-value of 10000 and a shuntimpedance $Z_o$ = 450 MΩ/m. All parts of the model are electrolytically copper plated.

Table 1: Characteristic parameters of the IH-tank

| | |
|---|---|
| Design ion | $^{238}U^{28+}$ |
| Frequency | 108,48 MHz |
| Input energy | 0,3 MeV/u |
| Output energy | 1,4 MeV/u |
| Radial acceptance | 60 π mm mrad |
| Normalized acceptance | 1,5 π mm mrad |
| Longitudinal acceptance | 150 π keV/u deg. |
| Tank length | 3,55 m |
| Tank diameter | 68 cm |
| Pulse frequency | 100 Hz |
| Duty cycle | 50 % |
| Eff. voltage | 10,4 MV |
| Peak RF power | 100 kW |
| Eff. shunt impedance | 310 MΩ/m |
| Max. electric field | 150 kV/cm |

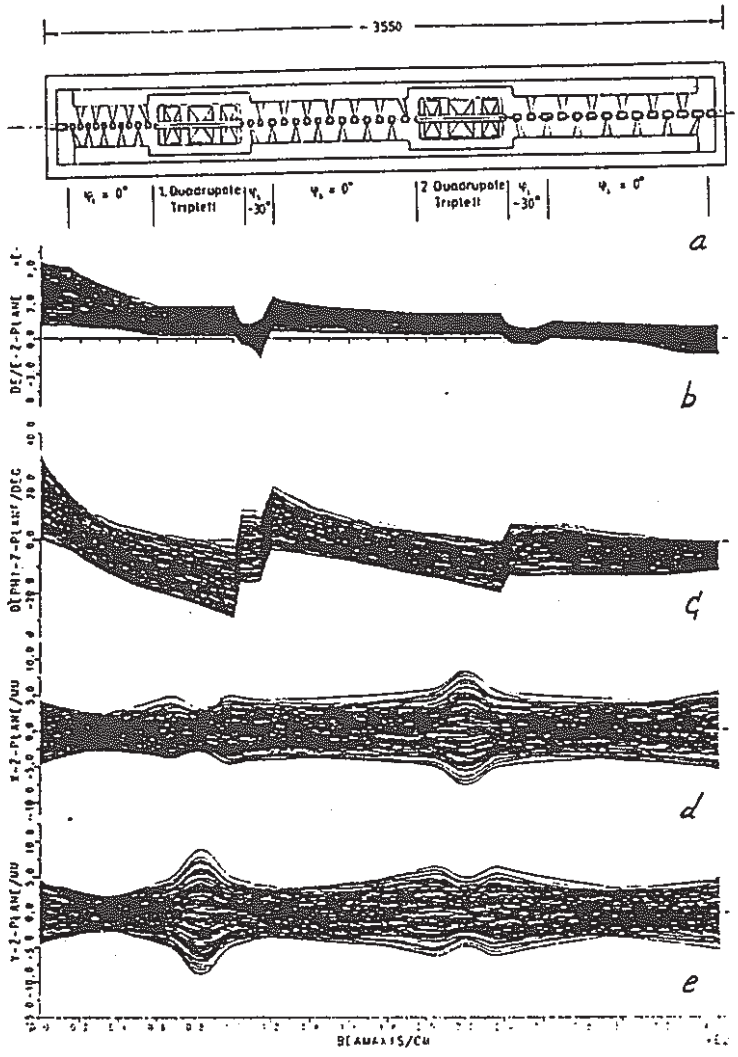


Fig. 1: Geometry of the accelerator structure and raytracing plots. Fig. 1 ab show the particles position in relation to the synchronous particle which is redefined at the points of non continuity. The structure is a combination of accelerating-, rebunching-, and transversal focussing sections.

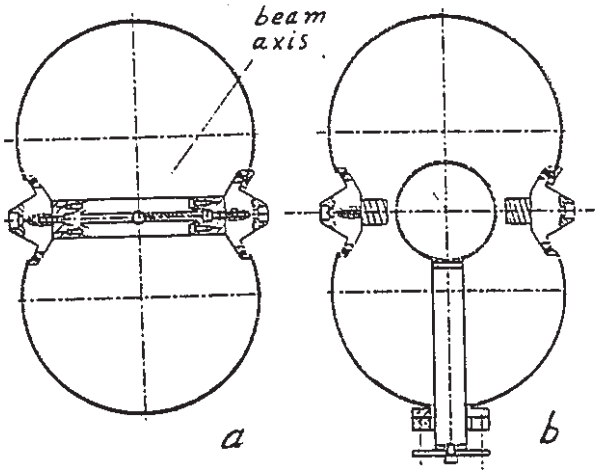


Fig. 2: Cross sectional views of the 1:2,5 scaled RF model at the drifttube structure (a) and at the quadrupole housings position (b).

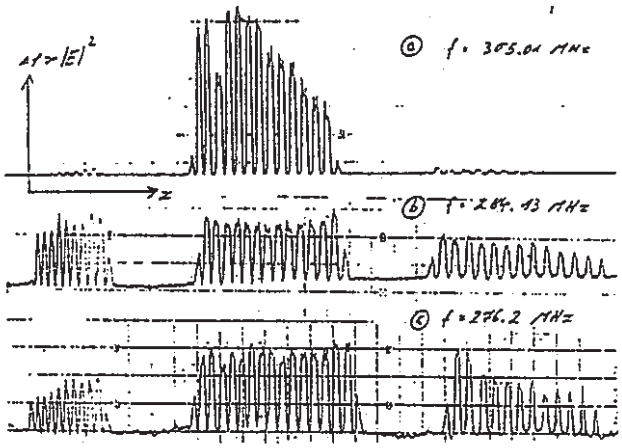


Fig. 3: Perturbation measurement of the electric field distribution along the beam axis. The capacitive coupling between cavity and lense housings is increased from (a) across (b) to (c).

## Transport of high beam intensities

The generation and acceleration of high intensity heavy ion beams is still an open question. In many cases it would be attractive to have an ion source which generates short pulses with highly charged ions so that poststripping is totally avoided or at least minimized. By that way the necessary particle current out of the ion source can be reduced drastically.

The following calculations demonstrate an efficient way to accelerate heavy ion beams with $q/A \geq 0{,}088$ at an injection energy $W_i = 0{,}6$ MeV/u and at beam intensities up to $I_e = 100$ emA.

## Space charge routine

The program LORAS was modified and a space charge routine was added. Particle-particle interaction is used, the number of particles being up to 500 usually. The sequence of space charge impulses on the particles can be controlled by defining the maximum allowed radial deviation caused by space charge forces between two steps for a particle on the bunch surface. To estimate roughly the space charge force at the pulse surface, a homogeneous density distribution inside the extreme values of particles positions is assumed. During acceleration sections, the maximum is one space charge impulse per $\beta\lambda/2$-cell. Mirror charges at the drift tube walls are neglected.

A structure for high beam intensities

Two tanks of the type described in the previous chapter but each coantaining only one quadrupole triplett, are combined to accelerate the design particle $^{238}U^{28+}$ from $W_i$ = 0,6 MeV/u up to $W_f$ = 2,4 MeV/u. The resonance frequency is $f_r$ = 108 MHz, the total length is l = 8 m. The beam transport at zero current and at $I_e$ = 70 emA is shown in figs. 4 a-d. If the operation parameters like RF voltage level and magnetic field gradient of the magnetic lenses are kept constant, we get particle losses at about $I_e$ > 30 emA in longitudinal direction at positive RF phase angles. If the voltage amplitude is increased in the percentage range the particle losses can be reduced again and the beam current can be further increased.

In that example with $I_e$ = 70 emA the voltage amplitude in the first tank was increased by 1,5 %, in the second tank by 3 %, all magnetic field gradients were increased by 1,5 %.

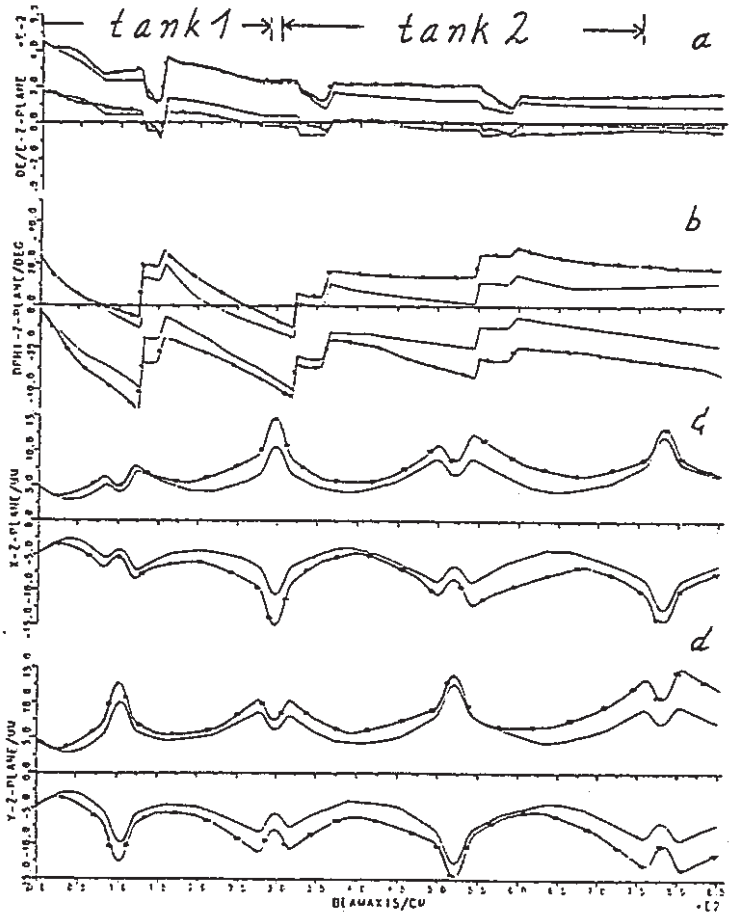


Fig. 4: Preliminary results of space charge investigations on that special type of accelerating structure.
Parameters: 2 tanks; $f_r$ = 108 MHz; $W_i$ = 0,6 MeV/u; $W_f$ = 2,4 MeV/u; q/A = 0,084; $E_{eff}$ = 2,7 MV/m;
The injected ellipses in phase space have areas $\varepsilon_{tr}$ = 30 π mm mrad, $\varepsilon_{long}$ = 100 keV/u deg.
——•——: beam envelopes at I = 70 emA;
————: beam envelopes at I = 0 emA;

References


[1] E. Nolte, G. Geschonke, K. Berdermann, R. Oberschmid, R. Zierl, M. Feil, A. Jahnke, M. Kress and H. Morinaga,
Nucl. Instr. and Meth. 158 (1979) 311.
[2] E. Nolte, R. Geier, W. Schollmeier and S. Gustavsson,
Nucl. Instr. and Meth. 210 (1982) 281.
[3] U. Ratzinger, E. Nolte, R. Geier, K. Gärtner and H. Morinaga
Nucl. Instr. and Meth. A 263 (1988) 261.
[4] J. Klabunde,
These proceedings.